



28th Summer School and International Symposium on the Physics of Ionized Gases

Aug. 29 - Sep. 2, 2016, Belgrade, Serbia

CONTRIBUTED PAPERS

&

ABSTRACTS OF INVITED LECTURES,
TOPICAL INVITED LECTURES, PROGRESS REPORTS
AND WORKSHOP LECTURES

Editors:

Dragana Marić, Aleksandar Milosavljević,
Bratislav Obradović and Goran Poparić



University of Belgrade,
Faculty of Physics



Serbian Academy
of Sciences and Arts

**28th Summer School and International
Symposium on the Physics of Ionized
Gases**

S P I G 2016

CONTRIBUTED PAPERS

&

ABSTRACTS OF INVITED LECTURES,
TOPICAL INVITED LECTURES, PROGRESS REPORTS
AND WORKSHOP LECTURES

Editors

Dragana Marić, Aleksandar Milosavljević,
Bratislav Obradović and Goran Poparić

University of Belgrade,
Faculty of Physics

Serbian Academy
of Sciences and Arts

Belgrade, 2016

CONTRIBUTED PAPERS & ABSTRACTS OF INVITED
LECTURES, TOPICAL INVITED LECTURES, PROGRESS
REPORTS AND WORKSHOP LECTURES

of the 28th Summer School and International Symposium on
the Physics of Ionized Gases

August 29 – September 2, 2016, Belgrade, Serbia

Editors:

Dragana Marić, Aleksandar Milosavljević,
Bratislav Obradović and Goran Poparić

Publisher:

University of Belgrade, Faculty of Physics,
Belgrade
Studentski trg 12, P. O. Box 44
11000 Belgrade, Serbia

Computer processing:

Tatjana Milovanov

Printed by

Skripta Internacional, Mike Alasa 54, Beograd

Number of copies

200

ISBN 978-86-84539-14-6

©2016 by University of Belgrade, Faculty of Physics

All rights reserved. No part of this book may be reproduced, stored or
transmitted in any manner without the written permission of the Publisher.

PREFACE

This publication of Faculty of Physics, University of Belgrade contains the Contributed papers and abstracts of Invited Lectures, Topical Invited Lectures, Progress Reports and associated Workshops' Lectures that will be presented at the 28th Summer School and International Symposium of the Physics of Ionized Gases – SPIG 2016. The symposium will be held at the Serbian Academy of Sciences and Arts in Belgrade, Serbia, from August 29th to September 2nd, 2016. The symposium is organized by the Faculty of Physics, University of Belgrade and Serbian Academy of Sciences and Arts, with the support of the Ministry of Education, Science and Technological Development, Republic of Serbia.

The SPIG conference covers a wide range of topics, bringing together leading scientists worldwide to present and discuss state of art research and the most recent applications, thus stimulating a modern approach of interdisciplinary science. The Invited lectures and Contributed papers are related to the following research fields: Atomic Collision Processes (Electron and Photon Interactions with Atomic Particles, Heavy Particle Collisions, Swarms and Transport Phenomena), Particle and Laser Beam Interactions with Solids (Atomic Collisions in Solids, Sputtering and Deposition, Laser and Plasma Interaction with Surfaces), Low Temperature Plasmas (Plasma Spectroscopy and other Diagnostic Methods, Gas Discharges, Plasma Applications and Devices) and General Plasmas (Fusion Plasmas, Astrophysical Plasmas and Collective Phenomena). The 28th SPIG includes two workshops that are closely related to the conference topics: the workshop on X-ray Interaction with Biomolecules in Gas Phase (XiBiGP) and the 4th International Workshop on Non-Equilibrium Processes (NonEqProc).

The Editors would like to thank the members of the Scientific and Advisory Committees of SPIG 2016 for their efforts in proposing the invited lectures and review of the contributed papers, as well as the chairmen of the associated workshops for their efforts and help in organizing the workshops and selection of invited talks. We particularly acknowledge the support of all members of the Local Organizing Committee for their help in the organization of the Conference. We are grateful to sponsors of the conference: RoentDek Handels GmbH and the European Physical Journal D.

Finally, we would like to thank all the invited speakers and participants for taking part in 28th SPIG and to wish them a pleasant stay in Belgrade, inspired and valuable moments and a very successful conference.

Editors: Dragana Marić, Aleksandar Milosavljević,
Bratislav Obradović and Goran Poparić

Belgrade, 2016.

ACKNOWLEDGEMENT

**28th SUMMER SCHOOL AND INTERNATIONAL
SYMPOSIUM ON THE PHYSICS OF IONIZED GASES**

is organized by

**University of Belgrade,
Faculty of Physics, Belgrade, Serbia**

and

**Serbian Academy of
Sciences and Arts**

with the support of the

**Ministry of Education, Science and Technological Development,
Republic of Serbia**

with the technical support of the

PANACOMP - Zemlja Čuda d.o.o.

and sponsored by:

**RoentDek Handels GmbH
The European Physical Journal D**

SPIG 2016

SCIENTIFIC COMMITTEE

D. Marić, Serbia (Co-Chair), Serbia
A. R. Milosavljević (Co-Chair), Serbia
D. Borka, Serbia
S. Buckman, Australia
J. Burgdörfer, Austria
J. Cvetić, Serbia
M. Danezis, Greece
Z. Donko, Hungary
V. Guerra, Portugal
D. Ilić, Serbia
M. Ivković, Serbia
D. Jovanović, Serbia
K. Lieb, Germany
I. Mančev, Serbia
N. J. Mason, UK
K. Mima, Japan
Z. Mišković, Canada
L. Nahon, France
B. Obradović, Serbia
G. Poparić, Serbia
P. Roncin, France
I. Savić, Serbia
Y. Serruys, France
N. Simonović, Serbia
M. Škorić, Japan
M. Trtica, Serbia

ADVISORY COMMITTEE

D. Belić
N. Bibić
M. S. Dimitrijević
S. Đurović
N. Konjević
M. Kuraica
J. Labat
G. Malović
B. P. Marinković
Z. Mijatović
M. Milosavljević
Z. L.J. Petrović
L. Popović
J. Purić
B. Stanić

ORGANIZING COMMITTEE

Faculty of Physics Belgrade
Serbian Academy of Sciences and Arts

G. Poparić (Co-chair)
B. Obradović (Co-chair)

M. Ristić (Co-Secretary)
M. Vojnović (Co-Secretary)

N. Konjević
M. Vičić
N. Cvetanović
G. Sretenović
V. Kovačević
I. Krstić

SPIG 2016 CONFERENCE TOPICS

Section 1.

ATOMIC COLLISION PROCESSES

- 1.1. Electron and Photon Interactions with Atomic Particles
- 1.2. Heavy Particle Collisions
- 1.3. Swarms and Transport Phenomena

Section 2.

PARTICLE AND LASER BEAM INTERACTION WITH SOLIDS

- 2.1. Atomic Collisions in Solids
- 2.2. Sputtering and Deposition
- 2.3. Laser and Plasma Interaction with Surfaces

Section 3.

LOW TEMPERATURE PLASMAS

- 3.1. Plasma Spectroscopy and Other Diagnostics Methods
- 3.2. Gas Discharges
- 3.3. Plasma Applications and Devices

Section 4.

GENERAL PLASMAS

- 4.1. Fusion Plasmas
- 4.2. Astrophysical Plasmas
- 4.3. Collective Phenomena

CONTENTS

Section 1. ATOMIC COLLISION PROCESSES

Invited Lectures

I. B. Abdurakhmanov, A. W. Bray, I. Bray, I. I. Fabrikant, D. V. Fursa,
A. S. Kadyrov, C. M. Rawlins, J. S. Savage and M. C. Zammit
*Convergent Close-Coupling Theory for Collisions in Atomic and
Molecular Physics*..... 3

Lorenzo Avaldi
Spectroscopy and Dynamics of Molecules of Biological Interest..... 4

Till Jahnke
Small Helium Clusters: Few Atoms, Many Phenomena..... 5

Topical Invited Lectures

D. Céolin
*High Energy Photoemission as a Probe of the Electronic Structure of KCl
Aqueous Solution*..... 6

R. Delaunay, M. Gatchell, A. Domaracka, A. Mika, M. H. Stockett,
L. Adoui, H. Zettergren, H. Cederquist, B. A. Huber and P. Rousseau
*Molecular Growth Inside of (Polycyclic Aromatic) Hydrocarbon Clusters
Induced by Ion Collisions*..... 7

J. P. Sullivan
Positron Scattering Measurements from Biologically Relevant Molecules... 8

Progress Reports

Miloš Lj. Ranković , Alexandre Giuliani and Aleksandar R. Milosavljević
*Electron Impact Action Spectroscopy of Mass/Charge Selected
Macromolecular Ions*..... 9

Anita Ribar, Georg Alexander Holzer, Štefan Matejčík and Stephan Denifl
Electron Interactions with Doped Neon Clusters..... 10

Michał Ryszka, Elahe Alizadeh and Sylwia Ptasinska
*Low Energy Electron-Induced Fragmentation of Nicotine and
N-Methylpyrrolidine*..... 11

Contributed Papers

| | |
|--|----|
| 1.1. Viktor Ayadi, Péter Földi, Péter Dombi and Károly Tőkési <i>Initial Phase Space Dependent Tunnel Ionization of the Hydrogen Atom.....</i> | 12 |
| 1.2. A. Bunjac, D. B. Popović and N. S. Simonović <i>Photoionization of Sodium by a Few Femtosecond Laser Pulse - Time-Dependent Analysis.....</i> | 16 |
| 1.3. A. Bunjac, D. B. Popović and N. S. Simonović <i>Strong-Field Ionization of Sodium in the Quasistatic Regime.....</i> | 20 |
| 1.4. R. Celiberto, V. Laporta, R. K. Janev and J. M. Wadehra <i>Resonant Vibrational Excitation of Ro-Vibrationally Excited H₂ and D₂ by Electron Impact.....</i> | 24 |
| 1.5. Nikola Filipović, Vladan Pavlović and Ljiljana Stevanović <i>Effect of Magnetic Field on Structural Properties of Confined Hydrogen Atom.....</i> | 28 |
| 1.6. S. Fritzsche, D. Seipt, A. A. Peshkov and A. Surzhykov <i>Interaction of Atoms and Ions with Twisted Light.....</i> | 32 |
| 1.7. N. P. Kucska, T. Mukoyama and K. Tőkési <i>Ionization of Rubidium by Electron Impact.....</i> | 36 |
| 1.8. Jelena Maljković, Paulina Maciejewska and Janina Kopyra <i>Dissociative Electron Attachment to Benzene Chromium Tricarbonyl.....</i> | 39 |
| 1.9. M. Z. Milošević and N. S. Simonović <i>Calculations of Ionization Rates for Alkali-Metal Atoms in Electric Field...</i> | 43 |
| 1.10. M. Z. Milošević and N. S. Simonović <i>Calculations of Electron Detachment Rates for Hydrogen Negative Ion in Electric Field.....</i> | 47 |
| 1.11. Zehra Nur Ozer and Umran Atmaca <i>Double Differential Cross Sections of Acetylene at 350 eV by Electron Impact.....</i> | 51 |
| 1.12. Zehra Nur Ozer and Mevlut Dogan <i>Electron Impact Ionization of Carbon Containing Molecules.....</i> | 55 |
| 1.13. Y. Y. Qi, J. G. Wang and R. K. Janev <i>Oscillator Strengths of Hydrogen-Like Ions in Quantum Plasmas.....</i> | 59 |
| 1.14. M. M. Vojnović, M. M. Ristić, M. P. Popović and G. B. Poparić <i>Total and Partial Cross Sections for Electron Impact Ionization of N₂.....</i> | 63 |

| | |
|---|-----|
| 1.15. D. Jakimovski and R. K. Janev <i>Polarization of Lyman α Radiation from $H^+ + H$ Collisions in Debye Plasmas</i> | 67 |
| 1.16. D. Jakimovski and R. K. Janev <i>Electron Capture in $H^+ - H$ Collisions with Cosine-Debye-Hückel Screened Interaction</i> | 71 |
| 1.17. L. Liu, C. H. Liu, J. G. Wang and R. K. Janev <i>Spin-Resolved Electron Capture in $Be^{3+} + Li$ Collisions</i> | 75 |
| 1.18. Ivan Mančev and Nenad Milojević <i>Projectile Angular Distribution in Single Electron Capture from Helium by Protons</i> | 79 |
| 1.19. Nenad Milojević and Ivan Mančev <i>Thomas Peak in Fast $H^+ - He$ Collisions</i> | 83 |
| 1.20. Y. Wu, L. Liu, X. H. Lin, J. G. Wang and R. K. Janev <i>Cross Section for Spin-Resolved Electron Capture in $He^+ - H$ Collisions</i> | 87 |
| 1.21. M. M. Aoneas, M. M. Ristić, M. M. Vojnović and G. B. Poparić <i>Rate Coefficients for Electron Impact Ionization of CO_2 in RF Electric Field</i> | 92 |
| 1.22. M. M. Aoneas, M. M. Ristić, M. M. Vojnović and G. B. Poparić <i>Excitation of the $A^3\Sigma_u^+$ State of the Nitrogen Molecule in RF Electric Field</i> | 96 |
| 1.23. Marija Grofulović, Luís L. Alves and Vasco Guerra <i>Swarm Analysis and Dissociation Cross Sections for CO_2</i> | 100 |
| 1.24. J. Mirić, D. Bošnjaković, I. Simonović, Z. Lj. Petrović and S. Dujko <i>Monte Carlo Simulations of Electron Transport in CF_3I and SF_6 Gases</i> | 104 |
| 1.25. J. Mirić, I. Simonović, D. Bošnjaković, Z. Lj. Petrović and S. Dujko <i>Electron Transport in Mercury Vapor: Dimer Induced NDC and Analysis of Transport Phenomena in Electric and Magnetic Fields</i> | 108 |
| 1.26. Ž. Nikitović, M. Gilić, Z. Raspopović, M. Petrović and V. Stojanović <i>Cross Section and Transport Parameters for K^+ in Dimethoxy Ethane</i> | 112 |
| 1.27. Ž. Nikitović, Z. Raspopović and V. Stojanović <i>Transport Properties of He^+ in CF_4</i> | 116 |
| 1.28. I. Simonović, Z. Lj. Petrović, R. D. White and S. Dujko <i>Transport Coefficients for Electron Swarms in Liquid Argon and Liquid Xenon</i> | 120 |

| | |
|--|-----|
| 1.29. I. Simonović, Z. Lj. Petrović, R. D. White and S. Dujko <i>Transition of an Electron Avalanche into a Streamer in Liquid Argon and Liquid Xenon</i> | 124 |
| 1.30. V. Stojanović, J. Jovanović, D. Marić and Z. Lj. Petrović <i>Cross Sections for Scattering and Mobility of OH And H₃O⁺ Ions in H₂O</i> | 128 |

Section 2. PARTICLE AND LASER BEAM INTERACTION WITH SOLIDS

Invited Lecture

| | |
|--|-----|
| Philippe Roncin <i>Diffraction of Fast Atoms on Surfaces, Decoherence Due to Phonons, Electrons and Topological Defects</i> | 135 |
|--|-----|

Topical Invited Lectures

| | |
|--|-----|
| Li Baiwen, Zheng Chunyang, Cao Lihua and Ning Cheng <i>Recent Progress on Numerical Simulation for High-Energy Density Plasma (HEDP) at IAPCM</i> | 136 |
| Vito Despoja, Ivan Radović and Zoran L. Mišković <i>Interactions of Charged Particles with Double-Layer Graphene</i> | 137 |
| Christoph Lemell <i>Attosecond Streaking of Photoelectrons Emitted from Solids</i> | 138 |
| Károly Tökési, C. Lemell and J. Burgdörfer <i>Classical Trajectory Monte Carlo Method – „Watching Quantum Physics in Real Time”</i> | 139 |

Progress Reports

| | |
|---|-----|
| Miloš Burger <i>The Role of Spectroscopic Diagnostics in Studying Laser-Plasma Interaction</i> | 141 |
| M. V. Erofeev, V. S. Ripenko, M. A. Shulepov and V. F. Tarasenko <i>Plasma Treatment of Metal Surface by Nanosecond Diffuse Discharge at Atmospheric Pressure</i> | 142 |
| Xu Han, James Kapaldo, Ireneusz Janik and Sylwia Ptasinska <i>Estimation of Radiation Dose Equivalent in Aqueous Solutions Subjected to Atmospheric Pressure Plasma Jets</i> | 143 |

| | |
|---|-----|
| J. Kočišek, K. Grygoryeva, A. Pysanenko, J. Lengyel, J. Fedor and M. Fárník <i>Electron-Induced Reactions in Clusters</i> | 144 |
| Miloš Nenadović, Danilo Kisić, Svetlana Štrbac and Zlatko Rakočević <i>Morphological and Structural Properties of Silver and Gold Nanoparticles Obtained by Ion Implantation in High Density Polyethylene</i> | 145 |
| Zoran Ristić <i>In-Situ Analysis of the Pulsed Laser Deposition (PLD) Fabricated LaAlO₃/SrTiO₃ Heterostructures</i> | 146 |
| Roland Sachser and Michael Huth <i>Febid for Application in Material Science and Solid State Physics</i> | 147 |
| Sára Tóth, László Himics and Margit Koós <i>Generation of Highly Luminescent Color Centers in Nanocrystalline Diamond by CVD Method</i> | 148 |
| Ying-Ying Zhang, Yuan-Hong Song and You-Nian Wang <i>Interactions of Moving Charged Particles with Multi-Walled Carbon Nanotubes (MWNTs)</i> | 149 |
| Contributed Papers | |
| 2.1. D. Borka, C. Lemell, V. Borka Jovanović and K. Tőkési <i>Simulation of Electron Transmission through Platinum Capillaries</i> | 150 |
| 2.2. T. Djordjević, L. Karbunar, V. Despoja, I. Radović and Z. L. Mišković <i>Plasmon-Phonon Hybridization in Layered Structures Including Graphene</i> | 154 |
| 2.3. E. Giglio, K. Tőkési and R. D. DuBois <i>A Quantitative Study of Ion Guiding Between Two Glass Plates</i> | 158 |
| 2.4. M. D. Majkić, R. J. Dojčilović and N. N. Nedeljković <i>Final Charge and Energy Z-Distributions of Slow Ar^{Z+}, Kr^{Z+} and Xe^{Z+} Ions in Front of a Solid Surface</i> | 162 |
| 2.5. M. D. Majkić, N. N. Nedeljković, D. K. Božanić and R. J. Dojčilović <i>Rydberg State Population of Slow Ar^{XV}, Kr^{XV} and Xe^{XV} Ions Impinging a Solid Surface at Arbitrary Collision Geometry</i> | 166 |
| 2.6. G. U. L. Nagy, I. Rajta and K. Tőkési <i>2D Simulation of 1 MeV Proton Microbeam Transmission through an Insulating Macrocapillary</i> | 170 |

| | |
|---|-----|
| 2.7. N. N. Nedeljković, M. D. Majkić, M. A. Mirković and R. J. Dojčilović <i>Cascade Neutralization of Slow Highly Charged Ions Impinging a Solid Surface at Arbitrary Collision Geometry.....</i> | 174 |
| 2.8. V. Burakov, M. Nedelko, N. Tarasenko, A. Nevar and N. Tarasenko <i>Synthesis of Silicon Nanoparticles by Atmospheric Pressure Electrical Discharges in Liquid.....</i> | 178 |
| 2.9. Radmila Panajotović and Jasna Vujin <i>Modifications of Lipid/2D-Material Heterostructures by SEM.....</i> | 182 |
| 2.10. Kamran Akbari and Zoran L. Mišković <i>Terahertz Radiation from Multilayer Graphene Induced by a Fast Electron</i> | 186 |
| 2.11. M. V. Erofeev, E. Kh. Baksht, V. S. Ripenko, M. A. Shulepov and V. F. Tarasenko <i>Spatial Structure of Runaway Electron Preionized Diffuse Discharge and Its Impact on a Plane Anode.....</i> | 190 |
| 2.12. Dragan Pantić, Miloš Burger, Zoran Nikolić, Vladimir Milosavljević, Goran Poparić and Stevan Djeniže <i>Influence of Laser Irradiance, Ambient Gas Pressure and Internal Shockwaves on the Homogeneity of Laser Produced Plasma.....</i> | 194 |

Section 3. LOW TEMPERATURE PLASMAS

Invited Lectures

| | |
|--|-----|
| Pascal Boubert <i>Optical Diagnostics in High Enthalpy Plasmas.....</i> | 203 |
| Peter J. Bruggeman <i>Plasma-Liquid Interaction.....</i> | 204 |
| Pietro Favia <i>Plasma Processes for Life Sciences.....</i> | 205 |
| Masaru Hori <i>Plasma Science Towards Next-Generation Healthcare Innovations.....</i> | 206 |
| J. Meichsner, S. Nemschokmichal, R. Tschiersch and T. Wegner <i>Influence of Negative Ions on the Dynamics of Electric Gas Discharges.....</i> | 207 |
| R. Stamm, I. Hannachi, M. Meireni, C. Logeais, H. Capes, L. Godbert-Mouret, M. Koubiti, J. Rosato and Y. Marandet <i>Lines Shapes in Turbulent Plasmas.....</i> | 208 |

Topical Invited Lectures

| | |
|---|-----|
| Ronny Brandenburg, Milko Schiorlin, Rouven Klink and Abdollah Sarani <i>Barrier Discharges in CO₂ Containing Gases at Atmospheric Pressure....</i> | 209 |
| N. De Oliveira, D. Joyeux, K. Ito, B. Gans, J. C. Loison, K. Hickson and L. Nahon <i>High Resolution Absorption Spectroscopy of Transient Species in the VUV Range.....</i> | 211 |
| Marija Gorjanc <i>Application of Plasma for Development of Innovative Functional Textiles</i> | 213 |
| M. Macias-Montero, T. Velusamy and D. Mariotti <i>Synthesis of Quantum Dots by Atmospheric Pressure Plasmas and Their Integration in Photovoltaic Devices.....</i> | 214 |
| C. D. Pintassilgo and V. Guerra <i>Gas Heating Mechanisms in N₂-O₂ Plasmas.....</i> | 215 |
| J. Schulze, M. Daksha, B. Berger, A. Derzsi, I. Korolov and Z. Donko <i>Realistic Surface Coefficients for Secondary Electron Emission and Electron Reflection in PIC/MCC Simulations of Capacitive RF Plasmas....</i> | 216 |

Progress Reports

| | |
|---|-----|
| Teodora Gajo <i>Experimental Study of the Influence of Debye Shielding on the Stark Shift of Neutral Helium Lines in Dense Plasmas.....</i> | 217 |
| M. R. Gavrilović <i>Study of Single Pulse Laser Induced Breakdown on the Target in Water....</i> | 218 |
| S. Iséni, X. Damany, G. Sretenović, V. Kovačević, I. Krstić, S. Dozias, J.-M. Pouvesle, M. Kuraica and E. Robert <i>Electric Field and Discharge Properties of Single and Multiple Arrangement of Pulsed Atmospheric Plasma Streams.....</i> | 219 |
| Z. Navrátil, R. Josepson, N. Cvetanović, B. Obradović and P. Dvořák <i>Electric Field Measurement in Atmospheric Pressure Radiofrequency Discharge in Helium.....</i> | 220 |
| J. Rosato <i>Radiation Transport with Partial Coherence in Optically Thick Plasmas....</i> | 221 |
| E. T. Slikboer, Y. N. Nguyen, O. Guaitella, G. Sretenović, A. Obrušník and A. Sobota <i>Electric Fields in kHz-Driven Plasma Jets.....</i> | 222 |

| | |
|---|-----|
| Goran B. Sretenović | |
| <i>Measurements of the Electric Field Development in Helium Plasma Jets....</i> | 223 |

Contributed Papers

| | |
|--|-----|
| 3.1. M. T. Belmonte, L. Gavanski, R. J. Peláez, J. A. Aparicio, S. Djurović and S. Mar | |
| <i>Transition Probabilities of Some UV Kr II Spectral Lines.....</i> | 224 |
| 3.2. N. Cvetanović, O. Galmiz and A. Brablec | |
| <i>Spectroscopic Investigation of the Underwater Diaphragm Discharge.....</i> | 228 |
| 3.3. T. Gajo, M. Ivković, I. Savić, Z. Mijatović, S. Djurović and N. Konjević | |
| <i>The Influence of Debye Screening on the Shift of the He I 706.52 nm Spectral Line.....</i> | 232 |
| 3.4. L. Gavanski, M. T. Belmonte, I. Savić and S. Djurović | |
| <i>Stark Halfwidths of Several O II Spectral Lines.....</i> | 236 |
| 3.5. S. S. Ivković, B. M. Obradović, N. Cvetanović and M. M. Kuraica | |
| <i>Study of Gas Flow Influence on Homogenous Barrier Discharge in Helium</i> | 240 |
| 3.6. V. V. Kovačević, G. B. Sretenović, A. Sobota, O. Guaitella, I. B. Krstić, B. M. Obradović and M. M. Kuraica | |
| <i>Influence of the Liquid Target on the Electric Field Strength in Helium Plasma Jet.....</i> | 244 |
| 3.7. Dejan Maletić, Nevena Puač, Gordana Malović and Zoran Lj. Petrović | |
| <i>Influence of Air Added in the Helium Flow on the Plasma Bullet Formation.....</i> | 248 |
| 3.8. Z. Mijatović, S. Djurović, I. Savić, L. Gavanski, T. Gajo and R. Kobilarov | |
| <i>Shift of Hydrogen H_{β} Spectral Line Measured in Wall Stabilized Arc.....</i> | 252 |
| 3.9. Z. Navrátil, T. Morávek, J. Čech and J. Ráhel' | |
| <i>OES Diagnostics of Pre-Breakdown Light Emission in Coplanar APGD in Helium.....</i> | 256 |
| 3.10. Sanja S. Pavlović, Vladimir M. Milosavljević, Patrick J. Cullen and Goran B. Poparić | |
| <i>Optical Diagnostic and Modeling of RF Plasma Discharges in The N_2 - Ar Gas Mixtures.....</i> | 260 |
| 3.11. I. Savić, L. Gavanski, M. T. Belmonte and S. Djurović | |
| <i>Stark Halfwidths of Some Spectral Lines of Ionized Silicon.....</i> | 264 |

| | |
|---|-----|
| 3.12. M. Skočić, M. Burger and S. Bukvić <i>Self-Absorption in Laser Induced Plasma</i> | 268 |
| 3.13. Ilija Stefanović, Vladimir Stojanović, Jasmina Jovanović, Cedric Pattyn, Shahzad Hussain, Eva Kovačević and Johannes Berndt <i>Mass Spectra Analysis of RF Nitrogen Plasma for Functionalization of Carbon Nanostructures</i> | 272 |
| 3.14. M. Vinic, B. Stankov, M. Ivkovic and N. Konjevic <i>Characterization of an Atmospheric Pressure Pulsed Microjet</i> | 276 |
| 3.15. Julien Annaloro and Arnaud Bultel <i>State-To-State and Collisional-Radiative Modeling of the CO₂-N₂-Ar Plasma Chemistry for the Exomars Mission</i> | 280 |
| 3.16. S. Dujko, D. Bošnjaković and A. Luque <i>Electron Transport in the Planetary Atmospheres Due to Lightning Generated Electromagnetic Pulses</i> | 284 |
| 3.17. N. V. Ivanović, Dj. Spasojević, N. M. Šišović and N. Konjević <i>A Routine for Demixing of Polarization Components in Profiles of Hydrogen Balmer Spectral Lines</i> | 288 |
| 3.18. A. P. Jovanović, M. N. Stankov, V. Lj. Marković and S. N. Stamenković <i>The Influence of Pressure on the Post-Discharge Relaxation in Synthetic Air with Teflon Walls</i> | 292 |
| 3.19. M. Klas, L. Moravský, Š. Matejčik, B. Radjenović and M. Radmilović-Radjenić <i>Breakdown Voltages of Direct Current Microdischarges in Compressed Air</i> | 296 |
| 3.20. M. Klas, L. Moravský, Š. Matejčik, B. Radjenović and M. Radmilović-Radjenić <i>Characteristics of Radio-Frequency Hydrogen Microdischarges</i> | 300 |
| 3.21. V. Lj. Marković, A. P. Jovanović, M. N. Stankov and S. N. Stamenković <i>Surface Recombination of Nitrogen Atoms on Teflon in Afterglow Studied by the Electrical Breakdown Time Delay</i> | 304 |
| 3.22. Vincent Morel, Arnaud Bultel, Lazar Gavanski, Zoran Mijatovic and Stevica Djurovic <i>Departure from Equilibrium of Ultrashort Laser-Induced Aluminum or Tungsten Plasmas</i> | 308 |

| | |
|---|-----|
| 3.23. Marija Savić, Dragana Marić and Zoran Lj. Petrović <i>Monte Carlo Simulation of Radio Frequency Breakdown in Air and Oxygen</i> | 312 |
| 3.24. Jelena Sivoš, Nikola Škoro, Dragana Marić, Gordana Malović and Zoran Lj. Petrović <i>Analysis of Transit Time of Ions in Low - Current DC Discharge in Water Vapour</i> | 316 |
| 3.25. S. N. Stamenković, V. Lj. Marković, A. P. Jovanović and M. N. Stankov <i>The Field Assisted Electron Emission in Neon DC Glow Discharge</i> | 320 |
| 3.26. M. N. Stankov, A. P. Jovanović, V. Lj. Marković and S. N. Stamenković <i>Spectroscopic Investigation, Photographic Imaging and Numerical Modeling of Glow Discharge in Argon</i> | 324 |
| 3.27. Vladimir Stojanović, Nikola Škoro, Jelena Sivoš, Gordana Malović, Dragana Marić and Zoran Petrović <i>Modeling Emission from Water Vapor DC Discharge at Low Pressure</i> | 328 |
| 3.28. M. M. Vasiljević, G. Lj. Majstorović and N. M. Šišović <i>Gas Temperature Measurements in Hydrogen-Argon Mixture Grimm Glow Discharge</i> | 332 |
| 3.29. D. Bošnjaković, Z. Lj. Petrović and S. Dujko <i>A New Model of Resistive Plate Chambers Based on Hydrodynamic Approximation</i> | 336 |
| 3.30. L. Ellis-Gibbins, A. Traore, K. Krupa, J. C. Oller, F. Ferreira da Silva, P. Limao-Vieira and G. Garcia <i>Medium to Low Energy Anion Beams and Their Application to Biomolecule Fragmentation</i> | 340 |
| 3.31. J. Kapaldo, X. Han and S. Ptasińska <i>High Throughput Imaging for Studying the Spatial Effect of Cold Atmospheric Plasma Jets on Cell Cultures</i> | 344 |
| 3.32. Milica Matijević, Milovan Stoiljković, Miloš Momčilović, Jelena Savović, Jovan Ciganović and Miroslav Kuzmanović <i>Laser-Induced Breakdown Spectroscopy at a Solid-Aqueous Aerosol Interface</i> | 348 |
| 3.33. Cristóbal Melero, José Muñoz and María Dolores Calzada <i>Microwave Plasmas Applied to the Synthesis of High-Quality Substrate-Free Graphene</i> | 352 |

| | |
|---|-----|
| 3.34. Ž. Mladenović, S. Gocić, D. Marić and Z. Lj. Petrović <i>Influence of Electron Energy Distribution Function on Composition of Atmospheric Pressure He/O₂ Plasmas</i> | 356 |
| 3.35. J. Muñoz, J. A. Bravo, C. Melero and M. D. Calzada <i>Aluminum Surface Cleaning and Activation by an Atmospheric Pressure Ar-N₂ Microwave Afterglow</i> | 360 |
| 3.36. Nenad Selaković, Nevena Puač, Nevenka Gligorijević, Milena Čavić, Gordana Malović, Radmila Janković, Siniša Radulović and Zoran Lj. Petrović <i>Low Temperature Plasma Needle Reduces the Survival of Cancer Cells</i> | 364 |

Section 4. GENERAL PLASMAS

Invited Lecture

| | |
|---|-----|
| Hiroshi Azechi <i>Status and Future Prospects of Laser Fusion Research at Ise, Osaka</i> | 371 |
|---|-----|

Topical Invited Lectures

| | |
|--|-----|
| René W. Goosmann, on behalf of the XIPE collaboration <i>X-Ray Polarimetry: A New Way to Probe Astrophysical Plasma</i> | 372 |
| G. La Mura, G. Busetto, S. Ciroi, P. Rafanelli, M. Berton, E. Congiu, V. Cracco and M. Frezzato <i>Relativistic Plasmas in Agn Jets: From Synchrotron Radiation to γ-Ray Emission</i> | 373 |
| Jinghong Li <i>A Hybrid Transport-Diffusion Simulation in Laser Fusion</i> | 374 |
| E. Lyratzi <i>Investigating the Reasons of Variability in Si IV and C IV Broad Absorption Line Troughs</i> | 375 |

Progress Reports

| | |
|---|-----|
| Bin Li, Zhanjun Liu, Chunyang Zheng, Xiaoyan Hu, Liang Hao and Jiang Xiang <i>Numerical Simulation of Large Scale Laser Filamentation and Beam Smoothing for Inertial Confinement Fusion</i> | 376 |
| Ivan Milić <i>Diagnosing Plasma in the Solar Atmosphere Using Spectropolarimetry</i> | 377 |

A. Nina, V. M. Čadež, L. Č. Popović and V. A. Srećković
Diagnostics of Plasma in Ionospheric D-Region by VLF Radio Waves..... 378

Marija Vranić
*Laser-Matter Interaction at the Intensity Frontier: On the Path Towards
Laboratory Astrophysics*..... 379

Contributed Papers

4.1. M. Vlainic, J. Mlynar, O. Ficker, J. Havlicek, V. Weinzettl,
M. Imrisek, R. Panek, J.-M. Noterdaeme and the COMPASS Team
Influence of Runaway Electrons on Discharge Start-Up in COMPASS..... 380

4.2. C. Y. Zheng, C. Z. Xiao, Z. J. Liu and X. T. He
*Competition Between Stimulated Raman Scattering and Two-Plasmon
Decay in Fusion Plasmas*..... 384

4.3. Jovan Bajčetić, Dušan Raičević and Aleksandra Nina
*Solar Lya and X-Ray Influence on Radio Wave Propagation in
Ionospheric D-Layer Plasma*..... 385

4.4. V. Borka Jovanović, P. Jovanović and D. Borka
*A Short Overview of Our Contribution to Green's Catalogue of Galactic
Supernova Remnants*..... 389

4.5. V. Borka Jovanović, P. Jovanović, D. Borka and S. Capozziello
Fundamental Plane of Elliptical Galaxies and $f(R)$ Gravity..... 393

4.6. D. Jevremović, V. Vujčić, A. A. Mihajlov, V. A. Srećković,
Lj. M. Ignjatović, M. S. Dimitrijević, S. Erkapić and N. Milovanović
*MOL-D: Database for Specific Collisional Processes and Web Service
Within the Serbian Virtual Observatory and the Virtual Atomic and
Molecular Data Center Consortium*..... 397

4.7. Gordana Jovanović
The Nature of Gravitational and Gravity Waves..... 401

4.8. Gordana Jovanović
The Role of Gravity in the Acoustic Waves Reflection..... 405

4.9. Jelena Kovačević Dojčinović and Luka Č. Popović
*Stratification in the Broad Line Region of Active Galactic Nuclei: $H\beta$ vs.
 $H\gamma$ Line Shapes*..... 409

4.10. A. A. Mihajlov, V. A. Srećković, Lj. M. Ignjatović, Z. Simić and
M. S. Dimitrijević
Atom Rydberg-Atom Processes in the Stellar Atmospheres..... 413

| | |
|---|-----|
| 4.11. A. Nina, S. T. Mitrović, V. M. Čadež, L. Č. Popović, P. Kolarž, A. Kolarski and J. Bajčetić <i>Detection of Plasma Variations in Period of Earthquake Occurred Near Kraljevo in 2010 by Electromagnetic Waves Propagation</i> | 417 |
| 4.12. A. Nina, S. Simić, V. A. Srećković, A. Djulaković and L. Č. Popović <i>Short-Term Disturbances of the Low Ionosphere Induced by γ-Ray Bursts</i> | 421 |
| 4.13. N. M. Sakan, V. A. Srećković, Lj. M. Ignjatović and A. A. Mihajlov <i>Bond - Bound State Transitions in the Frame of Coulomb Cut-Off Model Potential</i> | 425 |
| 4.14. D. Savić, R. Goosmann, F. Marin, V. L. Afanasiev, L. Č. Popović and D. Ilić <i>Measuring Black Hole Masses in Active Galactic Nuclei Using Polarization in Broad Line Profiles</i> | 429 |
| 4.15. Zoran Simić, Milan S. Dimitrijević and Vladimir Srećković <i>Stark Broadening of Bismuth IV Spectral Lines in A Type Stellar Atmospheres</i> | 433 |

The Workshop on X-ray Interaction with Biomolecules in Gas Phase (XiBiGP)

| | |
|---|-----|
| Sadia Bari <i>Structure and Dynamics of Gas-Phase Biomolecules</i> | 439 |
| M. C. Castrovilli, D. Ayuso, A. Trabattoni, S. De Camillis, A. Palacios, P. Decleva, J. Greenwood, F. Martín, M. Nisoli and F. Calegari <i>XUV Induced Ultrafast Dynamics in Bio-Relevant Molecules</i> | 440 |
| A. De Fanis, T. Baumann, M. Ilchen, T. Mazza, M. Meyer, Y. Ovcharenko and H. Zhang <i>The NQS Station (Nano-Size Quantum System), as Part of the SQS Instrument (Small-Quantum-System) at the SASE3 Branch of the European XFEL</i> | 441 |
| Sergio Díaz-Tendero <i>Unusual Fragmentation Mechanisms in Ionized Biomolecules in the Gas Phase</i> | 442 |
| Ronnie Hoekstra <i>Large Molecules Break-Dancing in the Spot Light</i> | 443 |
| F. Holzmeier, I. Fischer, S. Nandi, T. Wolf and M. Gühr <i>Auger Spectroscopy of HNC O Reveals Dissociative Photoionization Dynamics in Thymine</i> | 444 |

| | |
|--|-----|
| Kuno Kooser, Dang Trinh Ha, Marta Tarkanovskaja, Eero Itälä, Helena Levola and Edwin Kukk <i>Size Selective Spectroscopy of Molecular Clusters</i> | 445 |
| Robert Seidel <i>Electronic Structure of Small Biologically Relevant Molecules in Aqueous Solutions Studied by Photoelectron Spectroscopy</i> | 446 |
| S. D. Tošić, P. Bolognesi, L. Avaldi, R. Richter and B. P. Marinković <i>Fragmentation of Halothane Molecule by Synchrotron Radiation</i> | 447 |

The 4th International Workshop on Non-Equilibrium Processes (NonEqProc)

| | |
|--|-----|
| Roberto Celiberto and Vincenzo Laporta <i>Molecular Excitations by Electron-Impact in Non-Equilibrium Aerospace and Fusion Plasmas</i> | 451 |
| L. Ellis-Gibbings, K. Krupa, A. Traore, A. Verkhovtsev and G. Garcia <i>Modelling Low Energy Particle Tracks in Biologically Relevant Media</i> | 452 |
| Vasco Guerra, Carlos Teixeira and Daniil Marinov <i>Modelling Heterogeneous Reactions of Oxygen-Containing Plasmas on Silica Surfaces</i> | 453 |
| Kinga Kutasi, Cédric Noel, Thierry Belmonte and Vasco Guerra <i>Tuning the Afterglow Plasma Composition in Ar/N₂/O₂ Mixtures: Characteristics and Applications of a Flowing Surface-Wave Microwave Discharge System</i> | 454 |
| Svetlana Radovanov <i>New Trends in Low Energy Ion Implantation</i> | 455 |
| N. Škoro, D. Marić, V. Stojanović, J. Sivoš, G. Malović and Z. Lj. Petrović <i>Heavy-Particle Processes in Low-Pressure Water Vapour Discharge</i> | 456 |
| Vladimir Stojanović <i>Denpoh-Nambu Theory in Modelling Low Pressure Discharges</i> | 457 |
| Peter W. Stokes, Bronson Philippa, Daniel Cocks and Ronald D. White <i>A Generalised Boltzmann Equation for Non-Equilibrium Charged Particle Transport Via Localised and Delocalised States</i> | 458 |
| J. P. Sullivan <i>A Positron Reaction Microscope</i> | 459 |

| | |
|---|-----|
| J. G. Wang, L. Liu, Y. Wu, S. B. Zhang and R. K. Janev <i>Atomic Collision Processes in Hot, Dense Plasmas</i> | 460 |
| Achim Czasch <i>Single-Particle Counting: Applications in Atomic and Molecular Physics</i> | 463 |
| Author Index..... | 467 |

Section 1.

ATOMIC COLLISION PROCESSES

CONVERGENT CLOSE-COUPPLING THEORY FOR COLLISIONS IN ATOMIC AND MOLECULAR PHYSICS

I. B. Abdurakhmanov¹, A. W. Bray², I. Bray¹, I. I. Fabrikant³,
D. V. Fursa¹, A. S. Kadyrov¹, C. M. Rawlins¹, J. S. Savage¹ and
M. C. Zammit⁴

¹*Department of Physics, Astronomy and Medical Radiation Science,
Curtin University, Perth, WA, Australia* ²*Research School of Physics and
Engineering, Australian National University, Canberra ACT, Australia*
³*Department of Physics and Astronomy, University of Nebraska, Lincoln,
Nebraska, USA* ⁴*Theoretical Division, Los Alamos National Laboratory,
Los Alamos, New Mexico, USA*

We review recent developments and applications of the convergent close-coupling (CCC) theory. These include: Positronium scattering on (anti)protons: (anti)hydrogen formation [1], and threshold behaviour [2]. Electron scattering on molecular hydrogen [3]. Proton scattering on atomic hydrogen [4]. A novel approach to solving close-coupling equations in momentum space [5].

REFERENCES

- [1] A. S. Kadyrov, C. M. Rawlins, A. T. Stelbovics, I. Bray, and M. Charlton, *Phys. Rev. Lett.* **114**, 183201 (2015).
- [2] I. I. Fabrikant, A. W. Bray, A. S. Kadyrov, and I. Bray, *Phys. Rev. A* **94**, 012701 (2016).
- [3] M. C. Zammit, J. S. Savage, D. V. Fursa, and I. Bray, *Phys. Rev. Lett.* **116**, 233201 (2016).
- [4] I. B. Abdurakhmanov, A. S. Kadyrov, and I. Bray, *J. Phys. B* **49**, 03LT01 (2016).
- [5] A. W. Bray, I. B. Abdurakhmanov, A. S. Kadyrov, D. V. Fursa, and I. Bray, *Comp. Phys. Comm.* **203**, 147 (2016).

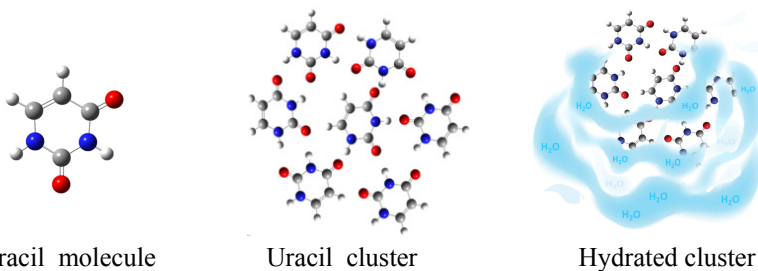
SPECTROSCOPY AND DYNAMICS OF MOLECULES OF BIOLOGICAL INTEREST

Lorenzo Avaldi

*CNR-Istituto di Struttura della Materia
Area della Ricerca di Roma 1, CP10 Monterotondo Scalo, Italy*

Gas phase studies of molecules of biological interest [1] represent the most suitable approach to disentangle the intrinsic properties of the molecules from those due to the interaction with the environment. Electron and ion spectroscopic techniques combined with ab-initio calculations and DFT methods allow to probe and to understand the basic mechanisms of radiation damage in elementary biomolecules, for example DNA/RNA bases, as well as how radiosensitiser molecules function.

Synchrotron radiation at Elettra (Trieste) [2-3] and ion beams at GANIL (Caen) [3-4] have been used to perform electron photoemission, mass spectrometry, electron-ion and ion-ion coincidence experiments on biomolecules of increasing complexity from DNA bases to larger biomolecules, e.g. nucleosides, and embedding the biomolecule in homogeneous and hydrated clusters.



Acknowledgements: Work partially supported by the Serbia– Italy Joint Research Project ‘A nanoview of radiation-biomatter interaction’, the COST Action XLIC (CM1204) and the Eurofel project .

REFERENCES

- [1] Prince K. C. *et al.*, J. Electron Spectrosc. Relat. Phenom. 204, 335 (2015).
- [2] Bolognesi Paola *et al.* , Phys.Chem.Chem.Phys.17, 24063 (2015).
- [3] Maclot Sylvain *et al.*, Phys Rev. Lett. (2016) to be published.
- [4] Markus P. *et al.*, Phys. Chem. Chem. Phys. 18, (2016) 16721.

SMALL HELIUM CLUSTERS: FEW ATOMS, MANY PHENOMENA

Till Jahnke

*Institut für Kernphysik, Goethe-Universität, Max-von-Laue-Str.1
60438 Frankfurt am Main, Germany*

Even though helium atoms are known to be chemically inert, small helium molecules are formed at low temperatures due to Van der Waals forces. It turns out that the smallest helium molecule consisting of only two helium atoms (the helium dimer) has the largest molecular ground state in the universe: with a binding energy of only 100 neV its internuclear distance extends to several hundred Angstroms with a mean internuclear distance of approx. 100 times the size of a hydrogen atom. This huge size is caused by the fact that the helium atoms tunnel deeply into the classically forbidden region (i.e. the region of the binding potential that is classically blocked due to energy reasons) making the helium dimer a so called “quantum halo”. A similarly intriguing species is the helium trimer, i.e. the triatomic helium molecule. While being not as huge as the helium dimer, recent experiments revealed that it is “a molecule without a shape”. Furthermore, it has been predicted that the trimer might exist as a so called “Efimov state” which occurs solely due to three-body interactions.

The first part of the talk will present experimental results on the shape of the vibrational wavefunctions of the helium dimer and trimer quantum halos and demonstrate the existence of a naturally occurring Efimov state in the helium trimer.

Despite of its huge internuclear distance, a phenomenon called “Interatomic Coulombic Decay” (ICD) was observed some time ago in the helium dimer. ICD is an interatomic deexcitation mechanism where an electronic excitation energy is transferred from one atom of the dimer to its atomic neighbour causing the ejection of a low energy electron from that neighbour. As ICD happens on a timescale that is similar to that of nuclear motion in the dimer, and as the efficiency of ICD depends strongly on the internuclear distance of the two participating atoms, the decay dynamics of ICD are very complex.

The second part of the talk will present the nuclear dynamics that occur during and after Interatomic Coulombic Decay as investigated in time-resolved experiments for differently sized helium clusters.

HIGH ENERGY PHOTOEMISSION AS A PROBE OF THE ELECTRONIC STRUCTURE OF KCl AQUEOUS SOLUTION

D. Céolin

*Synchrotron SOLEIL, l'Orme des Merisiers, Saint-Aubin, 91192 Gif-sur-Yvette
Cedex, France*

Author Email: denis.ceolin@synchrotron-soleil.fr

I will present the first high energy photoelectron spectroscopy (HAXPES) experiment performed in the liquid phase at the GALAXIES beamline (SOLEIL Synchrotron, France) [1]. This technique allows us to probe the electronic properties and the relaxation dynamics of core-excited ions placed in a liquid medium. We used our recently commissioned in-vacuum microjet setup specifically designed for the HAXPES setup to focus on the measurements of the Auger and resonant Auger spectra of a potassium chloride aqueous solution (0.5M).

2D maps (Auger kinetic energy vs. photon energy) were obtained by scanning the photon energy in the vicinity of the K^+1s and Cl^+1s ionization potentials and by collecting the emitted electrons corresponding to a $KL_{2,3}L_{2,3}(np)$ (resonant Auger decay (np being the Rydberg orbitals to which the $1s$ electron is promoted)). The present results are somewhat similar to our previous results obtained for the gas phase Ar (iso-electronic to K^+ and Cl^+) [2] but also exhibit several interesting differences.

Remarkably, we do not observe a clear evidence of chlorine–water delocalized states in contrast to the Cl^+2p core-excited spectra [3]. On the contrary, the presence of water molecules surrounding K^+ leads to the presence of extra structures in the KLL Auger spectrum that could be associated to a transfer of charge from the solvent to the core-excited potassium ion. Theoretical calculations are underway to interpret the data and eventually confirm this hypothesis.

REFERENCES

- [1] J.-P. Rueff et al, Journal of Synchrotron Radiation 22, (2015) 175
- [2] D. Céolin et al., Physical Review A, 91, (2015) 022502
- [3] B. Winter et al., JACS, 130, (2008) 713

MOLECULAR GROWTH INSIDE OF (POLYCYCLIC AROMATIC) HYDROCARBON CLUSTERS INDUCED BY ION COLLISIONS

R. Delaunay¹, M. Gatchell², A. Domaracka¹, A. Mika¹, M.H. Stockett²,
L. Adoui¹, H. Zettergren², H. Cederquist², B.A. Huber¹, and P. Rousseau¹

¹*Normandie Univ, ENSICAEN, UNICAEN, CEA, CNRS, CIMAP,
14000 Caen, France*

²*Department of Physics, Stockholm University,
AlbaNova University Center, S-10691 Stockholm, Sweden*

Due to the mass of the projectile, atomic collisions are specific as both electrons and nuclei can be excited, respectively through the friction on the electronic cloud and billiard-like binary collisions. The latter can open specific fragmentation channels due to their localised character.

Considering the collisions of atomic projectiles with clusters, these fragmentation channels lead to the formation of highly reactive species inside of the cluster. Thus, intra-cluster reactivity could occur producing species which are stabilised by the buffer effect due to the cluster environment. Indeed the formation of C_{119}^+ [3] and a rich molecular growth [4] have been observed respectively in clusters of C_{60} fullerene and pyrene, a polycyclic aromatic hydrocarbon (PAH).

This intra-cluster reactivity induced by ion collisions opens up new perspectives to understand the processing of molecular species in space, e.g. such process could play an important role in the chemical physics of planetary atmospheres such as the one of Titan. The formation of cyclic structures from linear hydrocarbons will be discussed.

Acknowledgements: Research performed at ARIBE, the low-energy ion beam facility of GANIL (Caen, France) within the framework of the Laboratoire International Associé DYNAMO.

REFERENCES

- [1] H. Zettergren et al., Phys. Rev. Lett. 110, 185501 (2013).
- [2] R. Delaunay et al., J. Phys. Chem. Lett. 6, 1536 (2015).

POSITRON SCATTERING MEASUREMENTS FROM BIOLOGICALLY RELEVANT MOLECULES

J. P. Sullivan

*Plasma Research Laboratories, Research School of Physics and Engineering,
Australian National University, Canberra, Australia*

Positron Emission Tomography (PET) is a widely used medical imaging technique, however there is still room for greater understanding of the effects induced by positrons introduced to the human body during the course of a PET scan. Our research group at the Australian National University is undertaking a broad reaching research project, in conjunction with modelling colleagues in Australia and Europe, to help better understand these effects.

In this talk, I will present experimental results which measure the interactions of low energy positrons with molecules relevant to biological processes, such as water and RNA/DNA base analogues [1,2]. The importance of positronium formation and other inelastic processes will be highlighted, along with an empirical model to describe the positronium formation process in terms of simple molecular parameters [3]. This data is incorporated into new models of positron transport in liquids, and the latest simulations of these transport processes will also be presented, along with plans for the future of this work.

Acknowledgements: This work is supported by the Australian Research Council.

REFERENCES

- [1] W. Tattersall et al., *J. Chem. Phys.* **140**, 044320 (2014)
- [2] E. K. Anderson et al., *J. Chem. Phys.* **141**, 034306 (2014)
- [3] J. R. Machacek et al., *J. Phys. B*, **49** 064003 (2016)

ELECTRON IMPACT ACTION SPECTROSCOPY OF MASS/CHARGE SELECTED MACROMOLECULAR IONS

Miloš Lj. Ranković¹, Alexandre Giuliani^{2,3} and Aleksandar R. Milosavljević^{1,2}

¹ *Institute of Physics Belgrade, University of Belgrade, Pregrevica 118,
11080 Belgrade, Serbia*

² *SOLEIL, l'Orme des Merisiers, St Aubin, BP48, 91192 Gif sur Yvette Cedex,
France*

³ *INRA, UAR1008, CEPIA, Rue de la Géraudière, BP 71627, 44316 Nantes,
France*

With the advent of modern mass spectrometry tools, as well as the electrospray ionization techniques, it has become possible to study large macromolecules in the gas phase. Recently Milosavljević et al [1] performed the action near edge X-ray absorption fine structure (NEXAFS) of a protein, by coupling the soft X-ray beamline PLEIADES at SOLEIL synchrotron with a linear quadrupole ion trap mass spectrometer. Here, we present the results from an electron impact action spectroscopy of trapped Ubiquitin protein, by coupling the same mass spectrometer with a focusing electron gun [2, 3]. We also compare the electron and photon impact results.

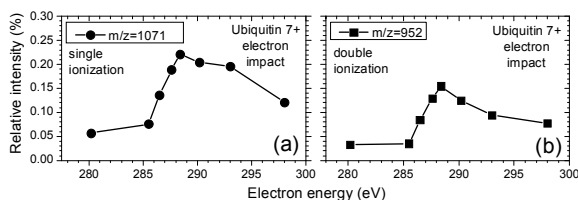


Figure 1. Single (a) and double (b) ionization yields from Ubiquitin 7+ precursor activated by electron impact.

Acknowledgements: This work was supported by ANR, France, under project ANR-08-BLAN-0065, MESTD of Republic of Serbia project #171020, and COST action STSM CM1301.

REFERENCES

- [1] A. R. Milosavljević et al, *J. Phys. Chem. Lett.* 6, 16 (2015).
- [2] M. Lj. Ranković, et al, *Appl. Phys. Lett.* 108, 064101 (2016).
- [3] M. Lj. Ranković et al, *Eur. Phys. J. D* 70, 7 (2016).

ELECTRON INTERACTIONS WITH DOPED NEON CLUSTERS

Anita Ribar^{1,2}, Georg Alexander Holzer¹, Štefan Matejčík² and Stephan Denifl¹

¹ *Institut für Ionenphysik und Angewandte Physik, Universität Innsbruck, Technikerstr.25, A-6020 Innsbruck, Austria*

² *Faculty of Mathematics, Physics and Informatics, Comenius University in Bratislava, Mlynská dolina F2, 842 48 Bratislava, Slovakia*

Atomic and molecular cluster matrices differ strongly in temperature and phase. Neutral helium clusters are known to be liquid (even super-fluid) independently of the presence of dopants in these clusters [1], while pure liquid neon- and hydrogen cluster start to be solid after embedment of few single molecules [2]. The commonness of the mentioned (semi)-liquid and extremely cold cluster (~0.4-10 K) is their strongly repulsive interaction with an excess electron which leads for electron injection to the formation of an electron bubble inside the cluster, where the excess electron is localized [3]. Moreover, the cluster surface represents an energetic barrier for an incoming electron, i.e. the electron needs sufficient kinetic energy to overcome this barrier. By doping these clusters with molecules which may form long-lived anions upon electron attachment, specific cluster properties upon electron capture can be studied over a wide range of cluster sizes [4]. A pronounced modification of the cross sections for electron attachment and subsequent dissociation can be expected. On our setup specific molecules will be embedded in the neon cluster matrix and anion formation will be studied for the first time by means of a high resolution electron monochromator which is combined with a quadrupole mass spectrometer.

Acknowledgements: This work was supported by FWF (P24443).

REFERENCES

- [1] S. Denifl, Eur. Phys. J. Special Topics 222, 2017 (2013)
- [2] R. von Pietrowski, M. Rutzen, K. von Haeften, S. Kakar, T. Möller, Z. Phys. D 40, 22 (1997)
- [3] A. Mauracher, M. Daxner, J. Postler, S.E. Huber, S. Denifl, P. Scheier, J.P. Toennies, J. Phys. Chem. Lett. 5, 2444 (2014)
- [4] E. J. Al Maalouf, J. Reitshammer, A. Ribar, P. Scheier, S. Denifl, Eur. J. Phys. Submitted.

LOW ENERGY ELECTRON-INDUCED FRAGMENTATION OF NICOTINE AND N-METHYLPYRROLIDINE

Michal Ryszka¹, Elahe Alizadeh² and Sylwia Ptasinska^{1,3}

¹*Radiation Laboratory, University of Notre Dame, Notre Dame, IN 46556, USA*

²*Department of Medical Imaging, College of Medicine,*

University of Saskatchewan, Saskatoon, SK S7N 5E5, Canada

³*Department of Physics, University of Notre Dame, Notre Dame, IN 46556, USA*

Nicotine, a naturally occurring alkaloid obtained from the tobacco plant, is a commonly used stimulant. Its psychoactive as well as behavioural effects and metabolic responses in the human body have been investigated extensively in previous years, both in *in vivo* and *in vitro* [1]. Nicotine stimulates a subclass of acetylcholine receptors in the brain, increases the heart rate and is responsible for the development of tobacco addiction [2]. Moreover, nicotine-mediated inhibition of apoptosis contributes to pathogenesis of cancer in humans, as well as decreases the efficacy of cancer therapies [3]. In this project we have investigated the anion yields resulting from DEA to nicotine and *N*-methylpyrrolidine using our recently constructed [4] crossed electron/molecule beam experimental set-up in the energy range between 0 eV and 15 eV. In contrast to 70 eV electron impact ionisation, direct cleavage of the pyridine – *N*-methylpyrrolidine bridge is not the dominant fragmentation channel in DEA to nicotine. The observed fragment anions indicate fragmentation at the pyrrolidine side of the molecule, confirmed by the observation of analogous fragments from DEA to *N*-methylpyrrolidine. Isotopic studies were performed in order to identify the observed anions.

Acknowledgements: This material is based upon work supported by the U.S. Department of Energy Office of Science, Office of Basic Energy Sciences under Award Number DE-FC02-04ER15533.

REFERENCES

- [1] K. Fattinger, D. Verotta, N.L. Benowitz, *J Pharm Exp Ther* **281**, 1238 (1997)
- [2] F. E. Pontieri, G. Tanda, F. Orzi and G Di Chiara, *Nature* **382**, 255 (1996)
- [3] S C Wright, J Zhong, H Zheng, J W Larrick, *FASEB Journal* **7** 1045 (1993)
- [4] M. M. Dawley, S. Ptasinska, *Int. J Mass Spectrom.* **365-366**, 143 (2014)

INITIAL PHASE SPACE DEPENDENT TUNNEL IONIZATION OF THE HYDROGEN ATOM

Viktor Ayadi¹, Péter Földi^{2,3}, Péter Dombi^{1,3} and Károly Tökési^{3,4}

¹*MTA "Lendület" Ultrafast Nanooptics Group, Wigner Research Centre for Physics, Konkoly-Thege M. út 29-33, H-1121 Budapest, Hungary*

²*Department of Theoretical Physics, University of Szeged, Tisza Lajos kör út 84, H-6720 Szeged, Hungary*

³*ELI-ALPS, ELI-HU Non-pro_t Ltd., Dugonics tér 13, H-6720 Szeged, Hungary*

⁴*Institute for Nuclear Research, Hungarian Academy of Sciences, H-4001 Debrecen, P.O. Box 51, Hungary*

Abstract. The tunnel ionization of hydrogen atom is studied using both a full quantum mechanical and a semiclassical method. As quantum treatment, we applied the direct integration of the time dependent Schrödinger equation (TDSE). In the semiclassical approximation (SCA), it is assumed that wavepacket propagation in the post-tunneling process can be well described within the classical framework. With these two methods, we analyze the similarities and deviations for above threshold ionization (ATI). We found that the 3 dimensional semiclassical method can describe reasonably well the momentum correlation pattern of the ATI peaks. With the semiclassical approximation we clearly identify and separate the regions in momentum distributions of the ejected electrons according to initial conditions.

1. INTRODUCTION

Understanding the ionization process during atomic collisions is fundamental both from the experimental and theoretical points of view. Especially, it is a challenging theoretical task to describe the ionization cross sections near the threshold region. It was shown that the interaction of a short, few-cycle infrared laser pulse with an atom characterized initially by superposition of two stationary states exhibits strong signatures of atomic coherence [1]. Along this line, we calculate the above threshold ionization (ATI) spectra and the angular distribution of electrons ejected from the hydrogen atom in the tunneling regime for the ground state.

The calculations to be presented below use both full quantum mechanical and semiclassical methods. We applied the direct integration of the time dependent Schrödinger equation (TDSE) and the semiclassical approximation (SCA) [2-4]. The latter approach is similar to the Classical Trajectory Monte

Carlo (CTMC) method, and it is based on the inclusion of the classical phase information of the motion. Over the past years SCA has widely been used for investigation of laser-atom collision, partly because it is much simpler than any other quantum treatment of the problem and it holds also the possibility of the visualization of the electron trajectories in a certain momentum map. This fact is true even when a large number of electron trajectories have to be determined, typically 100 million, for the accurate description of the tunnel ionization.

In the first part of this paper, we show that the full quantum mechanical model and the semiclassical approach provides very similar results for the momentum distribution of the liberated electrons in the process of tunnel ionization. Based on this, later on we focus on the semiclassical model and investigate the correlations between the initial phase-space positions of the (bound) electrons and their final momentum distribution. This allows us to assign an intuitive picture to the ionization mechanism, by identifying the initial conditions that correspond to the well separated interference maxima in the final momentum distributions.

2. THEORY

In our simulations we use a few-cycle linearly polarized infrared laser pulse. The polarization vector of the field is fixed along the z axis as excitation source. The vector potential of the external laser pulse is assumed to be polarized in the z direction.

2.1. Time dependent Schrödinger equation

We use atomic units and solve the time dependent Schrödinger equation (TDSE) numerically in the coordinate representation. Various numerical methods can be used for the solution of the TDSE as a partial differential equation, for example: the method of lines, split step Fourier, etc. For our purposes, the most efficient approach was found to be based on spherical harmonics expansion. The 2 dimensional momentum distributions for the TDSE were calculated from the wave function similar as in [5].

2.2. Semiclassical approach (SCA)

For any two-step step semiclassical model we first need initial conditions (starting point and initial velocity) for electron trajectories. To obtain a starting point for a trajectory we first need to determine the tunnel exit point, which can be found by studying the Schrödinger equation in the static limit. For the second step of our model, we have to evolve the electrons "born" in the first step according to the Newtonian equations of motion, and we also have to assign a phase by the formula, which can derived by investigating the lowest order contribution of the Feynman path integral. Finally we have to calculate the asymptotic velocities of the electron according to Kepler rules, and then coherently sum the energy bins of the 2 dimensional distribution.

3. RESULTS

With TDSE and SCA methods, we analyze the similarities and deviations for ionization of the hydrogen atom (Fig. 1). We found that the 3 dimensional semiclassical method can describe reasonably well the momentum correlation pattern of the ATI peak. We also show good agreement between the results obtained by TDSE method and the semi-classical method for the ground state. Semiclassical simulations have many advantages. First, these methods can be easily applied to systems with nontrivial geometries. Second, semiclassical simulations can help to identify the specific mechanism responsible for the relevant phenomena, and provide an illustrative picture of this mechanism in terms of classical trajectories. Therefore, we analyzed the different regions of Fig 1. We sorted the events according to the certain part of (p_z-p_ρ) as a function of initial velocities and tunnel exit points. We clearly identify and separate the regions in momentum distributions of the ejected electrons according to initial conditions.

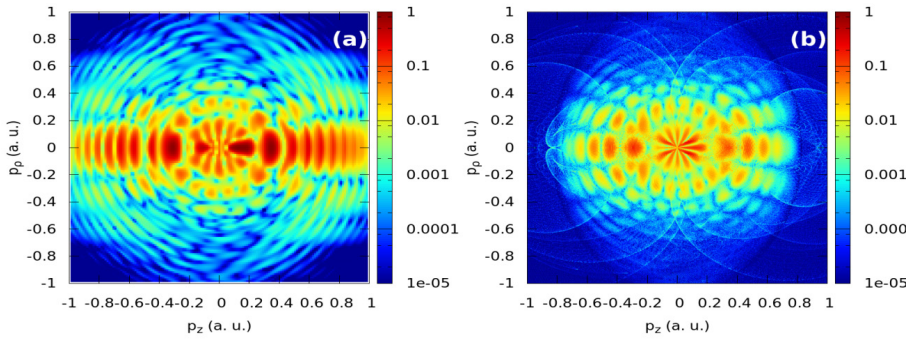


Figure 1. Ionization probability densities for the H atom as a function of the electron parallel and perpendicular momentum measured from the polarization vector ε , which coincides with the Oz axis. a) TDSE, b) SCA. The vector potential of the external laser pulse is: $A_0 = \sin(\omega t) \sin^2(\pi t / \tau)$, where $A_0 = 0.05$ a.u., $\omega = 0.056$ a.u., and $\tau = 885$ a.u..

The separation is especially noticeable for the distribution of the birth time of electrons arriving to different bumps of the momentum distribution. We illustrated the corresponding regions with typical electron trajectories.

Acknowledgements

This work was supported by the Hungarian Scientific Research Fund OTKA Nos. NN 103279 and K103917, by the COST Actions CM1204 (XLIC) and CM1405 (MOLIM).

REFERENCES

- [1] V. Ayadi, M. G. Benedict, P. Dombi, P. Földi, submitted for publication
- [2] M. Li, J. W. Geng, H. Liu, Y. Deng., C. Wu, L. Y. Peng, Q. Gong, Y. Liu, Phys Rev Lett. **112**, 113002 (2014).
- [3] B. Hu, J. Liu, S. G. & Chen, Phys. Lett. A **236**, 533(1997).
- [4] R. P. Feynman, Rev. Mod. Phys. **20**, 367 (1948).
- [5] Chelkowski, S. and Bandaruk, A. D., Phys. Rev. A. **71**, 053815 (2005).

PHOTOIONIZATION OF SODIUM BY A FEW FEMTOSECOND LASER PULSE – TIME-DEPENDENT ANALYSIS

A. Bunjac, D. B. Popović and N. S. Simonović

Institute of Physics, University of Belgrade, P.O. Box 57, 11001 Belgrade, Serbia

Abstract. Multiphoton ionization of sodium by a few femtosecond duration laser pulse is examined using the single-electron model where the valence electron moves in an effective core potential and the external electromagnetic field. The photoelectron angular and momentum distributions are studied by inspecting the evolution of the electron wave function until some time after the end of the pulse. The AC Stark shift of the lowest state is estimated and the appearance of the above threshold ionization is observed.

1. INTRODUCTION

Interaction of strong laser fields with atoms may lead to the photoionization of the later even when the single photon energy is lower than the ionization potential of atom. This process is known as the multiphoton ionization (MPI). Contrary to the single photon ionization, where the ionization rate is large even at very low intensities, the probability for multiphoton processes is much lower and they occur only at sufficiently strong fields. From the theoretical point of view this means that a perturbative treatment, that is a valid approach in describing the single photon ionization, usually fails when applying to MPI. A clear indication of the non-perturbative regime is the so-called above threshold ionization (ATI), in which the atom absorbs more photons than the minimum required. Here we study the MPI of the sodium atom in strong laser fields by solving numerically the time-dependent Schrödinger equation for this system within the single-electron approximation. A similar analysis has been recently done for lithium [1].

2. THE MODEL

Within the single-electron model and the frozen core approximation the dynamics of the valence (active) electron of sodium atom in an

alternating electric field $F(t)$ is described by Hamiltonian (in atomic units)

$$H = \frac{\mathbf{p}^2}{2} + V_{\text{core}}(r) - F(t)z. \quad (1)$$

The effective core potential (ECP) $V_{\text{core}}(r)$ describes the interaction of the valence electron with the atomic core (inner electrons + atomic nucleus). For this purpose we shall use the Hellmann's pseudopotential [2]

$$V_{\text{core}}(r) = -\frac{1}{r} + \frac{A}{r} e^{-ar}. \quad (2)$$

The parameters $A = 21$ and $a = 2.54920$ [3] provide the correct value for the ionization potential of sodium $I_p = 5.1391 \text{ eV} = 0.18886 \text{ a.u.}$ and reproduce approximately the energies of singly-excited states (see Fig. 1).

We consider the linearly polarized laser pulse of the form

$$F(t) = F_{\text{peak}} \sin^2(\pi t/T_p) \cos(\omega t), \quad 0 < t < T_p \quad (3)$$

(otherwise $F(t) = 0$). Here ω , F_{peak} and T_p are the frequency of laser field, the peak value of its electric component and the pulse duration, respectively. Due to the axial symmetry of the system the magnetic quantum number m of the valence electron is a good quantum number for any field strength. Since in the sodium ground state (when $F = 0$) the orbital and magnetic quantum numbers of this electron are equal zero, in calculations we choose $m = 0$.

3. THE METHOD

The photoionization process is simulated by calculating the evolution of the initial wave function $\psi(\mathbf{r}, 0)$, which is the lowest eigenstate of Hamiltonian (1) at $t = 0$ (then $F = 0$), until some time after the end of the pulse. This can be done by taking an adequate representation of the evolution operator $U(t, t + \Delta t)$ and integrating numerically the relation $\psi(\mathbf{r}, t + \Delta t) = U(t, t + \Delta t)\psi(\mathbf{r}, t)$ with a sufficiently small time step Δt . Here we use of the second-order-difference (SOD) scheme [4]

$$\psi(\mathbf{r}, t + \Delta t) = \psi(\mathbf{r}, t - \Delta t) - 2i\Delta t H \psi(\mathbf{r}, t) \quad (4)$$

that is for this purpose adapted to cylindrical coordinates. Due to the axial symmetry of the system described by the Hamiltonian (1) this observable as well as the electron's wave function do not depend on the azimuthal angle and the dynamics reduces to two degrees of freedom (ρ and z).

4. RESULTS

We study the photoionization of the sodium atom by a 760 nm ($\omega = 0.06 \text{ a.u.}$) laser pulse of the form (3) with the peak intensity $1.72 \times 10^{12} \text{ W/cm}^2$ ($F_{\text{peak}} = 0.007 \text{ a.u.}$) and 10 fs duration ($T_p = 413.4 \text{ a.u.}$).

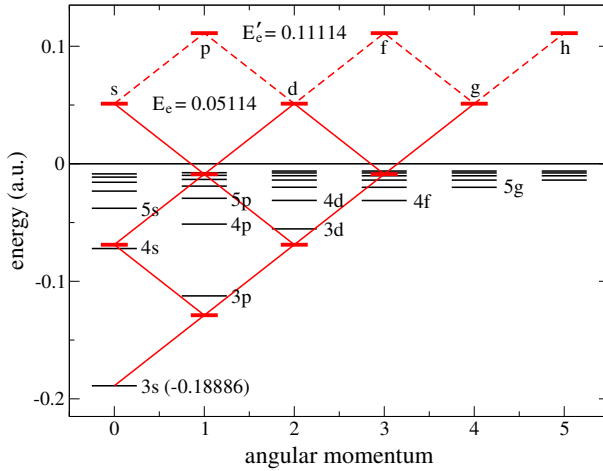


Figure 1. Energy scheme of sodium including the lowest excited states as well as possible four-photon and five-photon (ATI) absorption pathways ($\omega = 0.06$ a.u.) from the $3s$ ground state to the continuum.

The energy level diagram (Fig. 1) illustrates that from the ground state ($3s$) at least four photons with $\omega = 0.06$ are required to reach the continuum. Then, the excess energy of the photoelectrons is expected to be $E_e = 0.05114$ a.u.

The probability distribution $|\psi(\mathbf{r}, t)|^2$ of the active (valence) electron is shown in Fig. 2 at $t = 1000$ a.u. and $t = 1200$ a.u. The outgoing wave determines the photoelectron angular distribution. Apart from the strong emission along the laser polarization ($\vartheta = 0^\circ$ and 180°) the distribution shows also maxima at $\vartheta \approx 45^\circ$, $\vartheta = 90^\circ$ and $\vartheta \approx 135^\circ$. The observed distribution relates to a superposition of the accessible emitted partial waves. In the case of four-photon absorption s , d and g partial waves can be emitted

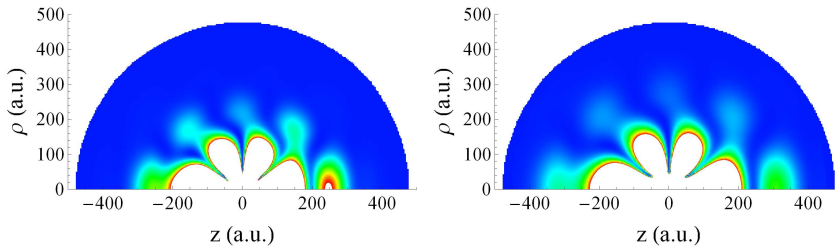


Figure 2. Probability distribution $|\psi(\mathbf{r}, t)|^2$ of the active electron of the sodium atom affected by the laser pulse (3) with $\omega = 0.06$ a.u. and $F = 0.007$ a.u. at: $t = 1000$ a.u. (left) and $t = 1200$ a.u. (right). The outgoing wave (with five maxima) determines the photoelectron angular distribution.

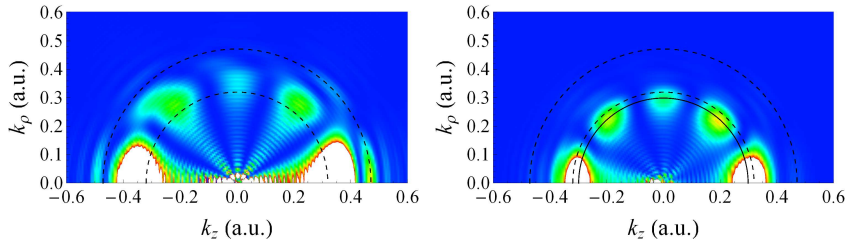


Figure 3. The photoelectron momentum distribution for the process shown in Fig. 1 at: $t = 800$ a.u. (left) and $t = 1000$ a.u. (right). Dashed semicircles denote the expected values of the momentum for the four-photon (MPI) and five-photon (ATI) processes at low laser intensities. The full semicircle corresponds to an average value of maxima in the calculated photoelectron momentum distribution at $t = 1000$ a.u.

(see Fig. 1). The maxima/minima structure of the outgoing wave in Fig. 2 indicate that in this case the g partial wave is dominant (four minima).

The photoelectron momentum distribution shows a similar angular structure, but the maxima are approximately located at semicircles of radius $k_e \equiv (2E_e)^{1/2} = 0.3198$ a.u. At shorter times after the ionization the photoelectrons momenta are larger than k_e (see Fig. 3(a)), but later they approach the asymptotic values (see Fig. 3(b)). The remaining difference can be attributed to the AC Stark shift.

Besides the regular MPI with four photons, in Fig. 3 the ATI structure related to the five-photon absorption can be observed. In the latter case, according to the energy level diagram in Fig. 1, the photoelectron excess energy in the weak field limit should be $E'_e = 0.05114$ a.u. ($k'_e = .4715$ a.u.) and p , f and h partial waves can be emitted. The ATI structure in Fig. 3 is indeed located near k'_e and contains five minima that is a feature of h waves.

Acknowledgements

This work was supported by the COST Action No. CM1204 (XLIC). We acknowledge support from the Ministry of Education, Science and Technological Development of Republic of Serbia under Project No. 171020.

REFERENCES

- [1] M. Schuricke et al, Phys. Rev. A **83**, 023413 (2011).
- [2] H. Hellmann, J. Chem. Phys. **3**, 61 (1935).
- [3] M. Z. Milošević and N. S. Simonović, Phys. Rev. A **91**, 023424 (2015).
- [4] A. Askar and A. S. Cakmak, J. Chem. Phys. **68**, 2794 (1978).

STRONG-FIELD IONIZATION OF SODIUM IN THE QUASISTATIC REGIME

A. Bunjac, D. B. Popović and N. S. Simonović

Institute of Physics, University of Belgrade, P.O. Box 57, 11001 Belgrade, Serbia

Abstract. Strong field ionization of sodium in the quasistatic regime is examined by studying the valence electron wave packet dynamics in the static electric field. The lowest state energies and ionization rates obtained by this method for different strengths of the applied field agree well with the results determined using other methods. It is shown that, if the Keldysh parameter is significantly lower than one (quasistatic regime), the probability of ionization by a laser pulse can be obtained from the static rates.

1. INTRODUCTION

When atom is irradiated by a sufficiently strong electromagnetic field the multiphoton ionization may occur although the single photon energy is lower than the ionization potential of this atom. If the field is, however, so strong that it is comparable to the atomic potential, it distorts the later forming a potential barrier through which the electron can tunnel. Finally, at extremely strong fields the barrier is suppressed below the energy of the atomic state and the so-called over-the-barrier ionization (OBI) occurs. The transition between multiphoton and tunnelling regimes is governed by the Keldysh parameter $\gamma = \omega (2I_p)^{1/2}/F$ [1], where ω , F and I_p are the frequency of electromagnetic field, the peak value of its electric component and the ionization potential of the atom (in atomic units). If $\gamma \gg 1$ (low-intensity/short-wavelength limit) the multiphoton ionization dominates, whereas for $\gamma \ll 1$ (high-intensity/long-wavelength limit) the tunnel ionization or OBI does.

Tunnel ionization is successfully described by the semiclassical theory due to Ammosov, Delone and Krainov (ADK) [2]. It is based on the quasistatic approximation which assumes that for $\gamma \ll 1$ the electric field changes slowly enough that the static tunnelling rate can be calculated for each instantaneous value of the field. Then the tunnelling rate for the alternating field can be obtained by averaging the static rates over the field

period. Here we present the results for ionization rates of the sodium atom in quasistatic field obtained by the wave-packet propagation method and compare them with the ADK values, as well as with the results obtained recently by the complex-rotation method [3]. Also we demonstrate that, if the Keldysh parameter is significantly lower than one, the probability of ionization by a laser pulse can be obtained from the static rates.

2. THE MODEL

The valence electron of alkali metal atoms can be considered as moving in an effective potential describing the interaction between this electron and the atomic core (inner electrons + atomic nucleus). The simplest effective core potential (ECP) applicable for these atoms is the Hellmann's pseudopotential [4]

$$V_{\text{core}}(r) = -\frac{1}{r} + \frac{A}{r} e^{-ar}. \quad (1)$$

(Atomic units are used throughout the text.) We shall for the sodium atom use the values $A = 21$ and $a = 2.54920$ from Ref. [3] which provide the correct value for the ionization potential $I_p = 5.1391 \text{ eV} = 0.18886 \text{ a.u.}$

Using this single-electron model we study the sodium atom under the influence of a quasistatic electric field F . Within the so-called frozen core approximation the dynamics of the valence electron is described by Hamiltonian

$$H = \frac{\mathbf{p}^2}{2} + V_{\text{core}}(r) - Fz. \quad (2)$$

The core potential and the external field form a potential barrier with the saddle point at the z -axis. Since the electron can tunnel through or escape over the barrier, the atom has a nonzero probability of ionizing for any field strength $F \neq 0$. Thus, all states of the system described by Hamiltonian (2) have a resonant character. We shall consider the resonance with the lowest energy that is characterized by the magnetic quantum number $m = 0$.

3. THE METHOD

The energy spectrum of Hamiltonian (2) (for static fields) can be obtained from the autocorrelation function $c(t) = \langle \psi(0) | \psi(t) \rangle$, where the initial state $|\psi(0)\rangle$ is the lowest eigenstate of Hamiltonian (2) when $F = 0$ and $|\psi(t)\rangle$ is the corresponding state at a later time t (then $F \neq 0$). The evolution of the lowest state is calculated using the so-called second-order-difference (SOD) method [5]. The eigenenergies of (2) appear as Lorentzian peaks in the power spectrum of the autocorrelation function $|\text{FT}[c(t)]|^2$, where $\text{FT}[c(t)]$ is the Fourier transform of $c(t)$. These peaks contain the information about the resonance positions E and widths Γ (i.e. decay rates $w = \Gamma/\hbar$).

The tunnelling rates determined numerically will be compared with those given by the ADK theory [2]. For alkali-metal atoms in the ground state one has $l = m = 0$ and the ADK formula (for static fields) reduces to

$$w = |C_{n^*0}|^2 I_p \left(\frac{2F_0}{F}\right)^{2n^*-1} e^{-\frac{2F_0}{3F}}, \quad (3)$$

where $n^* = (2I_p)^{-1/2}$, $F_0 = (2I_p)^{3/2}$, and $|C_{n^*0}|^2 = 2^{2n^*}/[n^* \Gamma(n^*+1) \Gamma(n^*)]$. Since for alkali metals the energy of the lowest state changes rapidly with F , the ADK rates can be significantly improved by applying the correction $I_p \rightarrow -E(F) = I_p - \Delta E(F)$ in (3), which accounts for the Stark shift $\Delta E(F)$ of the lowest energy level. For $F \ll 1$ this shift can be expanded in a series, giving

$$E(F) = E(0) + \Delta E(F) = -I_p - \frac{1}{2}\alpha F^2 - \frac{1}{24}\gamma F^4. \quad (4)$$

The dipole polarizability and the second dipole hyperpolarizability for sodium are $\alpha = 162.7 \pm 0.8$ and $\gamma = (9.56 \pm 0.48) \times 10^5$, respectively.

4. RESULTS

The lowest state energies and widths (ionization rates) for the sodium atom at different strengths of the applied static electric field calculated by the wave-packet method [7] are shown in Fig. 1, together with the values obtained recently by the complex-rotation method [3]. The results are in a good agreement in the considered field domain. The energies and rates estimated from the Stark shift expansion (4) and the ADK theory, respectively, agree well with the presented numerical values in the tunnelling regime.

We consider further the linearly polarized laser pulse of the form

$$F(t) = F_{\text{peak}} \sin^2(\pi t/T_p) \cos(2\pi t/T_c), \quad 0 < t < T_p \quad (5)$$

(otherwise $F(t) = 0$) and take $F_{\text{peak}} = 0.01$ a.u. We choose the optical cycle period $T_c = 1931$ a.u. ($\lambda = 14 \mu\text{m}$) that provides $\gamma = 0.2$ and the pulse duration $T_p = 4T_c$. The quasistatic rate $w(F(t))$ for this pulse, obtained using the corrected ADK formula (see Eq. (3) and the text below), is shown in Fig. 1(b). In Fig. 1(c) the corresponding (quasistatic) ionization probability

$$P_{\text{ion}}^{(\text{qs})}(t) = 1 - \exp\left[-\int_0^t w(F(t')) dt'\right] \quad (6)$$

is compared with the probability P_{ion} obtained by calculating the evolution of the time-dependent system [6] defined by Hamiltonian (2) with the alternating field $F(t)$ of the form (5). $P_{\text{ion}}^{(\text{qs})}(t)$ and $P_{\text{ion}}(t)$ approach each other whenever $F = 0$, allowing us to determine the ionization probability at $t = T_p$ from the static rates [7]. The difference between $P_{\text{ion}}(T_p)$ and $P_{\text{ion}}^{(\text{qs})}(T_p)$ in this example ($\gamma = 0.2$) is less than 1%, but it increases for larger values of γ .

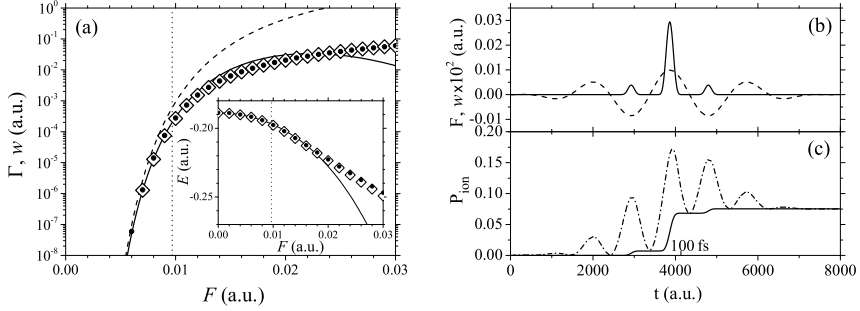


Figure 1. (a) Ionization rates of the sodium atom at different strengths of the static electric field F obtained by the wave-packet propagation method (full circles), by the complex-rotation method [3] (open 'diamonds'), by the ADK formula (3) (dashed line) and by the ADK formula with the Stark shift correction (4) (full line) are shown. The inset shows the numerical values for the lowest state energies (symbols) and those determined by the 4th order expansion formula (4) (full line). Vertical dotted lines mark the field strengths dividing the tunnelling and OBI areas (at $F = 0.00969$ for sodium). (b) The laser pulse of the form (5) with $F_{\text{peak}} = 0.01$ a.u., $T_c = 1931$ a.u., $T_p = 4T_c$ (dashed line) and the related quasistatic ionization rate $w(F(t))$ for sodium (full line). (c) The ionization probability obtained from the quasistatic rate (full line) and by solving the time-dependent problem exactly (dash-dot line).

Acknowledgements

This work was supported by the COST Action No. CM1204 (XLIC). We acknowledge support from the Ministry of Education, Science and Technological Development of Republic of Serbia under Project No. 171020.

REFERENCES

- [1] L. V. Keldysh, Sov. Phys. JETP **20**, 1307 (1965).
- [2] M. V. Ammosov, N. B. Delone, and V. P. Krainov, Sov. Phys. JETP **64**, 1191 (1986).
- [3] M. Z. Milošević and N. S. Simonović, Phys. Rev. A **91**, 023424 (2015).
- [4] H. Hellmann, J. Chem. Phys. **3**, 61 (1935).
- [5] A. Askar and A. S. Cakmak, J. Chem. Phys. **68**, 2794 (1978).
- [6] F. Grossmann, *Theoretical Femtosecond Physics* (Springer-Verlag, Berlin, 2008).
- [7] A. Bunjac, D. B. Popović, and N. S. Simonović, Eur. Phys. J. D **70**, 116 (2016).

RESONANT VIBRATIONAL EXCITATION OF RO-VIBRATIONALLY EXCITED H₂ AND D₂ BY ELECTRON IMPACT

R. Celiberto^{1,2}, V. Laporta², R.K. Janev³, and J.M. Wadehra⁴

¹*Dipartimento di Ingegneria Civile, Ambientale, Edile, del Territorio e di Chimica, Politecnico di Bari, Bari, Italy*

²*Istituto di Nanotecnologia - CNR, Bari, Italy*

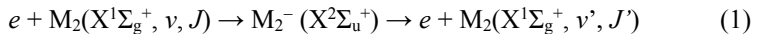
³*Macedonian Academy of Sciences and Arts, P. O. Box 428, 1000 Skopje, Macedonia*

⁴*Physics Department, Wayne State University, Detroit, Michigan 48202, USA*

Abstract. The process of resonant vibrational excitation of ro-vibrationally excited H₂ and D₂ molecules in their ground electronic state by electron impact is studied by the local-complex-potential model of resonant theory of electron-molecule collision processes. The cross sections for this process are presented for a selected number of initial vibrational and rotational states in the collision energy range from threshold to 20 eV. It is demonstrated that the cross section for a vibrational transition $\nu \rightarrow \nu'$ ($\nu' > \nu$) increases with increasing the rotational state J in the vibrational level ν ; this increase being larger when the difference $\nu' - \nu$ increases. In contrast, for the vibrationally elastic transition ($\nu' = \nu$) the cross section decreases with increasing the initial rotational level.

1. INTRODUCTION

In the present paper we study the vibrational excitation process



where M_2 stands either for H₂ or D₂. ν and ν' are the vibrational quantum numbers of initial and final vibrational states respectively, and J the corresponding rotational quantum numbers of the ν level. $M_2^-(X^2\Sigma_u^+)$ designates the lowest $^2\Sigma_u^+$ resonant state of M_2 molecule. Cross section for H₂ molecule have been already published in Ref. [1] for a limited range of incident energies. Here we extend the calculation from the threshold to 20 eV and to the D₂ molecule. Process (1) plays an important role not only in the chemistry of early Universe and in the galaxy and star formation [2], but also in the fusion reactor divertor plasmas [3]. It has a critical role, in fact, in the kinetics of H⁻ and D⁻ sources for the neutral hydrogen beam heating of thermonuclear fusion plasmas [4] as prime

competitor of the basic H^- and D^- formation process (the dissociative decay channel of the intermediate $X^2\Sigma_u^+ H_2$ resonance).

2. THEORETICAL MODEL

The local-complex-potential (LCP) model of resonant electron-molecule processes, used in the present study, is described in detail elsewhere [5]. The cross section for the reaction (1) in this model is given by [5, 6] (atomic units are used throughout this paper, unless otherwise explicitly indicated)

$$\sigma_{v,J,v',J} = \frac{2\pi^2}{k_i^2} \left| \int_0^\infty dR \langle \chi_{v',J}(R) | \Gamma_X^{1/2}(R) | \xi_{v,J}(R) \rangle \right|^2 \quad (2)$$

where $k_i = (2\varepsilon_i)^{1/2}$ is the incident electron momentum (ε_i is its energy), $\Gamma_X(R)$ is the partial width of the $X^2\Sigma_u^+ M_2$ resonance for decay to the $M_2(X^1\Sigma_g^+, v', J)$ state and R is the internuclear distance. In the LCP approximation the radial resonant wave function $\xi_{v,J}(R)$ is solution of the equation

$$\left[-\frac{1}{2\mu} \frac{d^2}{dR^2} + V^-(R) - \frac{i}{2} \Gamma(R) - E \right] \xi_{v,J}(R) = \left[\frac{\Gamma_X(R)}{2\pi} \right]^{1/2} \chi_{v,J}(R) \quad (3)$$

where μ is the reduced mass of the nuclei, $V^-(R)$ and $\Gamma(R)$ are potential energy and the total width of the $X^2\Sigma_u^+$ resonant state, and $E = \varepsilon_i + E_{v,J}$ is the total energy ($E_{v,J}$ being the energy of v, J ro-vibrational state). The potential energy curve $V^-(R)$, the partial $\Gamma_X(R)$ and total $\Gamma(R)$ widths of $X^2\Sigma_u^+$ resonant state, given in Ref. [6] up to $R = 4a_0$, have been appropriately (by analytic fit functions) extrapolated to large internuclear distances when used in Eqs. (2) and (3).

Equation (3) has been solved by using the Green's function method. The computational procedure is described in detail in Ref. [8].

3. CROSS SECTION RESULTS

In the present work we assume that the rotational motion of the molecule is much slower than its vibrational motion and the cross section calculations were performed only for the $vJ \rightarrow v'J$ transitions. In the figures below we present cross sections for these transitions that characterize the dependence of cross section magnitude and energy behavior on v, v' and J quantum numbers.

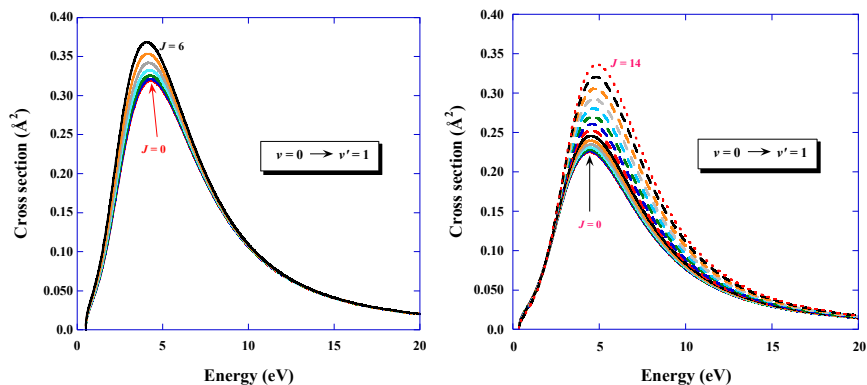


Figure 1. Cross section for the excitations $0, J \rightarrow 1, J$ with $J = 0-6$ for H_2 (left panel) and $J = 0-14$ for D_2 (right panel).

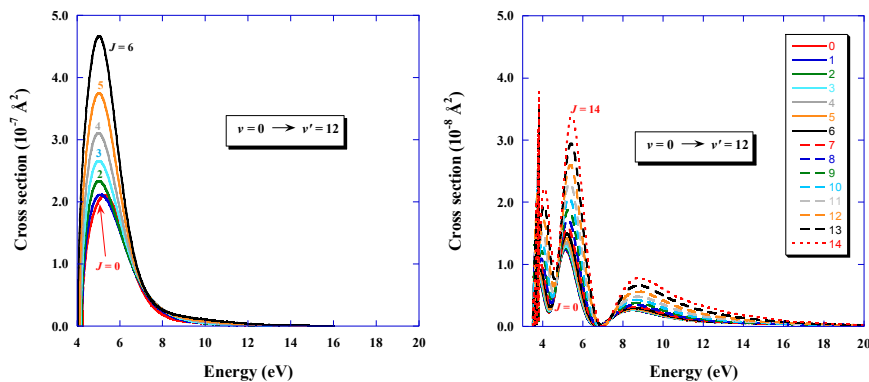


Figure 2. Same as in Fig.1 but for $0, J \rightarrow 12, J$ transitions.

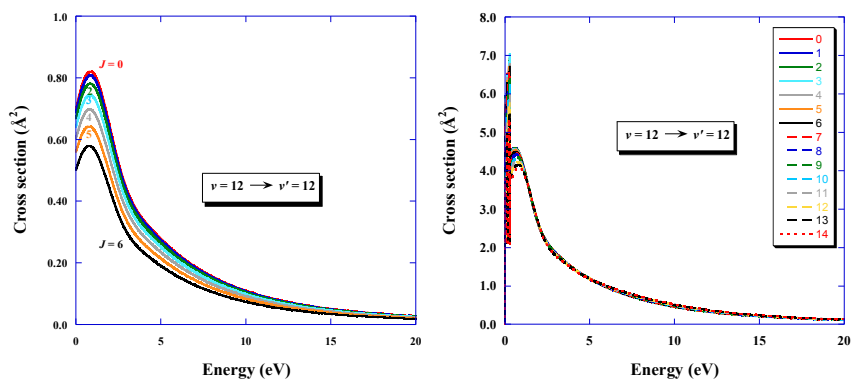


Figure 3. Vibrationally elastic cross sections for the $12, J \rightarrow 12, J$ transitions for various values of J .

The increase of the cross section for both H₂ and D₂ with increasing J for the $\nu J \rightarrow \nu' J$ ($\nu' > \nu$) transitions is related to the decrease of the transition energy from the νJ energy level to the energy of resonant state, while its decrease in the case of elastic transition is related to the increased decay of resonant state in the competing detachment channel. The elastic case for deuterium, however, the cross section behavior with J is less clear (see Fig. 3, right panel) as the curves almost overlap.

REFERENCES

- [1] M. Capitelli et al, Plasma Phys. Control. Fusion **53** 124007 (2011)
- [2] S. Lepp, P.C. Stancil and A. Dalgarno, J. Phys. B: At. Mol. Opt. Phys. **35**, R57 (2002)
- [3] D.E. Post, J. Nucl. Mater. **220**, 143 (1995)
- [4] M. Bacal, Nucl. Fusion **46**, S 250 (2006)
- [5] J.N. Bardsley and F. Mandl, Rep. Prog. Phys. **31**, 815 (1968)
- [6] R. Celiberto, R.K. Janev, J.M. Wadehra and A. Laricchiuta, Phys. Rev. A **77**, 012714 (2008)
- [7] T.D. Stibbe and J. Tennyson, J. Phys. B: At. Mol. Opt. Phys. **31**, 815 (1998)
- [8] R. Celiberto, R.K. Janev, V. Laporta, J. Tennyson and J.M. Wadehra, Phys. Rev. A **88**, 062701 (2013)

EFFECT OF MAGNETIC FIELD ON STRUCTURAL PROPERTIES OF CONFINED HYDROGEN ATOM

Nikola Filipović, Vladan Pavlović and Ljiljana Stevanović

*Department of Physics, Faculty of Sciences and Mathematics, University of Niš,
Višegradska 33, 18000 Niš, Serbia*

Abstract. Hydrogen atom in plasma is studied through the model of hydrogen atom confined by impenetrable sphere. The energy and dipole matrix element of the transition between the ground and first excited state with $m = 0$ are calculated using the variational Lagrange mesh method. Spontaneous emission coefficient of the $2p_0$ state is also calculated. The behavior of the quantities with applied magnetic field strength for several values of the radius of confinement is studied in details.

1. INTRODUCTION

Model of confined hydrogen atom (CHA) is introduced in physics in order to explain the polarizability of the gas of hydrogen atoms under high pressure. Later, it found its application in many diverse fields of physics, from atomic and molecular physics to condensed matter physics. CHA is one of the methods (approaches) in studying partially ionized plasmas and atoms embedded in neutral media [1, 2]. Recently, the model was used to investigate same structural properties of hydrogen atom embedded in Debye plasma [3].

In this contribution, we study the spontaneous emission of the hydrogen atom in plasma environment under magnetic field. In order of simplicity, we take the state $2p_0$ into consideration and found how magnetic field influences its spontaneous emission coefficient.

2. MODEL

Hamiltonian of the hydrogen atom embedded in plasma environment and subjected to external magnetic field of strength B , written in atomic units ($m_e = |e| = \hbar = 1$) is:

$$H = -\frac{1}{2} \frac{\partial^2}{\partial r^2} + \frac{1}{2r^2} L^2 + \frac{1}{2} BL_z + \frac{1}{8} B^2 r^2 \sin^2 \theta - \frac{1}{r} + V_c, \quad (1)$$

where

$$V_c(r) = \begin{cases} 0, & r \leq R, \\ \infty, & r > R, \end{cases} \quad (2)$$

is the confining potential, L and L_z are the orbital momentum operator and the z -component of the orbital momentum operator, respectively. Here, R is the radius of confinement. Eigen-problem of Hamiltonian (1) is solved by using the Lagrange mesh method [4] representing the wave function by the following expansion:

$$\psi(r, \theta, \varphi) = \sum_{k=1}^N \sum_{l'=|m|}^L c_{kl'} f_k\left(\frac{r}{R}\right) Y_{l'm}(\theta, \varphi). \quad (3)$$

where the basis functions f_i are constructed from shifted Legendre polynomials [4]. In Eqs. (3) and (4), $c_{kl'}$ are the coefficients of the expansion, $x = r/R$ and m stands for the magnetic quantum number. Hamiltonian matrix elements are given in [5].

Using previous results, the electric dipole transition matrix element between the states $|i\rangle$ and $|j\rangle$ with the same value of m , can be calculated by the following expression:

$$\begin{aligned} d_{ji} &= \langle j|z|i\rangle = \\ &= (-1)^m \sqrt{\frac{2}{3}} R \sum_{k,k',l,l'} c_{kl}^{(1)} c_{k'l'}^{(2)} x_k \delta_{kk'} \sqrt{(2l+1)(2l'+1)} \begin{pmatrix} l & 2 & l' \\ -m & 0 & m \end{pmatrix} \begin{pmatrix} l & 1 & l' \\ 0 & 0 & 0 \end{pmatrix}. \end{aligned} \quad (5)$$

Spontaneous emission coefficient between the given states are calculated by using the following formula:

$$\gamma_{ji} = \frac{4}{3} \alpha^3 (\Delta E_{ji})^3 |d_{ji}|^2, \quad (6)$$

where $\Delta E_{ji} = E_j - E_i$ is the transition energy, with α being the fine structure constant, $\alpha \approx 1/137$.

3. RESULTS AND DISCUSSION

In this work, we calculated the transition energy, electric dipole transition matrix element, the coefficient of the spontaneous emission of the $2p_0$ state. Therefore, we are interested only in the transition $1s_0 \leftrightarrow 2p_0$ (states with $m = 0$). Moreover, to obtain the energies and wave functions of CHA, we used the Lagrange mesh with $N = 40$, and $L = 12$.

The transition energy ΔE_{21} between the ground and the first excited state as function of the applied magnetic field strength is given on the left panel of Fig. 1. for different values of the confining radii $R = 2, 6, 10$ and 20 . It can be seen that, when R is small, ΔE_{21} slightly decreases when B increases. On the contrary, ΔE_{21} increases with the increase of B in the case when the confinement radius is larger, and that increase is more significant than the decrease of the same quantity for $R = 2$. Different behavior of ΔE_{21} with the increase of B can be understood by knowing that the spatial confinement is much more dominant than the magnetic field confinement for small R (represented by the third and the fourth term in Eq. (2)), while in the case of R being large enough, this behavior is inverted.

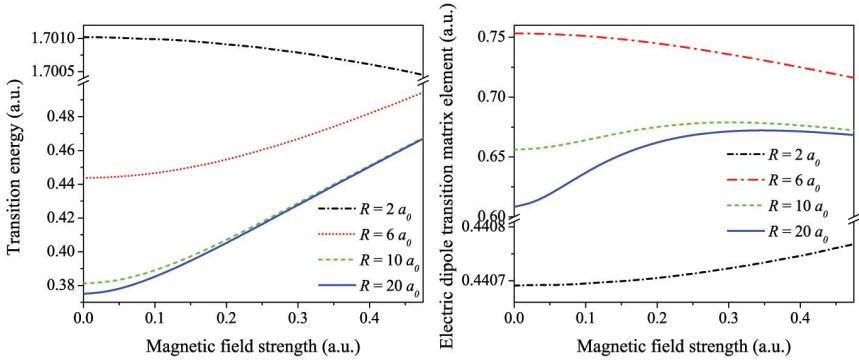


Figure 1. Transition energy and electric dipole transition matrix element between the ground and the first excited state as functions of the applied magnetic field strength, for several values of R .

The functional dependence of d_{21} on B , for $R = 2, 6, 10$ and 20 is given on the right panel of Fig. 1. We notice again that the behavior of these quantities differs for small and for large confinement radii. For $R = 2$, the electric dipole transition matrix element slightly increases with the increase of the applied magnetic field strength, while for larger R the opposite behavior is noticed in the area where B is large enough. Moreover, it can be seen that, in the same area of large B , the enlargement of the confinement radius leads to the free hydrogen atom limit, as expected. This behavior may be explained in the similar way as the one from the left side of Fig. 1.

The spontaneous emission coefficient between the ground and the first excited state with respect to B for $R = 2, 6, 10$ and 20 is given on Fig. 2. Similar behavior as for the transition energy is observed. This can be explained by looking at the Eq. (6) – γ_{21} has the cubic dependence on ΔE_{21} , while it increases with the increase of d_{21} only with the square dependence – less dominant than the one of the transition energy.

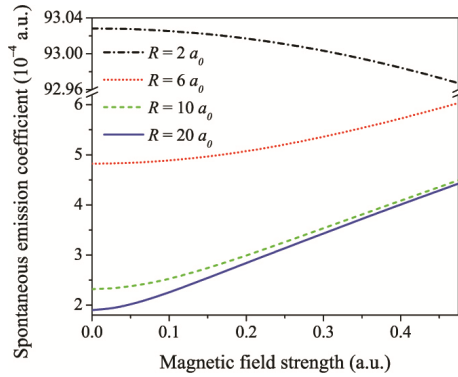


Figure 2. Coefficient of the spontaneous emission with respect to the magnetic field strength, for several values of R .

4. CONCLUSION

In this paper, we calculated the transition energy, electric dipole transition matrix element and the coefficient of the spontaneous emission of the $2p_0$ state of the hydrogen atom embedded in plasma environment as functions of the external magnetic field. It can be concluded that all of these show nonlinear dependence on the external magnetic field, and in particular that: (i) transition energy slightly decreases when magnetic field increases for small radii and increases for large radii, (ii) the electric dipole transition matrix element slightly increases with the increase of the applied magnetic field strength for small radii, and opposite for large, (iii) similar behavior is noticed for the spontaneous emission coefficient as for the transition energy.

Acknowledgements

This work is partially supported by our Ministry under the grant NO 171028 and NO 171025.

REFERENCES

- [1] G. M. Harris, J. E. Roberts and J. G. Trulio, Phys. Rev. 119, 1832 (1960).
- [2] H. C. Graboske, D. J. Harwood and F. J. Rogers, Phys. Rev. 186, 210 (1969).
- [3] B. Saha, P. K. Muherjee and G. H. F. Dierksen, Astron. Astrophys. 396, 337 (2002).
- [4] D. Baye, K. D. Sen, Phys. Rev. E 78, 026701 (2008).
- [5] Lj. Stevanović, N. Filipović and V. Pavlović, Opt. Quant. Electron. 48, 231 (2016).

INTERACTION OF ATOMS AND IONS WITH TWISTED LIGHT

S. Fritzsche^{1,2}, D. Seipt¹, A. A. Peshkov^{1,2} and A. Surzhykov^{3,4}

¹*Helmholtz-Institut Jena, D-07743 Jena, Germany*

²*Friedrich-Schiller-Universität Jena, D-07743 Jena, Germany*

³*Physikalisch-Technische Bundesanstalt, D-38116 Braunschweig, Germany*

⁴*Technische Universität Braunschweig, D-38106 Braunschweig, Germany*

Abstract. The excitation and ionization of (many-electron) atoms and simple molecules by twisted light have been investigated within the framework of density matrix theory. Expressions were derived especially for the alignment of the excited states as well as the angular distribution of the emitted (photo-) electrons and/or the subsequent fluorescence radiation, if the incident photons are initially prepared in a twisted Bessel beam or for a coherent superposition of such beams. Emphasis was placed to the question how the (transverse) phase structure of the incident radiation affects the scattering of light or the photoionization of atoms and molecules. For example, it was found that both, the population of the excited atoms and the angular distribution of the emitted particles are sensitive to the transverse momentum and the (projection of the) total angular momentum of the incident radiation.

1. INTRODUCTION

Research on optical vortices, popularly known also as *twisted* light, has attracted much interest during the past two decades. In particular, the spin and orbital angular momentum distributions of such light beams have been explored in quite detail. In contrast, rather little is yet known about their interaction with (clouds of) atoms and molecules and how the angular momentum of the light affects the subsequent fluorescence or photoelectron emission. In recent years, we have therefore investigated the photoexcitation and ionization of atoms and simple molecules. In this contribution, we here summarize some recent results on the fluorescence and photoelectron emission if the incident radiation has some well-defined (projection of the) total angular momentum and if the atoms or molecules are localized with regard to the beam (axis).

2. THEORETICAL BACKGROUND

The formation of excited atomic states in collisions with ions, electrons, or photons is described most conveniently by means of the density-matrix theory [1,2]. In this framework, for example, the overall system 'target atom + incident photon(s)' is treated consistently in the photoexcitation and ionization process of atoms and is described by the initial- and final-state statistical (or density) operators, respectively. These operators are connected by the transition operator T that is characteristic for the given interaction. If, for the sake of simplicity, we just consider the excitation of a hydrogic atoms by twisted light, the transition operator reads as [3]

$$\hat{V}^{(\text{tw})} = \alpha \mathbf{A}_{\varkappa m_\gamma k_z \lambda}(\mathbf{r}) \hat{\mathbf{p}}. \quad (1)$$

Although this operator is formally similar to an incident plane-wave radiation, the vector-potential $\mathbf{A}_{\varkappa m_\gamma k_z \lambda}$ differs for a Bessel beam since it now describes a (twisted) wave which propagates along the quantization axis with the longitudinal momentum k_z and well-defined projection of the total angular momentum (TAM), $J_z = m_\gamma$. Here, we assume in addition that the absolute value of the transverse momentum, $|\mathbf{k}_\perp| = \varkappa$ and, thus, the energy of the photons, $\omega = k/\alpha = \sqrt{k_z^2 + \varkappa^2}/\alpha$, are fixed. In fact, such a *Bessel* state of light is described by the vector potential [3,4]:

$$\begin{aligned} \mathbf{A}_{\varkappa m_\gamma k_z \lambda}(\mathbf{r}) &= \int \mathbf{e}_{\mathbf{k}\lambda} e^{i\mathbf{k}\mathbf{r}} a_{\varkappa m_\gamma}(\mathbf{k}_\perp) e^{-i\mathbf{k}_\perp \mathbf{b}} \frac{d^2 k_\perp}{(2\pi)^2}, \end{aligned} \quad (2)$$

which can be written as a superposition (integral) of the standard plane-wave components with the amplitude

$$a_{\varkappa m_\gamma}(\mathbf{k}_\perp) = (-i)^{m_\gamma} e^{im_\gamma \phi_k} \sqrt{\frac{2\pi}{k_\perp}} \delta(k_\perp - \varkappa). \quad (3)$$

In Eq. (2), moreover, the factor $e^{-i\mathbf{k}_\perp \mathbf{b}}$ specifies the position of the target atom within the incident wave-front. This difference is important since, in contrast to a plane-wave, the twisted beam has a complex spatial structure.

While the formalism developed by us in Ref. [3] can be employed for studying the photoexcitation of any atom, detailed calculations were performed for the low-lying $3s \ ^2S_{1/2} (J_i = 1/2) + \gamma \rightarrow 3p \ ^2P_{3/2} (J_f = 3/2)$ transition in neutral sodium. From the analysis of the alignment parameters we found, for instance, that the population of the photoexcited atomic are sensitive not only with regard to the kinematic parameters of the Bessel beams, such as the ratio of transverse-to-longitudinal momenta of the incident light, but also to their relative phase and the difference of the projections of the total angular momenta for superpositions of two (or more) Bessel beams. Furthermore, it was shown how the parameters of the (incident) twisted radiation affects also the angular distribution of the subsequent decay photons [3].

3. PHOTOIONIZATION OF H_2^+ MOLECULAR IONS

In addition to the photoexcitation of atoms, we also investigated the photoionization of H_2^+ molecular ions for Bessel beams of twisted light [5]. Detailed computations were carried out especially for the angle-differential photoionization cross sections and for a macroscopic target of randomly-distributed but initially aligned ions. For example, Fig. 1 displays the cross sections as function of the polar angle ϑ_f of the photoelectrons for three different photon energies. In these computations, both the alignment ($\gamma = 45^\circ$) and azimuthal angle of the emitted electrons ($\varphi_f = 0^\circ$) are fixed. As seen from this figure, the differential cross section $d\sigma^{\text{tw}}/d\Omega_f$ does not longer *vanish* for $\vartheta_f = 0^\circ$, quite in contrast to an incident plane wave, an effect that can be understood by the polarization (vector) of the twisted light [5]. For quite similar reasons, the cross section for twisted light is generally larger also than for plane-waves radiation.

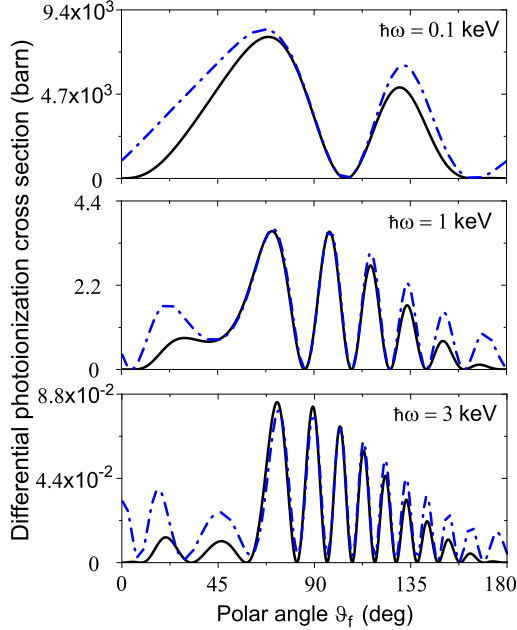


Figure 1. (Color online) Angle-differential photoionization cross section as a function of the polar angle ϑ_f (of the detector) for H_2^+ molecular ions under the angle $\gamma = 45^\circ$, and if the photo electrons are observed in the xz plane ($\phi_f = 0^\circ$). Plane-wave results (black solid lines) are compared with the photoionization by means of a Bessel beam with opening angle $\theta_k = 30^\circ$ (blue dashed lines) and are shown for the three different photon energies: $\hbar\omega = 0.1$ keV (upper panel), $\hbar\omega = 1$ keV (middle panel), $\hbar\omega = 3$ keV (bottom panel), respectively. Figure taken from Ref. [5]

While the angle-differential photoionization cross sections occur to be *insensitive* with regard to (the projection of the) TAM m for any macroscopic target, even if the molecular ions are supposed to be aligned, such an m -dependence can be expected if the size of the target becomes comparable with the variations in the transverse intensity pattern of the Bessel beams. An explicit dependence on m may also occur for a superposition of two (or more) Bessel beams with different m .

4.SUMMARY

We have applied the framework of density matrix theory to explore the photoexcitation of hydrogenic [6] and many-electrons atoms [3]. These studies showed that the angular momentum of *twisted light* provides not only an additional degree of freedom for the photons but also affects the photoabsorption, photoionization as well photon scattering of atoms and molecules. Sizeable effects were found especially for the alignment parameters of residual ions as well as for the angular distribution of the emitted photons and electrons, even if the results are averaged over the spatial intensity distribution of the beams. — A similar behaviour were found also for the scattering of twisted electrons, though the physics and applications are quite different in the latter case [7].

REFERENCES

- [1] K. Blum, *Density Matrix Theory and Applications* (Plenum, New York, 1996).
- [2] V. V. Balashov, A. N. Grum-Grzhimailo and N. M. Kabachnik, *Polarization and Correlation Phenomena in Atomic Collisions* (Kluwer Academic/Plenum Publishers, New York, 2000).
- [3] A. Surzhykov *et al*, Phys. Rev. A 91, 013403 (2015).
- [4] O. Matula, A. G. Hayrapetyan, V. G. Serbo, A. Surzhykov and S. Fritzsche, J. Phys. B 46, 205002 (2013).
- [5] A. Peshkov, S. Fritzsche and A. Surzhykov, Phys. Rev. A 92, 043415 (2015).
- [6] M. Scholz-Marggraf *et al*, Phys. Rev. A 90, 013425 (2014).
- [7] V. Serbo *et al*, Phys. Rev. A 92, 012705 (2015).

IONIZATION OF RUBIDIUM BY ELECTRON IMPACT

N. P. Kucska¹, T. Mukoyama¹ and K. Tőkési^{1,2}

¹ *Institute for Nuclear Research, Hungarian Academy of Sciences,
H-4001 Debrecen, P.O. Box 51, Hungary*

² *ELI-ALPS, ELI-HU Non-profit Ltd., Dugonics tér 13, H-6720 Szeged, Hungary*

Abstract. In this work, the cross sections for ionization by electron impact of rubidium 5s shell have been calculated by Classical trajectory Monte Carlo method, the binary-encounter approximation (BEA) and we also used the semi-empirical formula of Lotz. The kinetic energy of the projectile is in the range between 5 and 100 keV. We compared our results with other theoretical and experimental data.

1. INTRODUCTION

We have many experimental investigations of the ionization process by electrons and other charged particles from the beginning of the twentieth century. At the same time only a limited number of theoretical studies exists for Rubidium, however this simple element holds a possibility to test theoretical models.

It is a challenging task for classical theories to determinate the cross sections of multi-electron ion-atom collisions. The main difficulty is caused by the many-body feature of the collision, involving the projectile, target nucleus, and target electron(s).

The CTMC method is quite successful in dealing with the atomic collision processes, and it has the benefit that we can make classical examinations of the three-body interactions during the simulation in a nonperturbative manner [1,2]. In the present study different simulations for the collision of rubidium with positron and electron are presented. Beside the CTMC method we also applied the binary encounter approximation (BEA) and the formula of Lotz [3]. Our results are compared with other calculations and measurements.

2. THEORY

The classical treatment of various collision problems has been quite successful to obtain ionization cross sections. In particular the classical trajectory Monte Carlo (CTMC) method is widely used [1]. It is a non-perturbative method and hence all

the interactions between colliding particles can be taken into account exactly within the framework of the classical dynamics.

We describe the collision system as a three-body model: the projectile (e^+/e^-), an atomic electron (e^-), and the remaining rubidium ion (Rb^+). A three-body, three-dimensional CTMC calculation is performed as described by Olson and Salop [2]. The target atom modeled like a tiny solar system, in which the electron moving on Kepler orbit around the nucleus. Coulomb forces, what affects the three-body system are represented by Hamilton's equations, which are solved by numerical integration using a fourthorder Runge-Kutta-Gill method.

We evaluate the relative energy of the particles. If the electron's total energy is positive relative to the rubidium ion, then an ionization event is recorded

We investigated the ionization cross sections for rubidium using two models. The difference between the two models is in handling the effect of the other electrons.

At first Coulomb force acting between the colliding particles. In this case we calculate the effective charge of the valance electron by Slater's rules [4].

In the second approach we represented the rubidium atom with Garvey model potential[5]. The two parameters of the potential; ξ and η represents quantum mechanical effects by taking into account of the independent particle model.

3. RESULTS AND DISCUSSION

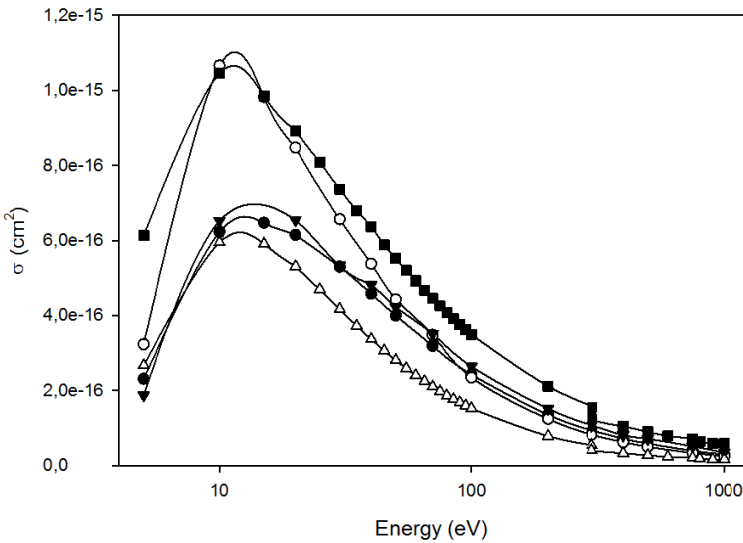


Figure 1. Electron-impact ionization cross sections of rubidium 5s shell. Inverse circle: present the conventional CTMC results using the effective static target nucleus charge, solid triangle: present CTMC results with Garvey-type model potential, inverse triangle: present BEA simulation, solid square: semi-empirical formula of Lotz[5], solid circle: BED simulation [6].

The binding energy of the rubidium 5s shell valence electron is 0,1504a.u. (4,1912 eV) based on the theoretical data of the ionization energy. The mass of Rubidiumatom is 156918,88 a.u, Applying the first model, the corresponding effective nuclear charge is $Z_{\text{eff}}= 2.2$.

We also made the simulations with the Garvey type model potential. In this casethe parameters of the potential, according to ref. 5, are $\xi=0,1686$ and $\eta=0,1619$. Fig. 1. shows the ionization cross sections of Rb 5s shell by electron impact. While the data of CTMC with static potential used are in agreement with Lotz calculations, the CTMC results using Garvey model potential during the simulations are in agreement with the BEA and with the results published in ref. 6.

Acknowledgments

This work was supported by the Hungarian Scientific Research Fund OTKA Nos. NN 103279, K103917 and by the COST Action CM1204 (XLIC).

REFERENCES

- [1] K. Tőkési, G. Hock, Nuclear Instruments and Methods in Physics Research Section B: Beam Interactions with Materials and Atoms 124 (1997) 398.
- [2] R.E. Olson, A. Salop, Physical Review A 16 (1977) 531.
- [3] W. Lotz, Zeitschrift für Physik 206 (1967) 205.
- [4] J.C. Slater, Physical Review 36 (1930) 57.
- [5] R.H. Garvey, C.H. Jackman, A.E.S. Green, Physical Review A 12 (1975) 1144.
- [6] Y.-K. Kim, J. Migdalek, W. Siegel, J. Bieroń, Physical Review A 57 (1998) 246.

DISSOCIATIVE ELECTRON ATTACHMENT TO BENZENE CHROMIUM TRICARBONYL

Jelena Maljković ^{1*}, Paulina Maciejewska ² and Janina Kopyra ²

¹ *Laboratory for Atomic Collision Processes, Institute of Physics Belgrade,
University of Belgrade, Pregrevica 118, 11080 Belgrade, Serbia*

² *Faculty of Sciences, Siedlce University, 3 Maja 54, 08-110 Siedlce, Poland*

Abstract. We have investigated dissociative electron attachment to benzene chromium tricarbonyl, $M = C_r(C_6H_6)CO_3$. This molecule was in our interest because it is a possible Focused Electron Beam Induced Dissociation (FEBID) precursor. Measurements were done utilizing an experimental setup settled in Siedlce, Poland. The obtained mass spectra were recorded for the energies from 0 eV to 14 eV, with 2 eV step. The compound showed a very rich fragmentation pattern.

1. INTRODUCTION

In the present work a dissociative electron attachment (DEA) to benzene chromium tricarbonyl has been investigated. In DEA processes electron is captured by molecule forming a temporary negative ion, which can decompose into negative fragment and one or more neutral counterparts. This molecule has been in our interest because it is potential Focused Electron Beam Induced Deposition (FEBID) precursor. FEBID is a direct-writing technique in which the metallic deposit is deposited onto a substrate with nanometer resolution. In this technique a highly focused, high-energy electron beam impinges on a substrate and due to collisions produces lower energy back-scattered electrons and secondary electrons. It is nowadays very well known that these low energy electrons (LEEs) contribute to the processes resulting in the formation of the deposits. However, in the case when LEEs lead to partial fragmentation of the target molecules this results in the formation of deposit with limited purity and resolution.

The benzene chromium tricarbonyl molecule belongs to organometallic compounds. It has piano stool geometry with planar arrangement of aryl group and three carbonyl groups which act as “legs” (Figure 1). This molecule has been investigated previously. Rees and Copens [1] have been studied the crystal structure of this molecule at 78 K, both by X-ray and neutron diffraction. The electronic structure of transition metal in benzene chromium tricarbonyl has been

investigated by using SCF MO calculations [2]. Uemura and coauthors [3] have investigated direct regioselective lithiation of chromium benzenetricarbonyl.

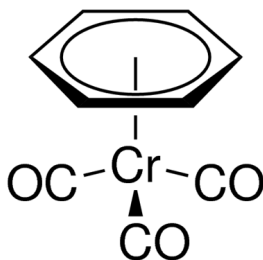


Figure 1. Structure of benzene chromium tricarbonyl molecule.

2. EXPERIMENT

The experiments were performed by means of crossed beam apparatus settled at Siedlce University, Poland. Description of the experimental set-up has been given elsewhere [4]. Briefly, it consists of a trochoidal electron monochromator (TEM), a quadrupole mass analyzer (QMA) and a secondary electron multiplier, all enclosed into vacuum chamber. Incident electron beam, with energy resolution of FWHM= 150-200meV and electron current $I \approx 10$ nA, orthogonally intersects with molecular beam resulting in the formation of fragment anions. Molecular beam emanates from the oven which was heated by two halogen bulbs. These lamps prevent condensation of the target molecules at the lenses and also provide sufficient vapour pressure of the target molecules and also and provide stable experimental conditions. Working temperature was around 95 °C. Negative ions are extracted directly from the collision region by a small electric field, towards a QMA and detected by single pulse counting techniques. The calibration of the energy scale was achieved by measuring SF_6 signal, with intense resonance near 0 eV. Base pressure was in the range of $\sim 10^{-8}$ mbar while the working pressure around 3×10^{-5} mbar.

3. RESULTS

Preliminary results of dissociative electron attachment to benzene chromium tricarbonyl are shown. Resonant features of anion yields indicate that underlying processes are DEA, as the only effective below ionization energy, $IE \approx 7$ eV [5]. Mass spectra has been obtained in the incident electron energy range from 0 eV up to 14 eV. Molecule showed rich anion formation: $(M - CO)^- = 186$ a.m.u., $(M - (CO)_2)^- = 158$ a.m.u, $(M - (CO)_3)^- = 130$ a.m.u, $(M - C_6H_6)^- = 136$ a.m.u, $Cr^- = 52$ a.m.u., $Cr(CO)^- = 80$ a.m.u, $(Cr(CO)_2)^- = 108$ a.m.u. and $Cr(CO)^- = 80$ a.m.u. The most intense reaction channel is the loss of one carbonyl group, which is also shown by other authors [6] in DEA process to $W(CO)_6$. Reaction channel associated with loss of all three CO groups, Figure 2, has a threshold

around 3eV. Three resonances are present in the anion yield curve. We can speak here about metastable decays, also shown in [6]. Sequential process, where $(M - CO)^-$ decays to $(M - (CO)_2)^-$ and $(M - (CO)_2)^-$ decays to $(M - (CO)_3)^-$ can occur in this presently studied compound.

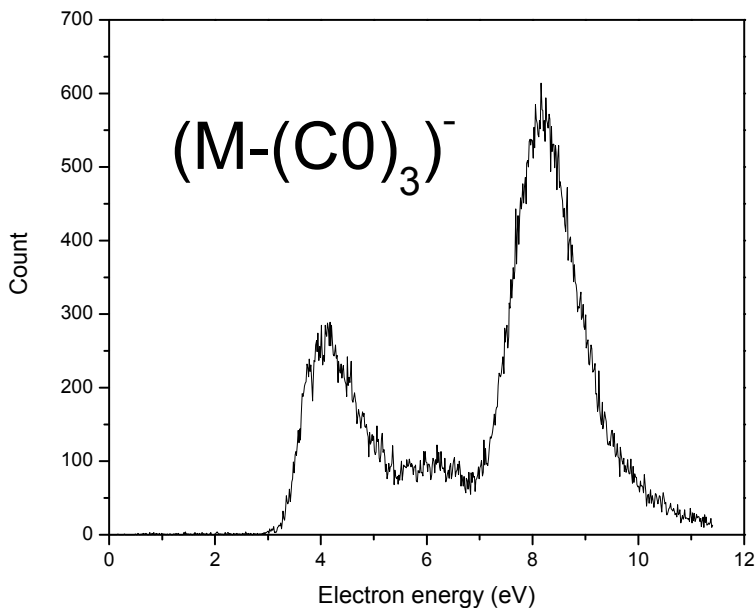


Figure 2. Anion yield of $(M - (CO)_3)^-$ formed by electron impact.

4. CONCLUSION

DEA processes have been investigated on benzene chromium tricarbonyl, a potential FEBID precursor. The obtained action tandem mass spectra have showed rich anion formation. The release of one, two and three CO groups has been noticed that is a consequence of a prompt decomposition of the temporary negative ion. In addition, a sequential processes can contribute to the overall intensity of the above mentioned fragment anions.

Acknowledgements

This work was supported by the Polish Ministry of Science and Higher Education (Project No. 277/S/11), Ministry of Education and Science of Republic of Serbia (Project No. 171020). This work was conducted within the framework of the COST Action CM1301 (CELINA).

REFERENCES

- [1] B. Rees and P. Copens, *Acta Cryst. B* 29, 2515 (1973).
- [2] M.F. Guesta, I.H. Hillierb, B.R. Higginsonc and D.R. Lloydc, *Molecular Physics: An International Journal at the Interface Between Chemistry and Physics*, 29, 113 (1975).
- [3] M. Uemura, N. Nishikawa, K. Take, M. Ohnishi, K. Hirotsu, T. Higuchi and Y. Hayashi, *J. Org. Chem.*, 48, 2349 (1983).
- [4] C. Koenig-Lehmann, J. Kopyra, I. Dabkowska, J. Kočišek and E. Illenberger, *Phys. Chem. Chem. Phys.*, 10, 6954 (2008).
- [5] <http://www.webbook.nist.gov>
- [6] K. Wnorowski, M. Stano, C. Matias, S. Denifl, W. Barszczewska and S. Matejíček, *Rapid Commun. Mass Spectrom.* 26, 2093 (2012).

CALCULATIONS OF IONIZATION RATES FOR ALKALI-METAL ATOMS IN ELECTRIC FIELD

M. Z. Milošević¹ and N. S. Simonović²

¹*Faculty of Science and Mathematics, University of Niš, Višegradska 33, 18000 Niš, Serbia*

²*Institute of Physics, University of Belgrade, P.O. Box 57, 11001 Belgrade, Serbia*

Abstract. The lowest state energies and widths (ionization rates) of alkali-metal atoms in the static electric field are calculated for different field strength by the complex rotation method using the single-electron model. The results are compared with the corresponding values obtained using the Stark shift expansion and the Ammosov-Delone-Krainov rate formula. A good agreement is obtained for the field strengths corresponding to the tunnelling regime. It is shown that a corrected rate formula, which takes into account the Stark shift of the lowest level, significantly improves the agreement with numerically determined values.

1. INTRODUCTION

Ionization of atoms in an external electric field is a process that is efficiently explained by the quantum-mechanical tunnelling. To a good approximation it can be described within the single-electron picture. The external field distorts the potential of atomic residue forming a potential barrier through which the electron can tunnel. As a consequence all atomic states become decaying (resonances). At stronger fields the barrier can be suppressed below the energy of atomic state and in that case over-the-barrier ionization (OBI) occurs. From the quantum mechanical point of view, however, there is no essential difference between these two kinds of ionization processes, but in the semiclassical approach they are treated in different ways. Tunnel ionization is successfully described by the Ammosov-Delone-Krainov (ADK) semiclassical theory [1]. It accurately predicts tunnelling rates in experiments with atomic ionization in strong fields and shows excellent agreement with exact numerical calculations in the low field limit of the tunnelling regime. At stronger fields, however, the ADK rates may significantly deviate from the exact values, especially in the OBI regime.

For atoms with low ionization potentials, as in the case of alkali-metal atoms, the OBI regime begins at much lower values of the field strength than for hydrogen or noble gases. Thus, for these atoms the application of the ADK theory may be very limited. In order to determine the ionization rates for alkali-metal atoms in electric field more accurately, keeping the single-electron description, here we use the complex rotation method that is very efficient for calculating the resonant states.

2. THE MODEL

Within the frozen core approximation the dynamics of the valence (active) electron of alkali-metal atoms in a static electric field F is described by Hamiltonian (in atomic units)

$$H = \frac{\mathbf{P}^2}{2} + V_{\text{core}}(r) - Fz. \quad (1)$$

$V_{\text{core}}(r)$ is the effective core potential (ECP) which describes the interaction between the valence electron and the atomic core (inner electrons + atomic nucleus). The total potential $V(\mathbf{r}) = V_{\text{core}}(r) - Fz$ contains a potential barrier with the saddle point at the z-axis. Its position $z = z_{\text{sp}}$ and the value $V_{\text{sp}} = V(\mathbf{r}_{\text{sp}})$ can be determine from the rule $(\partial V/\partial z)_{x=y=0} = 0$. As mentioned in Introduction, a consequence of the presence of the barrier is that all states of the system described by Hamiltonian (1) have a resonant character. We shall consider the resonance with the lowest energy that is characterized by the magnetic quantum number $m = 0$.

The simplest ECP applicable for alkali-metal atoms is the Hellmann's pseudopotential [2]

$$V_{\text{core}}(r) = -\frac{1}{r} + \frac{A}{r} e^{-ar}. \quad (2)$$

The parameters A and a for sodium and kalium are given in Table 1.

Table 1

| atom | I_p | α | γ | F_s | A | a |
|------|---------|-----------------|-------------------------------|---------|-----|---------|
| Na | 0.18886 | 162.7 ± 0.8 | $(9.56 \pm 0.48) \times 10^5$ | 0.00969 | 21 | 2.54920 |
| K | 0.15952 | 290.8 ± 1.4 | $(3.6 \pm 1.1) \times 10^6$ | 0.00697 | 6.5 | 1.34523 |

The value of the field strength $F = F_s$ which separates the tunnelling and OBI regimes is defined by the condition $E(F) = V_{\text{sp}}(F)$. The dependence $E(F)$ can be estimated from the Stark shift $\Delta E(F)$ of the lowest energy level. For $F \ll 1$ this shift can be expanded in a series, giving

$$E(F) = E(0) + \Delta E(F) = -I_p - \frac{1}{2}\alpha F^2 - \frac{1}{24}\gamma F^4. \quad (3)$$

The dipole polarizability, the second dipole hyperpolarizability and the corresponding F_s values for sodium and kalium are given in Table 1.

3. THE COMPLEX ROTATION METHOD

A resonant state $\psi(\mathbf{r})$ is an eigensolution of the Schrödinger equation which asymptotically behaves as a purely outgoing wave with complex eigenenergy E_{res} . The real and imaginary parts of E_{res} determine the energy (position) and the width of resonance, $E = \text{Re}(E_{\text{res}})$, $\Gamma = -2\text{Im}(E_{\text{res}})$. The decay rate of the resonant state is then $w = \Gamma/\hbar$. The basic idea of the complex rotation method [4] is to make the resonance wave function $\psi(\mathbf{r})$ square integrable by a complex rotation of the coordinate, $\psi(\mathbf{r}) \rightarrow \psi_\theta(\mathbf{r}) = \psi(e^{i\theta}\mathbf{r})$, where θ is a real parameter called the 'rotation angle'. Such a 'rotated' state $\psi_\theta(\mathbf{r})$ is an eigenfunction of the so-called complex rotated Hamiltonian H_θ obtained from the original Hamiltonian H by the transformations $\mathbf{r} \rightarrow e^{i\theta}\mathbf{r}$, $\mathbf{p} \rightarrow e^{-i\theta}\mathbf{p}$. The spectrum of Hamiltonian (1) can be computed by diagonalizing the corresponding rotated Hamiltonian in a square integrable basis which is complete in a sense that it covers the continuous part of the spectrum, too. For this purpose we have used here the Sturmian basis [5].

4. THE CORRECTED ADK FORMULA

The tunnelling rates determined numerically will be compared with the rates given by the ADK theory [1]. For alkali-metal atoms in the ground state one has $l = m = 0$ and the ADK formula (for static fields) reduces to

$$w = |C_{n^*0}|^2 I_p \left(\frac{2F_0}{F} \right)^{2n^*-1} \exp\left(-\frac{2F_0}{3F}\right), \quad (4)$$

where $n^* = (2I_p)^{-1/2}$ is the effective principal quantum number, $F_0 = (2I_p)^{3/2}$, and $|C_{n^*0}|^2 = 2^{2n^*}/[n^* \Gamma(n^*+1) \Gamma(n^*)]$. Since for alkali-metal atoms the energy of the lowest state changes rapidly with F , the ADK rates (4) can be significantly improved by applying the correction

$$I_p \rightarrow -E(F) = I_p - \Delta E(F), \quad (5)$$

which accounts for the Stark shift (3).

5. RESULTS

The lowest state energies and widths (ionization rates) for the kalium and sodium atoms at different values of applied electric field, obtained numerically by the complex rotation method are shown in Fig. 1, together with the corresponding values given by the Stark shift expansion (3) and by the ADK formula (original and corrected), respectively. The results for

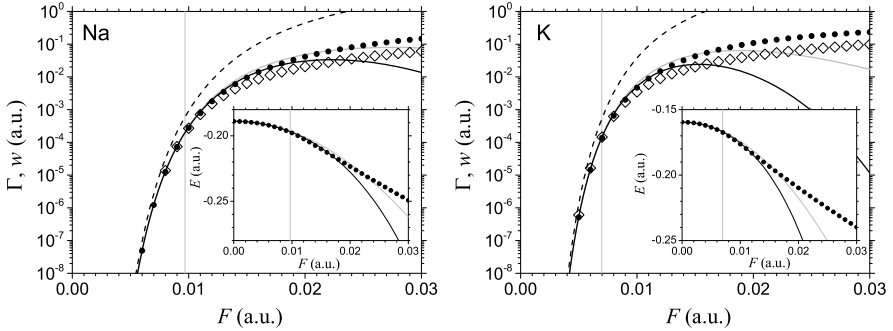


Figure 1. The lowest state widths (ionization rates) of sodium (Na) and potassium (K) in the static electric field F determined: numerically (diamonds); by the ADK formula (dashed lines); by the ADK formula with 2nd/4th order Stark shift correction (full gray/black lines); and by the ADK formula corrected using numerically calculated energy (black dots). The corresponding energies (obtained numerically and by the use of Eq. (3)) are shown in the insets (dots and full lines, respectively). Vertical gray lines mark the field strengths F_s dividing the tunnelling and OBI areas for each atom.

other alkali-metal atoms are given in Ref. [3]. A good agreement between the numerical results and those obtained using formulae (3) and (4) is found in the tunnelling domain ($F < F_s$). The correction (5) in the ADK formula significantly reduces deviations of the ADK rates compared to numerically determined values even in the OBI regime ($F > F_s$).

Acknowledgements

This work was supported by the COST Action No. CM1204 (XLIC). We acknowledge support from the Ministry of Education, Science and Technological Development of Republic of Serbia under Project No. 171020.

REFERENCES

- [1] M. V. Ammosov, N. B. Delone, and V. P. Krainov, *Sov. Phys. JETP* **64**, 1191 (1986).
- [2] H. Hellmann, *J. Chem. Phys.* **3**, 61 (1935).
- [3] M. Z. Milošević and N. S. Simonović, *Phys. Rev. A* **91**, 023424 (2015).
- [4] Y. K. Ho, *Phys. Rep.* **99**, 1 (1983); A. Buchleitner, B. Grémaud and D. Delande, *J. Phys. B: At. Mol. Opt. Phys.* **27** 2663 (1994).
- [5] J. Avery and J. Avery, *Generalized Sturmians and Atomic Spectra* (Singapore: World Scientific, 2006)

CALCULATIONS OF ELECTRON DETACHMENT RATES FOR HYDROGEN NEGATIVE ION IN ELECTRIC FIELD

M. Z. Milošević¹ and N. S. Simonović²

¹*Faculty of Science and Mathematics, University of Niš, Višegradska 33,
18000 Niš, Serbia*

²*Institute of Physics, University of Belgrade, P.O. Box 57, 11001
Belgrade, Serbia*

Abstract. The lowest state energies and detachment rates for the hydrogen negative ion at different strengths of the applied electric field are determined by solving the eigenvalue problem of the full two-electron Hamiltonian and alternatively by using single-electron models. It is demonstrated that the single-electron description of the lowest state of ion, that is a good approximation for weak fields, fails in over-the-barrier detachment regime and partially in the tunnelling regime. An accurate formula for the detachment rate is determined by fitting the two-electron data to the expression estimated using single-electron descriptions.

1. INTRODUCTION

The hydrogen negative ion (H^-) is a weakly bound system which has only one bound state – the ground state. This is a consequence of the fact that the interaction between electrons in this ion, unlike to helium atom and two-electron positive ions, is comparable in magnitude to that between the nucleus and electrons. The binding energy of H^- is $E_B = 0.75420 \text{ eV}$ (0.027716 a.u.) [1]. The electron detachment from H^- in electric field can be described by the quantum-mechanical tunnelling. A strong field distorts the potential of atomic residue forming a potential barrier through which the electron can tunnel. At a sufficiently strong field, however, the barrier is suppressed below the energy of the bound state and over-the-barrier detachment (OBD) occurs. Perelomov, Popov and Terentev (PPT) were the first who derived the correct tunnelling rate formula for an arbitrary atom [2]. For negative ions in the ground state this formula reduces to

$$w = C_{\kappa}^2 \frac{F}{\kappa} \exp\left(-\frac{2\kappa^3}{3F}\right), \quad (1)$$

where F is the field strength and $\kappa = (2E_B)^{1/2}$. The coefficient in the pre-exponential factor determined from Hartree-Fock calculation for H^- has the value $C_\kappa = 1.15$. For stronger fields, however, the formula significantly overestimate the exact rates (see Fig. 1(b)). One of the goals in this paper is to determine exact rates for this ion and find an adequate empirical formula.

2. TWO-ELECTRON DESCRIPTION

The Hamiltonian describing the full dynamics of two electrons of H^- in a static electric field F reads (in atomic units)

$$H = -\frac{1}{2}(\Delta_1 + \Delta_2) - \frac{1}{r_1} - \frac{1}{r_2} + \frac{1}{r_{12}} - F(z_1 + z_2), \quad (2)$$

where \mathbf{r}_i and $-\frac{1}{2}\Delta_i$ are the position and the kinetic energy operator of the i -th electron, respectively, and $r_{12} = |\mathbf{r}_1 - \mathbf{r}_2|$. Due to presence of the barrier all eigenstates of (2) have the resonant character when $F \neq 0$, including the lowest which is an exact bound state for $F = 0$. The width Γ of the lowest state determines the electron detachment rate $w(F) = \Gamma(F)/\hbar$ (hereafter we set $\hbar = 1$ and use atomic units). The eigenstates of (2) are calculated numerically using the complex rotation (scaling) method [3]. The calculations are performed in the basis whose elements are the symmetrized products of Sturmian functions [4] for each electron. Fig. 1 shows the lowest state energies and widths of H^- at different strengths of the applied electric field obtained using this method, together with the results obtained using the single-electron description that will be considered in the next section. It can be seen from Fig. 1(a) that for weak fields the lowest state energy $E(F)$ decreases by increasing the field strength according to the Stark shift expansion formula $\Delta E \equiv E(F) - E(0) = -\alpha F^2/2! - \gamma F^4/4! - \dots$. Here $E(0) = -0.5 + E_B$ is the ground state energy of the free ion, whereas $\alpha = 206$ and $\gamma = 8.03 \cdot 10^7$ are the corresponding values for the dipole polarizability and the second dipole hyperpolarizability. The width $\Gamma(F)$, on the other hand, grows rapidly with F (Fig. 1(b)). It is consistent with earlier *ab initio* calculations obtained by a different method [5].

3. SINGLE-ELECTRON DESCRIPTION

The configuration of the ground state of H^- suggests a one-electron description where the outer (loosely bound) electron moves in a short-range potential $V(\mathbf{r})$ describing the attraction by the neutral atomic residue [1]. Then, in the presence of an electric field F the outer electron may be considered as moving in the total potential $V_{\text{tot}} = V(\mathbf{r}) - Fz$. $V(\mathbf{r})$ is usually calibrated to give the value $-E_B$ for the lowest energy level $\epsilon(F)$ at $F = 0$. When $F \neq 0$ the total potential has a potential barrier that explains the resonant character of states. The saddle point of the barrier is located at

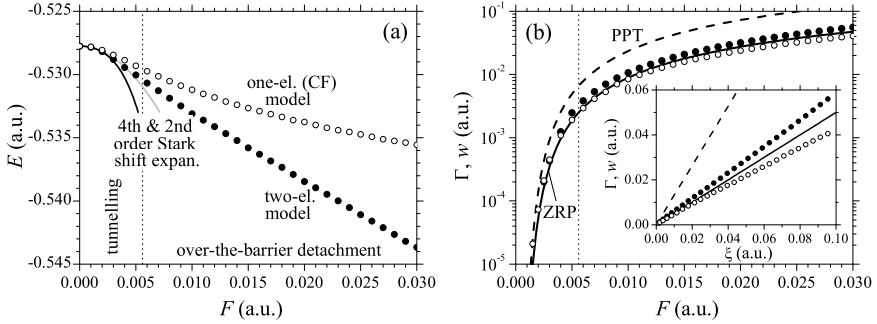


Figure 1. (a) The lowest state energy E and (b) width Γ (detachment rate w) of H^- as functions of the strength of applied electric field F . The full and open circles denote the results obtained numerically using the full two-electron and the CF single-electron (Eq. (3)) model, respectively. The full gray and black lines in part (a) represent the lowest state energy $E(F)$ obtained using the 2nd and the 4th order expansion for the Stark shift, respectively. The dashed and the full line in part (b) show the rate $w(F)$ given by the PPT and the ZRP theory (Eq. (1) with $C_\kappa^2 = 1.32$ and 0.5), respectively. The inset shows the same rates as functions of the variable ξ .

the z -axis. Its position $\mathbf{r}_{\text{sp}} = (0, 0, z_{\text{sp}})$ and height $V_{\text{sp}} = V_{\text{tot}}(\mathbf{r}_{\text{sp}}; F)$ for a given F can be determined from the rule $(\partial V_{\text{tot}}/\partial z)_{x=y=0} = 0$. The field strength F_{S} that separates the tunnelling and OBD regimes is defined by the condition $\epsilon(F_{\text{S}}) = V_{\text{sp}}(F_{\text{S}})$.

The simplest short-range potential that can be used to describe the dynamics of a weakly bound electron in negative ions is the so-called zero-range potential (ZRP) $V(\mathbf{r}) = -a\delta(\mathbf{r})$ ($a > 0$) [6]. This potential supports only one bound state with the binding energy $E_{\text{B}} = a^2/2$. The eigenvalue problem of the single-electron Hamiltonian with $V_{\text{tot}} = -a\delta(\mathbf{r}) - Fz$ admits for weak fields a solution in a closed analytical form [6]. The lowest state energies and widths are represented respectively by the Stark shift expansion with the polarizability $\alpha = 1/(16E_{\text{B}}^2) \approx 81.5$ and by Eq. (1) with $C_\kappa^2 = 1/2$. Hence, the PPT and ZRP rate formulae differ only by the value of C_κ .

A more realistic single-electron model of H^- consists of the loosely bound electron moving in an effective potential which is the sum of a short-range potential and the polarization term. A widely used potential of this type is the Cohen-Fiorentini (CF) potential [7]

$$V = -\left(1 + \frac{1}{r}\right)e^{-2r} - \frac{\alpha_{\text{H}}}{2r^4}e^{-r_0^2/r^2}, \quad (3)$$

where $\alpha_{\text{H}} = 9/2$ is the polarizability of the hydrogen atom and the parameter $r_0 = 1.6$ provides the correct value for the binding energy. The value of F that separates the tunnelling and OBD regimes obtained using the potential (3) is $F_{\text{S}} = 0.0056$. The calculations were performed using the complex rotation method [3] and the Sturmian basis [4]. At low values of

F the energies ($E(F) = \epsilon(F) - 0.5$ a.u.) obtained by the CF model approximately agree with the two-electron results (see Fig. 1(a)). At stronger fields, however, the difference between these results increases, particularly in the OBD area. The rates determined using the CF model agree with the two-electron results approximately for $F < F_S/2$, see Fig. 1(b). Otherwise the single-electron calculations underestimate the two-electron results.

4. CONCLUSIONS

Deviations of the energies and detachment rates obtained using the single-electron description of the hydrogen negative ion in electric field from those obtained using the full two-electron description indicate that the single-electron picture in principle is not valid at stronger fields. This fact may be explained by the change of form of the two-electron wave function at different field strengths [8]. As we have seen in Sec. 3 a difference between the detachment rate formulae for H^- obtained from the ZRP model and the PPT theory is only in the constant in the pre-exponential factor (that is 0.5 and 1.32, respectively). The rates obtained using the two-electron model also fit well to Eq. (1). Hence, the optimal value for C_κ can be estimated from these data. For this purpose we express w in terms of the variable $\xi = (F/\kappa) \exp(-2\kappa^3/(3F))$. Then Eq. (1) reduces to the linear dependence $w = C_\kappa^2 \xi$ (see the inset in Fig. 1(b)). The linear fit of the two-electron data for $F < F_S$ and for $F > F_S$ gives $C_\kappa^2 = 0.65$ and 0.58 , respectively.

Acknowledgements

This work is supported by the COST Action CM1204 (XLIC). N. S. S. acknowledges support by the Ministry of education, science and technological development of Republic of Serbia under Project 171020.

REFERENCES

- [1] T. Andersen, Phys. Rep. **394**, 157 (2004).
- [2] A. M. Perelomov, V. S. Popov and M. V. Terent'ev, Sov. Phys. JETP **23** 924 (1966).
- [3] Y. K. Ho, Phys. Rep. **99**, 1 (1983); A. Buchleitner, B. Grémaud and D. Delande, J. Phys. B: At. Mol. Opt. Phys. **27** 2663 (1994).
- [4] J. Avery and J. Avery, *Generalized Sturmians and Atomic Spectra* (Singapore: World Scientific, 2006)
- [5] S. I. Themelis and C. A. Nicolaides, Phys. Rev. A **49**, 3089 (1994).
- [6] Yu. N. Demkov and V. N. Ostrovskii *Zero-range potentials and their applications in atomic physics* (Plenum Press, New York, 1988)
- [7] J. S. Cohen and G. Fiorentini, Phys. Rev. A **33**, 1590 (1986).
- [8] M. Z. Milošević and N. S. Simonović, accepted for publication in J. Phys. B: At. Mol. Opt. Phys. (2016).

DOUBLE DIFFERENTIAL CROSS SECTIONS OF ACETYLENE AT 350 eV BY ELECTRON IMPACT

Zehra Nur Ozer* and Umran Atmaca

*Afyon Kocatepe University, Physics Department, e-COL Laboratory,
Afyonkarahisar, Turkey*

Abstract. We will present the experimental double differential cross sections (DDCSs) for electron impact ionization of C_2H_2 at different impact electron energies. Data were taken by fixing the incident electron energy at 350 eV and then measuring the secondary electron spectrum at 10^0 intervals.

1. INTRODUCTION

Electron collision properties of C_2H_2 take more attention in planetary and commentary atmosphere studies. C_2H_2 is one the smallest, symmetric polyatomic molecules and the smallest member of the hydrocarbon family. Its interaction with electrons, photons and ions are very important and the knowledge of electron impact ionization cross sections for this molecule is useful in understanding the fundamental processes of applications of hydrocarbons in molecular chemistry, astrophysics and plasma physics. The data regarding the ionization cross sections would prove all important also for theoreticians on developing new models of polyatomic molecules.

Information about ionizing collision can be obtained by measuring double differential cross sections (DDCSs) for detection of one of the outgoing electrons. DDCSs due to the electron impact on C_2H_2 have been measured only by Opal et al. [1] at high electron impact energy (500 eV) as we know. Due to the experimental difficulties, there are limited numbers of experimental studies on the electron impact ionization cross sections of C_2H_2 molecule in the literature. However, there are several studies on the differential cross sections (DCSs) of this molecule. Some of the recent joint theoretical and experimental studies of electron scattering on this molecule were published by Iga et al. [2] at intermediate energies and by Gauf et al. for low energies [3]. The ionization dynamics of the innermost orbital of C_2H_2 were measured using (e,2e) experiments by Avaldi et al. [4]. This work present the first and only cross sections performed by (e,2e) experiments at intermediate incident energy and on the deepest orbital of this molecule.

In this study, we will present the experimental DDCSs for electron impact ionization of C_2H_2 at different impact electron energies. Data were taken by fixing the incident electron energy and then measuring the secondary electron spectrum at 350 eV at 10° intervals and at different detection energies.

2. EXPERIMENT

We have measured the DDCSs of C_2H_2 molecule for 350 eV electron impact energy and 30° to 130° angular range. The apparatus originally developed for coincidence measurements meaning to measure triple differential cross sections (TDCSs). The experimental set up consists of an electron gun, two hemispherical electron energy analyzers, Faraday cup and target gas line. The experimental set up is described in previous studies in detail [5-7]. Besides, using the same apparatus but disabling the coincidence circuit DDCS measurements can be taken. In DDCS experiments, the electron beam is directed into a gas target perpendicular to the scattering plane and one of the outgoing electrons after ionization event is analyzed by hemispherical electron energy analyzer and detected by a channel electron multiplier (CEM). DDCS spectrum can be obtained by measuring of energy and angular distributions of one of the two outgoing electrons by a detector (CEM).

3. RESULTS AND DISCUSSIONS

In this work, for electron impact ionization of C_2H_2 have been measured in a crossed beam experiment and angular dependence of cross sections for detected electrons are presented. DDCS results at 350 eV incident electron energy and at detected electron energies of 125 eV and 250 eV is given in Figure 1. All counting rates are normalized to unity and no other corrections have been made.

It is clear from the figure that the angular position of the binary peak changes if the energy of the outgoing electron is increased. These types of studies are very important in collision physics because of the importance of their cross sections in many applications. These cross sections are used as input parameters to modeling codes for various purposes and last but not least supporting theoretical calculations to the come extent.

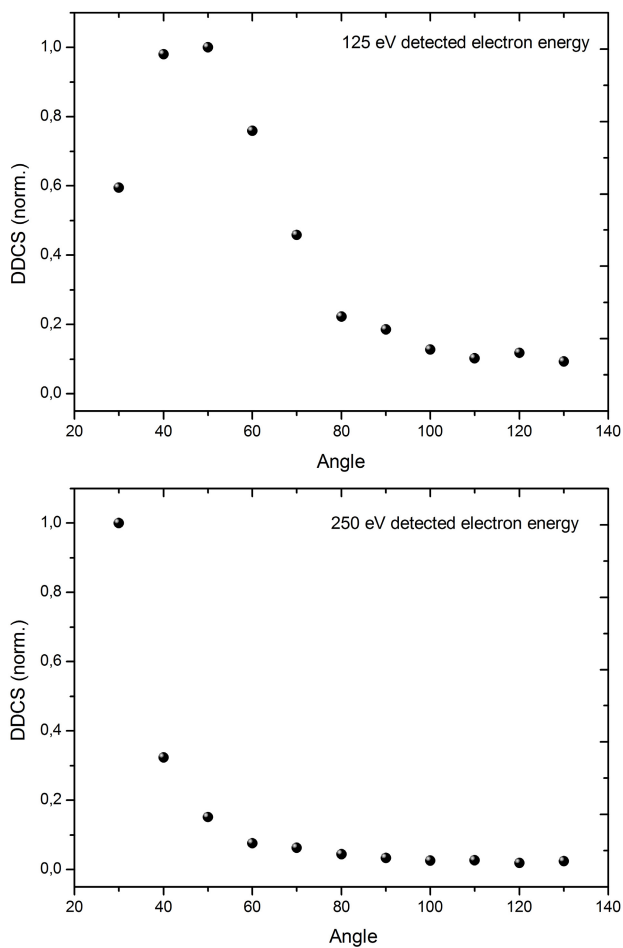


Figure 1. Experimental DDCS results obtained at incident energy of 350 eV. Angular distributions for ejected electron energy of 125 eV for a) CH₄ [6], b) CO₂ at 25° to 130° scattered electron angles.

To the best of our knowledge DDCSs data for C₂H₂ molecule at this energy level is presented for the first time in the literature. The experimental data is planned to use in theoretical analysis by collaboration with theoreticians that work on this molecule.

Acknowledgements

This work is supported by BAPK the grant NO: 15.HIZ.DES.131 and 15.FEN.BİL.15.

REFERENCES

- [1] C. B. Opal, W. K. Peterson and E. C. Beaty, *J. Chem. Phys.* 55, 4100 (1971).
- [2] I. Iga, M. Lee, P. Rawat, L. M. Brescansin, L. E. Machado, *European Physical Journal D-Atomic, Molecular, Optical and Plasma Physics*, 31(1), 45-51 (2004).
- [3] A. Gauf, C. Navarro, G. Balch, L. R. Hargreaves, M. Khakoo, C. Winstead, V. Mckoy, *Phys. Rev. A*, 87(1), 012710 (2013).
- [4] L. Avaldi, R. Camilloni, G. Stefani, *Phys. Rev. A*, 41(1), 134 (1990).
- [5] M. Yavuz, Z. N. Ozer, M. Ulu, C. Champion, M. Dogan, *The Journal of chemical physics*, 144(16), 164305, (2016).
- [6] M. Dogan, M. Ulu, Z. N. Ozer, M. Yavuz, and G. Bozkurt, *Journal of Spectroscopy*, (2013).
- [7] Z. N. Ozer, H. Chaluvadi, M. Ulu, M. Dogan, B. Aktas, and D. Madison, *Phys. Rev. A* 87, 042704 (2013).

ELECTRON IMPACT IONIZATION OF CARBON CONTAINING MOLECULES

Zehra Nur Ozer* and Mevlut Dogan

*Afyon Kocatepe University, Physics Department, e-COL Laboratory,
Afyonkarahisar, Turkey*

Abstract. We have measured the ionization cross sections of CO₂ and CH₄ molecules at different impact energies according to angular dependence of secondary electrons that are produced after an ionization event. We will present the current experimental cross section data obtained in e-COL laboratory for these molecules at intermediate electron impact energies during the conference.

1. INTRODUCTION

Carbon containing molecules are present in planetary atmospheres and interstellar media and they play an important role in chemistry of environment. Carbon is used in the chemical vapour deposition industry and in the production of reactive species in plasmas. The phrase of carbon based life or organic molecules define that carbon atoms form the backbone of almost all the important biological molecules floating around in our bodies. Electron impact processes with carbon and as well as carbon based molecules play important roles in various applied sciences. Carbon atoms form a number of interesting simple molecules like CO₂, CH₄,...etc. Though it is no wonder then that carbon based molecules are the best suited to collision studies. Measurements have been made for energy and angular distributions of electrons of these two molecules by electron impact from the beginning dates of collision physics. However, very few results of the ionization cross sections are presented for tri atomic or tetra atomic molecules involving CO₂ and CH₄ targets.

To provide information on ionization of these molecules and develop viable models of the processes, electron scattering cross sections of such targets are needed. CO₂ has an important role in applied fields of astrophysics, plasma chemistry, and environment and also in life. Some of the recent work of the ionization cross sections for this molecule is published in [1-4]. On the other hand, CH₄ is also significant molecule for atmospheres of some planets such as Uranus, and Neptune. Ionization cross section data is essentially needed for this molecule to model the ionosphere composition and also for electron energy deposition studies. Recent published papers on the ionization of CH₄ showed

fairly good agreement between theory and experiment but disagreement at low ejection energies [5-6].

We can summarize the work on these two molecules in the literature in the following way; although significant progress has been made both in the experimental studies and theoretical approaches for electron impact studies, the agreement between experimental results and theoretical calculations is unluckily unsatisfying. Thus, to obtain large variety of the collision cross section data, we have measured the ionization cross sections of CO₂ and CH₄ molecules at different impact energies according to angular dependence of secondary electrons that are produced after an ionization event. We will present the current experimental cross section data for these molecules at different electron impact and ejected energies during the conference.

2. EXPERIMENTAL SET UP

We have used an electron impact spectrometer at low and intermediate incident electron energies and with a constant energy resolution of analyzers around 1 eV. The experimental apparatus has previously been described in detail [6-9]. The apparatus consists basically of two hemispherical deflector electron energy analyzers with channel electron multipliers (CEMs), a Faraday cup, a target gas line and an electron gun in the vacuum chamber and the apparatus is completed with control units and electronics from outside of the vacuum system. The background pressure in the vacuum chamber was about $6 \cdot 10^{-6}$ mbar with the gas beam turned on. The electron beam was monitored by Faraday cup and ≈ 2 μ A of measured beam kept constant during the measurements. The electrons produced from a tungsten filament are collimated to 2 mm beam diameter in the interaction region and then crosses with the molecular gas target beam.

In the ionization cross section measurements, the scattered and ejected electrons are detected by electron energy analyzers and energy and angular distribution of outgoing electrons are measured. For every single ionization spectra, incident and ejected electrons energies are fixed and only angular distribution of outgoing electron counts were measured. These type cross section results are presented as double differential cross sections (DDCSs) in the literature.

3. RESULTS AND DISCUSSIONS

DDCSs have been measured after ionization electron collisions with CH₄ and CO₂ molecules at intermediate electron energies using a conventional electron spectrometer. An electron energy analyzer is used to measure angular distributions of ejected electrons with emission angles of 30° to 130°.

An example spectrum of DDCSs for CH_4 and CO_2 is given in Figure 1 at 350 eV incident electron energy and at 125 eV ejected electron energy. These curves are obtained by measuring the angular distributions of electrons scattered by the target at fixed ejected electron energies and counting rate for particles scattered by these targets gases in the vacuum chamber. All counting rates normalized to unity when the graphs are presented.

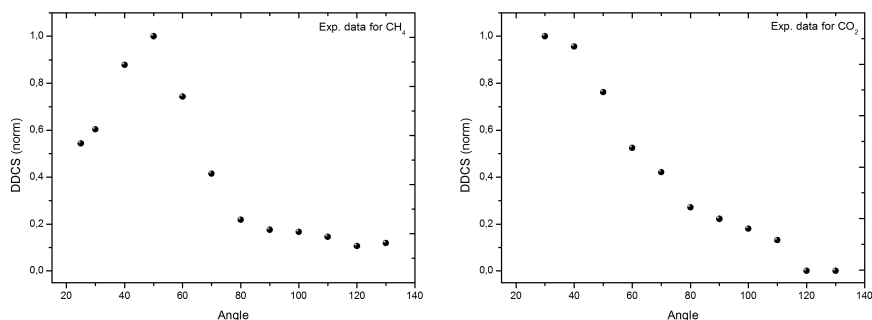


Figure 1. Experimental DDCS results obtained at incident energy of 350 eV. Angular distributions for ejected electron energy of 125 eV for a) CH_4 [6], b) CO_2 at 25° to 130° scattered electron angles.

It was found that the outgoing electrons may be called as fast electrons that are scattered in the forward direction and slow electrons or slow electrons which are distributed isotropically into all angles.

These type of studies have an important impact on both understanding of the nature of molecular systems and on the evolution of quantum mechanics. On the other hand, the development of theoretical approximation is clearly needed for molecular targets. Collaboration with theoreticians are being done for further studies on these molecules.

Acknowledgements

This work is supported by BAPK the grant No 14.FENED.06, 15.FEN.BIL.15 and 15.FENED.03.

REFERENCES

- [1] **Z. N. Ozer, E. Ali, M. Dogan, M. Yavuz, O. Alwan, A. Naja, D. Madison**, Physical Review A, 93(6), 062707(2016).
- [2] O. Alwan, O. Chuluunbaatar, X. Assfeld, A. Naja and B. Joulakian. J. Phys.B: At. Mol. Opt. Phys. 47, 225201 (2014).
- [3] K. Anzai, H. Kato, M. Hoshino, H. Tanaka, Y. Itikawa, L. Campbell, M. J. Brunger, S. J. Buckman, H. Cho, F. Blanco, G. Garcia, P. Limão-Vieira, and O. Ingólfsson, Eur. Phys. J. D 66, 36 (2012).
- [4] A. Lahmam-Bennani, E. M. Staicu Casagrande and A. Naja , J. Phys. B: At. Mol. Opt. Phys. 42, 235205 (2009).
- [5] M. Yavuz, Z. N. Ozer, M. Ulu, C. Champion, M. Dogan, The Journal of chemical physics, 144(16), 164305, (2016).
- [6] M. Yavuz, N. Isik, Z. N. Ozer, M. Ulu, M. Dogan, M. Sahlaoui and Bouamoud M. Can. J. Phys. 92(12) 1676-1680, (2014).
- [7] M. Dogan, M. Ulu, Z. N. Ozer, M. Yavuz, and G. Bozkurt, Journal of Spectroscopy, (2013).
- [8] H. Chaluvadi, Z. N. Ozer, M. Dogan, C. Ning, J. Colgan, and D. Madison, J. Phys.B: At. Mol. Opt. Phys. 48, 155203 (2015).
- [9] Z. N. Ozer, H. Chaluvadi, M. Ulu, M. Dogan, B. Aktas, and D. Madison, Phys. Rev. A 87, 042704 (2013).

OSCILATOR STRENGTHS OF HYDROGEN-LIKE IONS IN QUANTUM PLASMAS

Y. Y. Qi¹, J. G. Wang² and R. K. Janev³

¹*School of Mathematics & Physics and Information Engineering,
Jiaxing University, Jiaxing 314001, P.R. China*

²*Data Center for High Energy Density Matter, Institute of Applied Physics and
Computational Mathematics, P. O. Box 8009, Beijing 100088, P. R. China.*

³*Macedonian Academy of Sciences and Arts, P. O. Box 428, 1000 Skopje,
Macedonia*

Abstract. The properties of bound-bound transitions in a hydrogen-like ion embedded in dense quantum plasmas are investigated. The oscillator strengths, and radiative transition probabilities are calculated for the Lyman transitions up to $n=5$ as function of the screening parameter in electron-nucleus interaction. Comparison is made of these quantities with those of a hydrogen-like ion in weakly coupled Debye plasmas.

1. INTRODUCTION

Quantum plasmas are characterized with temperatures lower than the electron Fermi temperature $T_F (= \hbar^2 (3\pi^2)^{2/3} n_e^{2/3} / 2m_e)$ and electron densities n_e such that that de Broglie wavelength $\lambda_B = \hbar / m_e v_{th}$ (m_e, v_{th} and \hbar being the electron mass, thermal velocity and the reduced Planck constant) is close to or larger than the average inter-particle distance (i.e. $n_e \lambda_B^3 \geq 1$). Quantum effects (such as tunneling, quantum diffraction, etc.) start to play important role in these plasmas. Quantum plasmas are met in metals, nanoscale structures (such as nanowires, quantum dots), semiconductor devices and in compact astrophysical objects (e.g. neutron stars, white dwarfs). The interaction between a positive charge Z and an electron in such plasmas is described by the modified Debye-Hückel screening potential [1-3]

$$V(r) = -\frac{Ze^2}{r} \exp(-r/K) \cos(r/K) \quad (1)$$

where[3] $K = \sqrt{2} / k_q$ is the screening length, $k_q = (2m_e \omega_{pe} / \hbar)^{1/2}$ is the quantum wavenumber and ω_{pe} is the electron plasma frequency. Debye-Hückel potential differs from the potential (1) only by the absence of the cosine factor in (1) and by the different screening length $D = (k_B T_e / 4\pi e^2 n_e)^{1/2}$. It describes the charged -particle interaction in hot weakly coupled classical plasmas.

2.BASIC PROPERTIES OF POTENTIAL (1)

Since the potential (1) decreases faster than $-r^{-2}$ when $r \rightarrow \infty$, for any finite value of K it can support only a finite number of bound state, implying that with the decrease of K the energy of a bound nl state decreases and at certain critical value K_{nl} the state becomes unbound. Also, under the scaling transformations $\rho = Zr, \kappa = ZK, \varepsilon_{nl}(\kappa) = E_{nl}(Z, K) / Z^2$ the radial Schrödinger equation is transformed into the one for the hydrogen atom. We note that the Debye-Hückel potential has the same properties. In Fig. 1 we show the dependences of scaled binding energies of $1s, 2l$ and $3l$ states of hydrogen-like ion as function of scaled screening parameter $\lambda = 1 / \kappa$. They are compared with those in the Debye-Hückel potential for which $\lambda = 1 / ZD$. The decrease of binding energy of nl states with increasing the screening strength is much faster in the quantum plasmas (QP) than in the weakly coupled classical plasmas (WCP). The critical screening strengths of these states are also indicated in the upper axis of the figure.

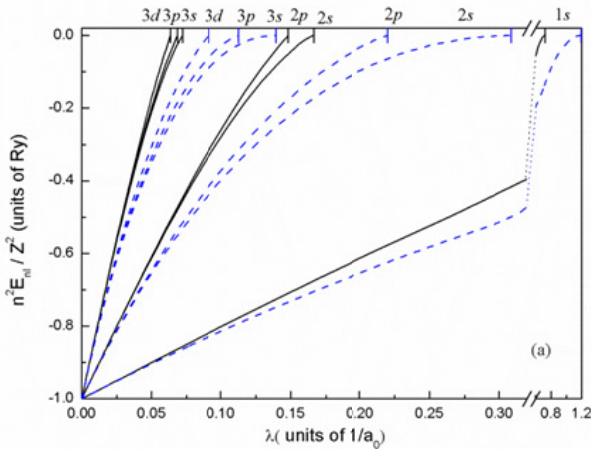


Figure 1. Scaled energies of $n \leq 3$ states of hydrogen-like ion as function of screening parameter in QP (solid lines) and WCP (dashed lines) plasmas.

3. OSCILLATOR STRENGTHS AND RADIATIVE TRANSITION PROBABILITIES

The oscillator strength for the $|nl\rangle \rightarrow |n'l'\rangle$ transition is given by (in atomic units)

$$f_{nl,n'l'}(\kappa) = \frac{2\omega_{nl,n'l'}}{3} \frac{(l+1)}{(2l+1)} \left| \langle P_{n'l'} | \rho | P_{nl} \rangle \right|^2 \quad (2)$$

where $\omega_{nl,n'l'} = \varepsilon_{n'l'} - \varepsilon_{nl}$ is the transition frequency and P_{nl} , $P_{n'l'}$ are the radialelectron wave functions. The wave functions and energies of bound states were obtained by solving the radial Schrödinger equation by the fourth-order symplectic integration scheme. (For details see Ref. [4]). The absorption oscillator strengths for the $1s \rightarrow np$ transitions are shown in Fig.2 as function of the screening parameter

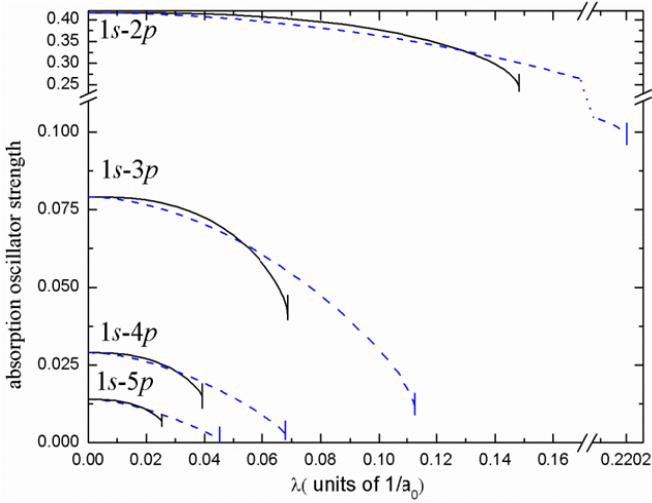


Figure 2. Absorption oscillator strengths $f_{1s,np}$ ($n \leq 5$) for the Lyman series of hydrogen-like ion as function of screening parameter λ in QP (solid lines) and WCP (dashed lines).

The decrease of the oscillator strengths with increasing the screening parameter in the potential reflects the increase of transition frequency $\omega_{nl,n'l'}$ (cf. Eq. (2) and Fig. 1)

The radiative decay probability $A_{n'l',nl}(Z,K)$ for the transition $|n'l'\rangle \rightarrow |nl\rangle$ in a hydrogen-like ion in quantum plasmas can be expressed in terms of

hydrogen atom radiative transition probability $A_{n'l',nl}(\kappa)$ with the potential (1) as (in atomic units)

$$A_{n'l',nl}(Z,K) = Z^4 A_{n'l',nl}(\kappa), \quad A_{n'l',nl}(\kappa) = 2 \frac{2l'+1}{2l'+1} \alpha^3 \omega_{nl',n'l'}^2(\kappa) f_{nl',n'l'}(\kappa) \quad (3)$$

where α is the fine structure constant. The scaled radiative transition probabilities for the $np \rightarrow 1s$ ($n \leq 5$) transitions as function of screening parameter are shown in Fig.3 in quantum (solid lines) and weakly coupled (dashed lines) plasmas.

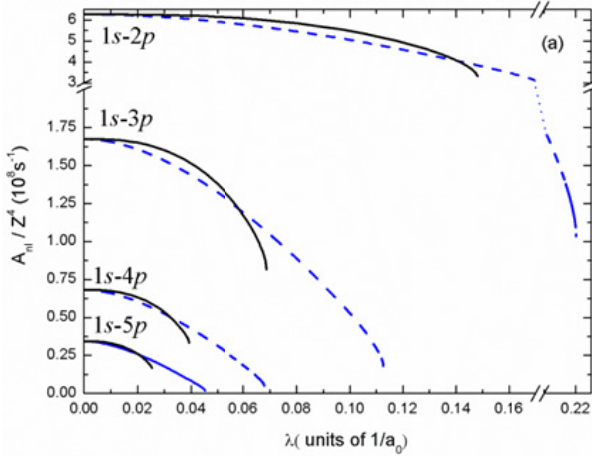


Figure 3. Scaled radiative transition probabilities of hydrogen-like ion as function of screening parameter λ for $np \rightarrow 1s$ ($n \leq 5$) transitions.

REFERENCES

- [1] V.L. Bonch-Bruevich and V.B. Glasko, Sov. Phys. Doklady **4**, 147 (1959)
- [2] G.L. Hall, Phys. Chem. Solids **23**, 1147 (1962)
- [3] P.K. Shukla and B. Eliasson, Phys. Lett. **A372**, 2897 (2008)
- [4] Y.Y. Qi, J.G. Wang and R.K. Janev, Phys. Rev. A **78**, 062511 (2008)

TOTAL AND PARTIAL CROSS SECTIONS FOR ELECTRON IMPACT IONIZATION OF N₂

M. M. Vojnović¹, M. M. Ristić², M. P. Popović¹ and G. B. Poparić¹

¹*University of Belgrade, Faculty of Physics, Belgrade, Serbia*

²*University of Belgrade, Faculty of Physical Chemistry, Belgrade, Serbia*

e-mail: Goran_Poparic@ff.bg.ac.rs

Abstract. This paper presents preliminary results obtained by using a new trochoidal electron spectrometer with ion mass analyzer, developed in our laboratory. High resolution electron beam, produced by use of the trochoidal electron spectrometer is crossed at right angles with a beam of molecules. Charged particles produced by simple ionization of nitrogen and ion fragments from dissociative ionization are separated by means of a time-of-flight technique. Description of the instrument, principles of operation and experimental characteristics are described here in detail.

1. INTRODUCTION

Electron impact ionization of molecules provides useful information on molecular structure and enables determination of parameters needed for description of gas discharges related to astrophysical and atmospheric phenomena, as well as for practical applications in various plasma technologies.

In our previous work a double trochoidal electron spectrometer [1] has been used to measure the ratio of the differential cross sections at 0° and 180° for electron impact excitation of molecules. Electron beam modulation and time of flight technique, in the pulse mode operation, enabled the separation of contributions of forward and backward scattered electrons. The new electron spectrometer design relies on a similar configuration. The energy resolution of the electron beam in this electron spectrometer is about 50meV.

In a new experiment, the time-of-flight (TOF) mass analyzer technique is applied to select produced ion species, which are directed to the electrostatic lens and subsequently to the channeltron detector.

The design of TOF mass analyzers has been changing lately to fulfill the requirements of various technology applications, e. g. in vacuum technology, fast switching of high voltage DC signal, lasers devices, mass sampling of large molecular and ionic species, studies of bio-organics etc. [2].

This experimental device is primarily designed to enable measurements of relative total cross sections for electron-impact ionization of molecules, as well as determination of partial cross sections inferred from mass spectra.

2. EXPERIMENTAL SETUP

Schematic of the experimental setup is presented in the Figure 1 [3]. The electron beam is produced by a directly heated hair-pin tungsten filament. It is collimated by using homogeneous axial magnetic field, generated by a pair of Helmholtz coils that surround the vacuum chamber of the spectrometer. Magnetic field keeps the electrons along the field direction, but it also enables energy selection of the electron beam. For the latest purpose - trochoidal electron monochromator (TEM) is used.

Apart from monochromator, the electron spectrometer consists of an analyzer and a collision chamber, where electrons are crossed with the gas beam. The role of additional electrodes is mainly focusing of the surfaces, but some are used to eliminate stray secondary electrons from the surfaces.

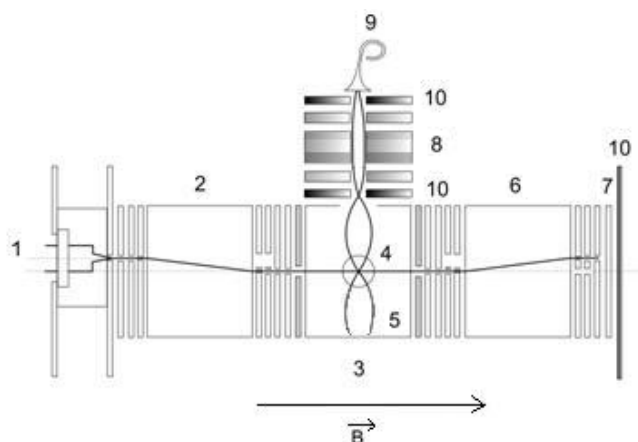


Figure 1. Experimental scheme. Cathode (1), monochromator with electron optics (2), collision chamber (3), gas introduction (4), repelling electrode (5), electron energy analyzer with electron optics (6), collecting electrode (7), ion lenses (8), channeltron (9), carriers (10). (Electron and ion beam trajectories are presented by full lines.)

Electrons are produced by thermoelectron emission from a filament (1). The extraction electrodes pull the electron beam to the monochromator (2). Electric field, established between electrodes of the dispersion element of the monochromator and set perpendicular to the electron path and thereby to magnetic field lines, bends the beam trajectory to the exit aperture. Electrons are then accelerated to the collision volume (3), defined by two pair of electrodes which are at the ground potential. A beam of gas molecules is introduced (4) in this volume, at right angles to the direction of the electron beam. After the

collision volume, electrons continue through the analyzer (6) to the anode (7). The analyzer is mainly used as a Faraday cage, but also for resolution testing.

In a short time interval (about a few tens of ns) a positive potential is applied to an electrode behind the monochromator to enable the electron beam. After this time interval a high voltage pulse of +250 V is applied to the electrode of collision volume (5) to push away the created ions to the ion lens system (8) and then to the entrance of detector (9) with a potential of -2 kV. The ion optics consists of three electrodes for ion focusing. A channel electron multiplier is used for detection of ion fragments. Measured ion flight-time is converted to analog voltage pulse by means of time-to-amplitude converter (TAC) device. In this way, the ion fragments are mass-separated since ions with different mass-to-charge ratio have different flight-times. This technique of mass spectrometry is known as the time-of-flight technique.

The present experiment is suitable for positive ions detection, but negative ions could be detected with a slight adaptation. The possibility of the negative charged ions detection relies on the advantage of the axial magnetic field presence that acts strongly upon light electrons, keeping them separated from heavy anions.

3. RESULTS

The first results of this experiment, presented in Figures 2 and 3 [3], are obtained for the nitrogen molecule. Figure 2 shows the comparison of our measured values to data recommended by Itikawa [4], which are based on measurements performed by Straub et al. [5].

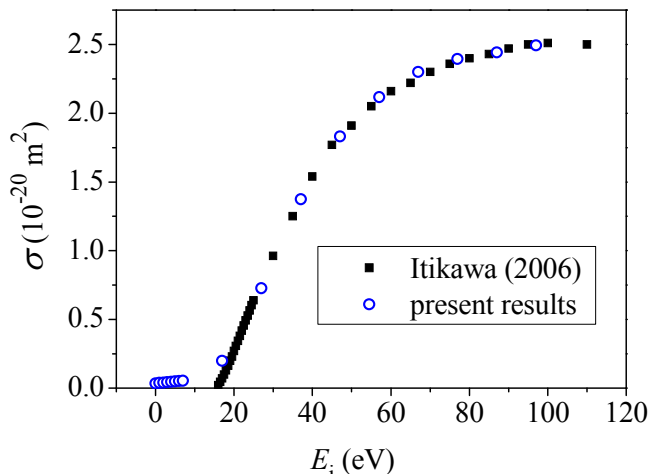


Figure 2. Normalized total ionization cross sections for electron-impact of N_2 as a function of incident electron energy

Our results are normalized to the cross sections of Itikawa [4] at electron energy of 100 eV. Electron energy is also calibrated by results of Itikawa [4]. The

contribution obtained below the threshold for ionization is due to poorly optimized resolution. Overall, an excellent agreement is obtained.

By applying pulses of 500 ns width on the repelling electrode of collision volume, with a repetition rate of 5 kHz, we obtained the TOF spectra presented in the Figure 3. Measurement was performed for the value of incident electron energy of 82 eV. Peaks that belong to N^+ and N_2^+ ions are clearly pronounced and are well separated. The smallest peak originates from the hydrogen arising from the residual gas.

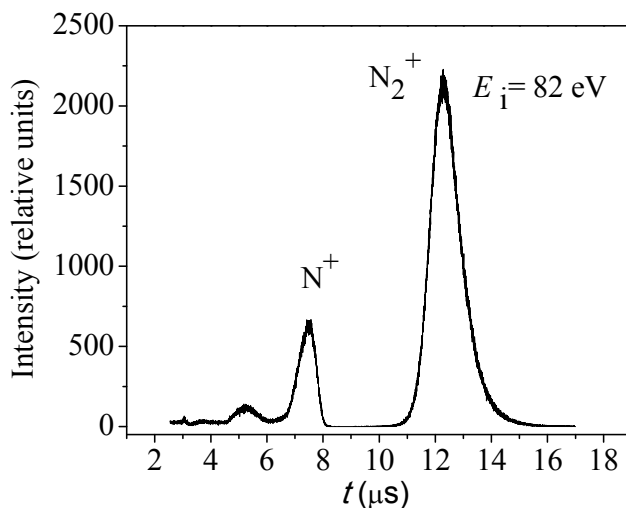


Figure 3. TOF mass spectrum at the value of incident energy of 82 eV.

Acknowledgements

This work is supported in part by the Ministry of Education, Science and Technological Development of the Republic of Serbia, under the contract NO 171016.

REFERENCES

- [1] M. Vikić, G. Poparić, D. S. Belić, *Rev. Sci. Instrum.* **69** 1996 (1998).A.
- [2] Bhowmick, S. C. Gadhari, J. V. Yakhmi, V. C. Sahni “Development of a new high resolution reflection time of flight mass spectrometer”, Technical Physics and Prototype Engineering Division, Bhabha Atomic Research Centre (2005).
- [3] M. M. Vojnović, PhD thesis, University of Belgrade (2016).
- [4] Y. Itikawa, *J. Phys. Chem. Ref. Data* **35** 31 (2006).
- [5] H. C. Straub, P. Renault, B. G. Lindsay, K. A. Smith, and R. F. Stebbings, *Phys. Rev. A* **54**, 2146 (1996).

POLARIZATION OF LYMAN α RADIATION FROM $H^+ + H$ COLLISIONS IN DEBYE PLASMAS

D Jakimovski¹ and R K Janev²

¹*Department of Natural Sciences and Mathematics, Sts. Cyril and Methodius University, Skopje, P. O. Box 162, 1000 Skopje, Macedonia*

²*Macedonian Academy of Sciences and Arts, P. O. Box 428, 1000 Skopje, Macedonia*

Abstract. The polarization of Lyman α radiation resulting from proton-hydrogen atom collisions in hot, dense weakly coupled plasmas is studied by the two-centre atomic orbital close-coupling method. The interaction between charged particles in such plasmas is represented by the Debye-Hückel potential. The degree of Lyman α polarization is calculated for a number of screening lengths of the potential in the 1-200 keV collision energy range and compared with the result for the pure Coulomb interaction. The large differences observed between the polarization values in the plasma screened and unscreened Coulomb interaction cases are explained in terms of properties of Debye-Hückel potential.

1. INTRODUCTION

In the present work we study the polarization of Lyman α radiation produced in proton collisions with ground state hydrogen atom through the processes



taking place in a hot, dense weakly coupled plasma in which the interaction between a positive charge Z and an electron is adequately described by the Debye-Hückel potential (in atomic units) [1]

$$V(r) = -\frac{Ze^2}{r} e^{-r/D} \quad (2)$$

where the screening length D depends on plasma electron temperature and density only.

The linear polarization of Lyman α radiation is given by [2, 3]

$$P = \frac{3(\sigma_{2p0} - \sigma_{2p1})}{7\sigma_{2p0} + 11\sigma_{2p1}} \quad (3)$$

where in the case of $H^+ + H$ collision $\sigma(2p_{0,1})$ is the total cross section for population of magnetic substates $2p_{0,1}$ by the charge exchange and excitation processes (1a) and (1b).

In order to demonstrate the effects of plasma screening on the Lyman α polarization we shall also calculate the polarization in the pure Coulomb case using the same computational method.

In the case of unscreened Coulomb potential, the linear polarization of Lyman α radiation (or the related anisotropy parameter $A_{20} = 6P/(P-3)$ [2, 3]) has been measured in Refs. [4, 5] and theoretically investigated by various coupled channel methods (see, e.g. [5, 6] and references therein).

2. BASIC PROPERTIES OF DEBYE-HÜCKEL POTENTIAL AND COMPUTATIONAL METHOD

The screened potential (2) has two important properties: for any finite value of the screening length D it supports only a finite number of bound states and it lifts the l -degeneracy of energy levels [7]. The first of these two properties implies that with decreasing D the energy of any nl state decreases and at a certain critical value D_{nl}^c it becomes zero (the nl state becomes unbound). The values of D_{nl}^c for the hydrogen atom ($Z=1$) have been calculated in Ref. [7] and for the states with $n \leq 4$ they are given in Table 1.

Table 1. Values of critical screening lengths (in units of a_0) for the states with $n \leq 4$ [7].

| n/l | 0 | 1 | 2 | 3 |
|-------|-------|-------|-------|-------|
| 1 | 0.84 | | | |
| 2 | 3.22 | 4.54 | | |
| 3 | 7.17 | 8.87 | 10.95 | |
| 4 | 12.69 | 14.73 | 17.21 | 20.07 |

In our calculations of cross sections for reactions (1a) and (1b) with the screened and unscreened Coulomb potential, involved in the expression (3) for P , we have employed the two-centre atomic orbital close-coupling (TC-AOCC) method, described in detail elsewhere [8]. In applying this method for description of processes (1a) and (1b) in a Debye plasma with specified screening length D , only the states which remain bound in the potential (2) for that value of D participate in the collision dynamics. We have considered Debye plasmas with screening lengths $D = 6a_0, 9a_0, 12a_0$

and $22a_0$. According to Table 1, for these screening lengths bound in the potential (2) are only the states with $n \leq 2$; (for $D = 6a_0$), the states with $n \leq 2$ plus the $3s$ and $3p$ states (for $D = 9a_0$), all states with $n \leq 3$ (for $D = 12a_0$) and all states with $n \leq 4$ plus the $5s$ state (for $D = 22a_0$). In the TC-AOCC calculations with the unscreened Coulomb interaction we have used an expansion basis that includes all bound states with $n \leq 7$ on both centers plus 176 continuum pseudostates placed on the projectile when calculating the electron capture and on the target when calculating the excitation.

3. RESULTS OF THE CALCULATIONS

The results of our calculations of Lyman α radiation are shown in Figure 1. The result for the pure Coulomb interaction is compared with the experimental data from Refs. [4] and [5]. The difference between the results with screened and unscreened Coulomb interaction is found to be very large. The largest difference appears in the 5-25keV energy range where it increases with decreasing the screening length. The origin of observed differences is the decrease of electron binding energy and the reduction of the number of bound states in the potential when the screening length decreases.

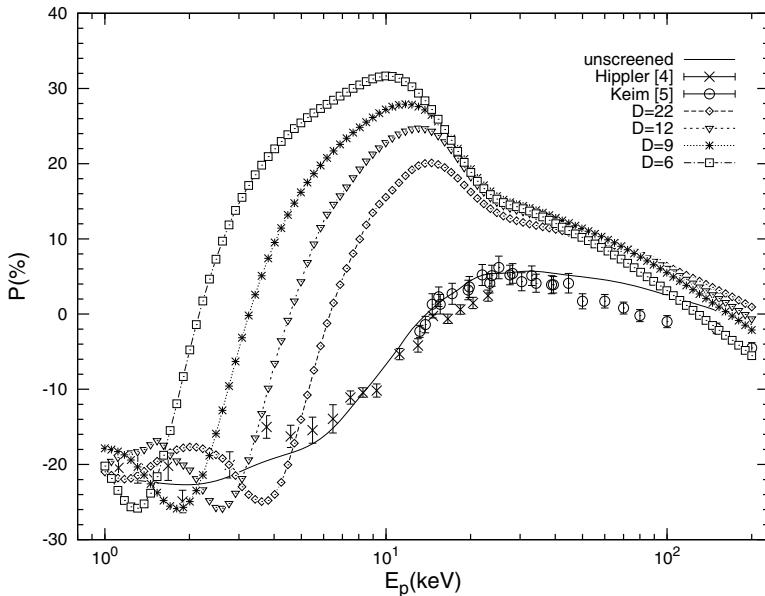


Figure 1. Polarization of Lyman α radiation resulting from $H^+ + H$ collisions in Debye plasmas, for the unscreened and screened Coulomb interaction for a number of screening lengths D (units a_0).

The oscillatory structures in P, observed in the energy region below 4keV, originate from similar oscillations of $2p_{0,1}$ excitation and electron capture cross sections in this energy region, resulting from the coupling of excitation and capture channels. We also note that in the energy region above 25-30keV the capture cross sections rapidly decrease with increasing the energy and the degree of Lyman α polarization is determined dominantly by the $2p_{0,1}$ excitation cross sections.

REFERENCES

- [1] D. Salzman, *Atomic Physics in Hot Plasmas* (Oxford University Press, Oxford, 1998).
- [2] I. C. Percival and M. J. Seaton, *Phil. Trans. R. Soc. A* 251,113 (1958)
- [3] U. Fano and J.H. Macek, *Rev. Mod. Phys.* 45, 553 (1973)
- [4] R. Hippler, H. Madeheine, W. Horbich, H. Kleinpoppen and H. O. Lutz, *Phys. Rev. A* 38, 1662 (1988)
- [5] M. Keim, A. Werner, D. Hasselkamp, K.-H. Schartner, H. J. Lüdde, A. Achenbach and T. Kirchner, *J. Phys. B: At. Mol. Opt. Phys.* 38, 4045 (2005)
- [6] S. K. Avazbaev, A. S. Kadyrov, A. B. Abdurakhmanov, D. V. Fursa and I. Bray, *Rev. A* 93, 022710 (2016)
- [7] F. J. Rogers, H. C. Graboske and D. J. Harwood, *Phys. Rev. A* 1, 1577 (1970)
- [8] W. Fritsch, and C. D. Lin, *Phys. Rep.* 202, 1 (1991)

ELECTRON CAPTURE IN H⁺-H COLLISIONS WITH COSINE-DEBYE-HÜCKEL SCREENED INTERACTION

D. Jakimovski¹ and R. K. Janev²

¹*Faculty of Natural Sciences and Mathematics, Sts Cyril and Methodius University, P.O. Box 162, 1000 Skopje, Macedonia* ²*Macedonian Academy of Sciences and Arts, P.O. Box 428, 1000 Skopje, Macedonia*

Abstract. The electron capture process in proton-hydrogen atom collisions with a cosine-Debye-Hückel screened interaction is studied by employing the two-centre atomic orbital close coupling (TC-AOCC) method. The $n \leq 3$ state-selective capture cross sections have been calculated for a number of representative screening lengths of the potential and compared with the results for the pure Coulomb interaction.

1. INTRODUCTION

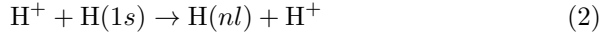
The plasma screening effects on atomic structure and collision processes have been subject to numerous studies in last several decades. Most of these studies have been performed for the weakly coupled classical plasmas in which the interaction between charges is described by the Debye-Hückel potential [1]. In cold, dense plasmas with temperatures lower than the electron Fermi temperature and densities such that de Broglie wavelength is larger than the average interparticle distance the quantum effects (tunneling, quantum diffraction, etc.) start to become important (quantum plasmas). The interaction between a positive charge Z and an electron in such plasmas has the form [2]

$$V(r) = -\frac{Z}{r} e^{-r/\kappa} \cos(r/\kappa) \quad (1)$$

where the screening length $\kappa = 2^{1/2}/k_q$, $k_q = (2\omega_p)^{1/2}$ is the electron quantum wavenumber (in atomic units) and ω_p is the electron plasma frequency.

Atomic structure properties and collision processes involving the cosine-Debye-Hückel (CDH) potential (1) have received considerable attention in recent years (see, e.g. [3,4] and references therein). In the present

paper we study the dynamics of electron capture proces in proton-hydrogen atom collisions



taking place in a quantum plasma.

2. PROPERTIES OF CDH POTENTIAL AND COMPUTATIONAL METHOD

The potential (1) decreases faster than r^{-2} when $r \rightarrow \infty$ and for any finite value of κ it can support only a finite number of bound states [5]. The Coulomb degeneracy of angular momentum states of one-electron atomic system is also lifted in this potential. The finiteness of the number of bound states implies that the energy of any nl bound state decreases with decreasing κ . At a certain critical value κ_{nl}^c the binding energy of an nl state becomes zero and the state enters the continuum. The critical screening lengths of nl ($n \leq 6$) states are given in Table 1. We shall

Table 1. Critical screening lengths $\kappa_{nl}^c(a_0)$ for CDH potential for $\text{H}(nl)$ states, $n \leq 6$

| n/l | 0 | 1 | 2 | 3 | 4 | 5 |
|-------|---------|---------|---------|---------|---------|---------|
| 1 | 1.3858 | - | - | - | - | - |
| 2 | 5.9974 | 6.7474 | - | - | - | - |
| 3 | 13.7982 | 14.5534 | 15.7278 | - | - | - |
| 4 | 24.7339 | 25.4687 | 26.7343 | 28.3758 | - | - |
| 5 | 38.7660 | 39.5007 | 40.8161 | 42.5855 | 44.6999 | - |
| 6 | 55.9179 | 56.6496 | 57.9944 | 59.8509 | 62.1138 | 64.7020 |

study the collision dynamics of reaction (2) by the atomic orbital close-coupling method, described in detail elsewhere [6]. In order to demonstrate the plasma screening effects on the cross sections of reaction (2) we shall calculate the cross sections with both the screened potential (1) and with the pure Coulomb interaction. In the expansion basis for the screened case we shall include all projectile states with $n \leq 6$ and all target states with $n \leq 4$. In the unscreened case the expansion basis includes all bound states with $n \leq 7$ on each of the centres plus 176 continuum pseudostates centered on the projectile.

3. CROSS SECTION RESULTS

In Figure 1 we show the cross sections for electron capture to $1s$, $2l$ and $3l$ states for the screened case with $\kappa = 16a_0$ (panels (a)) and for the unscreened case (panel (b)). For this value of κ bound in the potential

(1) are only the states with $n \leq 3$, while the states with $n = 4, 5$, and 6 are in the continuum (see Table 1). The comparison shows that the $1s$ cross sections in the two cases are almost identical but for the other nl cross sections this is true only for $E > 30$ keV. Below ~ 20 keV the $2l$ and $3l$ cross sections in both screened and unscreened case exhibit oscillations, with those in the screened case being more pronounced. The closeness of the $1s$ cross sections in the screened and unscreened case is due to the fact that for this value of κ the energy of $1s$ state does not differ much from that in the unscreened case. The oscillatory structures of $2l$ and $3l$ cross sections in the low energy region are due to the coupling of electron capture and excitation channels. The cross sections for capture to $1s$, $2s$ and $2p$ states for the $\kappa = 8a_0$ screened case are shown in Figure 2. In Figure 3 we show the capture cross section for the screening length $\kappa = 2.5a_0$ when only the $1s$ state is bound in the potential (1). Shown in this figure is also total capture cross section of Ref. [4] calculated with the classical trajectory Monte Carlo (CTMC) method.

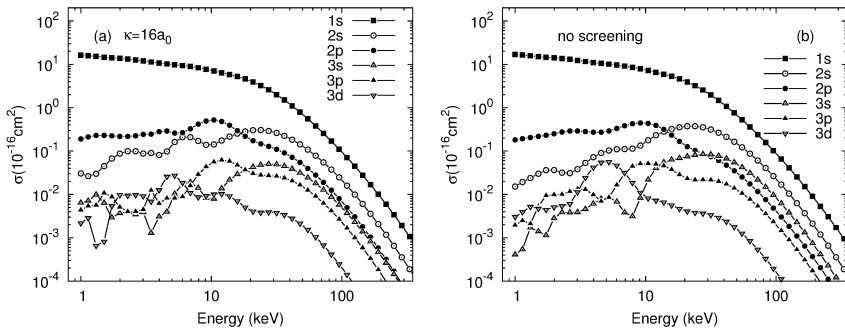


Figure 1. Cross sections for capture to $1s$, $2l$ and $3l$ states for the screened case with $\kappa = 16a_0$ (panels (a)) and for the unscreened case (panel (b)).

It is observed that in the overlapping energy range the total capture CTMC cross section is smaller than the present TC-AOCC cross section, their difference showing a tendency of increasing for lower energies. This is due to the fact that the classical radial electron density distribution of $1s$ hydrogen state in the potential (1) extends to up to $r = 2.1a_0$ only [4], while the quantum-mechanical distribution of $1s$ state in the potential (1) extends to infinity. It is well known that in the electron capture process (particularly in the symmetric resonant case) the dominant contribution to the capture at low collision energies comes from the distant (asymptotic) parts of electron density distributions of initial and final states.

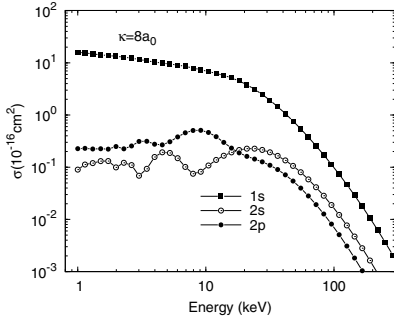


Figure 2. Cross sections for capture to $1s$, $2s$ and $2p$ states for the screened case with screening length $\kappa = 8a_0$.

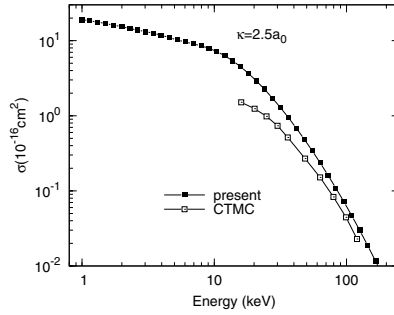


Figure 3. Capture cross section for the screening length $\kappa = 2.5a_0$. CTMC is the total capture cross section from Ref. [4].

REFERENCES

- [1] D. Salzman, *Atomic Physics in Hot Plasmas*, (Oxford Univ. Press, Oxford, 1998).
- [2] P. K. Shukla and B. Eliasson, *Phys. Lett. A* **372**, 2897 (2008)
- [3] N. F. Lai, Y. C. Lin, C. Y. Lin and Y. K. Ho, *Chinese J. Phys.* **51**, 73 (2013)
- [4] L.-Y. Zhang, X. Qi, X.-Y. Zhao, D.-Y. Meng, G.-Q. Xiao, W.-S. Duan and L. Yang, *Phys. Plasmas* **20**, 113301 (2013)
- [5] L. D. Landau and E. M. Lifshitz, *Quantum Mechanics: Non-Relativistic Theory* (Pergamon, London, 1958)
- [6] W. Fritsch, and C. D. Lin, *Phys. Rep.* **202**, 1 (1991)

SPIN-RESOLVED ELECTRON CAPTURE IN $\text{Be}^{3+} + \text{Li}$ COLLISIONS

L. Liu¹, C. H. Liu², J. G. Wang¹ and R. K. Janev³

¹*Data Center for High Energy Density Matter, Institute of Applied Physics and Computational Mathematics, P. O. Box 8009, Beijing 100088, P. R. China.*

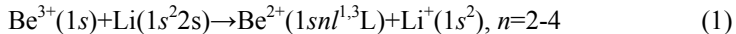
²*Institute of Modern Physics, Chinese Academy of Science, Lanzhou 730000, P. R. China*

³*Macedonian Academy of Sciences and Arts, P. O. Box 428, 1000 Skopje, Macedonia*

Abstract. Spin-resolved total and state-selective electron capture cross sections have been calculated by employing the quantal molecular orbital close-coupling method (QMOCC) and the two-center atomic orbital close-coupling (TC-AOCC) method in the 10^{-4} -2.5 keV/u and 0.5-100keV/u energy ranges, respectively. The reported cross sections are urgently required in the thermonuclear fusion research.

1. INTRODUCTION

In the present paper we study the electron capture processes



by using the QMOCC and TC-AOCC methods in the 10^{-4} -2.5 keV/u and 0.5-100keV/u energy ranges, respectively. The motivation for this study is the need for cross section data for these processes on the n , l and spin resolved level in the current thermonuclear fusion research. Beryllium is the selected as material for the first wall of International thermonuclear experimental reactor (ITER) [1] and lithium is the prime candidate for the liquid metal divertor in fusion reactors [2]. The considered processes have not been studied before to this level of channel resolution.

2. COMPUTATIONAL METHODS

The QMOCC method for ion-atom collision dynamics is described in detail in [3]. It solves a set of coupled second-order differential equations for the amplitudes of the expansion of total electron wave function over the adiabatic states of BeLi^{2+} molecular ion. All states of BeLi^{2+} ion indicated in Eq. (1) have

been included in the expansion. The eigenfunctions and eigenenergies of BeLi^{2+} converging in the separated atom limit to the atomic states of Be^{2+} as function of internuclear axis R were determined by employing the multireference single- and double- excitation configuration interaction computer (MRDCI) program [4]. The potential energy curves for the important Σ states involved in reactions (1) are shown in Fig.1. The figure shows that in the region of internuclear distances between $\sim 20a_0$ and $30a_0$ the potential curves of initial $11^1\Sigma$ and $10^3\Sigma$ states exhibit avoided crossings with the potential curves of the $n=4$ group of molecular states having the same symmetry. These are the regions of strong radial couplings between the initial and $n=4$ exit reaction channels. At small internuclear distances rotational couplings between molecular are also involved in the collision dynamics through which the $n=3$ and $n=2$ exit channels are populated.

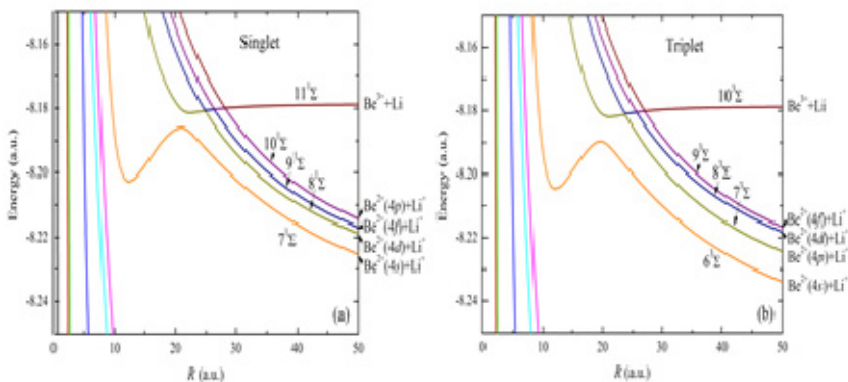


Figure 1. Potential energy curves of the singlet and triplet Σ states of BeLi^{2+} .

The TC-AOCC method for description of ion-atom collision dynamics is described in detail in [5]. The method solves a set of coupled first-order differential equations for the amplitudes of total electron wave function expanded over traveling atomic orbitals centered on the target and the projectile. In the present calculations all $\text{Be}^{2+}(1snl^{1,3}L)$ states with $n \leq 10$ and all $\text{H}(nl)$ states with $n \leq 4$ were included in the expansion. The interaction of active electron in the electron transfer process with the Be^{3+} ion core is described with a model potential, different for the singlet and triplet manifolds of Be^{2+} ion states. The model potentials reproduce the experimental singlet and triplet energy levels of Be^{2+} [6] to within 1.7% and 1.9%, respectively.

We note that the coupled equations for the singlet and triplet manifolds of states in both QMOCC and TC-AOCC method are mutually uncoupled.

3. CROSS SECTION RESULTS

The total QMOCC and TC-AOCC cross sections for electron capture to the singlet and triplet states of Be^{2+} are shown in Fig.2. The figure shows that in the overlapping energy range the results of two calculations agree quite well for both spin manifolds. We note that the predominant contribution to the total singlet and triplet cross sections comes from the reaction channels of the $n=4$ group of states. The TC-AOCC singlet and triplet cross sections are close to each other in the entire energy range considered due to the fact that energy difference between the singlet and triplet of $n=4$ states of Be^{2+} ion is very small. However, the singlet and triplet QMOCC cross sections differ significantly from each other in the energy region below 100eV/u due to the difference between the couplings of singlet and triplet molecular states. The sensitivity of QMOCC cross sections to the interstate couplings is clearly manifested not only in the magnitudes of the cross sections but also in their energy dependence.

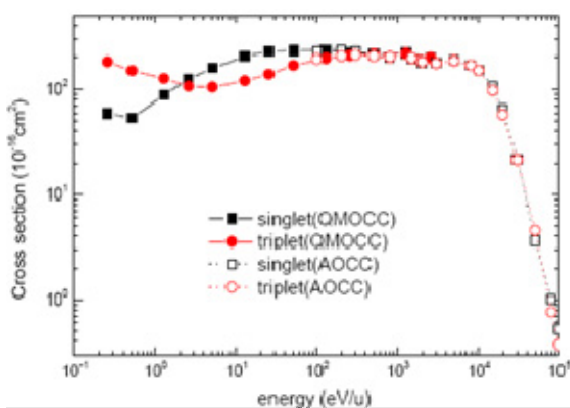


Figure 2. QMOCC and AOCC cross sections for capture to singlet and triplet Be^{2+} states.

In Fig. 3 we show our QMOCC and TC-AOCC cross section results for capture to the singlet and triplet $\text{Be}^{2+}(1s4l)$ states. The smooth connection of QMOCC and TC-AOCC results in the overlapping energy range is observed only for the capture to $4s$, $4d$, $4f$ singlet and $4s$, $4p$ (partially) triplet states. The reason for the mismatch of the cross sections for the other (weak) channels is the fact that both methods in this energy range are at the limit of their applicability. As the figure shows in the energy region below $\sim 1\text{keV/u}$ both the magnitudes and energy behavior of all $4l$ cross sections in the singlet and triplet manifolds of states are quite different; a manifestation of the different capture dynamics within the two manifolds. An insight in the capture dynamics can be gained by analyzing the distribution and the strength of radial couplings along the

internuclear distance and the extension and strength of rotational couplings operating at small internuclear distances.

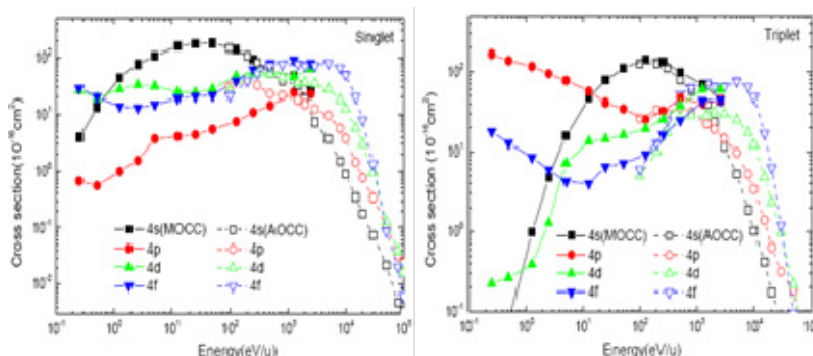


Figure 3. QMOCC and TC-AOCC Cross sections for capture to $4l$ singlet and triplet states of Be^{2+} .

REFERENCES

- [1] A. Loarte *et al.*, Nucl. Fusion 47, S203 (2007)
- [2] E. L. Tabares. Plasma Phys. Control. Fusion 58, 014014 (2015)
- [3] B. Zygelman *et al.*, Phys. Rev. A 46, 3846 (1992)
- [4] R. J. Buenker and R. A. Phillips, J. Mol. Struct.: THEOCHEM 123, 291 (1985)
- [5] W. Fritsch, and C. D. Lin, Phys. Rep. 202, 1 (1991)
- [6] Yu. Ralchenko, A. E. Kramida, J. Reader, and NIST ASD Team, NIST Atomic Spectra Database (35,R57-R80 (2002).version 3.1.5), 2008, <http://physics.nist.gov/asd3>

PROJECTILE ANGULAR DISTRIBUTION IN SINGLE ELECTRON CAPTURE FROM HELIUM BY PROTONS

Ivan Mančev and Nenad Milojević

*Department of Physics, Faculty of Sciences and Mathematics,
University of Niš, P.O.Box 224, 18000 Niš, Serbia*

Abstract. The prior form of the four-body boundary-corrected first Born approximation (CB1-4B) is applied to calculate the differential cross sections for single electron capture in fast collisions of a bare projectile with a heliumlike target. The CB1-4B method exhibit an unphysical and experimentally unobserved dip who is examined. As an illustration, computations are carried out for one-electron capture from helium by protons. The obtained theoretical differential cross sections are in reasonable agreement with the available experimental results.

1. Introduction

Collisional processes in which two nuclei and two electrons take part represent pure four-body problems. Such a simple four-body system provides substantial information for a better comprehension of the fundamental dynamics in more involved few-body collision systems. A large number of theoretical studies have been performed using different four-body methods for studying various one- and two-electron transitions in scattering of completely stripped projectiles on heliumlike atomic systems or in collisions between two hydrogenlike atoms or ions, as recently reviewed in Refs.[1]-[7]. The CB1-4B approximation is a fully quantum mechanical four-body formalism and it strictly preserves the correct boundary conditions in both collisions channels [4]-[7]. In the present work we report the theoretical differential cross sections for single electron capture from helium atomic systems by protons. Atomic units will be used throughout unless otherwise stated.

2. Theory and results

We consider single electron capture in collisions of a completely stripped projectile with a heliumlike target:

$$Z_P + (Z_T, e_1, e_2)_{1s^2} \longrightarrow (Z_P, e_1)_\Sigma + (Z_T, e_2)_{1s^1}, \quad (1)$$

where Z_K is the charge of the K th nucleus ($K=T, P$). The parentheses symbolize the bound states in the initial and final channels. Symbol Σ denotes the formation of hydrogenlike atomic systems (Z_P, e_1) in any state. Let \vec{s}_1 and \vec{s}_2 (\vec{x}_1 and \vec{x}_2) be the position vectors of captured electron e_1 and non-captured electron e_2 relative to the nuclear charge of the projectile Z_P (target Z_T). Further, let \vec{R} denote the position vector of Z_P with respect to Z_T .

The prior form of the transition amplitude for process (1) in the CB1-4B reads as [1]:

$$T_{if} = \iiint d\vec{x}_1 d\vec{x}_2 d\vec{R} \varphi_P^*(\vec{s}_1) V_i^c \varphi_T^*(\vec{x}_2) \varphi_i(\vec{x}_1, \vec{x}_2) e^{-i\vec{\alpha} \cdot \vec{R} - i\vec{v} \cdot \vec{x}_1} (vR + \vec{v} \cdot \vec{R})^{i\xi}, \quad (2)$$

$$V_i^c = V_R + V_{S1} + V_{S2}, \quad V_R = \frac{2Z_P}{R}, \quad V_{S1} = -\frac{Z_P}{s_1}, \quad V_{S2} = -\frac{Z_P}{s_2}. \quad (3)$$

Here, $\xi = (Z_P - Z_T + 1)/v$ where v is the velocity of the projectile. The momentum transfer $\vec{\alpha}$ is: $\vec{\alpha} = \vec{\eta} - (v/2 - \Delta E/v)\hat{v}$, with $\Delta E = E_i - E_f$ where E_i is the binding energy of the two electron target and $E_f = -Z_P^2/2 - Z_T^2/2$. Quantity η is the transverse momentum transfer $\vec{\eta} = (\eta \cos \phi_\eta, \eta \sin \phi_\eta, 0)$ with the property $\vec{\eta} \cdot \vec{v} = 0$. The bound state wave functions of the hydrogenlike atomic systems $(Z_P, e_1)_{1s^1}$ and $(Z_T, e_2)_{1s^1}$ are denoted by $\varphi_P(\vec{s}_1)$ and $\varphi_T(\vec{x}_2)$, respectively. The wave function of the two electron ground state of the target $(Z_T, e_1, e_2)_{1s^2}$ is labeled by $\varphi_i(\vec{x}_1, \vec{x}_2)$. The complete perturbation V_i^c from Eq. (3) contains three Coulomb electrostatic interactions. Therein, the repulsive potential $2Z_P/R$ describes the Rutherford scattering which dominates at larger scattering angles in differential cross sections. Potential $V_{S1} = -Z_P/s_1$ is the Coulomb attractive interaction between Z_P and the target electron e_1 . Interaction $V_{S2} = -Z_P/s_2$ is the Coulomb attractive potential between Z_P and the target electron e_2 . The potentials $Z_P(1/R - 1/s_1)$ and $Z_P(1/R - 1/s_2)$ are of a short range at $R \rightarrow \infty$, it follows that V_i^c also behaves as a short range potential at infinitely large distances between the two aggregates. After analytical calculation [1] the transition amplitude is obtained in terms of the two-dimensional integrals. Two-dimensional numerical integrations are performed by means of the Gauss-Legendre quadratures. Differential cross sections (DCS) for capture into all the final states of hydrogenlike atomic systems are obtained by applying the Oppenheimer n^{-3} scaling law: $\left(\frac{dQ}{d\Omega}\right)_{\text{tot}} = 1.202 \left(\frac{dQ}{d\Omega}\right)_{1s}$,

where $\left(\frac{dQ}{d\Omega}\right)_{1s} (a_0^2/sr) = \frac{\mu^2}{4\pi^2} |T_{if}|^2$ is differential cross sections for capture into 1s state of (Z_P, e_1) and $\mu = m_P m_T / (m_P + m_T)$ is the reduced mass of the incident and target nuclei of mass m_P and m_T , respectively. The presented calculation is general and it can be applied to both symmetric and non-symmetric charge-exchange reactions. The DCS are presently carried out for the following near-symmetric charge-exchange reaction:



Theoretical results with the available experimental data for reaction (4) at energy 100 keV are shown in Fig.1. The lines represent DCS

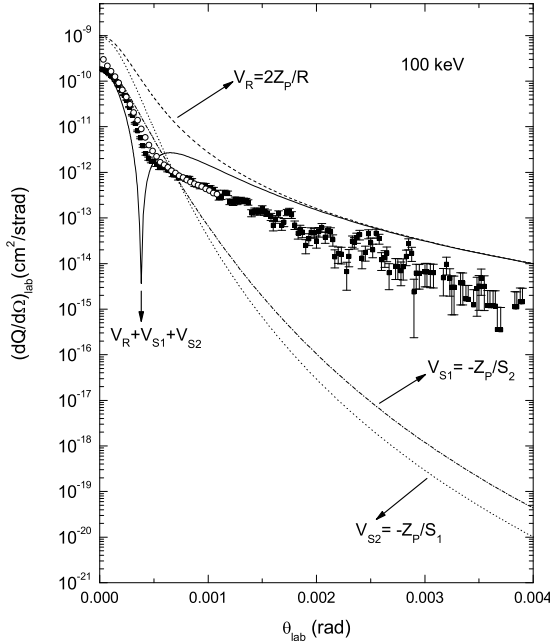


Figure 1. Separate contributions from three different potentials in the complete perturbation V_i^c at the incident energy 100 keV (present computation): dashed curve ($2Z_P/R$), dash-dotted curve ($-Z_P/s_2$), dotted curve ($-Z_P/s_1$) and solid curve ($V_i^c = 2Z_P/R - Z_P/s_1 - Z_P/s_2$). Experimental data: ■ Schöffler *et al* [9], ○ Guo *et al* [10].

for four-parameter wave function of Löwdin [8]: $\varphi_i(\vec{x}_1, \vec{x}_2) = N(a_1 e^{-\alpha_1 x_1} + a_2 e^{-\alpha_2 x_1})(a_1 e^{-\alpha_1 x_2} + a_2 e^{-\alpha_2 x_2})$, $a_1 = 2.7626$, $a_2 = 1.9104$, $\alpha_1 = 1.4287$, $\alpha_2 = 2.7022$ with the binding energy $E_i = -2.861525$. The normalization constant N is $\pi N = (a_1^2/\alpha_1^3 + a_2[2a_2/\alpha_2^3 + 16a_1/(\alpha_1 + \alpha_2)^3])^{-1}$. As can be seen from Fig. 1 the CB1-4B method exhibit an unphysical and experimentally unobserved dip due to a severe cancellation of potentials with different signs contained in the complete perturbation $2Z_P/R - Z_P/s_1 - Z_P/s_2$. The

angle at which this dip occurs is sometimes called the dark angle. In this case the dip is around 0.38 mrad and is followed by a broad maximum and a tail due to the internuclear Rutherford collision $2Z_P/R$ taking place at larger scattering angles. Fig. 1 is a particularly clear illustration of the origin of this dip. Thus, in the close vicinity of scattering angles 0.38 mrad dip follows from destructive interference of contributions of different signs $-Z_P/s_1$, $-Z_P/s_2$ and $2Z_P/R$ in the transition amplitude Eq. (2). All contributions no peak structure. No Thomas peak is detected by the CB1-4B method which, as the first-order approximation, neglects the intermediate continuum states of the captured electron. Thus the broad (around 0.65 mrad) and the Thomas peak should not be confused with each other. The curves due to $-Z_P/s_1$ and $-Z_P/s_2$ cross each other once at 0.71 mrad where the contribution from $-Z_P/s_2$ is dominated above 0.71 mrad and below 0.71 mrad is opposite. From Fig. 1 we can see that the DCS for the complete perturbation V_i^c (solid line) are in excellent agreement with the experimental results at scattering angles from 0 to 0.12 mrad, but at angles above 0.56 mrad theoretical results slightly overestimate the measurements.

Acknowledgements Authors thank the Ministry of Education, Science and Technological Development of the Republic of Serbia for support through Project No. 171020.

REFERENCES

- [1] I. Mančev, N. Milojević, Dž. Belkić, Phys. Rev. A 81, 022710 (2010).
- [2] I. Mančev, N. Milojević, Dž. Belkić, Phys. Rev. A 86, 022704 (2012).
- [3] I. Mančev, N. Milojević, Dž. Belkić, Phys. Rev. A 88, 052706 (2013).
- [4] Dž. Belkić, R. Gayet and A. Salin, Phys. Rep. 56, 279 (1979).
- [5] Dž. Belkić, I. Mančev and J. Hanssen, Rev. Mod. Phys. 80, 249 (2008).
- [6] Dž. Belkić, *Principles of Quantum Scattering Theory* (Institute of Physics, Bristol, 2004).
- [7] Dž. Belkić, *Quantum Theory of High-Energy Ion-Atom Collisions* (Taylor & Francis, London, 2008).
- [8] P. Löwdin, Phys. Rev. 90, 120 (1953).
- [9] M.S. Schöffler, J. Titze, L.Ph.H. Schmidt, T. Jehnke, N. Neumann, O. Jagutzki, H. Schmidt-Böcking, R. Dörner and I. Mančev, Phys. Rev. A 79, 064701 (2009).
- [10] D. L. Guo, X. Ma, S. F. Zhang, X. L. Zhu, W. T. Feng, R. T. Zhang, B. Li, H. P. Liu, S. C. Yan, P. J. Zhang, and Q. Wang, Phys. Rev. A 86, 052707 (2012).

THOMAS PEAK IN FAST $H^+ - He$ COLLISIONS

Nenad Milojević and Ivan Mančev

*Department of Physics, Faculty of Sciences and Mathematics,
University of Niš, P.O.Box 224, 18000 Niš, Serbia*

Abstract. Single charge exchange in collisions between protons and helium atomic systems is investigated by means of the four-body boundary-corrected continuum-intermediate-states (BCIS-4B) method. The BCIS-4B approximation is expected to predict double scattering of the captured electron on two nuclei as a quantum-mechanical counterpart of the Thomas classical two-step billiard-type collision. The differential cross sections obtained by means of BCIS-4B method are compared with the available experimental data.

1. Introduction

Charge transfer process in fast ion-atom collisions is very important in many branches of physics such as astrophysics, plasma physics, hadron radiotherapy, etc. The present work is aimed at a thorough theoretical investigation of single electron capture from helium atomic systems by bare projectiles using the four-body boundary-corrected continuum-intermediate-state (BCIS-4B) method [1]. A classical double-step or Thomas collision mechanism plays an important role in the process of single electron capture from helium by fast protons, and this Thomas peak is investigated with special attention. The BCIS-4B method is a fully quantum-mechanical four-body formalism and it strictly preserves the correct boundary conditions in both collisional channels. The boundary conditions or equivalently the asymptotic convergence problem [2, 3, 4] are of essential importance for ion-atom collisions whenever the aggregates are charged in the asymptotic channels. This is a second-order theory which provides a fully adequate description of the fact that, in an intermediate stage of collision, the captured electron moves in a Coulomb field rather than propagating freely according to a plane wave formalism of the usual i.e. the Jackson-Schiff first Born approximation with the incorrect boundary conditions. Atomic units will be used throughout unless otherwise stated.

2. Theory and results

We consider single charge exchange in collision of fast proton with helium targets. The quantum-mechanical non-relativistic scattering theory will be used throughout without accounting for the spin effects. In such a case, we shall consider that e_1 is captured, while e_2 remains in the target rest. This charge exchange process under study is symbolized as:



where symbol Σ denotes the formation of atomic hydrogen $\text{H}(\Sigma)$ in any state. Let \vec{s}_1 and \vec{s}_2 (\vec{x}_1 and \vec{x}_2) be the position vectors of e_1 and e_2 relative to the projectile H^+ (target He^{2+}). Further, let \vec{R} denote the position vector of H^+ with respect to He^{2+} .

Therefore, the prior form of the eikonal transition amplitude in the BCIS-4B approximation [1] for process (1) becomes:

$$T_{\text{if}}(\vec{\eta}) = [N^-(1/v)]^* \int \int \int d\vec{x}_1 d\vec{x}_2 d\vec{R} \varphi_{\text{P}}^*(\vec{s}_1) \varphi_{\text{T}}^*(\vec{x}_2) \left(\frac{2}{R} - \frac{1}{s_1} - \frac{1}{s_2} \right) \\ \times \varphi_{\text{i}}(\vec{x}_1, \vec{x}_2) e^{-i\vec{\alpha} \cdot \vec{R} - i\vec{v} \cdot \vec{x}_1} {}_1F_1(i/v, 1, ivx_1 + i\vec{v} \cdot \vec{x}_1) (vR + \vec{v} \cdot \vec{R})^{i/v}, \quad (2)$$

where the momentum transfer $\vec{\alpha}$ is: $\vec{\alpha} = \vec{\eta} - \alpha_z \hat{v}$, $\alpha_z = v/2 - \Delta E/v$, with $\Delta E = \epsilon_i - \epsilon_f$ and $\epsilon_f = -5/2$. The transverse component of the change in the relative linear momentum of a heavy particle is denoted by $\vec{\eta} = (\eta \cos \phi_\eta, \eta \sin \phi_\eta, 0)$ where $\vec{\eta} \cdot \vec{v} = 0$. The functions $\varphi_{\text{P}}(\vec{s}_1)$ and $\varphi_{\text{T}}(\vec{x}_2)$ represent the bound-state wave function of $\text{H}(1s^1)$ and $\text{He}^+(1s^1)$, respectively. Likewise, the wave function of the two-electron ground state of the target $\text{He}(1s^2)$ is labeled by $\varphi_{\text{i}}(\vec{x}_1, \vec{x}_2)$. Quantity $N^-(1/v) {}_1F_1(i/v, 1, ivx_1 + i\vec{v} \cdot \vec{x}_1)$ is the electronic continuum Coulomb wave function in the attractive potential $-1/x_1$, where $N^-(1/v) = e^{-\pi/2v} \Gamma(1 + i/v)$. The differential cross section is given by: $\frac{dQ}{d\Omega} (a_0^2/sr) \equiv \left(\frac{dQ}{d\Omega} \right)_{1s} = \frac{\mu^2}{4\pi^2} |T_{\text{if}}(\vec{\eta})|^2$, where $\mu = m_1 m_2 / (m_1 + m_2)$ is the reduced mass of the incident and target nuclei of mass $m_1 = m_{\text{H}^+}$ and $m_2 = m_{\text{He}^{2+}}$, respectively. After analytical calculation [1] the original nine-dimensional integral for transition amplitude from Eq. (2) can be reduced to a two-dimensional integral. The Gauss-Legendre quadrature is employed for the numerical integration of the two-dimensional integral. The number of integration points is $N_{GL} = 368$. Differential cross sections (DCS) for capture summed over all the final states of atomic hydrogen according to the Oppenheimer n^{-3} scaling law can be written as:

$$\left(\frac{dQ}{d\Omega} \right)_{\Sigma} = 1.202 \left(\frac{dQ}{d\Omega} \right)_{1s}. \quad (3)$$

Theoretical results with the available experimental data for reaction (1) at energy 7.5 MeV are shown in Fig.1.

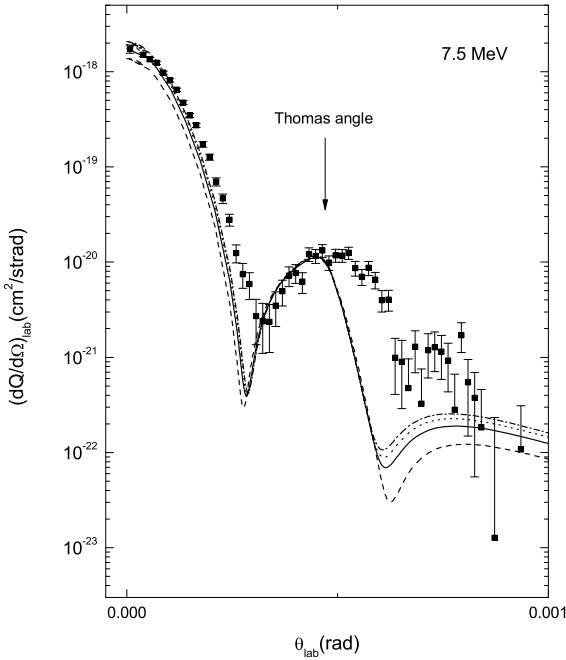


Figure 1. Differential cross sections (DCS) as a function of scattering angle $\theta \equiv \theta_{\text{lab}}$ (rad) in the laboratory frame of reference at incident energy $E = 7.5$ MeV for the single electron capture by protons from $\text{He}(1s^2)$. The theoretical results: the dashed curve-DCS(Hy), the full curve-DCS(S), the dashed dot curve-DCS(G) and the dot line-DCS(L). Experimental data: \bullet Fischer *et al* [9].

The lines represent DCS for different wave function $\varphi_i(\vec{x}_1, \vec{x}_2)$: a) the dashed line-uncorrelated one-parameter Hylleraas wave function [5]: $\varphi_i(\vec{x}_1, \vec{x}_2) = (\alpha^3/\pi)e^{-\alpha(x_1+x_2)}$, $\alpha = 1.6875$ with the binding energy $\epsilon_i = -2.847656$ (DCS is labeled with DCS(Hy)); b) the full line-the two-parameter wave function of Silverman *et al* [6]: $\varphi_i(\vec{x}_1, \vec{x}_2) = N(e^{-\alpha_1 x_1 - \alpha_2 x_2} + e^{-\alpha_2 x_1 - \alpha_1 x_2})$, $\alpha_1 = 2.183171, \alpha_2 = 1.18853$ and $\epsilon_i = -2.8756614$ (DCS is labeled with DCS(S)); c) the dashed dot line-the three-parameter function of Green *et al* [7]: $\varphi_i(\vec{x}_1, \vec{x}_2) = N(e^{-\alpha_1 x_1} + ae^{-\alpha_2 x_1})(e^{-\alpha_1 x_2} + ae^{-\alpha_2 x_2})$, $a = 0.6, \alpha_1 = 1.455799, \alpha_2 = 2.911598$ with the binding energy $\epsilon_i = -2.86167$ (DCS is labeled with DCS(G)), and d) the dot line-four-parameter wave function of Löwdin [8]: $\varphi_i(\vec{x}_1, \vec{x}_2) = N(a_1 e^{-\alpha_1 x_1} + a_2 e^{-\alpha_2 x_1})(a_1 e^{-\alpha_1 x_2} + a_2 e^{-\alpha_2 x_2})$, $a_1 = 2.7626, a_2 = 1.9104, \alpha_1 = 1.4287, \alpha_2 = 2.7022$ with the binding energy $\epsilon_i = -2.861525$ (DCS is labeled with DCS(L)), where N is the normalization constant. The term $-1/s_1$ and the confluent hypergeometric functions ${}_1F_1(i/v, 1, ivx_1 + i\vec{v} \cdot \vec{x}_1)$ from the corresponding Coulomb wave give the contribution from double scattering effects. Such effects are a quantum-mechanical counterpart of the classical Thomas billiard-type $\text{H}^+ - e_1 - \text{He}^{2+}$

collisions. The result is the Thomas peak at $\theta_{\text{lab}} = (1/m_{\text{H}^+}) \sin(60^\circ) \simeq 0.47$ mrad. Potential $-1/s_2$ also describes capture of e_1 . Here, H^+ first interacts with e_2 via $-1/s_2$ and, in the end, it is electron e_1 which is captured by the projectile. This is mediated by the static correlations of the two electrons in the bound state of the helium wave function $\varphi_i(\vec{x}_1, \vec{x}_2)$. Such an effect coupled with the presence of the Coulomb wave functions in Eq. (2) yield the second Thomas peak at the same angle $\theta_{\text{lab}} \approx 0.47$ mrad. Thus, for single charge exchange (1), at sufficiently high impact energies, differential cross sections computed using Eq. (2) should clearly exhibit two double-scattering effects with two pronounced peaks for two Thomas processes ($\text{H}^+ - e_1 - \text{He}^{2+}$ and $\text{H}^+ - e_1^{\text{S}} - e_2^{\text{S}}$). The superscript S on the two electrons in the $\text{H}^+ - e_1^{\text{S}} - e_2^{\text{S}}$ Thomas process is used to indicate that this Thomas peak is enabled by the static correlations of electrons in the target wave function $\varphi_i(\vec{x}_1, \vec{x}_2)$. From Fig. 1 we can see that the all curves have the same shape. We conclude that, in the case of reaction (1), the BCIS-4B method is relatively weakly dependent upon the choice of the bound-state wave function of helium atom. The discrepancy between them becomes significant above 0.59 mrad, where: $\text{DCS(G)} > \text{DCS(L)} > \text{DCS(S)} > \text{DCS(Hy)}$. All results from the BCIS-4B method are seen to be in very good agreement with the experimental data.

Acknowledgements Authors thank the Ministry of Education, Science and Technological Development of the Republic of Serbia for support through Project No. 171020.

REFERENCES

- [1] I. Mančev, N. Milojević and Dž. Belkić, *Phys. Rev. A* **91**, 062705 (2015).
- [2] Dž. Belkić, *Principles of Quantum Scattering Theory* (Institute of Physics, Bristol, 2004).
- [3] Dž. Belkić, I. Mančev and J. Hanssen, *Rev. Mod. Phys.* **80**, 249 (2008).
- [4] Dž. Belkić, *Quantum Theory of High-Energy Ion-Atom Collisions* (Taylor & Francis, London, 2008).
- [5] E. Hylleraas, *Z. Phys.* **54**, 347 (1929).
- [6] J.N. Silverman, O. Platas, F.A. Matsen, *J.Chem.Phys.* **32**, 1402 (1960).
- [7] L. Green, M. Mulder, M. Lewis and J.W. Woll, *Phys. Rev.* **93**, 757 (1954).
- [8] P. Löwdin, *Phys. Rev.* **90**, 120 (1953).
- [9] D. Fischer, K. Stöckel, H. Cederquist, H. Zettergren, P. Reinhed, R. Schuch, A. Kállberg, A. Simonsson, and H. T. Schmidt, *Phys. Rev. A* **73**, 052713 (2006).

CROSS SECTION FOR SPIN-RESOLVED ELECTRON CAPTURE IN $\text{He}^+\text{-H}$ COLLISIONS

Y. Wu¹, L. Liu¹, X. H. Lin^{1,2}, J. G. Wang¹ and R. K. Janev³

¹*Data Center for High Energy Density Matter, Institute of Applied Physics and Computational Mathematics, P. O. Box 8009, Beijing 100088, P. R. China.*

²*School of Physics, Beijing Institute of Technology, Beijing, 100081, P. R. China*

³*Macedonian Academy of Sciences and Arts, P. O. Box 428, 1000 Skopje, Macedonia*

Abstract. Electron-capture and excitation processes in $\text{He}^+\text{+H}$ collisions have been studied by using the full quantum-mechanical molecular orbital close-coupling (QMOCC) and the two-center atomic orbital close-coupling (TC-AOCC) methods in the energy ranges 10^{-2} -5keV/u and 0.1-100keV/u, respectively. The spin-resolved state-selective cross sections for these processes in the $\text{He}^+\text{+H}$ collision system are reported for the first time. The spin-averaged total electron capture cross sections are compared with the results of available experimental and previous theoretical results in the overlapping energy ranges.

1. INTRODUCTION

The electron capture and excitation processes in $\text{He}^+\text{+H}$ collisions have been subject to numerous studies in the past due to their important role in both laboratory and astrophysical plasmas. In magnetic fusion plasmas these processes affect the helium and hydrogen atom transport and radiation and can be used for diagnostic purposes [1, 2]. The previous experimental and theoretical studies of these processes [3-14] have been focused on determination of their total cross sections, covering usually limited energy ranges. In plasma diagnostic and particle transport studies state-selective information on these processes is required in a broad energy range. The aim of the present work is to provide such cross section information on a spin-resolved, state-selective level by using the full quantum-mechanical molecular-orbital close-coupling (QMOCC) method in the 10-5000eV/u energy range and the two-center atomic orbital close-coupling (TC-AOCC) method in the 0.1-100keV/u energy range. Total and spin-average state-selective electron capture and excitation cross sections, resulting from the present calculations, will also be reported and compared with the available experimental data and the results of the most involved theoretical calculations in the literature.

2. COMPUTATIONAL METHODS

Details of the QMOCC method for ion-atom collisions can be found elsewhere [15]. The QMOCC method involves the solution of a coupled set of second-order differential equations using the log-derivative method of Johnson [16]. In the expansion basis for our QMOCC calculations we have included the lower twelve $^1\Sigma$, six $^1\Pi$ states, and eleven $^3\Sigma$, six $^3\Pi$ states of HeH^+ molecule. The coupled equations for the singlet and triplet manifolds of states were solved separately. The spin-averaged cross section is then obtained as a weighted sum of corresponding singlet (weight $\frac{1}{4}$) and triplet (weight $\frac{3}{4}$) cross sections. The eigenfunctions and eigenenergies of HeH^+ as function of internuclear axis R were determined by employing the multireference single- and double- excitation configuration interaction (MRDCI) computer program [17, 18]. The adiabatic potential energy curves for the states involved in the QMOCC calculations are given in Fig. 1.

The TC-AOCC method for study of the dynamics in ion-atom collision systems is described in detail elsewhere [19]. It requires determination of single-center electronic states over which the total scattering wave function is expanded and used in the time-dependent Schrödinger equation to generate the coupled equations for the state amplitudes. Note that the expansion basis for the TC-AOCC calculations included all singlet and triplet bound states on He with $n \leq 7$ plus 63 pseudostates, and all the states with $n \leq 4$ centered on H. In the QMOCC calculations, all Σ and Π molecular states of HeH^+ , correlating asymptotically to the $n \leq 3$ atomic states of He and H, were included in the expansion basis.

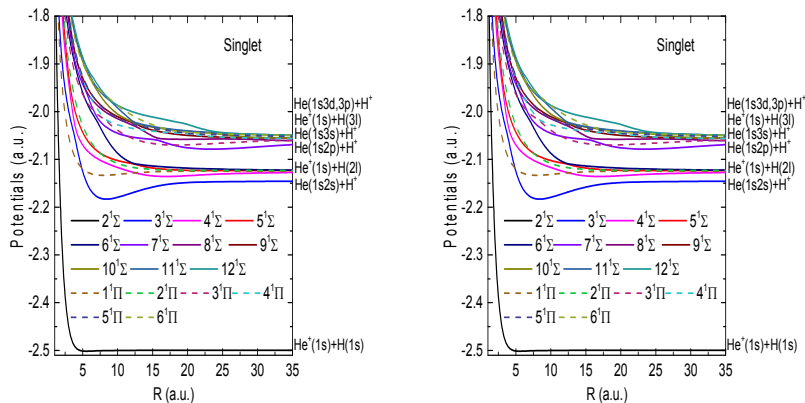


Figure 1. Potential energy curves of the singlet and triplet states of HeH^+ .

3. CROSS SECTION RESULTS

The total electron capture cross sections for the $\text{He}^+\text{-H}$ collision are displayed in Fig. 2 in the energy range of $10^{-6}\text{-}10^2\text{keV/u}$. It can be found in this figure that the present QMOCC and TC-AOCC results are in good mutual agreement in the overlapping energy region below $\sim 3\text{keV/u}$.

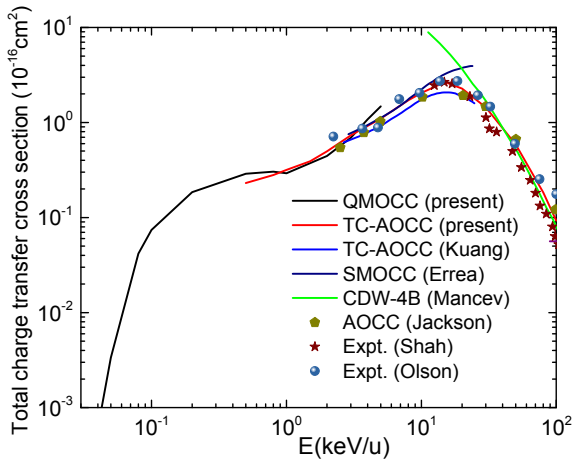


Figure 2. Total electron capture cross section for the $\text{He}^+\text{-H}$ collisions.

Fig. 3 shows the QMOCC and TC-AOCC cross sections for capture to the singlet and triplet $\text{He}(1s2p)$ states. It can be remarked that the TC-AOCC cross section for capture to 2^1P state is larger than that for capture to 2^3P state for energies below $\sim 3\text{keV/u}$, while above this energy the opposite is true. The QMOCC 2^1P and 2^3P cross sections are in similar relationship with regard to the energy $\sim 1\text{keV/u}$.

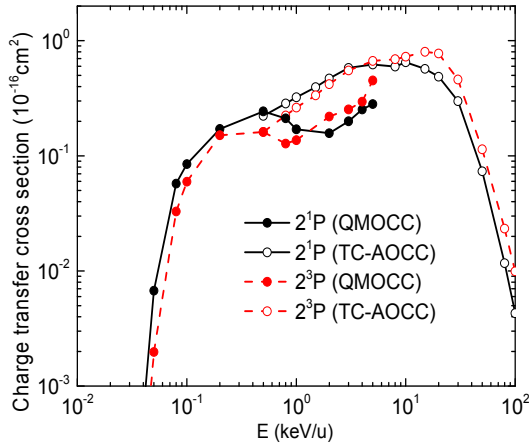


Figure 3. Cross sections for electron capture to the singlet and triplet states of $\text{He}(1s2p)$ in $\text{He}^+\text{-H}$ collisions.

REFERENCES

- [1] A. Laorte, B. Lipschultz, A.S. Kukushkin *et al.* Nucl. Fusion **47**, S203, (2007)
- [2] D.Reiter, M.Baeva, O.Marchuk. R.K.Janev, in: *Atomic and molecular data and their applications* (Eds. T.Kato et al) AIP Conf. Proc. Series, **771**, 3 (2006)
- [3] R. E. Olson, A. Salop, R. A. Phaneuf and F. W. Meyer, Phys. Rev. A **16**, 1867 (1977)
- [4] M.B. Shah and H.B. Gilbody, quoted as “private communication” in ref.[12] below.
- [5] J.D.A. Mc Kee, J.R. Sheridan, J. Geddes and H.B. Gilbody, J. Phys. B: At. Mol. Phys. **10**, 1679 (1977)
- [6] J.E. Aldag, J.L. Peacher, P.J. Martin, V.C. Sutcliffe, J.M. Geroge, E.Reed, T.J. Kvale, D.M. Blankenship and J.T. Park, Phys. Rev. A **23**, 1062 (1981)
- [7] J. Geddes, A. Donnelly, M. P. Hughes, D. P. Higgins and H. B. Gilbody, J. Phys. B: At. Mol. Opt. Phys. **27**, 3037 (1994)
- [8] A. Donnelly, G. Geddes and H.B. Gilbody, J. Phys. B: At. Mol. Opt. Phys. **24**, 165 (1991)
- [9] D. Jackson, H. A. Slim, B. H. Bransden and D. R. Flower, J. Phys. B **25**, L127 (1992)

- [10] A. M. Ermolaev, D. Jackson, N. Shimakura and T. Watanabe, *J. Phys. B* **27**, 4991 (1994)
- [11] J. Kuang, Z. Chen and C. D. Lin, *J. Phys. B* **28**, 2173 (1995)
- [12] I. Mancev, *Phys. Rev. A* **75**, 052716 (2007)
- [13] A. Macías, A. Riera and M. Yáñez, *Phys. Rev. A* **27**, 213 (1983)
- [14] L. F. Errea, L. Méndez, and A. Riera, *Z. Phys. D* **14**, 229 (1989)
- [15] B. Zygelman, D. L. Cooper, M. J. Ford, A. Dalgarno, J. Gerratt, and M. Raimondi, *Phys. Rev. A* **46**, 3846 (1992)
- [16] B. R. Johnson, *J. Comput. Phys.* **13**, 445 (1973)
- [17] R. J. Buenker and R. A. Phillips, *J. Mol. Struct. Theochem.* **123**, 291 (1985)
- [18] S. Krebs and R. J. Buenker, *J. Chem. Phys.* **103**, 5613 (1995)
- [19] W. Fritsch and C. D. Lin, *Phys. Rep.* **202**, 1 (1991)

RATE COEFFICIENTS FOR ELECTRON IMPACT IONIZATION OF CO₂ IN RF ELECTRIC FIELD

M. M. Aoneas¹, M. M. Ristić², M. M. Vojnović¹ and G. B. Poparić¹

¹*Faculty of Physics, University of Belgrade, Studentski trg 12-16, P. O. Box 44, 11000 Belgrade, Serbia*

²*Faculty of Physical Chemistry, University of Belgrade, Studentski trg 12-16, P. O. Box 47, 11158 Belgrade, Serbia*

Abstract. Rate coefficients for electron impact ionization of CO₂ molecule in the presence of time-dependent electric field are presented. Non-equilibrium electron energy distribution functions have been obtained by using a Monte Carlo simulation of electron movement in CO₂ gas for various frequencies of radio-frequency (RF) electric field: 50, 100, 200 and 500 MHz. Calculations have been performed for the reduced electric field value of 200 Td. The time modulation of ionization rate coefficients for different values of frequencies was studied. This research provides the data useful for modeling plasma generated by RF discharge.

1. INTRODUCTION

CO₂ molecule is the most abundant molecule of Venus and Mars atmospheres and it plays significant role in the global warming of the Earth. This places e-CO₂ collisions, the basic processes involving this species, at an important place in the study of the phenomena in these planets' atmospheres. Apart from that, the CO₂ gas is widely used in discharge based plasma generated in devices that use radio-frequency (RF) electric field [1, 2]. Electron impact ionization is the most important process for sustaining plasma in the plasma source. Complex models of these plasmas acquire systematic knowledge of rate coefficients.

The main goal of this work is the analysis of the time modulated ionization rate coefficient behavior under the influence of the various electric field frequencies. The non-equilibrium electron energy distribution functions (EEDFs) are obtained by using Monte Carlo simulation of electron transport through CO₂ gas, developed for the conditions of the RF electric field presence. In the earlier work of our group, a similar calculation had been performed for N₂ gas [3] and the most recent study for CO gas is yet to be published.

2. MONTE CARLO SIMULATION

The time-resolved Monte Carlo simulation code has been used for simulating the evolution of electron transport through CO₂ gas under the influence of spatially uniform RF electric field. It was assumed that in the initial moment all molecules are at the ground state. The simulation executes numerical calculation of the electron equations of motion in each time step (Δt) by Runge-Kutta method [4]. Low-density limit of gas discharge was assumed in the simulation. The EEDFs are sampled in each Δt within one cycle. After quasi-stationary state is reached, the results are averaged over many periods in order to obtain better statistics.

The input database of the simulation contains sets of, mostly experimentally obtained, differential and integral effective cross sections for electron-impact excitation and ionization of the CO₂ molecule. Part of these data was previously obtained by measurements performed in our Laboratory [5].

2. RESULTS AND DISCUSSION

The calculations have been performed at E_R/N (electric field reduced to number density N) value of 200 Td (1 Td = 10^{-21} Vm²). The time variation of the uniform external electric field $E(t)$ is given by the following equation:

$$\vec{E}(t) = \sqrt{2}E_R \vec{k} \cos(\omega t) \quad (1)$$

where E_R represents the effective reduced field strength, ω is angular frequency of the RF field and k is the unit vector in the field direction.

Initial kinetic energy of all electrons was chosen to be 5 eV in order to reach the steady state in a shorter time, thus minimizing the running time of the simulation. The number density of neutrals was $3.22 \cdot 10^{22}$ m⁻³, which corresponds to the gas pressure of 1 Torr (133.3 Pa). Rate coefficients for electron-impact ionization have been calculated at given conditions by using the relation [6]:

$$K(\langle \varepsilon \rangle) = \sqrt{2/m_e} \int_{\varepsilon_{thres}}^{+\infty} \sigma(\varepsilon) \sqrt{\varepsilon} \cdot f_e(\langle \varepsilon \rangle, \varepsilon) d\varepsilon \quad (2)$$

where $\langle \varepsilon \rangle$ is the mean electron energy, $\sigma(\varepsilon)$ is the excitation cross section for ionization, ε_{thres} is threshold energy and $f_e(\langle \varepsilon \rangle, \varepsilon)$ is the normalized EEDF.

Figure 1 presents the total ionization rate coefficients at frequencies of 50, 100, 200 and 500 MHz. A decrease of the rate coefficient's amplitude with increasing frequency follows from the inertness of the electrons caused by scattering and their incapability to adjust to temporal variations of the external electric field. For the same reasons there is a phase delay between rate coefficients and electric field, which is increased with increasing frequency. The effect of the amplitude decrease and the phase lag increase with increasing frequency is very pronounced.

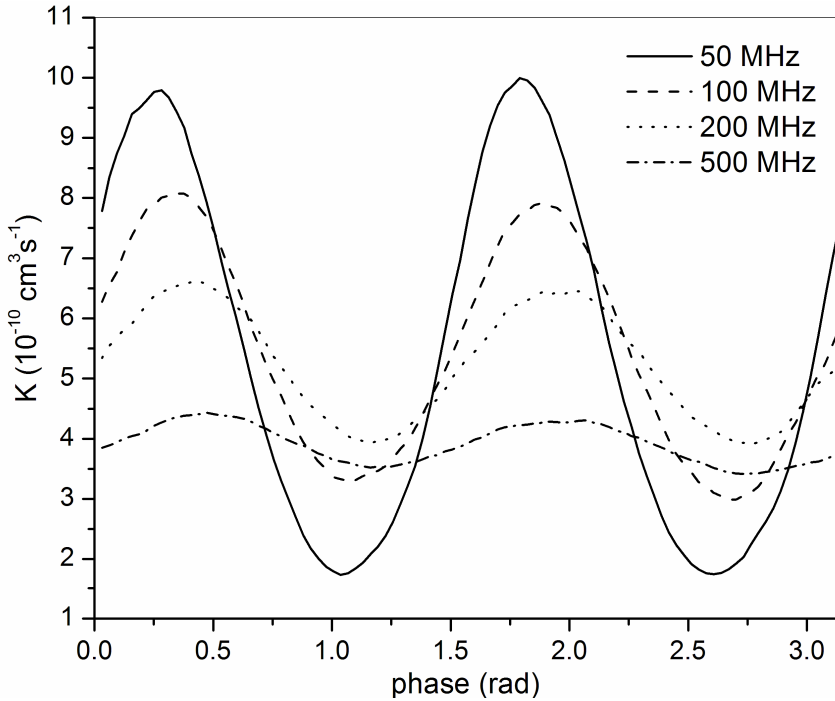


Figure 1. Time modulations of ionization rate coefficient K_{ion} for E_R/N value of 200 Td, in carbon dioxide at 1 Torr for 50, 100, 200 and 500 MHz.

4. CONCLUSIONS

Rate coefficients for electron-impact ionization of carbon dioxide in time modulated electric field have been calculated. Non-equilibrium EEDFs have been obtained by Monte Carlo simulation of electron movement through CO₂ gas under the influence of RF electric field. The obtained results give the insight into collision dynamics under these conditions. The dependence of rate coefficients on the applied electric field frequencies was studied and discussed. The results of this study are necessary input data for modeling non-equilibrium plasmas.

Acknowledgements

This work was performed under the Project 171016 of the Ministry of Science and Education of the Republic of Serbia.

REFERENCES

- [1] L.F. Spencer and A. D. Gallimore, *Plasma Chem Plasma Process* 31, 79 (2011).
- [2] M.P. Srivastava and A. Kobayashi, *Transactions of JWRI* 39, No. 1 (2010).
- [3] M.P. Popović, M. M. Vojnović, M. M. Aoneas, M. M. Ristić, M. D. Vičić and G. B. Poparić, *Physics of Plasmas* 21, 063504 (2014).
- [4] R. Morrow, *J. Comp. Phys.* 43, 1 (1981).
- [5] G. B. Poparić, M. M. Ristić and D. S. Belić, *J. Phys. Chem. A*, 114(4), 1610 (2010).
- [6] P. Chantry, *Final Technical Report ARPA*, Order No 3342 (1978).

EXCITATION OF THE $A^3\Sigma_u^+$ STATE OF THE NITROGEN MOLECULE IN RF ELECTRIC FIELD

M. M. Aoneas¹, M. M. Ristić², M. M. Vojnović¹ and G. B. Poparić¹

¹*Faculty of Physics, University of Belgrade, Studentski trg 12-16, P. O. Box 44, 11000 Belgrade, Serbia*

²*Faculty of Physical Chemistry, University of Belgrade, Studentski trg 12-16, P. O. Box 47, 11158 Belgrade, Serbia*

Abstract. Rate coefficient for electron impact excitation into $A^3\Sigma_u^+$ state in the N_2 molecule has been calculated in non-equilibrium conditions in the presence of radio-frequency (RF) electric field. A Monte Carlo simulation has been applied to determine non-equilibrium electron energy distribution functions within one period of the RF electric field. The results have been obtained for frequency values of 13.56, 50, 100 and 500 MHz, at reduced electric field amplitude value of 200 Td (1 Td = 10^{-21} Vm²). Rate coefficients of excitation into the $A^3\Sigma_u^+$ state under the influence of the field frequency change were studied and it is presented in this paper.

1. INTRODUCTION

Nitrogen molecule as the most abundant part of the Earth's atmospheres and the atmospheres of Mars, Venus, Titan and Triton, attracts much interest in various aspects of molecular, environmental and industrial physics and chemistry [1]. Many interesting properties of low temperature nitrogen plasma under the RF electric field have been studied; i. e. nitriding processes and corrosion resistance of some steels [2-3]. Alongside with the ionization, which our group has studied recently [4], excitation of nitrogen into various electronic states is also recognized as an important process in plasma nitriding. Experimental measurements have confirmed that molecules in N_2 excited in metastable $A^3\Sigma_u^+$ state can have up to three orders of magnitude higher density in plasma compared to the density of N_2^+ [5]. Similar situation is also recognized in DC nitrogen plasmas [6]. Existence of long living $A^3\Sigma_u^+$ state of the nitrogen molecule, which bears the significant amount of energy necessary for nitriding of gallium, is found to be essential for growth of quality gallium-nitride films [7-8]. Electron-impact processes under the influence of RF electric field is necessary for technologies such as RF excited gas lasers, RF plasma reactors, based on the use of RF electric signal for excitation of the molecules. For modeling these devices it is important to understand the excitation and ionization mechanisms involved when RF electric field is applied.

Reactive plasmas maintained by RF or microwave sources have important role in the fabrication of microelectronic devices. Modeling of inductively or capacitively coupled plasmas driven by RF is preformed in order to elucidate the discharge structures [9-10]. The primary aim of this work is to analyze the time dependent characteristics of electron-impact excitation into $A^3\Sigma_u^+$ state in N_2 under the external RF electric field. The non-equilibrium rate coefficients are determined by sampling the electron energy distribution function in Monte Carlo simulation of electron transport.

2. MONTE CARLO SIMULATION

Monte Carlo simulation for electron transport trough N_2 gas molecules, previously described in [11], has been developed in the presence of RF electric field [4]. Time variation of electric field vector is given by:

$$\vec{E}(t) = \sqrt{2} E_R \vec{k} \cos(2\pi ft) \quad (1)$$

where E_R is the root mean square value of the electric field strength, f is frequency of the RF field, and k is the unit vector in the field direction. Differential equations of electron motion are solved by using Runge-Kutta method [12]. After each time step (Δt) the position and velocity of the electron were determined after the steady state is reached, and the electron energy is sampled in each time step within one period.

All scattering processes, both elastic and inelastic are included by using experimentally measured data and estimations of integral cross sections as a function of energy. We tested the simulation by comparing the results obtained for model gases and for the real gas, when we compared our values to experimentally measured transport properties in DC field and got great agreement.

3. RESULTS AND DISCUSSION

The initial electron kinetic energy in the simulation was 5 eV. The nitrogen gas pressure was 1 Torr (133.3 Pa). Number of simulated electrons was approximately 10^7 . Calculations were performed at E_R value of 200 Td, for RF electric field frequencies of 13.56, 50, 100 and 200 MHz. EEDF is sampled in order to calculate rate coefficients for considered process at specific time t , given by the following equation:

$$K(\langle \varepsilon, t \rangle, t) = \sqrt{2/m_e} \int_{\varepsilon_{thres}}^{+\infty} \sigma(\varepsilon) \sqrt{\varepsilon} \cdot f_e(\langle \varepsilon, t \rangle, \varepsilon, t) d\varepsilon \quad (2)$$

Where $\langle \varepsilon \rangle$ is the mean electron energy, $\sigma(\varepsilon)$ is the excitation cross section for the given process, ε_{resh} is the threshold energy for observed process $f_e(\langle \varepsilon, t \rangle, \varepsilon, t)$ is the normalized EEDF.

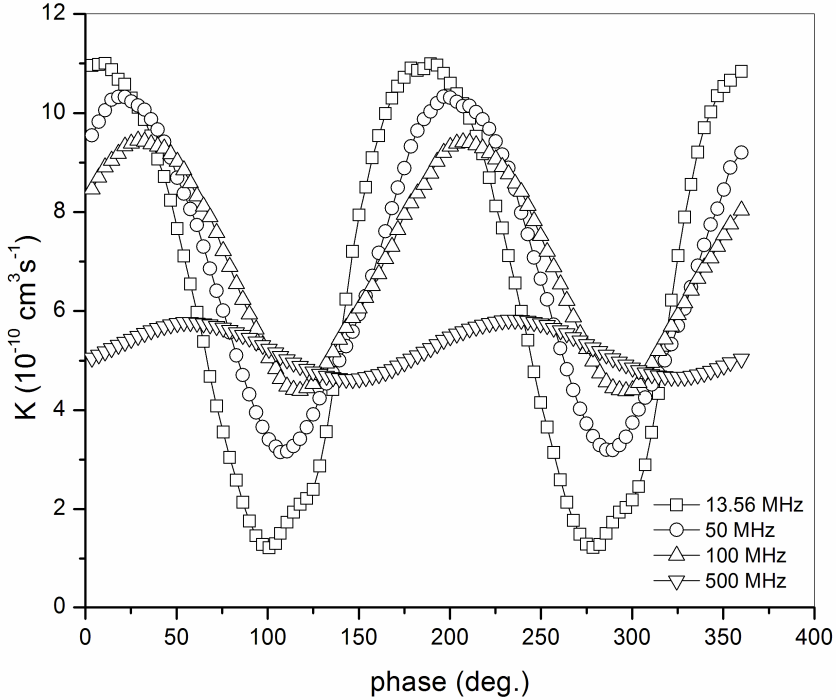


Figure 1. Rate coefficients for excitation into $A^3\Sigma_u^+$ state at $E_R = 200$ Td at frequencies 13.56, 50, 100, and 500 MHz.

Figure 1. presents the rate coefficients for electron-impact excitation into $A^3\Sigma_u^+$ state in N_2 gas at E_R value 200 Td at frequencies 13.56, 50, 100, and 200 MHz during one cycle. Rate coefficients for excitation into $A^3\Sigma_u^+$ state are decreasing, while phase delay is increasing with increasing frequency. This phenomenon is caused by incapability of electrons to follow and adjust to higher frequency changes of the RF electric field, as was noticed earlier in similar case where ionization rates were analyzed [4].

4. CONCLUSIONS

By using a Monte Carlo simulation, EEDFs have been sampled within one phase of the electric field. Rate coefficients for electron-impact excitation into $A^3\Sigma_u^+$ state of the N_2 molecule under the influence of RF electric field are obtained and their frequency dependence is discussed.

Acknowledgements

This work is partially supported by the Serbian Ministry of Education and Science under the grant No. 171016.

REFERENCES

- [1] P. C. Cosby, *J. Chem. Phys.* 98 (1993) 9544
- [2] E. Guiberteau, G. Bonhomme, R. Hugon, and G. Henrion, *Surf. Coat. Technol.* 97, 552–556 (1997)
- [3] F. Z. Bouanis, C. Jama, M. Traisnel, and F. Bentiss, *Corros. Sci.* 52, 3180–3190 (2010)
- [4] M. P. Popović, M. M. Vojnović, M. M. Aoneas, M. M. Ristić, M. D. Vičić and G. B. Poparić, *Phys. Plasmas* 21, 063504 (2014)
- [5] M. Baldwin, M. Fewell, S. Haydon, S. Kumar, G. Collins, K. Short and J. Tendys, *Surface and Coatings Technology* 98, 1187–1191 (1998)
- [6] A. Ricard, G. Henrion, H. Michel, M. Gantois, *Pure Appl. Chem.* 60, 747 (1988)
- [7] T. Kikuchi, A. Somintac, O. Ariyada, M. Wada, T. Ohachi, *Journal of Crystal Growth* 292, 221–226 (2006)
- [8] M. Newman, *Journal of Crystal Growth* 178 102–112 (1997)
- [9] J. P. Boeuf, P. Belengure and T. Hbid, *Plasma Sources Sci. Techol.* 3, 407 (1994)
- [10] K. Maeda, T. Makabe, N. Nakano, S. Bzenic and Z. Lj. Petrovic, *Phys Rev E* 55, 5901 (1997)
- [11] M. Ristić, G. B. Poparić and D. S. Belić, *Chem. Phys.* 410, 331 (2007)
- [12] R. Morrow, *J. Comp. Phys.* 43, 1 (1981)

SWARM ANALYSIS AND DISSOCIATION CROSS SECTIONS FOR CO₂

Marija Grofulović, Luís L. Alves and Vasco Guerra

*Instituto de Plasmas e Fusão Nuclear, Instituto Superior Técnico,
Universidade de Lisboa, Lisboa, Portugal*

Abstract. This work proposes a complete and consistent set of cross sections for electron collisions with carbon dioxide (CO₂), to be published in the IST-LISBON database with LXCat. The set is validated from the comparison between swarm parameters calculated using the LoKI (LisbOn KInetics) numerical code and the available experimental data. Superelastic collisions with CO₂(010) molecules are considered, as they are shown to be important at low reduced electric fields. The available dissociation cross sections are evaluated and discussed, and a strategy to obtain electron-impact dissociation rate coefficients is suggested.

1. INTRODUCTION

Carbon dioxide (CO₂) is an important component of several planetary atmospheres and a versatile industrial material. In recent years, its concentration in the Earth's atmosphere rapidly increased, causing the global warming problem. This severe issue put forward the idea of CO₂ conversion as one of the major scientific and technological challenges nowadays and has set the goals for fundamental experimental research and plasma modeling. The limiting step to achieve an efficient storage in high energy density chemical compounds produced from industrial CO₂ emissions is the dissociation [1]. To address this problem, a comprehensive knowledge of the electron kinetics is required. This work offers a complete and consistent set of cross sections for CO₂ to be published on the IST-LISBON database with LXCat. In addition, the existing dissociation cross sections are evaluated and a procedure for calculating the dissociation rate coefficient is recommended.

2. THE CROSS SECTION SET

The proposed cross section set was compiled mostly from Phelps [2] and it includes 17 cross sections defined up to 1000eV, describing dissociative attachment, effective momentum transfer, eleven vibrational excitation energy losses (corresponding either to the excitation of individual levels or groups of

vibrational levels), superelastic collisions with the $\text{CO}_2(010)$ vibrational state, excitation of two groups of electronic states and ionization. The modifications made in regard to the original set by Phelps are the following: the cross section for superelastic collisions with the $\text{CO}_2(010)$ state was included; the cross section for the electronic excitation at 10.5 eV and the ionization initially limited to 100 eV, were extended up to 1000 eV and replaced by the total ionization cross section from Itikawa [3], respectively; the momentum-transfer cross sections was modified for electron energies above 100 eV and slightly increased for electron energies below 0.1 eV; Some of the original vibrational excitation cross sections were deconvoluted into separate channels or groups of vibrational levels, as discussed in [4].

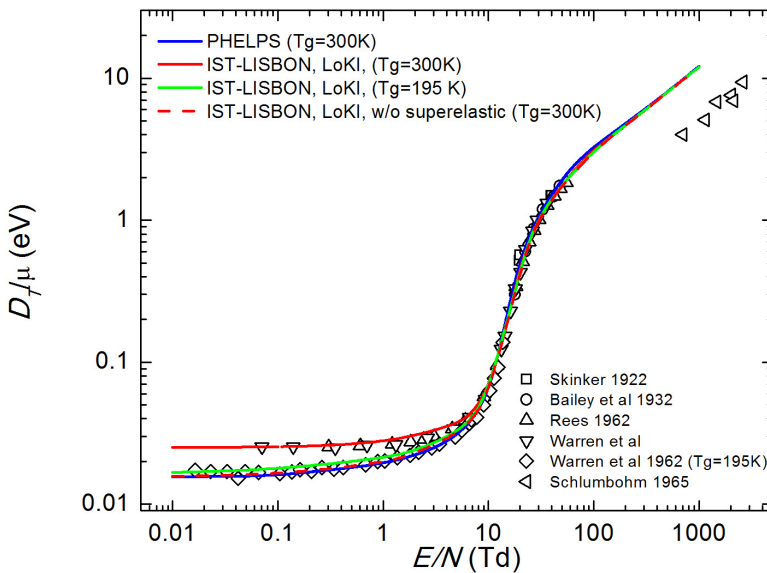


Figure 1. Measured and calculated characteristic energy in CO_2 as a function of E/N . The symbols are experimental data. The lines are calculation results obtained using the LoKI numerical code that solves the electron Boltzmann equation in two-term expansion, at different temperatures.

3. SWARM CALCULATIONS

The new IST-LISBON set yields accurate predictions of the swarm parameters when used as input data to the Boltzmann solver of the LoKI (LisOn KInetics) numerical code, that solves the electron Boltzmann equation in the usual two-term expansion in spherical harmonics. Figure 1 shows that the calculated characteristic energy exhibits the correct dependence with the gas temperature, very evident for $E/N < 10$ Td, only possible when superelastic

collisions are taken into account. In addition, the proposed cross sections are able to produce reduced electron mobility within 1% of the measurements for the lower values of E/N , as well as good predictions of the reduced Townsend ionization coefficient, (within 2%) for $E/N < 200$ Td.

Figure 2 shows that for $E/N < 70$ Td the major portion of the electron power gain from the electric field is transferred to CO_2 vibrations, which confirms an efficient input of electron energy into vibrational excitation and suggests the possibility of an effective dissociation channel through vibrational excitation, as proposed in [1].

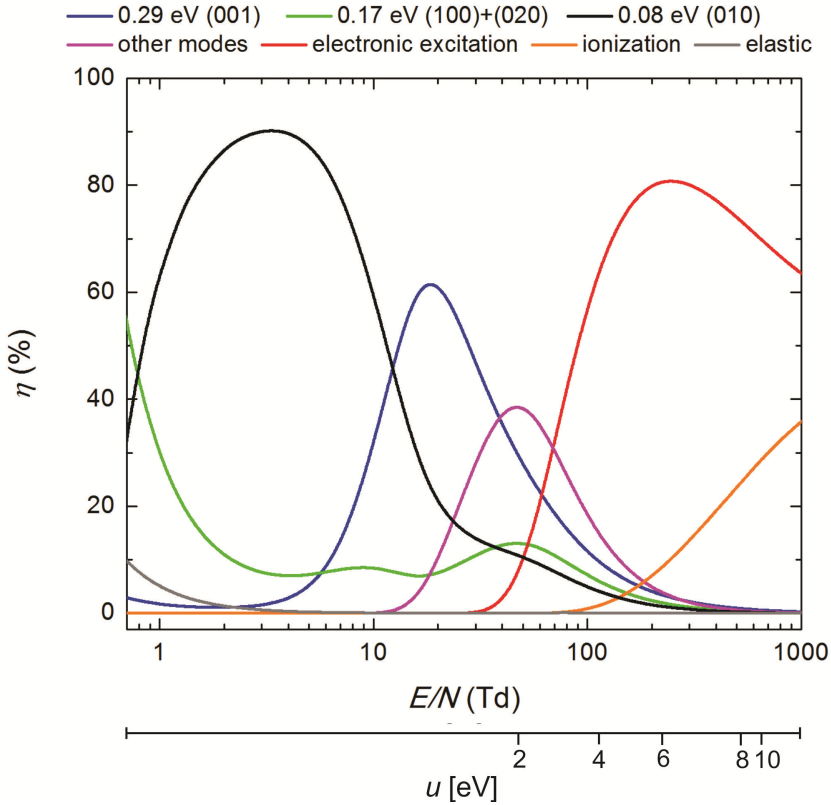


Figure 2. Electron fractional power transfer dissipated in the different channels, as a function of the reduced electric field, E/N .

4. DISSOCIATION

The plasma-based CO_2 energy storage has brought to attention the complexity of CO_2 dissociation, which is still not fully understood. In fact, there is no consensus on this matter. For instance: in [5] Phelps' cross section with

threshold at 7eV is considered to represent dissociation, while the 10.5 eV cross sections is assumed to correspond only to electronic excitation; Itikawa [3] included in his set the measured cross sections for the production of O(1S) with the threshold at 11.9 eV; Polak and Slovetsky [6] proposed calculated cross sections addressing i) the cross section related to the formation of O(3P)+CO(a3 π) and ii) cross sections of dissociation by excitation of allowed transitions. Their calculations are a good base for understanding and analyzing the problem of CO₂ dissociation, giving dissociation coefficients through mechanism i) similar to the ones obtained using the experimental cross section reported in [3] and total dissociation rates in agreement with the measurements from Corvin and Corrigan [7]. Therefore, at present we recommend using Polak and Slovetsky's cross sections for calculating the dissociation rate coefficient of CO₂. Work is in progress to verify the influence of the different cross sections in the overall kinetics of CO₂ plasmas.

Acknowledgements

This work was partially supported by the Portuguese FCT - Fundação para a Ciência e a Tecnologia, under Projects UID/FIS/50010/2013, PTDC/FIS-PLA/1420/2014 and grant PD/BD/105884/2014 (PD-F APPLAuSE).

REFERENCES

- [1] A. Fridman, Plasma Chemistry, Cambridge University Press, Cambridge, 2008.
- [2] J. J. Lowke, A. V. Phelps and B. W. Irwin, J. Appl. Phys. 44 (1973) 466471.
- [3] Y. Itikawa, J. Phys. Chem. Ref. 31 (2002) 749-767.
- [4] M. Grofulović, L.L. Alves and V. Guerra, J. Phys. D: Appl. Phys. (2016) (submitted for publication).
- [5] L. D. Pietanza, G. Colonna G, G. D'Ammando, A. Laricchiuta and M. Capitelli. Physics of Plasmas 23 (2016) 013515
- [6] L. S. Polak and D. I. Slovetsky, Int. J. Radiat. Phys. Chem. 8 (1976) 257-282
- [7] K. K. Corvin and S. J. B. Corrigan, J. Chem. Phys. 50 (1969) 2570.

MONTE CARLO SIMULATIONS OF ELECTRON TRANSPORT IN CF₃I AND SF₆ GASES

J. Mirić, D. Bošnjaković, I. Simonović, Z. Lj. Petrović and S. Dujko

*Institute of Physics, University of Belgrade,
Pregevica 118, 11080 Belgrade, Serbia*

Abstract. Electron transport coefficients in CF₃I and SF₆ gases are calculated using Monte Carlo simulations for a wide range of reduced electric field strengths. In order to compensate for the loss of electrons in simulation due to strong attachment, three different rescaling techniques are considered and applied. Among many observed phenomena, in case of SF₆ we highlight the reduction of mean electron energy with increasing electric field. In addition, we observe that for both gases bulk drift velocities exhibit negative differential conductivity which is not present in the flux drift velocity.

1. INTRODUCTION

Electron attachment in strongly electronegative gases, such as CF₃I and SF₆, has many industrial applications. For example, in high-voltage circuit breakers, it is the most significant process for the prevention of electric breakdown [1]. Electronegative gases are also used for plasma etching and cleaning in semiconductor fabrication [2].

On the other hand, electron attachment imposes practical difficulties in experiments for measurement of transport coefficients [1,3]. Considerable difficulties also appear in Monte Carlo simulations of electron transport in strongly electronegative gases at low electric fields where electron attachment is the dominant process. Due to this process, the number of electrons in a simulation can reach extremely low values leading to poor statistics or complete loss of electrons in the simulation [4,5]. In order to compensate for this loss of electrons, some sort of rescaling techniques must be used.

In this work, we discuss the existing rescaling techniques for Monte Carlo simulations of electron transport in strongly electronegative gases. Furthermore, we introduce our modified rescaling procedure and demonstrate how these techniques affect the calculated transport data for CF₃I and SF₆ gases.

2. RESCALING TECHNIQUES

The following rescaling techniques, applicable for Monte Carlo simulations, can be found in the literature:

1. Duplication of electrons randomly chosen from the remaining swarm at certain discrete time steps [6];
2. Duplication of the entire electron swarm (one or more times) at certain time steps [5] or at certain distance steps [7];
3. Introduction of an additional fictitious ionization [4] or attachment process [8] with a constant collision frequency.

An unaltered electron distribution function and its evolution are a common objective for all these techniques. In this work, the first technique will be referred to as discrete rescaling, the second as swarm duplication and the third as continuous rescaling. However, we introduce a modification to the third procedure where the fictitious ionization process is dynamically adjusted during the simulation in such way that the fictitious ionization rate is chosen to be equal to the attachment rate. Therefore, it is not necessary to define a fictitious ionization rate in advance and as a benefit, the number of electrons is kept nearly constant during the simulation.

3. RESULTS

In this section, we present the transport data for CF_3I and SF_6 gases, calculated using our Monte Carlo code [6,9] with three different rescaling techniques. The cross section set for electron scattering in SF_6 is taken from Itoh *et al.* [10]. In case of CF_3I , we use our modified cross section set [11] which is based on cross sections of Kimura and Nakamura [12]. This modification of the CF_3I set was necessary in order to provide a better agreement between the calculated data and the reference data measured in a pulsed Townsend experiment for pure CF_3I and its mixtures with Ar and CO_2 .

Figure 1(a) shows the variation of mean electron energy with E/n_0 in CF_3I . Calculations are performed assuming the three rescaling techniques. Excellent agreement between the cases of discrete rescaling and swarm duplication can be understood, having in mind that these two techniques are essentially the same. The only difference between the two is the fact that in case of discrete rescaling, the probability for duplication of an electron is determined by the ratio of current number and desired number of electrons, while in case of swarm duplication technique, this probability is set to unity i.e. the duplication is performed for all electrons. Continuous rescaling is also in a good agreement with the other two techniques.

In case of mean electron energy for the SF_6 gas, Figure 1(b) shows excellent agreement between the three rescaling techniques. Furthermore, one anomalous behavior is observed — a decrease of mean energy with increasing electric field. This phenomenon is associated with mutual influence of attachment heating and inelastic cooling. Since it is observed only in case of SF_6 ,

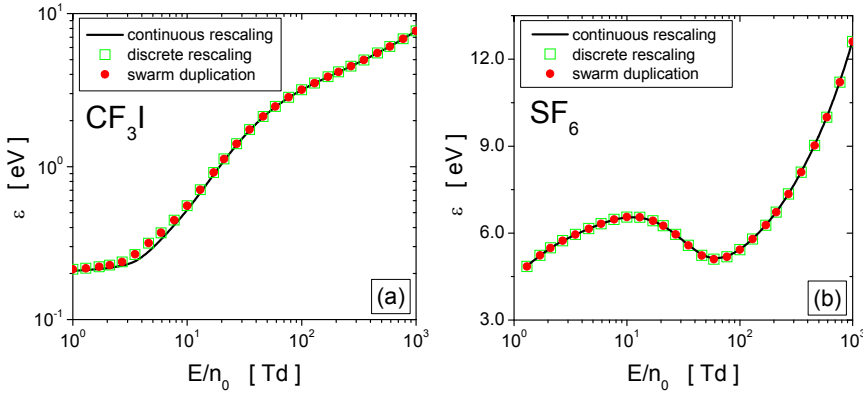


Figure 1. Mean electron energy in (a) CF_3I and (b) SF_6 gases as a function of reduced electric field. The profiles are calculated using three different rescaling techniques.

it is evident that the specific cross sections for electron scattering are essentially responsible for the occurrence of this phenomenon.

Figure 2 shows flux and bulk drift velocities in (a) CF_3I and (b) SF_6 gases, obtained with three rescaling techniques. For electrons in CF_3I , the drift velocities calculated using discrete rescaling and swarm duplication are again in excellent agreement while continuous rescaling at low electric fields gives slightly lower values than the other two techniques. For drift velocities in the SF_6 gas, all three rescaling techniques are in good agreement over the entire range of reduced electric fields considered in this work. We can conclude that the nature of the cross sections for electron scattering in CF_3I and SF_6 and their energy dependence are responsible for the differences between the results obtained using different rescaling techniques.

Two interesting phenomena are also observed in Figure 2. First, for

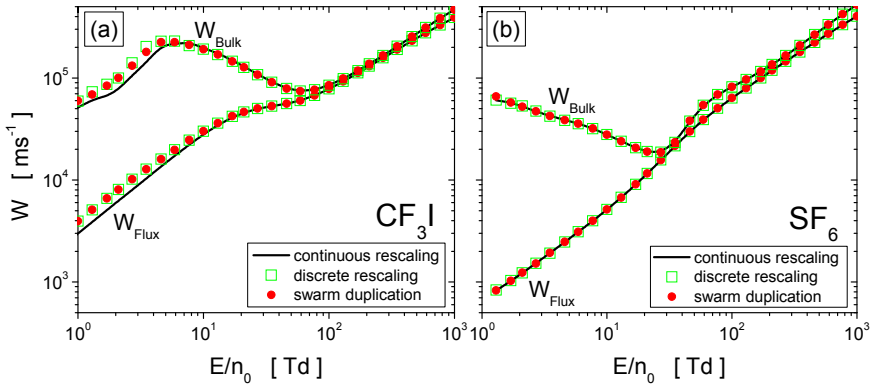


Figure 2. Variation of the drift velocity with E/n_0 for electrons in (a) CF_3I and (b) SF_6 gases. The profiles are calculated using three different rescaling techniques.

both gases the bulk drift velocity is higher than the flux drift velocity. In low energy range, this is a consequence of strong attachment heating (the consumption of slow electrons due to attachment) while in higher energy range the explicit effect of ionization is responsible. As a result, new electrons are preferentially created at the front of the swarm and/or slow electrons are consumed at the back of the swarm resulting in a forward shift of centre of mass of the swarm which is observed as an increase of bulk drift velocity over the flux drift velocity. The other phenomenon is a very strong NDC effect (negative differential conductivity) which is noticed for both gases, but only in case of bulk component drift velocity. This behavior appears to be common for all strongly electronegative gases since it is induced by explicit effects of electron attachment.

Acknowledgements

This work is supported by MPNTRRS Projects OI171037 and III41011.

REFERENCES

- [1] L. G. Christophorou and J. K. Olthoff, *Fundamental electron interactions with plasma processing gases*, (Springer, New York, 2004).
- [2] T. Makabe and Z. Lj. Petrović, *Plasma Electronics: Applications in Microelectronic Device Fabrication*, (CRC Press, New York, 2014).
- [3] Z. Lj. Petrović *et al.*, J. Phys. D: Appl. Phys. 42, 194002 (2009).
- [4] M. Yousfi, A. Hennad and A. Alkaa, Phys. Rev. E 49, 3264 (1994).
- [5] A. M. Nolan, M. J. Brennan, K. F. Ness and A. B. Wedding, J. Phys. D 30, 2865 (1997).
- [6] Z. M. Raspopović, S. Sakadžić, S. Bzenić and Z. Lj. Petrović, IEEE Trans. Plasma Sci. 27, 1241 (1999).
- [7] N. A. Dyatko and A. P. Napartovich, J. Phys. D 32, 3169 (1999).
- [8] Y. M. Li, L. C. Pitchford and T. J. Moratz, Appl. Phys. Lett. 54, 1403 (1989).
- [9] S. Dujko, R. D. White and Z. Lj. Petrović, J. Phys. D: Appl. Phys. 41, 245205 (2008).
- [10] H. Itoh, T. Matsumura, K. Satoh, H. Dane, Y. Nakano and H. Tagashira, J. Phys. D 26, 1975 (1993).
- [11] J. Mirić, O. Šašić, S. Dujko and Z. Lj. Petrović, Proc. 27th Summer School and International Symposium on the Physics of Ionized Gases (Belgrade) 2014, p. 122.
- [12] M. Kimura and Y. Nakamura, J. Phys. D 43, 145202 (2010).

ELECTRON TRANSPORT IN MERCURY VAPOR: DIMER INDUCED NDC AND ANALYSIS OF TRANSPORT PHENOMENA IN ELECTRIC AND MAGNETIC FIELDS

J. Mirić, I. Simonović, D. Bošnjaković, Z. Lj. Petrović and S. Dujko

*Institute of Physics, University of Belgrade,
Pregevica 118, 11080 Belgrade, Serbia*

Abstract. Transport coefficients for electron swarms in mercury vapor in the presence of electric and magnetic fields are calculated and analyzed using a multi term theory for solving the Boltzmann equation and Monte Carlo simulation technique. Particular attention is paid to the occurrence of negative differential conductivity (NDC) at higher gas pressures and temperatures. It is shown that the correct representation of the presence of mercury dimers and superelastic collisions plays a key role in the analysis of NDC. When both the electric and magnetic fields are present, another phenomenon arises: for certain values of electric and magnetic field, we find regions where swarm mean energy increases with increasing magnetic field for a fixed electric field. Spatially-resolved electron transport properties are calculated using a Monte Carlo simulation technique in order to understand these phenomena.

1. INTRODUCTION

In this work we discuss the transport of electrons in mercury vapor and its mixtures with argon under conditions relevant for metal vapor lamps. Current models of such lamps require knowledge of transport coefficients as a function of electric field strengths, gas pressures and temperatures. Recently developed inductively coupled plasma light sources require the knowledge of transport coefficients when both the electric and magnetic fields are present and crossed at arbitrary angles [1]. These transport coefficients can be either measured in swarm experiments or calculated from transport theory. To date, no experiments exist that can measure all the required transport coefficients, including rate coefficients, drift velocities, and diffusion coefficients for electrons in gases in the presence of electric and magnetic fields.

In the present work we solve the Boltzmann equation for electron swarms undergoing ionization in mercury vapor and its mixtures with argon in the presence of electric and magnetic fields crossed at arbitrary angles. For the E -only case we discuss the occurrence of negative differential conductivity (NDC) for

higher gas pressures and temperatures in the limit of lower electric fields. NDC is a phenomenon where the drift velocity decreases with increasing electric field. For electrons in mercury vapor this behavior of the drift velocity is attributed to the presence of mercury dimers.

In the second part of this work we investigate the electron transport in varying configurations of electric and magnetic fields. In particular, we discuss the following phenomenon: for certain values of electric and magnetic fields, we find regions where swarm mean energy increases with increasing magnetic field for a fixed electric field. The phenomenon is discussed using spatially-resolved transport data calculated in Monte Carlo simulations.

2. CROSS SECTIONS AND SIMULATION TECHNIQUES

The cross section for momentum transfer in elastic collisions is made as follows. For lower electron energies, we use a cross section from [2] while for higher energies, we use a cross section tabulated in MAGBOLTZ code [3]. Cross sections for electronic excitations for levels 3P_0 , 3P_1 and 3P_2 are retrieved from [4] while electronic excitations to 1S_0 and 1P_1 states as well as a cross section for higher states are also taken from MAGBOLTZ code. For electron-impact ionization, we have used a cross section from [5]. The effective cross section which describes vibration and electronic excitations of mercury dimers is derived using the experimental measurements of Elford [6]. Cross sections were slightly modified during the calculations to improve agreement between the calculated swarm parameters and the experimental values [6].

Electron transport coefficients are calculated from the multi term solution of Boltzmann's equation. A Monte Carlo simulation technique is used to verify the Boltzmann equation results and also for the calculations of spatially-resolved transport data.

3. RESULTS AND DISCUSSIONS

In Figure 1 (a) we show the variation of the drift velocity with E/n_0 for a range of gas pressures, as indicated on the graph. Calculations are performed in a wide range of pressures, from 20.2 to 108.4 Torr. The temperature of the background gas is 573K. The same range of pressures and temperatures was considered by Elford in his experiments [6]. We extend his measurements by considering the drift of electrons for six additional gas pressures. For E/n_0 less than approximately 2.5 Td the pressure dependence of the drift velocity is clearly evident. For higher E/n_0 , however, the drift velocity does not depend on the pressure. For pressures higher than approximately 200 Torr, we see that the drift velocity exhibits a region of NDC, i.e. over a range of E/n_0 values the drift velocity decreases as the driving field is increased. The conditions for the occurrence of NDC have been investigated previously [7]. For electrons in mercury vapor, NDC arises for certain combinations of elastic cross sections of dimer-free mercury vapor and inelastic cross sections of mercury dimers in

which, on increasing the electric field, there is a rapid transition in the dominant energy loss mechanism from inelastic to elastic. For pressures lower than 200 Torr the elastic cross section of dimer-free mercury vapor dominates the effective inelastic cross section of mercury dimers. Thus, the conditions for the occurrence of NDC are not set. For higher pressures, the phenomenon is promoted by either or both of (i) a rapidly increasing cross section for elastic collisions and (ii) a rapidly decreasing inelastic cross section. It is clear that the presence of dimers plays a key role in the development of NDC in mercury vapor.

In Figure 1 (b) we show a comparison between our calculations and experimental measurements of the drift velocity for a range of pressures. Our Monte Carlo results (figure 1 (b)) agree very well with those measured in the Bradbury-Nielsen time-of-flight experiment [6]. The agreement is achieved only after careful implementation of superelastic collisions in our calculations. Cross sections for superelastic collisions are calculated directly in our code from the principle of detailed balance.

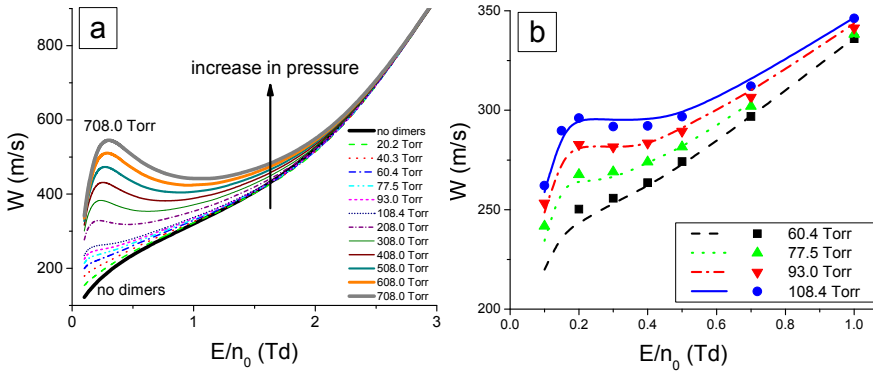


Figure 1. Variation of the drift velocity with E/n_0 for a range of pressures (a) and comparison between our Monte Carlo results and experimental measurements. Calculations are performed for electrons in mercury vapor. The temperature of the background gas is 573K.

In the last segment of this work we discuss the impact of a magnetic field on the electron transport in mercury vapor. The pressure and temperature of the mercury vapor are set to 1 Torr and 293K, respectively. As an example of our study, in figure 2 we show the variation of the mean energy with E/n_0 for a range of the reduced magnetic fields B/n_0 , in a crossed field configuration. In the limit of the lowest E/n_0 the electrons are essentially in the quasi-thermal equilibrium with the mercury vapor, independent of the strength of the applied magnetic field. In this regime, the longitudinal and transverse drift velocity components are dependent on both E/n_0 and B/n_0 while the diagonal diffusion tensor elements along the \mathbf{E} and $\mathbf{E} \times \mathbf{B}$ directions are dependent on B/n_0 only. The diffusion coefficient along the magnetic field direction is reduced to its thermal value as magnetic field only affects the diffusion in this direction indirectly, through the magnetic field's action to cool the swarm. Certainly one of the most striking

properties observed in the profiles of transport coefficients is an increase in the swarm mean energy with increasing magnetic field for a fixed electric field. The phenomenon is evident in the range $E/n_0=5-200$ Td for B/n_0 considered in this work. This behavior is contrary to previous experiences in swarm physics as one would expect the mean swarm energy to decrease with increasing B/n_0 for a fixed E/n_0 . The phenomenon could be associated with the interplay between magnetic field cooling and inelastic/ionization cooling, although the role of the cross sections in both phenomena is of course vital. The electron energy distribution function and spatially-resolved mean energy, rate coefficients and other properties are calculated using a Monte Carlo simulation technique in order to explain this phenomenon.

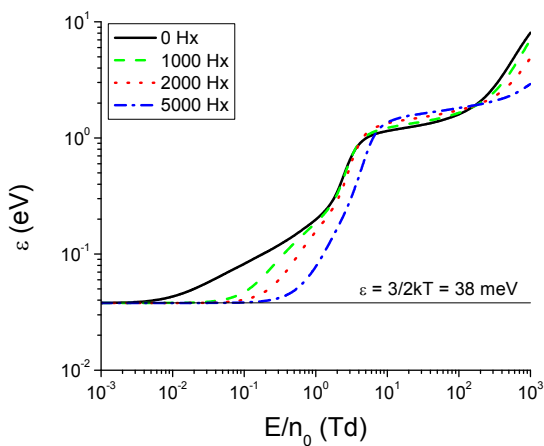


Figure 2. Variation of the mean energy with E/n_0 for a range of B/n_0 . Calculations are performed for electrons in mercury vapor.

Acknowledgements

This work is supported by MPNTRRS Projects OI171037 and III41011.

REFERENCES

- [1] G.G. Lister, J.E. Lawler, W.P. Lapatovich and V.A. Godyak, *Rev. Mod. Phys.* 76, 541 (2004)
- [2] J. P. England and M. T. Elford, *Aust. J. Phys.* 44, 647 (1991)
- [3] <http://magboltz.web.cern.ch/magboltz>
- [4] K. Bartschat, 3rd Int. Conf. on Atomic and Molecular Data and their Applications (New York: American Institute of Physics), 2003
- [5] L. J. Kieffer and G. H. Dunn, *Rev. Mod. Phys.* 38, 1 (1966)
- [6] M. T. Elford, *Aust. J. Phys.* 33, 231 (1980)
- [7] S.B. Vrhovac and Z.Lj. Petrovič, *Phys. Rev. E* 53, 4012 (1996)

CROSS SECTION AND TRANSPORT PARAMETERS FOR K^+ IN DIMETHOXY ETHANE

Ž. Nikitović, M. Gilić, Z. Raspopović, M. Petrović and V. Stojanović

*Institute of Physics, University of Belgrade, Pregrevica 118, 11080 Belgrade,
Serbia*

Abstract. In this work we present most probable reactions of alkali metal ion K^+ with dimethoxy ethane (DXE) molecule. Appropriate gas phase enthalpies of formation for the products were used to calculate scattering cross section as a function of kinetic energy. Three body association reaction of ion with DXE is studied and compared to experimental results. Calculated cross sections were used to obtain transport parameters for K^+ in DXE gas.

1. INTRODUCTION

Cold plasmas are often used in new technologies where they offer methods for nonintrusive production or modification of specific substances. Main characteristics of these plasmas are their high electron temperature and low gas temperature. Dimethoxy-containing compounds, such as dimethoxy ethane (DXE), can be produced from dimethyl ether by using dielectric barrier discharge (DBD) plasmas containing water vapor at atmospheric pressure [1]. As clear and colorless liquid at room temperature and atmospheric pressure, DXE is used as a precursor in production of ceramics or as a sole compound to make other chemicals such as those used in lithium batteries production, superconductor production and nanoparticles synthesis.

In this paper we firstly selected the most probable reactions of alkali metal ion K^+ with DXE molecule (and its most probable products) for thermodynamic threshold energies below about 15 eV. Appropriate gas phase enthalpies of formation [2] for the products were used to calculate thermodynamic thresholds.

2. CROSS SECTION SET

The scattering cross section of alkali ion K^+ on DXE are calculated by using the Denpoh-Nanbu (DN) theory [3] separating elastic from reactive collisions. DXE is known not to have dipole moment in its ground state. The dipole polarizability of $9.94 \times 10^{-30} \text{ m}^3$ [4] is used for the DXE target. Similar to

our recent papers [5] DN method is used to separate elastic from reactive endothermic collisions by accounting the thermodynamic threshold energy and branching ratio according to the Rice-Rampsperger-Kassel (RRK) theory [3]. Within the RRK theory the internal energy is being distributed among an empirical number of s equivalent effective modes of the complex selected from the total number of atoms involved in the complex.

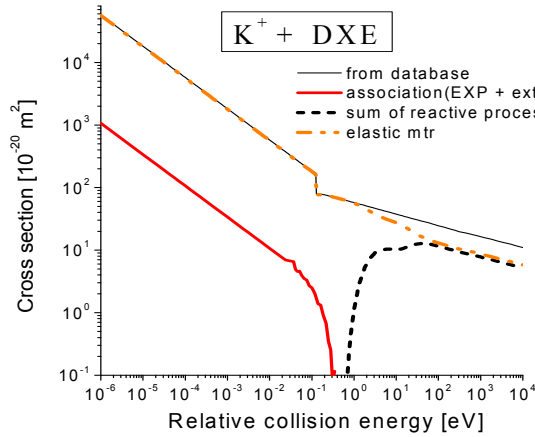


Figure 1. Cross section sets for K^+ in DXE.

Elastic momentum transfer cross section is modified in order to fit approximate mobility peak characteristic for presented systems. Swarm method [5, 6] is exploited to modify the cross section for elastic momentum transfer where for reduced mobility in the peak region (experimental [7] or theoretical values [8]) similarity with ions of equal or similar reduced mass is targeted. Elastic momentum transfer cross section for elastic collisions of K^+ with DXE is presented in Figure 1.

3. DISCUSSION AND RESULTS

Swarm parameters as a function of reduced electric field E/N in DC electric fields are generally applied to plasma modeling and simulations.

We have used a Monte Carlo code that properly takes into account thermal collisions [9]. The code has passed all the relevant benchmarks and has been tested in our work on several types of charged particles.

In Figure 2. we show the mean energy, which cannot be directly measured in experiments but a map of the mean energy versus E/N may be used

directly to provide the data in fluid models especially when the local field approximation fails.

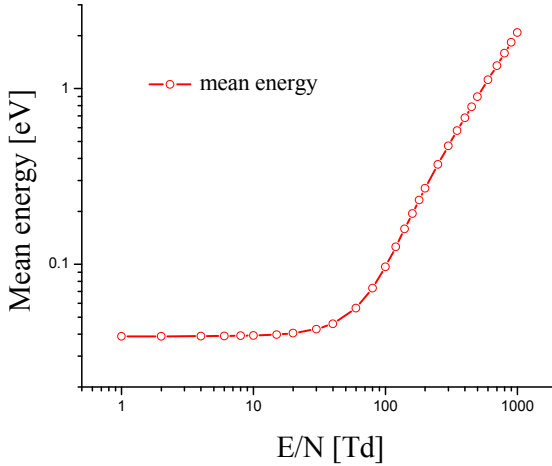


Figure 2. Mean energy of K^+ ions in DXE gas as a function of E/N at $T = 300$ K.

In Figure 3. we show the results of Monte Carlo simulation for reduced mobility as a function of E/N . Due to reactive collisions bulk and flux values of reduced mobility are separated.

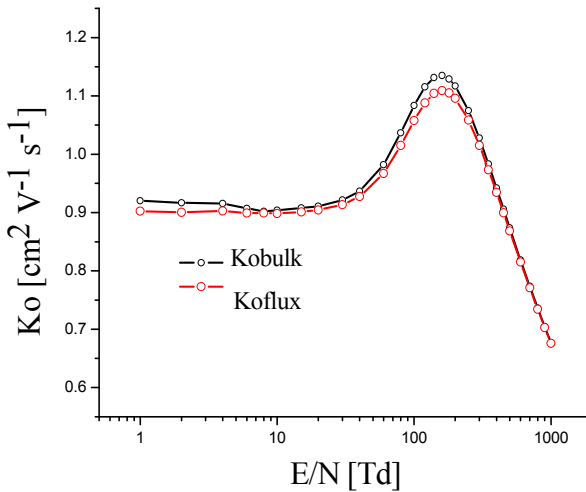


Figure 3. Reduced mobility of K^+ ions in DXE as a function of E/N at $T=300$ K.

The mobility K of an ion is the quantity defined as the velocity attained by an ion moving through a gas under the unit electric field. One often exploits the reduced or standard mobility defined as:

$$K_0 = \frac{v_d}{N_0 E} N, \quad (1)$$

where v_d is the drift velocity of the ion, N is the gas density at elevated temperature T and E is the electric field.

4. CONCLUSION

Calculated cross sections are used to obtain transport parameters for alkali metal ion K^+ in DXE gas.

The cross sections and transport data for technologically very important gas DXE have been determined by using simple theory. While it is a good basis for modeling it would be much better to add a data base of measured transport coefficients and then to perform the analysis again.

Acknowledgements

Results obtained in the Institute of Physics University of Belgrade under the auspices of the Ministry of Education, Science and Technology, Projects No. 171037 and 410011.

REFERENCES

- [1] Y. Wang, C. Liu, Y. Zhang, *Plasma Sci. & Technology* 7, No. 3, 2839 (2005).
- [2] S. G. Lias, J. E. Bartmess, J. F. Xebman and J. L. Holmes, R. D. Levin and W. G. Mallard, *J. Phys. Chem. Ref. Data, Supl. 1* Vol. 17, 1 (1988).
- [3] K. Denpoh and K. Nanbu, *J. Vac. Sci. Technol. A* 16 (3), 1201 (1998).
- [4] H. Koizumi, P. B. Armentrout, *J. Chem. Phys.* 119, 12819 (2003).
- [5] V. Stojanović, Z. Raspopović, J. Jovanović, Ž. Nikitović and Z. Lj. Petrović, *EPL* 101, 45003 (2013).
- [6] Ž. Nikitović, Z. Raspopović, V. Stojanović and J. Jovanović, *EPL* 108, 35004 (2014).
- [7] L. A. Viehland and E. A. Mason, *At. Data. Nucl. Data Tables* 60, 37 (1995).
- [8] http://nl.lxcat.net/data/set_type.php.
- [9] Z. Ristivojević and Z. Lj. Petrović, *Plasma Sources Sci. Technol.* 21, 035001 (2012).

TRANSPORT PROPERTIES OF He⁺ IN CF₄

Ž. Nikitović, Z. Raspopović and V. Stojanović

Institute of Physics, University of Belgrade, Pregrevica 118, 11080 Belgrade, Serbia

Abstract. In this paper we are presenting cross section set for scattering He⁺ ions in CF₄ that is assessed by using available experimental data for charge transfer cross sections. Monte Carlo method is used to calculate mean energy and drift velocity as a function of E/N and discussed as a consequence of non-conservative reactions at temperature $T=300$ K.

1. INTRODUCTION

Charge transfer reactions of ions with molecules are unavoidable elementary processes in modeling kinetics in terrestrial, industrial and astrophysical plasmas. In selected cases charge transfer reactions are known to represent the most significant part of a cross section set. Line spectra of excited atoms obtained in spectrometric measurements in CF₄ indicate that the charge transfer reaction is dominant process in collisions with inert gas ions. Thus, in this work we assessed cross section set for He⁺ in CF₄ by using existing experimental data [1] for charge transfer collisions producing radical ions of CF₄. Since no direct information is found in the literature how mobility of high recombination energy ions such as He⁺ ions behaves in CF₄ gas we also calculated transport parameters by using Monte Carlo simulation technique [2].

2. MONTE CARLO TECHNIQUE

The cross sections measured by Fisher *et al.* [1] were used to deduce elastic momentum transfer cross section (Figure 1) assuming total momentum transfer cross section σ_{mt} is known. At very low energies we assumed that σ_{mt} behaves as Langevin's cross section and elastic momentum transfer cross section is determined by deducing all reactive cross sections i.e productions of CF₂⁺ and CF₃⁺ ions. In the absence of association reaction [1] these were only processes that may affect mobility of He⁺ ions. Accordingly for average polarizability of CF₄ we adopted value of 3.86 Å³ used by Stojanović *et al.* [3] who found excellent agreement between experimental and calculated mobility of CF₃⁺ ions in CF₄.

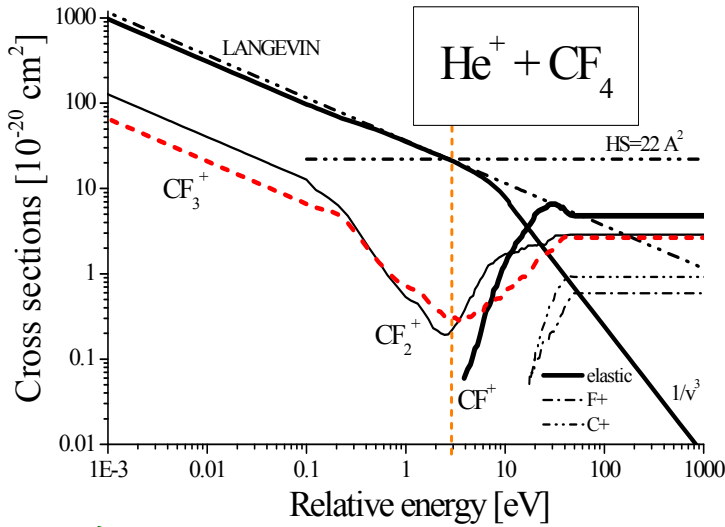


Figure 1. Cross section set for He^+ in CF_4 .

Further, extrapolation of elastic momentum transfer cross section trend beyond crossing point of Langevin's and hard sphere (HS) cross section [1] is done by smoothly connecting to $1/v^3$ trend [4, 5] where v is the center-of-mass velocity (see Figure 1).

At all ion kinetic energies above 50 eV reactive cross sections are extrapolated by constant values.

Effect of various extrapolations (short dot-dashed or dashed line in Figure 1) of unusual behavior at low energy, observed with measurements of the cross section leading to formation of CF_2^+ (where irrespective of the He^+ spin state exothermic behavior of reaction is expected) is found negligible on mobility.

3. DISCUSSION AND RESULTS

The transport coefficients include drift velocity, diffusion coefficients, ionization and attachment coefficients and chemical reaction coefficients for ions [2]. Excitation coefficients are also measured but seldom used in modeling.

Swarm parameters are generally applied in plasma modeling and simulations. At the same time, the non-equilibrium regime in discharges is well represented under a broad range of conditions by using Monte Carlo simulation scheme.

In this work we use Monte Carlo technique that accounts for a finite gas temperature of the background gas particles [6] to calculate swarm parameters of He^+ ions in CF_4 gas for temperature $T=300$ K.

In Figure 2 we show the characteristic energies (diffusion coefficient normalized to mobility eD/K in units of eV) based on longitudinal (D_L) and transversal (D_T) diffusion coefficients.

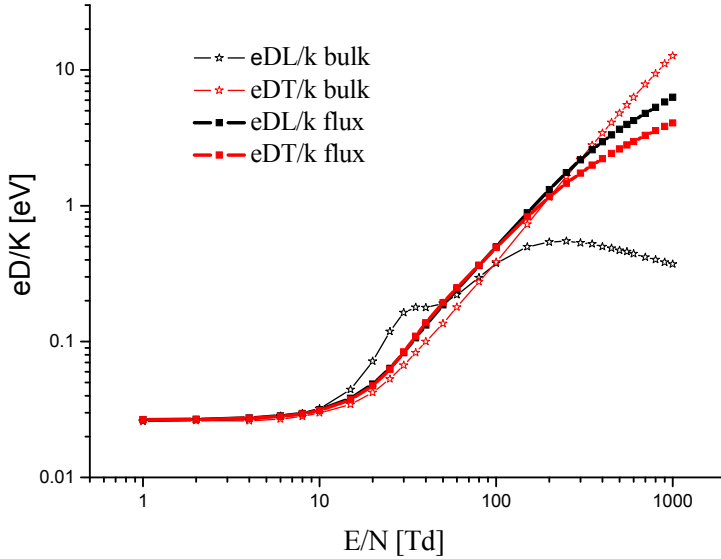


Figure 2. Characteristic energy of He^+ ions in CF_4 gas as a function of E/N at $T = 300$ K.

The bulk and flux drift velocities for He^+ in CF_4 as a function of E/N are given in Figure 3. The drift velocities obtained by Monte Carlo simulation are calculated in real space (bulk) and in velocity space (flux) values and are obtained as $\langle v \rangle$ and dx/dt , respectively. The bulk and flux values of the drift velocity begin to differ above 20 Td.

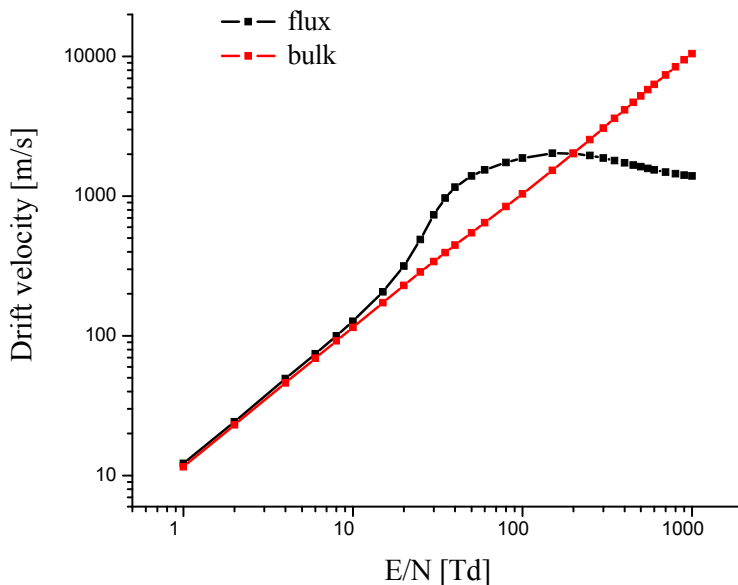


Figure 3. The bulk and flux drift velocity of He^+ ions in CF_4 as a function of E/N at $T=300$ K.

Acknowledgements

Results obtained in the Institute of Physics University of Belgrade under the auspices of the Ministry of Education, Science and Technology, Projects No. 171037 and 410011.

REFERENCES

- [1] E. R. Fisher, M. E. Weber and P. B. Armentrout, *J. Chem. Phys.* 92, 2296 (1990).
- [2] Z. Lj. Petrović, S. Dujko, D. Marić, G. Malović, Ž. Nikitović, O. Šašić, J. Jovanović, V. Stojanović and M. Radmilović-Radenović, *J. Phys. D: Appl. Phys.* 42, 194002 (2009).
- [3] V. Stojanović, Z. Raspopović, J. V. Jovanović, J. de Urquijo and Z. Lj. Petrović, *J. Phys. Conf. Ser.* 514, 012059 (2014).
- [4] P. S. Krstić and D. R. Schultz, *J. Phys. B: At. Mol. Opt. Phys.* 42, 065207 (2009).
- [5] Z. Raspopović, V. Stojanović and Ž. Nikitović, *EPL* 111, 45001 (2015).
- [6] Z. Lj. Petrović, Z. M. Raspopović, V. D. Stojanović, J. V. Jovanović, G. Malović, T. Makabe and J. de Urquijo, *Appl. Surf. Sci.* 253, 6619 (2007).

TRANSPORT COEFFICIENTS FOR ELECTRON SWARMS IN LIQUID ARGON AND LIQUID XENON

I. Simonović¹, Z. L.J. Petrović¹, R.D. White² and S. Dujko¹

¹*Institute of Physics, University of Belgrade,
Pregrevica 118, 11080 Belgrade, Serbia*

²*College of Science & Engineering, James Cook University, Townsville 4810,
Australia*

Abstract. We have developed a Monte Carlo code for the calculation of transport coefficients for electron swarms in non-polar liquids. Transport coefficients for electron swarms in liquid argon and liquid xenon are calculated for $10^{-3} \leq E/n_0 \leq 10^3$ Td. Effects caused by fluctuations of density are neglected. Calculated transport coefficients in liquid phase are compared with those in the gas phase and differences are addressed using physical arguments.

1. INTRODUCTION

Transport of charged particles in liquids is a growing field of research, which addresses some fundamental questions and has many important applications. One of the most attractive applications is the interdisciplinary field of plasma medicine, which requires a detailed description of the behavior of electrons in liquid water and structures found in the living tissue. Additional applications are found in the technology behind the liquid argon and liquid xenon time projection chambers which are designed for detection of cosmic radiation, and search for dark matter particles.

Knowledge of transport coefficients in the liquid phase is also necessary for modeling of electrical discharges in liquids. There were many attempts to calculate transport coefficients of electron swarms in liquids. Cohen and Lekner calculated cross sections for electrons in the liquid phase argon which include coherent scattering effects [1,2]. In addition, they solved the Boltzmann equation using the two term approximation. Atrazhev and Iakubov [3] developed effective cross sections for electrons in liquid argon, krypton and xenon, which, for small energies, depend on density only. Numerical values of these cross sections, at low energies, must be found empirically. They subsequently had performed calculations in the framework of Cohen-Lekner theory and they obtained good agreement with experiment. Boyle et al [4,5] have recently determined *ab initio* differential cross sections for the gas phase argon and xenon by solving Dirac-

Fock scattering equations. Their cross sections are in a good agreement with experiment. They have derived liquid phase cross sections from those for the gas phase. In their work, the Cohen-Lekner procedure was extended to consider multipole polarizabilities and a non-local treatment of exchange. The calculation of transport coefficients in their work was performed using a multi term solution of Boltzmann's equation.

2. THEORETICAL EVALUATION

We have developed a Monte Carlo code for the calculation of transport coefficients of swarms of electrons and positrons in the liquid phase. Elastic scattering is treated in a way which is similar to the method described in the paper by Tattersall et al [6]. This method uses the fact that in the liquid phase mean free paths for the transfer of energy and momentum are different, due to structure effects. This allows the correct representation of the net transfer of momentum and energy, by including additional collisional processes in which only momentum/energy are exchanged. The mean free paths for the transfer of energy and momentum are given by the following equations,

$$\Lambda_0 = \left(n_0 2\pi \int_0^\pi d\chi \sin \chi (1 - \cos \chi) \sigma_{sp}(\varepsilon, \chi) \right)^{-1}, \quad (1)$$

$$\Lambda_1 = \left(n_0 2\pi \int_0^\pi d\chi \sin \chi (1 - \cos \chi) \sigma_{sp}(\varepsilon, \chi) S(\Delta\vec{k}) \right)^{-1}, \quad (2)$$

where $\sigma_{sp}(\varepsilon, \chi)$ is the differential cross section for electron scattering on a single molecule, and $S(\Delta\vec{k})$ is the static structure factor. The validity of our code is verified by comparison with benchmark calculations for the Percus Yevick model liquid [6]. Due to the lack of an adequate theory for the treatment of inelastic collisions in liquids, we have implemented the following strategy. For electron-impact ionization, we applied the gas phase cross sections, with thresholds which are reduced to the values suggested in the literature. For excitations, however, we apply two different scenarios. In the first scenario, the excitations are completely neglected. This is the so-called two-level model in which only ground state and conduction band are present [7]. In the second scenario, the gas phase excitations, with thresholds which are lower than the reduced threshold for ionization, are included in our set of cross sections. The remaining excitations are neglected. Fluctuations of density, and effects which are produced by interaction of swarm particles with polar background molecules are not included. Therefore, the applicability of our code is limited to non-polar liquids in which bubble/cluster formation is not appreciable.

3. RESULTS AND DISCUSSIONS

In figure 1 we show the variation of ionization rate coefficient with E/n_0 for electrons in liquid and gas xenon. We see that the ionization rate coefficients for electrons in both liquid scenarios are significantly greater than the corresponding rate coefficient for electrons in the gas phase. This is in part due to the cooling action associated with the inelastic collisions in the gas system, and also due to the modifications of the scattering potential between the gas and liquid phases. Comparing the two liquid scenarios, the ionization rate is greater without excitations. The reason is obvious: the competitive processes that lead to electronic excitation in which electrons lose energy are removed. It should be noted that the difference between ionization rate coefficients for different liquid scenarios is more pronounced for electrons in liquid argon than for electrons in liquid xenon.

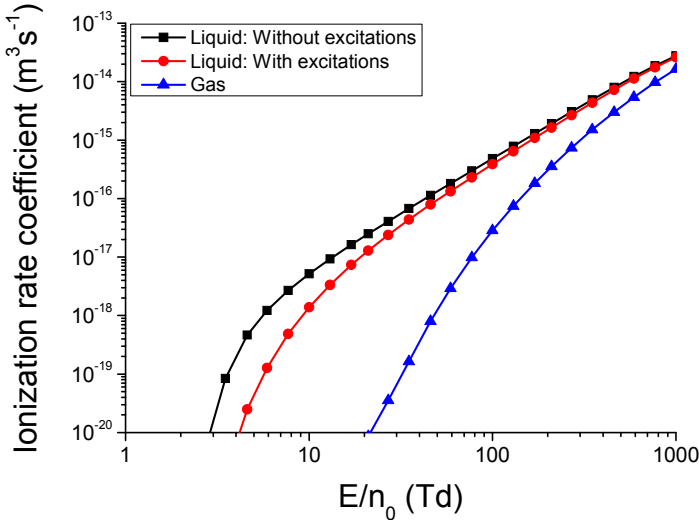


Figure 1. Variation of the ionization rate coefficient with E/n_0 for electrons in liquid and gas xenon.

In figure 2 we show the variation of the bulk drift velocity with E/n_0 for electrons in liquid and gas xenon. In the profile of the bulk drift velocity for electrons in the liquid phase, we observe negative differential conductivity (NDC). NDC is characterized by a decrease in the drift velocity despite an increase in the magnitude of applied electric field. While NDC has been demonstrated in the past to be a consequence of inelastic or non-conservative processes [8], its occurrence here is purely a result of including structure effects. The same effect has been already reported in the literature [3,4], and an analytic prescription for its occurrence has been presented [9,10]. For electrons in liquid Xe, NDC occurs for $0.01 \leq E/n_0 \leq 1$ Td. The corresponding range of mean energies is between 0.5 eV and 1.9 eV. In these field (energy) regions an

increase in the field leads to a sharp increase in the momentum-transfer cross section and hence a decrease in drift velocity. Structure induced NDC will be further investigated in our work, by simulating the spatially-resolved transport properties for electron swarms in liquid argon and liquid xenon.

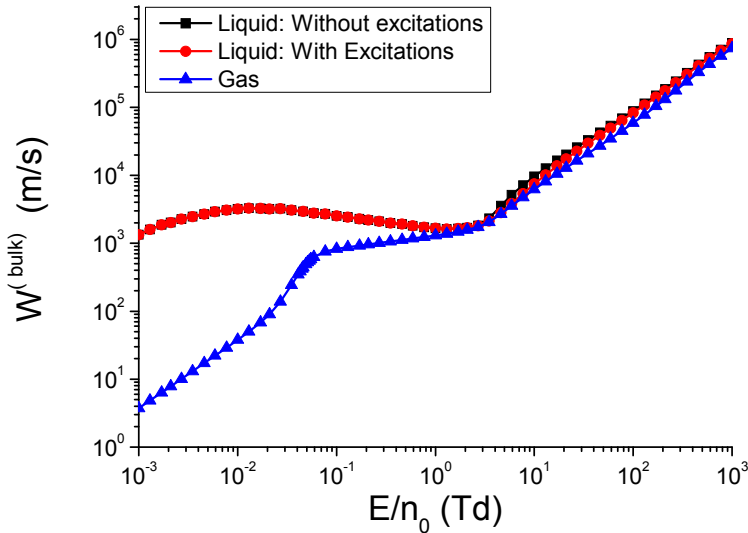


Figure 2. Variation of the bulk drift speed with E/n_0 for electrons in liquid and gas xenon.

Acknowledgements

This work was supported by MPNTRRS Projects OI171037 and III41011. RDW would like to thank the Australian Research Council.

REFERENCES

- [1] M. H. Cohen and J. Lekner, Phys. Rev. 158, 305 (1967)
- [2] J. Lekner Phys. Rev. 158, 130 (1967)
- [3] V.M. Atrazhev and I.T. Iakubov J. Phys. C 14, 5139 (1981)
- [4] G.J. Boyle et al. J. Chem. Phys. 142, 154507 (2015)
- [5] G.J. Boyle et al. arXiv:1603.04157v1 [physics.atom-ph]
- [6] W. J. Tattersall et al. Phys. Rev. E 91, 043304 (2015)
- [7] V M Atrazhev and E G Dmitriev J. Phys. C 18 (1985) 1205-1215.
- [8] S.B. Vrhovac and Z.Lj. Petrovič, Phys. Rev. E 53, 4012 (1996)
- [9] R.D. White et al, Phys. Rev. Lett. 102, 230602 (2009)
- [10] G.J. Boyle et al. New J. Phys. 14, 045011 (2012)

TRANSITION OF AN ELECTRON AVALANCHE INTO A STREAMER IN LIQUID ARGON AND LIQUID XENON

I. Simonović¹, Z. L.J. Petrović¹, R.D. White² and S. Dujko¹

*¹Institute of Physics, University of Belgrade,
Pregrevica 118, 11080 Belgrade, Serbia*

*²College of Science & Engineering, James Cook University, Townsville 4810,
Australia*

Abstract. In this work we investigate transition of an electron avalanche into a streamer, in liquid argon and liquid xenon, using 1.5 dimensional first-order fluid model. Electron transport coefficients used as input in fluid equations are calculated by our Monte Carlo simulation code. Streamer results in the liquid phase are compared to those in the gas phase.

1. INTRODUCTION

Electrical discharges in liquids have many important applications ranging from plasma medicine and water purification to transformer oils and miniaturized chemical analysis of liquid composition. However, detailed understanding of these discharges, which is necessary for their better stabilization and control, remains elusive, due to their complexity and diversity. Bubble formation and evolution, presence of impurities and solvation of electrons in polar liquids can all have significant impact on discharge dynamics in the liquid phase. Moreover, it is not possible to set up some experiments in liquids, the equivalent of which have been very useful for the study of gas discharges. Experiments which investigate electron avalanches in plane parallel geometry, in order to determine electron impact ionization coefficient, are one such example. In the case of liquids, high electric fields necessary for electron impact ionization, would lead immediately to breakdown [1]. This hinders the possibility to experimentally observe the gradual transition of an electron avalanche into a discharge, in a uniform external field. The presence of such experimental difficulties increases the importance of theoretical studies, both for the purpose of developing insight into the relevant physical phenomena, and for designing the future experiments. However, theoretical investigation of the behavior of charged particles in liquids also faces many problems. Many of those problems are related to accurate description of interaction between charged particles and the background molecules. The most recent advancement in the theoretical description of

transport of electrons in the liquid phase is presented in the papers by Boyle et al [2,3].

In this work we study the transition of an electron avalanche into a streamer in liquid argon and liquid xenon, in the presence of a constant external electric field, by employing 1.5 dimensional first-order fluid model. A similar study has been recently performed by Naidis [4] for electrons in liquid cyclohexane, although his simulations were done in point to plane geometry.

2. THEORETICAL EVALUATION

In this work we apply the first-order fluid model which is based on the drift-diffusion equation for electrons (1) and number balance equations for ions (2)

$$\frac{\partial n_e}{\partial t} = \frac{\partial}{\partial x} \left(D \frac{\partial n_e}{\partial x} - w n_e \right) + n_e (v_i - v_a), \quad (1)$$

$$\frac{\partial n_p}{\partial t} = n_e v_i, \quad \frac{\partial n_n}{\partial t} = n_e v_a, \quad (2)$$

where n_e , n_p and n_n are number densities of electrons, positive and negative ions, respectively, while w , D , v_i and v_a are drift velocity, longitudinal diffusion coefficient, and rate coefficients for ionization and attachment. The electric field produced by the space charge effects is given as follows

$$E(x,t) = \frac{e}{2\epsilon_0} \int_0^d \left(\text{sgn}(x-x') - \frac{x-x'}{\sqrt{(x-x')^2 + R_0^2}} \right) n_e(x',t) dx'. \quad (3)$$

Here we assume the cylindrically symmetric 2D charge distribution, where R_0 is a parameter of the model. The equations are solved numerically using 4th order Runge-Kutta method for the integration in time and 2nd order central differences for the spatial derivatives in 1 dimension. This corresponds to the so-called 1.5D dimensional model. Ions are considered stationary, since their velocity is negligible compared to the velocity of electrons for the time scale considered in this work.

Our fluid model is based on the local field approximation and requires the tabulation of electron transport coefficients as a function of the reduced electric field. We have used our Monte Carlo simulation code to calculate electron transport coefficients in both the gaseous and liquid systems. The code we use is similar to the Monte Carlo code developed by Tattersall et al [5]. We apply two scenarios regarding cross sections. In the first scenario excitations are completely neglected (No Excitation scenario) while in the second scenario, they are

approximated by the gas phase excitations (Excitation scenario). A more detailed introduction to our Monte Carlo code, and calculations of transport coefficients is given in our accompanying paper in the Proceedings of this conference. Comparison of the results, obtained by using these two scenarios, gives a rough estimate of the importance of accurate representation of excitations for modeling of streamer dynamics.

3. RESULTS AND DISCUSSION

In figures 1 and 2 we show the temporal evolution of the electron density in gas argon and liquid argon, respectively, for the several instants. The initially Gaussian electron density grows due to the ionization processes; then charge separation occurs in the electric field due to the drift of oppositely charged particles in opposite directions, and the initially homogeneous electric field is distorted; and finally, when the field in the ionized region becomes more and more screened, the ionization is reduced and the typical ionization front profiles of electron and ion densities and of the electric field are established. The initial ionization avalanche is then said to have developed into a streamer.

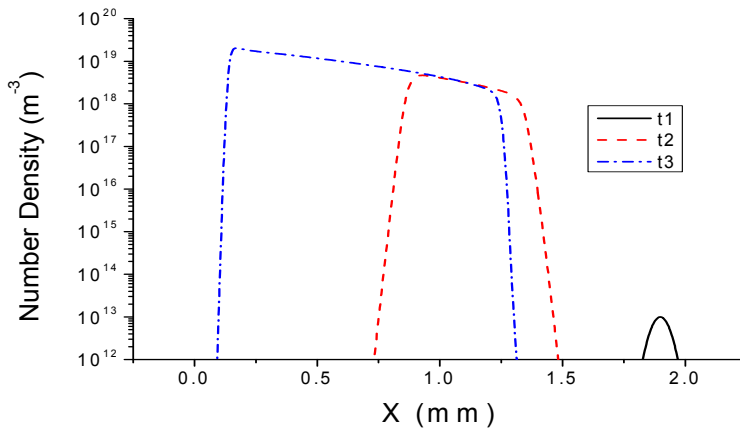


Figure 1. Transition of an electron avalanche into a streamer in the gas phase argon. Time moments t_1 , t_2 and t_3 correspond to 0ns, 9.2ns and 12ns respectively. The electric field vector is oriented to the right.

We observe that the transition of an electron avalanche into a streamer occurs much faster, and in a much smaller spatial range, in the liquid than in a gas system. It can also be seen that streamer dynamics is significantly different in the two scenarios regarding the treatment of excitations in the liquid phase. The

transition of an electron avalanche into a streamer is much faster in scenario without excitations, due to the absence of inelastic losses, which would decrease the rate for ionization. Thus, different estimations of the inelastic cross sections could yield great differences in the streamer properties. This suggests that accurate representation of the cross sections for excitations, in the liquid phase, is essential for modeling of discharges in liquids. The same holds for accurate description of cross sections for ionization.

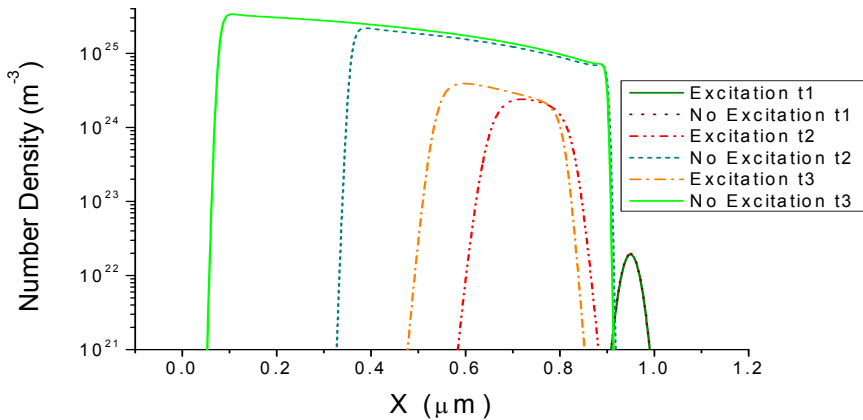


Figure 2. Transition of an electron avalanche into a streamer in the liquid argon. Time moments t1, t2 and t3 correspond to 0ps, 2.3ps and 2.9ps respectively. The electric field vector is oriented to the right.

Acknowledgements

This work was supported by MPNTRRS Projects OI171037 and III41011. RDW acknowledges the support from the Australian Research Council.

REFERENCES

- [1] N. Bonifaci et al. *J. Phys. D: Appl. Phys.* **30** (1997) 2717–2725
- [2] G.J. Boyle et al. *J. Chem. Phys.* **142**, 154507 (2015)
- [3] G.J. Boyle et al. arXiv:1603.04157v1 [physics.atom-ph]
- [4] G.V. Naidis *J. Phys. D: Appl. Phys.* **48** (2015) 195203
- [5] W. J. Tattersall et al. *Phys. Rev. E* **91**, 043304 (2015)

CROSS SECTIONS FOR SCATTERING AND MOBILITY OF OH⁻ AND H₃O⁺ IONS IN H₂O

V. Stojanović¹, J. Jovanović², D. Marić¹ and Z. Lj. Petrović^{1,3}

¹*Institute of Physics, University of Belgrade, Pregrevica 118,
11080 Belgrade, Serbia*

²*Faculty of Mechanical Engineering, University of Belgrade,
Kraljice Marije 16, 11000 Belgrade, Serbia*

³*also at Serbian Academy of Sciences and Arts, Knez Mihajlova 35,
11000 Belgrade Serbia*

Abstract. In an attempt to provide the data that are not yet available, we present cross sections sets and reduced mobility for OH⁻ and H₃O⁺ ions. Denpoh-Nanbu procedure (DNT) has been applied to calculate cross section sets for collisions of OH⁻ and H₃O⁺ ions with H₂O molecule. Reduced mobility for OH⁻ and H₃O⁺ ions in H₂O are calculated by using a Monte Carlo code over a wide range of E/N (E -electric field, N -gas density) at temperature $T=295$ K, in the low pressure limit.

1. INTRODUCTION

The interest in application of plasmas in medicine, some nanotechnologies and environmental remediation [1] has drawn the attention to studies of discharges in water and in proximity to water [2] although other liquids are of interest as well. More generally, all atmospheric discharges contain some degree of water vapour [3]. It is therefore of interest to determine how discharges are created in water vapour and to provide elementary transport data for the charged particles [1, 4].

We applied Denpoh-Nanbu [5] procedure to calculate cross section sets for collisions of OH⁻ and H₃O⁺ ions with H₂O molecule. Induced polarization and permanent dipole interaction in reactions of these ions with H₂O are taken into account. The OH⁻ set includes production of anions (OH⁻, H⁻, O⁻, O₂⁻, HO₂⁻) and electrons released in ion induced electron detachment, while the H₃O⁺ set includes production of cations (H⁺, H₂⁺, H₃⁺, H₂O⁺, O⁺, O₂⁺, O₂H⁺, OH⁺). Reduced mobility for OH⁻ and H₃O⁺ ions in H₂O are calculated by using a well tested Monte Carlo code over a range of E/N from 1 Td to 1200 Td at temperature $T=295$ K, in the low pressure limit.

The data are valid for low pressure water vapour or small amounts in mixtures. These data will provide a solid basis for calculation of ion-water molecule clusters properties that are most commonly found at higher pressures, and for modelling of discharges in liquids.

2. CALCULATION OF THE CROSS SECTIONS AND REDUCED MOBILITY

The scattering cross section sets for OH^- and H_3O^+ ions on H_2O molecule, are presented in Fig. 1 and Fig. 2, respectively. Cross section sets are initially calculated by applying Denpoh-Nanbu theory [5, 6] where we have taken into account that polarisation and dipole forces are expected to be important over the energy range from 20 meV to few eV. Since range of polarisation potential is a few eV, only processes with low threshold energies are taken into account.

For both ions we have used data for polarizability ($\alpha=1.45 \cdot 10^{-30} \text{ m}^3$) and dipole moment of H_2O as suggested by Clary [7]. Selected heats of formation and electron affinities are taken from from Ref. [8].

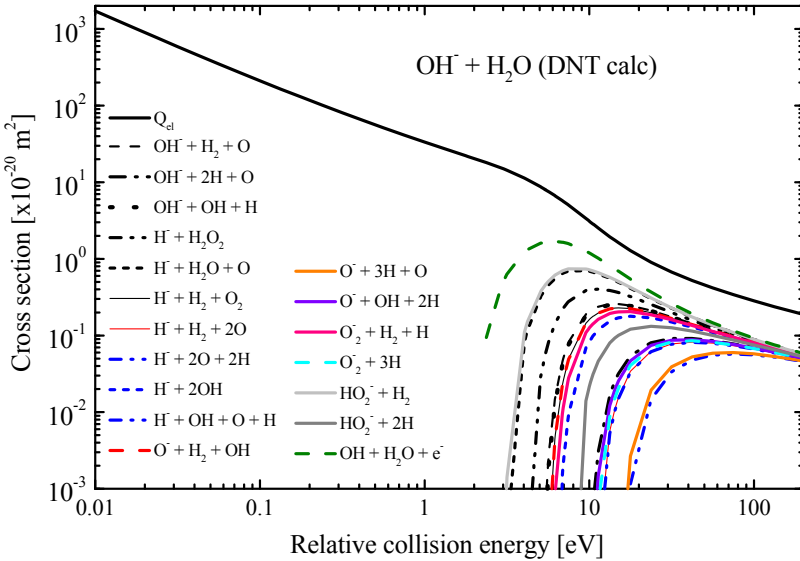


Figure 1. Cross section set for OH^- scattering on H_2O .

In Fig. 1 and Fig.2 we have shown cross section set for scattering of OH^- ion and H_3O^+ ions, respectively. Considering H_3O^+ ions obtained cross section set was used as initial in swarm procedure in which elastic momentum transfer cross section was further improved by assuring a good agreement between our Monte Carlo (MC) calculated reduced mobility and the available experimental results [9].

Reduced mobilities for OH^- and H_3O^+ ions in H_2O as a function of E/N are shown in Fig. 3. Reduced mobilities for OH^- and H_3O^+ ions in H_2O are calculated as a function of E/N at temperature $T = 295 \text{ K}$, for conditions where pressure effects can be assumed to be negligible. A Monte Carlo simulation method appropriate to calculate transport parameters [10, 11] for ions in gases at

elevated temperature [11] was used. In Monte Carlo simulations exothermic reactive collisions are followed in a similar way as all non-conservative collisions, i.e. followed swarm particle disappear from the swarm after the exothermic collision.

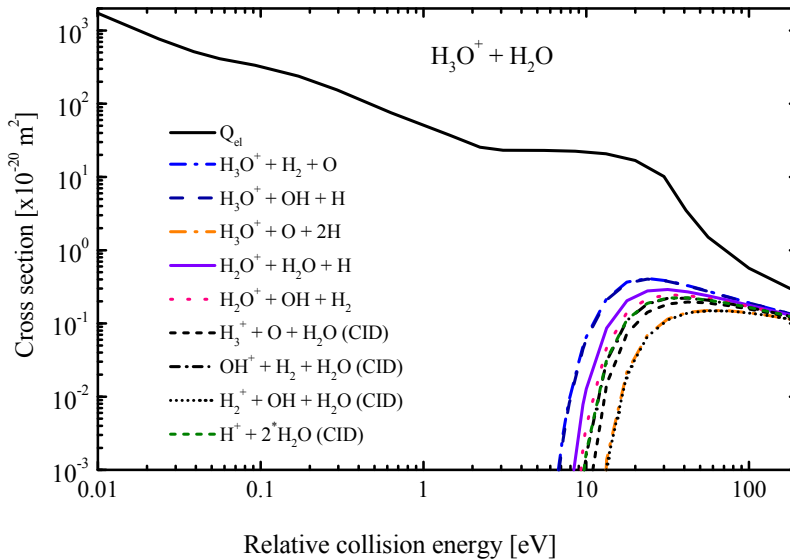


Figure 2. Cross section set for H_3O^+ scattering on H_2O .

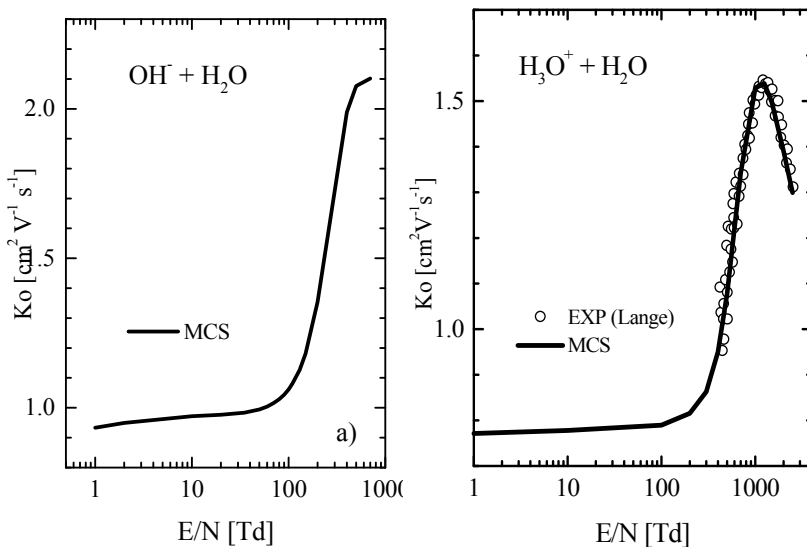


Figure 3. Reduced mobility as a function of E/N for a) OH^- ion and b) H_3O^+ ion.

3. CONCLUSION

In this paper the cross-section set has been obtained by using a simple theory. The Monte Carlo technique was applied to carry out calculations of reduced mobility as a function of reduced electric field. Due to the lack of experimental data, we were not able to test the accuracy of derived cross sections set for OH⁻ ions in H₂O. However, considering H₃O⁺ ions it is noteworthy saying that the agreement between calculated and measured reduced mobility is very good and for these ions the derived cross section set is more accurate but for further validation some additional experimental data such as diffusion coefficients are needed. Anyway, the obtained results are a good base for modelling, which could be further improved by adding a data base of the measured values of transport coefficients and then performing the analysis again.

Acknowledgment

This work is partly supported by Ministry of Education, Science and Technology of Republic Serbia projects ON171037 and III410011. Z.Lj.P. is also grateful to the SASA project F155.

REFERENCES

- [1] J. de Urquijo, E. Basurto, A.M. Juarez, K.F. Ness, R.E. Robson, M.J. Brunger, R.D.White, *J. Chem. Phys.* 141, 014308 (2014).
- [2] P. Bruggeman, D. Schram, M. Á. González, R. Rego, M. G. Kong, and C. Leys, *Plasma Sources Sci. Technol.* 18, 025017 (2009); P. Bruggeman and C. Leys, *J. Phys. D: Appl. Phys.* 42 053001 (2009).
- [3] T. Murakami, K. Niemi, T. Gans, D. O'Connell, W.G.Graham, *Plasma Sources Sci. Technol.* 22, 015003 (2013); W. Van Gaens, A. Bogaerts, *J. Phys. D* 46, 275201 (2013);
- [4] G. Ruíz-Vargas, M. Yousfi, and J. de Urquijo, *J. Phys. D* 43, 455201 (2010); R.D. White, W. Tattersall, G. Boyle, R.E. Robson, S. Dujko, Z.Lj. Petrović, A. Banković, M.J. Brunger, J.P. Sullivan, S.J. Buckman, G. Garcia, *Appl. Radia. Isotopes* 83, 77 (2014).
- [5] K. Denpoh and K. Nanbu, *J. Vac. Sci. Technol. A* 16 (1998) 1201
- [6] Z.Lj. Petrović , Z.M. Raspopović , V.D. Stojanović , J.V. Jovanović , G. Malović, T. Makabe, J. De Urquijo, *Appl. Surf. Sci.* 253 6619 (2007).
- [7] D.C. Clary, *Chem. Phys. Lett.* 232 267 (1995).
- [8] S.G. Lias, J.E. Bartmess, J.F. Liebman, J.L. Holmes. R.D. Levin, W.G. Mallard, *J. Phys. Chem. Ref. Data*, 17, supplement 1,1 (1988) .
- [9] F.D. Lange, *Int.J.Mass.Spectrosc.Ion.Proc.* 37 341-354 (1981).
- [10] R.E. Robson, R.D. White and Z. Lj.Petrović, *Rev. Mod. Phys.* 77 (2005) 1303; Robson R. E., *Aust. J. Phys.*, 44 (1991) 685.
- [11] Z. Ristivojević and Z.Lj. Petrović, *Plasma Sources Sci. Technol.* 21 035001 (2012).

Section 2.

PARTICLE AND LASER BEAM INTERACTION WITH SOLIDS

DIFFRACTION OF FAST ATOMS ON SURFACES, DECOHERENCE DUE TO PHONONS, ELECTRONS AND TOPOLOGICAL DEFECTS.

Philippe Roncin

Institut des Sciences Moléculaires dOrsay (ISMO), CNRS, Univ. Paris Sud, Université Paris Saclay, Orsay F-91405, France

Massive particles such as helium atoms offer a unique balance of very short wavelength associated with limited total energy allowing pm resolution [1, 2, 3]. However, the mass and the complexity i.e. the atomic structure of the particles also play a role to limit the coherence of the diffraction. We will discuss the contributions and the possible benefits and limitations to technique of fast atom diffraction. Elastic diffraction on a periodic system gives rise to diffraction spots having the same size as the primary beam. This simple statement is already very helpful to isolate the intensity associated with elastic diffraction carrying the structural information [3]. Whatever the process breaking energy conservation, the phase coherence with the elastic contributions will be lost and the but this does not mean that diffraction disappears. It become more complex and more interesting because it opens a window on the physical process responsible. We will try to detail the decoherence and the line-shape modification associated with various processes such a creation of phonons [4] or electron-hole pairs [5]. In favorable conditions, inelastic diffraction allows, for instance, a high sensitivity to tiny momentum transfer between electrons at the Fermi level and the projectile.

REFERENCES

- [1] J.R. Manson, H. Khemliche and P. Roncin, *Phys. Rev. B* **78**, 155408 (2008).
- [2] H. Winter and A. Schüller, *Progress in Surface Science* **86**, 169 (2011).
- [3] M. Debiossac *et al.*, *Phys. Rev. B.* **90** 155308 (2014)
- [4] P. Rousseau *et al.* *J. Phys. Conf. Ser.* **133**, 012013 (2008)
- [5] N. Bundaleski *et al.* *Phys. Rev. Lett.* **101**, 177601 (2008).

RECENT PROGRESS ON NUMERICAL SIMULATION FOR HIGH-ENERGY DENSITY PLASMA (HEDP) AT IAPCM

Li Baiwen, Zheng Chunyang, Cao Lihua and Ning Cheng

*Institute of Applied Physics and Computational Mathematics, Beijing 100094,
China*

Due to the rich physical phenomena both in wave-wave and wave-particle interaction and its widespread applications such as in astrophysics, particle acceleration, medical therapy and fusion science, and so on, the researches of interaction between ultra-intense laser and plasmas now is still a basic and important hotspot topic. In this report we mainly introduce our recent research activities, directions and some works in the field of laser-plasma interaction, which includes as follows: 1) Stimulated Raman cascade scattering, photon condensate, and electromagnetic soliton generation in under-dense plasma; 2) Mechanism of SRS and SBS, their coupling and competition in large-scale plasma; 3) Generation and mechanisms of Stimulated T-SEAWS instability and ion-vortices in sub-critical density plasma; 4) Physical mechanism and controlling of filamentation instability; 5) Formation and mechanism of high-quality and well-collimated return relativistic electron beam in under-dense plasma; 6) Generation and mechanism of monochromatic proton beams based on the interaction between ultra-shot ultra-intense laser and multi-component plasma; 8) Research of dynamic mechanism of gas-puff Z-pinch based on the particle-in-cell simulation.

Keywords: Laser-Plasma interaction; Stimulated Raman Scattering; Soliton; Instability

INTERACTIONS OF CHARGED PARTICLES WITH DOUBLE-LAYER GRAPHENE

Vito Despoja¹, Ivan Radović² and Zoran L. Mišković³

¹*Department of Physics, University of Zagreb, Bijenička 32, HR-10000 Zagreb, Croatia*

²*VINČA Institute of Nuclear Sciences, University of Belgrade, P.O. Box 522, 11001 Belgrade, Serbia*

³*Department of Applied Mathematics, and Waterloo Institute for Nanotechnology, University of Waterloo, Waterloo, Ontario, Canada N2L 3G1*

Nowadays we are witnesses of a development of one promising branch of applied physics, called plasmonics. Especially interesting issue is plasmonics in quasi-two-dimensional (q2D) crystals deposited on various dielectric substrates. Here arise the main questions: how to increase the 2D plasmon propagation length and how to excite 2D plasmon most efficiently. We will focus on describing the interaction between electronic excitations in two graphene layers with phonons in aluminium oxide (Al_2O_3) slab on which the graphene layers are deposited. Special attention will be paid to explain the hybridization between 2D plasmons and surface (TO) phonons. Because of multiple intersections of 2D plasmons and TO phonons the 2D plasmon moves to lower energies which allows it to be excited by charged particles moving at subthreshold speeds, $v < v_F$ [1]. We will present the results for wake potential induced by a charged particle which moves parallel to the graphene/dielectric interface. It will be shown how various substrates modify the efficiency of particle/plasmon coupling. The electronic excitations in graphene are obtained by using plane wave approach where we have addressed the problem of calculation of EELS spectra in the optical limit ($Q \rightarrow 0$) and how to avoid intersubcell Coulomb interaction [2].

REFERENCES

- [1] T. Marinković, I. Radović, D. Borka, Z. L. Mišković, *Plasmonics* **10** 1741-1749 (2015).
- [2] V. Despoja, D. Novko, K. Dekanić, M. Šunjić, L. Marušić, *Phys. Rev. B* **87**, 075447 (2013).

ATTOSECOND STREAKING OF PHOTOELECTRONS EMITTED FROM SOLIDS

Christoph Lemell

*Inst. for Theoretical Physics, Vienna University of Technology, Wiedner
Hauptstraße 8-10, A-1040 Vienna, Austria, EU*

Time-resolved photoemission from solid surfaces using the streaking technique as pioneered by Cavalieri et al. [1] probes the electron dynamics near surfaces on its natural time scale (escape times of photoelectrons ~ 4 a.u.). Additionally, surface streaking features a high surface sensitivity on the few-angstrom scale [2].

A problem inherent to streaking is the missing reference time t_0 , only relative delays of photoemission between different lines in the energy spectrum of released electrons are accessible. Deconvolution of the streaked photoelectron spectra from interacting many-electron systems has started recently with refined experimental techniques (target materials with one or multiple adlayers) [2] and advanced data-analysis methods (simulation of photoemission from nearly free-electron gas metals) [3].

In this presentation I will discuss our semiclassical model developed to simulate the motion of electrons under the combined influences of crystal atoms, other target electrons, and the external pump and streaking fields.

Acknowledgments: This work has been supported within the FWF special research programs SFB-041 (ViCoM) and SFB-049 (NextLite), doctoral program DK-W1243 (Solid4Fun), FWF project P21141-N16, and by the European COST Action CM1204 (XLIC).

REFERENCES

- [1] A. Cavalieri et al., *Nature (London)* **449**, 1029 (2007).
- [2] S. Neppl et al., *Nature (London)* **517**, 342 (2015).
- [3] C. Lemell, S. Neppl, G. Wachter, K. Tökesi, R. Ernstorfer, P. Feulner, R. Kienberger, and J. Burgdörfer, *Phys. Rev. B* **91**, 241101(R) (2015).

CLASSICAL TRAJECTORY MONTE CARLO METHOD – „WATCHING QUANTUM PHYSICS IN REAL TIME”

Károly Tökési^{1,2}, C. Lemell³ and J. Burgdörfer³

¹*Institute for Nuclear Research, Hungarian Academy of Sciences (Atomki),
Debrecen, Hungary, EU*

²*ELI-ALPS, ELI-HU Non-profit Ltd., Dugonics tér 13, Szeged, Hungary, EU*
³*TU WIEN, Austria*

Attosecond physics is a new and rapidly developing field driven by recent advances in laser technology. Attosecond science holds the promise to observe and to control the motion of electrons on their natural time scale. It is now possible to take snapshots of electrons in motion in atoms, molecules, and solids [1]. The long-lasting dream of chemists and physicists to watch and to control in real time the formation and breaking of chemical bonds or electrons leaving an atom is now closer to realization than ever. These experimental advances pose considerable challenges for theory.

Time-resolved photoemission experiments employing attosecond streaking of electrons emitted by an extended ultraviolet pump pulse and probed by a few-cycle near-infrared pulse found a time delay of about 100 as between photoelectrons from the conduction band and those from the 4f core level of tungsten [2]. We present a microscopic simulation of the emission time and energy spectra employing a classical transport theory. Our calculations reproduced well both the emission spectra and streaking images. We found delay times near the lower bound of the experimental data.

Photoemission spectra feature also complex correlation satellite structures signifying the simultaneous excitation of single or multiple plasmons. The time delay of the plasmon satellites relative to the main line can be resolved in attosecond streaking experiments [3]. Time-resolved photoemission thus provides the key to discriminate between intrinsic and extrinsic plasmon excitation. We demonstrate the determination of the branching ratio between intrinsic and extrinsic plasmon generation for simple metals.

Acknowledgement: This work was supported by the Hungarian Scientific Research Fund OTKA Nos. NN 103279, K103917 and by the COST Action CM1204 (XLIC).

REFERENCES

- [1] R. Kienberger, E. Goulielmakis, M. Uiberacker, A. Baltuska, V. Yakovlev, F. Bammer, A. Scrinzi, T. Westerwalbesloh, U. Kleineberg, U. Heinzmann, M. Drescher, and F. Krausz, *Nature (London)* 427, 817 (2004).
- [2] C. Lemell, B. Solleder, K. Tókési, and J. Burgdörfer, *Phys. Rev. A* 79, 062901 (2009).
- [3] C. Lemell, S. Neppl, G. Wachter, K. Tókési, R. Ernstorf, P. Feulner, R. Kienberger, and J. Burgdörfer, *Real-time observation of collective excitations in photoemission*, *Phys. Rev. B: Rapid Communication*, 91, 241101(R) (2015).

THE ROLE OF SPECTROSCOPIC DIAGNOSTICS IN STUDYING LASER-PLASMA INTERACTION

Miloš Burger

University of Belgrade, Faculty of Physics, PO Box 44, 11001 Belgrade, Serbia

Absorption of infrared nanosecond laser radiation by copper plasma is investigated under low pressure helium environment. The laser irradiance threshold for the onset of the significant plasma absorption is determined using high precision mass measurements. The value of about 2 GW/cm is verified with results obtained using standard techniques of optical emission spectroscopy. Both electron density and electron temperature of the plasma plume exhibit significant increase when applied irradiance exceeds the threshold value. In addition, fast plasma imaging and image processing were used to reveal the distribution of species involved, including an intermixing zones. It is shown that plasmas produced in low pressure helium environment are profoundly non-uniform, and that radially resolved analysis is required. These results are beneficial for LIBS (laser-induced breakdown spectroscopy) and PLD (pulsed-laser deposition) research communities, as well as for researchers dealing with modeling of laser-matter interactions.

PLASMA TREATMENT OF METAL SURFACE BY NANOSECOND DIFFUSE DISCHARGE AT ATMOSPHERIC PRESSURE

M.V. Erofeev, V.S. Ripenko, M.A. Shulepov and V.F. Tarasenko

Institute of High Current Electronics, Akademicheskyy ave., 2/3, Tomsk, Russia

In this work we present experimental results on the generation of diffuse discharge initiated by runaway electron beam and X-rays in pulsed-periodic mode in nitrogen at atmospheric pressure, and its application for metal surface modification. A runaway electron preionized diffuse discharge (REP DD) [1] was formed by applying of nanosecond high voltage pulses with amplitude up to 50 kV to electrode of small curvature radius at a pulse repetition frequency of up to 2 kHz. In such regime, a specific input power up to 10 MW/cm³ per pulse was realized. Measured maximal value of an electron concentration in the plasma of the pulse-periodic REP DD in atmospheric-pressure nitrogen achieved in the middle of the interelectrode gap and was $\sim 4 \cdot 10^{14}$ cm⁻³, and gas temperature was 820 K [2]. The aim of this work is to investigate the possibilities of surface modification of copper, stainless steel, aluminum, niobium and titanium in the plasma of REP DD, formed in nitrogen flow. The study shows that REP DD treatment after exposure of 10⁵ shots provides ultrafine surface cleaning of all metals from carbon contamination. At the same time, it is found that all materials subjected to REP DD are involved in surface oxidation. Moreover, the surface energy of the treated specimens increased up to 4 times, whereas the other surface properties like microhardness or roughness remain almost unchanged. Thus, plasma treatment by runaway electron preionized diffuse discharge has enabled us to create an optimum metal surface without mechanical damages that is important for further coating, printing, painting, and adhesive bonding.

Acknowledgements: The work is performed in the framework of the Russian Science Foundation (the project #14-29-00052).

REFERENCES

- [1] V. F. Tarasenko, *Runaway Electrons Preionized Diffuse Discharge*, p. 598, (Nova Science Publishers, New York, 2015).
- [2] D. A. Sorokin, M. I. Lomaev and V. F. Tarasenko, Proc. SPIE. 9810, 98101M-2 (2015).

ESTIMATION OF RADIATION DOSE EQUIVALENT IN AQUEOUS SOLUTIONS SUBJECTED TO ATMOSPHERIC PRESSURE PLASMA JETS

Xu Han^{1,2}, James Kapaldo^{1,2}, Ireneusz Janik² and Sylwia Ptasinska^{1,2}

¹*Department of Physics, University of Notre Dame, Notre Dame, 46556 IN, USA*

²*Radiation Laboratory, University of Notre Dame, Notre Dame, 46556 IN, USA*

Radiation chemical dosimetry methods were performed to estimate the concentration of intermediate and stable products generated upon exposure of aqueous solutions to atmospheric pressure plasma jets (APPJs). The rates of product formation were determined from the linear product concentration dependencies on plasma exposure times. We observed that these rates can be altered by the adjustments of specific parameters in APPJ source. Upon change of the high voltage pulse frequency from 0.5 to 1.5 kHz the product formation rates tripled. They were also affected by the geometry of the sample as well as its axial and equatorial position in relation to the axis of the plasma jet. The effective sample exposure profile was determined based on the dependence of the observed rates on the thickness of the samples as well as the size of the sample surface. For the given APPJ parameters we obtained the ratio of product formation rate to plasma energy absorption rate. This ratio represents an equivalent of chemical radiation yield (a $G(X)$ value) and defines molar concentration of product X generated upon absorption of 1 Joule of energy by the exposed sample. The G value of ferric ion, $G(\text{Fe}^{3+})_{\text{APPJ}}$, in Fricke dosimeter solutions exposed to plasma jets is much lower than the lowest literature values reported for exposures to high linear energy transfer (LET) ionizing radiation sources. Extrapolating the dependence of depth of ionization penetration on $G(\text{Fe}^{3+})$ indicates that plasma penetration into the aqueous sample must be extremely shallow. Based on $G(\text{Fe}^{3+})_{\text{APPJ}}$ we were able to estimate the equivalents of radiation dose absorbed by solutions subjected to various plasma jet exposure times.

Acknowledgements: The research described herein was supported by the Division of Chemical Sciences, Geosciences and Biosciences, Basic Energy Sciences, Office of Science, United States Department of Energy through grant number DE-FC02-04ER15533.

ELECTRON-INDUCED REACTIONS IN CLUSTERS

J. Kočíšek¹, K. Grygoryeva¹, A. Pysanenko¹, J. Lengyel¹, J. Fedor¹, M. Fárník¹

¹*J. Heyrovský Institute of Physical Chemistry v.v.i., Academy of Sciences of the Czech Republic, Dolejkova 3, 18223 Prague, Czech Republic*

The talk will map our recent progress in studies of electron induced processes in clusters. Clusters are small aggregates of matter that allow studies of a bulk chemistry using gas phase methods. This approach allows the identification of main changes induced by an environment on elementary processes such as an electron impact, or an electron attachment. First, we will discuss general trends that we observed in the model systems of nitrophenol, nitrophenol clusters and heterogeneous clusters of nitrophenol, water and argon [1]. Second, consequences for the practical surface chemistry will be shown on the case study of technical FeCO₅ molecule deposited on the surface of argon clusters [2].

Acknowledgements: The work was supported by the Czech Science Foundation (Grant No. 16-10995Y and 14-14082S).

REFERENCES

- [1] J. Kočíšek, K. Grygoryeva, J. Lengyel, M. Fárník, J. Fedor, EPJ D 70, 98 (2016)
- [2] J. Lengyel, J. Kočíšek, M. Fárník, J. Fedor, J. Phys. Chem. C 120, 7397 (2016)

MORPHOLOGICAL AND STRUCTURAL PROPERTIES OF SILVER AND GOLD NANOPARTICLES OBTAINED BY ION IMPLANTATION IN HIGH DENSITY POLYETHYLENE

Miloš Nenadović¹, Danilo Kisić¹, Svetlana Štrbac² and Zlatko Rakočević¹

¹ *INS Vinca, Laboratory of Atomic Physics, University of Belgrade,
Mike Alasa 12–14, 11001 Belgrade, Serbia*

² *ICTM Institute of Electrochemistry, University of Belgrade, Njegoseva 12,
11001 Belgrade, Serbia*

High density polyethylene (HDPE) has been implanted with Ag⁺ and Au⁺ ions using the energies of 60 and 200 keV respectively. The source of silver ions was the preheated silver fluoride - AgF salt (Fluka, p.a.), while the gold ions were extracted from a high purity gold wire [1]. The fluences of implanted silver and gold ions were 1, 5 and 10·10¹⁵ ions/cm². The working temperature of the samples was kept constant at 20 °C using the target cooling system. Transmission electron microscopy (STEM) and field emission gun – scanning electron microscopy (FEG-SEM) showed the existence of nanoparticle clusters. X ray photoelectron spectroscopy (XPS) revealed the presence of silver but not confirmed gold on the expected electronic peaks. The surface topography was observed by atomic force microscopy (AFM), while the surface composition changes were analyzed using phase imaging AFM. Force modulation microscopy (FMM – AFM) showed significant difference in the cross-sectional analysis. The ions projected range and radiation damage zone are very different in shape and size, depending on ions type and energy [2].

Acknowledgements: This work is supported by Serbian Ministry for Education and Science under the grant NO 45005.

REFERENCES

- [1] M.Nenadović, J.Potočnik, M.Ristić, S Štrbac and Z.Rakočević, Surf. Coat. Tech. 206, 4242 (2012).
- [2] J.M. Charrier, *Polymeric Materials and Processing: Plastics, Elastomers and Composites*, Hanser Publishers, Munich, New York, 1991.

***IN-SITU* ANALYSIS OF THE PULSED LASER DEPOSITION (PLD) FABRICATED $\text{LaAlO}_3/\text{SrTiO}_3$ HETEROSTRUCTURES**

Zoran Ristić

VINCA Institute of Nuclear Sciences, Belgrade University, Belgrade, Serbia

The recent advances made in modern material physics, in the field of (transition metal) oxide electronics, were made possible, in large part, by the ability to exert control on the nanoscale/atomic level when creating these systems - thin films, interfaces, heterostructures etc. The role of pulsed laser deposition (PLD) in these advances is especially significant since PLD is usually the tool of choice due to its versatility, simplicity, cost-effectiveness, speed and, at certain degree, due to its scalability.

The model transition metal oxide (TMO) system that generated a lot of attention in recent years is that of $\text{LaAlO}_3/\text{SrTiO}_3$. Here an interface formed between two wide-band-gap non-magnetic insulators exhibits electrical conductivity [1] as well as superconductivity [2] and even magnetic properties [3]. In this work, with goal to better understand the origin of electrical conductivity in this model system, the power of *in-situ* PLD and scanning tunneling spectroscopy/microscopy (STS/STM) was used in addition to other characterization techniques.

REFERENCES

- [1] A. Ohtomo, H. Y. Hwang, Nature 427 (6973): 423–426 (2004)
- [2] S. Gariglio, N. Reyren, A. D. Caviglia, J.-M. Triscone, Journal of Physics: Condensed Matter 21 (16): 164213 (2009)
- [3] J. A. Bert, B. Kalisky, C. Bell, M. Kim, Y. Hikita, H. Y. Hwang, K. A. Moler, Nature Physics 7(10): 767–771 (2011)

FEBID FOR APPLICATION IN MATERIAL SCIENCE AND SOLID STATE PHYSICS

Roland Sachser and Michael Huth

Physikalisches Institut, Goethe-University, Frankfurt am Main, Germany

Focused electron beam induced deposition (FEBID) is a versatile technique for direct writing of nanostructures down to the scale of about 10nm [1]. A precursor gas adsorbes on the surface of a substrate in a scanning electron microscope (SEM) and is dissociated by the electron beam. Via rastering the beam over a defined area the deposit is formed. For application, pure metallic structures are desirable, but the typically used organometallic precursors mostly lead to carbon-rich deposits. Especially the commonly used precursor MeCpPtMe₃ results in only about 20 at. % metal content, showing electrically insulating behavior. Various techniques allow to modify the electrical properties of the deposit. Via additional electron beam irradiation after deposition the conductivity can be tuned continuously [2,3]. Applying oxygen or H₂O vapor atmosphere during irradiation allows further purification to pure Pt [4,5]. Using a pulsed oxygen flux at substrate temperatures of 150°C allows purification to pure Pt structures without the need of additional irradiation [6]. The different post-treatment approaches and their influence on the electrical transport properties will be discussed. Additionally, an outlook to exemplary applications will be given.

Acknowledgements: Support by the German Academic Exchange Service (DAAD) is gratefully acknowledged.

REFERENCES

- [1] I. Utke, P. Hoffmann and J. Melngailis, *J. Vac. Sci. Technol. B* 26, 1197 (2008).
- [2] F. Porrati, R. Sachser, C. H. Schwalb, A. S. Frangakis and M. Huth, *J. Appl. Phys.* 109, 063715 (2011).
- [3] R. Sachser, F. Porrati, C. H. Schwalb and M. Huth, *Phys. Rev. Lett.* 107, 206803 (2011).
- [4] H. Plank, J. H. Noh, J. D. Fowlkes, K. Lester, B. B. Lewis and P. D. Rack, *ACS Appl. Mater. Interfaces* 6, 1018 (2014).
- [5] C. Elbadawi, M. Toth and C. J. Lobo, *ACS Appl. Mater. Interfaces* 5, 9372 (2013).
- [6] R. Sachser, H. Reith, D. Huzel, M. Winhold and M. Huth, *ACS Appl. Mater. Interfaces* 6, 15868 (2014).

GENERATION OF HIGHLY LUMINESCENT COLOR CENTERS IN NANOCRYSTALLINE DIAMOND BY CVD METHOD

Sára Tóth, László Himics and Margit Koós

*Institute for Solid State Physics and Optics, Wigner Research Center for Physics,
Hungarian Academy of Sciences, Budapest, H-1525 Budapest, P.O.Box 49.,
Hungary*

Nanodiamond grains with intensive light emission in the near-infrared region has an important application potential in the field of quantum technology [1] or biological imaging [2]. Advantages of metal-related light emitting optical centers are the emission concentrated into a narrow band region with a weak vibronic sideband caused by the relatively low electron-phonon coupling at room temperature. In this work we report on the creation of Ni-Si impurity related complex defect center in nanodiamond grains under microwave plasma assisted chemical vapor deposition (MW CVD) growth process. This complex center accounts for the previously undocumented fluorescence system with zero phonon line (ZPL) emission at 865 nm (1.433 eV) and band width of 1.5 nm (2.4 meV) at room temperature. By varying deposition conditions the Ni-Si impurity related complex defect center was formed in nanodiamond grains of 80-200 nm average sizes. Some variation of ZPL peak position and line width have been detected in nanodiamond grains prepared at different conditions, as well as in numerous nanodiamond grains prepared at the same conditions. The variations of local stress field may explain the spread of ZPL spectral parameters.

Acknowledgements: This work was supported by the Hungarian Science Foundation under contract number NKFI K-115805.

REFERENCES

- [1] C. Kurtsiefer, S. Mayer, P. Zarda and H. Weinfurter, Phys. Rev. Lett. 85 (2000) 290.
- [2] Dean Ho (Editor), Nanodiamonds, Applications in Biology and Nanoscale Medicine (Springer, 2010).

INTERACTIONS OF MOVING CHARGED PARTICLES WITH MULTI-WALLED CARBON NANOTUBES (MWNTS)

Ying-Ying Zhang, Yuan-Hong Song* and You-Nian Wang

*Key Laboratory of Materials Modification by Laser, Ion and Electron Beams
(Ministry of Education), School of Physics and Optoelectronic Technology,
Dalian University of Technology, Dalian 116024, China*

Channeling of energetic charged particles through carbon nanotubes (CNTs) has drawn great interest since their potential application in nano-electronics and biomedicine. A semi-classical kinetic model combined with the Molecular Dynamics (MD) method was adopted to investigate the moving trajectory in single-walled carbon nanotubes^[1], showing the ions can be channeled with consecutive reflections off the wall or even along helical trajectories, which is affected by the exact geometrical array of the carbon atoms on the nanotube surface. For multi-walled carbon nanotubes, which are much more easily produced as an aligned array of straight parallel tubes in experiments, the multi-peak curves in the stopping power and the self-energy of the moving ions have been observed by Miskovic^[2]. In this research, we find the outer and inner tubes of triple-walled carbon nanotubes (TWNTs) may give important contribution to the peaks of the self-energy curves, corresponding to one or two small narrow peaks in the low speed region. Besides, the total potential with the introduction of the REBO potential^[1] and the induced potential, which has a deep potential well at radial distances midway between the center and the wall, are analyzed in the interaction investigation for MWNTs. As the analogous structures of graphene and CNTs, all our results may be important for the further research in the field of graphene.

Acknowledgements: This work is partially supported by National Natural Science Foundation of China (No. 11275038).

REFERENCES

- [1] Y. Y. Zhang, J. Z. Sun, Y. H. Song, Z. L. Mišković, Y. N. Wang, Carbon 71 (2014) 196.
- [2] S. Chung, D. J. Mowbray, Z. L. Mišković, F. O. Goodman, Y. N. Wang, Radiat. Phys. Chem. 76 (2007) 524.

SIMULATION OF ELECTRON TRANSMISSION THROUGH PLATINUM CAPILLARIES

D. Borka¹, C. Lemell², V. Borka Jovanović¹ and K. Tőkési³

¹*Atomic Physics Laboratory (040), Vinča Institute of Nuclear Sciences,
University of Belgrade, P.O. Box 522, 11001 Belgrade, Serbia*

²*Institute for Theoretical Physics, Vienna University of Technology,
Wiedner Hauptstraße 8-10, A-1040 Vienna, Austria, EU*

³*Institute for Nuclear Research, Hungarian Academy of Sciences (Atomki),
4026 Debrecen Bem tér 18/c, Hungary, EU*

Abstract. In this work we present a realistic computer simulation of electron transmission through a platinum (Pt) capillary based on a Monte Carlo Simulation (MCS) and classical transport theory. We compare our results with experimental data for 200 eV electrons entering a macrocapillary under a 6 deg tilt angle. In the simulation both elastic and inelastic scattering of primary electrons colliding with the inner Pt surface as well as secondary electron emission from the capillary wall are taken into account. In order to reach good agreement between simulated and experimental energy spectra modeling of trajectories undergoing multiple scattering off the internal capillary wall is more important than expected.

1. INTRODUCTION

Interactions of charged particles with capillaries have attracted great research interest over the past years (see, e.g., [1,2] and references therein). First reports on electron guiding through insulating capillaries date back to 2007 [3, 4]. Later, it was shown [5] that electron transmission through insulating capillaries appears to be fundamentally different from guiding of highly charged ions (HCI). While the latter is mediated by Coulomb repulsion due to the formation of charge patches on the inner wall of the insulating capillary, electrons are scattered both elastically and inelastically in close interactions with the capillary wall. Furthermore, inelastic scattering may lead to generation of low-energy secondary electrons which may also escape the capillary. As a consequence of multiple scattering events a prominent fraction of electrons transmitted through the capillary have lost part of their energy [3,4,6]. Of course, also for electrons Coulomb deflection enhances the total transmission rate, however with an unknown contribution. We therefore concentrate in this study on the interaction of electrons with metallic capillaries to separate the physics of close interactions of electrons with the inner capillary wall from long-range Coulomb deflections.

Detailed experimental analysis of the interaction sequence of electrons inside the capillary is hindered by the fact the electrons cannot change their charge state. In our simulation, however, we can identify and follow the trajectories of all electrons including secondary electrons and analyze their respective contributions to the total energy spectrum.

2. THEORY

Our simulation is based on a well-established electron transport code to model scattering of electrons at surfaces [7,8]. The trajectory between subsequent scattering events is calculated semi-analytically taking the image-charge potential within the capillary into account [9]. In brief, we model elastic and inelastic scattering of primary electrons colliding with the inner Pt surface and also secondary electron generation inside the material. Doubly differential elastic scattering cross sections are calculated using the static field approximation with non-relativistic Schrödinger partial wave analysis [10]. For the description of inelastic scattering cross sections we use the dielectric response formalism [11–13]. The bulk and surface energy loss functions for Pt are derived from an analytic expansion of the measured loss function without momentum transfer [14], $Im\{-\epsilon^{-1}(q=0, \omega)\}$ (optical data), into the $q-\omega$ plane (see, e.g., [15,16]). Inside the capillary wall, the trajectory is determined by stochastic scattering events depending on the elastic and inelastic mean free paths. In case of inelastic scattering a secondary electron is created with kinetic energy equal to the energy loss of the primary. Subsequently, the secondary trajectory is followed, as well. Initial conditions (starting point, energy, polar and azimuthal angles) for our Monte-Carlo simulation are chosen randomly from suitable distributions to match experimental conditions [6].

3. RESULTS AND DISCUSSION

Depending on their entry point, electrons transmitted through the capillary may have suffered more than one deflection from the inner capillary wall influencing their energy distribution upon exit. In Fig. 1 we present theoretically obtained kinetic energy spectra of 200 eV electrons escaping a Pt capillary (length 40.8 mm, diameter 3.3 mm [6]) having experienced up to five scattering events for a tilt angle of 6 deg. While for single and double scattering features from elementary excitations (surface and bulk plasmons) can be clearly discerned, a feature-less spectrum dominated by secondary electron transmission is found for 5 scattering events. Measured spectra are convolutions of the distributions shown in Fig. 1. For the case studied here, we find a dominant contribution of the single- and double-scattering spectra (see inset in Fig. 2, 46.8% and 45.8%, respectively) with small admixtures from trajectories with more scattering events (3 scat. 4.97%, 4 scat. 1.49%, and 5 scat. 0.91%). Fig. 2 shows experimental data (filled black circles, taken from [6]) for 200 eV electrons transmitted through a Pt capillary tilted by 6 deg together with

simulated spectra for single scattering only (blue line) and a weighted sum of spectra accounting for up to 5 scattering events (red line). Theoretical spectra have been calculated down to 80 eV. Despite their small overall contribution (less than 10%) trajectories with 3 and more scattering event must not be neglected in order to reach agreement between experiment and simulation. In particular, the low-energy part of the spectrum can only be reproduced when accounting for the correct geometry of scattering problem and modeling the complete trajectory of electrons especially for entry points close to the capillary wall.

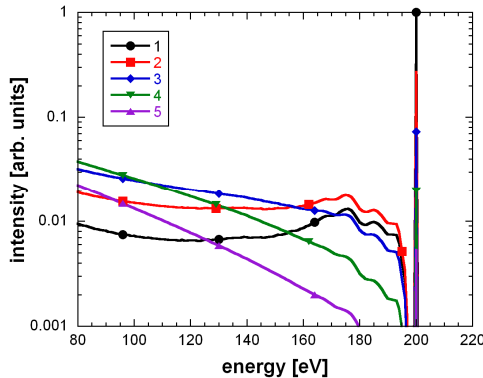


Figure 1. Theoretically obtained reduced kinetic energy spectrum of electrons escaping the Pt capillary experienced 1 (black), 2 (red), 3 (blue), 4 (green) and 5 (purple) scattering events, respectively.

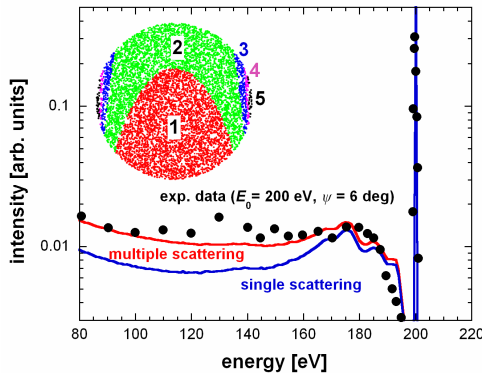


Figure 2. Experimental and simulated energy spectra for 200 eV electrons transmitted through a Pt capillary. Blue line: single scattering; red line: up to 5 scattering events. Inset: entrance surface of the capillary with the number of scattering events shown as colors (1: red, 2: green, 3: blue, 4: purple, 5: black).

We have presented a Monte-Carlo simulation of electron transmission through a Pt capillary. We have successfully modeled experimental data for a primary energy of 200 eV and 6 deg tilt angle of the capillary. The spectra were compared in the energy range between 80 eV and 200 eV. The energy spectrum

of electrons after transmission contains prominent low-energy contributions due to multiple inelastic scattering and secondary electron emission. Close to the elastic peak single- and double-scattering trajectories dominate. The obtained theoretical spectrum is in good agreement with the experimental results. Our calculations are an important step towards a better understanding of electron transmission through nano- and microcapillaries. Using metallic capillaries allows us analyzing electron transmission without the influence of electrostatic charge-up of the internal capillary wall on the electron trajectory.

Acknowledgements

This project was supported by Bilateral Austrian-Serbian project “Interaction of charged particles with capillaries” number 451-03-01039/2015-09/25 (D.B., C.L., and V.B.J.), by the Ministry of Education, Science and Technological Development of the Republic of Serbia through the project 45005 (D.B. and V.B.J.), by the Hungarian Scientific Research Fund OTKA Nos. NN 103279 and K103917 (K.T.).

REFERENCES

- [1] C. Lemell, J. Burgdörfer and F. Aumayr, *Prog. Surf. Sci.* **88**, 237 (2013).
- [2] N. Stolterfoht and Y. Yamazaki, *Phys. Rep.* **629**, 1 (2016).
- [3] A.R. Milosavljević, Gy. Viktor, Z.D. Pešić, P. Kolarz, D. Šević, B.P. Marinkovic, S. Matefli-Tempfli, M. Matefli-Tempfli and L. Piraux, *Phys. Rev. A* **75**, 030901(R) (2007).
- [4] S. Das, B.S. Dassanayake, M. Winkworth, J.L. Baran, N. Stolterfoht and J.A. Tanis, *Phys. Rev. A* **76**, 042716 (2007).
- [5] K. Schiessl, K. Tökési, B. Solleder, C. Lemell and J. Burgdörfer, *Phys. Rev. Lett.* **102**, 163201 (2009).
- [6] A.R. Milosavljević, M.Lj. Ranković, D. Borka, J.B. Maljković, R.J. Berezky, B.P. Marinkovic and K. Tökési, *Nucl. Instr. Meth. Phys. Res. B* **354**, 86 (2015).
- [7] R. Shimizu, Y. Kataoka, T. Ikuta, T. Koshikawa and H. Hasimoto, *J. Phys. D: Appl. Phys.* **9**, 101 (1976).
- [8] K. Tökési, D. Varga, L. Kövér and T. Mukoyama, *J. Electron Spectrosc. Relat. Phenom.* **76**, 427 (1995).
- [9] K. Tökési, L. Wirtz, C. Lemell and J. Burgdörfer, *Phys. Rev. A* **64**, 042902 (2001).
- [10] F. Salvat and R. Mayol, *Comput. Phys. Commun.* **74**, 358 (1993).
- [11] H. Ritchie, *Phys. Rev.* **106**, 874 (1957).
- [12] H. Ritchie and A.L. Marusak, *Surf. Sci.* **4**, 234 (1966)
- [13] Z.-J. Ding and R. Shimizu, *Surf. Sci.* **222**, 313 (1989).
- [14] W.S.M. Werner, K. Glantschnig and C. Ambrosch-Draxl, *J. Phys. Chem. Ref. Data* **38**, No. 4 (2009).
- [15] C. J. Powell, *Surf. Sci.* **44**, 29 (1974).
- [16] D. R. Penn, *Phys. Rev. B* **35**, 482 (1987).

PLASMON-PHONON HYBRIDIZATION IN LAYERED STRUCTURES INCLUDING GRAPHENE

T. Djordjević¹, L. Karbunar², V. Despoja³, I. Radović¹ and Z.L. Mišković⁴

¹*Vinča Institute of Nuclear Sciences, University of Belgrade, P.O. Box 522, Belgrade, Serbia*

²*School of Electrical Engineering, University of Belgrade, Bulevar Kralja Aleksandra 73, Belgrade, Serbia*

³*Department of Physics, University of Zagreb, Bijenička 32, Zagreb, Croatia*

⁴*Department of Applied Mathematics, and Waterloo Institute for Nanotechnology, University of Waterloo, Waterloo, Ontario, Canada*

Abstract. We present a method to introduce several graphene sheets into the non-retarded Green's function for a layered structure containing polar insulators, which support transverse optical phonon modes. Dispersion relations are derived to illustrate hybridization of Dirac plasmons in two graphene sheets with phonon modes in an oxide spacer layer between them.

1. INTRODUCTION

Recent developments in the area of Nano-Plasmonics are concerned with integrating graphene sheets and other two-dimensional (2D) materials with various dielectric materials in order to design novel devices that operate in the Terahertz to mid-infrared range of frequencies [1,2]. Particularly interesting is the possibility to control the doping density of charge carriers in graphene via chemical or electrical means, which enables the tunability of the dispersion relation of graphene's Dirac plasmon [2]. However, insulating spacer layers between graphene sheets in such nanoscale devices are typically composed of strongly polar materials, such as SiO₂, Al₂O₃ and other oxides, which support pronounced transverse optical (TO) phonon modes in the above mentioned frequency range [3]. Those phonon modes can provide efficient means for damping of Dirac plasmons and they may undergo strong hybridization with the Dirac plasmons in the nearby graphene sheets, thereby modifying the dispersion of the collective modes in layered structures that involve graphene sheets [4].

This plasmon-phonon hybridization (PPH) may be explored by moving charged particles, e.g. in a high-resolution electron energy loss spectroscopy (HREELS). We have recently shown that the wake effect in the dynamically screened potential induced by a slow charge moving parallel to a graphene sheet on a SiO₂ substrate can be used as a sensitive probe for the PPH [5]. In Ref. [5] we have used a classical dielectric formalism in the non-retarded limit to solve the Poisson equation with suitable boundary conditions. However, in the case of complex layered structures of dielectrics, it is preferable to use the available electrostatic Green's functions (GFs) for those structures [6] as a starting point. Then, owing to the 2D nature of the polarization function of graphene, it is possible to solve analytically the Dyson-Schwinger (DS) equation for the GF describing a layered structure that contains any number of graphene sheets. Using this GF allows one to develop closed-form expressions for the induced potential and the related polarization forces of interest in HREELS [5,6].

In this work, we illustrate the process of solving the DS equation for a "sandwich" structure consisting of two graphene sheets with an oxide layer between them.

2. GREEN'S FUNCTION FORMALISM

We assume that the layered structure is translationally invariant in the directions of the position vector $\mathbf{r} = \{x, y\}$ in a system of Cartesian coordinates $\{x, y, z\}$, allowing us to perform a 2D spatial ($\mathbf{r} \rightarrow \mathbf{q}$) and a temporal ($t \rightarrow \omega$) Fourier transform (FT) of all relevant quantities. Then the DS equation for the FT of the full GF, $\tilde{G}(\mathbf{q}; z, z'; \omega)$, is

$$\tilde{G}(z, z') = \tilde{G}_0(z, z') + \frac{1}{4\pi} \int_{-\infty}^{\infty} \tilde{G}_0(z, z'') \check{V}(z'') \tilde{G}(z'', z') dz'', \quad (1)$$

where we have dropped \mathbf{q} and ω to simplify the notation. Here, $\tilde{G}_0(z, z') \equiv \tilde{G}_0(\mathbf{q}; z, z'; \omega)$ denotes the GF for the structure *without* graphene, e.g., as given in Ref. [6]. One can include N graphene sheets placed in the planes $z = z_n$ by defining the interaction potential $\check{V}(z) \equiv \check{V}(\mathbf{q}; z; \omega)$ in Eq. (1) as

$$\check{V}(z) = -4\pi e^2 \sum_{n=1}^N \chi_n \delta(z - z_n), \quad (2)$$

where $\chi_n \equiv \chi_n(\mathbf{q}, \omega)$ is the polarization function of the n th graphene sheet. Notice that different graphene sheets may be doped with different densities of charge carriers, and hence they may have different Fermi energies E_F .

We limit our interest to a sandwich structure with $N = 2$ graphene sheets placed at $z_1 = 0$ and $z_2 = h$. Hence, from Eqs. (1) and (2),

$$\tilde{G}(z, z') = \tilde{G}_0(z, z') - e^2 \chi_1 \tilde{G}_0(z, z_1) \tilde{G}(z_1, z') - e^2 \chi_2 \tilde{G}_0(z, z_2) \tilde{G}(z_2, z'). \quad (3)$$

We next set $z = z_1$ and $z = z_2$ in Eq. (3) to obtain a system of algebraic equations for the unknown values of $\tilde{G}(z_1, z')$ and $\tilde{G}(z_2, z')$,

$$\left[1 + e^2 \chi_1 \tilde{G}_0(z_1, z_1)\right] \tilde{G}(z_1, z') + e^2 \chi_2 \tilde{G}_0(z_1, z_2) \tilde{G}(z_2, z') = \tilde{G}_0(z_1, z'), \quad (4)$$

$$e^2 \chi_1 \tilde{G}_0(z_2, z_1) \tilde{G}(z_1, z') + \left[1 + e^2 \chi_2 \tilde{G}_0(z_2, z_2)\right] \tilde{G}(z_2, z') = \tilde{G}_0(z_2, z'). \quad (5)$$

For a layer of oxide with the (relative) dielectric function $\varepsilon_{\text{ox}}(\omega)$, which occupies region $0 \leq z \leq h$ and is surrounded by vacuum, one finds [6]

$$\tilde{G}_0(z_1, z_1) = \tilde{G}_0(z_2, z_2) = \frac{2\pi}{q\varepsilon_{\text{ox}}} \frac{(1-\lambda)(1-\lambda\Delta)}{1-\lambda^2\Delta}, \quad (6)$$

$$\tilde{G}_0(z_1, z_2) = \tilde{G}_0(z_2, z_1) = \frac{2\pi}{q\varepsilon_{\text{ox}}} \sqrt{\Delta} \frac{(1-\lambda)^2}{1-\lambda^2\Delta}, \quad (7)$$

where $\lambda = (1 - \varepsilon_{\text{ox}})/(1 + \varepsilon_{\text{ox}})$ and $\Delta = e^{-2qh}$. Using Eqs. (6) and (7) one can solve Eqs. (4) and (5) to obtain $\tilde{G}(z_1, z')$ and $\tilde{G}(z_2, z')$, which need to be substituted in the right-hand side of Eq. (3) to yield a final expression for the full GF, $\tilde{G}(z, z')$.

One can derive a dispersion relation for all eigenmodes in a sandwich structure with two graphene sheets by making the determinant of the coefficients in the left-hand sides of the system in Eqs. (4) and (5) vanish. As an illustration, we assume that the graphene sheets have equal polarization functions, $\chi_1 = \chi_2 = \chi$, in which case we obtain two dispersion relations corresponding to anti-symmetric and symmetric coupling between collective modes at the opposite surfaces of this sandwich structure,

$$1 + \varepsilon_{\text{ox}} \tanh(qh) + \frac{4\pi e^2}{q} \chi = 0, \quad \text{and} \quad 1 + \varepsilon_{\text{ox}} \coth(qh) + \frac{4\pi e^2}{q} \chi = 0. \quad (8)$$

3. RESULTS AND CONCLUDING REMARKS

To obtain dispersion relations of our sandwich structure, we use $\varepsilon_{\text{ox}}(\omega)$ from Ref. [3] for a 5 nm thick layer of Al_2O_3 , which includes two TO phonon modes at 48 meV and 71 meV with zero damping. If we take the long wavelength limit of the polarization function for both graphene sheets, $\chi = -q^2 E_F / (\pi \hbar^2 \omega^2)$ with $E_F = 200$ meV, then each of the dispersion relations in Eq. (8) becomes a cubic equation in ω^2 and it may be in principle solved analytically. The resulting six dispersion curves are shown in the left panel of Fig. 1 for symmetric (red curves) and anti-symmetric coupling (green curves) of two pairs of the surface TO phonons and two Dirac plasmons. Alternatively, one may plot the so-called loss function, $-\Im[1/\varepsilon(q, \omega)]$ where $\varepsilon(q, \omega)$ is the dielectric function of the entire sandwich structure obtained by an *ab initio* method [7]. In the right panel of Fig. 1 we see that the peak positions in the loss function follow quite closely the analytically obtained dispersion curves in the left panel, showing versatility of the GF approach.

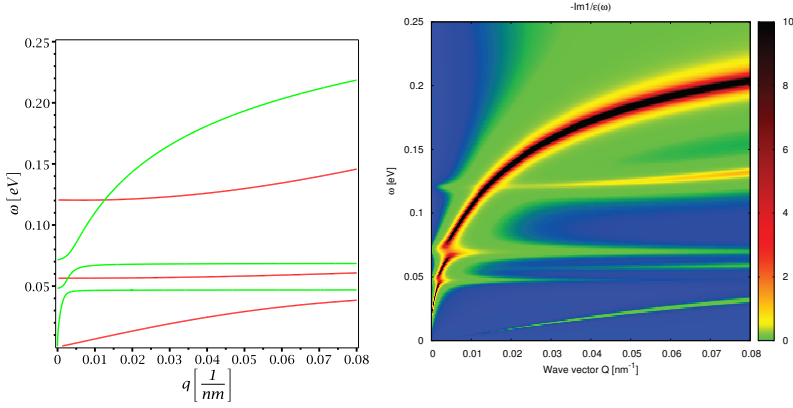


Figure 1. Analytical result for dispersion relations of hybridized modes, Eq. (8), (left) and *ab initio* result for loss function, $-\Im [1/\varepsilon(q, \omega)]$, (right) in Al_2O_3 layer between two graphene sheets with Fermi energies $E_F = 0.2$ eV.

Acknowledgements

T.Dj., L.K. and I.R. acknowledge support from the Ministry of Education, Science and Technological Development of the Republic of Serbia (Projects No. 171023, 32039, and 45005, respectively). V.D. acknowledges support from the Ministry of Science, Education and Sports of the Republic of Croatia. Z.L.M. acknowledges support from the Natural Sciences and Engineering Research Council of Canada.

REFERENCES

- [1] F. Xia, H. Wang, D. Xiao, M. Dubey and A. Ramasubramaniam, *Nature Photon.* 8, 899 (2014).
- [2] F. J. García de Abajo, *ACS Photonics* 1, 135 (2014).
- [3] M. V. Fischetti, D. A. Neumayer and E. A. Cartier, *J. Appl. Phys.* 90, 4587 (2001).
- [4] H. Yan, T. Low, W. Zhu, Y. Wu, M. Freitag, X. Li, F. Guinea, P. Avouris and F. Xia, *Nature Photon.* 7, 394 (2013).
- [5] T. Marinković, I. Radović, D. Borka and Z. L. Mišković, *Plasmonics* 10, 1741 (2015).
- [6] R. Aničić and Z. L. Mišković, *Phys. Rev. B* 88, 205412 (2013).
- [7] D. Novko, M. Šunjić and V. Despoja. *Phys. Rev. B* 93, 125413 (2016).

A QUANTITATIVE STUDY OF ION GUIDING BETWEEN TWO GLASS PLATES

E. Giglio¹, K. Tőkési^{2,3*} and R.D. DuBois⁴

¹*Centre de Recherche sur les Ions, les Matériaux et la Photonique (CIMAP),
F-14000, Caen, France, EU*

²*Institute for Nuclear Research, Hungarian Academy of Sciences (Atomki),
4026 Debrecen Bem tér 18/c, Hungary, EU*

³*ELI-ALPS, ELI-HU Non-profit Kft., Dugonics tér 13, H-6720 Szeged,
Hungary, EU*

⁴*Missouri University of Science and Technology, Rolla, MO USA*

Abstract. The transmission of a 1 keV Ar⁺ beam between two glass plates (microscope slides) 508 mm long, 25.4 mm wide and 0.925 mm thick was studied. The plate separation was 1.25 mm. The beam was collimated by three 0.5 mm apertures, one centered between the plates, the other two positioned to transmit beams between the outer surface of one of the glass plates and a parallel metal plate. One of the bypass beams was at the same height as the “guided” beam, the other was 3 beam diameters lower. We present studies with the goal to provide quantitative information about the buildup and decay of charge on the glass plates and how this correlates with the observed guiding.

1. INTRODUCTION

Since the original discovery of ion beam guiding by insulating capillaries, numerous studies have been performed [1-6]. The vast majority of these provide qualitative information about the transmitted intensity as a function of time and/or angle between the capillary axis and the original beam direction. Models of the stochastic buildup of charge on the capillary surfaces have been used to simulate these properties [2]. However, quantitative information about the charge buildup, i.e., the deposition and redistribution, is needed for testing and improving these models.

In an earlier study of low energy ion beam guiding by a cylindrical glass capillary, we provided some experimental information about how rapidly the charge decayed away plus simulated the beam transmission [4]. In another study a highly charged ion beam was guided [2] and then moved to pass close by the outside of the charged capillary. The beam was observed to have a time dependent deflection as the capillary charge decayed away. However, in both

studies, the geometries plus the data acquired were incompatible with providing information about the spacial and temporal behavior of the capillary charge.

Here, a new study employing well defined geometry is described. We used a 1 keV Ar^+ beam guided by two parallel glass microscope slides. Measurements of the currents on the glass slides and being transmitted, plus images of the transmitted beams were used to provide information about the amount of deposited charge and the times required to charge and discharge the plates.

2. EXPERIMENT

The present guiding study was performed at the Missouri University of Science and Technology. To provide a well defined geometry, the beam was collimated to 0.5 mm diameter by an aperture centered between two glass plates (microscope slides) 508 mm long, 25.4 mm wide and 0.925 mm thick. The plate separation was 1.25 mm. The plates were set in parallel shallow grooves in an aluminum holder. Similar grooves in a vespel holder kept the plates parallel in the vertical direction. The aperture and plate assembly were mounted on a rotatable xyz manipulator. Although only a single aperture was used, based upon lens positions and geometrical factors the total beam divergence was estimated to $\sim 0.1^\circ$.

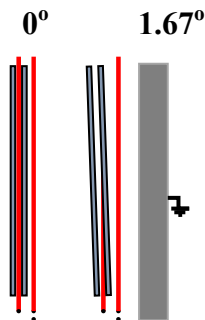


Figure 1. Geometry of present setup showing an overhead view of the guiding assembly and the guided and bypass beams (the red lines) for 0° and 1.67° tilt angles. The collimating apertures are as viewed by the incoming beam.

In addition to the “guided beam”, two “bypass beams” of 0.5 mm in diameter and offset horizontally by 3 mm were produced by two additional apertures. One of the bypass beams was at the same vertical level as the guided beam, the other was 1.75 mm lower. Thus, as shown in Fig. 1, with the plates aligned along the beam axis the guided and bypass beams traveled uninterrupted between and outside the glass plates whereas for a small rotation the guided beam impacted the inner surface of one plate while the bypass beams again passed uninterrupted on the other side of the same plate. In order to provide predictable electric field conditions in the bypass region, a grounded plane was positioned 7 mm away from the closest glass plate.

A larger collimator of ~ 6 mm diameter was placed approximately 2 cm upstream from the three input apertures and a defocused beam was used in order

to simultaneously illuminate all three input apertures as uniformly as possible. A metal plate on a horizontal manipulator located between the large and the three small input apertures could be positioned to block the guided beam without disturbing the bypass beams or, using a small aperture in this plate, just the guided beam could pass. To monitor the guided and bypass beams, a 50 mm diameter channelplate with a 2D anode was located approximately 15 cm downstream from the exit of the glass plates. With only a small bias voltage applied, the transmitted currents impacting the plate could be measured using sensitive electrometers or when the beam intensity was reduced and high voltage was applied, images and intensities for each of the guided and bypass beams could be recorded. To ensure stable conditions, the beam current was monitored either on the input aperture assembly or on the plate on the horizontal positioner. In addition, the current impacting and ultimately exiting the glass plates through their lower surfaces into the aluminum holder was recorded. Outputs from the electrometers were digitized and sent to a PC with a second PC added for the imaging measurements.

3. RESULTS

Using our setup, several studies were performed to provide quantitative information about the buildup and decay of charge on the glass plates and how this correlates with the observed guiding. In the work presented here the bypass beams were prohibited from entering the guiding assembly.

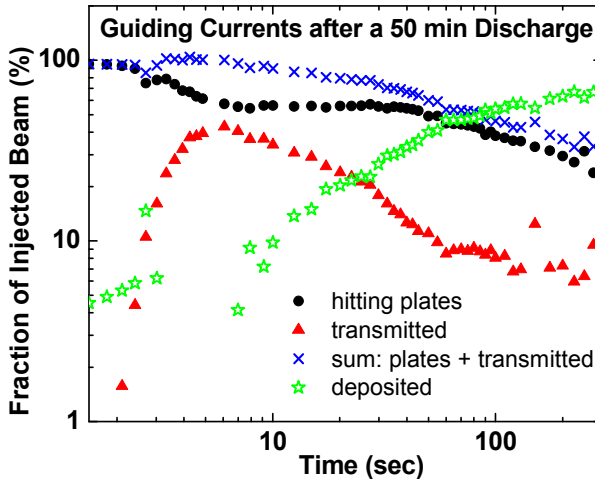


Figure 2. The relative amounts of injected beam hitting the glass plates and being transmitted, plus their sum and the missing component that is deposited in the plates.

By using a beam intensity of ~ 100 pA, the relative amounts of current hitting the glass plates and being transmitted were measured as a function of time. But the higher beam current also means guiding begins quite quickly. Data obtained after allowing the glass plates to discharge for 50 minutes are shown. As seen, the transmitted current immediately increases while the current hitting the plates decreases. Ultimately, both decrease. Their sum is seen to systematically decrease which indicates that some of the injected beam is deposited in and on the glass plates. This study using higher currents shows that guiding begins immediately or very shortly after beam injection but very quickly guiding begins. With the onset of guiding, data obtained following a 50 and 60 minute discharge illustrate that the initial increase in transmission correlates with a decrease in the amount of the injected beam that impacts the glass plates. Ultimately, approximately $\frac{1}{2}$ to $\frac{3}{4}$ of the injected charge is deposited in the plates.

Acknowledgements

This work was funded by the French National Research Agency (ANR) in the P2N 2012 program (ANR-12-NANO-008) for the PELIICAEN project. This work was also supported by the TeT No. 12 FR-1-013-0007, by the Hungarian Scientific Research Fund OTKA No. NN 103279 and by the and by the European Cost Actions CM1204 (XLIC) and CM1405 (MOLIM).

REFERENCES

- [1] N. Stolterfoht et al., Pys. Rev. Lett. **88**, 133201 (2002).
- [2] K. Schiessl, W. Palfinger, K. Tökési, H. Nowotny, C. Lemell, and J. Burgdörfer, Phys. Rev. A **72** (2005) 062902.
- [3] R.D. DuBois and K. Tökési, Nucl. Instr. Meth. Phys. Res. B. **279**, 186 (2012).
- [4] E. Giglio, R.D. DuBois, A. Cassimi, K.Tökési, Nucl. Instr. and Meth. Phys. Res. **B354** (2015) 82.
- [5] I. Rajta et al., Nucl. Instr. Meth. Phys. Res. B. **354**, 328 (2015).
- [6] G.U.L. Nagy et al., Eur. Phys. J. D. **69**:102 (2015).

FINAL CHARGE AND ENERGY Z-DISTRIBUTIONS OF SLOW Ar^{Z+} , Kr^{Z+} AND Xe^{Z+} IONS IN FRONT OF A SOLID SURFACE

M. D. Majkić¹, R. J. Dojčilović² and N. N. Nedeljković³

¹*University of Pristina, Faculty of Technical Sciences, Kosovska
Mitrovica, Serbia*

²*University of Belgrade, Vinča Institute of Nuclear Sciences, PO Box 522,
Belgrade, Serbia*

³*University of Belgrade, Faculty of Physics, PO Box 368, Belgrade, Serbia*

Abstract. We consider the final ionic charge $Q_{\text{fin}}^{(Z)}$ and the kinetic energy gain $\Delta E^{(Z)}$ of slow highly charged ions interacting with solid surface at arbitrary collision geometry, within the framework of the two-state vector model for the population dynamics and the micro-staircase model for the cascade neutralization. We analyze the case of the Ar^{Z+} , Kr^{Z+} and Xe^{Z+} ions. The core polarization of these ions is significantly different; however, the obtained charge states and kinetic energy gains are nearly the same, depending only on the collision geometry and ionic velocity. This result could be important in the analysis of the surface nanostructures, produced by these ions impinging upon a solid surface.

1. INTRODUCTION

Highly charged ions (HCI, charge $Z \gg 1$) impinging upon a solid surface can be partially neutralized via successive population of the intermediate Rydberg states. This process is well known and has been extensively studied previously. More recently, the quasi-resonant two-state vector model (TVM) appropriate for the study of the process at small but nonthermal ionic velocities has been developed [1]. In this case the fine structure of the neutralization cascade $Q = Z \rightarrow Q = Z - 1 \dots$ becomes important, i.e. it is necessary to use the appropriate micro-staircase model, which takes into account the specific quantum features of the population dynamics [1].

In this study, by using the quasi-resonant TVM and the micro-staircase model we calculate the ionic charge $Q_{\text{fin}}^{(Z)}$ and the kinetic energy

gain $\Delta E^{(Z)}$ in front of a solid surface, at ion-surface distance $R = R_{\min}$, i.e. at the time of its "impact" on surface. We consider the Ar^{Z+} , Kr^{Z+} and Xe^{Z+} ions, for $Z \in [10, 45]$, impinging upon a solid surface at arbitrary angle of incidence Φ_{in} , at velocities $v \in [0.01, 0.25]$ (in a.u.).

2. Z-DISTRIBUTIONS $Q_{\text{fin}}^{(Z)}$ AND $\Delta E^{(Z)}$

Within the framework of the micro-staircase model, the charge $Q_{\text{fin}}^{(Z)}(R)$ of the ion at distance R from the surface and the kinetic energy gain $\Delta E^{(Z)}(R)$ due to the action of the surface-image force are given by [1]

$$Q_{\text{fin}}^{(Z)}(R) = Q_{\min}^{(Z)}(R) - \sum_{j=j_{\min}^{(Q)}}^{\tilde{j}_{\max}^{(Q)}} P^{(Q,j)}, \quad Q = Q_{\min}^{(Z)}, \quad (1)$$

where $Q_{\min}^{(Z)} = \left\{ \max Q; R_c^{(Q,j_{\max}^{(Q)}+1)} < R \right\}$ is the ionic charge corresponding to the last macro-step, and

$$\Delta E^{(Z)}(R) = \frac{Q_{\text{fin}}^{(Z)2}}{4R} + \sum_{Q=Q_{\min}^{(Z)}}^Z \sum_{j=j_{\min}^{(Q)}}^{j_{\text{fin}}^{(Q)}} \frac{f^{(Q,j)}}{4R_c^{(Q,j)}}, \quad (2)$$

where $f^{(Q,j)} = P^{(Q,j)} \left[2Q - 2 \sum_{k=j_{\min}^{(Q)}}^j P^{(Q,k)} + P^{(Q,j)} \right]$, respectively. The sets of Rydberg levels (numerated by j ; $n_A = n_Z - j + 1$) populated in the neutralization cascade are defined by the values $\tilde{j}_{\max}^{(Q)}$, $j_{\min}^{(Q)}$ and $j_{\text{fin}}^{(Q)}$ [1]. The quantities $P^{(Q,j)}$ are the maxima of the population probabilities of the Rydberg levels participating in the process, and $R_c^{(Q,j)}$ are the corresponding neutralization distances [1].

In Fig. 1 we present the Z -distributions $Q_{\text{fin}}^{(Z)}$ and $\Delta E^{(Z)}$ given by Eq. (1) and Eq. (2), respectively, for Xe^{Z+} ion impinging upon a solid surface (work function ϕ) at velocity $v = 0.25$ a.u., for $\Phi_{\text{in}} = \pi/2, 3\pi/8$ and $\pi/4$. We consider the ion-surface distance $R_{\min} = 3.5$ a.u. In Fig. 1 we also present the grazing incidence case [2] and the classical overbarrier (COB) quantity $\Delta E^{(\text{class},Z)} = \phi Z^{3/2}/3\sqrt{2}$ [3]; the charge $Q_{\text{fin}}^{(\text{class},Z)} = 0$. Characteristic feature for the considered velocity and ionic charges Z is an incomplete neutralization: $Q_{\text{fin}}^{(Z)} \neq 0$. With increasing of Z the final ionic charge and the kinetic energy gain increase, for all considered geometries. With decreasing of the angle of incidence the final ionic charge, as well as the kinetic energy gain, decrease. In the case of grazing incidence ($\Phi_{\text{in}} \approx 0$), the value of the kinetic energy gain is relatively small and nearly coincide with the COB value, Fig. 1(b).

In Fig. 2 we present the Z -distributions $Q_{\text{fin}}^{(Z)}$ and $\Delta E^{(Z)}$ for Ar^{Z+} , Kr^{Z+} and Xe^{Z+} ions, for $\Phi_{\text{in}} = \pi/2$ and $\Phi_{\text{in}} = \pi/4$ and $R_{\min} = 3.5$ a.u. For

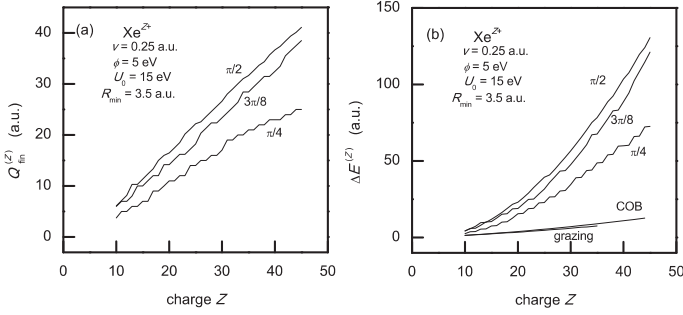


Figure 1. (a) Final charge state $Q_{\text{fin}}^{(Z)}$ and (b) kinetic energy gain $\Delta E^{(Z)}$ at ion-surface distance $R_{\text{min}} = 3.5$ a.u. of the Xe^{Z+} ion at velocity $v = 0.25$ a.u. for the angle of incidence $\Phi_{\text{in}} = \pi/2, 3\pi/8$ and $\pi/4$. Grazing and COB curves are from Ref. [2] for $v = 0.18$ a.u. and Ref. [3], respectively.

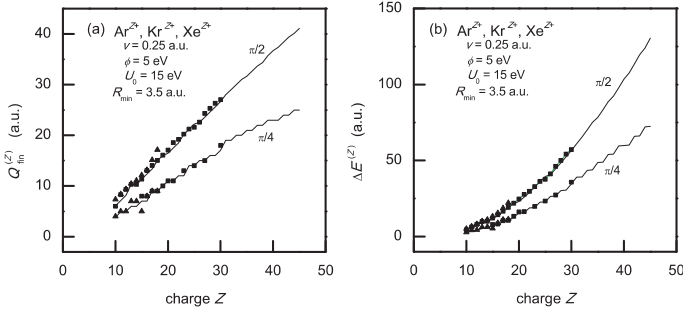


Figure 2. (a) Final charge state $Q_{\text{fin}}^{(Z)}$ and (b) kinetic energy gain $\Delta E^{(Z)}$ at ion-surface distance $R_{\text{min}} = 3.5$ a.u. of the Ar^{Z+} , Kr^{Z+} and Xe^{Z+} ions (symbols Δ and \square , and full line, respectively), for $\Phi_{\text{in}} = \pi/2$ and $\Phi_{\text{in}} = \pi/4$.

the same core charge Z these ions have different core polarization. However, the final ionic charge and the kinetic energy gain are nearly the same. It is a consequence of the fact that (although different Rydberg states of these ions are populated in each particular step of the cascade neutralization) the population is at nearly the same ion-surface distances $R_c^{(Q,j)}$.

In Fig. 3 we analyze the velocity effect: we consider the Z -distributions $Q_{\text{fin}}^{(Z)}$ and $\Delta E^{(Z)}$ for Xe^{Z+} ion at ion-surface distance $R_{\text{min}} = 3.5$ a.u. for $v = 0.01$ a.u., $v = 0.1$ a.u. and $v = 0.25$ a.u., and $\Phi_{\text{in}} = \pi/2$ and $\Phi_{\text{in}} = \pi/4$. From Fig. 3 one can see that for $v = 0.25$ a.u. and normal incidence ($\Phi_{\text{in}} = \pi/2$) the final ionic charge is close to the initial value Z ; for $\Phi_{\text{in}} = \pi/4$ the neutralization becomes significant, but still the neutralization is incomplete. In both cases the kinetic energy gain is large. For smaller ionic velocity $v = 0.01$ a.u. the neutralization process is almost complete and the kinetic energy gain is relatively small. With decreasing of

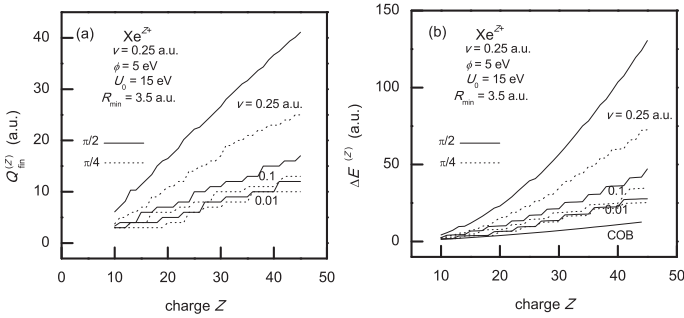


Figure 3. (a) Final charge state $Q_{\text{fin}}^{(Z)}$ and (b) kinetic energy gain $\Delta E^{(Z)}$ at ion-surface distance $R_{\min} = 3.5$ a.u. of the Xe^{Z+} ion at velocity v , for $\Phi_{\text{in}} = \pi/2$ and $\Phi_{\text{in}} = \pi/4$. COB curve is $\Delta E^{(\text{class},Z)}$ [3].

the ionic velocity (and/or) decreasing of the angle of incidence, the TVM kinetic energy gain approaches the COB velocity independent value [3].

The obtained velocity dependent Z -distributions $Q_{\text{fin}}^{(Z)}$ and $\Delta E^{(Z)}$ represent important information for the energy partition in the surface. The results can be most directly used in the analysis of nanostructures (craters), obtained by the impact of individual HCI on the conducting surfaces [4, 5].

Acknowledgements

This work was supported in part by the Ministry of Education, Science and Technological Development of the Republic of Serbia (Projects 171016, 172056 and 45020).

REFERENCES

- [1] N. N. Nedeljković, M. D. Majkić, D. K. Božanić and R. J. Dojčilović, *J. Phys. B: At. Mol. Opt. Phys.* 49, 125201 (2016)
- [2] N. N. Nedeljković, M. D. Majkić and S. M. D. Galijaš, *J. Phys. B: At. Mol. Opt. Phys.* 45, 215202 (2012)
- [3] C. Lemell, H. P. Winter, F. Aumayr, J. Burgdörfer and F. Meyer, *Phys. Rev. A* 53, 880 (1996)
- [4] J. M. Pomeroy, A. C. Perrella, H. Grube and J. D. Gillaspay, *Phys. Rev. B* 75, 241409(R) (2007)
- [5] R. E. Lake, J. M. Pomeroy, H. Grube and C. E. Sosolik, *Phys. Rev. Lett.* 107, 063202 (2011)

RYDBERG STATE POPULATION OF SLOW ArXV, KrXV AND XeXV IONS IMPINGING A SOLID SURFACE AT ARBITRARY COLLISION GEOMETRY

M. D. Majkić¹, N. N. Nedeljković², D. K. Božanić^{3,4} and R. J. Dojčilović³

¹*University of Pristina, Faculty of Technical Sciences, Kosovska Mitrovica, Serbia*

²*University of Belgrade, Faculty of Physics, PO Box 368, Belgrade, Serbia*

³*University of Belgrade, Vinča Institute of Nuclear Sciences, PO Box 522, Belgrade, Serbia*

⁴*DESIRS Beamline, Synchrotron SOLEIL, Saint Aubin BP 48, 91192 Gif sur Yvette, France*

Abstract. We consider the population dynamics of the Rydberg states of slow highly charged ArXV, KrXV and XeXV ions, impinging upon a solid surface at arbitrary angle of incidence. We use the two-state vector model recently adapted for the calculation of the intermediate population probabilities in the quasi-resonant case. According to the model, the population probabilities depend both on the collision geometry and ionic velocity. An increase of the ionic core polarization (ArXV \rightarrow KrXV \rightarrow XeXV) induces an increase of the population probability maxima and the localization of the population process is shifted toward a smaller ion-surface distances.

1. INTRODUCTION

Interest in the interaction of slow highly charged ions (HCI) with solid surfaces was renewed due to the recently observed phenomena that the surface nanostructures can be obtained by the impact of these ions on solid surfaces, with neutralization energy participating in the energy distribution profile, see [1] and references therein. The quantities relevant for analyzing of the surface structures are in direct correlation with the population dynamics of the Rydberg states of HCI approaching a solid surface. For that reason, recently [2] the two-state vector model (TVM) has been adapted to the arbitrary collision geometry and ionic velocities relevant for experiments (perpendicular velocity $v_{\perp} < 0.3$ a.u. and parallel velocity $v_{\parallel} < 0.15$ a.u.).

The TVM was obtained for quasi-resonant electron transitions and has been used to analyze the population dynamics of the Xe^{Z+} ions [2]. In the present article, we extend the analysis to different ions, considering the ArXV, KrXV and XeXV ions as an example. Considering these ions, we elucidate the role of the ionic core polarization. The results are viable only under the resonant conditions, for the HCI escaping a solid surface in the normal direction [3] at velocity $v = v_{\perp} \ll 1$ a.u. and in the grazing incidence geometry ($v_{\perp} \approx 0, v_{\parallel} \in [0.003, 0.18]$ a.u.) [4, 5].

2. QUASI-RESONANT TVM

The quasi-resonant TVM is described in details in [2]; within the model, the state of an active electron is described simultaneously by two state vectors $|\Psi_1(t)\rangle$ and $|\Psi_2(t)\rangle$ evolving in two opposite directions in time: from the preselected state (electron in solid) and from the postselected state (electron in the ionic Rydberg state). At ion-surface distance R these states are determined by the parabolic quantum numbers $\mu_M = (\gamma_M, n_{1M}, m_M)$ and the spherical quantum numbers $\nu_A = (\gamma_A, l_A, m_A)$, see Fig. 1. The quantities γ_M and $\gamma_A(R)$ are the energy parameters corresponding to the electron energy in solid (metal) ($E_M = -\gamma_M^2/2 \equiv k^2/2 - U_0$) and atomic energy $E_A = -\gamma_A^2/2$, respectively. The state $|\Psi_1(t)\rangle$ in the system S , which

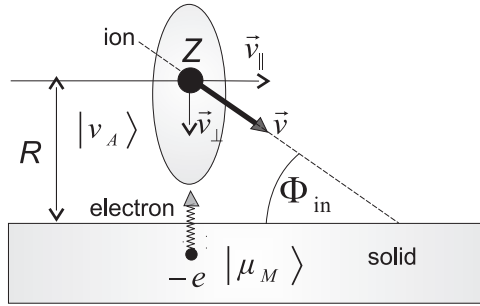


Figure 1. Collision geometry and electron capture process, schematically.

moves with velocity \vec{v}_{\parallel} along the surface, and the state $|\Psi_1^{(0)}(t)\rangle$ for $v_{\parallel} = 0$ are connected kinematically. Effectively, the electron momenta in solid are shifted: $\vec{k} \rightarrow \vec{k}' = \vec{k} - \vec{v}_{\parallel}$, so that $\gamma_M \rightarrow \gamma'_M$, where $\gamma_M'^2 - \gamma_M^2 = k^2 - k'^2$. Electrons, which for $v_{\parallel} = 0$ occupy the metallic states corresponding to the energies $-U_0 < E_M < -\phi$, where ϕ is the solid work function, now are distributed according to the velocity modified angle averaged Fermi-Dirac distribution $\langle f \rangle_{\Omega_{k'}}$ [2, 4]. The state $|\Psi_2(t)\rangle$ in the S and the state $|\Psi_2^A(t)\rangle$ in the rest frame of the moving ion (which moves at velocity \vec{v}_{\perp} in respect to S) differ by the Galilei phase factor $\exp[i(\vec{v}_{\perp} \cdot \vec{r} - v_{\perp}^2 t/2)]$ [2, 3].

The population probability $P_{\nu_A}(t)$ of the Rydberg state $|\nu_A\rangle$ is ex-

pressed by $P_{\nu_A}(t) = 1 - \exp[-T_{\nu_A}(t)]$, where $T_{\nu_A}(t)$ is the transition probability, given by [2]

$$T_{\nu_A}(t) = f_\varepsilon T_{\nu_A}^{(0)} \frac{v_\perp}{\gamma_A |\tilde{\beta}|} \langle f \rangle_{\Omega_{k'}} f_\gamma(\gamma'_M) (\gamma'_M + \gamma_A)^2 \left(1 + \frac{2\tilde{\alpha}}{\tilde{\beta}} \frac{1}{R} \right) R^{2\tilde{\alpha}} e^{-2\tilde{\beta}R}, \quad (1)$$

where $v_\perp = -dR/dt$. The quasi-resonant transition probability differs from the corresponding expression for the resonant electron transitions [4] by the factor $f_\varepsilon = f_\varepsilon(R; v_\parallel, v_\perp)$ [2]. In Eq. (1), $\tilde{\alpha} = Z/\tilde{\gamma}_A - 1/2 + 1/4\gamma'_M$ and $\tilde{\beta} = \gamma'_M + (\tilde{\gamma}_A - \gamma'_M)/2$, where $\tilde{\gamma}_A$ is the energy parameter of the considered Rydberg state in the absence of interaction with solid and $\gamma'_M = \gamma_A(R)$. The quantities $T_{\nu_A}^{(0)}$, $\langle f \rangle_{\Omega_{k'}}$ and $f_\gamma(\gamma'_M)$ are given explicitly in [4].

3. RESULTS

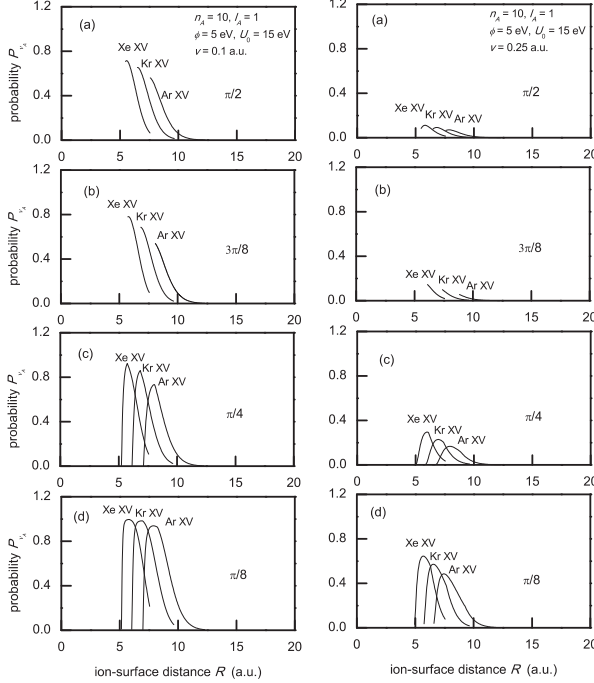


Figure 2. Population probabilities $P_{\nu_A}(t)$ via ion-surface distances R for the ArXV, KrXV and XeXV ions at velocities $v = 0.1$ a.u. (left panel) and $v = 0.25$ a.u. (right panel), for angle of incidence (a-d): $\Phi_{\text{in}} = \pi/2, 3\pi/8, \pi/4$ and $\pi/8$. Probabilities are for the solid work function $\phi = 5$ eV and the depth of the solid potential well $U_0 = 15$ eV.

In Fig. 2 we present the probability $P_{\nu_A}(t)$ via ion-surface distances R ; outside of the presented R -intervals $\langle f \rangle_{\Omega_{k'}} = 0$. We consider the popula-

tion of the Rydberg state $n_A = 10, l_A = 1, m_A = 0$ of the ArXV, KrXV and XeXV ions, for some characteristic angle of incidence Φ_{in} and ionic velocities $v = 0.1$ a.u. and $v = 0.25$ a.u. The probabilities are peak-shaped, with maxima $P_{\nu_A}^{\text{max}}$ at $R = R_{\text{max}}$. The increasing of the population probability when the ion approaches the surface (decreasing of R) in the initial stages of the population process can be attributed to the pure electron capture. With further decrease of R , i.e. for $R < R_{\text{max}}$, population probability decreases, which means that the reionization channel partially suppresses the neutralization. For the normal incidence case ($\Phi_{\text{in}} = \pi/2$) and for $\Phi_{\text{in}} = 3\pi/8$, the process mainly consists of pure population, without reionization.

For the considered population process, from Fig. 2 we see that with increasing of the ionic core polarization (ArXV \rightarrow KrXV \rightarrow XeXV), the population maxima $P_{\nu_A}^{\text{max}}$ increase. The corresponding ion-surface distances R_{max} decrease, i.e. with increasing of the ionic core polarization the population process is shifted toward the surface. This effect is due to the increasing of $\tilde{\gamma}_A$ with increasing of the core polarization: $\tilde{\gamma}_A = 1.509$ a.u., 1.613 a.u. and 1.736 a.u. for the ArXV, KrXV and XeXV ions, respectively. The quantities $P_{\nu_A}^{\text{max}}$ increase with decreasing of the angle of incidence (Fig. 2(a) \rightarrow Fig. 2(d)), what is the consequence of decreasing of v_{\perp} and increasing of v_{\parallel} with decreasing of Φ_{in} . The neutralization process, for all geometries, takes place at almost the same ion-surface distance $R \approx R_{\text{max}}$. We can also recognize the decreasing of the probability maxima with increasing of the projectile velocity ($v = 0.1$ a.u. $\rightarrow v = 0.25$ a.u.). This effect is less significant for smaller angle of incidence ($\Phi_{\text{in}} = \pi/8$). We note that for the grazing incidence case ($\Phi_{\text{in}} = 0$), the probability increases with increasing of the ionic velocity [2, 5].

Acknowledgements

This work was supported in part by the Ministry of Education, Science and Technological Development of the Republic of Serbia (Projects 171016, 172056 and 45020).

REFERENCES

- [1] F. Aumayr et al, J. Phys: Condens. Matter 23, 393001 (2011)
- [2] N. N. Nedeljković, M. D. Majkić, D. K. Božanić and R. J. Dojčilović, J. Phys. B: At. Mol. Opt. Phys. 49, 125201 (2016)
- [3] N. N. Nedeljković and M. D. Majkić, Phys. Rev. A 76, 042902 (2007)
- [4] N. N. Nedeljković, M. D. Majkić and S. M. D. Galijaš, J. Phys. B: At. Mol. Opt. Phys. 45, 215202 (2012)
- [5] M. D. Majkić, N. N. Nedeljković and S. M. D. Galijaš, J. Phys: Conf. Series 399, 012009 (2012)

2D SIMULATION OF 1 MEV PROTON MICROBEAM TRANSMISSION THROUGH AN INSULATING MACROCAPILLARY

G.U.L. Nagy¹, I. Rajta¹ and K. Tökési^{1,2}

¹*Institute for Nuclear Research, Hungarian Academy of Sciences (Atomki),
4026 Debrecen Bem tér 18/c, Hungary*

²*ELI-ALPS, ELI-HU Non-profit Kft., Dugonics tér 13, H-6720 Szeged, Hungary*

Abstract. The transmission of 1 MeV proton microbeam through an insulating macrocapillary is simulated according to our recent experiments. The beam was inserted into the capillary under 1° incident angle, which is large enough to prevent the geometrical transmission of the beam due to the aspect ratio of the capillary. In the simulation the XZ section is taken from the experiments, which is the rotation plane of the target. The key processes leading to the ion guiding phenomenon are studied. Time evolution of the beam transmitted through the capillary is observed. The first results are in agreement with our experiments.

1. INTRODUCTION

Charged particle beams are able to pass through insulating capillaries keeping their initial kinetic energy and charge state, even if the capillary target is tilted with respect to the direction of the incident beam, preventing the geometrical transmission. The phenomenon is called charged particle guiding and caused by the self-organized charge-up of the insulating material. Guiding of slow, highly charged, heavy ions is extensively studied since the discovery of the guiding effect [1]. Although the phenomenon is interesting from theoretical points of view, practical applications of it can be found rather in the MeV energy range, such as particle induced X-ray emission analysis (PIXE) [2] or cell irradiation [3,4]. This gave us the motivation to start our investigations using 1 MeV proton microbeam. Guiding of MeV energy ions is so far attributed to multiple small angle scattering, which is actually a different process from guiding, and which leads to the energy broadening and energy loss of the incident ion beam [5,6].

In Atomki a new experimental set-up was constructed in order to experimentally study the guiding of 1 MeV focused proton beam through an insulating macrocapillary [7]. The experiments were successful and we proved that it is possible to guide an ion beam of 1 MeV energy through an insulating capillary target in initial energy and charge state [8,9].

Now, as a continuation of our previous work, we started to develop a classical trajectory Monte-Carlo simulation code to reproduce our experimental data in order to study the key processes responsible for the guiding of the swift ion beam. In the simulation, the proton implantation into the insulating material is considered, as well as the Coulomb forces act on the projectile ions due to the accumulated charge on the inner capillary wall. Charge relaxation due to the leakage currents are taken into account. Elastic scattering of the incident ions by the surface atoms is also introduced in order to distinguish between atomic or electronic processes, and the collisionless guiding phenomenon. The first results of the simulation show strong correlation with our previous experiments.

2. SIMULATION

The simulation code is set up so that it releases a proton microbeam of 1 MeV kinetic energy focused on the entrance of the capillary (see Figure 1). The divergence (half opening angle) of the microbeam in the XZ plane is 0.29° , therefore the beam is broadening according to this during it is approaching the inner capillary wall.

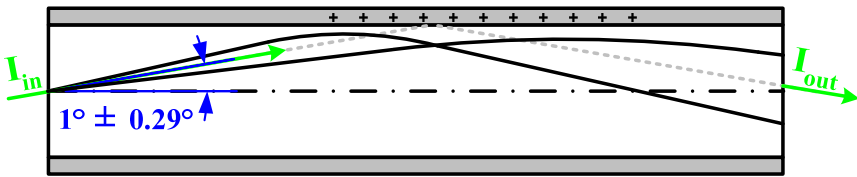


Figure 1. Schematic drawing of the simulation (note that the X and Z directions are not to scale). The 1 MeV proton microbeam, whose focal point is on the entrance of the capillary, is released in 1° angle of incidence and with $\pm 0.29^\circ$ half opening angle.

The geometry of the whole simulation is identical to our experiments, including both the main parameters of the beam and the dimensions of the capillary. This means that the length of the capillary is set to $l = 44.5$ mm and its diameter is $d = 800$ μm .

When the protons hit the surface, they are either implanted into the target material leaving a positive charge in the surrounding area, or they are scattered from a nucleus of the target so that they can leave the material and continue travelling towards the capillary exit or to the opposite wall of the target. During their travel inside the material, different atomic and electronic processes result in the energy loss of the incident particles. When charge is implanted into the material, it will interact with the protons arriving later through Coulomb repulsion. When enough charge is accumulated on the capillary wall, it will start to deflect the arriving protons, first modifying their trajectory and their impact

position with the capillary, later entirely preventing the collisions between the projectiles and the target atoms.

In parallel with the charge accumulation, leakage currents are induced due to the formed electric potential on the wall. Since the outer surface of the capillary is not conductive (e.g. it is not evaporated with a metal layer), the charges more likely travel along the inner surface, since the ground potential is at the entrance and at the exit of the capillary both on the inner and outer surfaces. Although some effects of charge migration into the bulk might take place like in other works dealing with macrocapillaries [10,11], so far we have neglected this effect.

3. RESULTS

In the recent work the time evolution of the transmission of the proton microbeam is investigated. The intensity of the beam leaving the capillary is expressed relative to the intensity entering it (I_{out}/I_{in}), giving us the efficiency of the transmission in percents. The probability of scattering the incident protons is set according to our experiments.

We found, that the transmission starts to increase right after we let the beam enter into the capillary. This is coherent with the experiments, as well as a continuous, incident beam intensity dependent increase of the transmission. Figure 2 shows an example, where the simulation was running for 400 and 800 seconds using 1 pA and 0.5 pA incoming beam intensity, which is enough for the beam to terminate at above 90% relative transmission. However, since we are in only two dimensions, the absolute values of any time dependent processes (e.g. the elapsed time itself, or the beam current) are not comparable with the reality.

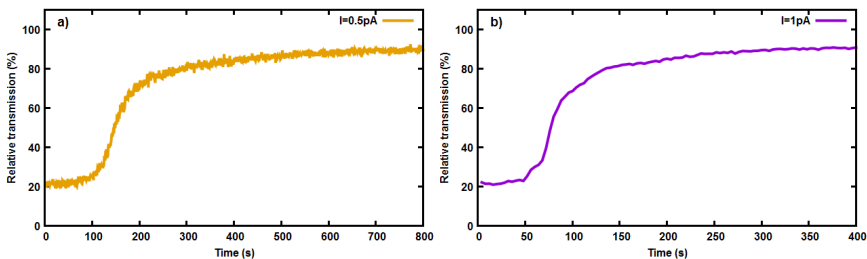


Figure 2. Time evolution of the proton microbeam transmission I_{out}/I_{in} through the insulating capillary in case of **a)** 0.5pA incident intensity and **b)** 1pA incident intensity.

As it is seen, by increasing the incident beam intensity, the time needed to reach a plateau in the transmission is decreasing nearly reciprocally as we measured and showed in Ref. [9]. In case of 1 pA incoming intensity, the transmission can be considered stable from around 350 seconds, while in case of 0.5 pA incident intensity, it just stabilized at around 700 seconds. This is explained by the total charge implanted into the capillary, $q=I*t$. Although the energy dependent elastic scattering cross section and the time dependent charge

relaxation might influence this relation, the former is neglected because of the small energy loss of the impinging protons, and the latter is a relatively slow process, which therefore shows also negligible effects in the above intensity range.

These first results are very promising, motivating us to further develop the code and to complete our model in order to approach the reality as much as possible, and to become able to get insight of what is happening inside the capillary.

Acknowledgements

This work was supported by the Hungarian Scientific Research Fund OTKA Nos. NN 103279 and K103917, by the COST Actions CM1204 (XLIC) and CM1405 (MOLIM).

REFERENCES

- [1] N. Stolterfoht et al., *Pys. Rev. Lett.* **88**, 133201 (2002).
- [2] J. Hasegawa et al., *Nucl. Instr. Meth. Phys. Res. B.* **269**, 3087 (2011).
- [3] Y. Iwai et al., *Appl. Phys. Lett.* **92**, 023509 (2008).
- [4] T. Ikeda et al., *Surface & Coatings Technology* **206**, 859 (2011).
- [5] M.J. Simon et al., *Nucl. Instr. Meth. Phys. Res. B.* **330**, 11 (2014).
- [6] G.Y. Wang et al., *Scientific Reports* **5**: 15169 (2015).
- [7] G.U.L. Nagy et al., *Aip. Conf. Proc.* **1525**, 40 (2013).
- [8] I. Rajta et al., *Nucl. Instr. Meth. Phys. Res. B.* **354**, 328 (2015).
- [9] G.U.L. Nagy et al., *Eur. Phys. J. D.* **69**:102 (2015).
- [10] N. Stolterfoht, *Phys. Rev. A.* **89**, 062706 (2014).
- [11] N. Stolterfoht, *Nucl. Instr. Meth. Phys. Res. B.* **354**, 51 (2015).

CASCADE NEUTRALIZATION OF SLOW HIGHLY CHARGED IONS IMPINGING A SOLID SURFACE AT ARBITRARY COLLISION GEOMETRY

N. N. Nedeljković¹, M. D Majkić², M. A. Mirković³ and R. J. Dojčilović⁴

¹*University of Belgrade, Faculty of Physics, PO Box 368, Belgrade, Serbia*

²*University of Pristina, Faculty of Technical Sciences, Kosovska Mitrovica, Serbia*

³*University College of Civil Engineering and Geodesy, Belgrade, Serbia*

⁴*University of Belgrade, Vinča Institute of Nuclear Sciences, PO Box 522, Belgrade, Serbia*

Abstract. We consider the interaction of slow highly charged XeXXV ion ($Z = 25$) at velocity $v = 0.1$ a.u. with solid surface at arbitrary angle of incidence. We analyze the influence of interaction geometry on the values of the ionic kinetic energy gain and the final ionic charge. Recently elaborated two-state vector model is used to calculate the corresponding population probabilities and neutralization distances. Cascade neutralization $Z \rightarrow Z - 1 \rightarrow Z - 2 \dots$ of the ion is treated within the framework of the appropriate micro-staircase model. Within the model the kinetic energy gain and the final ionic charge significantly depend on the collision geometry.

1. INTRODUCTION

Highly charged ions (HCI, charge $Z \gg 1$) impinging upon a solid surface can be partially neutralized via successive population of the intermediate Rydberg states (principal quantum number $n_A \gg 1$), which results in the neutralization cascade $Q = Z \rightarrow Q = Z - 1 \dots$. The cascade can be considered within the framework of the micro-staircase model [1], which represents a generalization of the staircase model appropriate for the grazing incidence [2]. Within the model, one can obtain the kinetic energy gain $\Delta E^{(Z)}(R)$ of the ionic projectile at distance R from the surface, for the arbitrary angle of incidence. Simultaneously, model yields the final ionic charge $Q_{\text{fin}}^{(Z)}(R)$. The micro-staircase model is based on the quasi-resonant two-state vector model (TVM) [1], appropriate for the calculation of the

intermediate population probabilities and neutralization distances for the low, but nonthermal ionic velocities v .

In our previous studies of the cascade neutralization, only the grazing incidence ($\Phi_{\text{in}} = 0$) [2] and normal incidence $\Phi_{\text{in}} = \pi/2$ [1] have been considered, using the staircase and micro-staircase models, respectively. In the present article, we apply the micro-staircase model to obtain the quantities $\Delta E^{(Z)}(R)$ and $Q_{\text{fin}}^{(Z)}(R)$, for arbitrary angle of incidence, considering the XeXXV ion as an example.

2. MICRO-STAIRCASE MODEL

The most general analysis of the multielectron population of the HCI interacting with solid surface is within the framework of the system of rate equations, by taking into account the population-reionization rates (together with the rates of other relevant electron exchange processes) [3]. The kinetic energy gain for the complete neutralization predicted by this approach is close to the value $\Delta E^{(\text{class},Z)}$ [4], obtained within the simple staircase-model for the classical over-barrier electron transitions. The result is velocity independent and can be used in the case of thermal ionic velocities. On the other hand, in the case of grazing incidence, the staircase-model combined with the resonant TVM predicts the velocity dependent expression for $\Delta E^{(Z)}$ [2]; the velocity effect is weak and the kinetic energy gain is in accordance with $\Delta E^{(\text{class},Z)}$.

In the case of small but nonthermal ionic velocities, and for arbitrary collision geometry, the kinetic energy gain $\Delta E^{(Z)}(R)$ has to be calculated by the micro-staircase model [1]. The specific feature of the model is an incomplete neutralization; simultaneously with $\Delta E^{(Z)}(R)$ one obtains the final ionic charge $Q_{\text{fin}}^{(Z)}(R) \neq 0$. According to the model, within the particular macro-step ($Q = Z, Z - 1, \dots$), the series of Rydberg levels $n_A = n_Z - j + 1$ are populated, where n_Z corresponds to the first populated level. Taking into account the population probabilities, characterized by the corresponding maxima $P^{(Q,j)}$, the macro step $Q \rightarrow Q - 1$ has the following micro-staircase structure:

$$Q \rightarrow Q - P^{(Q,j_{\text{min}}^{(Q)})} \rightarrow \dots \rightarrow Q - \sum_{j=j_{\text{min}}^{(Q)}}^{j_{\text{max}}^{(Q)}} P^{(Q,j)} \approx Q - 1; \quad (1)$$

each micro-cascade occurs at ion-surface distance $R_c^{(Q,j)}$. Within the model, the charge of the ion at distance R from the surface is given by [1]

$$Q_{\text{fin}}^{(Z)}(R) = Q_{\text{min}}^{(Z)}(R) - \sum_{j=j_{\text{min}}^{(Q)}}^{\bar{j}_{\text{max}}^{(Q)}} P^{(Q,j)}, \quad Q = Q_{\text{min}}^{(Z)}, \quad (2)$$

where $Q_{\min}^{(Z)}(R) = \left\{ \max Q; R_c^{(Q, j_{\max}^{(Q)} + 1)} < R \right\}$ is the ionic charge corresponding to the last macro-step, for a given R . The set of relevant Rydberg states is defined by the quantities $j_{\max}^{(Q)}, j_{\min}^{(Q)}$ and $\tilde{j}_{\max}^{(Q)}$, defined in [1].

At ion-surface distance R the kinetic energy of MCI is given by $E_k^{(Z)}(R) = E_{k0} + \Delta E^{(Z)}(R)$, where E_{k0} is the initial kinetic energy of the ion of charge Z . The kinetic energy gain, under the action of the surface image force is given by $\Delta E^{(Z)}(R) = \int_R^\infty [q^2(R)/4R^2] dR$, where $q(R) = Q_{\text{fin}}^{(Z)}(R)$; within the micro-staircase model, we have [1]

$$\Delta E^{(Z)}(R) = \frac{Q_{\text{fin}}^{(Z)2}}{4R} + \sum_{Q=Q_{\min}^{(Z)}}^Z \sum_{j=j_{\min}^{(Q)}}^{j_{\text{fin}}^{(Q)}} \frac{P^{(Q,j)} \left[2Q - 2 \sum_{k=j_{\min}^{(Q)}}^j P^{(Q,k)} + P^{(Q,j)} \right]}{4R_c^{(Q,j)}}, \quad (3)$$

where $j_{\text{fin}}^{(Q)} = j_{\max}^{(Q)}$ for $Q = Z, Z - 1, \dots, Q_{\min}^{(Z)} + 1$ and $j_{\text{fin}}^{(Q)} = \tilde{j}_{\max}^{(Q)}$ for $Q = Q_{\min}^{(Z)}$.

3. RESULTS

In Fig. 1 we present the ionic charge $Q_{\text{fin}}^{(Z)}(R)$ and the kinetic energy gain $\Delta E^{(Z)}(R)$ via ion-surface distances R , for XeXXV ion ($Z = 25$), for some characteristic angles of incidence Φ_{in} and initial ionic velocity $v = 0.1$ a.u. By approaching the surface of the HCI (decreasing of R) the ionic charge decreases due to the cascade neutralization (left panel). Simultaneously the ion is accelerated toward the surface, so that the ionic kinetic energy increases; the corresponding kinetic energy gain increases with decreasing of R , right panel. The smallest ion-surface separation R_{\min} used in Fig. 1 corresponds to the population of the Rydberg states $n_A = 5$ ($R_{\min} = 1.5$ a.u. for $\Phi_{\text{in}} = \pi/2$, $R_{\min} = 2$ a.u. for $\Phi_{\text{in}} = 3\pi/8, \pi/4$ and $\Phi_{\text{in}} = \pi/8$, and $R_{\min} = 15$ a.u. for the grazing incidence case).

From Fig. 1 we can see that the final ionic charge and the kinetic energy gain significantly depend on the collision geometry. With decreasing of the angle of incidence: (a) \rightarrow (e), i.e. with decreasing of the perpendicular and increasing of the parallel components of the ionic velocity, the final ionic charge decreases, at a given R and at smallest considered distance from the surface. Specific situation is for the grazing incidence of XeXXV ion, which is almost neutralized in front of the surface, Fig. 1(e). With decreasing of the angle of incidence, the value of the kinetic energy gain proportionally decreases.

Acknowledgements

This work was supported in part by the Ministry of Education, Science and Technological Development of the Republic of Serbia (Projects 171016,

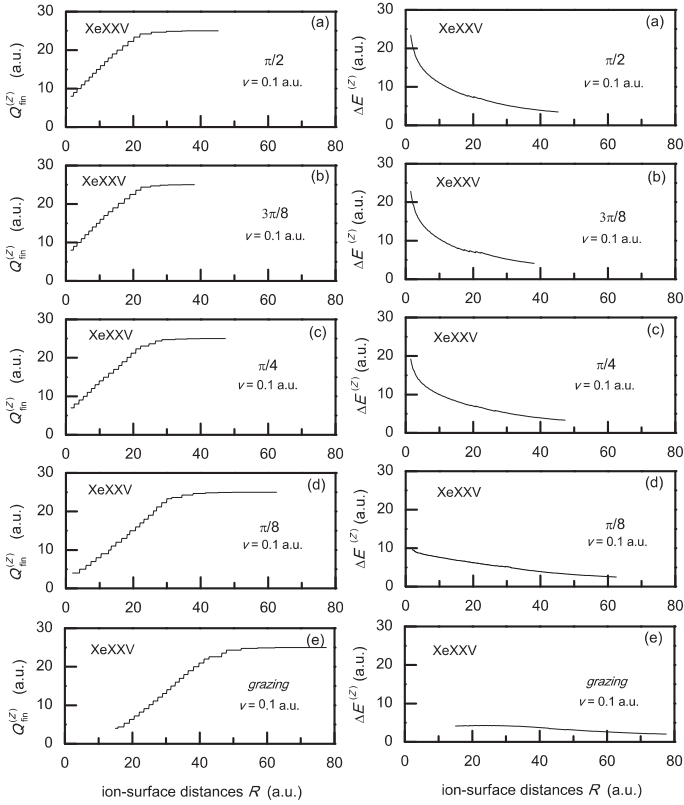


Figure 1. (a)-(e) Ionic charge $Q_{\text{in}}^{(Z)}$ (left panel) and kinetic energy gain $\Delta E^{(Z)}$ (right panel) at ion-surface distance R for the XeXXV ion at velocity $v = 0.1$ a.u., for the angles of incidence Φ_{in} equal to $\pi/2$, $3\pi/8$, $\pi/4$, $\pi/8$ and for the grazing incidence, respectively. The solid work function is $\phi = 5$ eV and the depth of the solid potential well is $U_0 = 15$ eV.

172056 and 45020).

REFERENCES

- [1] N. N. Nedeljković, M. D. Majkić, D. K. Božanić and R. J. Dojčilović, J. Phys. B: At. Mol. Opt. Phys. 49, 125201 (2016)
- [2] N. N. Nedeljković, M. D. Majkić and S. M. D. Galijaš, J. Phys. B: At. Mol. Opt. Phys. 45, 215202 (2012)
- [3] J. Ducrée J, H. J. Andrä and U. Thumm, Phys. Rev. A 60, 3029 (1999)
- [4] C. Lemell, H. P. Winter, F. Aumayr, J. Burgdörfer and F. Meyer, Phys. Rev. A 53, 880 (1996)

SYNTHESIS OF SILICON NANOPARTICLES BY ATMOSPHERIC PRESSURE ELECTRICAL DISCHARGES IN LIQUID

V. Burakov, M. Nedelko, N. Tarasenko, A. Nevar and N. Tarasenko

*B. I. Stepanov Institute of Physics, National Academy of Sciences of Belarus
68 Nezalezhnasti Ave. 220072 Minsk, Belarus*

Abstract. In this paper, we have developed electrical discharge technique in liquids for the controlled synthesis of silicon quantum dots. Optical emission spectroscopy method has been applied to evaluate parameters of the generated plasma in liquid. The phase composition, morphological, structural, and optical properties of the synthesized nanoparticles (NPs) have been investigated.

1. INTRODUCTION

In recent years silicon nanoparticles (Si-NPs) have attracted much attention due to a unique combination of their size-dependent optoelectronic properties and their biocompatibility, which could be used in a wide range of medical and technological applications, in particular, in biological imaging and therapy, lasers and light emitting diodes, memory devices, energy source and sensor devices. Therefore it is of great interest to study the properties of Si nanocrystals, their production methods, applications, and the ways of their characterization.

For silicon, new optoelectronic properties can be observed when the NP size is reduced below 10 nm (weak quantum confinement). But, when the diameter is comparable or below the silicon Bohr radius (~4.2 nm) the strong quantum confinement regime is observed [1]; in this case the silicon NPs are referred to as quantum dots (QDs).

Over the last decades, several methods for the synthesis of Si-NPs including Si-QDs have been proposed, which include plasma-based, laser-based and wet chemistry methods.

In the present work, we prepared nearly spherical Si-NPs by spark discharge between bulk silicon electrodes in water and ethanol. Special attention has been paid to the selection of the optimal conditions for a formation of NPs with the required composition based on the determination of electrical discharge plasma parameters, such as temperature and density of plasma components, since the discharge characteristics, as well as the temperature and composition of the liquid medium substantially influence the erosion of the electrode material and the

nature of plasma-chemical processes in the discharge. Investigation of the morphology, structure and optical properties of the synthesized nanocrystals in dependence on the electrical discharge plasma parameters is important for the determination of the possible ways of their practical application.

2. EXPERIMENTAL DETAILS

A reactor containing two electrodes submerged into liquid was used for generation of Si-NPs from the material of electrodes. The power supply provided an alternating current (ac) spark or arc discharges with a repetition rate of 100 Hz. The discharge was initiated by applying a high-frequency voltage of 11 kV. The optimal distance between the electrodes was about 0.3-0.5 mm. The peak current of the pulsed spark discharge was 60 A with a pulse duration of 30 μ s. The peak current and pulse duration of arc discharge were 10 A and 4 ms, respectively.

The basic plasma diagnostics consist in measuring the evolution of voltage and current during a discharge. In our experiments the waveforms of the current and voltage were measured by a digital fast oscilloscope. The discharge current was monitored by means of the current viewing resistor. The length of the single spark discharge pulse was almost two orders of magnitude shorter than that in the arc mode. Therefore spark discharge mode results in more intensive erosion of the electrodes.

Spectroscopic studies of plasma were performed using the diffraction spectrograph equipped with a CCD linear array. The light emitted by the plasma was focused by lens with focal length of 15 cm on the entrance slit of the spectrometer with a 1200 grooves/mm grating in order to investigate the spectral region from 300 nm to 700 nm.

The phase composition, morphology and structure of the synthesized NPs were analyzed by SAED, XRD, TEM and SEM techniques.

3. RESULTS AND DISCUSSION

XRD analysis was performed for the formed Si powder after drying of the colloidal solution aiming to determine the phase composition of the synthesized particles. The main diffraction peaks corresponded to lattice plane of cubic structured silicon. Analysis of the phase composition of the powders showed that NPs with the cubic silicon structure are major in the samples produced by the spark discharge both in water (90 vol.%) and ethanol (95 vol.%) with a small impurity of the oxide phase (SiO₂) in the samples synthesized in water and carbide phase (SiC) in the powder obtained in ethanol. No features of amorphous silicon were observed in XRD pattern.

Figure 1 shows the TEM image of Si-NPs synthesized by spark electrical discharge in water. TEM observations indicate that Si-NPs generated in water are nearly spherical, isolated (without agglomeration) and similar in morphology. Nearly all particles have a size in the range of 3-8 nm. The maximum of the size distribution was found to be around 5 nm.

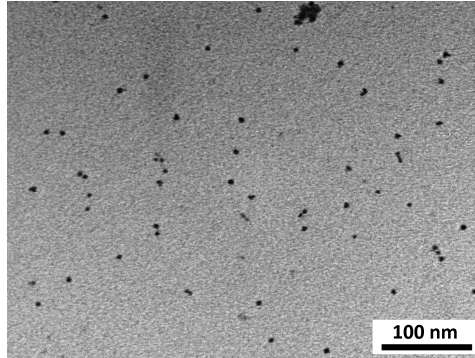


Figure 1. TEM image of the Si-NPs produced via spark discharge in water.

Raman spectroscopy provides important information about the microstructure of Si-NPs generated by pulse spark discharge. Figure (2a) shows Raman spectra of Si-NPs synthesized in water compared to bulk Si. It is well known that the bulk Si crystal displays a narrow optical phonon band at $\approx 521.3 \text{ cm}^{-1}$. When Si crystallites become small enough ($\leq 10 \text{ nm}$), the Raman phonon band broadens and shifts down in energy. In our experiment the position of the Raman peak for Si-NPs is shifted to lower wave numbers ($\Delta\omega \approx 3.5 \text{ cm}^{-1}$) compared to that of the bulk Si, indicating the existence of tiny Si grains.

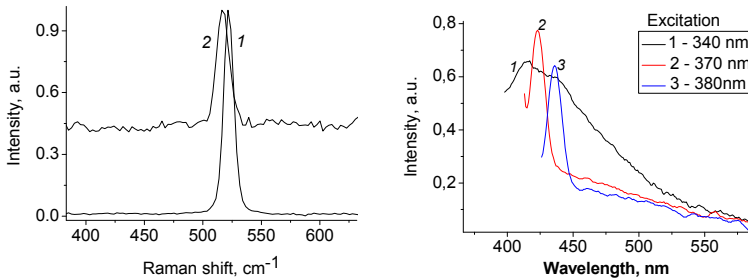


Figure 2. a) Raman scattering spectrum of the Si-NPs synthesized in water via spark discharge (curve 2) in comparison to the bulk silicon (curve 1); b) Photoluminescence spectra of silicon NPs obtained with different excitation wavelength

The Si-NPs synthesized exhibited a violet-blue photoluminescence at the room temperature and can be useful for development of light-emitting optoelectronic devices. The main characteristic of these spectra is the dependence of the luminescence band on the excitation wavelength and, in particular, a monotonous shift of the PL band maximum to the longer wavelength, from 350 to 570 nm, when increasing the excitation wavelength from 300 to 500 nm. A typical example of such behavior is presented in Figure 2b.

It is well known that bulk Si has no photoluminescence because of its narrow and indirect band gap. As the diameter of Si particles shrinks to several nanometers, it is possible that nanoparticles become efficient light emitters due to the quantum confinement effect. The photoluminescence of Si nanostructures can be explained by the radiative recombination of electron-hole pairs generated in a quantum confined system. Besides, impurities or defects introduced into Si can act as radiative centers.

Most probably, the Si NPs are formed through the mechanism of the primary nucleation of the evaporated atoms from the electrodes in the plasma plume and a growth of the embryonic particles. As shown by the results of spectroscopic studies the discharge takes place in a gas mixture consisting of atoms of the electrode material and decomposition products of the liquid. The presence of silicon atoms in the discharge plasma is confirmed by spectroscopic studies (Figure 3). Termination of NPs growth occurs in result of their interaction with cold liquid surrounding the discharge zone.

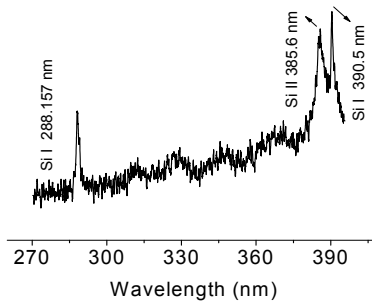


Figure 3. Emission spectra of the electrical discharge plasma between silicon electrodes submerged in water

4. CONCLUSION

The non-equilibrium atmosphere pressure discharge in liquid-phase media has been applied for the production of semiconductor Si NPs. Spectroscopic diagnostics of the electrical discharge plasma in liquids (water, ethanol) was carried out in order to optimize the formation of NPs under the discharge conditions. The nano-sized silicon particles with an average diameter of about 5 nm were synthesized, and a mechanism of their formation was suggested.

Acknowledgements

This work is partially supported by the Belarusian Foundation for Fundamental research by under the Grant № F15MS-024.

REFERENCES

- [1] K-Y. Cheng, R. Anthony, U.R. Kortshagen and R.J. Holmes, *Nano Lett.* 11, 1952 (2011).

MODIFICATIONS OF LIPID/2D-MATERIAL HETEROSTRUCTURES BY SEM

Radmila Panajotović and Jasna Vujin

*Institute of Physics, University of Belgrade, Pregrevica 118, 11080 Belgrade,
Serbia*

Abstract. The use of 2D-materials as solid support for lipids in the organic Field-Effect Transistors has been in expansion in recent years, particularly for their increased sensitivity to detecting small molecular concentrations. Molecular binding and charge transfer in these devices is governed by the chemical and electrical properties of the interface, as well as by its homogeneity and roughness. In our experiment we used the Scanning Electron Microscope (SEM) to modify the surface of thin lipid/graphene and lipid/WS₂ films. We showed that in these heterostructured film surface potential modifications can be achieved without significant morphological changes in the interface.

1. BACKGROUND

Lipid films in the form of mono-, bi- or multipliers supported on solid surfaces [1] are one of the center-points in the fields of biotechnology, organic material science and Bioelectronics. These assemblies are usually engineered through chemical or mechanical processing, which allow them to be tailored to a specific application, such as biochemical sensing. Recently, the use of 2D-materials as solid support for lipid heterostructures, particularly graphene and transition metal dichalcogenides, has been suggested, especially as a component of organic FET (Field-Effect Transistor) devices [1, 2]. In terms of sensing properties, it is crucial to these devices to possess the largest possible binding surface; hence the need for a porous substrate that will provide for this feature. To this end, thin films of graphene and other 2D-material substrates produced from liquid exfoliation seem to be good candidates because of their structure consisting of multilayered flakes with edges exposing dangling bonds. At the same time, such films allow the formation of uniform and homogenous lipid films as a stable and versatile platform for molecular binding in FET sensing devices.

Electrical properties of these heterostructures are crucial for their operation. As the pure lipid layer is likely to have high resistivity (of the order of M Ω) and is supported either on a conductive (graphene) or semiconductive (WS₂) substrate, our idea was to use the source of electrons that is routinely used in imaging, the Scanning Electron Microscope (SEM), to modify electric properties of the surface of such heterostructures. Since the SEM employs an intense high-

energy electron beam that is participating in elastic and inelastic collisions within both the lipid film and solid substrate that supports them, based on the earlier studies [3-5], we expected to see significant changes both in morphology and electric potential of the samples. We showed that the SEM beam tuned to its typical values of power and energy for imaging organic samples could be used as a lithography tool for electrical and chemical modification of lipid/2D-material heterostructures, without inducing significant changes in the morphology of the surface.

2. EXPERIMENT

2.1. Sample preparation

Graphene and WS₂ powder were dispersed in the solvent to produce the colloidal solution of desired concentration and then sonicated and centrifuged in order to homogenize and exfoliate. Thin films were first produced at the water/air (graphene) or toluene/air (WS₂) interface and then transferred to the SiO₂ substrate by using the Langmuir-Blodgett technique. The structure of these films consists of several nm-thick and tens to hundred-nm wide flakes. Low-concentration (0.1 mM) aqueous solution of deuterated phospholipid (1,2-dipalmitoyl-sn-glycero-3-phosphocholine) DPPC-D62 liposomes was drop-casted on thin graphene and WS₂ films. After the 15 min incubation, the samples were rinsed with DI H₂O to remove the excess liposomes.

2.2 Experimental technique

Morphology and surface potential of the samples before and after exposure to the electron beam from SEM (Tescan Mira 3) were measured in ambient conditions on the NTegra Prima Atomic Force Microscope in the semi-contact mode. For measurements of the surface potential the Au-TiN tip of about 35 nm curvature radius was used in the Kelvin Probe Force Microscopy mode. The samples were exposed to the 30 keV electron beam, scanning an area of 5x5 μm for 5 min and with the beam intensity typically used for high-resolution imaging. The spot size of the electron beam at this energy was ~ 7 nm. Raman spectroscopy was used in order to assess the chemical status of the samples before and after electron irradiation.

3. RESULTS

In order to study an overall effect of the keV-energy focused electron beam on our heterostructures consisting of lipids supported on graphene and WS₂ thin films, we performed the AFM, KPFM, and Raman spectroscopy measurements. The topography and surface potential scans of DPPC/graphene and DPPC/WS₂ are presented in Figures 1 and 2, respectively. It is evident from the topography scans that the 30 keV electron beam is not producing visible changes on the surface in neither of the three profile cross sections. The rough-

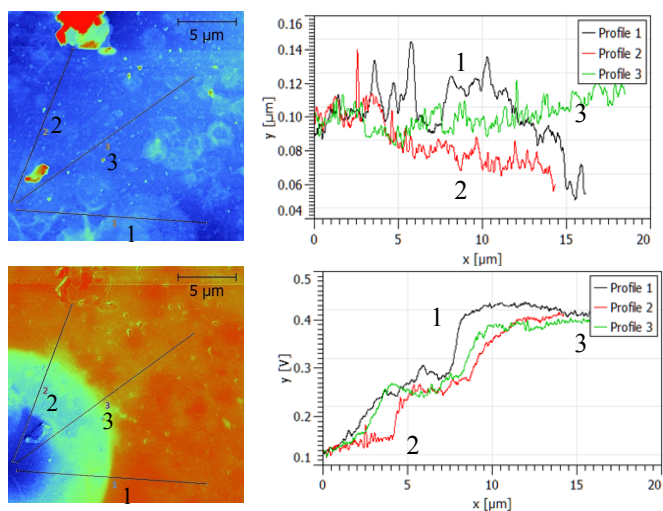


Figure 1. Topography (top row) and surface potential (bottom row) of DPPC/Graphene heterostructures on SiO_2 after irradiation by 30 keV electrons from SEM. Graphs on the right represent profiles of the topography and surface potential along the lines marked on 2D-scans.

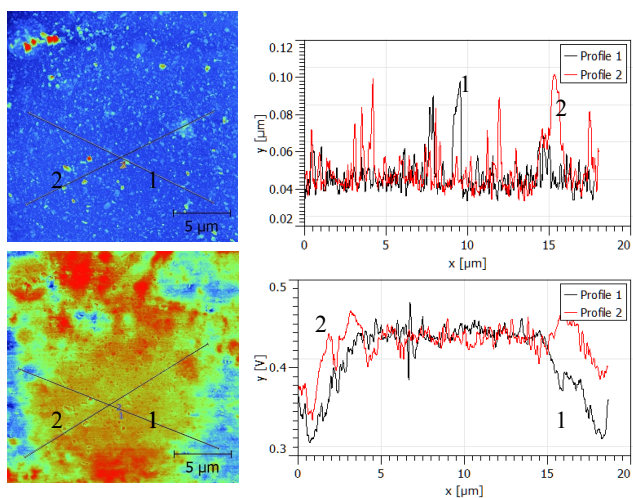


Figure 2. Topography (top row) and surface potential (bottom row) of DPPC/ WS_2 heterostructures on SiO_2 after irradiation by 30 keV electrons from SEM. Graphs in the middle of the top and bottom rows represent profiles of the topography and surface potential along the lines marked on 2D-scans (top left and bottom left).

ness of the surface is rather small and the peaks correspond to the large grained areas, which are present before electron irradiation. On the other hand the effect of the electron beam is clearly modifying the electrostatic status in the scanned area, reducing the surface potential for almost 300 mV with respect to the surrounding non-irradiated area in lipid/graphene samples and increasing it for about 150 mV in lipid/WS₂ samples. Evidently, the injection of the charge in the case of the lipid/WS₂ is very uniform in the scanned area, while the lipid/graphene trace is more diffuse. Two factors may be the reason for such effects - one that graphene is a conductor and WS₂ a semiconductor, therefore the charge stays more localized in the lipid/WS₂ than in the other sample. The other may be that the flakes in the graphene film are arranged differently than in WS₂ (they are larger and thicker) so that the secondary electrons scatter more within the lipid film than in the graphene substrate. The striking feature on lipid/graphene heterostructure is that the induced chemical changes are mostly limited to the reorientation and modifications in lipid tails, consisting of simple hydrocarbon chains, which was confirmed by Raman spectroscopy.

4. CONCLUSION

The electronic properties of lipid/2D-material are modulated by charged lipid bilayer. The high-energy electron beam from SEM, with moderate intensity could be used as a tool for shaping the electric charge path at the interface without significantly affecting the roughness of the surface. At the same time, chemical changes are limited to the reorientation of lipid molecules due to the modifications in their alkane chains.

Acknowledgements

This work is supported by the Ministry of education, science and technological development of the Republic of Serbia under the grant IO 171005. We thank Mr. Vladimir Lazović for the technical help with the use of Scanning Electron Microscope.

REFERENCES

- [1] Ann E. Oliver, Atul N. Parikh, *Biochimica et Biophysica Acta*, 1798, 839-850 (2010)
- [2] Nathaniel S. Green, Michael L. Norton, *Analytica Chimica Acta*, 853, 127-142 (2015)
- [3] Yuqing Wang, Yi Feng, Yangming Chen, Fei Mo, Gang Qian, Dongbo Yu, Yang Wang and Xuebin, Zhang, *Phys.Chem.Chem.Phys*, 17, 2678 (2015)
- [4] R. Panajotović, S. Ptasinska, V. Lyamayev, and K. Prince, *Rad. Appl.*, 1(1), 46-50 (2016)
- [5] R. F. Egerton, P. Li . Malac, *Micron*, 35, 399-409 (2004)

TERAHERTZ RADIATION FROM MULTILAYER GRAPHENE INDUCED BY A FAST ELECTRON

Kamran Akbari¹ and Zoran L. Mišković^{1,2}

¹*Department of Applied Mathematics, University of Waterloo, Waterloo &*

²*Waterloo Institute for Nanotechnology, University of Waterloo, Waterloo, Ontario, Canada N2L 3G1*

Abstract. We discuss a fully retarded electromagnetic theory of the transition radiation from several parallel layers of graphene, induced by a fast electron traversing those layers perpendicularly. We find asymmetry between radiation patterns that are emitted in the direction of moving electron and in the opposite direction. This asymmetry arises from interference effects, which are absent when the electron traverses single layer of graphene.

1. INTRODUCTION

Two-dimensional (2D) materials have recently come into intense focus of research for applications in the area of Nano-photonics [1]. In that context, properties of the so-called Dirac plasmon in doped graphene open a promising route to new developments in the area of Plasmonics in the Terahertz (THz) frequency range [2]. Quite recently, several studies appeared exploring the possibility to use fast electron beams to generate electromagnetic radiation from graphene in a broad range of frequencies [3,4]

Optical properties of nanostructures have been efficiently studied in transmission electron microscopes (TEM) using high energy electron beams (~ 100 keV), which can provide spatially-resolved plasmon excitation patterns in those structures via the technique called electron energy loss spectroscopy (EELS) [5]. In addition, the interaction with fast electrons in a TEM induces radiation from the target material known as cathodoluminescence, which can be measured in a broad range of frequencies via parabolic mirrors [5].

We have recently studied theoretically the effects of retardation in EELS of single-layer graphene [6] and found that a significant fraction of the energy deposited in graphene at the THz range of frequencies is emitted in the form of transition radiation (TR) [7]. In particular, we have shown that presence of the Dirac plasmon polariton (DPP) mode in graphene gives rise to the possibly observable effects in the angular distributions of the emitted TR at the sub-THz range.

We present here our preliminary results on the TR from a multi-layer graphene (MLG) consisting of spatially separated, parallel graphene sheets. While this configuration is of interest for integrating graphene into plasmonic nanostructures [1,2], we assume here that the MLG is placed in vacuum to avoid interferences with other mechanisms of radiation, which may be induced when a fast charged particle traverses different dielectric regions [7]. Choosing an example of electron moving perpendicularly upon MLG at the half of the speed of light c , our results may be found useful in the context of EELS in a TEM configuration [5].

2. THEORETICAL MODEL

We use the Hertz vector, $\mathbf{\Pi}(\mathbf{R}, t)$ [6], where $\mathbf{R} = \{x, y, z\}$ is a point in a three-dimensional Cartesian coordinate system. Performing the Fourier transform (FT) with respect to time, both the magnetic and the electric fields may be obtained from

$$\mathbf{H}(\mathbf{R}, \omega) = -i\frac{\omega}{c}\nabla \times \mathbf{\Pi}(\mathbf{R}, \omega), \quad (1)$$

$$\mathbf{E}(\mathbf{R}, \omega) = \nabla(\nabla \cdot \mathbf{\Pi}(\mathbf{R}, \omega)) + \frac{\omega^2}{c^2}\mathbf{\Pi}(\mathbf{R}, \omega). \quad (2)$$

We assume that an electron with charge e moves along the z axis at constant speed v and traverses N graphene layers that are placed in the planes $z = z_l$ with $l = 1, 2, \dots, N$. Thus, it is convenient to perform a 2D FT with respect to the in-plane coordinates, $\mathbf{r} = \{x, y\} \mapsto \mathbf{k} = \{k_x, k_y\}$, so that the total induced Hertz vector may be written as [6]

$$\mathbf{\Pi}_{ind}(\mathbf{k}, z, \omega) = -\frac{2\pi}{\omega\kappa} \sum_{l=1}^N e^{i\kappa|z-z_l|} \mathbf{j}_l(\mathbf{k}, \omega), \quad (3)$$

where $\kappa(k, \omega) = \frac{\omega}{c} \sqrt{1 - (\frac{ck}{\omega})^2}$ for $|\omega| > ck$ with $k = \sqrt{k_x^2 + k_y^2}$, and $\mathbf{j}_l(\mathbf{k}, \omega)$ is the induced current in the l th graphene layer.

For simplicity, we assume that the dynamic response of the l th graphene layer is described by an in-plane scalar conductivity function, $\sigma_l(k, \omega)$, where the index l indicates that, in general, graphene layers can have different transport properties depending in their respective charge carrier densities n_l , which may be different. Thus, we substitute $\mathbf{j}_l(\mathbf{k}, \omega) = \sigma_l(k, \omega)\mathbf{E}_{\parallel}(\mathbf{k}, z_l, \omega)$ in Eq. (3), where the tangential components of the total electric field in the plane $z = z_l$ may be assumed to only possess the longitudinal component, $\mathbf{E}_{\parallel}(\mathbf{k}, z_l, \omega) = \hat{\mathbf{k}}E_{\parallel}(k, z_l, \omega)$. Using Eq. (3) in Eq. (2) we obtain a system of equations

$$E_{\parallel}(k, z_l, \omega) = -\frac{2\pi\kappa}{\omega} \sum_{l'=1}^N e^{i\kappa|z_l-z_{l'}|} \sigma_{l'}(k, \omega) E_{\parallel}(k, z_{l'}, \omega) - ikA \frac{e}{v} e^{iz_l \frac{\omega}{v}}, \quad (4)$$

whose solution gives a self-consistent set of tangential electric fields $E_{\parallel}(k, z_l, \omega)$ in all graphene layers. The last term in Eq. (4) represents a contribution from the

electric field in the l th layer arising from the incident electron, with an amplitude of the interaction given by $A(k, \omega) = 4\pi / \left(\frac{\omega^2}{v^2} - \frac{\omega^2}{c^2} + k^2 \right)$.

Substituting the solutions of Eq. (4) for all $E_{\parallel}(\mathbf{k}, z_l, \omega)$ into Eq. (3) one can find the induced magnetic and electric fields from Eqs. (1) and (2), respectively. Thus, the total energy emitted from MLG in the form of radiation is given in terms of the flux of the Poynting vector across a closed surface S by

$$W_{\text{rad}} = \frac{c}{(2\pi)^2} \int_0^{\infty} d\omega \Re \oint\!\!\!\oint_S dS \hat{\mathbf{n}} \cdot [\mathbf{E}_{\text{ind}}(\mathbf{R}, \omega) \times \mathbf{H}_{\text{ind}}^*(\mathbf{R}, \omega)], \quad (5)$$

which may be written in two equivalent forms [6], viz.

$$W_{\text{rad}} = \iint d^2\mathbf{k} \int_0^{\infty} d\omega \omega F_{\text{rad}}(\mathbf{k}, \omega) = \iint d^2\hat{\Omega} \int_0^{\infty} d\omega \mathcal{D}(\theta, \omega). \quad (6)$$

The middle term in the above expression defines probability density $F_{\text{rad}}(\mathbf{k}, \omega)$ for the radiative energy loss $\hbar\omega$ of the incident electron with the momentum transfer $\hbar\mathbf{k}$ to the target, whereas the last term defines spectral distribution of radiation $\mathcal{D}(\theta, \omega)$ [7] emitted at frequency ω in a direction having the angle θ with respect to the direction of motion of the incident electron with $d^2\hat{\Omega} = \sin\theta d\theta d\varphi$ being an infinitesimal solid angle.

3.RESULTS AND CONCLUDING REMARKS

For the THz range of frequencies one may use the Drude model for conductivity of a graphene layer doped with the charge carrier density n [2],

$$\sigma_D(\omega) = \frac{i v_B v_F k_F}{\pi \omega + i\gamma} \quad (7)$$

where $v_B = e^2/\hbar \approx c/137$ is the Bohr velocity, $v_F \approx c/300$ is the Fermi speed of graphene, $k_F = \sqrt{\pi|n|}$ is its Fermi wavenumber, and γ is the damping rate. We find it useful to use normalized values of the wavenumber, $\bar{k} = k/k_c$, and frequency, $\bar{\omega} = \omega/\omega_c$, where $k_c = v_B v_F k_F/c^2$ and $\omega_c = ck_c = v_B v_F k_F/c$. For typical doping densities of $|n| \sim 10^{13} \text{ cm}^{-2}$, one has $k_c \sim 1.36 \times 10^{-5} \text{ nm}^{-1}$ and $\hbar\omega_c \sim 2.69 \text{ meV}$ (or $\nu_c = \omega_c/(2\pi) \sim 0.65 \text{ THz}$).

In Fig. 1 we analyze the distribution of radiation emitted from two graphene layers a distance $d = 1/k_c$ apart having equal doping densities and equal damping rates $\gamma = 0.01 \omega_c$, traversed by an electron at the speed $v = c/2$. In the left panel of Fig. 1 we show the normalized probability density $\bar{F}_{\text{rad}} = \pi\omega_c^2 k_c F_{\text{rad}}/(4e^2)$ for $\bar{k} = 1$. One notices an asymmetry in the frequency dependencies of the radiation emitted in the direction of electron motion (downstream, red dotted curve) and in the opposite direction (upstream, blue dashed curve), which add up to give the total radiated density (solid black curve). In the right panel of Fig. 1 we show a polar plot of the normalized spectral distribution, $c\mathcal{D}/e^2$, as a function of the emission angle θ relative to the electron trajectory for various values of the reduced

frequency $\bar{\omega}$. This panel also shows asymmetry in the angular patterns emitted in the upstream (blue curves on the left) and downstream (red curves on the right) directions relative to the electron motion, which may be experimentally detectable.

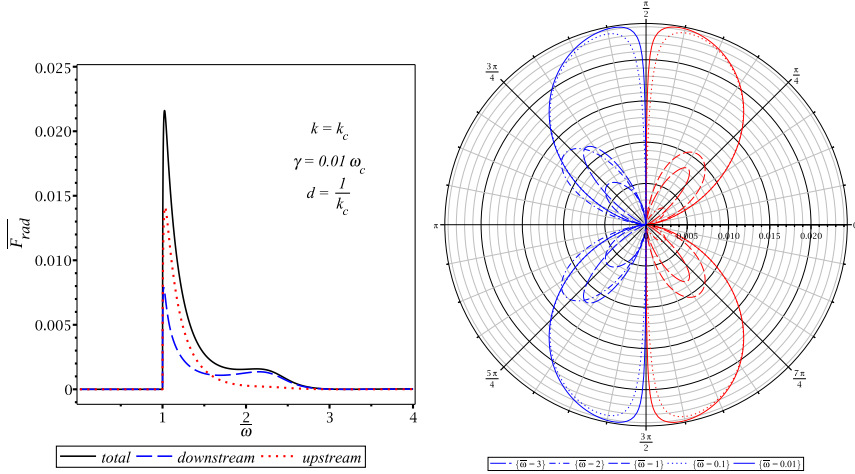


Figure 1. Probability density of the radiative energy loss $F_{\text{rad}}(k, \omega)$ (left panel) and the spectral distribution of radiation $\mathcal{D}(\theta, \omega)$ (right panel) from two graphene layers.

Acknowledgements

This work is supported by NSERC.

REFERENCES

- [1] F. Xia, H. Wang, D. Xiao, M. Dubey, and A. Ramasubramaniam, *Nature Photonics* 8, 899 (2014).
- [2] F.J. García de Abajo, *ACS Photonics* 1, 135 (2014).
- [3] T. Zhan, D. Han, X. Hu, X. Liu, S.-T. Chui and J. Zi, *Phys. Rev. B* 89, 245434 (2014).
- [4] L.J. Wong, I. Kaminer, O Ilic, J.D. Joannopoulos, and M. Soljacic, *Nature Photonics* 10, 46 (2016).
- [5] F.J. García de Abajo, *Rev. Mod. Phys.* 82, 209 (2010).
- [6] Z.L. Miskovic, S. Segui, J.L. Gervasoni and N.R. Arista, submitted (2016).
- [7] V.L. Ginzburg and V.N. Tsytovich, *Transition Radiation and Transition Scattering*, (Adam Hilger, Bristol, 1990).

SPATIAL STRUCTURE OF RUNAWAY ELECTRON PREIONIZED DIFFUSE DISCHARGE AND ITS IMPACT ON A PLANE ANODE

M.V. Erofeev, E.Kh. Baksht, V.S. Ripenko, M.A. Shulepov and V.F. Tarasenko

Institute of High Current Electronics, Akademichesky ave., 2/3, Tomsk, Russia

Abstract. The spatial structure of a diffuse discharge initiated by runaway electrons in nonuniform electric field and the influence of its plasma on the surface of a plane anode have been studied. It is shown that runaway electron preionized diffuse discharge makes it possible to uniform process of the anode surface at atmospheric pressure in contrast to a spark discharge, which results in microcraters formation and thereby surface erosion.

1. INTRODUCTION

Advanced high voltage nanosecond pulse generators can operate both in single pulse and in repetitive pulsed mode at a pulse repetition frequency of up to several kilohertz. Due to them, tangible progress has been reached in recent years in investigation and application of runaway electron preionized diffuse discharges (REP DD) initiated in different gases under atmospheric pressure [1-3]. As the pressure increased, a transformation of the diffuse discharge into spark was observed, whereas for surface plasma processing it is necessary to provide uniform effect on a metal or dielectric surface. Of most importance in this respect are the spatial structure of the discharge and the uniformity of its action on the surface being processed. The aim of this work was to study, using a CCD camera, the discharge structure transition from diffuse to spark discharge and its act on a plane anode surface.

2. EXPERIMENTAL DETAILS

In our experiments, we used a NPG-18/3500N high-voltage generator. The incident voltage had negative polarity, amplitude of ~ 20 kV, and FWHM of 6 ns; the discharge current was up to 200 A. The discharge plasma was formed in nitrogen by applying high voltage pulses to the interelectrode gap which was varied between 2 and 9 mm. Under such conditions, the specific input power reached up to 10 MW/cm^3 . The cathode was pointed and was made of steel. The anode was plane and was the electrode on which copper plates were arranged being covered by carbon with thickness of 7 μm before plasma treatment.

Irradiance of discharge plasma was registered using an HSFC-PRO CCD camera, which was synchronized with the FPG18/3500N generator with a subnanosecond accuracy. After the plane electrode was processed under different conditions, its surface properties were examined with a LOMO MIKMED-1 v.2 optical microscope.

3. RESULTS AND DISCUSSION

Figure 1 presents the waveform of the diffuse discharge current and photos of the discharge which were taken during this pulse using CCD camera. The exposure time of each frame was 3 ns. The beginning of the current pulse was chosen as the starting time and coincided with discharge plasma irradiance. Amplitude of the discharge current was 170 A with pulse width of 10 ns, the electrodes were spaced 6 mm apart. Under the given condition, the discharge has the form of a diffusely glowing cone and hold it along the whole current pulse. The experiments show that the diffuse discharge does not leave any visible traces on the anode surface.

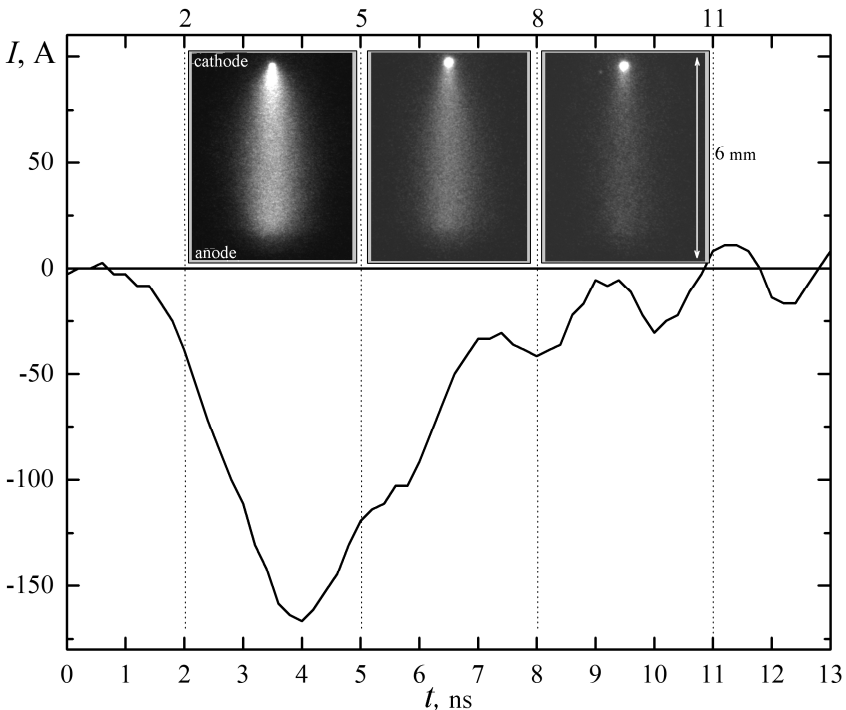


Figure 1. Waveform of the discharge current and photos of the discharge which were taken along the current pulse.

As the interelectrode gap shortens, the diffuse discharge with anode spot, that is an intermediate stage of transition from diffuse to spark discharge, was

realized. Figure 2 shows integral photo of the diffuse discharge with anode spot and its autograph on the anode surface. Diameter of the brightly radiating anode spot was about 0.5 mm, and it corresponds to the dimension of the autograph representing itself a set of microcraters with diameters of 5–40 μm .

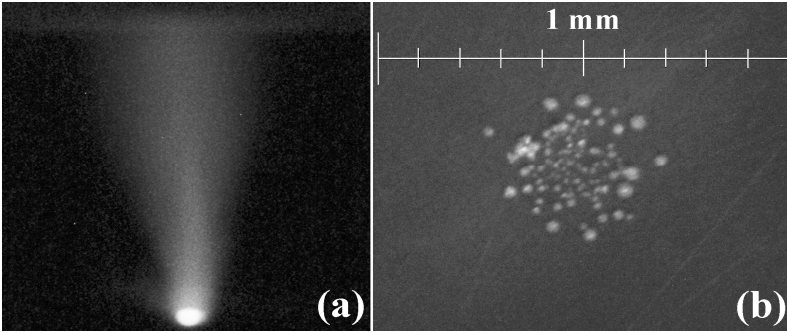


Figure 2. (a) – integral photo of the diffuse discharge with anode spot. (b) – autograph from the anode spot left on the anode surface.

Figure 3 presents the current waveform of the spark discharge, its photos and spark autograph on the anode surface at the 2-mm-wide interelectrode gap. In this case, the discharge current was 230 A.

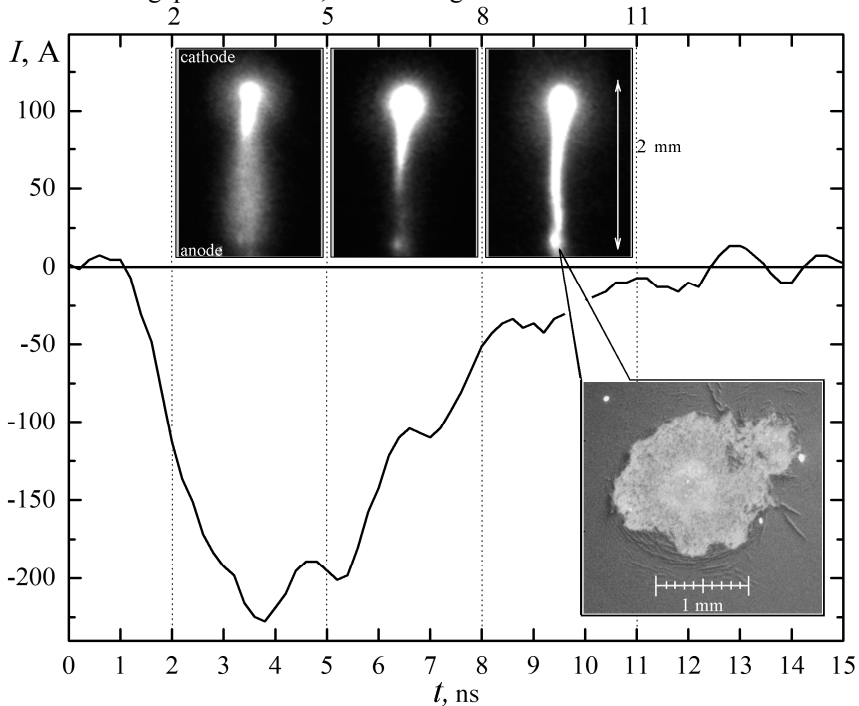


Figure 3. Waveform of the spark discharge current, its photos and spark autograph left on the anode surface.

On the first frame (fig. 3), a bright diffuse discharge with cone-like form is observed, which bridges the gap within the 2–5 ns after breakdown. On the second frame (5–8 ns), it is seen that bright spot has shown up on the anode surface before the spark bridged the interelectrode gap. Within 8–11 ns (the third frame), the spark has bridged the gap. Under the given conditions, the discharge represents two glowing regions: central spark channel with diameter of 0.4 mm and peripheral diffuse shell with diameter of 0.7–1 mm. The spark channel has intense effect on the anode carbon cover and leaves on it solid trace up to 2 mm in diameter. At the same time, deformation in the form of radially dispersing surface waves is observed on the regions adjacent to the borders of carbon cover. This deformation could be result of the shock or sonic wave generated by spark discharge. In some cases, aggregation of microcraters with 20, 40, 80 and 160 μm in diameter appear on the periphery of the solid trace. The total number of the microcraters is more than 100.

4. CONCLUSION

It is established that diffuse channel is the initial stage of the discharge radiation; then anode spot, channel with high glow intensity based on the anode spot and spark channel are consecutively formed. Spark formation finished within 10–15 ns after the onset of the discharge. Microstructure of spark and diffuse channels with anode spot autograph have been detected. The traces of such discharge represents itself an aggregation of up to 100 microcraters with dimeters of 20–160 μm . It was also shown that diffuse discharge does not leave erosive action on an anode surface or on its carbon cover.

Acknowledgements

This work was supported by the Russian Science Foundation under the grant number 14-29-00052.

REFERENCES

- [1] C. Zhang, M. V. Erofeev, Z. Fang, M. A. Shulepov, Z. Zhou, V. F. Tarasenko and T. Shao, *Laser and Particle Beams* 34, 202 (2016).
- [2] V. F. Tarasenko, *Runaway Electrons Preionized Diffuse Discharge*, p. 598, (Nova Science Publishers, New York, 2015).
- [3] M. V. Erofeev, E. Kh. Baksht, V. F. Tarasenko and Yu. V. Shut'ko, *Tech. Phys.* 58, 200 (2013).

INFLUENCE OF LASER IRRADIANCE, AMBIENT GAS PRESSURE AND INTERNAL SHOCKWAVES ON THE HOMOGENEITY OF LASER PRODUCED PLASMA

Dragan Pantić², Miloš Burger^{1*}, Zoran Nikolić¹, Vladimir Milosavljević¹,
Goran Poparić¹ and Stevan Djenize¹

¹*University of Belgrade, Faculty of Physics, POB 44, Belgrade, Serbia*

²*Directorate of measures and precious metals, Belgrade, Serbia*

**Corresponding author. Email: milosb@ff.bg.ac.rs*

Abstract. Impacts of varying the intensity of Nd:YAG nanosecond infrared 1064 nm laser radiation and background gas pressure on morphology and internal structure of plasma plume were objectives of the present study. We employ methods of fast imaging spectroscopy of laser generated copper plasma applying irradiance in the order of 10^9 W cm^{-2} under moderate pressure helium atmosphere. Behavior of both ionized and neutral species was observed up to 1 μs after the laser pulse. With an increase of laser irradiance and background gas pressure, notable differences in plasma propagation mechanisms are observed and mainly attributed to internal shockwave dynamics within the plasma plume.

1. INTRODUCTION

Laser-induced plasma (LIP) emits continuous, ionic, atomic and eventually molecular spectra depending on the elements involved. Theoretical and experimental efforts in studying LIP have a constantly rising trend due to broad range of applications ie. laser-induced breakdown spectroscopy (LIBS) [1], extreme ultraviolet (EUV) lithography [2], nanoparticle production [3] or pulsed laser deposition (PLD) [4]. In order to optimize experimental parameters in formerly mentioned applications, morphology investigation is an essential step. Standard experimental techniques capable of observing an early stage dynamics of both plasma plume and shockwave are time-resolved shadowgraphy [3] and Schlieren photography [5]. However, these techniques cannot provide information about radially-resolved distributions of the elements within the plasma. Time-resolved spectroscopic imaging is therefore applicable for studying hydrodynamic expansion of laser induced plasma as well as its radiative characteristics [6]. This technique allows one to determine spatial separation between different excited states and elements in the plasma applying band-pass optical filters [7,8]. Here, we study effects of varying nanosecond (IR) laser intensities and background gas pressure on species distributions within the copper-helium plasma for irradiance below and above strong shielding threshold value of about 2 GW cm^{-2} reported in our previous paper [9].

2. EXPERIMENTAL

All measurements were conducted with fundamental harmonic of Nd:YAG laser (EKSPLA, model NL 311), delivering pulses of 6 ns at 1064 nm wavelength. The laser beam was focused onto high purity copper (99.9%) sample surface using a plano-convex lens of 100 mm focal length. The sample surface position was kept in front of the lens focal distance and remained fixed during measurements (spot size of 570 μm). The laser pulse energies measurements were performed using a power-meter (Coherent, model Field-Max II TOP), coupled with pyroelectric sensor. Two laser pulse energies were applied in this study: 15 mJ (1.0 GW cm^{-2}) and 45 mJ (3.0 GW cm^{-2}). In order to perform experiments in a controlled environment, the samples were placed inside of the closed vacuum chamber, mounted on an automated x - y - z translation stage. The remaining air was evacuated by means of mechanical pump and the chamber was filled with helium. For detection of the plasma spectral emission, the plume was imaged side-on onto an ICCD camera (Andor, model iStar DH740), cooled down to -20°C . Spectroscopic images of different emitting species were obtained using the narrow-band optical filters placed in front of an ICCD. The spectral lines selected for representing emission of the neutral species were Cu I 521.82 nm and He I 587.56 nm. Behavior of ions is monitored by observing Cu II 490.97 nm line emission. Central wavelengths of the narrow band filters were 520 nm, 490 nm and 589 nm for Cu I, Cu II and He I, respectively. The continuum emission contribution to the former lines intensities was estimated by measuring emission from neighboring spectral regions using narrow-band filters with central wavelengths at 483 nm and 550 nm. These contributions were subtracted from spectral line images as well as correcting on transmission curves of the filters for each image. All recordings were captured using 1 ns ICCD gate width. An image is the result of averaging 30 recordings with continuous sample movement (1 shot – 1 place).

3. RESULTS AND DISCUSSION

The emission images of copper neutral, ionic and helium neutral species obtained using two different irradiance values under 200 Torr of helium pressure are shown on Fig. 1. For the sake of clarity, corresponding intensities were normalized to its maximal value. These images reveal highly transient character of the plasma during the first microsecond after the laser pulse, especially at 3.0 GW cm^{-2} (Fig. 1. (b)). By looking at the spectral emission of neutral copper species at later delay times, one can observe change in propagation direction of the most intense (interior) region of the vapor plume along the axial expansion of the plasma. We define interior emission as a part of vapor plume having intensity above 90% of the maximum emission intensity. At 1.0 GW cm^{-2} the change occurs at 500 ns, while it appears about 50 ns earlier at 3.0 GW cm^{-2} . The change in propagation direction may be explained by formation of the internal shockwave (IS) in the vapor plume during its supersonic expansion. IS is formed to balance the velocity and high back-pressure generated by the external shockwave [10,11]. Therefore IS propagates in both forward and backward directions within the vapor plume, between contact surface (between the vapor plume and the compressed background gas) and sample surface [12].

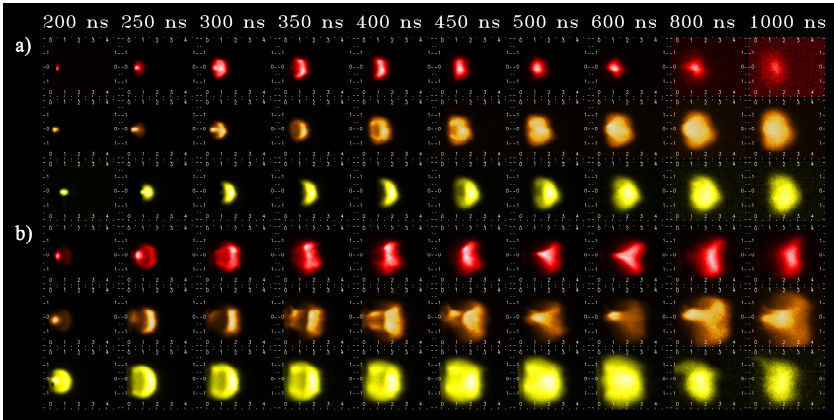


Figure 1. Spatial distributions of emitting species within the plasma plume generated using ns-laser irradiance of (a) 1.0 GW cm^{-2} and (b) 3.0 GW cm^{-2} . Red and orange colors indicate Cu II and Cu I emission, respectively; while yellow represents He I emission. The scale is millimetric.

Fig. 2. presents dynamics of intense emission regions (interior) and front positions of copper species (Cu I and Cu II). At 1.0 GW cm^{-2} , an abrupt expansion of intense emission regions of copper ions and neutrals ends at an approximate delay of 350 ns. After the first 350 ns the strong slowdown of both Cu ions and neutrals is evident, lasting to about 450 and 500 ns respectively. The notable loss of kinetic energy is due to internal shockwave, acting on the species within the expanding plume. Actually, the bulk of ions and neutrals tend to move in opposite direction preventing the background gas from filling up the region initially occupied by the copper species. This behavior seems to be strongly entangled with plasma plume deceleration. After 600 ns delay, species within the plasma plume predominantly returned to their initial propagation direction and velocities of each species corresponded to that of the overall plume expansion. At 3.0 GW cm^{-2} irradiance, after initial acceleration and subsequent deceleration, the neutrals revert sooner (450 ns) compared to 1.0 GW cm^{-2} irradiance case. In contrast, the ions manage to fairly resist to the shockwave influences staying just to a smaller extent in the middle of region dominated by neutrals. The reason for this behavior may be attributed to confluent effect of IS and strong vortex forces tending to push away the copper particles. As being a lighter species, ions are more subjective to these forces. In addition, the intense emission regions of Cu I and Cu II tend to form a conical shape (see Fig. 1. (b)). This shape is dictated by the presence of intense vortex region [12]. The vortex region is induced in the vicinity of sample by the high velocity gradients between sample surface and plume. This region tends to get larger as the first internal shockwave reaches the sample surface. During the subsequent interaction between the internal shockwave and sample, the large vortex region affects primarily the peripheral part of IS, therefore forming the conical shape of intense emission region. At 3.0 GW cm^{-2} irradiance, this characteristic behavior is more pronounced and occurs about 100 ns earlier. The former is attributed to significantly larger kinetic energy introduced by more intense pulse.

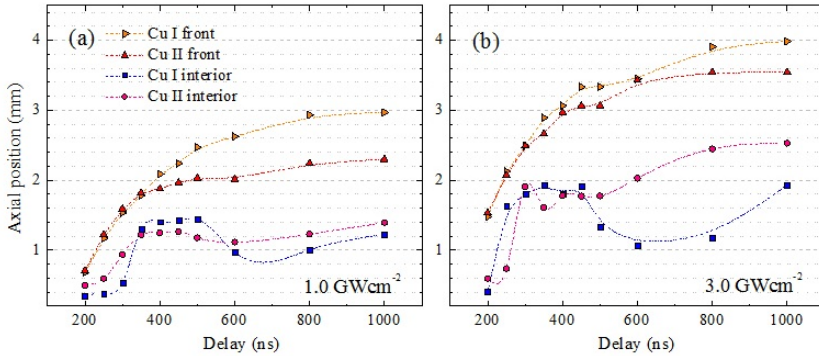


Figure 2. Dynamics of intense emission regions (interior) and front positions of copper species (Cu I and Cu II) for performed ablations at: 1.0 GW cm⁻² and (b) 3.0 GW cm⁻². An ordinate axis presents a distance from the sample surface.

Consequently, the vortex forces are more intense, affecting only the shape of ablated (copper) species and changing their propagation from concave through conical to convex. Similar observation was reported by Wen et al. [12] for copper plasma expansion into 1 atm of helium for laser irradiance of about 3.5 GW cm⁻², where conical shape is formed at 100 ns. This indicates that a strong pressure dependence should also be expected. In order to confirm these assumptions, the background pressure was increased to 400 Torr. Since the shear stress in the boundary layer is proportional to the relative velocity between the vapor plume and the stationary sample, faster expansion (due to the higher irradiance applied) generates greater shear and a stronger vortex ring [12]. Recorded images correspond to higher laser irradiance of 3.0 GW cm⁻² (Fig 3.), showing that for 400 Torr of applied pressure conical shape of copper ionic species start to form approximately at 400 ns (100 ns earlier than under 200 Torr).

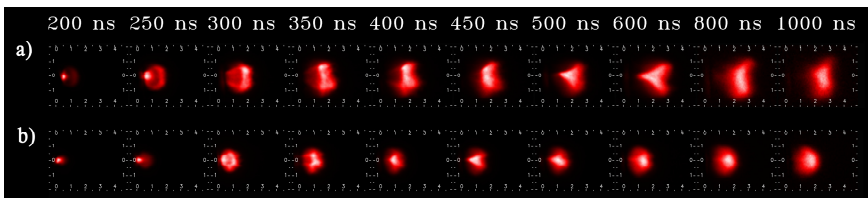


Figure 3. Spatial distributions of copper ionic species within the plasma plume at (a) 200 Torr and (b) 400 Torr of helium pressure. The scale is millimetric.

4. CONCLUSION

The fact that the bulk of neutral species experience change in direction of propagation under IS influence is already known from the literature. For the first time we report IS influence on ions. Depending on applied laser irradiance, ions may exhibit different

behavior compared to neutral species and react to IS more instantly. Furthermore, IS propagation within the plasma plume may significantly contribute to its deceleration. This should be of interest to researchers dealing with laser-material interaction modeling, as the hydrodynamic treatment proves inevitable in accompanying standard collision-radiative approach. On the other hand, LIBS diagnostics should (if possible) include imaging spectroscopy and morphological studies prior to extraction of plasmas thermodynamic parameters. Even the relatively small change in laser irradiance may distort homogeneity of plasma species, which should be additionally verified from the analysis of radially resolved emission profiles.

Acknowledgements

This research has been supported by the Ministry of education, science and technological development of the Republic of Serbia (project ON171008).

REFERENCES

- [1] R. Noll, *Laser-induced breakdown spectroscopy fundamentals and applications* (Springer-Verlag, Berlin, Heidelberg, 2012).
- [2] J. R. Freeman, S. S. Harilal, and A. Hassanein, "Enhancements of extreme ultraviolet emission using prepulsed Sn laser-produced plasmas for advanced lithography applications", *J. Appl. Phys.* 110(8), 083303 (2011).
- [3] S.-B. Wen, X. Mao, R. Greif, and R. E. Russo, "Experimental and theoretical studies of particle generation after laser ablation of copper with a background gas at atmospheric pressure", *J. Appl. Phys.* 101(12), 123105 (2007).
- [4] R. K. Singh and J. Narayan, "Pulsed-laser evaporation technique for deposition of thin films: Physics and theoretical model", *Phys. Rev. B* 41(13), 8843–8859 (1990).
- [5] M. Lackner, S. Charareh, F. Winter, K. F. Iskra, D. Rüdissler, T. Neger, H. Kopecek, and E. Wintner, "Investigation of the early stages in laser-induced ignition by Schlieren photography and laser-induced fluorescence spectroscopy", *Opt. Express* 12(19), 4546-4557 (2004).
- [6] D. B. Geohegan, "Fast intensified-CCD photography of YBa₂Cu₃O_{7-x} laser ablation in vacuum and ambient oxygen", *Appl. Phys. Lett.* 60(22), 2732-2734 (1992).
- [7] F. Garrelie, J. Aubreton, and A. Catherinot, "Monte Carlo simulation of the laser-induced plasma plume expansion under vacuum: Comparison with experiments", *J. Appl. Phys.* 83(10), 5075-5082 (1998).
- [8] V. Motto-Ros, Q. L. Ma, S. Grogire, W. Q. Lei, X. C. Wang, F. Pelascini, F. Surma, V. Detalle, and J. Yu, "Dual-wavelength differential spectroscopic imaging for diagnostics of laser-induced plasma", *Spectrochim. Acta B* 74-75, 11 - 17 (2012).
- [9] M. Burger, D. Pantić, Z. Nikolić, and S. Djeniže, "Shielding effects in the laser-generated copper plasma under reduced pressures of He atmosphere", *J. Quant. Spectrosc. Radiat. Transf.* 170, 19-27 (2016).

- [10] S.-B. Wen, X. Mao, R. Greif, and R. E. Russo, "Expansion of the laser ablation vapor plume into a background gas. I. Analysis", *J. Appl. Phys.* 101(2), 023114 (2007).
- [11] N. Arnold, J. Gruber and J. Heitz, "Spherical expansion of the vapor plume into ambient gas: an analytical model", *Appl. Phys. A* 69(1), S87–S93 (1999).
- [12] S.-B. Wen, X. Mao, R. Greif, and R. E. Russo, "Laser ablation induced vapor plume expansion into a background gas. II. Experimental analysis", *J. Appl. Phys.* 101(2), 023115 (2007).

Section 3.

LOW TEMPERATURE PLASMAS

OPTICAL DIAGNOSTICS IN HIGH ENTHALPY PLASMAS

Pascal Boubert¹

¹*CORIA, Université de Rouen, 76800 Saint-Etienne-du-Rouvray, France*

Collisional radiative models achieve more and more accurate and successful descriptions of physics and chemistry in non-equilibrium plasmas. The validation of those models remain nevertheless a relevant issue and a challenge for experimentalists. Moreover, the coupling of radiation and chemistry with aerodynamics has sometimes to be addressed. Local parameters are then to be measured within plasma flows in order to ensure a whole understanding of energy exchanges. Static pressures, flow velocities, densities and temperatures (when they are suitable) are the key parameters which have to be measured. Probes showed they could be used in some thermodynamic conditions but with a limited spatial accuracy and a disturbance of the medium. Optical diagnostic techniques, especially laser techniques, have been widely used in application at moderate temperatures and atmospheric pressure such as combustion. In low pressure, high enthalpy plasmas some issues has to be considered and fixed but those techniques help to bring data non reachable by probes, with an excellent space and, sometimes, time accuracy and without any perturbations.

The example of plasmas generated to reproduce the interaction of heat shield with an atmosphere during a space probe entry illustrates the case of subsonic and hypersonic flows, equilibrium and non-equilibrium plasmas, and homogeneous and heterogeneous chemically reactive media. Spontaneous Raman Scattering (SRS) and Laser Induced Fluorescence (LIF) and their respective variations will be described with results about velocity, density and temperature measurements. Simultaneous investigations will be discussed as well as the use of techniques developed in other conditions than high enthalpy plasmas (Krypton Tagging Velocimetry, Femtosecond laser electronic excitation tagging, Vibrationally excited NO monitoring). The modelling of laser experiments, including radiative and collisional processes, especially thanks to spectroscopic databases, allows to increase the accuracy of measurements and to take into account non-linear phenomena such as stimulated Raman scattering, saturations and amplified spontaneous emission. Some prospects can be found in those complex behaviors.

PLASMA-LIQUID INTERACTION

Peter J. Bruggeman

*University of Minnesota, Department of Mechanical Engineering,
111 Church Street SE, Minneapolis, MN 55455 USA*

Plasma-liquid interactions represent a growing interdisciplinary area of research involving plasma science that is of growing importance for many new applications. This presentation will provide an overview of the state-of-the-art of this multidisciplinary area and identify several key research challenges [1]. These challenges will be illustrated specifically for non-equilibrium plasmas used for biomedical applications and synthesis of nanoparticles. The review will focus on the plasma kinetics in the gas phase, the transfer of reactivity from the gas to the liquid phase and the liquid phase chemistry responsible for the biological effects and material interactions.

Acknowledgements: This work is partially supported by the "Plasma Science Center on Control of Plasma Kinetics" of the United States Department of Energy, Office of Fusion Energy Science (DE-SC0001319), a Department of Energy Early Career Research Award (DE-SC0016053) and the National Science Foundation (PHY 1500135).

REFERENCES

- [1] P.J. Bruggeman, M.J. Kushner, B.R. Locke et al, Plasma-liquid interaction: a review and roadmap, *Plasma Sources Sci. Technol.* (accepted)

PLASMA PROCESSES FOR LIFE SCIENCES

Pietro Favia

Department of Chemistry, University of Bari 70126 Bari, Italy

PLASMA SCIENCE TOWARDS NEXT- GENERATION HEALTHCARE INNOVATIONS

Masaru Hori

*Department of Electric Engineering and Computer Science,
Plasma Nanotechnology Research Center (PLANT), Nagoya University, Japan*

INFLUENCE OF NEGATIVE IONS ON THE DYNAMICS OF ELECTRIC GAS DISCHARGES

J. Meichsner, S. Nemschokmichal, R. Tschiersch and T. Wegner

*University of Greifswald, Institute of Physics, Felix-Hausdorff-Str. 6,
17489 Greifswald, Germany*

Radio frequency oxygen discharge (CCP, ICP) as a model system for electronegative plasmas was investigated. The presence of negative ions is discussed regarding the discharge operation modes, electron heating and plasma stability, respectively. Line integrated electron and negative ion densities were measured by 160 GHz Gaussian beam microwave interferometry combined with laser photodetachment, [1]. Phase resolved optical emission spectroscopy and probe measurements provide information about the electron heating mechanisms and spatio-temporal behavior of the plasma density. The oxygen CCP reveals attachment-induced ionisation instability depending on pressure and RF power, [2]. Additionally, the formation of negative secondary ions on the powered electrode of an asymmetric CCP was evaluated by ion mass spectrometry. In oxygen ICP a decreasing electronegativity was observed during E–H mode transition. Furthermore, a diffuse helium barrier discharge near atmospheric pressure with small oxygen admixture was evaluated regarding the influence of negative ions on the breakdown behavior, [3]. In particular, the laser photodetachment experiments show a change in breakdown voltage and discharge current when firing the laser during the pre-phase of the discharge, only. The comparison with simulation implies that an additional formation of negative secondary ions on the negatively charged dielectric might be responsible for the large electronegativity in the discharge pre-phase.

Acknowledgements: This work was supported by the DFG via Collaborative Research Centre “Fundamentals of Complex Plasmas” TRR24.

REFERENCES

- [1] K. Dittmann, C. Küllig, and J. Meichsner, *Plasma. Phys. Control. Fusion* 54, 124038 (2012)
- [2] C. Küllig, Th. Wegner, and J. Meichsner, *Phys. Plasmas* 22, 043515 (2015)
- [3] R. Tschiersch, S. Nemschokmichal, and J. Meichsner, *Plasma Sources Sci. Technol.* 25, 025004 (2016).

LINES SHAPES IN TURBULENT PLASMAS

R. Stamm, I. Hannachi, M. Meireni, C. Logeais, H. Capes, L. Godbert-Mouret,
M. Koubiti, J. Rosato and Y. Marandet

*Laboratoire PIIM, UMR 7345 Aix-Marseille Université / CNRS,
Centre de Saint-Jérôme, F-13397 Marseille Cedex 20, France*

In a quiet plasma near to equilibrium, many plasma processes are strictly reproducible. Such a regular behavior is however not always the rule, and it is often possible to observe random fluctuations and oscillations in an unstable plasma. Plasma turbulence is a state of the plasma where instabilities have permitted a significant development of fluctuations and oscillations. Many different instabilities exist in a plasma, each one leading to a specific turbulent process and requiring a particular approach. In this work we will review only turbulent plasmas which may be investigated by observing the line shapes emitted by atoms and ions in the plasma. If line broadening is dominated by Doppler effect, the line shape reflects the velocity distribution of the emitters along the line of sight. In a plasma at equilibrium, it is then possible to obtain the temperature of the emitters. If non thermal movements take place on the line of sight, the line shape no longer corresponds to a maxwellian velocity distribution at the emitter temperature. The study of line shapes may then provide valuable information on the nature of turbulence, and this has been used in astrophysical and laboratory plasmas. In denser plasmas, the broadening of line shapes is often dominated by Stark effect. Turbulent fluctuations on the line of sight can modify the measured Stark profile, which can be expressed in function of statistical properties of the fluctuating plasma parameters. Another cause of Stark profile changes is the presence of turbulent waves in the plasma. Such waves can also modify different part of the line shape. We will present a line shape model suited to the case of nonlinear wave collapse, a phenomenon appearing in plasmas submitted to an external source of energy, such as a beam of charged particles. The nonlinear coupling of Langmuir, ion sound and electromagnetic waves changes the structural and radiative properties of the plasma. Wave packets concentrate in regions of low densities, and evolve to shorter scales and higher intensities. We have proposed a line shape model for calculating the effect of wave packet collapse on a hydrogen emitter.

Acknowledgements: This work is supported in part by the funding agency Campus France (Pavle Savic PHC project 36237PE).

REFERENCES

- [1] P. A. Robinson, Rev. Mod. Phys. **69**, 507(1997).

BARRIER DISCHARGES IN CO₂ CONTAINING GASES AT ATMOSPHERIC PRESSURE

Ronny Brandenburg, Milko Schiorlin, Rouven Klink and Abdollah Sarani

*Leibniz Institute for Plasma Science and Technology (INP Greifswald),
Felix-Hausdorff-Str. 2, D-17489 Greifswald, Germany*

Plasma assisted carbon capture utilization (PA-CCU) by using of excess energy from renewable sources is an approach to reduce carbon dioxide (CO₂) emission and conserve electrical energy as chemicals [1]. This contribution will report about the effect of the admixture of nitrogen to CO₂ on the chemistry as well as the discharge physics in Dielectric Barrier Discharges (DBDs). The effect of admixture on the conversion into carbon monoxide (CO) was systematically investigated in a coplanar DBD at atmospheric pressure and the energetic yield of CO generation resulted in values up to 60 g/kWh. The highest energy yield was achieved in a gas mixture CO₂:N₂=30/70 [2].

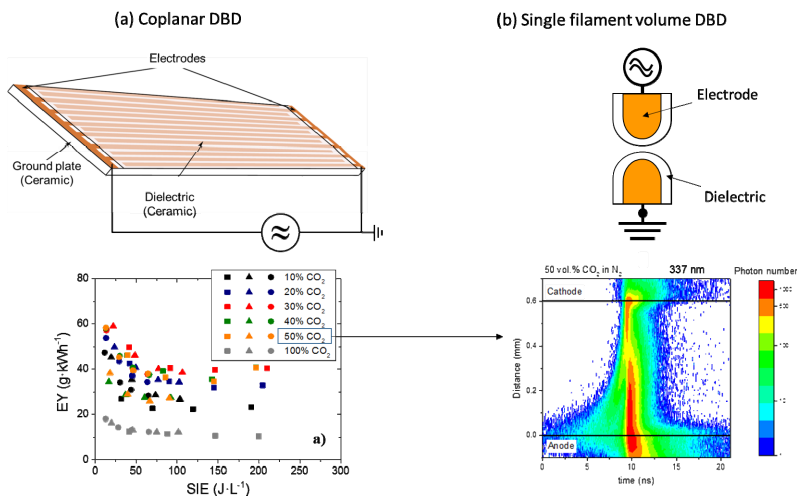


Figure 1. Scheme of the discharge arrangements (top): (a) coplanar DBD and (b) single filament DBD. Bottom left: Energy yield EY of CO generation in coplanar DBD. Bottom right: Spatio-temporal distribution of filament luminosity for 50 % CO₂ in N₂.

The spatio-temporal resolved development of single filaments in different CO₂:N₂ gas mixtures and the corresponding discharge current pulses were investigated in a single filament volume DBD arrangement. The discharge development proceeds in a similar way as in O₂:N₂ gas mixtures [3], i.e. a Townsend pre-phase, a cathode directed ionization wave, anode glow and decay phase. The results show an optimized energy input into single filaments for gas compositions with 10 to 30 % CO₂ and a significant quenching of the luminosity by CO₂ molecules.

Acknowledgements: The authors would like to thank Wolfgang Reich and Michael Schmidt for technical help and Klaus-Dieter Weltmann for support and helpful discussions. The research leading to these results has received funding from the European Union Seventh Framework Programme (FP7/2007-2013) under grant agreement n°316216.

REFERENCES

- [1] F. Brehmer, S. Welzel, M.C.M. van de Sanden, R. Engeln, *J. Appl. Phys.* 116, 123303 (2014).
- [2] M. Schiorlin, R. Klink, R. Brandenburg, *Eur. J. Phys. Appl. Phys.*, in print (2016).
- [3] K. V. Kozlov, R. Brandenburg, H.-E. Wagner, A.M. Morozov, P. Michel, *J. Phys. D: Appl. Phys.* 38, 4, 518-529 (2005).

HIGH RESOLUTION ABSORPTION SPECTROSCOPY OF TRANSIENT SPECIES IN THE VUV RANGE

N. de Oliveira¹, D. Joyeux¹, K. Ito¹, B. Gans², J.C. Loison³, K. Hickson³ and
L. Nahon¹

¹*Synchrotron Soleil, Orme des Merisiers St Aubin BP 48,
91192 Gif sur Yvette Cedex, France*

²*Institut des Sciences Moléculaires d'Orsay, Rue Henri Becquerel,
91405 Orsay Cedex, France*

³*Institut des Sciences Moléculaires, Université de Bordeaux,
33405 Talence Cedex, France*

Radical compounds are of particular importance as key highly reactive intermediate species in chemical reactions, including combustion processes, and are found in abundance in low density natural environments such as interstellar medium, or planetary and exoplanetary atmosphere. Reliable values of electronic transition probabilities, excited states lifetimes, line positions are necessary to feed the models and/or to determine abundances and column densities. However, reactive transient species such as radicals are known to be difficult to produce in column density suitable for detection in absorption, this is partly the reason why experimental data for the electronic states of radicals is quite limited especially in the VUV range.

An experimental branch dedicated to high resolution absorption spectroscopy has been developed over the past years on the DESIRS synchrotron beamline (Nahon et al., 2012). This permanent facility is based upon a unique Fourier transform spectrometer (FTS) designed to cover the UV-VUV (300 – 40 nm) spectral range with an ultimate resolving power in the range of 10^6 and absolute line position accuracy of 1.5×10^{-7} (de Oliveira et al., 2011). Besides, a large number of dedicated sample environments have been developed including windowless gas cells that can be cooled down or heated up, a free molecular beam and various windowed cells (de Oliveira et al., 2016). Recently, a windowed DC discharge set-up has been built for the production and study of transient species in absorption, allowing us to obtain VUV absorption spectroscopic data so far on OH, CH₃, SO₂ and SH radicals. A broad overview of the FTS branch will be

shown in this presentation with a focus on experimental data obtained with the newly developed discharge cell for the study of transient species.

REFERENCES

- [1] Nahon, L., De Oliveira, N., Garcia, G. A., Gil, J. F., Pilette, B., Marcouillé, O., Lagarde, B., & Polack, F. (2012). *J. Synchrotron Radiat.* **19**, 508–520.
- [2] De Oliveira, N., Roudjane, M., Joyeux, D., Phalippou, D., Rodier, J.-C., & Nahon, L. (2011). *Nat. Photonics.* **5**, 149–153.
- [3] N. de Oliveira, D. Joyeux, M. Roudjane, J.-F. Gil, B. Pilette, L. Archer, K. Ito & L. Nahon (2016), *J. Synchrotron Radiat.*, **23**, doi:10.1107/S1600577516006135.

APPLICATION OF PLASMA FOR DEVELOPMENT OF INNOVATIVE FUNCTIONAL TEXTILES

Marija Gorjanc

*University of Ljubljana, Faculty of Natural Sciences and Engineering,
Aškerčeva 12, SI-1000 Ljubljana*

Functional textiles are higher performance products which have been engineered to meet the specific requirements for the end-use and have special properties, i.e. anti-UV radiation, antibacterial, super-hydrophobic, super-oleophobic, therapeutic and healing, sensing and smart. The innovative functional properties of textiles cannot be engineered only by the means of conventional wet-chemical procedures, but by using plasma technology as well [1-3]. This work will review the synergistic effect of plasma technology and chemical active components, such as nanoparticles, phase change materials and sol-gel for development of innovative functional textiles.

Acknowledgements: This work was financially supported by ARRS, grant number P2-0213.

REFERENCES

- [1] M. Gorjanc, K. Jazbec, M. Mozetič, M Kert. UV Protective Properties of Cotton Fabric Treated with Plasma, UV Absorber and Reactive Dye. *Fibers and Polymers*, 2014, vol.15, no.10, 2095-2104.
- [2] J. Vasiljević, M. Gorjanc, B. Tomšič et al. The surface modification of cellulose fibres to create super-hydrophobic, oleophobic and self-cleaning properties, *Cellulose*, 2013, vol. 20, no. 1, 277-289.
- [3] K. Jazbec, M. Šala, M. Mozetič, A. Vesel, M. Gorjanc. Functionalization of cellulose fibres with oxygen plasma and ZnO nanoparticles for achieving UV protective properties. *Journal of nanomaterials*, 2015, vol. 2015, article ID 346739.

Synthesis of quantum dots by atmospheric pressure plasmas and their integration in photovoltaic devices

M. Macias-Montero, T. Velusamy, D. Mariotti

Nanotechnology & Integrated Bio-Engineering Centre (NIBEC), University of Ulster, BT37 0QB,
UK. E-mail: m.macias-montero@ulster.ac.uk

Section 3. Low Temperature Plasmas

Non-thermal atmospheric pressure plasmas (APPs) have attracted great interest due to the potential cost reductions in manufacturing and processing of materials for a wide range of applications [1]. Although APPs present several challenges, considerable progress has been achieved in recent years with an increasing number of industrial and commercial applications utilizing different forms of APPs. One of the most attractive applications of APPs is the synthesis and processing of nanomaterials with specific focus on materials for energy applications.

In this contribution, we will present recent advances in the synthesis of quantum confined nanoparticles [2,3]. In particular, the focus will be on the synthesis of silicon quantum dots (QDs) and CuO QDs. Silicon at the nanoscale offers a range of interesting features that have motivated intense research for a wide range of applications. Contrary to bulk semiconductors, varying the size of the QDs allows controlling the electron confinement, which affects the bandgap as well as the full band energy diagram. We will discuss a range of synthesis conditions using APP that enable the production of crystalline Si QDs. The analysis includes theoretical models that highlight key mechanisms of nanoparticle heating [4]. Additionally, the use of advanced diagnostics has permitted us to experimentally characterise the energy band diagram of APP produced Si QDs [5]. On the other hand, the intrinsic flexibility of APP allows their combination with liquid media. A method based on the use of a hybrid plasma-liquid cell has enabled the direct synthesis of CuO QDs. CuO is a versatile p-type material for energy applications capable of imparting diverse functionalities. The possibility of manipulating the CuO bandgap, through quantum confinement is an exciting opportunity as it makes CuO an attractive material for a wide range of applications. APP synthesis yields high quality and high purity ultra-small CuO QDs with strong quantum confinement properties.

Finally, the applicability of APPs in different aspect of photovoltaic device fabrication will be discussed, presenting opportunities and challenges for large scale nanomanufacturing. The implementation of APP synthesized materials in fully-inorganic photovoltaic devices will be presented, including the use of the above mentioned Si QDs and CuO QDs as active components in these devices.

[1] D. Mariotti *et al.* *J. Phys. D Appl. Phys.* 43, 323001 (2010).

[2] D. Mariotti *et al.* *Nanoscale* 5, 1385, (2013).

[3] S. Askari *et al.* *J. of Phys. D: Appl. Phys.* 48 314002 (2015).

[4] S. Askari *et al.* *Appl. Phys. Lett.* 104, 163103 (2014).

[5] M. Macias-Montero *et al.* *Nanoscale* 8, 6623 (2016).

GAS HEATING MECHANISMS IN N₂-O₂ PLASMAS

C. D. Pintassilgo^{1,2}, V. Guerra¹

¹*Instituto de Plasmas e Fusão Nuclear, Instituto Superior Técnico,
Universidade de Lisboa, 1049-001 Lisboa, Portugal*

²*Departamento de Engenharia Física, Faculdade de Engenharia,
Universidade do Porto, 4200-465 Porto, Portugal*

In spite of the intensive research work carried out over the past decades in pure N₂ and in N₂-O₂ plasma discharges, the theoretical study of the mechanisms of energy transfer to gas heating in these gases, with the exception of air-like mixtures (N₂-20%O₂), has not received too much attention. We present in this work a detailed description of these mechanisms in pure N₂ and N₂-O₂ for fractional concentrations of oxygen molecules [O₂]/N_g (where N_g is the total gas number density) up to 80%.

The present study is based on the coupled solutions to the gas thermal balance equation and a system of rate balance equations for the most important neutral and ionic heavy-species produced in these plasmas, including vibrational kinetics. A complete set of gas heating mechanisms is taken into account, together with gas cooling by heat conduction to the wall. The simulations provide the temporal evolution of the energy transferred to the translational mode (gas heating) from electron impact collisions, vibrational excitation, exothermic chemical reactions, deactivation of electronically excited species at the wall, and the recombination of atoms on the wall.

The fundamental aspects concerning energy transfer to the translational mode are identified for both N₂ and N₂-O₂ situations, namely (i) fast gas heating; (ii) gas cooling as a consequence of vibrational-vibrational energy exchanges; (iii) efficient gas heating through vibrational-translational relaxation and (iv) plasma-wall interaction.

Acknowledgements: This work was partially supported by the Portuguese FCT-Fundação para a Ciência e a Tecnologia, under Project UID/FIS/50010/2013.

REALISTIC SURFACE COEFFICIENTS FOR SECONDARY ELECTRON EMISSION AND ELECTRON REFLECTION IN PIC/MCC SIMULATIONS OF CAPACITIVE RF PLASMAS

J. Schulze^{1,2}, M. Daksha^{1,2}, B. Berger^{1,2}, A. Derzsi³, I. Korolov³, Z. Donko³

¹*Department of Physics, West Virginia University, USA*

²*Institute for Electrical Engineering, Ruhr-University Bochum, Germany*

³*Institute for Solid State Physics and Optics, Wigner Research Centre for
Physics, Hungarian Academy of Sciences, Hungary*

In most PIC/MCC simulations of radio frequency capacitively coupled plasmas (CCPs) several simplifications are commonly made: (i) fast neutrals are not traced, (ii) heavy particle induced excitation and ionization are neglected, (iii) secondary electron emission from boundary surfaces due to neutral particle impact is not taken into account, (iv) the secondary electron emission coefficient is guessed and assumed to be constant, i.e. independent of the incident particle energy and the surface conditions, and (v) the electrodes are assumed to perfectly absorb electrons. Here, we examine the validity of these simplifications under conditions typical for plasma processing applications [1,2]. We study the effects of including fast neutrals, using realistic energy-dependent secondary electron emission coefficients for ions and fast neutrals, and using different electron reflection probabilities in simulations of CCPs operated in argon at 13.56 MHz and at different neutral gas pressures. By switching individual processes on and off in the simulations we identify their individual effects on the ionization dynamics and plasma parameters. We find a significant effect of using realistic surface coefficients on the plasma density, the ion flux to the electrodes, and electron heating mode transitions under most conditions. Using different surface coefficients at both electrodes is found to induce a discharge asymmetry and to lead to the generation of a DC self bias that affects the ion energy distributions at boundary surfaces. In dual-frequency CCPs using realistic γ -coefficients is found to affect the separate control of the ion flux and the mean ion energy. Finally, a novel computationally assisted spectroscopic technique to measure effective γ -coefficients in-situ in the plasma (γ -CAST) is presented [3].

REFERENCES

- [1] A. Derzsi et al. 2015 Plasma Sourc. Sci. Technol. 24 034002
- [2] I. Korolov et al. 2015 Plasma Sourc. Sci. Technol. 25 015024
- [3] M. Daksha et al. 2016 J. Phys. D 49 234001

EXPERIMENTAL STUDY OF THE INFLUENCE OF DEBYE SHIELDING ON THE STARK SHIFT OF NEUTRAL HELIUM LINES IN DENSE PLASMAS

Teodora Gajo

¹*University of Novi Sad, Faculty of Sciences, Trg Dositeja Obradovića 4,
21000 Novi Sad, Serbia*

The results of an experimental study of the Stark shifts of neutral helium lines at 706.52, 728.14, 471.32, 501.57, 667.82 and 447.15 nm are presented in this work. The plasma source was a linear pulsed arc working at 200 milibars in a mixture of helium and hydrogen. The plasma electron density in the range $(0.6 - 7) \cdot 10^{23} \text{ m}^{-3}$ was obtained from the peak separation of the He I 447.15 nm line and cross-checked by the use of H I 486.13 nm line. The plasma temperature in the range (14600 - 20200) K was determined from relative intensities of eight impurity Si II lines. Details of the experimental setup that enables a relatively quick Stark shift determination technique is presented. The results of these measurements are presented together with the corresponding plasma parameters and compared to other experimental and theoretical data. Where it was possible, a best fitting formula was obtained from the available experimental data which can be used in plasma density diagnostics. The influence of Debye screening is carefully examined from the semiclassical point of view. The comparison of experimental results obtained in this work with the semiclassical results suggests that Debye screening has an important role on higher electron densities. Also, based on all the available experimental data, appropriate correction factors are suggested for the semiclassical Stark shift calculations for the examined lines.

STUDY OF SINGLE PULSE LASER INDUCED BREAKDOWN ON THE TARGET IN WATER

M.R. Gavrilović¹

¹*Institute of physics, University of Belgrade, 11080 Belgrade, P.O. Box 68, Serbia*

Direct elemental analysis of bulk liquids and submerged targets with laser induced breakdown (LIB) spectroscopy requires understanding of many factors influencing the process [1]. In this study, complex phenomena that arise during single pulse LIB on submerged solid target in the distilled water are studied by experimental techniques, fast schlieren and shadow photography, optical emission spectroscopy and transmission and scattering measurements Nd:YAG laser source operated at 1064 nm, with 20 ns pulse duration and 40 mJ energy was used for the plasma initiation. Obtained results indicate that it is possible to produce long lasting plasma underwater by applying single pulse laser ablation [2].

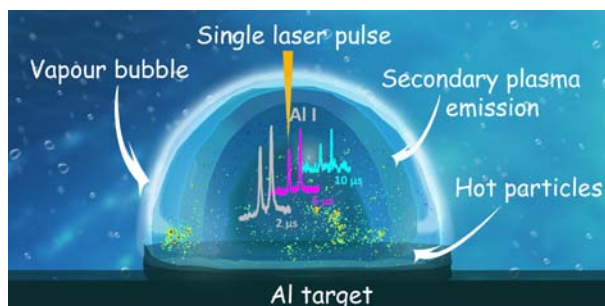


Figure 1. Graphical illustration of the processes occurring after the interaction of the single laser pulse with the pure aluminium target inside water

Acknowledgements: This work is supported by the Ministry of Education, Science and Technological development of Republic Serbia under project NO 171014.

REFERENCES

- [1] V. Lazić, S. Jovičević, Spectrochim. Acta Part B 101, 288 (2014).
- [2] M.R. Gavrilović, M. Cvejić, V. Lazić, S. Jovičević, Phys. Chem. Chem. Phys. 18, 14629 (2016)

ELECTRIC FIELD AND DISCHARGE PROPERTIES OF SINGLE AND MULTIPLE ARRANGEMENT OF PULSED ATMOSPHERIC PLASMA STREAMS

S. Iséni¹, X. Damany¹, G. Sretenović², V. Kovačević², I. Krstić²,
S. Dozias¹, J.-M. Pouvesle¹, M. Kuraica² and E. Robert¹

¹*GREMI, UMR 7344, CNRS/Université d'Orléans, France*

²*Faculty of Physics, University of Belgrade, Serbia*

In this study, one focuses on the diagnostic of single and *multiple* pulsed atmospheric plasma streams (PAPS) with the investigation of electric field (EF) [1]. The authors will present the results of EF strength obtained with two different methods. The first technique is a custom made electro optic sensor based on the Pockels effect [2], allowing for recording simultaneously two orthogonal components of the EF vector, time and spaced resolved [1]. The second method uses Stark polarization emission spectroscopy of the He I line at 492.19 nm [3]. Depending on the experimental conditions, both methods will be either complementary or compared with each other. The outcomes will bring information about the reliability of each methods and are of high interest for the validation of numerical simulation results.

Acknowledgments: This work was supported by the bilateral project PHD Pavle Savic 2016 (n° 36216UA). X.D. acknowledges his grant funding INEL/Région Centre Val de Loire.

REFERENCES

- [1] E. Robert, T. Darny, S. Dozias, S. Iseni and J.-M. Pouvesle, *Phys. Plasmas*, 22, 122007 (2015).
- [2] G. Gaborit, P. Jarrige, F. Lecoche, J. Dahdah, E. Duraz, C. Volat and L. Duvillaret, *IEEE Trans. Plasma Sci.*, 42, 1265 (2014).
- [3] G. Sretenović, I. Krstić, V. Kovačević, B. Obradović, and M. Kuraica, *J. Phys. D. Appl. Phys.*, 47, 102001 (2014).

ELECTRIC FIELD MEASUREMENT IN ATMOSPHERIC PRESSURE RADIOFREQUENCY DISCHARGE IN HELIUM

Z. Navrátil¹, R. Josepson¹, N. Cvetanović², B. Obradović³ and P. Dvořák¹

¹*Department of Physical Electronics, Faculty of Science, Masaryk University, Kotlářská 2, 611 37 Brno, Czech Republic*

²*Faculty of Transport and Traffic Engineering, University of Belgrade, Vojvode Stepe 305, 11000 Belgrade, Serbia*

²*Faculty of Physics, University of Belgrade, Studentski trg 12, 11001 Belgrade, Serbia*

In this work, electric field in helium γ -mode atmospheric pressure radiofrequency discharge was measured using Stark polarization spectroscopy. Time-correlated single photon counting enabled to measure the time development of spectral profile of He I 492.2 nm line with a temporal resolution of 0.8 ns during the sheath formation. From the measured profiles, which were fitted with pseudo-Voigt profiles for forbidden ($2^1P - 4^1F$) and allowed ($2^1P - 4^1D$) helium lines, electric field could be directly determined from the wavelength distance between forbidden and field-free allowed line [1].

The obtained electric field of 32 kV/cm is in agreement with the full sheath-averaged value of 40 kV/cm estimated from homogeneous charge density RF sheath model. The observed rectangular temporal profile of the electric field suggests, that the sheath conductivity is substantially increased in γ -mode discharge at current density of 3 A/cm².

Acknowledgements: The work was supported by projects GA13-24635S of Czech Science Foundation, CZ.1.05/2.1.00/03.0086 and LO1411 (NPU I).

REFERENCES

- [1] N. Cvetanović *et al*, J. Phys. D: Appl. Phys. 48, 205201 (2015)

RADIATION TRANSPORT WITH PARTIAL COHERENCE IN OPTICALLY THICK PLASMAS

J. Rosato

Laboratoire PIIM, UMR 7345 Aix-Marseille Université / CNRS, Centre de Saint-Jérôme, F-13397 Marseille Cedex 20, France

In standard textbooks on radiative transfer, it is assumed that the radiation field intensity obeys a Boltzmann-like transport equation and this equation is derived heuristically from conservation relations, using that the photon emission and absorption processes are source and loss terms. We examine the validity of this interpretation by reconsidering the radiative transfer problem from the first principles. Using a phase space formulation of quantum electrodynamics [1], we examine a method to account for finite coherence length and time in the emission and extinction coefficients. The model is confronted to the standard radiative transfer theory. New calculations of atomic line spectra in laboratory and astrophysical plasmas are performed.

Acknowledgements: This work is supported in part by the funding agency Campus France (Pavle Savic PHC project 36237PE).

REFERENCES

- [1] J. Rosato, Phys. Rev. Lett. 107, 205001 (2011).

ELECTRIC FIELDS IN kHz-DRIVEN PLASMA JETS

E.T. Slikboer¹, Y.N. Nguyen¹, O. Guaitella², G. Sretenović³, A. Obrušník⁴, A. Sobota¹

¹*EPG, Eindhoven University of Technology, the Netherlands*

²*LPP, Ecole Polytechnique, Palaiseau, France*

³*LPP, Faculty of Physics, University of Belgrade, Serbia*

⁴*LPP, Department of Physical Electronics, Faculty of Science, Masaryk University, Brno, Czech Republic*

What is the role of the flow in non-thermal atmospheric pressure plasma jets operating in ‘bullet mode’? What is the influence of the target? How to they affect fundamental plasma properties such as electric field profile along the plasma plume? The answers are relevant both for the understanding of the processes in atmospheric pressure non-thermal plasmas and for the applications on materials sensitive to high temperatures, (bio)materials that are not resistant to vacuuming or even fully drying, (bio)targets that are sensitive to significant current transfer.

This paper will give an overview of the recent work in the electric field measurements in atmospheric pressure plasma jets that operate in the bullet mode. A kHz-driven jet in helium is used with flow rates up to 2 SLM, like the one reported on in [1].

Acknowledgements: A.S. would like to thank the European Cooperation in Science and Technology Action COST TD1208 for the financial support for a short-term scientific mission. G.S. would like to thank the Ministry of Education and Science of the Republic of Serbia for financial support through Project 171034 and Project 33022. A.O. is a Brno PhD Talent scholarship holder funded by Brno city municipality.

REFERENCES

- [1] O. Guaitella and A. Sobota, *J.Phys.D:Appl.Phys.* 48, 255202 (2015)

MEASUREMENTS OF THE ELECTRIC FIELD DEVELOPMENT IN HELIUM PLASMA JETS

Goran B. Sretenović

University of Belgrade, Faculty of Physics, PO Box 44, 11001 Belgrade, Serbia

The subject of presented work is the study of emission and propagation of streamers in atmospheric pressure plasma jets in helium. Atmospheric-pressure helium plasma jets have been studied by optical emission spectroscopy and electrical measurements.

The focus of the research was on the spatially and temporally resolved measurements of the electric field in streamers in helium [1,2]. Using the method of Stark polarization spectroscopy, temporal development of the electric field was observed in steps which were in range of 20–500 ns. Such temporal resolution was complemented by the spatial resolution of 0.025 mm [3]. Depending on the plasma jet configuration, the maximal electric field strength in the bullet/streamer head was between 10 and 20 kV cm⁻¹. Electric field measurements are accompanied by the electrical and spectroscopic diagnostics of the discharge evolution. It was found that without the grounded electrode downstream from the nozzle, the jet develops as the cathode directed streamer. Contrarily, when a grounded electrode is present, development of the plasma jet is very similar to the evolution of the single microdischarge in air. Finally, the direct relation between electric field strength and the velocity of the plasma bullet is demonstrated.

Acknowledgements: This work was supported by the Ministry of Education and Science of the Republic of Serbia through Project 171034 and Project 33022.

REFERENCES

- [1] G. B. Sretenović, I. B. Krstić, V. V. Kovačević, B. M. Obradović, and M. M. Kuraica, *Appl. Phys. Lett.*, 99 (16) 161502 (2011).
- [2] G. B. Sretenović, I. B. Krstić, V. V. Kovačević, B. M. Obradović, and M. M. Kuraica, *IEEE Trans. Plasma Sci.* 40, 2870 (2012).
- [3] G. B. Sretenović, I. B. Krstić, V. V. Kovačević, B. M. Obradović, and M. M. Kuraica, *J. Phys. D: Appl. Phys.* 47, 102001 (2014).

TRANSITION PROBABILITIES OF SOME UV Kr II SPECTRAL LINES

M. T. Belmonte¹, L. Gavanski², R. J. Peláez³, J. A. Aparicio¹,
S. Djurović² and S. Mar¹

¹*Universidad de Valladolid, Departamento de Física Teórica, Atómica y Óptica,
Paseo de Belén 7, E-47011 Valladolid, Spain*

²*University of Novi Sad, Faculty of Sciences, Department of Physics,
Trg Dositeja Obradovića 4, 21000 Novi Sad, Serbia*

³*LaserProcessing Group, Instituto de Óptica, CSIC, Serrano 121,
E-28006 Madrid, Spain*

Abstract. Experimentally obtained transition probabilities for some ultraviolet Kr II lines, expressed in absolute units, are presented in this paper. For the measurement, intensities of spectral lines emitted by a plasma generated in a low-pressure pulsed arc were used. The electron density was in the range of $(1.5 - 3.4) \times 10^{22} \text{ m}^{-3}$, while the temperature was between 28 000 K and 35 000 K.

1. INTRODUCTION

In this paper, we report experimental results of transition probabilities for some UV lines of singly ionized krypton. Transition probability data, for a number of Kr II spectral lines from the UV spectral region, have been published recently in [1]. Here we give an extension of those measurements. These data are of interest for plasma diagnostic purposes, especially for the determination of the plasma temperature using a method based on spectral line intensities [2]. These data are also important for the development of light and laser sources [3, 4] as well as in astrophysics [5-7].

The absolute values of the transition probability data were obtained by measuring the relative spectral line intensities. Seven spectral lines with well known transition probability data were used to transform our relative measurements into absolute ones.

2. EXPERIMENT

As the plasma source, we used a low pressure pulsed arc. It was a Pyrex glass tube, 175 mm long and 19 mm in internal diameter. The pulses were made by discharging a 20 μF capacitor bank, charged up to 7.8 kV. The plasma life was about 200 μs . Pure krypton was continuously flowing through the discharge tube under a pressure of 120 Pa.

The spectra were recorded by using a 1.5 m spectrometer equipped with a 2400 lines/mm grating. At the exit of the spectrometer, an ICCD camera was mounted. The spectra were observed along the discharge tube, 2 mm off the tube axis at the instants 50, 60, 100 and 110 μs after the beginning of the discharge. The exposure time ranged between 2 and 5 μs . Every line profile was checked for the presence of the self-absorption effect.

The electron density, in the range of $(1.5 - 3.4) \times 10^{22} \text{ m}^{-3}$, was measured by a two-wavelength interferometric technique, using two He-Ne lasers radiating at 543.5 nm and 632.8 nm. The laser beams passed 2 mm off the tube axis, opposite to the optical measurements. The axial homogeneity of the plasma and the cylindrical symmetry enabled simultaneous optical and interferometric measurements. The estimated error for the electron density determination is about 5%. The electron temperature was obtained by using the Boltzmann plot technique. According to [8], the plasma was in PLTE. For this purpose, we used seven Kr II lines (459.280, 460.402, 461.529, 461.917, 482.519, 483.208 and 484.661 nm) with well known transition probabilities [9, 10]. The temperature was between 28000 and 35000 K. The estimated errors were lower than 10%.

3. RESULTS

The results are shown in Table 1. The first column contains the transitions, while in the second column the corresponding wavelengths are given. The Table is arranged in order of increasing wavelength. The wavelength and transition data are taken from the NIST Atomic Spectra Database [9], except for

Table 1. Measured transition probability data for some UV Kr II spectral lines.

| Transition | Wavelength (nm) | A_{ki} (10^8 s^{-1}) | Exp. error |
|---|--------------------|---------------------------------------|---------------|
| $(^1\text{D})5s \ ^2\text{D}_{5/2} - (^3\text{P}_1)4f \ ^2[3]_{7/2}^\circ$ | 220.840 | 0.019 | 18% |
| $(^3\text{P})4d \ ^4\text{D}_{5/2} - (^3\text{P})6p \ ^4\text{D}_{7/2}^\circ$ | 224.531 | 0.080 | 7% |
| $4d \ ^4\text{F}_{3/2} - 5f \ ^2\text{F}_{5/2}^\circ$ | 230.267 | 0.084 | 18% |
| $4d \ - (^3\text{P}_1)4f \ ^2[3]_{5/2}^\circ$ | 248.750 | 0.313 | 18% |
| $(^3\text{P})5p \ ^2\text{D}_{5/2}^\circ - (^1\text{D})5d \ ^2\text{P}_{3/2}$ | 266.122 | 0.189 | 18% |
| $(^3\text{P})4d \ ^2\text{P}_{3/2} - (^1\text{S})5p \ ^2\text{P}_{1/2}^\circ$ | 271.027 | 0.065 | 18% |
| $4d \ - (^3\text{P}_1)4f \ ^2[3]_{7/2}^\circ$ | 277.459 | 0.042 | 18% |
| $(^3\text{P})5p \ ^4\text{S}_{3/2}^\circ - (^1\text{D})5d \ ^2\text{F}_{5/2}$ | 277.796 | 0.137 | 18% |
| $(^3\text{P})4d \ ^4\text{P}_{5/2} - (^3\text{P})6p \ ^4\text{D}_{7/2}^\circ$ | 312.602 | 0.022 | 25% |

the 230.267 nm line, for which there are no data in this Database. For this line, we used transition notation from Striganov and Sventitskii Tables [11]. The third column contains the measured transition probabilities in absolute units. In the last column the estimated experimental errors are presented. As the reference lines, employed to transform relative transition probabilities into absolute units, we used the same lines that we had used for the temperature determination.

Examples of spectra with some of the considered lines are given in Figs. 1 and 2. Even if the lines 248.750 nm and 248.762 nm were blended, we were able to separate and fit their profiles as shown in Fig. 1.

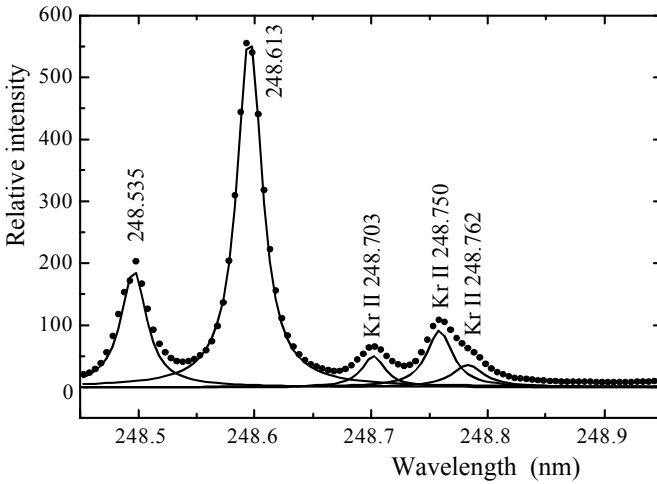


Figure 1. Part of the ionized krypton spectrum close to the 248.750 nm line.

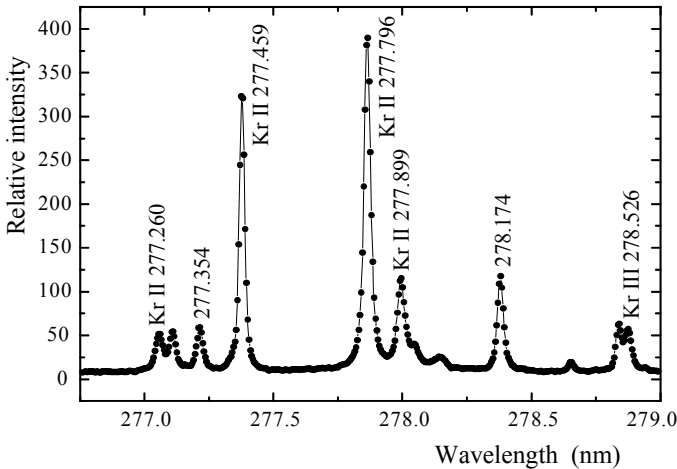


Figure 2. Part of the ionized krypton spectrum close to the 277.459 nm and 277.796 nm spectral lines.

There are no transition probability data in the literature for the considered lines and the present data are given here for the first time.

Acknowledgements

This work was supported by the Ministry of Education, Science and Technological development of Republic Serbia, under Project 171014.

M. T. Belmonte thanks the University of Valladolid for her PhD scholarship.

R. J. Peláez acknowledges the grant JCI-2012-13034 from the Juan de la Cierva Programme.

REFERENCES

- [1] M. T. Belmonte, L. Gavanski, R. J. Peláez, J. A. Aparicio, S. Djurović and S. Mar, *Month. Not. Roy. Astron. Soc.* 456, 518 (2016).
- [2] H. R. Griem, *Plasma Spectroscopy*, McGraw-Hill Book Company, New York (1964).
- [3] M. A. Cayless and A. M. Marsden, *Lamps and Lighting*, 3rd edn. Edward Arnold, London (1983).
- [4] K. Shimoda, *Introduction to laser physics*, Springer Series in Optical Sciences, Springer, Berlin (1984).
- [5] W. P. Bidelman, *Astrophys. J.* 67, 111 (1962).
- [6] H. L. Dinerstein, *Astrophys. J.* 550, L223 (2001).
- [7] B. Sharpee, Y. Zhang, R. Williams, E. Pellegrini, K. Cavagnolo, J. A. Badwin, M. Philips and X. W. Lui, *Astrophys. J.* 659, 1265 (2007).
- [8] H. R. Griem, *Phys. Rev.* 131, 1170 (1963).
- [9] NIST Atomic Spectra Database: <http://physics.nist.gov/asd>
- [10] S. Mar, J. A. del Val, F. Rodríguez, R. J. Peláez, V. R. Gonzalez, A. B. Gonzalo, A. de Castro and J.A. Aparicio, *J. Phys. B: At. Mol. Phys.* 39, 3709 (2006).
- [11] A. R. Striganov and N. S. Sventitskii, *Tables of Spectral Lines of Neutral and Ionized Atoms*, Plenum, New York (1968).

SPECTROSCOPIC INVESTIGATION OF THE UNDERWATER DIAPHRAGM DISCHARGE

N. Cvetanović¹, O. Galmiz² and A. Brablec²

¹*University of Belgrade, Faculty of Transport and Traffic Engineering,
Vojvode Stepe 305, 11000 Belgrade, Serbia*

²*Department of Physical Electronics, Masaryk University, Kotlarska 2,
61137 Brno, Czech Republic*

Abstract. The diaphragm underwater discharge developed for textile treatment was investigated using optical emission spectroscopy. The gas temperature obtained from nitrogen molecular band was used to obtain the H α Stark broadening and estimate the electron density. This preliminary results show that the discharge filaments are formed within the air bubble while electron density is within the expected values for underwater discharges.

1. INTRODUCTION

The diaphragm underwater discharge is designed and made at the Faculty of Sciences, Masaryk University, Brno [1, 2]. The specific design of the discharge is made preferably for application of textile plasma H₂O treatment. For this reason the reactor consists of narrow slit electrodes mounted on a plastic diaphragm and submerged in water. Between the electrodes and the diaphragm a textile ribbon is moved, made of polypropylene. The plasma is formed as a large number of filaments under the water surface, along the surface of the textile, see Ref. [1]. This paper gives preliminary results obtained from time-integrated optical emission spectroscopy. The parameters of the plasma filaments were estimated from molecular bands and broadening of Balmer alpha line.

2. EXPERIMENT

Details of the discharge configuration can be found in references [1] and [2], here only essential information is given. The discharge was generated using a diaphragm electrode; where a narrow slit of 0.1×1×40 mm was positioned between two metallic electrodes at 2 cm mutual distance, see Fig. 1. The polypropylene textile is moved between the electrodes and consequently the plasma filaments are formed along the textile surface and can be investigated by observing radiation in the vicinity of the electrode.

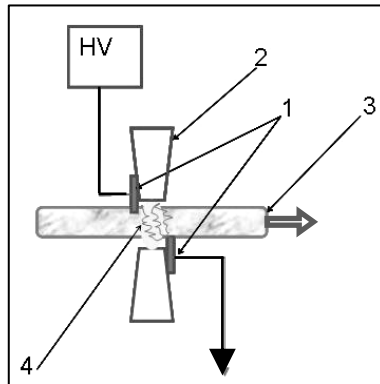


Figure 1. Configuration of underwater diaphragm discharge: 1–electrodes; 2–diaphragm; 3–polypropylene nonwoven fabric; 4–discharge.

The discharge was driven by a high voltage pulse power source typically at 30 kV voltage and frequency of 10 Hz. To obtain the overall spectrum with low resolution Avantes Sensiline spectrometer was used (FWHM 1.3 nm). Spectroscopic observations were done orthogonally to the textile surface by focusing radiation at different axial positions (from the diaphragm onwards) to the entrance of the optical fiber connected to the high resolution spectrometer. The Horiba FHR1000 spectrometer (grating 2400 gr.mm⁻¹, instrumental FWHM 0.017 nm) with a CCD cooled detector was used for time-integrated detection.

3. RESULTS

The overall spectrum from the underwater diaphragm discharge is given in Fig. 2. The most prominent structures in the spectrum are C₂ and CN molecular bands. The gas temperature was estimated by measuring rotational temperature from the N₂ second positive system. Unfortunately the H_β line could not be used for diagnostics due to its very low intensity and overlap with molecular spectra and continuum radiation. Therefore the broadened Balmer alpha line was used for electron density measurements.

The example of H_α line from the underwater discharge, taken at the position near the maximum intensity is shown in Fig. 3. To obtain the goodness of the fit the line had to be fitted with two Voigt functions corresponding to two phases in streamer development (effect already observed in high pressure pulse discharges) [3]. The wider component (FWHM ~ 2 nm) is emitted from a fully developed streamer/filament and corresponds to high electron density. The narrow component (FWHM ~0.25 nm) is emitted at lower electron density during plasma decay, with most of the broadening due to the van der Waals mechanism. The existence of a narrower component in the fit indicates that the breakdown occurs within the air micro-bubble. The width of the both components includes Van der Waals broadening at pressures 1-10 bar which is a characteristic value for breakdown in air bubbles.

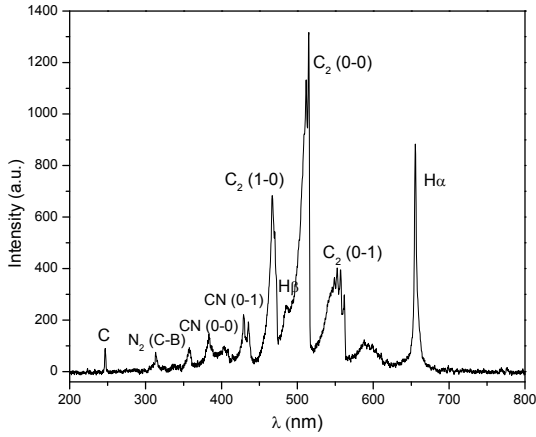


Figure 2. The overall spectrum of underwater diaphragm discharge with low resolution.

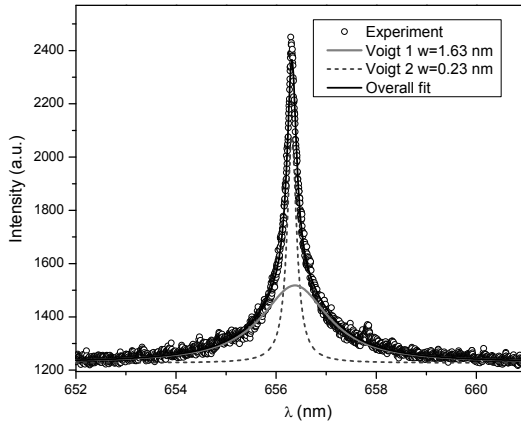


Figure 3. The example of measured H_{α} and the corresponding fit.

The contribution to the width coming from collisional broadening (i.e. Lorentz width) was obtained by subtracting Doppler and instrumental contribution as recommended in [3, 4], and then the electron density was calculated from the width of the Stark component of the Lorentzian [3, 4].

The estimated electron density depends on the presumed pressure and since the H_{β} line profile was not obtained, the comparison of the two line profiles to attain information on pressure was not possible. However, the calculated electron density from H_{α} should produce a very broad H_{β} (~6 nm) which approximately corresponds to the observed spectrum in its region. Table 1 gives the measured widths of the line with obtained densities for the maximum and minimum expected pressure. The measured gas temperature, at the position of given H_{α} measurement, was (1200 ± 300) K. By careful examination of the Voigt

profiles in Fig. 3, one may observe that the wider component is slightly shifted towards the longer wavelengths. The value of the observed shift, agrees fairly good with the expected Stark shift at electron density given in Table 1.

Table 1. Line widths and estimated densities: w - Voigt widths from fit, w_s -Stark widths, w_{vdw} -Van der Waals widths. Estimated uncertainty for Ne is $\sim 20\%$.

| p (bar) | w_1 (nm) | w_2 (nm) | w_{vdw} (nm) | w_{s1} (nm) | w_{s2} (nm) | Ne_1 (cm^{-3}) | Ne_2 (cm^{-3}) |
|------------|---------------|---------------|-------------------|------------------|------------------|-------------------------|-------------------------|
| 1 | 1.63 | 0.23 | 0.0245 | 1.60 | 0.202 | $1.75 \cdot 10^{17}$ | $8.3 \cdot 10^{15}$ |
| 10 | 1.63 | 0.23 | 0.245 | 1.38 | ≈ 0 | $1.38 \cdot 10^{17}$ | $< 10^{14}$ |

As can be seen, in the case of higher presumed pressure (order of magnitude from atmospheric) the wider component gives significantly smaller density while the narrower component is then broadened only by Van der Waals. This can also be taken as evidence that the pressure is not higher than 10 bar. The higher electron density in Table 1, obtained from the wider fit profile corresponds to the ones found in similar experiments of underwater plasma filaments [5].

4. CONCLUSION

The diaphragm underwater discharge developed for textile treatment was investigated using optical time-integrated emission spectroscopy. The gas temperature obtained from molecular bands was used to obtain the Stark broadening and resulting electron density. This preliminary results show that the discharge filaments are formed within the air bubble while electron density is within the expected values for this kind of discharge.

Acknowledgements

The present work was supported by the project LO1411 (NPU I) funded by the Ministry of Education, Youth and Sports of the Czech Republic. It was also done within the COST Action TD1208.

REFERENCES

- [1] G. Neagoe, A. Brablec, J. Ráhel, P. Slaviček And M. Zahoran, Chem. Listy 102, s1490 (2008).
- [2] O. Galmiz, A. Brablec, Z. Navrátil, Chem. Listy 106, s1443 (2012).
- [3] A. Yu. Nikiforov, Ch. Leys, M. A. Gonzalez and J. L. Walsh Plasma Sources Sci. Technol. 24, 034001 (2015).
- [4] N. Konjević, M. Ivković, N. Sakan, Spectrochim. Acta B 76, 16 (2012).
- [5] M. Simek, M. Clupek, V. Babicky, P. Lukes and P. Sunka, Plasma Sources Sci. Technol. 21, 055031 (2012).

THE INFLUENCE OF DEBYE SCREENING ON THE SHIFT OF THE He I 706.52 nm SPECTRAL LINE

T. Gajo¹, M. Ivković², I. Savić¹, Z. Mijatović¹, S. Djurović¹ and N. Konjević³

¹*University of Novi Sad, Faculty of Sciences, Trg Dositeja Obradovića 4,
21000 Novi Sad, Serbia*

²*University of Belgrade, Institute of Physics, P.O. Box 68,
11081 Belgrade, Serbia*

³*University of Belgrade, Faculty of Physics, P.O. Box 368,
11081 Belgrade, Serbia*

Abstract. Results of the Stark shift of the He I 706.52 nm spectral line and the influence of Debye screening at higher electron densities is presented here. A linear pulsed arc was used as the plasma source having an electron density in the range $(0.6 - 7) \cdot 10^{23} \text{ m}^{-3}$ and electron temperature in the range (14600-20200) K. The experimental results were compared to the semiclassical theoretical shift values calculated with and without the inclusion of Debye screening. The results are in very good agreement with the theoretical ones that take into account the influence of Debye screening if the theory is corrected on all available experimental values of the Stark parameters.

1. INTRODUCTION

The spectral lines of neutral helium are examined in great detail theoretically, as well as experimentally. However, in the majority of theoretical studies, the effect of Debye screening has been left out. Usually the correction due to Debye screening has to be calculated separately so the Stark parameters could be corrected [1]. Recently a quantum statistical study of Stark broadening has been given in [2]. This study compares the results of two different approximations: binary, without the inclusion of Debye screening and dynamical, where dynamical screening is taken into account. Another approach is described in [3] where Stark broadening is treated by simulations using molecular dynamics of independent particles. In this approach Debye screening is approximately taken into account by using Debye screened potentials. The analysis of these theoretical approaches and their comparison with experimental results can be found in [2-4].

Since Debye screening starts to affect the Stark parameters at higher electron densities, the aim of this work was to find the dependence of the shift

values on the electron density at these, higher values. Then, the dependences were compared with the available results given by different theories and experiments.

2. EXPERIMENT

2.1 Experimental setup and line shift measurements

The plasma source used here was a linear pulsed arc in helium with a small amount of hydrogen as the working gas at 200 milibars. The details of the plasma source and experimental setup can be found in Refs. [4] and [5]. The construction of the plasma source enabled a relatively simple technique for Stark shift measurements. During the spectral recordings, except the examined broad line profiles at different times of the plasma decay (measured from the maximum of the discharge current I_{max}), narrow unshifted profiles of the same line appeared (Figure 1). The origin of these profiles is the plasma jet formed at the outer region of the electrodes. The Stark shifts of the examined lines were determined as the difference in the wavelength position between the narrow line and the position of the broad line maximum as described in [5].

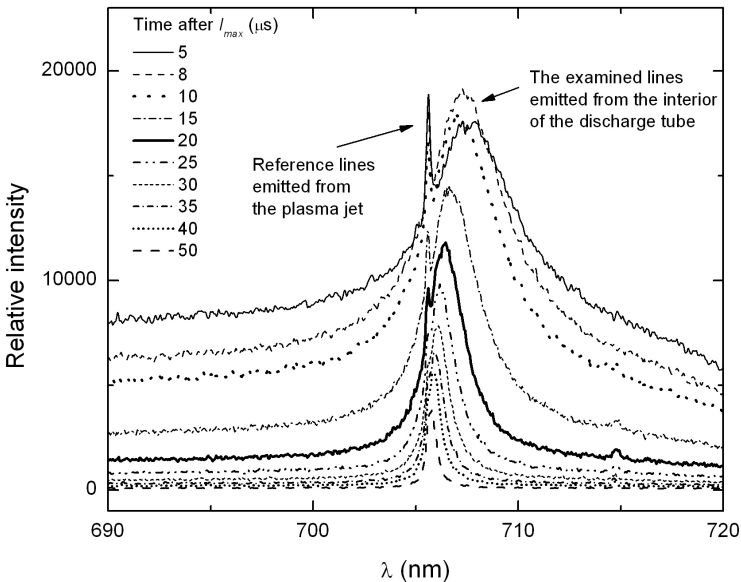


Figure 1. Profiles of the He I 706.52 nm spectral line at different times after the discharge current maximum I_{max} . Illustration of the line shift measurement.

2.2 Plasma diagnostics

The plasma electron density ranging from 0.6 to $7 \cdot 10^{23} \text{ m}^{-3}$ was determined from the peak separation of the He I 447.15 nm line using equations

given in [6]. The electron temperature in the range (14600-20200) K was determined from the relative intensities of eight Si II spectral lines at 385.60, 386.26, 412.81, 413.09, 595.76, 597.89, 634.71 i 637.14 nm. These lines appeared in the recorded spectrum as impurity lines originating from the glass wall of the discharge tube.

3. RESULTS AND DISCUSSION

The Stark shifts of He I 706.52 nm at different plasma parameters were determined. The actual results of measured shifts are given in [5] and their comparison with the results of other experiments and theories is presented graphically in the same paper, but without any correction to Debye screening or other. The agreement among the experimental results is good, however the results of other authors are given in the density range of $(0.3 - 2.07) \cdot 10^{23} \text{ m}^{-3}$ where Debye screening has no significant influence on the shift. In Figure 2 the comparison of experimental results obtained in this work and the results of Griem's theory [1] with and without screening are compared.

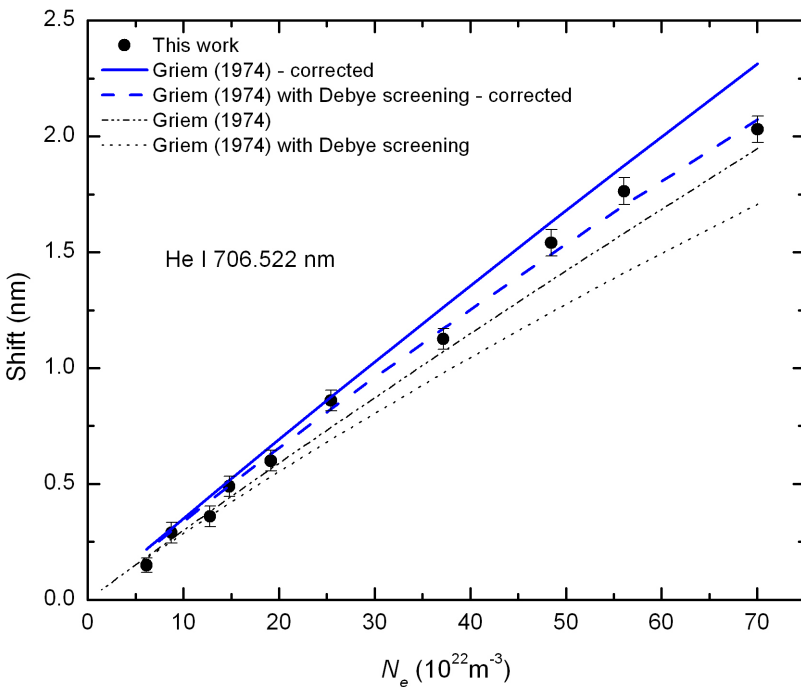


Figure 2. Comparison of the experimental and theoretical [1] shift values for the He I 706.52 nm spectral line including corrections to Debye screening and to all available experimental results. Detailed explanation on obtaining the results of this theory can be found in [4].

The agreement of Griem's theory without Debye screening and the experimental results is within 11%, while for the theory corrected to Debye screening the average deviation increased to 17%. In order to resolve this unexpected result, an additional correction of this theory has been carried out. The average of the correction factors concluded from the experimental results reported in Critical Review papers [7], [8], [9] and [10] has been used considering only the data with the highest accuracy. In this way the electron impact width w_e and shift d_e were corrected by multiplying them with the correction factors $w_m/w_{th} = 0.96$ and $d_m/d_{th} = 1.24$. The index "m" stands for the measured values of half-widths and shifts, while "th" for their values given by Griem's theory. The agreement between Griem's theory that takes into account Debye screening corrected to the measured values of half-widths and shifts has decreased to 7%, while the agreement with corrected Griem's theory without screening is inside 11%. The results of Griem's theory corrected in the above mentioned way are also presented in Figure 2. Based on this result, it can be seen that the experimental results are in almost perfect agreement with Griem's theory with Debye screening corrected on measured values of the Stark parameters. Also, it can be concluded that Debye screening affects the values of Stark shifts at higher electron densities.

Acknowledgements

This work is financed by Serbian Ministry of Education, Science and Technological Development under the project OI 171014.

REFERENCES

- [1] H. R. Griem, *Spectral Line Broadening by Plasmas*, (Academic Press, New York, 1974).
- [2] B. Omar, S. Günter, A. Wierling, G. Röpke, Phys. Rev. E 73, 056405 (2006).
- [3] M. Gigosos, S. Djurović, I. Savić, D. González-Herrero, Z. Mijatović, R. Kobilarov, A&A 561, A135 (2014).
- [4] T. Gajo, M. Ivković, N. Konjević, I. Savić, S. Djurović, Z. Mijatović, MNRAS 455, 2969 (2016).
- [5] M. Ivković, T. Gajo, I. Savić, N. Konjević, J. Quant. Spectrosc. Radiat. Transfer 161, 197 (2015).
- [6] M. Ivković, M. A. Gonzalez, S. Jovičević, M. A. Gigosos, N. Konjević, Spectrochimica Acta Part B 65, 234 (2010).
- [7] N. Konjević, M. S. Dimitrijević, W. L. Wiese, J. Phys. Chem. Ref. Data 13, No. 3, 619 (1984).
- [8] N. Konjević, W. L. Wiese, J. Phys. Chem. Ref. Data 19, No. 6, 1307 (1990).
- [9] N. Konjević, A. Lesage, J. R. Fuhr, W. L. Wiese, J. Phys. Chem. Ref. Data 31, No. 3, 819 (2002).
- [10] A. Lesage, New Astronomy Reviews 52, 471 (2009).

STARK HALFWIDTHS OF SEVERAL O II SPECTRAL LINES

L. Gavanski¹, M. T. Belmonte², I. Savić¹ and S. Djurović¹

¹*University of Novi Sad, Faculty of Sciences, Department of Physics,
Trg Dositeja Obradovića 4, 21000 Novi Sad, Serbia*

²*Universidad de Valladolid, Departamento de Física Teórica, Atómica y Óptica,
Paseo de Belén 7, E-47011 Valladolid, Spain*

Abstract. Experimental Stark halfwidths of several O II spectral lines are presented in this paper. The spectral lines were emitted from a T-tube plasma with an electron density of $1.45 \times 10^{23} \text{ m}^{-3}$ and electron temperature of 15 000 K. The obtained experimental results were compared with available experimental data from other authors, as well as with some calculated and some available theoretical Stark halfwidth results.

1. INTRODUCTION

In this paper, we report the experimental results of Stark halfwidths (FWHM) for some spectral lines of ionized oxygen. This work is an extension of a recent paper [1]. Oxygen spectral lines can be of interest for both laboratory and astrophysical plasmas. The Stark halfwidths of these lines can be used for plasma diagnostic purposes. As well as for plasma diagnostics, in the study of stellar plasmas, these data are used for the determination of chemical abundances of elements and the investigation of radiative transfer through stellar atmospheres [2]. A huge amount of spectroscopic data is necessary for this purpose.

2. EXPERIMENT

The plasma was produced in an electromagnetically driven T-tube with an internal diameter of 27 mm. The tube was filled with pure helium up to 300 Pa. The distance between the electrodes and the reflector was 140 mm. The capacitor bank with capacity of 4 μF , charged up to 20 kV, was used for the discharge through the T-tube. The discharge current was monitored by a Rogowski coil and an oscilloscope. The spectroscopic data were collected by means of an ICCD camera. The camera was mounted on a 1-m spectrometer, with a 1200 g mm^{-1} grating. The inverse linear dispersion was 0.833 nm mm^{-1} .

The oxygen in the tube appears as an impurity due to the erosion of the T-tube glass walls.

The electron temperature of 15000 K was obtained from a Boltzmann plot of 12 O II lines for which transition probability values and other necessary data were taken from the NIST Atomic Spectra Database [3]. The estimated error is 16%. The electron density of $1.45 \times 10^{23} \text{ m}^{-3}$ was determined from the distance between the two peaks of the He I 447.148-nm line. For that purpose, we used the empirical formula from Ivković et al. [4]. The estimated error is 15%.

3. RESULTS

In this paper, we will focus on the low intensity spectral lines as well as on those blended with lines of high intensity. Part of the recorded spectrum containing the O II 413.280 nm line is shown in Fig. 1.

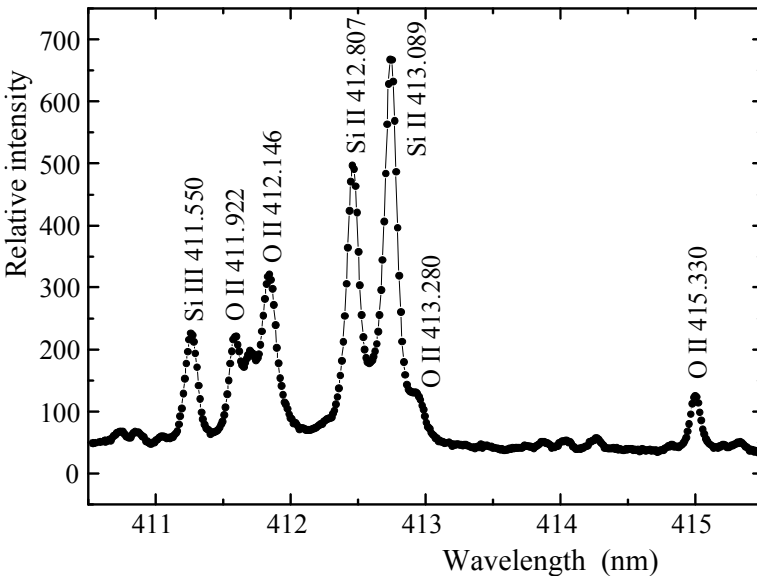


Figure 1. An example of part of the spectrum of interest.

In order to separate the Lorentzian and the Gaussian components of the spectral line halfwidths, the standard procedure employing the Voigt function was used [5]. The results for Stark halfwidths (FWHM) results are presented in Table 1. The observed lines belong to the 3s–3p, 3p–3d and 3d–4f transitions. The first two columns in Table 1 contain the line transition and wavelength. The next two columns show the plasma conditions. In the column denoted as w_m , both the measured Stark halfwidths and the experimental ones obtained by other

Table 1. Experimental Stark halfwidths of singly ionized oxygen spectral lines. All the terms belong to (3P) parent term except for the term denoted by *, which belongs to (1D) parent term.

| Transition | Wav. (nm) | N_e ($10^{23}m^{-3}$) | T_e (K) | w_m (nm) | w_m/w_{MSE} | w_m/w_{GR} | Ref |
|---------------------------------------|--------------|------------------------------|--------------|---------------|---------------|--------------|-----|
| $3s^4P_{3/2} - 3p^4P^{\circ}_{5/2}$ | 431.963 | 1.45 | 15000 | 0.0228 | 0.60 | 0.74 | TW |
| | | 1.00 | 40000 | 0.0261 | 1.61 | 1.59 | [8] |
| $3p^4D^{\circ}_{3/2} - 3d^4F_{3/2}$ | 407.884 | 1.45 | 15000 | 0.0272 | 0.59 | 0.62 | TW |
| | | 1.00 | 40000 | 0.0200 | 1.03 | 1.09 | [8] |
| * $3s^2D_{5/2} - 3p^2D^{\circ}_{5/2}$ | 435.126 | 1.45 | 15000 | 0.0272 | 0.86 | | TW |
| | | 1.00 | 40000 | 0.0225 | 1.68 | | [8] |
| $3p^4P^{\circ}_{1/2} - 3d^4P_{3/2}$ | 413.280 | 1.45 | 15000 | 0.0396 | 0.79 | 0.87 | TW |
| | | 0.52 | 25900 | 0.0130 | 0.95 | 1.05 | [6] |
| | | 1.00 | 40000 | 0.0299 | 1.41 | 1.56 | [8] |
| | | 0.76 | 12000 | 0.0312 | 1.06 | 1.17 | [9] |
| | | 0.91 | 13800 | 0.0360 | 1.10 | 1.21 | [9] |
| | | 1.45 | 15700 | 0.0374 | 0.76 | 0.84 | [9] |
| | | 1.82 | 18300 | 0.0462 | 0.81 | 0.89 | [9] |
| $3p^2D^{\circ}_{5/2} - 3d^2D_{5/2}$ | 439.594 | 1.45 | 15000 | 0.0538 | 0.87 | | TW |
| | | 0.81 | 60000 | 0.0254 | 1.39 | | [7] |
| $3p^2P^{\circ}_{3/2} - 3d^2D_{5/2}$ | 494.299 | 1.45 | 15000 | 0.0518 | 0.64 | 0.73 | TW |
| $3p^2P^{\circ}_{3/2} - 3d^2D_{3/2}$ | 495.571 | 1.45 | 15000 | 0.0525 | 0.65 | 0.74 | TW |
| | | 0.81 | 60000 | 0.0328 | 1.42 | 1.64 | [7] |
| $3d^4P_{3/2} - 4f^2[2]^{\circ}_{5/2}$ | 429.478 | 1.45 | 15000 | 0.0699 | 0.75 | | TW |
| | | 0.81 | 60000 | 0.0774 | 2.16 | | [7] |

authors are given [6 - 9]. The estimated experimental errors for the halfwidth values measured in this experiment were between 15 and 30%. The sixth and seventh columns contain a comparison between experimental and theoretical halfwidth values. For that purpose, calculations based on Ref. [10] (w_{MSE}) were made and the data from [11] (w_{GR}) were used. Some of the data are missing in [10].

All our results show lower Stark halfwidth values than those predicted by both theories. The ratios w_m/w_{MSE} and w_m/w_{GR} are between 0.6 and 0.87. The only result from [6] is in agreement with both theories. The results from [7] give considerably higher halfwidths than both theories; the ratio w_m/w_{Theory} ranges between 1.4 and 2.16. Only one result from [8] is in agreement with the theoretical results, but for the remaining three values this ratio is between 1.4 and 1.68. In Ref. [9] the authors report five results in one experiment, but for different plasma conditions. These results are not self-consistent. The ratio w_m/w_{MSE} varies between 0.76 and 1.13 while the ratio w_m/w_{GR} varies between 0.89 and 1.25. The high value of the w_m/w_{Theory} ratio indicates a possible problem with self-absorption. In this experiment, even if only traces of oxygen ions appeared, we checked the spectral lines for self-absorption, but did not detect this effect for any of the observed lines.

Acknowledgements

This work was supported by the Ministry of Education, Science and Technological development of Republic Serbia, under Project 171014.

M. T. Belmonte thanks the University of Valladolid for her PhD scholarship.

REFERENCES

- [1] L. Gavanski, M. T. Belmonte, I Savić and S. Djurović, *Month. Not. Roy. Astron. Soc.* 457, 4038 (2016).
- [2] M. S. Dimitrijević, *Astron. Astrophys. Trans.* 22, 389 (2003).
- [3] NIST Database: <http://physics.nist.gov/asd>
- [4] M. Ivković, M. Á. González, S. Jovičević, M. A. Gogosos, N. Konjević, *Spectrochim. Acta B* 65, 234 (2010).
- [5] J. T. Davies and J. M. Vaughan, *Astrophys. J.* 137, 1302 (1963).
- [6] M. Platiša, M. Popović and N. Konjević, *Astron. Astrophys.* 45, 325 (1975).
- [7] S. Djeniže, A. Srećković, J. Labat, and M. Platiša, *Z. Phys. D* 21, 295 (1991).
- [8] J. A. del Val, J. A. Aparicio, V. Gonzales and S. Mar, *Astron. Astrophys. Suppl. Ser.* 140, 171 (1999).
- [9] A. Srećković, V. Drinčić, S. Bukvić and S. Djeniže, *Phys. Scripta* 63, 306 (2001).
- [10] H. R. Griem, *Spectral Line Broadening by Plasmas*, Academic Press, New York (1974).
- [11] M. S. Dimitrijević and N. Konjević, *J. Quant. Spectrosc. Radiat. Transfer* 24, 451 (1980).

STUDY OF GAS FLOW INFLUENCE ON HOMOGENOUS BARRIER DISCHARGE IN HELIUM

S. S. Ivković¹, B. M. Obradović¹, N. Cvetanović² and M. M. Kuraica¹

¹ *University of Belgrade, Faculty of Physics, Studentski. trg 12,
11001 Belgrade, Serbia*

² *University of Belgrade, Faculty of Transport and Traffic Engineering,
V. Stepe 305, 11000 Belgrade, Serbia*

Abstract. Influence of gas flow rate on helium dielectric barrier discharge operating at atmospheric pressure in homogeneous mode, is investigated by studying electrical characteristics and space-time development of spectral lines. It was found that the breakdown voltage, current maximum and spectral lines emission of helium and hydrogen all depend on gas flow rate.

1. INTRODUCTION

It is well known that gas flow rate significantly influences the characteristics of dielectric barrier discharge (DBD). For instance, in reference [1] it was shown that laminar gas flow prevents the DBD discharge in nitrogen from transiting into filamentary mode. Also, in [2] it was shown that DBD discharge in helium is formed in multi-peak regime when operated in trapped gas, while when operating with gas flow only one current peak occurs per discharge half-period. Furthermore, the breakdown voltage is lower with trapped gas. In article [3] the influence of gas flow velocity was investigated in the range 0–17 cm/s in the discharge in helium at atmospheric pressure. It was determined that the breakdown voltage is highest with trapped gas (i.e. without flow), unlike the results of [2], and that it is reduced with increase of gas flow rate. In all of the mentioned articles the authors explain the effects by the reduction of the impurities due to increased gas flow (primarily N₂) which are introduced into the discharge from the barrier surface. This increases the number density of metastable species. Additionally, the gas flow cools down the barrier surfaces what enables the sufficient time of electron retaining on the barriers till the start of next discharge [4, 5]. These electrons then contribute to ignition and sustaining of the discharge.

2. EXPERIMENT

In our experiment the discharge is formed between two parallel metal electrodes ($40 \times 40 \text{ mm}^2$), both covered with Al_2O_3 dielectric ($105 \times 105 \text{ mm}^2$; $\epsilon_r = (9.4 \pm 0.3)$). The distance between the barriers is fixed at 4.8 mm. The discharge chamber is firstly evacuated down to 10^{-2} mbar, and then helium is introduced (purity 99.996%) up to atmospheric pressure. The gas flow is controlled using Omega FMA 5400/5500 flow controller. High voltage power supply is composed of three stages: signal generator, audio amplifier and high voltage transformer. The amplitude of the sine applied voltage was 1.75 kV at frequency of 16 kHz. Voltage is measured using high-voltage probe Tektronix P6015A, and current is monitored using Rogowski coil IPC CM-100-M (1 V/A). For the time-space resolved measurement of emission spectra the 1-m spectrometer with 1200 gr/mm grating was used. At the exit of the monochromator the ICCD detector with 1024 1024 pixels was used. With entrance slit of 30 μm , the instrumental FWHM was 0.032 nm.

3. RESULTS

Voltage and current waveforms were recorded for 18 different gas flow rates (in the range 0.05 – 5 l/min). At given amplitude and frequency of the applied voltage the discharge is established in a multi-peak regime with two or three current peaks. The change of gas flow significantly influences the electric characteristics of the discharge. Dependence of breakdown voltage and maximal value of discharge current on gas flow, for the first and second current peak are

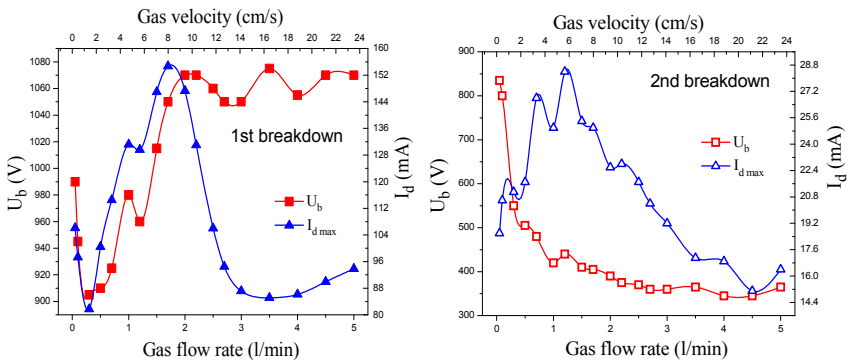


Figure 1. Dependence of breakdown voltage and maximal value of discharge current on gas flow, for the first and second current peak.

given in Fig 1. The dependence of breakdown voltage on flow rate for the second current peak corresponds to the results for single-peak discharge in [3]. Namely, it can be noted that breakdown voltage for the second breakdown decreases with increase of gas flow rate (Fig. 1). It may be concluded that with increase of flow rate, the destruction of metastables is reduced, in the extinguishing phase, after

the first breakdown. In this way, more metastables are engaged in the processes that provide the conditions for the second breakdown. This conclusion was also confirmed by the spectroscopic measurements.

To further investigate the influence of gas flow on development and characteristics of the discharge the space-time development of helium spectral line HeI 492.2 nm and hydrogen H_{β} line were studied. The spectral proximity of these lines enabled simultaneous recoding of both.

The intensity of HeI 492.2 nm line, for all gas flow rates, reaches its maximum at time instance of current maximum and decreases rapidly i.e. line emission lasts shorter than the first current peak. Also, the change of line maximum with gas flow reflects the change of amplitude of the first current peak, which is in agreement with [3]. It can be concluded that this atomic transition is predominantly excited through direct electronic excitation.

On the other hand the time development of H_{β} line is determined by the gas flow rate (Fig. 2).

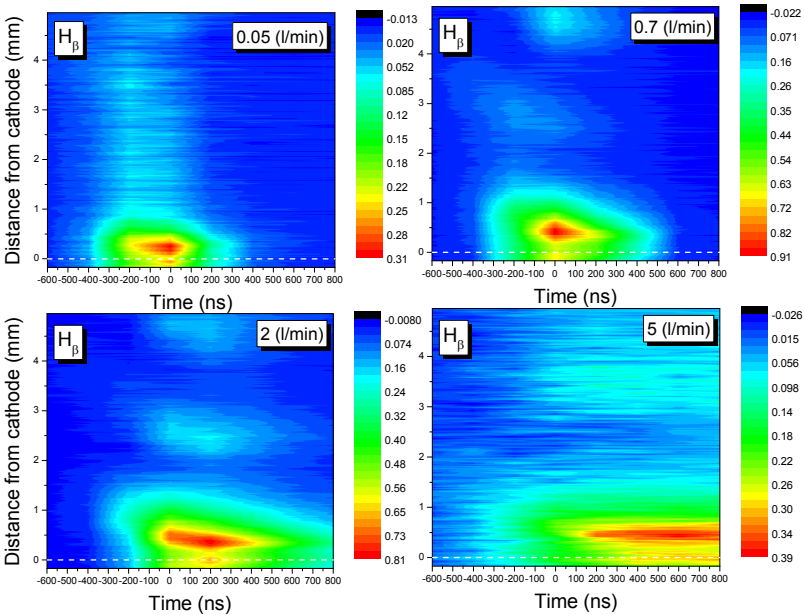


Figure 2. The spatiotemporal development of the intensity H_{β} line for different gas flow rates. Zero on the time scale corresponds to maximum of current peak.

At low flow rates (up to 0.7 l/min), the line H_{β} reaches its maximum at the time of current maximum indicating predominant excitation with direct electronic excitation. The rapid quenching of H_{β} line indicates that destruction of metastables is very efficient, which, in turn, suggests significant presence of

impurities (predominantly nitrogen) [6]. The values of breakdown voltage for the second breakdown confirm this conclusion (Fig. 1).

At high flow rates (over 2 l/min), the line H_{β} reaches its maximum after the time of current maximum and lasts longer. Here, with increase of gas flow rate the delay of line maximum from the current maximum is increased and its emission is prolonged. This behavior of H_{β} line indicates that, in the higher range of flow rates, it is predominantly excited via processes that involve helium metastable states, which agrees with conclusions in Ref. [7]. Therefore, the increase of gas flow leads to reduction of impurities and slower destruction of metastables. This, in turn, leads to increase of voltage drop required for the second breakdown.

4. CONCLUSION

Investigations were performed to study the influence of gas flow rate on helium dielectric barrier discharge. The discharge operated at atmospheric pressure in homogeneous mode. Measurements of electrical waveforms were accompanied with measurement of space-time development of spectral lines. The effect of gas flow rate was observed on the breakdown voltage, current maximum and spectral lines emission of helium and hydrogen. This influence of the gas flow rate is related to the concentration of impurities and consequent rate of metastables destruction.

Acknowledgements

This work is supported by the Ministry of Education, Science and Technological Development of the Republic of Serbia through the Project No 171034 and the Project No 33022.

REFERENCES

- [1] Gherardi N and Massines F, *IEEE Trans. Plasma Sci.*, **29** N^o3 536 (2001)
- [2] Chiper A S and Popa G, *Journal of applied physics*, **113** 213302 (2013)
- [3] Luo H, Liang Z, Wang X, Guan Z and Wang L, *J. Phys. D: Appl. Phys.* **41** 205205 (2008)
- [4] Golubovskii Yu B, Maiorov V A, Behnke J and Behnke J F, *J. Phys. D: Appl. Phys.* **36** 39 (2003)
- [5] Wang D, Wang Y and Liu C, *Thin solid films* **506-507** 384-388 (2006)
- [6] Massines F, Segur P, Gherardi N, Khamphan C and Ricard A, *Surface and Coatings Technology*, **174-175** 8-14 (2003)
- [7] Navrátil Z, Brandenburg R, Trunec D, Brablec A, St'ahel P, Wagner H-E and Kopecký Z, *Plasma Sources Sci. Technol.* **15** 8 (2006)

INFLUENCE OF THE LIQUID TARGET ON THE ELECTRIC FIELD STRENGTH IN HELIUM PLASMA JET

V. V. Kovačević¹, G. B. Sretenović¹, A. Sobota², O. Guaitella³, I. B. Krstić¹,
B. M. Obradović¹ and M. M. Kuraica¹

¹*University of Belgrade, Faculty of Physics, PO Box 44, 11001 Belgrade, Serbia*

²*Eindhoven University of Technology, EPG, Postbus 513, 5600MB Eindhoven,
The Netherlands*

³*LPP, Ecole Polytechnique, Route de Saclay, 91128 Palaiseau, France*

Abstract. In this paper we present electric field distribution in He plasma jet impinging the surface of different liquids. Dielectric barrier discharge (DBD) plasma jet with constant He flow of 1000 SCCM, operating at applied voltage of 2 kV and 30 kHz, was positioned above the liquid surface. Electric field measurement was performed using Stark polarization spectroscopy when Petri dish with distilled water or physiological saline (0.85 % NaCl) was positioned 10 mm below the plasma jet nozzle. Obtained axial distributions of the electric field show that maximal values of the field are similar for different targets.

1. INTRODUCTION

In recent years atmospheric pressure plasma jets have been extensively investigated and recognized as an emerging tool in the field of plasma medicine and biology [1]. Plasma jets are source of reactive oxygen and reactive nitrogen species which play important role in redox biology and medical applications [2]. Among reactive species, it is known that electric field can be the cause of various effects observed in experiments on biological samples [3] and it determines the production of charged particles, consequently the plasma chemistry, which can play a very significant role in the rupture of the outer membrane of bacterial cells [4]. In our previous study of spatio-temporal development of the plasma jet in helium for two different electrode configurations it was found that without the grounded electrode downstream from the nozzle the maximal value of electric field was about 10 kV/cm. Contrarily, when a grounded electrode is present, a maximal electric field of 20 kV/cm is obtained [5]. This suggests great influence of target on jet properties, especially in plasma medicine cells in tissue or in in vitro experiments are surrounded by liquid, thus plasma-liquid interaction is important to understand the plasma-cell interaction and design of the most favorable experimental conditions. The aim of this study was to investigate the

influence of the liquid targets on the electric field strength in helium plasma jet. Namely, distilled water and NaCl solution, positioned downstream the jet, were selected as test liquids since these are most commonly used in research of interaction of plasma with biological samples.

2. EXPERIMENT

In this study, we present our recent research on helium plasma jet interacting with the liquid surface. Here we focus on spatially resolved measurements of the electric field strength along the jet axis when water is positioned below the jet nozzle as a target. The atmospheric pressure plasma jet in use has already been described in detail elsewhere [6, 7]. Powered electrode is needle with the inner diameter of 0.8 mm centered inside the Pyrex capillary (inner diameter 2.5 mm, outer diameter 4 mm). Metal ring on the outer side of the capillary is used as the grounded electrode. The thickness of the ground was 3 mm, and the gap between the two electrodes was 5 mm, while the distance from the grounded electrode to the end of capillary was 20 mm. Helium flow was set to 1000 SCCM by mass flow controller. The power supply provided a sine voltage at 2 kV in amplitude and 30 kHz frequency. Liquid samples were set in a Petri dish and a constant distance between jet nozzle and liquid surface of 10 mm was adjusted.

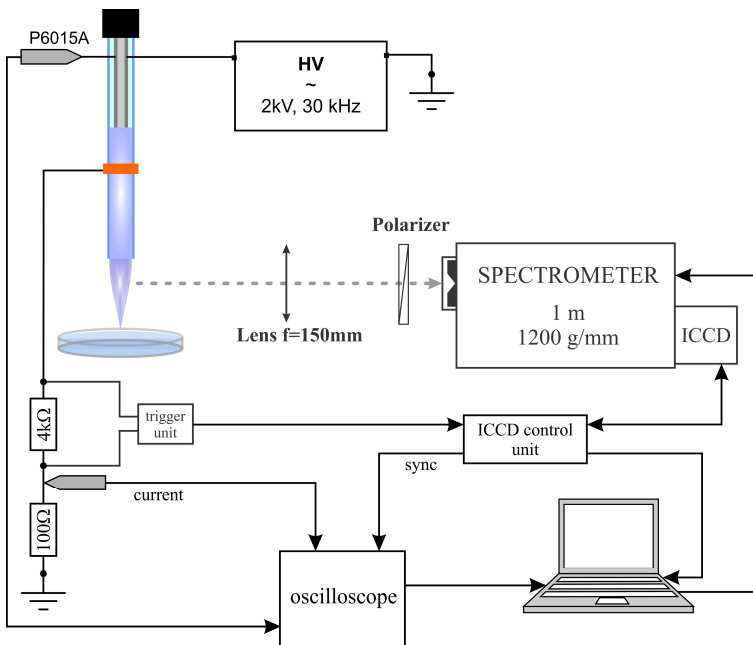


Figure 1. The schematic overview of the experimental setup.

Distilled water and physiological saline (NaCl solution 0.85%, 8.5g NaCl per 1000ml water) were used as targets. Electric field strength was measured by non-perturbing method based on Stark effect of helium lines developed by Kuraica and Konjević [8], and it was already applied for the electric field measurements in He plasma jets [5,9,10].

3. RESULTS

The electric field measurements are presented in Fig. 2. Figure 2 shows the distribution of the electric field along the plasma plume when it contacts distilled water or physiological saline. It is clear that measured electric field rises with the distance from the capillary reaching the maximum value of about 25 kV/cm when distilled water was treated. When plasma jet operates without target, measured electric field strength at 9 mm from the exit of the capillary was about 18 kV/cm. Also, if distilled water is positioned at 5 mm from the capillary exit maximal value of the electric field will reach 20 kV/cm (results are not shown here). Spatial development of the electric field along the jet axis for two liquids almost overlap, with slight increase of the electric field strength in the vicinity of the liquid surface when distilled water was target. One should have in mind that initial conductivity of distilled water was 2.5 $\mu\text{S}/\text{cm}$ while that of physiological saline was 14.94 mS/cm.

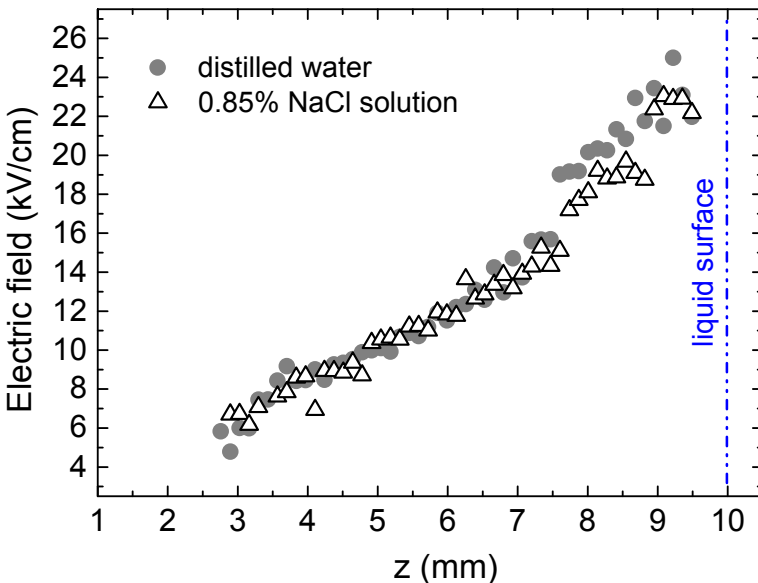


Figure 2. Electric field strength in the plume of the plasma jet when distilled water and NaCl solution were positioned 10 mm from the exit of capillary.

The results suggest that the type of the treated solution does not influence considerably axial distribution of the electric field strength nor its magnitude. Such conclusion is significant for research in the field of plasma medicine where interaction of plasma and biological sample occurs through different liquids. Our recent research implies that discharge configuration crucially affects the properties of the plasma plume and influence of different targets will be further investigated.

Acknowledgements

This work was supported by the Ministry of Education and Science of the Republic of Serbia through Project 171034 and Project 33022. This work was carried out within the framework of the COST TD1208 network.

REFERENCES

- [1] T. von Woedtke, S. Reuter, K. Masur, and K.-D. Weltmann, *Phys. Rep.* 530, 291 (2013).
- [2] D. B. Graves, *J. Phys. D. Appl. Phys.* 45, 263001 (2012).
- [3] M. Moisan, P. Levif, J. Séguin, and J. Barbeau, *J. Phys. D. Appl. Phys.* 47, 285404 (2014).
- [4] M. Laroussi, *Plasma Process. Polym.* 2, 391 (2005).
- [5] G. B. Sretenović, I. B. Krstić, V. V Kovačević, B. M. Obradović, and M. M. Kuraica, *J. Phys. D. Appl. Phys.* 47, 102001 (2014).
- [6] A. Sobota, O. Guaitella, and A. Rousseau, *Plasma Sources Sci. Technol.* 23, 025016 (2014).
- [7] O. Guaitella and A. Sobota, *J. Phys. D. Appl. Phys.* 48, 255202 (2015).
- [8] M. M. Kuraica and N. Konjević, *Appl. Phys. Lett.* 70, 1521 (1997).
- [9] G. B. Sretenović, I. B. Krstić, V. V Kovačević, B. M. Obradović, and M. M. Kuraica, *Appl. Phys. Lett.* 99, 161502 (2011).
- [10] G. B. Sretenović, I. B. Krstić, V. V. Kovačević, B. M. Obradović, and M. M. Kuraica, *IEEE Trans. Plasma Sci.* 40, 2870 (2012).

INFLUENCE OF AIR ADDED IN THE HELIUM FLOW ON THE PLASMA BULLET FORMATION

Dejan Maletić¹, Nevena Puač¹, Gordana Malović¹ and Zoran Lj. Petrović^{1,2}

¹*Institute of Physics, University of Belgrade, Pregrevica 118, 11080 Belgrade*

²*Serbian Academy of Sciences and Arts, Knez Mihajlova 35, 11001 Belgrade, Serbia*

Abstract. The aim of this paper is to investigate the influence of addition of air into the working gas on the plasma jet development. Here we present the time resolved images of plasma jet for two helium/air mixtures (1% and 1.5% of air). It was found that the addition of 1% Air produces multiple plasma ‘bullets’ in the positive halfcycle of the excitation signal while in case of 1.5 % Air/He mixture plasma is much smaller in volume and with only few ‘bullets’ formed.

1. INTRODUCTION

Plasma jets are very useful plasma devices due to its simple design. These devices can be divided in two major groups by the type of the electrodes DFE Jet (Dielectric Free Electrode Jet) and DBD (Dielectric Barrier Plasma Jet) [1]. Various electrode configurations were investigated by numerous researchers [1-4]. The most common diagnostic technique for plasma jet analysis is fast time resolved iCCD imaging. Plasma propagation and development can be observed during the entire period of the excitation signal from the images taken by fast iCCD camera. In some cases fast plasma clusters (“plasma bullets”) can be observed. The velocities of the “bullets” are several kilometers per second [2]. Some researchers observed three plasma jet modes “chaotic”, “bullet” and “continuous” [5]. Each mode has a specific features. Formation of multiple plasma “bullets” were observed by S. Park et al in helium nitrogen mixture and they found that additional electrons originating from Penning ionization are playing important role in this phenomenon [6].

2. EXPERIMENTAL SETUP

Plasma jet used in this paper is consisted of the glass tube and two transparent electrodes. Inner diameter of the glass tube is 4 mm and outer diameter is 6 mm. The electrodes are made of the conductive foil made of indium tin oxide. The electrode width, gap between them and the distance of the powered electrode to edge of the glass tube is 15 mm. As a working gas we used

mixture of helium and synthetic Air. Percentage of Air in mixture is set to 1 and 1.5%. The flow rate was kept constant during all measurements at 3 slm. Powering system used in this experiment is consisted of a signal generator PeakTech 4025 and homemade power amplifier based on TDA7293 transistor and high voltage transformer. Voltage of the powering signal was 8 kV_{pp} and the power transmitted to the plasma was constant.

3. RESULTS AND DISCUSSION

Development and propagation of the plasma jet was investigated for two different concentration of Air in He by using fast iCCD camera. In figure 1. we present voltage-current signals with triggering positions for the 1% Air/He mixture. In figure 2 are presented images obtained in case of the 1%Air/He mixture and in figure 3. images for mixture 1.5%Air/He Time resolved images were obtained for the whole period of excitation signal (12.5 μ s) with the step between the successive images of 0.8 μ s. For the both cases exposure time was 2 ms, the gate width 25 ns and the gain 200.

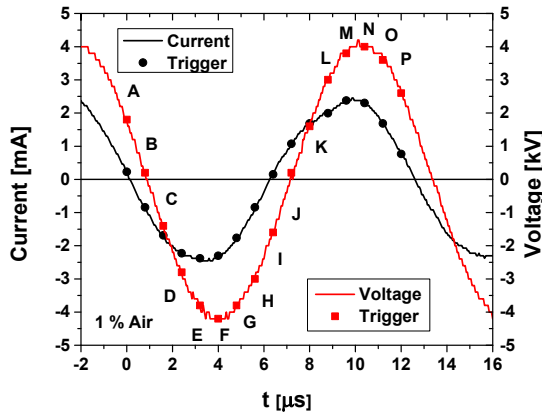


Figure 1. Voltage-current signals for the 1% Air/He plasma jet with triggering positions.

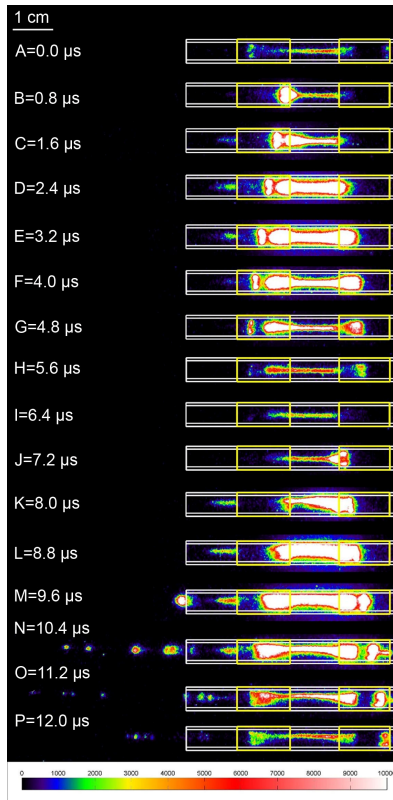


Figure 2. Time resolved images for the plasma jet at 3slm helium flow with 1% Air addition at power of 4W.

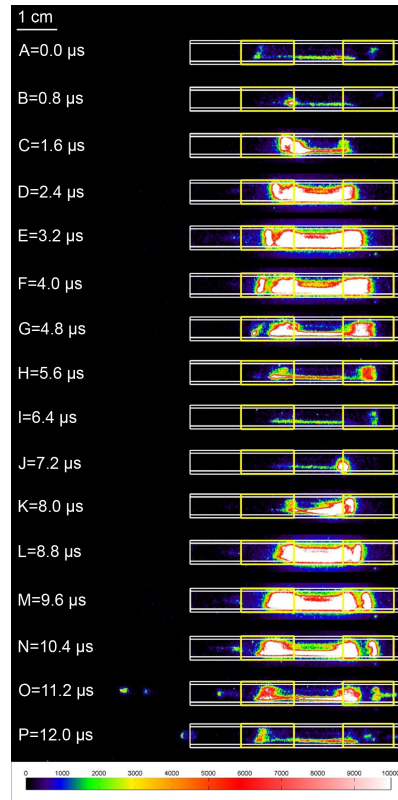


Figure 3. Time resolved images for the plasma jet at 3slm helium flow with 1.5% Air addition at power of 4W.

First we will discuss the 1% Air/He mixture case. Images from B ($0.8 \mu\text{s}$) to J ($7.2 \mu\text{s}$) are in negative and from K ($8.0 \mu\text{s}$) to A ($0.0 \mu\text{s}$) in positive halfcycle. We will start at point A ($0.0 \mu\text{s}$) when the voltage is still positive from the previous excitation period. At this point we have weak light emission between electrodes and inside the powered electrode. At the time point B ($0.8 \mu\text{s}$) new excitation period starts and the voltage is zero. Plasma is forming at the right edge of the powered electrode. The powered and grounded electrode are connected with the plasma channel through the whole excitation period. After the initial formation of the plasma in the powered electrode ionization front is moving towards the tube exit. The ionization front has a donut shape in the electrode region. After point J ($7.2 \mu\text{s}$) voltage rises and plasma starts to appear at the left edge of the grounded electrode. At point L ($8.8 \mu\text{s}$) plasma appears in the powered electrode which is different comparing to the pure helium plasma jet where there is no plasma inside the powered electrode in positive halfcycle [2]. Presence of Air promotes electron production due to Penning ionization inside

the discharge area. Higher concentration of electrons produces larger plasma and higher light emission. At the point M (9.6 μs) plasma “bullet” forms at the plasma jet nozzle. After initial “bullet” formation N (10.4 μs) four plasma clusters appear, similar like in Helium/Nitrogen mixture [6]. The distance between these clusters are around 10 mm and their size reduces as we go further from the jet nozzle. At points O (11.2 μs) and P (12.0 μs) outside the glass tube we have very weak emission.

The behavior of the plasma for the 1.5% of Air added to working gas is somewhat similar to the previous case. Plasma forms the channel between powered and grounded electrode throughout the whole excitation cycle. In the negative halfcycle plasma propagates only through the powered electrode and during the positive halfcycle there is propagation in both electrode region. Outside the glass tube there is almost no discharge. For our experimental parameters we could not produce plasma for the Air concentrations higher than 1.5%.

4. CONCLUSION

Small addition of the air into the working gas drastically changes the plasma jet development. Multiple plasma “bullet” are formed for the 1% of Air as a consequence of molecular reactions in the plasma. We observed up to four plasma “bullet” packages. Adding 1.5% of air totally disrupts the structure of the plasma jet, there is very weak plasma outside the glass tube. Further increase of Air percent in the gas mixture leads to total distinguishing of plasma.

Acknowledgements

This research has been supported by the Ministry of Education and Science, Serbia, under projects ON171037 and III41011.

REFERENCES

- [1] R. Zaplotnik, Z. Kregar, M. Bišćan, A. Vesel, U. Cvelbar, M. Mozetič and S. Milošević, *EPL*, 106, 25001 (2014).
- [2] N. Puač, D. Maletić, S. Lazović, G. Malović, A. Đorđević, and Z. Lj. Petrović, *Appl. Phys. Lett.* 101, 024103 (2012).
- [3] D. Maletić, N. Puač, N. Selaković, S. Lazović, G. Malović, A. Đorđević and Z. Lj. Petrović, *Plasma Sources Sci. Technol.* 24, 025006 (2015)
- [4] J. Shi, F. Zhong and J. Zhang, *Phys. Of Plasmas* 15, 013504 (2008).
- [5] J. L. Walsh, F. Iza, N. B. Janson, V. J. Law and M. G. Kong, *J. Phys. D: Appl. Phys.* 43, 075201 (2010).
- [6] S. Park, S. Youn Moon, and W. Choe, *Appl. Phys. Lett.* 103, 224105 (2013).

SHIFT OF HYDROGEN H_{β} SPECTRAL LINE MEASURED IN WALL STABILIZED ARC

Z. Mijatović, S. Djurović, I. Savić, L. Gavanski, T. Gajo and R. Kobilarov

*University of Novi Sad, Faculty of Sciences, Department of Physics,
Trg Dositeja Obradovića 4, 21000 Novi Sad, Serbia*

Abstract. The results of shifts of hydrogen H_{β} spectral line measurements are reported. The wall stabilized electric arc was used as a plasma source. Plasma was observed side-on, what enabled shift measurements since narrow and unshifted lines were emitted from peripheral regions of the arc column.

1. INTRODUCTION

Hydrogen spectral lines, particularly from Balmer series, have been the subject of examination in many theoretical and experimental works. Due to great number of papers, here will be cited references [1-3] where most of papers had been referred. The main attention was paid on H_{β} Balmer line because it was appeared as one of most reliable spectral line for plasma diagnostics purposes, especially for plasma electron density determination. Recently, interest for this line is again raised due to plasma diagnostics of laser induced plasmas (see for example [2]). The most of the papers has been devoted to theoretical calculation and experimental measurements of the shape of this line, relation between halfwidth and plasma electron density and various parameters related to asymmetry of this line. Only a few papers considered shift of this line, either theoretically [3, 4] or experimentally [5-7]. Here we report results of H_{β} line shift measurements in the plasma electron density range $(1.9 - 4.6) \cdot 10^{16} \text{ cm}^{-3}$, and plasma temperature of 11000 K.

2. EXPERIMENTAL

Wall stabilized electrical arcs used in these experiment were 5 and 6 mm in diameter. They were supplied with current stabilized power electrical source. Measurements were made for the currents between 22 and 32 A. Different diameters of used arcs enabled different plasma electron density values for the same currents. Plasma electron density range was $(1.9 - 4.6) \cdot 10^{16} \text{ cm}^{-3}$. Electron densities were determined from the halfwidths of H_{β} lines, accordingly to [1^b], recorded end-on for the same conditions as for recordings performed side-on.

From plasma composition data [8], temperature was determined to be 10300 - 11400 K.

Electrical arcs operated in argon under atmospheric pressure, while small amount of Ar/H₂ (96%:4%) mixture was introduced in the central part. Experimental setup is presented in Figure 1. Spectroscopic observations of plasma were done side-on. The central part of the arc column was focused on the entrance slit of 1-m spectrometer with 1200 g/mm grating. The ICCD (4.7×4.7 μm pixel size) camera was placed at the exit plane. The width of entrance slit was 30 μm what resulted in 0.04 nm instrumental halfwidth.

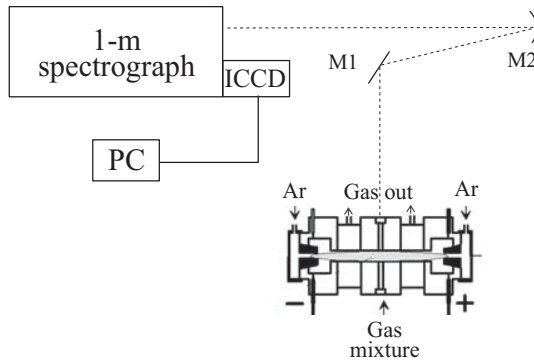


Figure 1. Experimental Set- up.

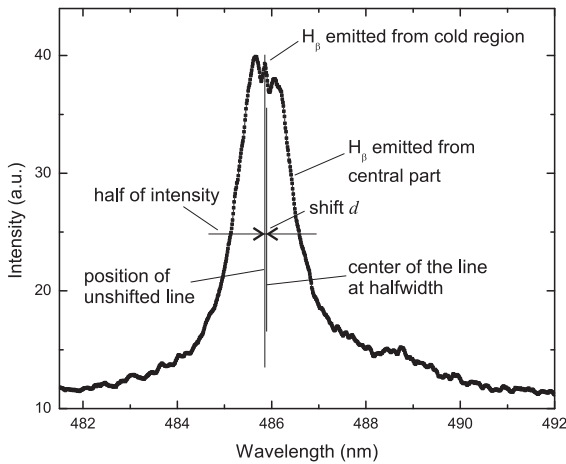


Figure 2. Recorded spectrum in H_β line spectral region

The shifted lines were emitted from the hot, central part of the arc columns. Plasma also spread into the region near the windows where it was cooled and emitted practically unshifted lines. Profiles emitted from that cold region were superimposed on profiles emitted from hot region and appeared as

small peaks in the central part of recorded spectra. Example of recorded spectrum in H_{β} line spectral region is presented in Figure 2.

3. RESULTS

The shifts were measured in relation to the peaks of H_{β} lines emitted from cold regions. In this region, of low plasma density, and low plasma temperature, H_{β} can be considered as unshifted. Obtained results, together with estimated errors are presented in Figure 3. The errors were estimated from uncertainty of determination of position of unshifted lines and uncertainty of position of shifted lines. As centers of shifted lines, central positions at HWHM were used. Here, we also present results of our previous measurements done using T-tube as a plasma source. Using this plasma source, plasma electron density in the range $(2.6 - 7.8) \cdot 10^{17} \text{ cm}^{-3}$ can be reached. Although plasma temperatures in these two sources are different, for shifts it is not so important since the main cause is electrical microfield in plasmas produced by electrons or ions, and not temperature [6]. Results from both measurements are presented in Figure 4. Full line is the best-fit line obtained from the shift measurements

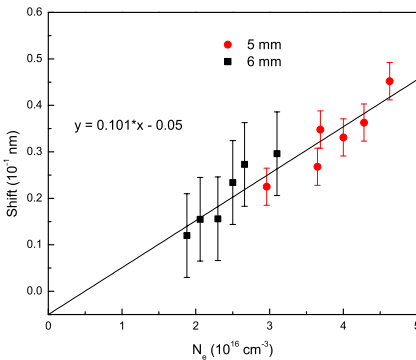


Figure 3. Shifts from the arcs.

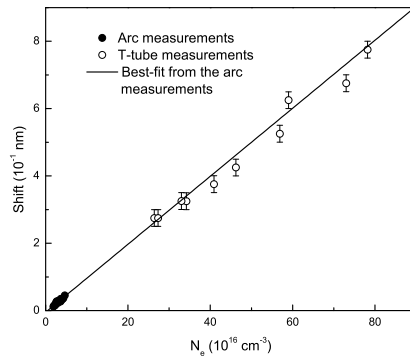


Figure 4. Shifts from the arcs and T-tube

using wall stabilized arc. For the results obtained from T-tube experiments, the value of shift for the lowest value of electron density is supposed to be the one predicted from the best-fit line. In that sense, results obtained from T-tube are continued on the results obtained from stabilized arc.

It should be stressed that theories [3,4], as well as consideration in [6] predict linear dependence of shifts on electron density. The theoretical values of shifts predicted by [3,4] are not included in Figure 3 because in [7] comparison between measured and theoretical values already commented.

As it can be seen from Figure 4, good agreement between two experiments of shift measurements can be found, considerably inside estimated experimental errors. It is important that these results were obtained from three plasma sources. Two of them are DC sources – wall stabilized arcs with internal

diameters of 5 and 6 mm and the pulsed source – T-tube. The difference in plasma electron density is about one order of magnitude.

Plasmas from wall stabilized arcs were observed side-on. Obtained results show good agreement with the linear dependence on electron density. For the measurements of the halfwidths of emitted spectral lines it is necessary to apply Abel inversion procedure. In presented shift measurements Abel inversion procedure was not applied. On the other hand, T-tube is known as radially homogeneous plasma source and Abel inversion procedure is not necessary to be applied, even for spectral lines halfwidth measurements. This implies that for shift measurements, along the radii, using plasma sources with similar radial temperature and electron density distribution profiles, Abel inversion procedure is not necessary. This could be important for LIBS and similar plasma sources when shift of H_{β} can be used for plasma density determination.

Acknowledgements

This work is financed by Serbian Ministry of Education, Science and Technological Development under the project OI 171014.

REFERENCES

- [1] H. R. Griem, *Plasma Spectroscopy*, (McGraw Hill, New York, 1964)^a; *Spectral Line Broadening by Plasmas*, (Academic Press, New York, 1974)^b; *Principles of Plasma Spectroscopy*, (Cambridge University Press, 1997)^c.
- [2] L. Pardini et al, *Spectrochimica Acta Part B* 88, 98 (2013).
- [3] H. R. Griem, *Phys. Rev. A* 28, 1596 (1983).
- [4] H. R. Griem, *Phys. Rev. A* 38, 2943 (1988).
- [5] W. L. Wiese, D. E. Kelleher and D. R. Paquette, *Phys. Rev. A* 6, 1132 (1972).
- [6] T. L. Pittman and D. E. Kelleher, in *Spectral Line Shapes*, ed. B. Wende, (De Gruyter, Berlin, 1981).
- [7] Z. Mijatović, M. Pavlov and S. Djurović, *Phys. Rev. A* 43, 6095 (1991).
- [8] C. H. Popenoe and J. B. Shumaker Jr., *J. Res. NBS, Phys. Chem.* 69A, 495 (1965).

OES DIAGNOSTICS OF PRE-BREAKDOWN LIGHT EMISSION IN COPLANAR APGD IN HELIUM

Z. Navrátil, T. Morávek, J. Čech and J. Ráhel'

*Department of Physical Electronics, Faculty of Science, Masaryk
University, Kotlářská 2, 611 37 Brno, Czech Republic*

Phase resolved photon counting was applied to record low-resolved optical spectra of pre-breakdown light emitted in coplanar barrier discharge in helium. Light emissions from species as OH^* , N_2^{+*} , He^* as well as thermoluminescence of Al_2O_3 ceramics were observed during the whole voltage period. Moreover, a light with continuum spectrum was observed shortly before the discharge breakdown. Assuming neutral bremsstrahlung as the origin of the continuum, electric field of 0.5-1 kV/cm was obtained in this discharge phase.

1. INTRODUCTION

Time evolution of light emission from helium APGD contains two intensity maxima corresponding to two current pulses occurring during the voltage period. Between these two maxima, light emission from excited species produced by metastables (as OH) can be observed [1]. Thermoluminescence of dielectric is another possible source of photons during this dark region [2]. Furthermore, a weak light wave travelling over the former cathode shortly before Townsend breakdown has been reported in coplanar helium APGD recently [3]. This light wave, probably analog to the known backward discharge of surface barrier discharge, appears, when the applied voltage is decreased and the electric field of the surface charge prevails. The light of this wave was observed about $20 \mu\text{s}$ before the current peak maximum. In this contribution, a photon counting was applied to measure the optical emission spectra of the observed pre-breakdown light in order to reveal the pre-breakdown light origin.

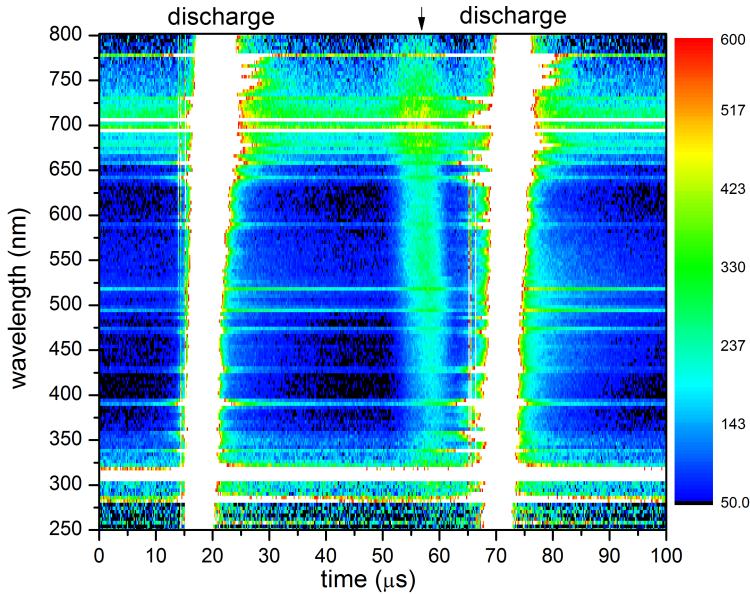


Figure 1. Light emission from coplanar barrier discharge in helium as a function of time and wavelength. Continuous-spectrum light emission is denoted with an arrow.

2. EXPERIMENTAL

The coplanar barrier discharge was generated above brass electrodes, with electrode gap set to 4.7 mm, immersed into insulation oil and covered by alumina dielectric plate (96% Al_2O_3 ; thickness 0.6 mm). The electrodes were placed into a small chamber equipped with a quartz window for optical diagnostics. Helium with purity 5.0 was flowing through the chamber at flow rate of 555 sccm, operating pressure was slightly above 1 atm. Discharge was driven by alternating voltage of frequency 9.4 kHz, generated with function generator (Agilent 33220A) and amplified to a high voltage signal with amplitude of 1.6 kV. UV/VIS photons from the discharge (250–800 nm), collected with a optical fibre located in front of the window, was first monochromatized (Jobin Yvon HR-640, grating 1200 gr/mm, used resolution 4 nm) and then counted by a single photon counter (Becker & Hickl SPC-150, PMT PMC-100-4). Using galvano controller card B&H GVD-120, the optical signal was correlated with the voltage signal; the time resolution was 0.2 μs . The measured spectra were corrected for instrument sensitivity using combined deuterium-halogen calibration lamp (AvaLight-DH-CAL).

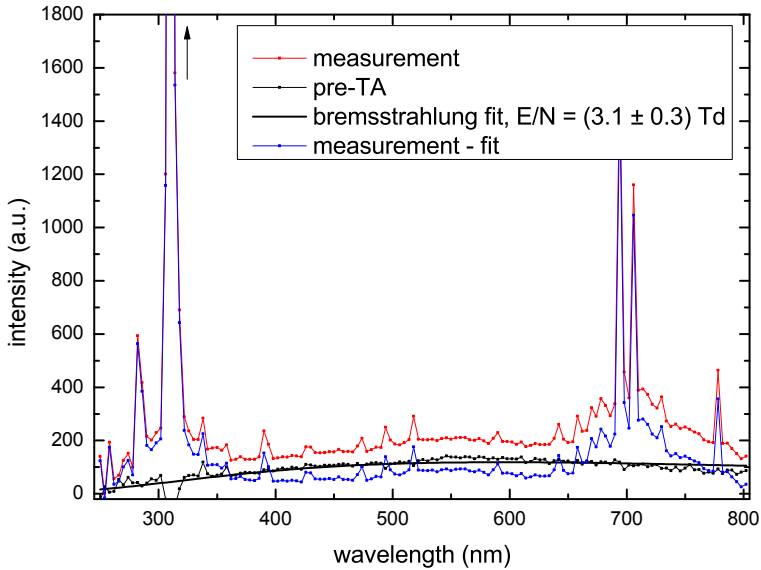


Figure 2. Spectrum of pre-breakdown light before Townsend avalanching. The extra-light emitted in this discharge phase is fitted with a model of neutral bremsstrahlung.

3.RESULTS

The phase-resolved optical spectra during one period of the coplanar barrier discharge in helium are displayed in Fig. 1. The color scale is chosen so that the low-level light emissions between the intensity maxima of two current peaks are visible. As can be seen in the figure, light emissions from species as OH^* (308 nm), N_2^{+*} (391 nm), He^* (706 nm) as well as thermoluminescence of Al_2O_3 ceramics (e.g. of Cr^{3+} at 695 nm) were observed during the whole voltage period. Moreover, a weak light with continuum spectrum was observed just during the time of pre-breakdown light wave [3] (denoted with an arrow in the plot). After that, the intensity is first decreased and then the light emission from Townsend avalanching is started. The measured spectrum, integrated over the duration of the pre-breakdown light emission (about 7 μs), is displayed in Fig. 2. The measured spectrum consists of long-lasting emissions (blue curve in Fig. 2) as well as of the continuous spectrum (black measured curve). This curve can be obtained by subtracting the intensity signal measured in earlier times. The continuum has a maximum at 550 nm. A possible origin of the continuum is neutral bremsstrahlung of electrons detached from the dielectric under low electric field. A fit of measured continuum with neutral bremsstrahlung model for helium provided electric field of 0.5-1 kV/cm in this discharge phase.

Acknowledgements: The work was supported by projects GA13-24635S of Czech Science Foundation, CZ.1.05/2.1.00/03.0086 and LO1411 (NPU I).

REFERENCES

- [1] Z. Navrátil *et al*, Plasma Sources Sci. Technol. 15, 8 (2006)
- [2] P. F. Ambrico *et al*, J. Phys. D. - Appl. Phys. 43, 325201 (2010)
- [3] T. Morávek *et al*, Eur. Phys. J. Appl. Phys., accepted 2016.

OPTICAL DIAGNOSTIC AND MODELING OF RF PLASMA DISCHARGES IN THE N₂ - Ar GAS MIXTURES

Sanja S. Pavlović¹, Vladimir M. Milosavljević^{2,3}, Patrick J. Cullen³
and Goran B. Poparić²

¹*Belgrade Polytechnic, Brankova 17, 11000 Belgrade, Serbia*

²*University of Belgrade, Faculty of Physics, Studentski trg 12, P.O. Box 44,
11000 Belgrade, Serbia*

³*Bio-plasma Research group, Dublin Institute of technology,
Dublin 1, Ireland*

Abstract. An optical diagnostic and an appropriate modeling of the radio frequency (RF) plasma discharges in N₂ - Ar gas mixtures have been conducted. A standard 13.56 MHz RF power supplier was employed with effective power value of 100 W. The optical diagnostic was conducted by measuring the relative intensities of Argon atomic spectral lines for several gas flow rates for N₂ and Ar gas mixtures used for plasma discharges. The modeling was included the simulations of RF plasma discharges and the estimations of relative intensities of Argon atomic spectral lines for different plasma conditions. The results of measurements and comparisons with the data obtained by calculation are presented in this work.

1. INTRODUCTION

The nitrogen molecule plays an important role in various aspects of technology and environmental physics. Nitrogen is also important for astrophysics, because it is found in the planetary atmospheres of Mars, Venus and also in the extraterrestrial space. Industrial physics use electron impact excitation and ionization of N₂ in many plasma and discharge technologies and applications. Diffuse discharge switches [1], plasma etching [2] and laser devices are based on these processes. In chemistry, processes in the plasma polymerization [3] and chemical detectors are related to the nitrogen molecule. Excitation and ionization of nitrogen are also important processes in various surface and coating technologies [4]. Plasma nitriding [5], a well-known surface hardening technique is related with gas mixtures where the presence of nitrogen is necessary. The argon gas also plays an important role in the nitrogen gas mixtures and in the above mentioned plasma technologies. Argon as a noble gas is very resistant to chemical reaction in plasma gas mixtures and very often serves as a buffer gas.

The argon atom is also very useful in plasma diagnostic due to sharp optical spectral lines in its optical spectrum.

2. EXPERIMENTAL SETUP

In order to perform an optical diagnostic of RF plasma discharges in the $N_2 - Ar$ gas mixtures we used the cylindrical 304 stainless steel chamber as a plasma chamber with a quartz view port at one of its side. The length of the cylinder is 400 mm and its diameter is 100 mm. In the center of the cylinder is an electrode from copper which diameter 6 mm. In order to control the gas mixture purity, a vacuum system with mass gas flow meters was used. The N_2 and Ar gases were introduced in the previously evacuated plasma's chamber by a vacuum pump, with controlled mass flows of the gases in order to achieve desired ratios in the gas mixtures. The high voltage RF generator was connected to the central electrode of the chamber, while the ground was connected to the outer body of the chamber. The standard 13.56 MHz frequency was applied for RF discharges. The pressure in gas mixtures was 1 mTorr and the voltage was 1200 V peak to peak. The power which was used during plasma discharges was in the range from 60 W to 100 W.

The optical system which enabled our optical measurements was consisted of a collimated lens, long optical path spectrometer with high resolution grating connected to a step-motor and a photomultiplier. The focusing lenses were adjusted to focus the spectral radiation of plasma discharges which took place at distance of 40 mm from the anode of the cylindrical tube system. High resolution optical spectrometer was used to record spectral lines from 300 to 790 nm. The resolution of recorded spectra was 0.01 nm, which was achieved by using a high resolution grating and long optical path of spectrometer of about 4 meters. The photomultiplier tube operated in continuous mode and the photoelectron current was measured for every angular position of grating with the spectra recorded using in-house software.

3. MODELING AND NUMERICAL SIMULATION

For the purpose of modeling the RF plasma discharges in $N_2 - Ar$ gas mixtures we used a Monte Carlo simulation. The simulation was developed earlier for RF plasma discharges in N_2 [6], and extended for $N_2 - Ar$ gas mixtures. The simulation follows the movement of electrons through gas mixtures in the conditions of the external RF electric field and allows all possible scattering processes to be happened. The probability of each possible scattering process was modeled in simulation by using its electron impact integral cross. The simulation includes the scoring of energies of tracked electrons which enabled us to obtain electron energy distribution functions (EEDFs) in the RF plasma discharges for different ratios of N_2 and Ar in the mixtures. By using the simulation generated EEDFs we determined rate coefficients for excitation of upper Ar electronic states which dominantly take part in optical emission spectra

during the RF plasma discharges. We used the determined rate coefficients for excitation of upper Ar electronic states and the probabilities of optical emissions into lower electronic states to estimate relative intensity of Ar optical spectral lines in the spectra.

4. RESULT AND DISCUSSION

The optical spectra of the RF plasma discharges in N₂ - Ar gas mixtures were measured at the various ratios of gases participation in the mixtures by tuning the gas flow rates. The optical measurements were performed in the spectral range from 300 nm to 795 nm. Beside argon atomic spectral lines, many nitrogen vibration spectral lines were observed in the spectra. For the purpose of diagnostics, we chose to analyze the relative intensities of the argon atomic spectral lines for different ratios of the participation of gases in the mixtures. The most intense argon atom spectral lines were chosen where spectral noise is the smallest thereby limiting the influence of experimental error. The chosen spectral lines had high energy of the upper atomic states, which enabled us to test the simulation obtained shape of tail region of electron energy distribution functions at different conditions of discharges. The chosen spectral lines are presented in table 1.

Table 1. Argon atom spectral lines chosen for plasma diagnostic.

| λ (nm) | Upper level | Energy of up. level (eV) | Rel. Intensity (NIST [7]) |
|----------------|--|--------------------------|---------------------------|
| 750.38 | $3s^23p^5(^2P^{\circ}_{1/2})4p\ 2[1/2]\ 0$ | 11.827 | 20000 |
| 751.46 | $3s^23p^5(^2P^{\circ}_{3/2})4p\ 2[1/2]\ 0$ | 11.623 | 15000 |
| 763.51 | $3s^23p^5(^2P^{\circ}_{3/2})4p\ 2[3/2]\ 2$ | 11.548 | 25000 |
| 772.42 | $3s^23p^5(^2P^{\circ}_{3/2})4p\ 2[1/2]\ 1$ | 11.723 | 10000 |

It is observed that the relative intensities of argon spectral lines in spectra were changed with changing the flow ratio of the N₂ - Ar gases in the gas mixtures. This changing of relative intensities of argon spectral lines in optical spectra could be explained by expected changing of shapes of electron energy distribution functions when different N₂ - Ar gas mixtures were used. This was just shown by comparing simulation obtained EEDFs for different N₂ - Ar gas mixtures.

In order to validate proposed modeling and numerical simulation we compared the relative intensity obtained experimentally and by the calculations. The relative intensities of argon atom spectral lines at flow ratio of (10/1.4) in the N₂ - Ar gas mixtures, which were experimentally obtained by optical measurements, are given in table 2. In the table are also shown calculated values of relative intensities. The values of relative intensities are normalized at the first of chosen lines to similar value in order to make the comparison easier. As can be seen from the table, a good agreement between experimentally obtained and calculated values was achieved. The difference is significant only for the spectral

line with the smallest intensity, where an influence of the spectral noise is not negligible.

It should be also noted that for some other flow ratios of N₂ and Ar in the gas mixtures the achieved agreements were less satisfied. It is possible that some other effects take part in RF discharges, such as non-radiative transfer of energy and an additional modeling have to be performed.

Table 2. Relative intensity of argon atom spectral lines at flow ratio of (10/1.4) in the in N₂ - Ar gas mixtures

| λ (nm) | Rel. Intensity | | Rel. difference |
|----------------|----------------|---------|-----------------|
| | Exp. | Calcul. | |
| 750.38 | 0.18 | 0.18 | 0 % |
| 751.46 | 0.30 | 0.27 | 10 % |
| 763.51 | 0.09 | 0.05 | 44 % |
| 772.42 | 0.56 | 0.54 | 3 % |

5. CONCLUSIONS

An optical diagnostic and modeling of radio frequency plasma discharges in the N₂ and Ar gas mixtures were performed in the work. Several gas ratios in mixtures of N₂ and Ar gases were analyzed. The optical diagnostic was conducted by measuring the relative intensities of Argon atomic spectral line emissions for different ratios of gases in the mixtures. The modeling included simulations of RF plasma discharges and numerical determination of relative intensities of Argon spectral lines. By comparing experimentally obtained data of relative intensities with those obtained by numerical calculations we partly verified proposed modeling, but disagreements at some values of gas ratio in the mixtures pointed out that an additional modeling is needed.

Acknowledgements

This work was supported in part by the Ministry of Education and Science of the Republic of Serbia by the Projects No. 171006 and No. 171016.

REFERENCES

- [1] S. R. Hunter and J. G. Carter, *J. Appl. Phys.* 58 3001 (1985).
- [2] W. Z. Collison, T. Q. Ni and, M. S. Barnes, *J. Vac. Sci. Technol. A* 16 100 (1998).
- [3] H. Yasuda and T. Hsu, *J. Polym. Sci.: Polym. Chem. Ed.* 15 81 (1977).
- [4] S. Gredelj, A. R. Gerson, S. Kumar, and G. P. Cavallaro, *Appl. Surf. Sci. A* 199, 183–194 (2002).
- [5] E. Guiberteau, G. Bonhomme, R. Hugon, and G. Henrion, *Surf. Coat. Technol.* 97, 552–556 (1997).
- [6] M. Popović, M. Aoneas, M. Vojnović, M. M. Ristić, M. D. Vičić and G. B. Poparić, *Physics of Plasmas* 21, 063504 (2014)
- [7] <http://physics.nist.gov/>

STARK HALFWIDTHS OF SOME SPECTRAL LINES OF IONIZED SILICON

I. Savić¹, L. Gavanski¹, M. T. Belmonte² and S. Djurović¹

¹*University of Novi Sad, Faculty of Sciences, Department of Physics,
Trg Dositeja Obradovića 4, 21000 Novi Sad, Serbia*

²*Universidad de Valladolid, Departamento de Física Teórica, Atómica y Óptica,
Paseo de Belén 7, E-47011 Valladolid, Spain*

Abstract. Experimental Stark halfwidths of some Si II and Si III spectral lines are presented in this paper. The spectral lines were emitted from a T-tube plasma with an electron density of $1.45 \times 10^{23} \text{ m}^{-3}$ and an electron temperature of 15000 K. The obtained experimental results were compared with available experimental results from other authors, as well as with some available theoretical Stark halfwidth results.

1. INTRODUCTION

In this paper, we report experimental results of Stark halfwidths (FWHM) for some spectral lines of singly and doubly ionized silicon. This work is an extension of a recent paper [1]. The silicon spectral lines can be of interest for both laboratory and astrophysical plasmas. In laboratory plasmas, silicon often appears as an impurity from the glass walls of the discharge tubes. As well as for plasma diagnostics, in the study of stellar plasmas, these data are used for the determination of chemical abundances of elements and the investigation of radiative transference through stellar atmospheres [2]. For this purpose, a huge amount of spectroscopic data is necessary.

2. EXPERIMENT

The plasma was produced in an electromagnetically driven T-tube with an internal diameter of 27 mm. The tube was filled with pure helium up to 300 Pa. A capacitor bank of 4 μF capacity, charged up to 20 kV, was used for the discharge through the T-tube. The spectroscopic data were collected by means of an ICCD camera. The camera was mounted on a 1-m spectrometer, with a 1200 g mm^{-1} grating and with inverse linear dispersion of 0.833 nm mm^{-1} . The silicon in the T-tube appeared as an impurity from the erosion of the glass walls.

The electron temperature of 15000 K was obtained from Boltzmann plot of 6 Si II lines, for which transition probability values and other necessary data

were taken from the NIST Atomic Spectra Database [3]. The estimated error is 11%. The electron density of $1.45 \times 10^{23} \text{ m}^{-3}$ was determined from the distance between the two peaks of the He I 447.148-nm line. For that purpose, we used the empirical formula from Ivković et al. [4]. The estimated error is 15%.

3. RESULTS

The results of the measured Stark halfwidths (FWHM) are presented in Table 1.

Table 1. Experimental Stark halfwidths of ionized silicon spectral lines are presented here. Both our halfwidth results and those from other authors are denoted as w_m , while theoretical results of Griem [13] are denoted as w_{GR} .

| Transition | Wav. (nm) | N_e (10^{23} m^{-3}) | T_e (K) | w_m (nm) | w_m/w_{OA} | w_m/w_{GR} | Ref |
|--|--------------|---------------------------------------|--------------|---------------|--------------|--------------|------|
| Si II | | | | | | | |
| 4p ² P _{1/2} - 4d ² D _{3/2} | 504.103 | 1.45 | 15000 | 0.362 | | 0.91 | TW |
| | | 1.00 | 10000 | 0.300 | 1.02 | 1.03 | [5] |
| | | 1.00 | 10000 | 0.350 | 0.87 | 1.21 | [6] |
| | | 1.00 | 10000 | 0.253 | 1.21 | 0.87 | [7] |
| | | 1.00 | 23000 | 0.390 | 0.52 | 1.46 | [8] |
| | | 1.00 | 16000 | 0.216 | 1.12 | 0.79 | [9] |
| | | 1.00 | 22000 | 0.208 | 0.99 | 0.78 | [9] |
| | | 0.98 | 35000 | 0.225 | 0.71 | 0.87 | [10] |
| | | 0.565 | 13900 | 0.140 | 1.05 | 0.85 | [11] |
| | | 0.662 | 16400 | 0.164 | 0.96 | 0.88 | [11] |
| | | 0.919 | 31500 | 0.205 | 0.77 | 0.84 | [11] |
| | | 1.00 | 16000 | 0.254 | 0.95 | 0.93 | [12] |
| | 1.00 | 20000 | 0.254 | 0.85 | 0.95 | [12] | |
| 3d ⁴ F ^o _{7/2} - 4p ⁴ D _{5/2} | 568.881 | 1.45 | 15000 | 0.121 | | | TW |
| 4p ³ D _{7/2} - 4d ³ F ^o _{9/2} | 520.241 | 1.45 | 15000 | 0.147 | | | TW |
| | | 1.00 | 16000 | 0.133 | 0.74 | | [12] |
| Si III | | | | | | | |
| 5p ¹ P ^o ₁ - 5d ¹ D ₂ | 761.236 | 1.45 | 15000 | 0.172 | | | TW |
| 4s ³ P ^o ₁ - 4p ³ P ₁ | 466.587 | 1.45 | 15000 | 0.131 | | | TW |

The first two columns in Table 1 contain the line transition and wavelength. The next two columns give the plasma conditions. In the column denoted as w_m , both our measured Stark halfwidths and the experimental ones obtained by other authors are given [5 - 12]. The estimated experimental errors for the halfwidth values measured in this experiment ranged between 15% and 30%. The sixth column contains a comparison between our results and those available from other authors (w_m/w_{OA}), while the seventh column gives the ratio between the experimental and the theoretical halfwidth values [13]. Some of the data are missing in [13].

We have analyzed in this paper lines of small intensity and those which are blended. The standard procedure of using the Voigt function [14] was employed in order to separate the Lorentzian and the Gaussian components of the spectral line halfwidths.

An example of the treatment of experimental data for part of the spectrum near the Si III 761.236 nm line is shown in Fig. 1. To get halfwidth value for this line, together with the deconvolution procedure, it was necessary to separate the profile of this line from the profile of Si III 380.654 nm line, which appears here in the second order of diffraction and the spectrum of which overlaps with the Si III 761.236 nm line.

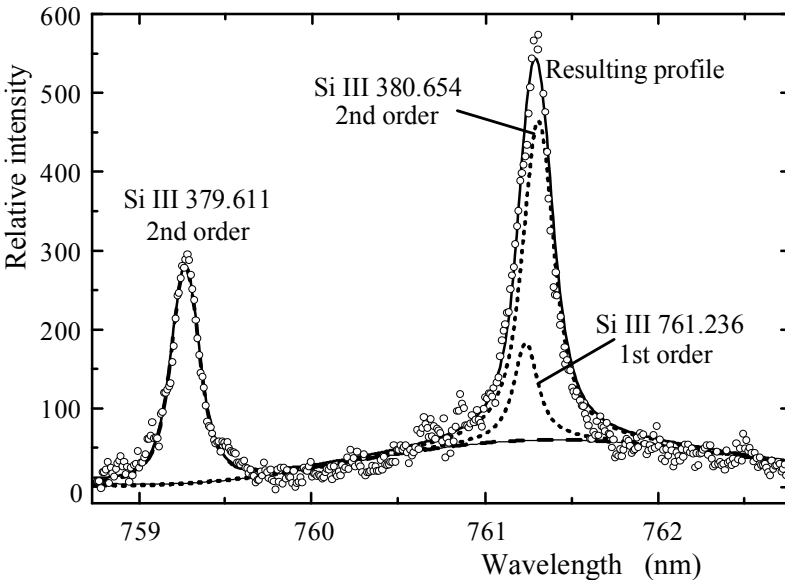


Figure 1. Part of the spectrum near the Si III 761.236 nm line.

A good agreement was found between our Stark halfwidth value and those from other authors [5, 6, 9-12] for the 504.103 nm line (see Table 1). The

w_m/w_{OA} ratio is between 0.71 and 1.12. Exceptions are the results from [7] and [8], where these ratios are 1.21 and 0.52. For the 520.241 nm line, the ratio between the presented value and the result from [12] is 0.74. In order to compare the results obtained under different plasma conditions, a linear dependence of the Stark halfwidths on electron density and temperature dependence, as $T^{-1/2}$, were used.

The agreement with the theory is also very good except for the result from [8], where w_m/w_{GR} is 1.46. For the other three lines, there are not any other available experimental or theoretical results.

Acknowledgements

This work was supported by the Ministry of Education, Science and Technological development of Republic Serbia, under Project 171014.

M. T. Belmonte thanks the University of Valladolid for her PhD scholarship.

REFERENCES

- [1] L. Gavanski, M. T. Belmonte, I. Savić and S. Djurović, *Month. Not. Roy. Astron. Soc.* 457, 4038 (2016).
- [2] M. S. Dimitrijević, *Astron. Astrophys. Trans.* 22, 389 (2003).
- [3] NIST Database: <http://physics.nist.gov/asd>
- [4] M. Ivković, M. Á. González, S. Jovičević, M. A. Gogosos, N. Konjević, *Spectrochim. Acta B* 65, 234 (2010).
- [5] M. H. Miller, University of Maryland, Technical Note BN-550 (1968).
- [6] A. Lesage and M. Miller, *C. R. Acad. Sci. Ser. B* 280, 645 (1975).
- [7] A. Lesage, S. Sahal-Brechot and M. H. Miller, *Phys. Rev. A* 16, 1617 (1977).
- [8] H. J. Kush and K. Schröder, *Astron. Astrophys.* 116, 255 (1982).
- [9] A. Lesage, B. A. Rathore, I. S. Lakičević and J. Purić, *Phys. Rev. A* 28, 2264 (1983).
- [10] C. Pérez, M. I. de la Rosa, A. M. de Frutos, V. R. Gonzalez and S. Mar, *Ann. Phys. (Paris)* 15, 115 (1990).
- [11] C. Pérez, I. de la Rosa, A. M. de Frutos and S. Mar, *Phys. Rev. E* 47, 756 (1993).
- [12] V. R. Gonzalez, J. A. Aparicio, J. A. del Val and S. Mar, *J. Phys. B: At. Mol. Opt. Phys.* 35, 3557 (2002).
- [13] H. R. Griem, *Spectral Line Broadening by Plasmas*, Academic Press, New York (1974).
- [14] J. T. Davies and J. M. Vaughan, *Astrophys. J.* 137, 1302 (1963).

SELF-ABSORPTION IN LASER INDUCED PLASMA

M. Skočić, M. Burger and S. Bukvić

University of Belgrade, Faculty of Physics, 11000 Belgrade, Serbia

Abstract. A simple analytical expression for self-absorption correction of a radially resolved spectrum is presented. Two spectra are recorded, F_2 recorded with a back mirror and F_1 recorded without. The corrected spectrum F_0 , free of self-absorption, is given by the simple expression. An example, illustrating proposed method for self-absorption correction is given in details.

1. Introduction

In typical arrangements spectroscopic observations of the laser induced plasma are accomplished side-on. In this way measured intensity represents 'integral value' of the light emission along the line of sight, see Fig.1. If an imaging CCD is applied as a detector, then one can measure simultaneously emission along numerous lines of the sight, each at different wavelength λ and offset y in respect to the axis of the plume. Set of intensities $F(\lambda, y)$ captured by the CCD is commonly called lateral profile. Within this paper we propose a simple way to correct lateral profiles affected by self-absorption applying 'back mirror' approach.

2. Self-absorption issues

When lateral profile $F(\lambda, y)$ is known, the emission function $\varepsilon(\lambda, r)$ can be evaluated by the inverse Abel transform [1], [2].

$$\varepsilon(\lambda, r) = -\frac{1}{\pi} \int_r^\infty \frac{dF(\lambda, y)}{dy} \frac{dy}{\sqrt{y^2 - r^2}} \quad (1)$$

If the plasma is not optically thin then recorded lateral profile $F(\lambda, y)$ is affected by self-absorption and inverse Abel transform is meaningless. Suitable approach to determine whether the plasma is free of self-absorption or not is based on use of duplicating or back mirror. The idea of the method

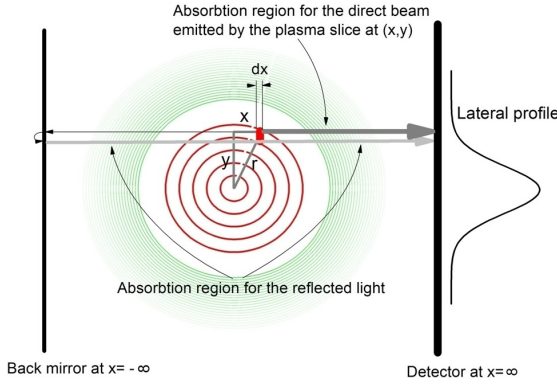


Figure 1. Concentric circles mimic radial emission function $\epsilon(r)$. For the purpose of simplicity emission area (red) and absorption area (green) are separated. With dark gray we indicate region of absorption for direct ray emitted by the plasma slice at (x, y) . With light gray is marked region of absorption for reflected beam.

is to record two images, $F_2(\lambda, y)$ with back mirror and $F_1(\lambda, y)$ without. In this manner reflected light is directed again through the plasma providing the way for estimating amount of self-absorption. In addition to the emission function $\epsilon(\lambda, r)$ we introduce axially symmetric absorption function, $k(\lambda, r)$, which is responsible for self-absorption. We consider amount of light originating from a plasma slice, having thickness dx and lying on the line of sight y at the position x , coming to the detector (Fig. 1)

$$dF_1 = e^{-\int_x^\infty k(\lambda, r) dx} \epsilon(\lambda, r) dx \quad (2)$$

If absorption is small ($\int_0^\infty k(\lambda, r) dx \ll 1$) self-absorption correction is possible, and above relation for measured intensity without back mirror $F_1(\lambda, y)$ simplifies to the following form:

$$F_1(\lambda, y) = F_0(\lambda, y) \left(1 - \int_0^\infty k(\lambda, r) dx \right) \quad (3)$$

Similarly, relation for measured intensity with back mirror in place is:

$$F_2(\lambda, y) = F_1(\lambda, y) + GF_1(\lambda, y) \left(1 - 2 \int_0^\infty k(\lambda, r) dx \right) \quad (4)$$

The value $G < 1$ quantifies reflected fraction of the light, taking in account reflectivity of the mirror, transmission of the lens, solid angle

etc. Relying on these equations one can evaluate corrected image F_0 which would be recorded by the detector in the case of negligible self-absorption.

$$F_0(\lambda, y) = \frac{2F_1(\lambda, y)}{1 + \frac{F_2(\lambda, y) - F_1(\lambda, y)}{GF_1(\lambda, y)}} \quad (5)$$

The term $\frac{F_2 - F_1}{GF_1}$ is in fact transmission. For optically thin plasma, $T = 1$, corrected image F_0 is equal to the image F_1 , recorded without back mirror. If self-absorption is present, intensity of the corrected image will be increased by a certain amount since $T < 1$.

3. Example

In Fig.2 we present two spectra recorded by the CCD camera, F_1 taken in usual way and F_2 recorded with back mirror. The corresponding FVB spectrum is presented in Fig.3 before and after correction. Tiny difference is caused by the self-absorption, in average about 0.02. Table 1 outlines values of the width and height for investigated lines after correction. One can notice that for Cu II 240.01 nm line self-absorption is negligible while for Cu II 240.33 nm width of the line is reduced for $\sim 5\%$ due to correction. More pronounced self-absorption in 240.33nm spectral line can be attributed to the significantly higher transition probability $A_{240.33} = 1 \times 10^8$ 1/s in respect to the $A_{240.01} = 0.078 \times 10^8$ 1/s.

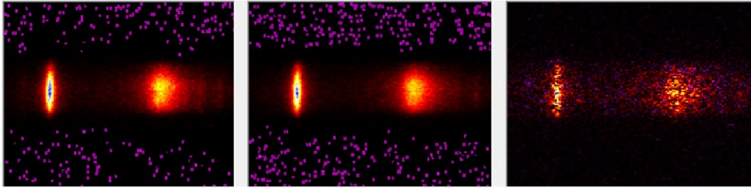


Figure 2. Cu II 240.01 nm and 240.33 nm spectral lines recorded without back mirror, the leftmost panel, and with the back mirror, the middle panel. The rightmost panel depicts a net effect of the back mirror; the picture is obtained subtracting the image recorded without back mirror from the one recorded with the back mirror.

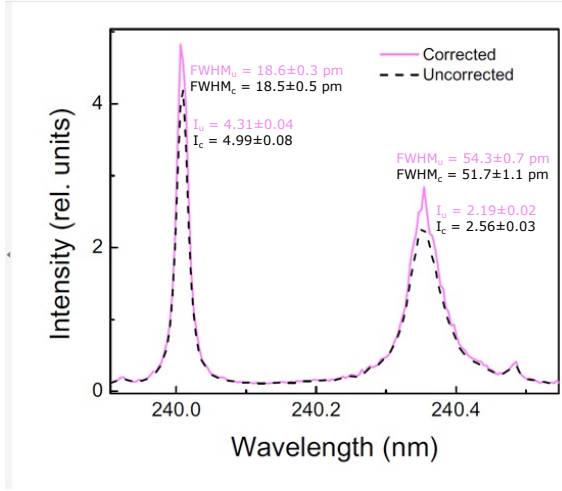


Figure 3. Spectrum of 240.01 nm and 240.33 nm Cu II spectral lines in FVB mode of the ICCD camera. With black we present uncorrected profiles, while corrected spectrum is plotted in light magenta.

Table 1. FWHM and Height of the lines are evaluated by fitting the line shapes to the Lorentzian profile (all coefficients free).

| Cu II 240.01 nm | | |
|-----------------|------------------|---------------------|
| | FWHM (pm) | Height (Rel. Units) |
| Uncorrected | 18.55 ± 0.26 | 4.306 ± 0.035 |
| Corrected | 18.50 ± 0.50 | 4.994 ± 0.078 |
| Cu II 240.33 nm | | |
| | FWHM (pm) | Height (Rel. Units) |
| Uncorrected | 54.32 ± 0.7 | 2.190 ± 0.016 |
| Corrected | 51.72 ± 1.1 | 2.559 ± 0.030 |

Acknowledgements

This work is part of the Determination of atomic parameters on the basis of spectral line profiles (ON 171008) project supported by the Ministry of Education and Science of the Republic of Serbia.

REFERENCES

- [1] R. N. Bracewell, McGraw-Hill, New York, (1978).
- [2] Lj.M. Ignjatović, A.A. Mihajlov, JQSRT 72 677-689 (2002)
- [3] M. Burger, M. Skočić, S. Bukvić, Spectrochimica Acta Part B 101 51-56 (2014)

MASS SPECTRA ANALYSIS OF RF NITROGEN PLASMA FOR FUNCTIONALIZATION OF CARBON NANOSTRUCTURES

Ilija Stefanović^{1,3}, Vladimir Stojanović², Jasmina Jovanović⁴, Cedric Pattyn¹,
Shahzad Hussain¹, Eva Kovačević¹ and Johannes Berndt¹

¹*GREMI UMR 7344 CNRS & Université d'Orléan, 45067 Orléans Cedex 2,
France*

²*Institute of Physics Belgrade, University of Belgrade, 11001 Belgrade, Serbia*

³*Faculty for Strategic and Operational Management,
University Union-Nikola Tesla, 11070, Belgrade, Serbia*

⁴*Faculty of Mechanical Engineering, University of Belgrade,
Kraljice Marije 16, 11000 Belgrade, Serbia*

Abstract. Low pressure (0.1 - 0.2 mbar) capacitively-coupled RF nitrogen plasma is used for plasma functionalization of carbon nanotubes. To optimize the functionalization, the samples are exposed at different distances (0 - 93 mm) from plasma source. To analyze the active species, the mass spectrometry is done at same positions. On short distances the majority of ion flux consists of N_2^+ ions. However, the large flux of N_2H^+ , H_2O^+ and H_3O^+ is detected too, which originate from relatively small amount of impurities. The possible ion-molecule reactions responsible for the detected ion fluxes are analyzed.

1. INTRODUCTION

The functionalized carbon nanotubes (CNTs) are used in biotechnology for creating bio-nanocomposites [1], in particular for fabricating components for biosensors [2]. The functionalization of CNTs with nitrogen containing functional groups is used to create chemical (covalent) binding with polymers [1]. Low-temperature nitrogen plasmas provide an important alternative way to functionalize CNTs with nitrogen [3].

In order to get the optimal parameters for low-temperature plasma polymerization the diagnosis and control of plasma properties is necessary [4]. Recently, it is shown for radiofrequency (RF) oxygen plasma that significant amount of impurity ions, especially water cluster ions, contribute to the total ion flux upon the distance of the mass spectrometer sampling orifice and plasma source [5]. The presence of impurity ions can, in some cases, help to improve functionalization of CNTs. Here, we will present the results of ion mass spectra of RF nitrogen plasma upon the different distances to plasma source. By

analyzing ion -molecule reactions in the reactor it is possible to explain the change of ion spectra from “nitrogen dominated” (near to the plasma source) to the “impurity dominated” (far away from the plasma source). These results will be correlated with the material analysis of CNTs functionalized at the same positions.

2. EXPERIMENT

Experimental set-up consists of discharge chamber equipped with vacuum system, providing the basic pressure of $5 - 7 \times 10^{-8}$ mbar. The system of mass flow controllers and valves ensures the continuous flow of gas mixture and the working pressure. RF power in the range of 3 W to 15 W is capacitively coupled to the discharge by using matching network. Plasma properties can be monitored with different diagnostic techniques, including infrared absorption spectroscopy, microwave interferometry, emission spectroscopy and electric probe. Here, we use mass spectrometer equipped with energy analyzer that is mounted on the mechanical rail and can be traveled to and from the plasma. The mass spectrometer is mounted perpendicular to the discharge axis and supplies the information about different neutral and ionic species, as well as ion energy distributions at different distances from the plasma source. The details on experimental set-up and procedure can be found in the literature [5].

3. EXPERIMENTAL RESULTS

Table 1. Total ion fluxes for different ions for two distances between the plasma and the sampling orifice. Discharge conditions are: pressure $p = 0.1$ mbar, electric power $P = 4$ W, working gas N_2 , flow - rate 50 sccm.

| <i>distance</i> (cm) | N_2^+ (c/s) | H_2O^+ (c/s) | $H(H_2O)^+$ (c/s) |
|----------------------|-------------------|-------------------|-------------------|
| 0 | $3.40 \cdot 10^7$ | $2.93 \cdot 10^7$ | $3.40 \cdot 10^7$ |
| 9.3 | 1340 | $1.33 \cdot 10^6$ | $1.59 \cdot 10^5$ |

Energy resolved ion distributions of some relevant positive ions are measured for different distances between sampling orifice of mass spectrometer and plasma. Energy resolved ion fluxes of specific ions are integrated over measured energy range to obtain the total ion fluxes, which are listed in Table 1. In addition, fluxes of N^+ , N_3^+ , N_4^+ , N_2H^+ , NO^+ , OH^+ , and ion clusters of water molecules $H^+(H_2O)_n$, ($n = 2, 3$) are also detected (not presented here).

As expected, close to the plasma the most prominent ion is N_2^+ . Nevertheless, even the abundance of water impurities are very low in comparison to the working gas (nitrogen) the flux of water ions and protonized water ions $H^+(H_2O)$ is very high and close to the flux of N_2^+ ion.

The relative ion contributions are dramatically changed with the distance. At 9.3 cm distance, the molecular nitrogen ions disappear, leaving the H_2O^+ as the most dominant constituent of the positive ion flux.

4. CHARGED PARTICLES TRANSPORT

It is obvious that change of mass spectra is induced by various ion reactions that occur during the travel of ions between plasma and the sampling orifice. It is why is necessary to analyze the ion transport processes in the presence of impurities. The first step is to select the proper set of cross sections for N_2^+ , N_2H^+ , H_2O^+ , H_3O^+ and NO^+ scattering on H_2O molecule. In this work we present assessed cross section set for scattering of N_2^+ on H_2O as probably most relevant for production of N_2H^+ impurity ions detected in our system.

Since only a few measurements of the cross sections exist for selected system we used Denpoh-Nanbu theory [6] to resolve between elastic and reactive cross sections assuming induced and permanent dipole interaction [7-9]. In Table 2 we show most probable reactions, based on thermo chemical values [10]. At hyperthermal collision energies, intermediate collision complex become too short-lived and thus measurements of Dressler *et al.*[6] (EXP, see Fig. 1) were included to cover that energy range. Rate constant for charge transfer reaction selected in Ref. [11] ($k=1.8 \cdot 10^{-9} \text{ cm}^3/\text{s}$ at 300 K) is in agreement with value calculated from charge transfer cross section presented in Fig. 1. If cross section for N_2H^+ production is extrapolated to low energies with the same trend as charge transfer cross section we obtained about 2.3 times lower rate constant at 300 K than suggested in Ref. [11].

Our preliminary Monte Carlo calculations [12] of transport parameters show that non conservative collisions strongly affect transport of N_2^+ in H_2O not only by producing N_2H^+ but also in significant variation of transport parameters in whole range of reduced electric field values [13].

Table 2. N_2^+ - H_2O reaction products and the corresponding thermodynamic threshold energies Δ .

| No | products | Δ (eV) |
|------|---------------------|---------------|
| P1 | $N_2^+ + H_2O$ (EL) | 0 |
| EXO1 | $H_2O^+ + N_2$ | 2.999 |
| EXO2 | $N_2H^+ + OH$ | 1.974 |
| P2 | $N_2^+ + H_2 + O$ | -5.059 |
| P3 | $N_2^+ + OH + H$ | -5.113 |
| P4 | $N_2^+ + O + 2H$ | -9.536 |
| P5 | $H_2O^+ + 2N$ | -6.799 |
| P6 | $N^+ + N + H_2O$ | -8.751 |
| P7 | $H_2^+ + O + N_2$ | -4.903 |
| P8 | $O^+ + H_2 + N_2$ | -3.096 |
| P9 | $H^+ + H + O + N_2$ | -7.553 |
| P10 | $NO^+ + H_2 + N$ | -1.999 |
| P11 | $N_2O^+ + H_2$ | -10.58 |

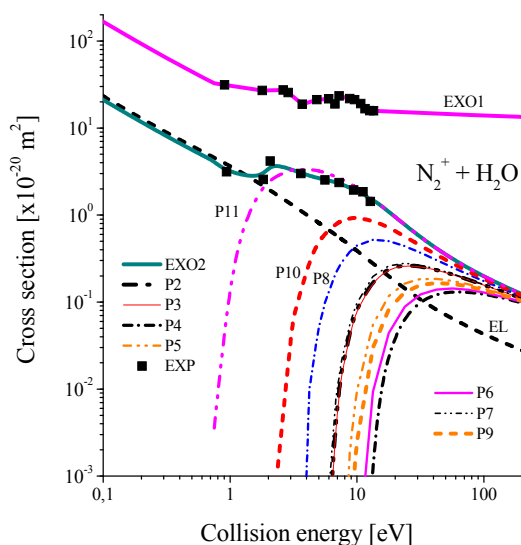


Figure 1. Cross section set for $N_2^+ + H_2O$ reaction as a function of collision energy. EL-the elastic momentum transfer cross section, EXOx- xth exothermic and Py-yth endothermic cross section (see Table 2).

Acknowledgements

Results obtained in the Institute of Physics University of Belgrade under the auspices of the Ministry of Education, Science and Technology, Project No. 171037. GREMI&Université d'Orléan are supported by Region Centre, France, through projects APR IR Capt'Eau and APRIR MEPS Flexible.

REFERENCES

- [1] L. Nagy, *et al*, Current Protein and Peptide Science, 15, 363 (2014).
- [2] A. Matsumoto and Y. Miyahara, Nanoscale, 5, 10702 (2013).
- [3] B. Khare, P. Wilhite, B. Tran, *et al*, J. Phys. Chem. B, 109, 23466 (2005).
- [4] K. Spasić, N. Škoro, *et al*, 32nd ICPIG P. 2.51 (2015) ; K. Spasić, N. Škoro, *et al*, 42nd IEEE Conf. Plasma Sci.(ICOPS) P. 2B-4 (2015).
- [5] I. Stefanović, V. Stojanović *et al* J. Phys. D: Appl. Phys. 49 265202 (2016).
- [6] K. Denpoh and K. Nanbu, J. Vac. Sci. Technol. A 16 (3), 1201(1998).
- [7] D.C. Clary, Chem. Phys. Lett. 232 267 (1995).
- [8] S. G. Lias *et al* J. Phys. Chem. Ref. Data, Supl. 1 Vol. 17, 1 (1988).
- [9] V. Stojanović, Z. Raspopović, *et al*, Eur. Phys. J. D 69, 63 (2015).
- [10] R.A. Dressler *et al* J.Chem.Phys., 92, 1117-1125 (1990).
- [11] L. W. Sieck *et al*, Plasma Chem. and Plasma Proc., 20, 235 (2000).
- [12] Z. Ristivojević and Z. Lj. Petrović, PSST 21, 035001 (2012).
- [13] R.E. Robson, R.D. White and Z. Lj.Petrović, Rev. Mod. Phys. 77 (2005) 1303.

CHARACTERIZATION OF AN ATMOSPHERIC PRESSURE PULSED MICROJET

M. Vinic¹, B. Stankov¹, M. Ivkovic¹ and N. Konjevic²

¹*Institute of Physics, University of Belgrade, Belgrade, Serbia*

²*Faculty of Physics, University of Belgrade, Belgrade, Serbia*

Abstract. The results of an experimental study of atmospheric pressure pulsed microjets in helium and gas mixture are presented. The images of plasma jet propagation were recorded and emission spectra from glass discharge tube and plasma jet were analyzed and compared. From helium spectral lines electron density was calculated for several different configurations of discharge source. Temporal dependence of electron density was determined. The influence of various capacitors and discharge voltages on plasma jet emission and propagation were studied also.

1. INTRODUCTION

Atmospheric pressure He microdischarges have many different configuration and many applications. Most of them are constructed in order to obtain cold plasmas for medical and plasma chemical applications. It can be used for cleaning, decontamination, etching, or coating surfaces at atmospheric pressure and low temperature. [1] One reason for why plasma jets are advantageous is because even though the electrons are hot, the overall gas is at room temperature. Another important advantage of using atmospheric plasmas is the possibility to process materials which are not resistant to vacuum. [2,3] The main disadvantage of such microdischarges is high consumption of He.

Here, we present attempt to construct and characterize low flow atmospheric pressure He single pulse plasma microjet.

2. EXPERIMENT

Schematic sketch of pulsed atmospheric pressure plasma jet is shown in Figure 1a. The experimental setup consists of microjet, focusing optic, radiation intensity detection system (imaging spectrometer equipped with ICCD camera), computer and electronics system for synchronization, detector gating and spectrum storage, Figure 1b:

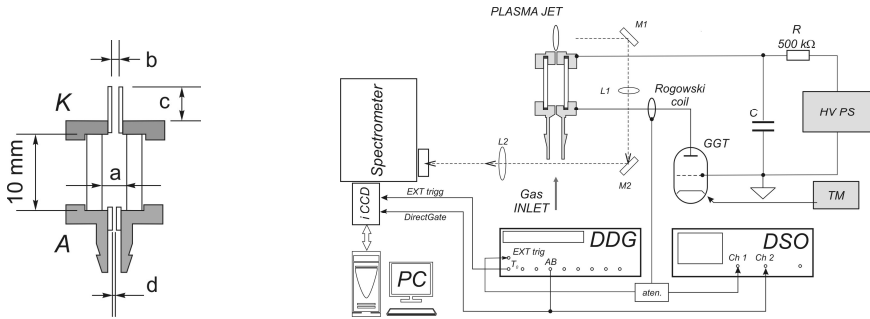


Figure 1. a) Microjet; b) Experimental setup.

Light emitted from microjet was focused by the use of lens L₁ having focal length of 32 cm. For the recordings of plasma jet images an additional lens L₂ was used having focal length of 17 cm.

Plasma image was projected on the 20 μm wide entrance slit of the 0.3 m imaging spectrometer Andor Shamrock 303, equipped with ICCD camera. The camera gating was performed with digital delay generator (DDG) by processing signal from Rogowsky coil which was used for current pulse measurements. The spectra were recorded at different delay times in respect to beginning of current pulse monitored by digital storage oscilloscope (DSO). The fast pulse discharge is driven by a different capacitors - C, charged with high voltage power supply - HV PS.

In microjet gas is fed through a hole in center of lower electrode (d), with passage trough glass tube and output through hole in an upper electrode (b) see Fig. 1a. Glass tubes with various inner diameters were used (a). In some cases, stainless steel tubes (SST) of different lengths were placed in upper hole (c), Table 1.

Table 1. List of different configurations of microjet.

| label | MJ1 | MJ2 | MJ3 | MJ4 | MJ5 | MJ6 | MJ7 | MJ8 | MJ9 | MJ10 | MJ11 | MJ12 |
|--------|------|------|------|------|------|------|------|------|------|------|------|------|
| a [mm] | 4 | 4 | 4 | 4 | 4 | 4 | 2 | 2 | 1 | 1 | 1 | 2 |
| b [mm] | 0.50 | 0.70 | 0.70 | 0.70 | 0.70 | 0.45 | 0.70 | 0.45 | 0.70 | 0.70 | 0.45 | 0.5 |
| c [mm] | 0 | 6 | 15 | 0 | 6 | 6 | 6 | 6 | 0 | 6 | 6 | 0 |
| d [mm] | 0.50 | 0.10 | 0.10 | 0.35 | 0.35 | 0.35 | 0.35 | 0.35 | 0.35 | 0.35 | 0.35 | 0.35 |

First step of our experiment was to record plasma images. After analyzing images, next step was to record spectrum of main discharge and plasma jet area. Helium and gas mixture (He with 1.5% CO₂ and 1.5% N₂) were used as carrier gasses. For the electron density determination we used the separation between allowed and forbidden component of He I 447.1 nm line [4].

3. RESULTS AND DISCUSION

Due to an insufficient space in this publication we show only several results out of large number of images and spectra recordings.

Images of jet propagation were recorded, see example in Figure 2. First image depicts emission from discharge tube and plasma jet. In order to record images of jet, emission from discharge tube was blocked. It was discovered that jet appears 1 μ s after beginning of discharge current, reaches maximum intensity at 2.5 μ s and lasts until 14 μ s. Based on these observations time and spatial position of subsequent measurements were selected. Another result from images appeared - in this type of discharge there is no plasma propagation, i.e. plasma stays in contact with upper electrode.

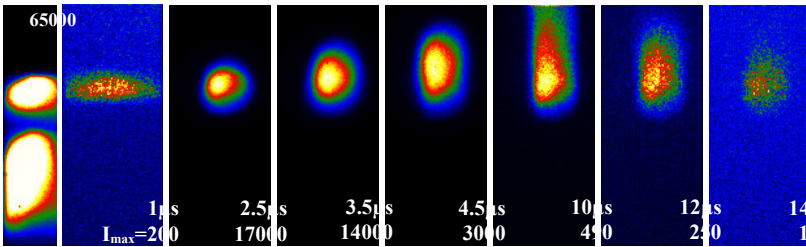


Figure 2. Images of jet evolvment. Each image is normalized to max light intensity.

In order to obtain aperiodic waveform of discharge current the resistor (0.4 Ω) connected in series with discharge was used. Figure 3 illustrates different current waveforms depending on used capacitor and applied voltage:

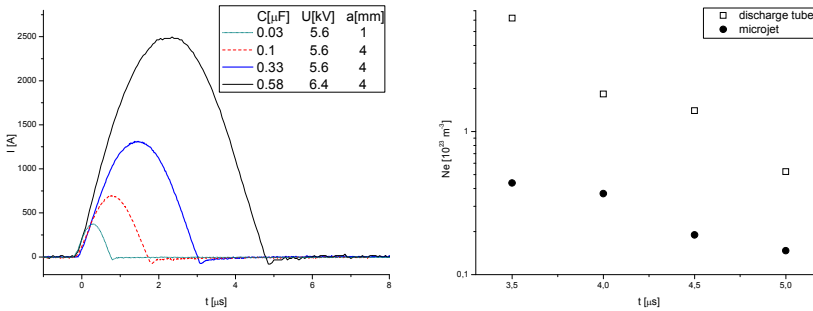


Figure 3. a) Current waveform depending of C and U; b) Temporal dependence of electron density for discharge tube and microjet (MJ12), C=0.33 μ F, U=3.6 kV.

Temporal dependence of Ne for microjet without SST is shown in Figure 3b. Strong continuum obstructed estimation of Ne at the beginning of discharge so first evaluated Ne value is at 3.5 μ s. At that moment, electron density in discharge tube is $6.2 \cdot 10^{23} \text{ m}^{-3}$, while Ne in jet is $4.4 \cdot 10^{22} \text{ m}^{-3}$.

The distinction between spectra from discharge tube and jet is shown in Figure 4a.

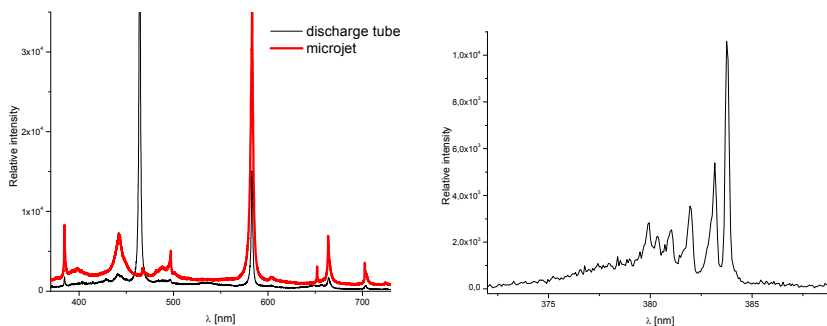


Figure 4. a) Comparison of spectra from discharge tube and microjet (MJ1), $C=0.33 \mu\text{F}$, $U=5.6 \text{ kV}$; b) N_2^+ FNS (MJ8), $C=0.33 \mu\text{F}$, $U= 5.6 \text{ kV}$.

Molecular bands of N_2 were detected in spectra when gas mixture was used as carrier gas, see Figure 4b. This is an indication that plasma jet temperature is low.

Acknowledgements

This work was financed by the Ministry of Education, Science and Technological Development of the Republic of Serbia under Project OI 171014 and TR 37019.

REFERENCES

- [1] M. Wolter, S. Bornholdt, M. Häckel, H. Kersten, *Journal of Achievements in Materials and Manufacturing Engineering* 37, 730 (2009)
- [2] Peter Bruggeman, Ronny Brandenburg, *J. Phys. D: Appl. Phys.* 46, 28 (2013)
- [3] M. Laroussi, T. Akan, *Plasma Process. Polym.* 4, 777 (2007)
- [4] M. Ivkovic, M.A. Gonzalez, S. Jovicevic, M.A. Gigosos, N. Konjevic, *Spectrochimica Acta Part B* 65, 234 (2010)

STATE-TO-STATE AND COLLISIONAL-RADIATIVE MODELING OF THE CO₂-N₂-Ar PLASMA CHEMISTRY FOR THE EXOMARS MISSION

Julien Annaloro¹ and Arnaud Bultel²

¹*CNES, 18 avenue Edouard Belin, 31401 Toulouse cedex 9, FRANCE*

²*CORIA UMR 6614 – CNRS, Université et INSA de Rouen, Campus universitaire du Madrillet, 76800 Saint-Etienne du Rouvray, FRANCE*

Abstract. The CoRaM-MARS collisional-radiative model has been elaborated to provide detailed information on the behavior of CO₂-N₂-Ar mixtures out of equilibrium. This model is based on a state-to-state description of the 21 different species taken into account and on a complete database of elementary processes. This model is applied to the Martian atmospheric entry conditions of the current Exomars mission.

1. INTRODUCTION

The correct modeling of the chemistry of plasmas produced during the atmospheric entry of a spacecraft requires the development of a state-to-state approach since the Local Thermodynamic Equilibrium (LTE) is not fulfilled [1]. This departure from LTE does not occur only in the shock layer developed in front of the spacecraft therefore in dissociation – ionization conditions. This departure also takes place in recombination situation, within the wake flow in the vicinity of the spacecraft's afterbody. The excited states departing from Boltzmann equilibrium with the ground states, the correct estimate of their population number density requires to consider each one as an independent variable and to treat the related number density as a full species driven by the corresponding conservation equation.

The next entry into the Martian atmosphere of the Schiaparelli module of the Exomars mission will take place October 19, 2016. This mission is driven by the European Space Agency (ESA). The role of the French National Space Agency CNES was to prepare several instruments of the spacecraft and to study the different phases of the atmospheric entry in collaboration with the ESA in the global framework of the sizing of the module [2]. Another interesting contribution of the CNES was also to implement couples of radiometers on the back shield. Observing two spectral regions located in the infrared ([2.6, 3.3] μm and [4.2, 5] μm), each set of radiometers will be used to reach the following objectives (1) the

determination of the radiative part of the total flux observed on the back shield and (2) an indirect estimate of the dissociation degree of the recombining plasma. Since the spectral windows correspond to radiation emitted by deexcitation of CO(X) and CO₂(X) vibrational states, the LTE departure requires to use a numerical tool able to provide relevant information on the vibrational ground states number density. The estimate of the dissociation degree will then be deduced.

The numerical tool is the collisional-radiative model CoRaM-MARS [3]. In the present communication, the model is quickly described. Calculations are reported in dissociation – ionization and recombination situations representative of the upstream shock layer and the downstream afterbody flow.

2. PHYSICAL MODEL

The collisional-radiative model CoRaM-MARS takes into account the species CO₂, N₂, C₂, O₂, CO, CN, NO, C, N, O, Ar, N₂⁺, C₂⁺, O₂⁺, CO⁺, CN⁺, NO⁺, C⁺, N⁺, O⁺, Ar⁺ on their main excited states [6]. In our state-to-state model, it is important to note that CO₂ on its ground electronic state can be vibrationally excited among 14 lower states (v₁,v₂,v₃) with a vibrational energy lower than 0.8 eV and among 106 states (i00,0j0,00k) with a vibrational energy higher than 0.8 eV. With this energy diagram, two important asymptotic behaviors are respected. At low vibrational excitation, the whole vibrationally dependent chemistry identified by Blauer and Nickerson [4] and Herzfeld and co-workers [5] can be used. At high vibrational excitation, considering only one-mode excitation is enough to match the order of magnitude of the global dissociation rate coefficient of CO₂ [6]. As far as we know, this approach is the more detailed among those reported in the literature. The electronic excited states are considered in vibrational equilibrium with electrons at the temperature T_e. The rotational energy storage mode is assumed at equilibrium with the heavy particles translation at the temperature T_A.

The collisional elementary processes leading to changes in the population number density are due to electron and heavy particle induced collisions. Vibrational and electronic excitation, dissociation, ionization, charge and neutral exchanges, dissociative recombination and the corresponding backward elementary processes are taken into account. The main radiative molecular systems and the spontaneous emission of atoms and atomic ions are also considered using escape factors to limit the radiative losses resulting from self-absorption. Finally, the radiative recombination is also implemented in the model. This complete set of elementary processes requires the treatment of almost 10⁶ rate coefficients and Einstein coefficients. Due to this high number, CoRaM-MARS has not been yet fully implemented in a computational fluid dynamics code. Relaxations in steady pressure and temperature conditions have been calculated.

3. RESULTS

The results reported hereafter have been obtained in the typical Martian entry conditions of the next Exomars mission corresponding to the elapsed time $t = 94$ s of the “cold steep trajectory” (capsule speed 3.84 km s^{-1} , upstream conditions $\rho_\infty = 11.86 \times 10^{-4} \text{ kg m}^{-3}$, $T_\infty = 155.3 \text{ K}$, $p_\infty = 35.28 \text{ Pa}$) [7]. For the dissociation – ionization flow within the shock layer, we have considered that the relaxation of the mixture occurs at $T_A = T_e = 7000 \text{ K}$ and $p = 10,000 \text{ Pa}$ close to the results of the Rankine-Hugoniot type assuming a frozen chemistry from the upstream conditions. Figure 1 illustrates in these conditions the evolution in time of the composition of a fluid particle moving from the shock front.

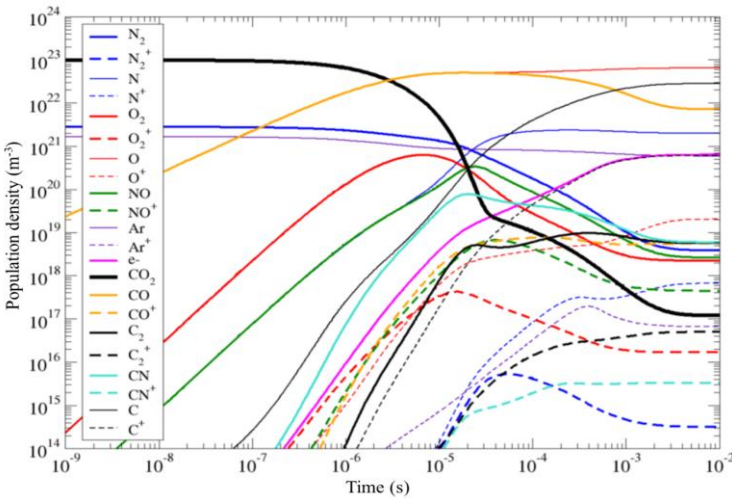


Figure 1. Temporal evolution of the population density of the species in typical dissociation – ionization conditions of the Exomars type at $T_A = T_e = 7000 \text{ K}$ and $p = 10,000 \text{ Pa}$.

We can note the strong dissociation of the CO_2 molecules whose population density collapses and the resulting formation of CO and O . The ionization degree reached at the final state is about 1 % which is lower than that observed in similar conditions in pure diatomic mixtures such as $\text{N}_2\text{-O}_2\text{-Ar}$ (Earth atmosphere), for instance. This is the direct result of the three vibrational modes of CO_2 whose excitation requires a higher amount of energy. In the present case, radiation plays a negligible role and the final state exactly corresponds to equilibrium.

In the case of recombination starting from representative conditions of the probe edge flow at $p = 1000 \text{ Pa}$ and $T_A = T_e = 5000 \text{ K}$ in the afterbody typical conditions ($p = 1000 \text{ Pa}$, $T_A = T_e = 2500 \text{ K}$), the CoRaM-MARS CR model leads to the results displayed on Fig. 2. The recombination is clearly observed, since CO_2 finally becomes the major species. We can also note the formation of a substantial amount of O_2 . The corresponding chemical relaxation time scales are

large (1 to 10 s), which means that the afterbody flow is in chemical non equilibrium. Indeed, a much lower hydrodynamic time scale is expected. This perfectly illustrates the relevance of the elaboration of such CR models.

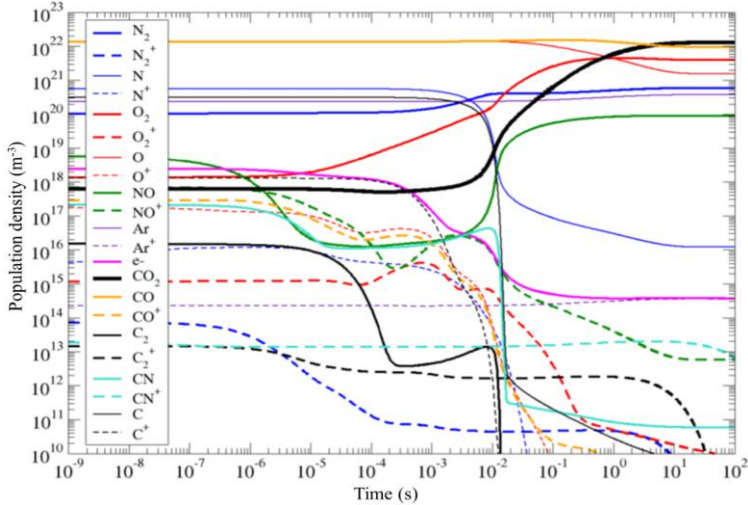


Figure 2. Temporal evolution of the population density of the species in typical recombination conditions of the Exomars type at $T_A = T_e = 2500$ K and $p = 1000$ Pa.

Acknowledgements

The authors acknowledge Drs V. Laporta, P. Rivière and Y. Babou for their collisional and radiative elementary data.

REFERENCES

- [1] A. Bultel and J. Annaloro, *Plasma Sources Sci. Technol.* 22, 025008 (2013)
- [2] P.W. Bousquet, A. Gaboriaud, P. Gaudon, P. Laudet, F. Chiavassa and F. Rocard, *Acta Astronautica* 81, 358 (2012) Communication on the Exomars mission by the CNES
- [3] J. Annaloro, A. Bultel and P. Omary, *J. Phys.: Conf. Series* 550, 012049 (2014)
- [4] J.A. Blauer and G.R. Nickerson, AIAA Paper no 74-536, AIAA 7th Fluid and Plasma Dynamics Conference, Palo Alto CA, June 1974
- [5] K.F. Herzfeld, *J. Chem. Phys.* 47, 743 (1967); R.N. Schwartz, Z.I. Slawsky and K.F. Herzfeld, *J. Chem. Phys.* 20, 1591 (1952)
- [6] J. Annaloro, PhD Dissertation, in French, University of Rouen (2013)
- [7] A. Le Brun and P. Omary, Proc. of the 4th Int. Workshop on Radiation of High Temperature Gases in Atmospheric Entry, ESA SP-689, Lausanne Switzerland (2011)

ELECTRON TRANSPORT IN THE PLANETARY ATMOSPHERES DUE TO LIGHTNING GENERATED ELECTROMAGNETIC PULSES

S. Dujko¹, D. Bošnjaković¹ and A. Luque²

¹*Institute of Physics, University of Belgrade, Serbia*

²*Institute for Astrophysics of Andalusia, Granada, Spain*

Abstract. In this work we apply our time-dependent multi term solution of Boltzmann's equation and Monte Carlo simulation technique to investigate the response of electrons with respect to lightning-generated electromagnetic pulses (EMP) in the planetary atmospheres. Temporal profiles of EMP are calculated externally by solving the appropriate set of Maxwell's equations. When considering the effect of lightning on the lower ionosphere of Saturn, the effects of a planetary magnetic field are included in our calculations assuming the crossed field configuration.

1. INTRODUCTION

Apart from Earth, lightning has been observed on several planets in the Solar system. While the occurrence of lightning on Venus is still an open issue, we possess clear evidences of lightning in all four gaseous and ice planets of the Solar system. At the giant planets, the Voyager, Galileo, Cassini, and New Horizons missions detected radio emissions attributed to lightning [1]. Since the Voyager 1, every spacecraft that has approached to Jupiter has imaged lightning flashes from its night side. The still-operating Cassini spacecraft detected optical images of lightning in Saturn as well as thousands of radio pulses termed Saturn electrostatic discharges (SED) emitted from electric storms. Lightning discharges are thought to occur in the deep H₂O clouds that exist in these atmospheres and are estimated to be roughly 10³ times more energetic than those on Earth.

It is well-documented that lightning discharges produce both an electromagnetic pulse (EMP), due to the rapid lightning current pulse, as well as a quasi-electrostatic (QE) field due to the removal of charge from the thundercloud [2]. When the QE field exceeds the breakdown threshold,

sprites can be initiated in the mesosphere while the EMP field similarly leads to heating, ionization, and optical emissions referred to as elves. In the atmosphere of Earth, elves are luminous glows extending at an altitude from 75 to 105 km with lateral dimensions of 100-300 km and an extremely short duration of less than 1 ms.

In this work we study the effect of lightning on the lower ionospheres of Earth and Saturn. We apply our time-dependent multi term solution of Boltzmann's equation and Monte Carlo simulation technique [3] to investigate transport properties of electrons due to lightning-generated electromagnetic pulses. Temporal profiles of EMP are calculated externally by solving the appropriate set of Maxwell's equations. The methods and techniques for solving the Boltzmann equation are by now standard and the reader is referred to our previous works [3, 4]. In addition to the multi term solution of Boltzmann's equation, we have used our time-resolved Monte Carlo simulation code that has been described in great detail in previous publications. Our Boltzmann and Monte Carlo codes have been verified for a number of benchmarks which prove their correctness and accuracy.

2. RESULTS AND DISCUSSION

2.1 Electron transport in the atmosphere of Saturn in dc electric and magnetic fields

In the first part of this work, we have calculated transport coefficients for electrons in the gas mixtures that mirror the planetary atmospheres. The common practice in previous studies of couplings between atmospheric layers due to lightning-generated EMP in Jupiter and Saturn was application of an altitude-dependent mobility in the Langevin equation as well as an altitude-dependent ionization rate required for the description of local changes in the ambient conductivity. The explicit effects of planetary magnetic fields were neglected. In this work, we investigate the way in which the transport coefficients and other properties are influenced by the local electric field and planetary magnetic field in the atmosphere of Saturn. Assuming the exponential decay of the pressure with the altitude and planetary magnetic field of 20 μT , it is found that the cyclotron frequency exceeds the collision frequency at altitudes where sprites can occur. The expected heights of occurrence of sprites above lightning discharges in the atmosphere of Saturn are calculated using the method of image charges.

As an illustrative example, in Figure 1 we show the variation of the rate coefficients for electron attachment and ionization with the reduced electric field E/N for different altitudes in the atmosphere of Saturn. We see that between 0 (which corresponds to the so-called 1 bar pressure) and 600 km the critical electric field is not affected by the planetary magnetic field. For higher altitudes, however, the critical electric field is increased. At higher altitudes due to B/N scaling the effect of a magnetic field is stronger

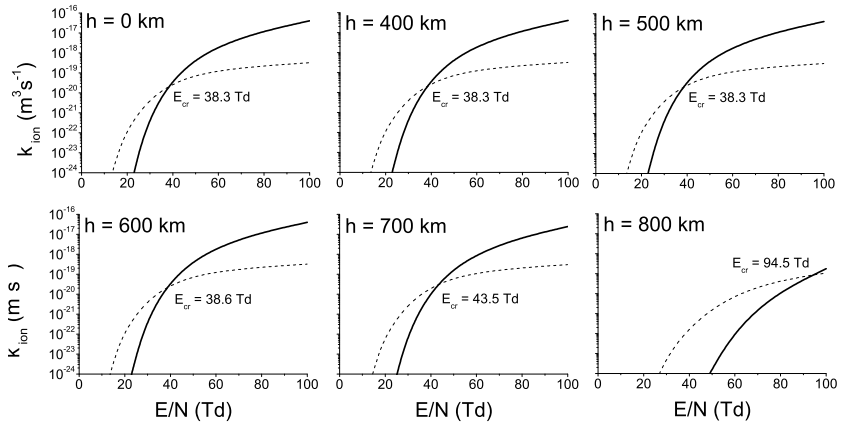


Figure 1. Variation of the rate coefficients for ionization (full curve) and electron attachment (dashed curve) with E/N for different altitudes in the atmosphere of Saturn. Critical electric fields are obtained at the point of intersection of curves for ionization and electron attachment.

which in turn leads to the depopulation of the high-energy electrons from the tail of the distribution function. As a consequence, the ionization rate is reduced.

2.2 Electron transport in the planetary atmospheres due to lightning-generated EMPs

We split the applications into two parts, electrons in the upper atmosphere of Earth and electrons in the upper atmosphere of Saturn. The duration of electromagnetic pulses is 5 ms for Earth and 10 ms for Saturn. Magnetic field amplitudes of EMP are weak (less than a few Hx, where $1 \text{ Hx} = 10^{-27} \text{ Tm}^{-3}$) and are neglected in our calculations. However, the effects of the global planetary magnetic field of Saturn are explicitly included in our calculations, assuming the crossed-field configuration. The effects of planetary magnetic field can be neglected for Earth. For both planetary atmospheres, we show temporal profiles of mean energy, drift velocity and rate coefficients for electron attachment and ionization as a function of the electric field amplitudes and altitudes. Non-local effects in time are observed in the profiles of the mean energy and the ionization rate due to the inability of the electrons to relax their energy on the time scale of the changes in the field. Non-local effects have not been observed in the profiles of drift velocity. This means that momentum relaxation occurs much faster than the energy relaxation in the gas mixtures that mirror the terrestrial and Saturnian atmospheres. As expected, non-local effects in time are more pronounced for higher altitudes and lower electric fields.

In Figure 2 we show the temporal profile of the mean electron energy and the profile of the lightning-generated EMP in the atmosphere of Saturn. Calculations are performed for an altitude of 750 km and the corresponding planetary magnetic field of 580 Hx. When a planetary magnetic field is taken into account, we see that the mean energy is significantly reduced. For altitudes lower than 600 km the impact of planetary magnetic field on temporal profiles of transport data is negligible. Among many important points, this study shows that modeling of nonlinear processes such as local changes in the ambient conductivity due to impact-ionization should take into account the non-local effects.

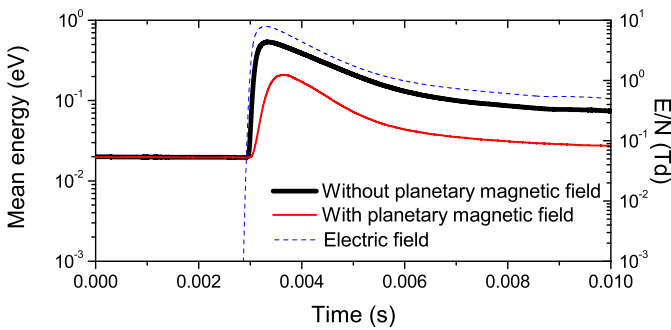


Figure 2. Temporal profile of the mean energy for electrons in the atmosphere of Saturn. Calculations are performed for the altitude of 750 km and along the axial axis of a discharge ($R = 0$ km).

REFERENCES

- [1] A. Luque, D. Dubrovin, F.J. Gordillo-Vzquez, U. Ebert, F.C. Parra-Rojas, Y. Yair, and C. Price, *J. Geophys. Res. Space Physics*, 119 (2014).
- [2] R.A. Marshall, *J. Geophys. Res.* 117, A03316 (2012).
- [3] S. Dujko, R.D. White, Z.Lj. Petrović and R.E. Robson, *Plasma Source Sci. Technol.* 20, 024013 (2011).
- [4] S. Dujko, R.D. White, Z.Lj. Petrović and R.E. Robson, *Phys. Rev. E* 81, 046403 (2010).

A ROUTINE FOR DEMIXING OF POLARIZATION COMPONENTS IN PROFILES OF HYDROGEN BALMER SPECTRAL LINES

N. V. Ivanović¹, Dj. Spasojević², N. M. Šišović² and N. Konjević²

¹*University of Belgrade, Faculty of Agriculture, Nemanjina 6, 11080 Belgrade, Serbia*

²*University of Belgrade, Faculty of Physics, 11001 Belgrade, P.O. Box 44, Serbia*

Abstract. Spatially resolved profiles of hydrogen Balmer lines have been recorded in a low current, low pressure, obstructed neon-hydrogen dc discharge of the Grimm type. The polarization dependent Stark splitting of the H_{α} line has been used to measure the electric field in the cathode fall region. Due to presence of mixing of polarization components in line spectra, a dedicated computer routine has been developed and utilized for their demixing.

1. INTRODUCTION

Polarization dependent Stark splitting of hydrogen Balmer lines has been commonly used for mapping electric field distribution in the cathode fall region of glow discharges not only in hydrogen, but also in mixtures of inert gases with hydrogen [1–3].

In this work, we have studied the Stark profiles of the H_{α} line emitted from the cathode fall region of an abnormal glow discharge in a neon-hydrogen mixture. Since we used spectrometer with high resolving power, in the recorded π -polarized line shape profile we have revealed a presence of peaks belonging to the σ -polarized component and vice versa. For determining the origin of the observed phenomenon, principal transmittance, extinction ratio, and other properties of an imperfect polarizer, as well as the effects of the light source inhomogeneity, instrumental polarization and sensitivity of the detector to the plane of polarization have to be tested experimentally and/or eliminated by calculations.

To this end a dedicated computer routine has been developed and implemented for fitting the polarized line shapes affected by the leakage of other polarization component.

2. EXPERIMENTAL

A modified Grimm glow discharge source was laboratory made after the Ferreira et al. design [4]. Hollow anode (30 mm long with inner diameter 8 mm) has a longitudinal slot (16 mm long and 1.5 mm wide) for side-on observations along the discharge axis, see figure 1. The water-cooled cathode holder has tungsten electrode, 18 mm long and 7.50 mm in diameter, which screws tightly into its holder to ensure good cooling.

All experiments were carried out with the neon-hydrogen mixture (99.2% Ne + 0.8% H₂). A continuous gas flow of about 300 cm³/min was sustained in the pressure range 5-10 mbar by means of a needle valve and two two-stage mechanical vacuum pumps. The reported values for gas pressure represent an average between measured values of gas inlet and outlet pressure.

To run the discharge a current stabilized power supply (0-2 kV, 0-100 mA) is used. A ballast resistor of 5.3 k Ω is placed in series with the discharge and the power supply.

Spectroscopic observations of the Grimm GD were performed side-on through an anode slit in translation steps of approximately 0.125 mm.

Prior entering spectrometer, the radiation from discharge was polarized by a plastic polarizer. Selection of the π - or σ -polarized profile was experimentally carried out by orienting the polarizer axis parallel or perpendicular to the discharge axis, i.e. electric field direction in the cathode fall. Under the π -polarization is understood the component of light with linear polarization along the electric field, and under a σ -polarization the component of light that is circularly polarized in the plane perpendicular to the direction of the electric field, see schematic representation in Figure 1.

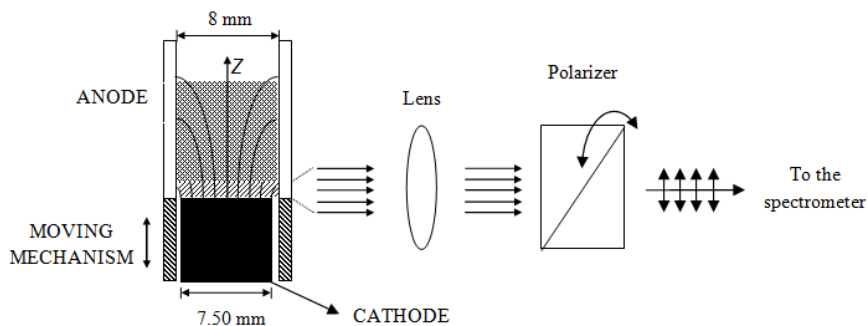


Figure 1. Schematic diagram of the central part of the Grimm GD and the experimental setup.

The radiation from the discharge source is focused with an achromatic lens (focal length 75.8 mm) with unity magnification, through the polarizer, onto the 20 μ m entrance slit (height restriction 2 mm) of 2 m focal length Ebert type spectrometer with 651 g/mm reflection grating blazed at 1050 nm. For the line shape measurements the reciprocal dispersion of 0.37 nm/mm is used throughout

this experiment. All spectral measurements were performed with an instrumental profile very close to a Gaussian with measured full width at half maximum (FWHM) of 8.2 pm.

3. NUMERICAL METHOD

Spectral profile of the Balmer H_α line consists of three components. The narrow and the broadened central components both originate from electron impact, i.e. from ionization, and from dissociative ionization and excitation, respectively. The third, usually called the excessively broadened wings, originates mainly from the energetic hydrogen atoms produced in charge exchange reactions, see Ref. 5 and references therein. In our model function, each of these components is described by a Gaussian. Due to dc electric field in the cathode fall region, their superposition is convolved with a convex combination of π and σ Stark shift operators, and finally convolved with the instrumental profile.

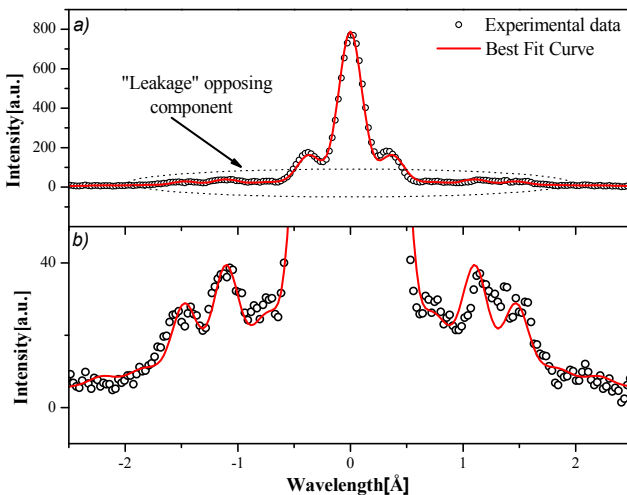


Figure 2. Experimental profile of the σ -polarized Balmer H_α line, observed side-on at 0.125mm from the cathode surface. Discharge conditions: $I=12.1$ mA, $U=914$ V, and $p=6$ mbar. The best fit curve was obtained using above described model function. The line intensity is given versus wavelength shift relative to the 656.281 nm central wavelength of the H_α line. On layer *a*) we present the overall profile, whereas on layer *b*) the profile part around base line is magnified so that the leaked π -component is visible.

4. RESULTS

Preliminary results show detailed agreement between experimental and model profiles, see Fig. 2. In addition, our results show that the determination of the electric field value is affected by the use of the demixed profile less than 1%. Further details of the procedure and examples of its application will be demonstrated at the Conference.

Acknowledgements

This work is supported by the Ministry of Education, Science and Technological Development of the Republic of Serbia under Projects 171014 and 171027.

REFERENCES

- [1] Dj. Spasojević, V. Steflekova, N. M. Šišović, and N. Konjević, *Plasma Sources Sci. Technol.* 21 025006 (8pp) (2012).
- [2] T. Wujec, H.W. Janus and W. Jeleński, *J. Phys. D: Appl. Phys.* 36 868–877(2003).
- [3] I. R. Videnović, N. Konjević and M. M. Kuraica, *Spectrochimica Acta B* 51, 1707 (1996).
- [4] N. P. Ferreira, H. G. C. Human and L. R. P. Butler, *Spectrochim. Acta B* 35, 287 (1980).
- [5] Dj. Spasojević, S. Mijin, N. M. Šišović, and N. Konjević, *Journal of Applied Physics* 119(5), 053301 (2016).

THE INFLUENCE OF PRESSURE ON THE POST-DISCHARGE RELAXATION IN SYNTHETIC AIR WITH TEFLON WALLS

A. P. Jovanović, M. N. Stankov, V. Lj. Marković and S. N. Stamenković

*Department of Physics, Faculty of Sciences and Mathematics, University of Niš,
33 Višegradska street, PO box 224, Niš, Serbia*

Abstract. In this paper, the analysis of the memory curves measured in a synthetic air is presented. The measurements are carried out at three different pressures with the Teflon foil tightly fitted to the walls of vacuum chamber. The dominant species responsible for memory effect in late afterglow are identified to be nitrogen atoms, recombining on the stainless steel cathode and producing initial electrons, while the main loss of these atoms is due to recombination on the walls. The order of surface recombination of nitrogen atom on Teflon is determined by using the analytical model, while the surface recombination coefficients are calculated by the numerical model.

1. INTRODUCTION

The aim of this paper is to investigate the influence of wall material and pressure on the memory curve. It is the extension of the earlier paper in which post-discharge relaxation in synthetic air is analyzed [1]. We will focus on the late relaxation only, in order to identify the order of the surface recombination of nitrogen atoms on Teflon walls, as well as corresponding coefficients. The research of surface recombination of nitrogen atoms in air (or $N_2 - O_2$ mixtures) was already reported in refs [2, 3]. The manuscript is organized as follows: brief description of experiment is given in the second section, followed by the description of theoretical model in the section three and discussion of the results of measurement and calculations in the section four. Finally, brief conclusion is given in the last section.

2. EXPERIMENTAL DETAILS

The measurements of memory curve (the mean time delay to breakdown as a function of the relaxation time [4]) are carried out on custom-made vacuum chamber. The vacuum chamber is made of borosilicate glass (with diameter $D_r = 5.5\text{ cm}$ and length $L = 16.5\text{ cm}$), with aluminum flange on one

side, used to connect it to the vacuum system. The Teflon (PTFE) foil is tightly fitted to the glass walls of the chamber, with the purpose to investigate nitrogen surface recombination on it. The cylindrical electrodes of diameter $D = 0.6\text{ cm}$ made of stainless steel (AISI 304) were used, with the inter-electrode space $d = 0.5\text{ cm}$ fixed for all measurements. The chamber is pumped out to the pressure of 10^{-3} Pa and then filled with gas at working pressure, in this case synthetic air (mixture of 78 percent of nitrogen, with less than 5 ppm of impurities, and 22 percent of oxygen, with less than 3.5 ppm of impurities). The measurements were carried out at three different pressures 400, 800 and 1200 Pa , at 50 percent overvoltage (600, 700 and 780 V , respectively), glow current $I_g = 300\text{ }\mu\text{A}$, with glow time of $t_g = 1\text{ s}$. Time delay is measured with Tektronix FCA3000 counter (time resolution of 100 ps) with 100 data for each relaxation time. The vacuum chamber was protected from light during the measurements.

3. THEORETICAL MODEL

The time delay measurements are used to analyze effect of the wall material and pressure on the relaxation of glow discharge in synthetic air. We primarily focus on the late afterglow, dominated by neutral particles. According to the model for synthetic air, presented in [1], the part of memory curve after 100 ms is dominated by a surface recombination of nitrogen atoms. Therefore, we will apply analytical model from [5], in order to determine the order of recombination of nitrogen atoms on Teflon surface. According to this theory, by finding the dependence between the mean time delay (which is inversely proportional to the number density of nitrogen atoms) and the relaxation time, the order of surface recombination can be determined [5]. If the linear dependence of the mean time delay \bar{t}_d and relaxation time τ is obtained, the first order of the surface recombination of nitrogen atoms occurs. On the other hand, if the square root of the mean time delay $\sqrt{\bar{t}_d}$ is linear with the relaxation time τ , the second order surface recombination occurs. Based on the slope and the interception of linear fit, the surface recombination coefficients can be determined, but their values are unreliable [1, 5]. Therefore, we will also use the numerical model to precisely determine the surface recombination coefficients.

The gas phase numerical model describes the loss of the nitrogen atoms on the walls due to the second order recombination and assumes that their density in the chamber is uniform, neglecting the number density diffusion profiles:

$$\frac{d[N]}{dt} = -\gamma_{NW}[N]^2 \quad (1)$$

where γ_{NW} is the surface recombination coefficient on the walls. The second order recombination on the stainless steel cathode is used [1], so the electron yield is equal to $Y = k_{NE}^{II} [N]^2 V_c$, where V_c is the volume of inter-electrode space and k_{NE}^{II} is the surface recombination coefficient on the electrodes. The initial densities of the nitrogen atom are calculated by 1D numerical model for the stationary state of nitrogen glow discharge [1].

4. RESULTS AND DISCUSSION

The memory curves measured at pressures of 400, 800 and 1200 Pa are presented in Fig. 1a. It can be seen that with the increase of pressure, the value of mean time delay increases, which implies the decrease of electron yield. This can be explained by the greater loss of dominant particles at higher pressure. In order to fully understand the processes responsible for the change of the electron yield, the numerical model which takes into account all the possible particles and reactions have to be used, which is out of the scope of this paper. Here, we are going to focus on the late afterglow only. According to the numerical model presented in [1], the charged particles decay until 100 ms, so only the neutral particles can be responsible for memory effect in the late afterglow. The only possible particles that can cause the electron emission from the cathode surface are metastable molecules and nitrogen atoms (by a surface recombination). However, the metastable molecules are strongly quenched by the oxygen and nitrogen atoms and molecules [1]. Therefore, the only possible particle that can explain the memory effect are the nitrogen atoms. First, we will try to determine the dependence of the mean time delay and relaxation time. In the earlier paper [1] discussing the synthetic air, the square root of mean time delay is linearized as a function of time delay, in the interval from 0.1s to 4s. This implies that some second order loss process of particles responsible for electron emission is occurring at these relaxation times [1]. This kind of linearization was explained by the second order surface recombination of nitrogen atoms on the glass surface. Let us assume that the same process is responsible for this case, as well.

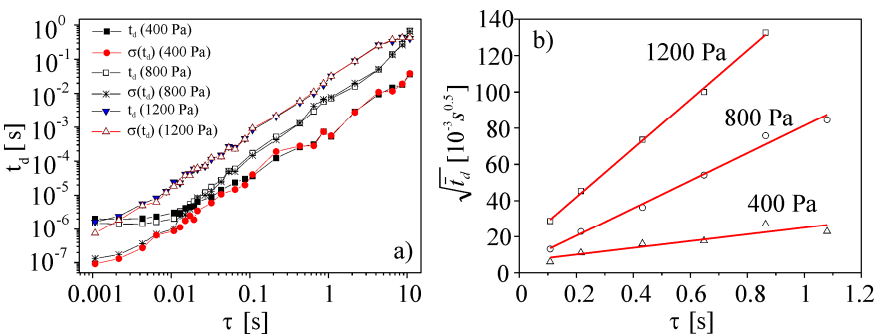


Figure 1. Memory curves in synthetic air with Teflon walls at different pressures

In the Fig. 1b, the square root of mean time delay is represented as a function of the relaxation time. The linearization in the interval from 0.1 to 1 s, at all pressures is observed, which is consistent with the earlier results [1]. However, this linearization implies that the surface recombination of the nitrogen atom at the Teflon surface is of the second order as well, same as for the borosilicate glass! We can also observe that the slope of the fit increases with the rise of the pressure. This means that the loss of nitrogen atoms increases when the pressure increases. The rate of surface recombination is determined from the slope of the fit in Fig. 1b by using the analytical model [5]. The rate of surface recombination of nitrogen atom at the pressure $p = 400 \text{ Pa}$ is $k_{NW}''[N] = 2.95/s$, at the pressure $p = 800 \text{ Pa}$ is $k_{NW}''[N] = 14.08/s$, while at the pressure $p = 1200 \text{ Pa}$ is $k_{NW}''[N] = 8.99/s$, thus the non-monotonic behavior with the pressure is observed. In order to precisely determine the surface recombination coefficients, the numerical model describing the surface recombination of nitrogen atoms on Teflon surface is used (1). The equation is numerically solved by the Runge-Kutta method. By fitting the experimental data, the following values of recombination coefficient are determined: $\gamma_{NW} = 10^{-14} \text{ cm}^3/s$ for the pressure $p = 400 \text{ Pa}$, $\gamma_{NW} = 10^{-14} \text{ cm}^3/s$ for the pressure $p = 800 \text{ Pa}$ and $\gamma_{NW} = 9 \times 10^{-13} \text{ cm}^3/s$ for the pressure $p = 1200 \text{ Pa}$.

5. CONCLUSION

The discussion of the memory curves measured at different pressures in synthetic air with Teflon walls is presented. The memory effect in the late afterglow is explained by the second order surface recombination of nitrogen atom on the Teflon surface and on the stainless steel electrodes. The simple numerical model is applied to fit experimental data and corresponding surface recombination coefficients are determined.

Acknowledgements

This work is supported by Ministry of Education, Science and Technological development of the Republic of Serbia under the grant ON 171025.

REFERENCES

- [1] A. P. Jovanović, V. Lj. Marković, S. N. Stamenković and M. N. Stankov, J. Phys. D: Appl. Phys. 48 465204 (2015)
- [2] K. Kutasi and J. Loureiro J. Phys. D: Appl. Phys. 40 5612–5623 (2007)
- [3] B. Gordiets, C. M. Ferreira, J. Nahorny, D. Pagnon, M. Touzeau and M. Vialle J. Phys. D: Appl. Phys. 29 1021 (1996)
- [4] Đ. A. Bošan Industrial R. and D. Report (Development of surge arresters), TD PO2, Comp Elektronska Industrija, former Zavodi R R (Niš, 1956)
- [5] V. Lj. Marković, M. M. Pejović and Z. Lj. Petrović Plasma Chem. Plasma Proc. 16 195 (1996)

BREAKDOWN VOLTAGES OF DIRECT CURRENT MICRODISCHARGES IN COMPRESSED AIR

M. Klas¹, L. Moravský¹, Š. Matejčík¹, B. Radjenović²
and M. Radmilović-Radjenić²

¹*Department of Experimental Physics, Comenius University, Mlynská dolina
F-2, 842 48 Bratislava, Slovakia*

²*Institute of Physics, University of Belgrade, Pregrevica 118, Belgrade, Serbia*

Abstract. This paper contains results of the experimental and simulation studies of the breakdown voltage curves of direct current microdischarges in compressed air. The obtained results agree well with the data taken from the literature. Based on the experimentally recorded breakdown voltage curve the effective yields have been estimated. The effective yields for all gap sizes have the same trends spread in the range from 2.3×10^{-4} up to 2.3×10^{-2} .

1. INTRODUCTION

Compressed air applications have made tremendous progress in recent years due to energy efficiency. According to proponents, compressed air also has a great potential as a clean, inexpensive, and infinitely renewable energy source. Its use is currently being explored as an alternative to fossil fuels. Although, studies of the breakdown characteristics in compressed gases are reported in a number of publications [1,2], many aspects are insufficiently explored, so this subject is still an active area of research.

In this paper, the electrical breakdown characteristics of uniform fields in compressed gases are studied. Measurements were carried out for the gap sizes from 5 microns up to 100 microns. In addition, effective yields have been determined from the measured breakdown voltage curves.

2. EXPERIMENTAL SET-UP

The measurements were performed high pressure brass chamber equipped with stainless steel electrodes with sphere to plane geometry. Schematic view of the apparatus with the electrode dimensions is shown in Figure 1. Electrode separation was varied from $5 \mu\text{m}$ to 1mm in the pd (pressure times the gap size) range 0.4-300 Torr x cm. One of the electrodes was fixed while the other one was movable continuously by the micrometer screw with the

resolution of $\sim 2\mu\text{m}$. Breakdown voltages were measured by Tektronix probe P6015A, Pearson current monitor 2877 and recorder by oscilloscope (Agilent DSO5032A).

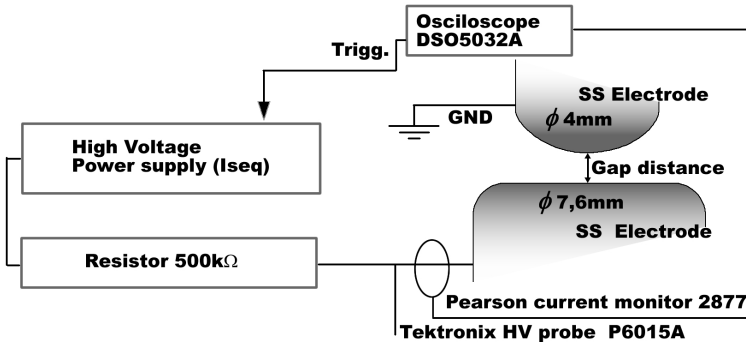


Figure 1. Experimental setup for the breakdown voltage measurements.

3. RESULTS

Figure 2 shows the dependence of the direct current (DC) breakdown voltage on pd value for various gaps sizes. At high pd values, breakdown voltage curves for all distances follow the standard scaling law. A departure from the scaling law is observed to the left hand branch of the Paschen curve where results of measurements performed for $5\mu\text{m}$ (black squares) are lower than those measured for larger interelectrode separations due to field emission processes and leading to the lower breakdown voltages [3]. Results of our measurements have the same tendencies as the experimental data taken from [4] (right yellow triangles) as well as from our previous publication [5] (orange down triangles). Differences between them could be attributed to differences between the experimental conditions, since the data from [4] and [5] were recorded at the fixed pressure of 760 Torr and at the fixed gap size of 100 microns, respectively. For the same reasons, the differences could be also observed between previously published PIC/MCC results [5] (crosses) and novel PIC/MCC results (stars).

Based on recorded breakdown voltages curves the dependence of the effective yield on the reduced electric field E/p (the electric field over the gas pressure ratio) has been estimated and shown in Figure 3. The effective yields for compressed air lay in the interval from 2.3×10^{-4} up to 2.3×10^{-2} . There is a good agreement with our previously published data taken from [5] (orange down triangles).

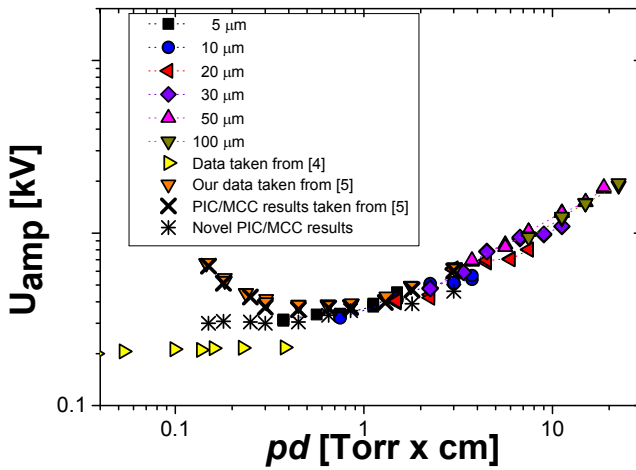


Figure 2. The DC breakdown voltage as a function of pd product.

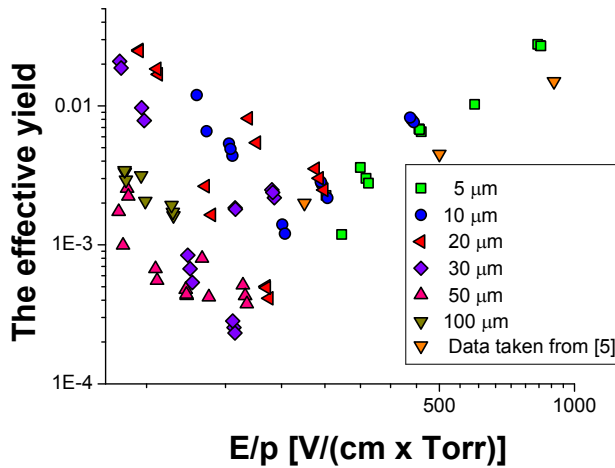


Figure 3. The effective yields obtained from the breakdown voltage curves shown in Figure 2.

Acknowledgements

This work is partially supported by VEGA grant agency project: VEGA 1/0417/15 and Slovak Research and Development Agency Projects: APVV-0733-11.

REFERENCES

- [1] L.B. Loeb, *Fundamental Processes of Electrical Discharges in Gases*, (J. Wiley and Sons, Inc., New York, 1939).
- [2] J.M. Meek, J.D. Craggs, *Electrical Breakdown of Gases*, (Oxford University Press, Oxford, UK, 1953).
- [3] M. Radmilovic-Radjenovic, B. Radjenovic, Z. Nikitovic, Š. Matejcik and M. Klas, *Nuclear Instruments and Methods in Physics Research B* 279, 103 (2012).
- [4] Yu.D. Korolev and G.A. Mesyats, *Physics of pulsed breakdown in gases*, (Uro-Press, Yekaterinburg, Ural, 1998).
- [5] M. Klas, S. Matejcik, B. Radjenovic and M. Radmilovic-Radjenovic, *Europhysics Letters* 95, 35002 (2011), 35002.

CHARACTERISTICS OF RADIO-FREQUENCY HYDROGEN MICRODISCHARGES

M. Klas¹, L. Moravský¹, Š. Matejčík¹, B. Radjenović² and
M. Radmilović-Radjenović²

¹*Department of Experimental Physics, Comenius University, Bratislava, Slovakia*

²*Institute of Physics, University of Belgrade, Pregrevica 118, Serbia*

Abstract. This paper contains images of radio-frequency hydrogen microdischarges generated between two electrodes separated by 100 microns. Two types of the electrode configurations were used: glass melting electrodes and electrodes with Bruce profile. The Bruce profile was found to be a good compromise in producing uniform fields with a negligible end effect. Images taken by camera Nikon D7100 with exposure time of few seconds indicate that discharge has more diffuse character as the operating frequency increases.

1. INTRODUCTION

Hydrogen plasmas have been widely employed in a number of technological processes, such as thin film deposition, passivation, isotropic etching of dielectric material and organic polymers [1,2]. On the other hand, radio frequency (RF) capacitively coupled plasma (CCP) sources have attracted much attention due to a wide range of applications from industrial surface processing of materials to advanced medical treatments of biomedical tissues [3,4]. Although these discharges have operated traditionally in large scales, there has been a recent interest in developing microplasmas and RF CCPs that operate at atmospheric pressures.

In this paper we display and analyze images of the development and propagation of high pressure hydrogen microdischarges for two types of the electrode configurations (glass melting electrodes and electrodes with Bruce profiles).

2. EXPERIMENTAL PROCEDURE

Experimental arrangement used in this study is shown in Figure 1. Discharge was generated in hydrogen (purity 6.0). Electrical probes were corrected on a phase shift due to length of cables and voltage probe P6015A (70 MHz) was calibrated at lower voltages with a Tektornix probe P6139B (500 MHz).

We employed two types of the electrode systems shown in Figure 2: The 1st type of the electrode configuration represents a glass melting electrode where molybdenum rod of diameter of 2mm is covered by molybdenum glass. The 2nd type consists of two bare planar molybdenum electrodes with rounded edges of the top electrode.

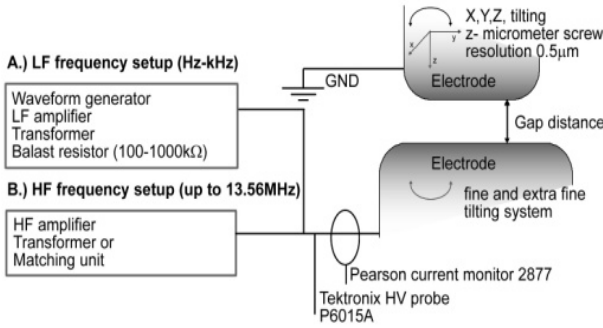


Figure 1. Schematic view of the experimental arrangements used for measurements in this study.

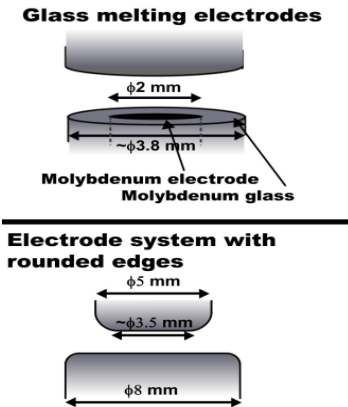


Figure 2. The 1st type (glass melting electrodes - MG) and the 2nd type (electrodes with Bruce Profile-BP) of the electrode configuration.

4. RESULTS

The Bruce profile electrode configuration produces uniform field with a negligible end effect and a nearly constant uniform field region as illustrated in Figure 3 [5].

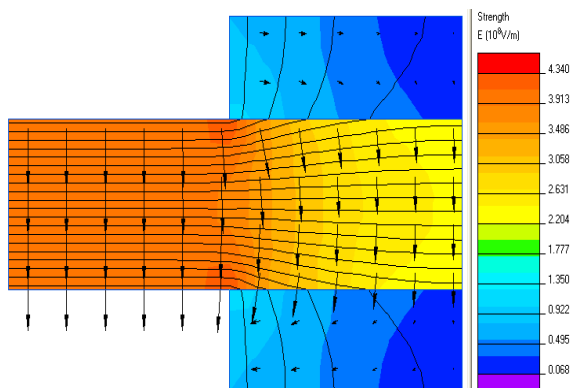


Figure 3. Distribution of the field generated between the electrodes with Bruce profile.

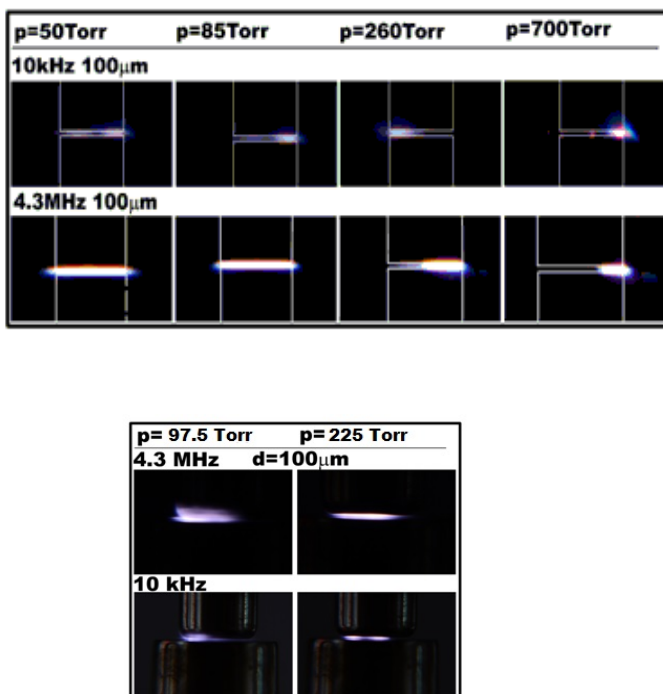


Figure 4. Images of discharges between: a) glass melting electrodes and b) electrodes with Bruce Profile separated by 100 microns at two frequencies (10 kHz and 4.3 MHz) and different pressures.

Images taken by camera Nikon D7100 with exposure time of few seconds of discharges formed between: a) glass melting electrodes and b) electrodes with Bruce profile are shown in Figure 4. These images clearly demonstrate the discharge propagation at two frequencies (10 kHz and 4.3 MHz), at various pressures, but the constant gap size of 100 μm . It is obvious that with increasing the operating frequency discharge has more diffuse character which is in accordance with the results of the theoretical study [6].

Acknowledgements

This work has been supported by the- project VEGA 1/0514/12 and the Slovak Research and Development Agency Projects.

REFERENCES

- [1] Y. Park, J.G. Lu and G. Rozgonyi, *Electron. Mater. Lett.* 6, 1 (2010).
- [2] B. Radjenović and M. Radmilović-Radjenović, *Electron. Mater. Lett.* 10, 1039 (2014).
- [3] M. Laroussi and X. Lu, *Appl. Phys. Lett.* 87, 113902 (2005).
- [4] X. Lu, M. Laroussi and V Puech, *Plasma Sources Sci. Technol.* 21, 034005 (2012).
- [5] F.M. Bruce, *Proc. IEE* 94, 138 (1947).
- [6] F. Iza, J. K. Lee, and M. G. Kong, *Phys. Rev. Lett.* 99, 075004 (2007).

SURFACE RECOMBINATION OF NITROGEN ATOMS ON TEFLON IN AFTERGLOW STUDIED BY THE ELECTRICAL BREAKDOWN TIME DELAY

V. Lj. Marković, A. P. Jovanović, M. N. Stankov and S. N. Stamenković

Department of Physics, Faculty of Sciences and Mathematics, University of Niš, Višegradaska 33, PO box 224, Niš, Serbia

Abstract. The surface recombination of nitrogen atoms on Teflon in afterglow of DC nitrogen discharge is studied by the time delay measurements as a function of relaxation time $\bar{t}_d(\tau)$ (memory curve). The surface recombination of nitrogen atoms on Teflon was reported to be the first order process in the number density of nitrogen atoms, with their exponential temporal evolution in afterglow and recombination coefficients independent on nitrogen atom number density. In our experiment, it was observed that the surface recombination of nitrogen atoms on Teflon surface is second order process in the number density of nitrogen atoms, with recombination coefficients depending on the initial nitrogen atom number density, whose calculation is in progress.

1. INTRODUCTION

Several authors have concluded in their experiments that the surface recombination of nitrogen atoms on Pyrex and Teflon is the first order process in the nitrogen atom number density $[N]$ at low pressure afterglow [1-3]. In this case, the temporal evolution of number density of nitrogen atoms $[N]$ in afterglow is exponential, giving a straight-line dependence when plotted in the semi-logarithmic scale. However, some authors concluded from their experiments that the process is second order or mixture of first and second order in nitrogen atom number density $[N]$ [4-8]. In the series of time delay measurements \bar{t}_d vs. relaxation time τ (memory curve) in nitrogen [9-11], argon [12] and air [13] it was shown that surface recombination of nitrogen atoms on molybdenum glass, iron and stainless steel is second order process (changing to first order at low $[N]$ number densities). Such process leads to the well known $1/[N]$ decay, which gives a straight-line dependence when plotted $1/[N]$ vs. τ in the linear-linear scale. In this contribution, we study the surface recombination of nitrogen atoms in afterglow of DC glow discharge in nitrogen on Teflon foil inserted into the vacuum chamber.

2. EXPERIMENTAL SETUP

The experimental setup is shown in Fig. 1. Vacuum system consists of turbo-molecular vacuum pump with diaphragm pump as a fore pump. Vacuum chamber is custom-made of borosilicate glass (8245 Schott technical glass, also known as molybdenum glass), with diameter $D = 5.5\text{ cm}$, length $L = 16.5\text{ cm}$ and aluminum flanges. The Teflon (PTFE) foil is tightly fitted into the vacuum chamber. The vacuum chamber is pumped out to the pressure of 10^{-3} Pa and then filled with nitrogen at 399 Pa (nitrogen, with less than 3 ppm of impurities). The measurements were carried out at the inter-electrode space $d = 0.5\text{ cm}$, 50 percent relative overvoltage (the static breakdown voltage was 375 V at this $p \cdot d$ value), glow current $I_g = 300\text{ }\mu\text{A}$ and glow time $t_g = 1\text{ s}$. The $\bar{t}_d(\tau)$ dependences (the memory curves) were measured with the stainless steel (AISI 304) cathode, with Tektronix FCA3000 counter (time resolution 100 ps) and 100 data in the series. During the measurements, the vacuum chamber was protected from external light (Fig. 1).

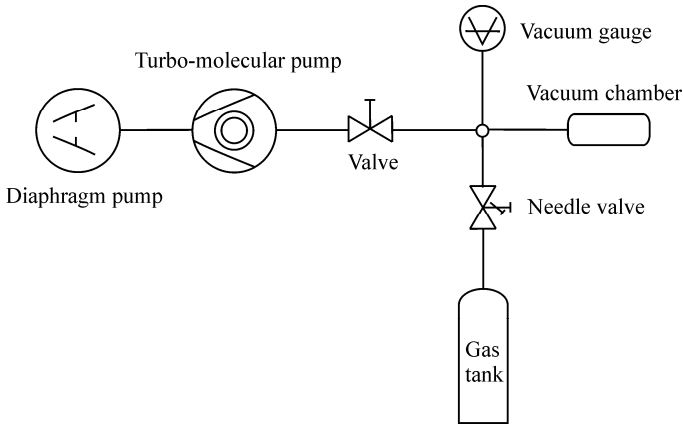


Figure 1. The experimental setup with turbo-molecular vacuum pump.

3. RESULTS AND DISCUSSION

For the first order surface recombination of nitrogen atoms on Teflon, the exponential number density decay in afterglow is obtained:

$$\frac{d[N]}{d\tau} = -k_{NW}^I [N] \Rightarrow [N] = [N]_0 \exp(-k_{NW}^I \tau), \quad (1)$$

where $[N]_0$ is the initial number density of nitrogen atoms and k_{NW}^I is the first order surface recombination coefficient on Teflon. For the electron yield Y of

electrons in the inter-electrode space initiating breakdown [9,10] for the second order process on stainless steel cathode, it is obtained

$$Y = k_{NE}^{II} [N]^2 V_c, \quad (2)$$

where k_{NW}^{II} is the second order surface recombination coefficient on the stainless steel cathode and V_c is the volume of the inter-electrode space. By applying the time delay measurements, when the formative time is the negligible part of the breakdown time delay, it holds that $\bar{t}_d \approx \bar{t}_s = \frac{1}{YP}$, where P is the breakdown probability [9]. By solving this system of equations, it is obtained $\bar{t}_d = \bar{t}_{d0} \exp(2k_{NW}^I \tau)$ and the linear dependence when plotted in semi-logarithmic scale with $k_{NW}^I = \ln(\bar{t}_d / \bar{t}_{d0}) / 2\tau$, where \bar{t}_{d0} is the intersection of mean breakdown time delay with ordinate axis at $\tau = 0$ s (Fig. 2a).

It is clear from Fig. 2a that experimental memory curve $\bar{t}_d(\tau)$ is not linear, which means that the surface recombination of nitrogen atoms on Teflon is not first order process in the number density of nitrogen atoms. On the other hand, when the surface recombination is the second order process

$$\frac{d[N]}{d\tau} = -k_{NW}^{II} [N]^2, \quad (3)$$

the temporal evolution is given by $1/[N] = 1/[N]_0 + k_{NW}^{II} \tau$.

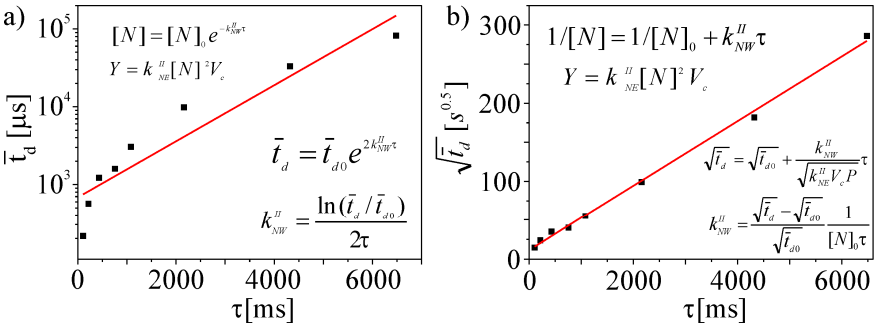


Figure 2. The memory curve with stainless-steel cathode and Teflon.

By using $Y = k_{NE}^{II} [N]^2 V_c$ and solving the system of equations, the square root of the mean time delay is linearized as a function of relaxation time (Fig. 2b)

$$\sqrt{\bar{t}_d} = \sqrt{\bar{t}_{d0}} + \frac{k_{NW}^{II}}{\sqrt{k_{NE}^{II} V_c P}} \tau \quad (4)$$

implying that surface recombination of nitrogen atom on Teflon surface is second order process with surface recombination coefficient given by

$$k_{NW}'' = \frac{\sqrt{\bar{t}_d} - \sqrt{\bar{t}_{d0}}}{\sqrt{\bar{t}_{d0}}} \frac{1}{[N]_0 \tau}. \quad (5)$$

Thus, for the second order surface recombination of nitrogen atoms on Teflon the recombination coefficient depends on the initial number density of nitrogen atoms, whose calculations are in progress.

4. CONCLUSION

The surface recombination of nitrogen atoms on Teflon in afterglow of DC nitrogen discharge is reported to be the second order process in nitrogen atom number density. Instead of exponential temporal evolution in afterglow and the recombination coefficients independent on nitrogen atom number density, the well-known $1/[N]$ decay is obtained with the recombination coefficients depending on the initial nitrogen atom number density.

Acknowledgements

This work is partially supported by Ministry of Education, Science and Technological development of the Republic of Serbia (grant ON 171025)

REFERENCES

- [1] T. Wentink Jr., J. O. Sullivan, and K. Wray, *J. Chem. Phys.* 29, 231 (1958).
- [2] J. Herron, J. Franklin, P. Bradt, V. Dibeler, *J. Chem. Phys.* 30, 879 (1959)
- [3] R. A. Young, *J. Chem. Phys.* 34, 1292 (1961)
- [4] I. Campbell and B. Thrush, *Proc. R. Soc. London, Ser A*, 296, 201 (1967)
- [5] M. A. A. Clyne and D. H. Stedman, *J. Phys. Chem.* 71, 3071 (1967).
- [6] K. M. Evenson and D. S. Burch. *J. Chem. Phys.* 45, 2450 (1966).
- [7] M. L. Rahman and J. W. Linnett, *Trans. Faraday Soc.*, 67, 170 (1971).
- [8] W. Brennen and E. C. Shane, *J. Phys. Chem.*, 75, 1552 (1971)
- [9] V. Lj. Marković, Z. Lj. Petrović and M. M. Pejović, *J. Chem. Phys.* 100, 8514 (1994)
- [10] V. Lj. Marković, M. M. Pejović and Z. Lj. Petrović, *Plasma Chem. Plasma Process.* 16, 195 (1996)
- [11] V. Lj. Marković, Z. Lj. Petrović and M. M. Pejović, *Jpn. J. Appl. Phys.* 34, 2466 (1995)
- [12] V. Lj. Marković, S. R. Gocić, S. N. Stamenković and Z. Lj. Petrović, *Phys. Plasmas* 12, 073502 (2005)
- [13] A. P. Jovanović, V. Lj. Marković, S. N. Stamenković and M. N. Stankov, *J. Phys D: Appl. Phys.* 48, 465204 (2015)

DEPARTURE FROM EQUILIBRIUM OF ULTRASHORT LASER-INDUCED ALUMINUM OR TUNGSTEN PLASMAS

Vincent Morel¹, Arnaud Bultel²,
Lazar Gavanski³, Zoran Mijatovic³ and Stevica Djurovic³

¹*Institut Pprime, UPR 3346, ISAE ENSMA,*

86961 Futuroscope Chasseneuil cedex, FRANCE

²*CORIA UMR 6614 – CNRS, Université et INSA de Rouen,*

Campus universitaire du Madrillet, 76800 Saint-Etienne du Rouvray, FRANCE

³*Department of Physics, Faculty of Sciences, University of Novi Sad,*

Trg Dositeja Obradovica 4, 21000 Novi Sad, SERBIA

Abstract. Using the collisional-radiative models CoRaM-Al and CoRaM-W, the departure from equilibrium of laser-induced plasmas on aluminum and tungsten is put forward when the background gas is at a pressure level similar to the one occurring after a shock within the WEST tokamak of the CEA Cadarache, France. This means that the Laser-Induced Breakdown Spectroscopy (LIBS) diagnostic performed in these conditions has to concern characteristic times close to the laser pulse.

1. INTRODUCTION

The Laser-Induced Breakdown Spectroscopy (LIBS) technique advances nowadays towards the status of a well-established diagnostics method [1]. This technique faces to the fundamental question of the departure of the plasma from thermochemical equilibrium [2, 3]. Indeed, since this technique is based on the analysis of the laser-induced plasma by Optical Emission Spectroscopy, deducing the ground state population density of the species, hence their relative abundance, cannot be directly performed if Local Thermodynamic Equilibrium (LTE) is not fulfilled.

Following the temporal evolution of a typical plasma, the successive factors that can cause its departure from equilibrium are (1) its interaction with the laser pulse during its formation, (2) the super- (hyper-) sonic expansion of the plasma, (3) its segregation caused by its expansion, and (4) the radiative losses. These reasons are more or less the same as those causing a departure from equilibrium in the case of other plasmas, i.e. an insufficient collisional coupling between particles with respect to other elementary processes. In the present case, deeper understanding can be achieved using modeling.

For several decades, many modeling studies have been devoted to fast moving plasmas, such as those obtained in shock tubes [4] or in the vicinity of objects entering the upper layers of a planetary atmosphere [5]. In particular, it has been proved that state-to-state approaches are totally relevant to study departures from excitation and chemical equilibrium. Indeed, they can lead to understand the behavior of the plasma when several types of elementary processes compete to each other. It is therefore logical to apply the same approach in the case of laser-induced plasmas, since the question of departure from equilibrium is central.

The present contribution reports the implementation of such approaches in a simplified computational fluid dynamics code able to reproduce the whole behavior of ultra-short laser induced plasmas obtained on aluminum and on tungsten. These two elements have been chosen for the following reasons. Aluminum is considered as a surrogate to beryllium (material considered for the ITER project) and tungsten results from our objective to measure by LIBS light elements implantation within the tungsten divertor wall of the WEST tokamak in the CEA center at Cadarache, France.

2. STATE-TO-STATE, COLLISIONAL-RADIATIVE AND FLUID DYNAMICS MODELS

State-to-state approaches are developed for the (aluminum or tungsten) metallic plasma in order to model situations out of thermochemical equilibrium. 64 states for Al, 124 states for Al^+ and 1 state for Al^{2+} have been considered for aluminum. For tungsten, we have considered 60 states of W and 74 for W^+ . These numbers of states result from a classical lumping procedure [6]. All these states are coupled together through collisional and radiative elementary processes (excitation, ionization and backward processes, spontaneous emission, radiative recombination) that form the CoRaM-Al model for aluminum and the CoRaM-W model for tungsten [6,7].

The plasma formed under ultra-short laser irradiation of the metallic sample is assumed hemispherically symmetric. It is assumed uniform and in mechanical interaction with a shock layer developed around the central aluminum or tungsten plasma within the background gas through a contact surface. The shock layer is assumed uniform as well and argon is considered as background gas. This shock layer is assumed out of thermochemical equilibrium. The related collisional-radiative (CR) model is detailed in [6].

Mass, momentum and energy conservations are used to predict behaviors illustrated in the upcoming section.

3. RESULTS

If the background gas pressure is atmospheric, the central metallic plasma remains close to the equilibrium. However, if this pressure is sufficiently decreased, departures from excitation and ionization equilibrium can be observed. Figures 1 and 2 illustrate the Boltzmann plots calculated at $p_0 = 10$ Pa

for aluminum and tungsten, respectively. This pressure level typically corresponds to the pressure just after a shock in the WEST tokamak.

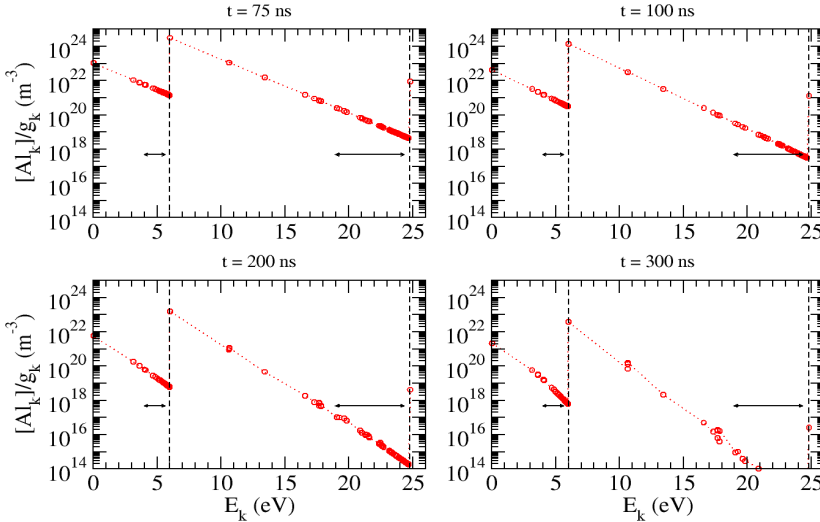


Figure 1. Boltzmann plots evolution after the laser (532 nm, 10 mJ, 10 J cm⁻²) irradiation of an aluminum sample at $p_0 = 10$ Pa (vertical dashed line: ionization limit of Al and Al⁺, arrows: upper levels of the transitions observable over the range 300 nm < λ < 800 nm).

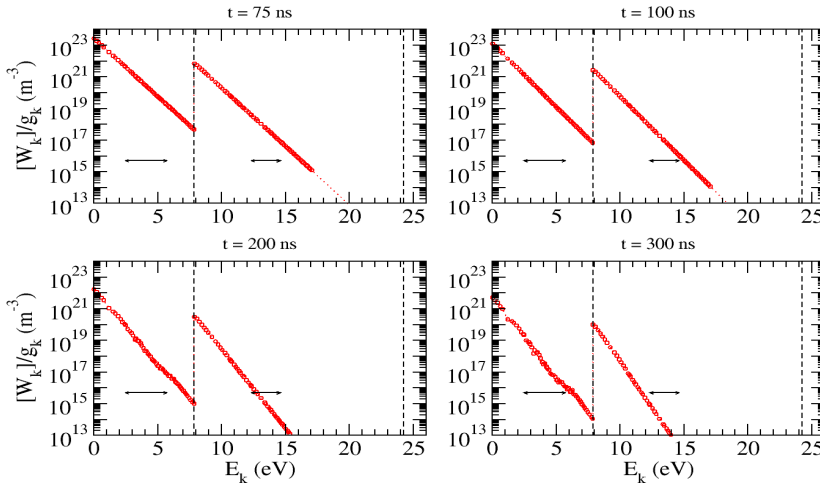


Figure 2. Same as Figure 1, but for tungsten.

At $t = 200$ ns, a departure from excitation equilibrium can be observed since the repartition is not linear. This departure increases at time $t = 300$ ns. This behavior is due to the collapse of the collision frequency resulting from the

decrease of the density of the plasma expanding in the background gas, which leads to a dramatic lack of confinement of the plasma. The double arrows correspond to upper states from which radiative transitions can be observed over the spectral range $300 \text{ nm} < \lambda < 800 \text{ nm}$. The related number densities are very weak and these spectral lines do not participate to the plasma emission. Only neutral number densities can therefore be measured using emission spectroscopy. The LIBS diagnostic developed for this type of situation has to be performed on the first hundreds of ns. It also suggests that detecting elements with high energy excitation states requires an alternative strategy based on the implementation of double pulse experiments.

4. CONCLUSION

Using the CoRaM-Al and CoRaM-W CR models for aluminum and tungsten, the departure from thermochemical equilibrium of ultra short laser-induced plasmas is studied. At low pressure, the confinement of the ablated material is not enough to maintain a sufficiently high level of the collision frequency: the plasma then strongly deexcites and recombines. The lifetime is then reduced and the plasma quickly displays a departure from equilibrium. A diagnostic such as LIBS has therefore to be used over the first hundreds of ns.

Acknowledgements

The authors acknowledge the financial support of the French Agence Nationale de la Recherche (ANR), through the program “Investissement d’avenir” (ANR-10-LABX-09-01), LabEx EMC³ and of the “Fédération de Recherche sur la Fusion par Confinement Magnétique FR-FCM-ITER”, France.

REFERENCES

- [1] A.W. Miziolek, V. Palleschi and I. Schechter, Laser-induced breakdown spectroscopy (LIBS), Fundamentals and applications, (Cambridge University Press, 2006)
- [2] G. Cristoforetti, A. De Giacomo, M. Dell’Aglia, S. Legnaioli, E. Tognoni, V. Palleschi and N. Omenetto, Spectrochim. Acta B 65, 86 (2010)
- [3] G. Cristoforetti, E. Tognoni and L. Gizzi, Spectrochim. Acta B 90, 1 (2013)
- [4] J. Annaloro, A. Bultel and P. Omary, J. Thermophys. Heat Transfer 28, 608 (2014)
- [5] A. Bultel and J. Annaloro, Plasma Sources Sci. Technol. 22, 025008 (2013)
- [6] V. Morel, A. Bultel, I. Schneider and C. Grisolia, submitted to Spectrochim. Acta Part B (2016)
- [7] V. Morel, A. Bultel, J. Annaloro, C. Chambrelan, G. Edouard and C. Grisolia, Spectrochim. Acta Part B 103-104, 112 (2015)

MONTE CARLO SIMULATION OF RADIO FREQUENCY BREAKDOWN IN AIR AND OXYGEN

Marija Savić, Dragana Marić and Zoran Lj. Petrović

Institute of Physics, University of Belgrade, Pregrevica 118, 11080 Belgrade

Abstract. We report results of a breakdown voltage, Paschen-like curves, obtained by Monte Carlo (MC) collision code for a radio frequency discharge, for frequency of 13.56MHz. Background gases are synthetic air and pure oxygen. MC code includes electrons and heavy particles, primarily ions. Effects of surface reflection and secondary electron emission on Paschen curve are discussed. Comparisons with the available experimental and simulation results are also shown. A satisfying agreement is achieved for synthetic air while the results for pure oxygen are different from experiment.

1. INTRODUCTION

Radio frequency discharges are widely used in industrial applications, from microelectronics [1] to biomedicine [2, 3]. Basic data for radio frequency plasma applications can be acquired from simulations and experimental results, and from recorded breakdown voltage curves. The DC breakdown voltages versus pd (p -pressure, d gap between two parallel electrodes) are known as Paschen curves. For RF breakdown pd scaling may be expected to work again but the curves are not determined by the Paschen law and yet these curves are often called Paschen curves in the literature. We shall call them RF breakdown or sometimes even Paschen-like curves but we shall never attempt to determine secondary electron yields from them.

A necessary condition for a self-sustained discharge is to have feedback between the electron growth toward instantaneous anode and their initialization at the cathode. In DC breakdown the necessary component is due to feedback by ion transport. In RF fields, however, electrons go in both direction so a discharge may be supported purely by electrons. First we introduce a model for radio frequency discharge in electron dominated regime. Further on, heavy particles are included.

2. RF BREAKDOWN CURVES AND DISCUSSION

Monte Carlo code used for breakdown analysis is developed and fully tested in our group. Code follows transport of electrons as well as heavy particles across the gap between electrodes. Electrodes are plane-parallel and infinite. At a beginning, electrons were released from a point in the middle of the gap. Any additional events are result of movement of particles due to electric field and solutions of kinetic and balance equations. Cross sections for oxygen are taken from Itikawa [4]. Air is synthetic, consisting of 20% of oxygen and 80% nitrogen. Cross sections for nitrogen are taken from Phelps [5]. In our previous paper we have examined radio frequency breakdown in argon under conditions when ion induced secondary emission is negligible (electron dominated regime) [6]. In this paper we move further by including ions and their contribution to secondary electrons emitted from electrodes surfaces.

Breakdown points are determined by slowly increasing voltage to approach the breakdown from below the curve (right hand side) and by increasing pressure to approach higher breakdown voltage branch (left hand side). Breakdown point is established as the one where number of electrons increases over the time (detailed discussion is given in [6]).

Figure 1 shows RF breakdown curves for synthetic air. We adjust two parameters to try to fit the experimental data, the first being the reflection coefficient for electrons on the surface of electrodes (R) and also the secondary electron yield γ (gamma) due to ion bombardment.

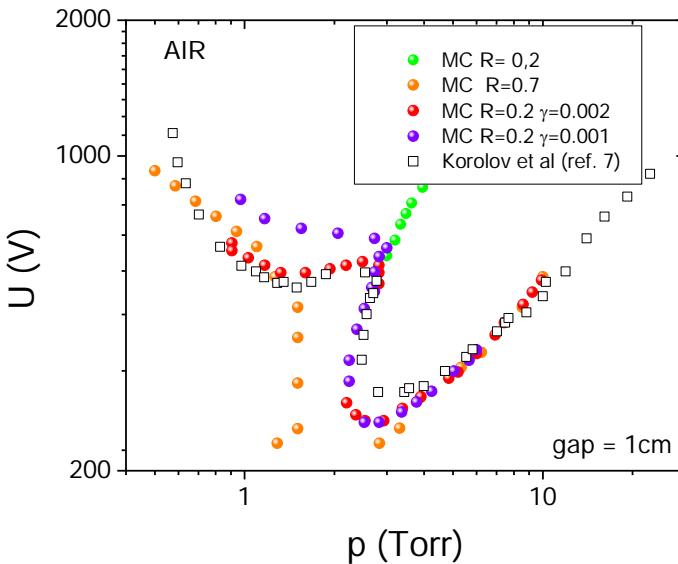


Figure 1. Paschen-like RF breakdown curves in synthetic air. Gap is 1cm, frequency 13.56MHz. Open points are the available results in literature [7].

At first, we examine MC simulation that includes only electrons with distance between electrodes of 1cm. By changing reflection coefficient one can observe deformation of Paschen curve by pushing breakdown point toward lower voltages, but there is no „second,, minimum, as Korolov et al [7] obtained in their experiment (also shown in figure 1).

Next thing to do was to include ions and their contribution to secondary electron emission. It was done by using Phelps-Petrovic analysis of surface and gas phase production of secondary electrons [8]. As a result, good agreement with Korolov et al. was achieved by an assumption that secondary electron yield for ions is 0.002.

Figure 2 presents our results and available experimental data for oxygen.

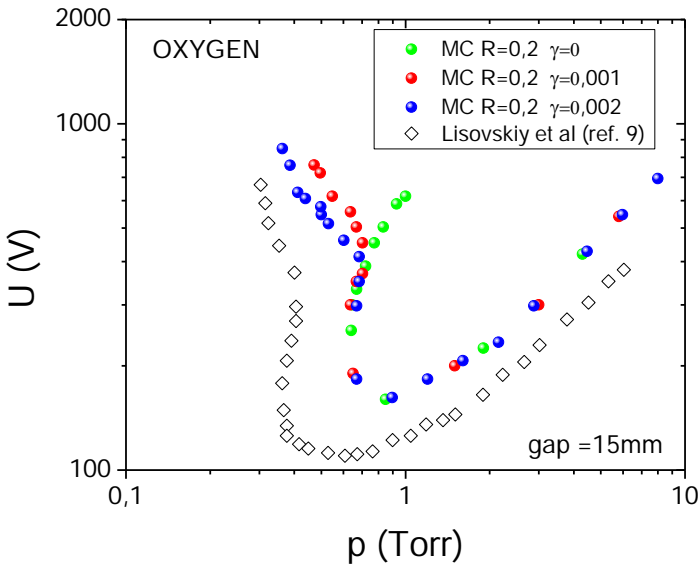


Figure 2. Paschen curves for RF breakdown in oxygen and gap of 15mm and frequency of 13.56MHz. Curves are plotted for different values of secondary electron yield γ ($=0, 0.001, 0.002$) and a constant reflection coefficient of $R=0.2$.

Unlike Paschen curve for synthetic air, we could not achieve a perfect agreement for oxygen as background gas with the available experimental data [9]. By fixing reflection coefficient to 0.2 and changing secondary electron yield from 0 to 0.002, we have managed to obtain the shape of the Paschen-like breakdown curve in accordance with experimental results, but our curve is somewhat translated to higher breakdown voltages. Disagreement is yet to be understood but in the DC breakdown it is easy to assign the magnitude of the breakdown voltage to the conditions at the surface. This, however cannot be

used here as in purely electron driven RF breakdown surface conditions are of limited effect.

We have presented results obtained by Monte Carlo code. For now, code includes electrons as well as heavy particles. Electrode surfaces are investigated by including particle reflection and secondary electron yields. We achieved satisfying agreement with experimental and simulation results for synthetic air, while for oxygen as a background gas, further analysis is required.

Acknowledgements

This work is supported by MESTD projects O171037 and III41011.

REFERENCES

- [1] T. Makabe and Z. Lj. Petrović, *Plasma Electronics: Applications in Microelectronic Device Fabrication*, 2nd edition (Taylor&Francis Group, 2015).
- [2] N. Puač, S. Živković, N. Selaković, M. Milutinović, J. Boljević, G. Malović, and Z. Lj. Petrović *Applied Physics Letters* 104, 214106 (2014)
- [3] S. Lazović, N. Puač, M. Miletić, D. Pavlica, M. Jovanović, D. Bugarski, S. Mojsilović, D. Maletić, G. Malović, P. Milenković and Z.Lj. Petrović, *New Journal of Physics*, 12 083037 (2010).
- [4] Y. Itikawa, *J.Phys.Chem.Ref.Data*, 38 1 (2009).
- [5] http://jila.colorado.edu/~avp/collision_data/electronneutral/ELECTRON.TXT
- [6] M. Savić, M. Radmilović-Radjenović, M. Šuvakov, S. Marjanović and Z. Lj. Petrović, *IEEE Transactions on Plasma Science*, 39 2556 (2011).
- [7] I. Korolov, A. Derzsi and Z. Donko, *J.Phys.D:Appl.Phys.* 47 475202 (2014).
- [8] A.V. Phelps and Z.Lj. Petrović, *Plasma Sources Sci. Technol.* 8 R21 (1999).
- [9] V. Lisovskiy, J-P Booth, K. Landry, D. Douai, V. Cassagne and V. Yegorenkov, *J.Phys.D:Appl.Phys.* 39 660 (2006).

ANALYSIS OF TRANSIT TIME OF IONS IN LOW - CURRENT DC DISCHARGE IN WATER VAPOUR

Jelena Sivoš¹, Nikola Škoro¹, Dragana Marić¹, Gordana Malović¹ and
Zoran Lj. Petrović^{1,2}

¹*Institute of Physics Belgrade, University of Belgrade, Pregrevica 118,
11080 Belgrade, Serbia*

²*Serbian Academy of Sciences and Arts, Knez Mihajlova 35, 11000 Belgrade,
Serbia*

Abstract. In this paper we present transit times of ions in water vapour discharges calculated by using the analytical model of Townsend low current discharge developed by Phelps and co-workers. Experimentally measured waveforms of the discharge current and voltage are used as input in the model. Measurements are done for electrode gaps 1.1, 2.1 and 3.1 cm and pressure (p) x electrode gap (d) of 0.3 and 0.6 Torr·cm. We compare calculated ion transit times with transit times of hydrogen ions H^+ , H_2^+ and H_3^+ in hydrogen discharge. Results indicate that H_2^+ is dominant ion in water vapour discharge for the moderate values of reduced electric fields (E/N).

1. INTRODUCTION

Development of novel devices and improvement of existing plasma applications used in bio-medicine, nanotechnology and environmental remediation [1, 2] has led to increase in studies of discharges in water and in contact with water. Since these discharges operate either in a gas mixture that contains a significant portion of water vapour or sometimes inside vapour bubbles within liquids, the main operation environment is gaseous. Therefore, it is important to study fundamental processes and properties of discharge in vapour of water. Effective way to achieve this is to measure parameters for simple geometry discharge of pure water vapour. Our aim is to investigate non-equilibrium parallel-plate DC discharge in water vapour established with different parameters and to obtain a reference set of data that can be used in modelling of breakdown, gas discharges and collisional plasmas. Here we show results of transit times of ions obtained from a simple discharge model by using experimentally determined frequency of damped oscillations and parameters of electrical circuit.

2. EXPERIMENTAL SET-UP

The discharge is established between two parallel-plate electrodes placed within a tightly fitting quartz tube. Separation of electrodes is adjustable. The cathode is made of copper, while the anode is quartz window with deposited thin, transparent and conductive platinum film. Water vapour is obtained from bi-distilled de-ionized water and introduced into the vacuum system at a slow flow rate. The electrical circuit allows discharge operation in the low-current DC regime as well as application of a voltage pulse imposed onto a running DC discharge. A more detailed description of the experiment and measurement technique can be found in [3].

3. RESULTS AND DISCUSSION

In our previous paper [3] it was shown that in water vapour discharges heavy particles – positive ions and fast neutrals that are created in charge transfer processes, can have significant contribution to the processes of excitation at moderate and high reduced electric fields (E/N). Initial assumption was that hydrogen ions and fast atoms are the most probable candidates, as the lightest products in water vapour discharges.

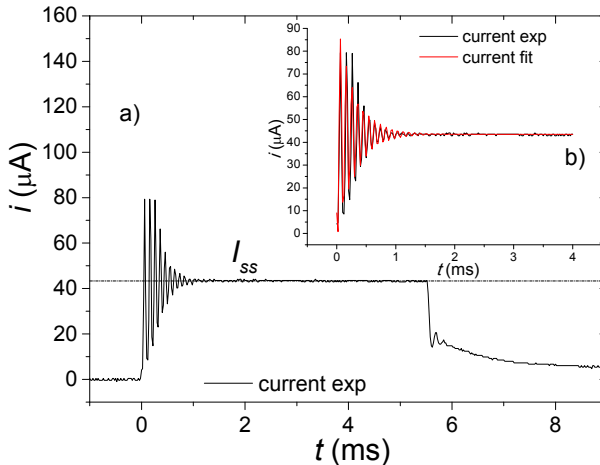


Figure 1. a) Waveform of current signal, where I_{ss} represents value of quasi-steady-state current, b) optimization (fitting) of the current waveform. The signal is measured for $pd = 0.3$ Torr \cdot cm, $d = 2.1$ cm, $R_s = 1.2$ M Ω , $R_m = 100$ k Ω , $I_{ss} = 43$ μA . Obtained damping coefficient is $k = 3.3$ kHz and angular frequency is $\omega = 64.9$ kHz.

In this paper, our aim is to identify dominant heavy species in water vapour discharge. We analysed discharge parameters by using the model developed by Phelps and co-workers [4], which is valid in low-current Townsend discharge where space charge does not represent a significant perturbation to the

applied electric field. The model allows to calculate transit time of ions using parameters of electrical circuit and experimentally determined angular frequency and damping coefficient. The data used for calculations are attained by fitting the current waveform of the discharge running in damped oscillations regime. In Figure 1 we show an example of such current signal, together with its optimization (fitting) curve in the inset. The experimentally measured current or voltage waveforms can be accurately fitted with function

$$i(t) = A \exp(-kt) \sin(\omega t) - B \quad (1)$$

where A and B are constants, ω is angular frequency and k is damping coefficient of oscillations.

Furthermore, by using formula which describes dependence between angular frequency of damped oscillations and current $\omega(I)$ for low current conditions [4], we can calculate transit time of ions in the case of water vapour

$$\omega^2 = \frac{\gamma_{ss}}{R_s C^2} \left[(R_s + R_m) \frac{\partial g}{\partial V} - \frac{k_1}{\gamma_{ss}} \right] \left[1 + \frac{\gamma_{ss} (k_1 - R_m \partial g / \partial V)}{\gamma_{ss} (1 + \gamma_{ss})} \right]^{-1} - k^2 \quad (2)$$

where C represents calculated effective capacitance of electrical circuit, R_s and R_m are resistances in the electrical circuit, $\partial g / \partial V$ is differential of the coefficient of electron multiplication g by discharge voltage V , γ_{ss} represents the effective yield of electrons per ion arriving at the cathode at the stationary discharge voltage value. The k_v term approximates contribution of “kinetic” ejection of electrons from the cathode surface and the k_1 term represents the first-order effects of space charge on the electric field, and thus, the electron yield at the cathode [4].

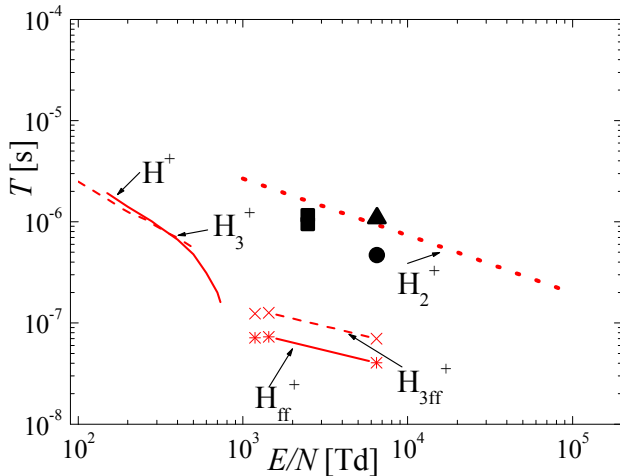


Figure 2. Transit time of ions T vs. reduced electric field E/N for discharges in water vapour and hydrogen. Water vapour discharge: full symbols – values from optimization of experimental dependence $\omega(I)$ using formula (2): ■– $d = 1.1$ cm, ●– $d = 2.1$ cm ▲– $d = 3.1$ cm. Hydrogen discharge: lines – transit time of

hydrogen ions from literature [5], lines + symbols – “free fall” (ff) time of ions [6].

In Figure 2 we show transit time of ions for discharges in water vapour calculated at different E/N values. We also show transit times of hydrogen ions H^+ , H_2^+ , H_3^+ , H_{ff}^+ , H_{3ff}^+ in hydrogen discharge [4, 6] for comparison. Our calculations are done for the discharge conditions where heavy-particle processes play important role in low-current regime [3], i.e. at $d = 1.1$ cm and $pd = 0.6$ Torr \cdot cm, which corresponds to the conditions of the minimum of Paschen curve, and $d = 2.1$ cm and $d = 3.1$ cm and $pd = 0.3$ Torr \cdot cm –the left hand-branch of Paschen curve. Analysis of obtained transit times indicates that H_2^+ is dominant ion in the range of moderate E/N s. More complex heavier ions would have significantly larger transit times. Our further investigation will be extended to the analysis to wider range of operating conditions.

Acknowledgements

This work is supported by the Serbian MESTD under project numbers ON 171037 and III 41011.

REFERENCES

- [1] K. R. Stalder, G. Nersisyan and W. G. Graham, *J. Phys. D: Appl. Phys.* 39, 3457S (2006).
- [2] T. Makabe and Z. Petrović, *Plasma Electronics: Applications in Microelectronic Device Fabrication* (Boca Raton, FL: Taylor&Francis, 2006).
- [3] J. Sivoš, N. Škoro, D. Marić, G. Malović and Z. Lj. Petrović, *J. Phys. D: Appl. Phys.* 48, 424011 (2015).
- [4] A. V. Phelps, Z. Lj. Petrović and B. M. Jelenković, *Phys. Rev. E* 47, 2825 (1993).
- [5] A. V. Phelps, *J. Phys. Chem. Ref. Data* 20, 557 (1991).
- [6] I. Stefanović and Z. Lj. Petrović, *Jpn. J. Appl. Phys.* 36, 4728-4732 (1997).

THE FIELD ASSISTED ELECTRON EMISSION IN NEON DC GLOW DISCHARGE

S. N. Stamenković, V. Lj. Marković, A. P. Jovanović and M. N. Stankov

*Department of Physics, Faculty of Sciences and Mathematics, University of Niš,
Višegradska 33, 18000 Niš, Serbia*

Abstract. The electron emission in DC glow discharge in neon with *Au-Ni* cathode spots was studied by measuring the breakdown time delay t_d as a function of working voltage U_w at low level of residual states (long relaxation time τ). It was found that voltage dependence of electron emission follows the Fowler-Nordheim equation and based on experimental data the effective work function ϕ and the effective emitting area S were estimated. In terms of late relaxation the field assisted electron ejection is supposed to be responsible for emission of electrons initiating breakdown.

1. INTRODUCTION

The phenomenon of electrical breakdown in gases takes place when the certain voltage is applied to the gas tube. However, the electrical breakdown does not occurs at the moment of voltage application (voltage greater than the static breakdown voltage U_s), but after some time called the breakdown time delay t_d . The breakdown time delay comprises statistical t_s and formative time delay t_f ($t_d = t_s + t_f$) [1].

The separation of statistical and formative time delay could be done by selecting appropriate experimental conditions [2]. In the case of high level of residual states, the t_f is the dominant part of time delay t_d , while, at low preionization, the formative time delay is negligible and $t_d \approx t_s$. That way, by selecting appropriate preionization level (relaxation time τ), only formative or statistical time delay was measured.

The breakdown time delay has stochastic character and depends on many different parameters such as working voltage U_w , relaxation time τ (afterglow period), gas pressure, dimension of the vessel, material, size and separation of electrodes, etc. The methods based on time delay measurements are very suitable in different areas of science and technology because of high sensitivity of time measurements. Modification of any aforementioned factors leads to the variation

of the time delay and by application of appropriate analytical and numerical models information on breakdown initiation and formation can be obtained.

In this paper, the measurements of breakdown time delay are used for studying the voltage dependence of electron emission in neon with galvanic gold layer on the electrodes.

2. EXPERIMENTAL DETAILS

The measurements are carried out on the gas tube made of borosilicate glass filled with research purity neon at the pressure of $1333 Pa$ with a nitrogen impurity below 1ppm. The electrodes were cylindrical (diameter $D = 6 mm$, interelectrode gap $d = 6 mm$) made of OFHC copper, deposited with sub-layer of nickel and hard galvanic gold layer. The static breakdown voltage was $U_s = 190 V$. The time delay measurements were carried out by applying rectangular voltage pulses with different working voltages, at the current $I_g = 100 \mu A$, glow time $t_g = 1 s$ and relaxation time $\tau = 1 s$. More detail about the experimental procedure including used measuring system and tube preparation can be found in [3].

3. RESULTS AND DISCUSSION

To investigate the voltage dependence or field assisted electron emission, the breakdown time delay was measured for different values of applied working voltage throughout the range $U_w \equiv U \approx U_s$ to $U \approx 2U_s$.

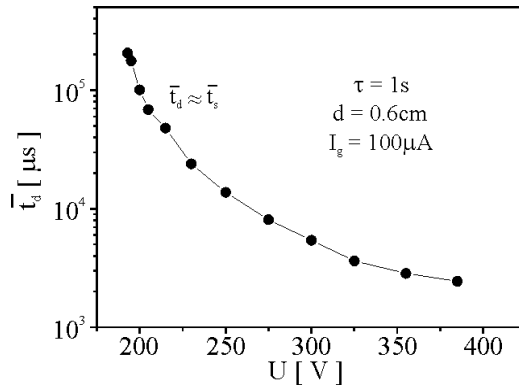


Figure 1. The voltage dependence of the breakdown time delay.

The $\bar{t}_d(U)$ dependence shown in Fig. 1 is obtained at low level of residual states and therefore electrical breakdown time delay is dominated by the statistical time delay $\bar{t}_d \approx \bar{t}_s = 1/YP$ where Y is the electron yield and P is the breakdown probability of one electron to cause a breakdown [1]. The decreasing of t_d at higher working voltages indicates increased electron emission i.e. voltage (field)

dependence of electron yield. By plotting $\ln(Y/U^2)$ against $1/U$, a straight line is obtained shown in Fig. 2.

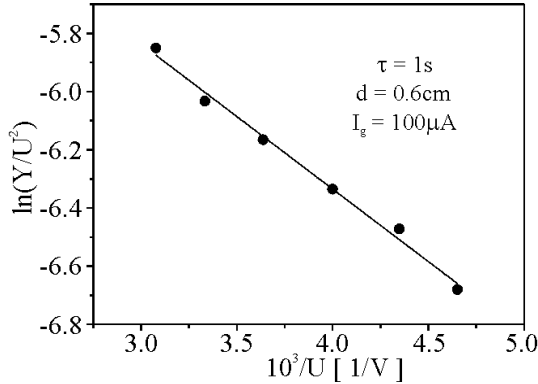


Figure 2. The Fowler-Nordheim plot (symbols – experiment; line – linear fit).

This dependence denotes functional relationship between Y and U in the form:

$$Y = A_{\text{exp}} U^2 \exp(-B_{\text{exp}}/U) \quad (1)$$

where A_{exp} is the intersection of the straight line with the ordinate axis and B_{exp} experimental value of the slope. Physical interpretation of experimentally established Eq. (1) could be obtained by its comparison with the Fowler-Nordheim equation for the field emission of electrons Y under the field $E = U/d$ [4]. In that manner, the effective work function ϕ and the effective emitting area S of the sources of initiatory electrons are estimated. Based on experimental data shown in Fig. 2, the aforementioned parameters get the values: $\phi \sim 0.5 \text{ meV}$ and $S \sim 10^{-19} \text{ cm}^2$. The very low values for work function and effective emitting area imply that, although the emission mechanism is voltage dependent, it is not pure field emission, i.e. the emission mechanism is not determined only by macroscopic field applied to the electrodes. Beside photoelectric and/or secondary electron emission, high recombination energy of nitrogen atoms (9.78 eV) may be also responsible for field assisted electron emission through adsorbed gas layers on the cathode surface [5,6]. Thus combined, multistep effect of different emission mechanisms is supposed, facilitated by relatively low external electric field.

A possible explanation of low work function is the presence of shallow electron traps formed on the cathode surface. Actually, due to diffusion of nickel atoms from intermediate barrier into the galvanic gold layer, number of impurities or inclusions increases and significantly affects properties of the gold film. As a result, semi-insulating regions are formed on the surface. The presence of such areas is proved by the scanning electron microscopy (SEM) images and energy dispersive X-ray (EDS) spectrum of the cathode surface (Fig. 3). The cathode spots (black dots in the Fig. 3) with reduced conductivity, as a mixture of nickel

and nickel oxide or other inclusions, may serve as electron traps whereby the trapped electrons have less binding energy than the intrinsic ones [7].

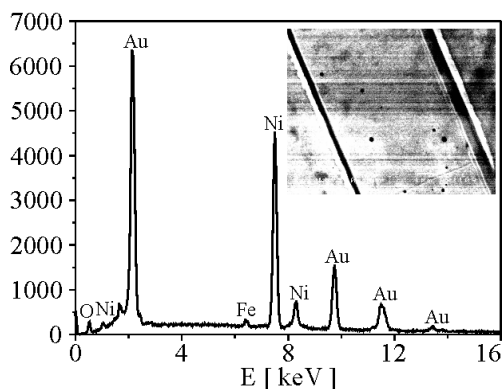


Figure 3. EDS spectrum and SEM image of the cathode surface.

Moreover, it was found that in the presence of semi-insulating region on the electrodes, surface charges could be deposited on such areas and thus affect electron emission. The deposited positive ions, produced in a discharge, may intensify electric field and field emission of electrons. The presence of the areas with reduced conductivity where the ions might be retained modifies the value of emitting areas by a factor of the order $\sim 10^9$ [8]. Taking into account this correction factor, the effective emitting areas get the values that have physical meaning, i.e. they may be attributed to electron traps on the cathode surface.

Acknowledgements

The authors are grateful to Ministry of Education, Science and Technological Development of the Republic of Serbia for partial support (project 171025).

REFERENCES

- [1] C. G. Morgan, *Electrical Breakdown of Gases*, edited by J.M. Meek, J.D. Craggs (John Wiley & Sons, Chichester, 1978).
- [2] V. Lj. Marković, S. N. Stamenković, S. R. Gocić and S. M. Djurić, *Eur. Phys. J. Appl. Phys.* 38, 73 (2007).
- [3] V. Lj. Marković, S. R. Gocić and S. N. Stamenković, *J. Phys. D: Appl. Phys.* 42, 015207 (2009).
- [4] R. H. Fowler and L. Nordheim, *Proc. R. Soc.* 119, 173 (1928).
- [5] V. Lj. Marković, Z. Lj. Petrović and M. M. Pejović, *J. Chem. Phys.* 100, 8514 (1994).
- [6] W. G. Huo, S. J. Jian, J. Yao and Z. F. Ding, *Phys. Plasmas* 21, 053505 (2014).
- [7] A. M. Abdul-Lettif, N. N. Rammo and M. N. Makadsi, *Surf. Interface Anal.* 32, 117 (2001).
- [8] F. L. Jones and C. G. Morgan, *Proc. R. Soc. A*, 215, 88 (1953)

SPECTROSCOPIC INVESTIGATION, PHOTOGRAPHIC IMAGING AND NUMERICAL MODELING OF GLOW DISCHARGE IN ARGON

M. N. Stankov, A. P. Jovanović, V. Lj. Marković and S. N. Stamenković

*Department of Physics, Faculty of Sciences and Mathematics, University of Niš,
Višegradska 33, PO Box 224, 18001 Niš, Serbia*

Abstract. The spectroscopic measurements of glow discharge in argon are performed and the axial distribution of intensity of emission line with wavelength 696.5 nm is presented. The extended fluid model is used for the modeling of stationary state of argon glow discharge. As the emission spectral line 696.5 nm corresponds to one of transitions from $2p_x$ to $1s_x$ states then the number density distribution of these argon states are compared with axial distribution of intensity of emission line.

1. INTRODUCTION

Gas discharges are widely applied in many different fields of science and technology: plasma treatments of different surfaces, light sources manufacturing, gas switches, medical treatment, etc [1, 2]. Wide application is the main reason of intensive investigation of gas discharges and electrical breakdowns from the middle of the 20th century [3]. Experimental investigation is very important for understanding of different processes during the establishment, as well as in the stationary state and relaxation of gas discharge. In addition to experimental studies, the theoretical analysis based on analytical and numerical models, are often necessary for complete understanding of gas discharges.

In this paper the investigation of stationary state of glow discharge in argon at pressure $p = 226.6$ Pa is performed. The extended fluid model is applied for determination of number density distribution of excited states of argon atom between the electrodes. These distributions are compared with the distribution of intensity of one spectral line from visible part of spectrum. The paper is organized as follows: in section 2 the theoretical description of extended fluid model is given, the details of experiment are presented in section 3, the results of experiment and modeling are presented in section 4 and finally, in section 5 the conclusion is given.

2. EQUATIONS

Fluid models are used very often for the modeling of different types of gas discharges. Three types of fluid models can be found in the literature [4, 5]: simple, extended and fluid model with nonlocal ionization. In this paper, one dimensional extended fluid model is applied for the modeling of stationary state of glow discharge in argon. This model consists of the following equations:

$$\frac{\partial n}{\partial t} + \nabla \Gamma = S, \quad (1)$$

$$\frac{\partial n^{ele} u^{ele}}{\partial t} + \frac{5}{3} \nabla \Gamma_u^{ele} = S_\varepsilon, \quad (2)$$

$$\nabla^2 \varphi = -\frac{e}{\varepsilon_0} (n^{ion} - n^{ele}), \quad (3)$$

where n is the number density of particles, Γ are the fluxes of particles, S is the source term, u^{ele} is the mean electron energy, Γ_u^{ele} is electron energy flux, S_ε is energy source term, φ is the electric potential, e is the electron charge and ε_0 is the vacuum permittivity. The equation (1) represents continuity equation for particle number density determination, while the equation (2) is energy balance equation for electron energy determination. For the calculation of electric potential between the electrodes, Poisson equation (3) is used.

3. EXPERIMENTAL DETAILS

The experimental measurements are performed on the gas tube filled with argon at the pressure $p = 226.6$ Pa. The tube is made of borosilicate glass 8245 (Schott technical glass) with two electrodes, one made of OFHC copper and the other made of stainless steel (AISI 304). The inter electrode distance is $d = 1$ cm and both electrodes have the same diameter $D = 2.2$ cm. The measurements are performed for the applied voltage of $U = 300$ V and glow current of $I_g = 150$ μ A. The spectrometer Ocean Optics HR2000+CG is used to obtain emission spectrum of glow discharge, while the camera with Sony CMOS Exmor RS IMX220S sensor is used for imaging of discharge axial profile.

4. RESULTS AND DISCUSSION

The emission spectrum of argon glow discharge is presented in Figure 1. This spectrum is recorded for the applied voltage of $U = 300$ V and glow current of $I_g = 150$ μ A. The certain lines are marked in the figure and they represent some of transitions from $2p_x$ to $1s_x$ states of argon atoms. In the Figure 2a the digitalized image of glow discharge is given. The regions with different intensity of light are marked with different colors, where the red color represents

the region with the highest intensity, while the blue one is the region with lowest intensity. This light consists of the spectral lines in the visible part of spectrum. We chose one line with wavelength of 696.5 nm in the visible part of spectrum and recorded its intensity at different distances from the cathode.

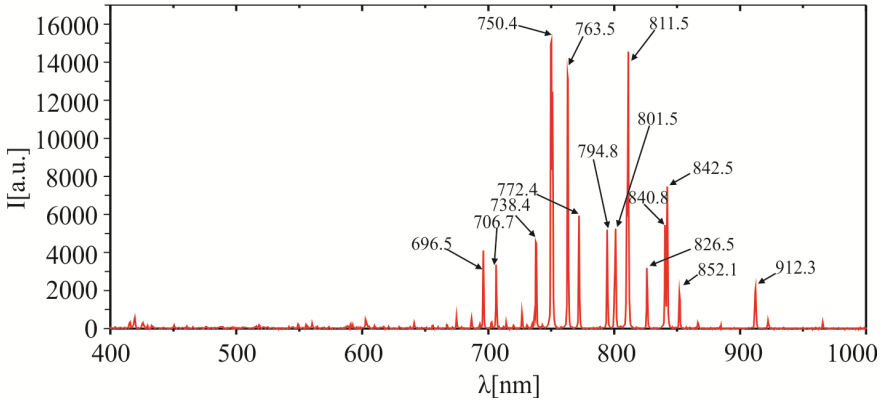


Figure 1. Emission spectrum of argon glow discharge at pressure $p = 226.6$ Pa.

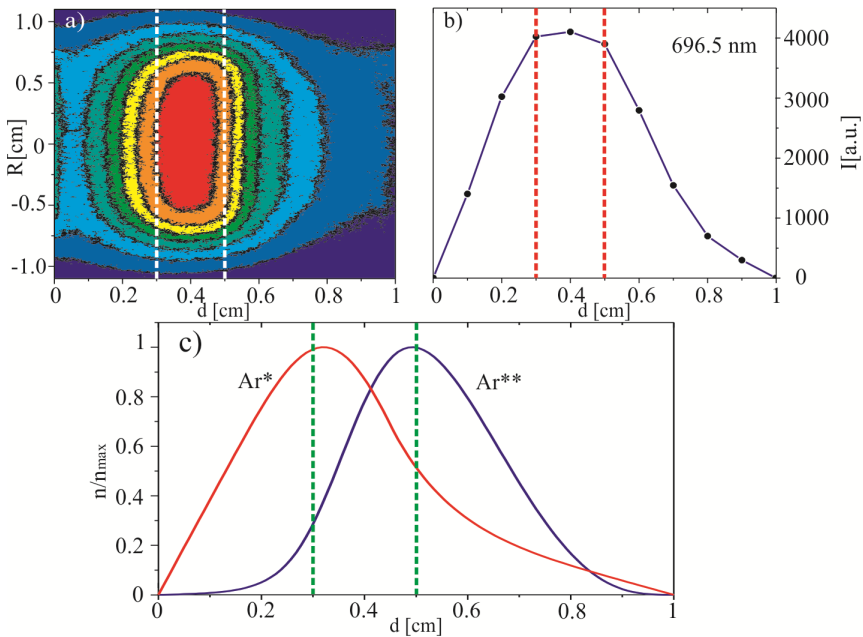


Figure 2. a) Digitalized image of argon glow discharge for the applied voltage of $U = 300$ V and glow current of $I_g = 150 \mu\text{A}$, b) axial distribution of spectral line intensity of wavelength 696.5 nm and c) the number density distributions of $\text{Ar}^*(1s_x)$ and $\text{Ar}^{**}(2p_x)$ states.

This line corresponds to transition from $2p_2$ state to $1s_5$ state. The measured intensity distribution is given in the Figure 2b. It can be seen that the light is most intensive in the region (0.3 cm-0.5 cm) where the intensity of line 696.5 nm has the maximum value (fig.2b). Beside the spectroscopic measurements, the numerical modeling of stationary state of glow discharge is carried out at the same conditions. The following particles are included in the modeling: electrons, Ar^+ ions, Ar_2^+ ions and Ar^* and Ar^{**} excited states. The states $1s_x$ are designated as Ar^* and represent four states with very close energies (11.5 eV-11.8 eV), while $2p_x$ states are designated as Ar^{**} and represent ten states also with very close energies (12.9 eV-13.5 eV). As the spectral line 696.5 nm represents one of the transitions from $4p$ to $4s$ states then it can be assumed that the region where this line has the highest intensity should be the region where the atoms in $2p_x$ and $1s_x$ states have the highest number densities. The number density distributions of these states, obtained from the modeling, are given in the Figure 2c. It can be noticed that the highest number densities of Ar^* and Ar^{**} excited states are in the region where spectral line 696.5 nm has the highest intensity, as it was assumed.

5. CONCLUSION

The stationary state of glow discharge in argon at pressure $p = 226.6$ Pa is studied by the spectroscopic measurement, as well as by the numerical modeling. The intensity of spectral line with wavelength of 696.5 nm is measured and its axial distribution is presented. This spectral line corresponds to one of transitions from $2p_x$ to $1s_x$ states and it is assumed that the intensity maximum of this line must be in the region where the argon atoms in $4s$ and $4p$ states have the highest number densities. Based on the results of modeling this assumption is confirmed.

Acknowledgements

The author is grateful to the Ministry of Education, Science and Technological development of the Republic of Serbia (projects 171025).

REFERENCES

- [1] J. E. Harry, Introduction to plasma technology (Wiley, Weinheim, 2010)
- [2] M. G. Kong et al, New J.Phys. 11, 115012 (2009)
- [3] J.M. Meek, J.D. Craggs, Electrical Breakdown of Gases (Clarendon Press, Oxford, 1953)
- [4] I. Rafatov, E. A. Bogdanov and A. A. Kudryavtsev, Phys. Plasmas 19, 093503 (2012)
- [5] M. N. Stankov et al, Chin. Phys. Lett. 32, 025101 (2015)

MODELING EMISSION FROM WATER VAPOR DC DISCHARGE AT LOW PRESSURE

Vladimir Stojanović, Nikola Škoro, Jelena Sivoš, Gordana Malović,
Dragana Marić and Zoran Petrović

Institute of Physics Belgrade, University of Belgrade, 11001 Belgrade, Serbia

Abstract. We follow transport of electrons, positive ions and fast H atoms in H₂O in high DC fields by using Monte Carlo simulation technique. Cross section sets for scattering of electrons, positive ions (H⁺, H₂⁺, OH⁺, H₂O⁺, H₃O⁺) and fast hydrogen atoms on H₂O were assessed and used as an input in Monte Carlo simulations. In this paper we show results of our Monte Carlo simulations (MCS) for spatially resolved H α emission for the conditions of high reduced electric fields E/N (N -gas density). Cross section for H α excitation of H₂O by fast H atoms is modified in order to obtain agreement with a range of experimental results for H α emission from moderate to high E/N .

1. INTRODUCTION

Interest in application of plasmas in medicine, nanotechnologies and environmental applications [1-5] has motivated studies of discharges in water and with water vapour as well as the water boundaries [6]. Current studies show that in such systems, discharge is produced in water vapour either from evaporating liquid electrode or in bubbles created by an induced phase transition within the liquid. Since all atmospheric discharges contain some degree of water vapour it is of an increased interest to determine how discharges are created in water [7-9] both liquid, at the interface between liquid and gas and in water vapour. Accurate knowledge of the electrical properties of water vapor and in particular its breakdown potential [10,11] are the basic information for modelling in various situations. Complicated chemistry and poor understanding for range of processes of particles interacting with gas and surface forced to further insights of such discharges. In this work our aim is to model spatially resolved H α emission in water vapor gas by using assembled cross sections for positive ions (H⁺, H₂⁺, OH⁺, H₂O⁺, H₃O⁺) and fast H neutrals scattered on H₂O and to explore effects of heavy particles.

2. MONTE CARLO SIMULATION

A Monte Carlo simulation (MCS) was employed to model the Townsend discharge with parameters used in the experiment and take into account boundary conditions, spatially dependent transport coefficients for electrons and heavy particles as well as distribution functions that may include a runaway component. Monte Carlo code for electron transport was coupled with similar particle codes involving ions and neutrals [12]. Cross sections for electron collisions were taken from the literature [13,14]. For heavy-particle processes we modified collision cross sections from the data reviewed by Phelps [15,16] and Miller and Green [17] assuming the dominant role of fast H atoms in excitation. For ions other than H^+ we exploited Denpoh-Nanbu theory [18,19] to calculate cross sections for elastic and reactive processes which were extrapolated towards high energy by a hard sphere cross section. Energy partition of ions dissociated at the cathode is according to data for pure H_2 discharge as well as integrated probability of escape [16]. Electrons reflected from the electrodes were also included in the simulation. As an output of the model we observed H emission coming from excitation induced by electrons and in heavy particle collisions.

3. RESULTS

Spatial discharge profiles recorded with $H\alpha$ filter have the same shape as the profiles of emission integrated in visual spectra [10]. This indicates that major contribution to overall emission comes from excited hydrogen atoms, both in the regime where electrons play a crucial part in excitation and also in the case of heavy-particle excitation. In order to clarify a particular role of H atoms and all possible heavy-particles involved, we have modified cross section for fast H [16] (dashed-dot-dot line in Fig. 1) by fitting Monte Carlo results for spatial emission to experimental emission data from moderate(not shown) to very high E/N .

Modified cross section for $H\alpha$ excitation by fast H atoms is presented by connected solid line in Fig.1. Energy distribution function (EDF) of fast H atoms at the cathode is shown in Fig. 1 for 6.1 kTd and 14.4 kTd ($1 \text{ Td}=10^{-21} \text{ Vm}^2$).

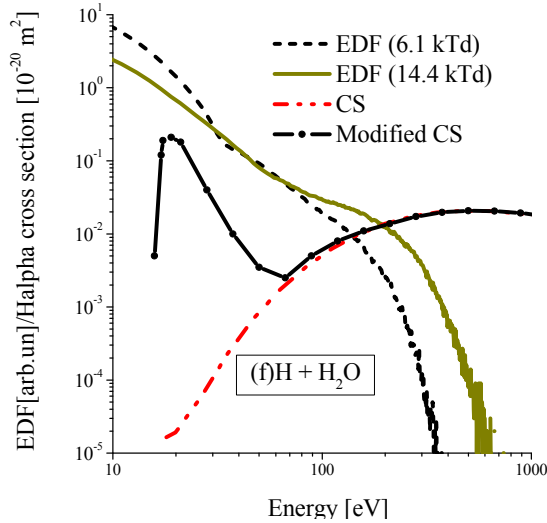


Figure 1. Cross sections for H α emission/EDF as a function of energy. Energy distribution function (EDF) of fast H particles 0.05 cm from the cathode.

In Fig. 2 we show comparison of Monte Carlo simulation (MCS) results with experimental data (EXP) at very high E/N . The experimental results are

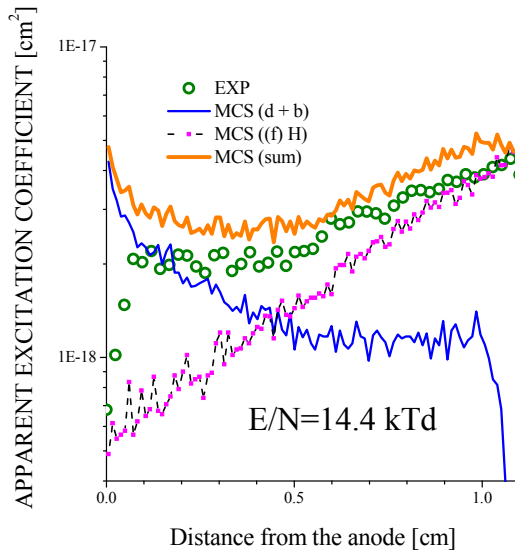


Figure 2. Comparison of the experimental and Monte Carlo simulation results for the apparent excitation coefficient as a function of the distance from the anode in pure water vapor discharge at $E/N=14.4$ Td.

normalized to the apparent (electron induced) excitation coefficient [16] at the anode. Total H α emission signal obtained from MCS (sum) consists of a sum of electron component (d + b) including backscattered electrons (b), and fast H component [(f) H] which accounts also for all fast H reflected back from the cathode.

Acknowledgements

Results obtained in the Institute of Physics University of Belgrade under the auspices of the Ministry of Education, Science and Technology, Projects No. 171037 and III 41011.

REFERENCES

- [1] K. R. Stalder, G. Nersisyan and W. G. Graham, *J. Phys. D: Appl. Phys.* **39** 3457 (2006).
- [2] T. Makabe and Z. Petrović *Plasma Electronics: Applications in Microelectronic Device Fabrication* (Boca Raton, FL: Taylor&Francis, 2006)
- [3] M. Laroussi, *Plasma Process. Polym.* **2**, 391 (2005).
- [4] Long and short term effects of plasma treatment on meristematic plant cells N. Puač, S. Živković, N. Selaković, M. Milutinović, J. Boljević, G. Malović, and Z. Lj. Petrović *Applied Physics Letters* **104**, 214106 (2014).
- [5] K. Kutasi and J. Loureiro, *J. Phys. D* **40**, 5612 (2007).
- [6] P. Bruggeman, D. Schram, M. Á. González, R. Rego, M. G. Kong, and C. Leys, *Plasma Sources Sci. Technol.* **18**, 025017 (2009); P. Bruggeman and C. Leys, *J. Phys. D: Appl. Phys.* **42** 053001 (2009).
- [7] G. Ruíz-Vargas, M. Yousfi, and J. de Urquijo, *J. Phys. D* **43**,455201 (2010).
- [8] Y. Itikawa and N. Mason, *J. Phys. Chem. Ref. Data* **34**, 1 (2005).
- [9] R. E. Robson, R. D. White, and K. F. Ness, *J. Chem. Phys.* **134**,_064319 (2011).
- [10] N. Škoro, D. Marić, G. Malović, W. G. Graham, and Z. Lj. Petrović, *Phys.Rev. E* **84**, 055401(R) (2011).
- [11] M. Radmilović-Radenović, B. Radenović, Ž. Nikitović, Š. Matejčik and M. Klas, *Nucl. Instr.Meth. in Phys.Res. B* **279** pp.103-105 (2012).
- [12] V. Stojanović, B. Jelenković, Z. Lj. Petrović *J. Appl. Phys.* **81** 1601-1603 (1997).
- [13] A.V. Phelps <http://www.lxcat.laplace.univ-tlse.fr> retrieved June 4, (2013).
- [14] Y. Itikawa, N. Mason *J. Phys. Chem. Ref. Data* **34** 1 (2005).
- [15] A. V. Phelps *J. Phys. Chem. Ref. Data* **19** 653-675 (1990).
- [16] A. V. Phelps *Phys. Rev. E* **79** 066401 (2009).
- [17] J. H. Miller, A. E. S. Green *Rad. Res.* **54** 343 (1973).
- [18] K. Denpoh and K. Nanbu, *J. Vac. Sci. Technol. A* **16** 1201 (1998).
- [19] V. Stojanović, Z. Raspopović, *et al* , *Eur. Phys. J. D* **69**, 63 (2015).

GAS TEMPERATURE MEASUREMENTS IN HYDROGEN-ARGON MIXTURE GRIMM GLOW DISCHARGE

M. M. Vasiljević¹, G. Lj. Majstorović² and N. M. Šišović¹

¹*University of Belgrade, Faculty of Physics, 11001 Belgrade,
P.O. Box 44, Serbia*

²*University of Defence, Military Academy, 11105 Belgrade,
Pavla Jurišića Šturma 33, Serbia
e-mail: gordana.majstorović@va.mod.gov.rs*

Abstract. Emission spectroscopy technique is used to measure gas temperature along the axis of cylindrical abnormal glow discharge parallel (side-on) to the copper cathode surface in hydrogen - argon mixture at low pressure. The rotational temperature of excited electronic states of H₂ was determined from the intensity distribution in the rotational structure of R branch of the $GK \rightarrow B$ (0-0) band using Boltzmann plot technique while the obtained of the ground vibrational state $X^1\Sigma_g^+$ ($v=0$) temperature T_0 is assumed equal to translational gas temperature T_{tr} . Under our experimental conditions, translational gas temperature is two times larger than the rotational temperatures of excited state $GK^1\Sigma_g^+$.

1. INTRODUCTION

Within the growing number of applications Glow Discharge Sources (GDS) are successfully used as an excitation source for analytical spectroscopy of metal and alloy samples [1, 2]. The most of GDS applications is based on original Grimm design [3, 4] with both direct current (DC) and radio frequency (RF) excitation.

For characterization of Grimm GDS, the knowledge of discharge parameter like the translational gas temperature T_{tr} of molecules and radicals is of particular importance since it determines the rate of chemical reactions.

In this study, OES technique is used to measure gas temperature in Grimm type discharge source in hydrogen - argon mixture at low pressure. For that purpose, $GK^1\Sigma_g^+$, $\nu' \rightarrow B^1\Sigma_u^+$, ν'' ($\nu' = \nu'' = 0$) band are recorded and analyzed in the cathode fall region of glow discharge.

2. EXPERIMENTAL

A detailed description of a modified Grimm GDS is given in [4] and thus only few important details will be mentioned here. The experiment was realized in hydrogen-argon (5% vol. Ar) mixture. The continuous flow of about $300\text{cm}^3/\text{min}$ of gas (at room temperature and atmospheric pressure) was sustained in the pressure range 5-10mbar by means of needle valve and two two-stage mechanical vacuum pumps. The reported results for gas pressure represent an average between gas inlet and outlet pressure measurements. To run the discharge a current stabilized power supply (0-2kV, 0-100mA) is used. A ballast resistor of $5.3\text{k}\Omega$ is placed in series with the discharge and the power supply.

The axial intensity distribution of radiation has been observed side-on through the anode slot, see Figure 1. The discharge tube was translated in approximately 0.125mm steps. The light from the discharge was focused with an achromatic lens (focal length 75.8mm) with unity magnification onto the $20\mu\text{m}$ entrance slit (height restriction 2mm) of 2m focal length Ebert type spectrometer with $651\text{g}/\text{mm}$ reflection grating blazed at 1050nm . For the line shape measurements the reciprocal dispersion of $0.37\text{nm}/\text{mm}$ is used throughout this experiment. All spectral measurements were performed with an instrumental profile very close to Gaussian form with measured full width at half maximum (FWHM) of 8.2pm .

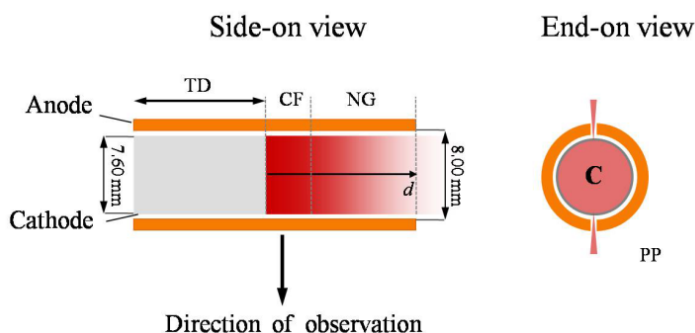


Figure 1. Schematic diagram of the central part of the Grimm GD for side-on and end-on observations. Symbols: TD – translation direction; CF – cathode fall region, NG – negative glow region, PP – protruding plasma, C – cathode.

3. RESULTS AND DISCUSSION

In the recent study, see Ref. [5], we have investigated the possibility of using R and/or P branches ($v'=v''=0$) of the $GK^1\Sigma_g^+, v', J' \rightarrow B^1\Sigma_u^+, v'', J''$ molecular system for temperature measurement in HCGD. The temperature obtained using limited number of spectral lines from R branch of $GK \rightarrow B$ transition agrees well with temperature measured from Q branch of Fulcher- α band, considered as the most reliable for temperature estimation. It was found

that for rotational and ground state $T_0(n', \nu')$ temperature monitoring it is possible to use first five lines of R-branch of $GK \rightarrow B''(\nu' = \nu'' = 0)$ band. Now, we investigate the possibility of using R branch of the $GK^1\Sigma_g^+, \nu', J' \rightarrow B^1\Sigma_u^+, \nu'', J''$ molecular system for temperature measurement in hydrogen-argon mixture Grimm GDS.

From the recorded spectra, see Figure 2, it was evident that R branch lines of the $GK^1\Sigma_g^+ \rightarrow B^1\Sigma_u^+(\nu' = \nu'' = 0)$ electronic transition are well resolved and have high enough intensities in the 453-463nm wavelength region (wavelength data are taken from [6]). The recorded rotational band of the ($GK^1\Sigma_g^+ \rightarrow B^1\Sigma_u^+$) hydrogen transition is used for evaluation of rotational temperature $T_{rot}(n', \nu')$ of excited state using Boltzmann plot (BP) technique.

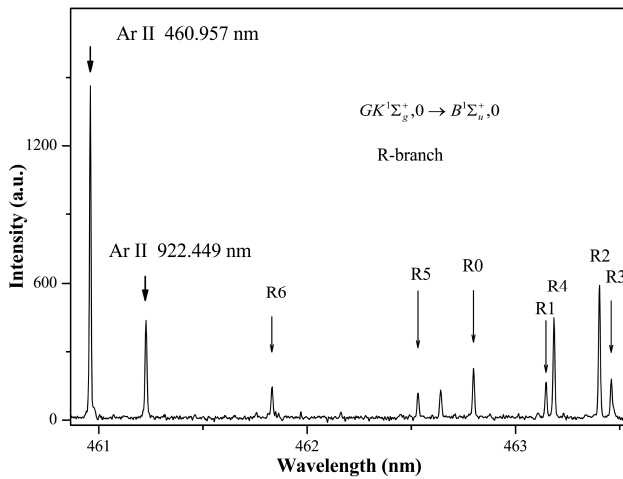


Figure 2. Emission spectra of rotational lines for $GK \rightarrow B(\nu' = \nu'' = 0)$ system; R-branch (with $\nu' = \nu'' = 0$) recorded in the second order of diffraction grating. Experimental conditions: cooper cathode Grim GD in $H_2 + 5\%Ar$ at $p = 4.5\text{mbar}$; $I = 13.4\text{mA}$; $U = 646\text{V}$.

In low pressure discharges, due to small collision frequencies, lower than the radiative decay of the excited state, the number of collisions is not sufficient to redistribute the rotational population. Within the framework of model discussed in [7], the rotational temperature of ground vibrational state $T_0(n', \nu')$ determined from the rotational population density distribution in an excited (n', ν') vibrational can be considered as a valid estimation of the ground state rovibrational temperature i.e. H_2 translational temperature T_{tr} . In our case the temperature recalculated [5] for the ground vibrational state $X^1\Sigma_g^+(\nu = 0)$ is two times larger than the rotational temperature of excited states since the rotational constants [8] for the upper $G^1\Sigma_g^+$ and ground $X^1\Sigma_g^+(\nu = 0)$ states are 28.4cm^{-1} and 60.853cm^{-1} , respectively.

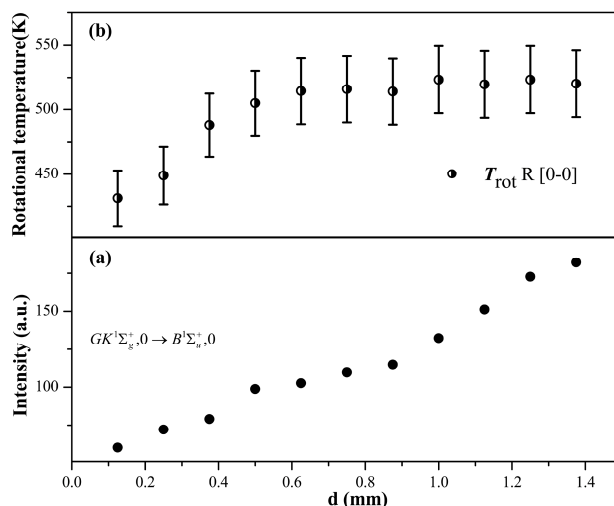


Figure 3. The dependence: (a) Relative intensity of R-branch of $GK \rightarrow B$ ($\nu' = \nu'' = 0$) band and (b) Rotational temperature of the excited state $GK^1\Sigma_g^+$ upon distance from cathode. Experimental conditions: cooper cathode Grim GD in $H_2 + 5\%Ar$ at $p = 4.5\text{mbar}$; $I = 13.4\text{mA}$; $U = 646\text{V}$.

Acknowledgements

This work is supported by the Ministry of Education, Science and Technological Development of the Republic of Serbia under Project 171014.

REFERENCES

- [1] N. Jakubowski, A. Bogaerts and V. Hoffmann, *Atomic Spectroscopy in Elemental Analysis*, (Sheffield: Cullen M., Blackwell Publishing, 2003) Glow discharges in emission and mass spectrometry.
- [2] J. A. C. Broekaert, *Glow Discharge Plasmas in Analytical Spectroscopy*, p. 28, (eds. R. K. Marcus and J. A. C. Broekaert, New York: Wiley, 2003).
- [3] W. Grimm, *Spectrochim. Acta B* 23, 443 (1968).
- [4] G. Lj. Majstorović, N. V. Ivanović, N. M. Šišović, S. Djurović and N. Konjević, *Plasma Sources Sci. Technol.* 22, 045015 (2013).
- [5] G. Lj. Majstorović, N. M. Šišović, *Journal of Research in Physics* 36, 1, (2012).
- [6] H. M. Crosswhite. *The hydrogen molecule wavelength tables* (Gerhard Heinrich Dieke, New York: Wiley-Interscience; 1972).
- [7] S. A. Astashkevich, M. Käning, E. Käning, N. V. Kokina, B. P. Lavrov, A. Ohl and J. Röpcke, *J. Q. S. R. T.* 56, 725 (1996).
- [8] G. Herzberg, *Molecular spectra and molecular structure vol I*, p. 125, (New York: Van Nostrand-Reinhold, 1950).

A NEW MODEL OF RESISTIVE PLATE CHAMBERS BASED ON HYDRODYNAMIC APPROXIMATION

D. Bošnjaković, Z. Lj. Petrović and S. Dujko

*Institute of Physics, University of Belgrade,
Pregrevica 118, 11070 Belgrade, Serbia*

Abstract. A novel approach based on hydrodynamic approximation is employed in fluid modeling of Resistive Plate Chambers (RPCs) which are used for timing and triggering purposes in many high energy physics experiments. The model is numerically implemented in a 1.5-dimensional scenario and is utilized for studying of streamer and signal development in two RPC configurations used at CERN. The results are compared with classical fluid model.

1. INTRODUCTION

Owing to their good efficiency, excellent timing resolution and low cost, Resistive Plate Chambers (RPCs) became widely used particle detectors for large area timing and triggering purposes in high energy physics experiments [1, 2]. They consist of one or many gas gaps sandwiched between the electrodes of high volume resistivity such as glass or bakelite. RPCs also found their way into other areas such medical imaging, cosmic ray physics and geophysics [3].

Many approaches were used in simulation and modeling of RPCs. Still, all RPC models, except the microscopic Monte Carlo model [4], require accurate electron transport data in gases as input. Numerical models based on fluid equations were used for studying the underlying physics and signal development in RPCs [5, 6]. However, these were based on classical fluid model where the diffusion flux was often neglected and the duality of transport data used as input was systematically ignored. Namely, in particle detector community, there seems to be a lack of awareness of the two types of transport data named ‘flux’ and ‘bulk’ [7]. The two may differ considerably when non-conservative collisions such as attachment and ionization are present.

In this work, we present a new approach in fluid modeling of RPCs which is solely based on hydrodynamic approximation. This model is employed for studying the signal development in two RPC configurations used in ALICE and ATLAS experiments at CERN. For comparison, the results are also calculated using classical fluid model with flux and bulk transport data as input.

2. THEORETICAL METHODS

The fluid model developed in this work is based on hydrodynamic approximation which assumes that the electron distribution function can be expanded in terms of gradients of the electron number density [8]. This assumption is strictly valid for weak gradients in absence of sources or sinks of electrons. Under these conditions, the continuity equation for electrons in one-dimensional scenario can be written as

$$\frac{\partial n_e}{\partial t} = \frac{\partial}{\partial x} \left(W_F \operatorname{sgn}(E) n_e + D_{L,F} \frac{\partial n_e}{\partial x} \right) + S_i - S_a + S_{\text{ph}}, \quad (1)$$

where the electric field \mathbf{E} is oriented along the x -axis while W_F , $D_{L,F}$ and S_{ph} denote flux drift velocity, flux longitudinal diffusion and source term due to photoionization, respectively. Using hydrodynamic approximation, the source terms due to ionization (S_i) and attachment (S_a) are also expanded as

$$S_m = S_m^{(0)} n_e + S_m^{(1)} \operatorname{sgn}(E) \frac{\partial n_e}{\partial x} + S_{L,m}^{(2)} \frac{\partial^2 n_e}{\partial x^2} \quad (m = i, a). \quad (2)$$

The ions can be considered as immobile on the timescale of fast electron signal. Therefore, the balance equations for number densities of positive (n_p) and negative ions (n_n) are written as

$$\frac{\partial n_p}{\partial t} = S_i + S_{\text{ph}} \quad \text{and} \quad \frac{\partial n_n}{\partial t} = S_a. \quad (3)$$

We assume that the charge is contained inside a cylinder, with radius R_0 along the x axis, and distributed uniformly in the radial direction. For this case, the expression for electric field along the x axis is given in [9]. Source term due to photoionization is calculated as in [10] and assumes that the photon production rate is proportional to the ionization rate.

Equations (1) and (3) are solved numerically imposing homogeneous Dirichlet boundary conditions at the gas gap boundaries. The numerical scheme uses second-order central finite differences for discretization of spatial derivatives and classical fourth-order Runge–Kutta 4 scheme for integration in time. Finally, the induced current is calculated using Ramo's theorem [11]

$$i(t) = e_0 \pi R_0^2 \frac{E_w}{V_w} \int_0^d n_e(x, t) W_F(|E(x, t)|) \operatorname{sgn}(E(x, t)) dx, \quad (4)$$

where E_w/V_w is the weighting field and d is the gas gap length.

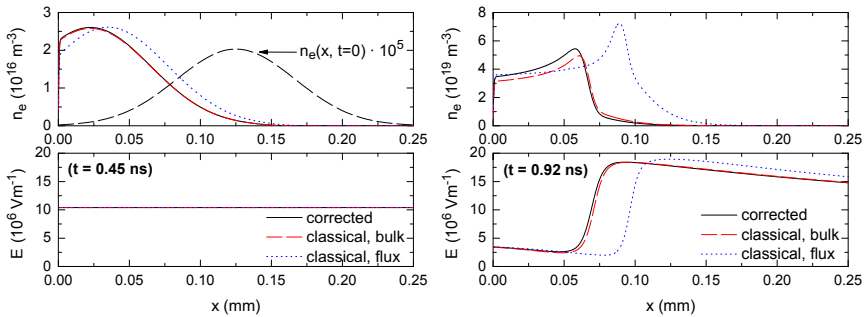


Figure 1. Electron number density and electric field along the gas gap of ALICE timing RPC at $t = 0.45$ ns during avalanche development (left), and $t = 0.92$ ns during positive streamer formation (right). The external electric field is set to 10.4 MV/m. Calculations are made using corrected fluid model and classical fluid model with flux and bulk transport data as input.

3. RESULTS AND DISCUSSION

The fluid model presented in previous section is used to study the streamer development and signal formation in ATLAS triggering RPC [1] and ALICE timing RPC [2]. For example, ALICE timing RPC uses five 0.25 mm gas gaps with a gas mixture of 90% $C_2H_2F_4$ + 5% iso- C_4H_{10} + 5% SF_6 . The transport data and source term expansion coefficients are calculated by our Monte Carlo code [12] using the cross section set for electron scattering in $C_2H_2F_4$ developed by our group [13], cross sections for iso- C_4H_{10} taken from MAGBOLTZ 7.1 code (developed by S. Biagi [14]), and cross sections for SF_6 taken from Itoh et al. [15].

For comparison, the results are calculated using both ‘corrected’ fluid model described in previous section and classical model with either bulk or flux transport data. Mathematically, the corrected model reduces to classical model if $S_m^{(1)} \equiv S_m^{(2)} \equiv 0$ ($m = i, a$). We assume that the initial electron distribution at $t = 0$ is a Gaussian representing 6 primary electrons. Figure 1 (left) shows the electron number density and electric field at time instant $t = 0.45$ ns during avalanche development in ALICE timing RPC. At this moment, there are no space charge effects and the profiles obtained using corrected model match with those obtained using classical model with bulk data. During the avalanche phase, the induced current grows exponentially with time (Figure 2). Afterwards, the exponential rise gradually stops due to both space charge effects and electron absorption at the anode. At about 0.92 ns, the positive streamer starts to develop (Figure 1, right) and the current rises again while the streamer progresses towards the cathode (Figure 2). The positive streamer stops at about 1 ns and starts to diminish while the induced current slowly drops to zero. In the streamer stage, there is an obvious difference between the profiles and induced currents for the

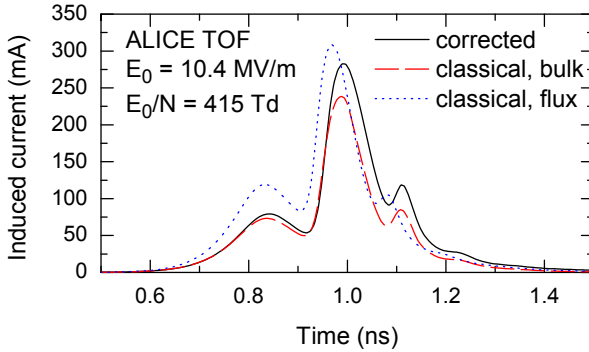


Figure 2. Induced current in ALICE timing RPC calculated using corrected fluid model and classical fluid model with flux and bulk transport data as input. The external electric field is set to 10.4 MV/m.

three modeling scenarios. The difference arise mainly due to different drift velocities and representation of the source term employed in these models.

Acknowledgements

This work is supported by MPNTRRS Projects OI171037 and III41011.

REFERENCES

- [1] The ATLAS Collaboration, *J. Instrum.* 3, S08003 (2008).
- [2] The ALICE Collaboration, *J. Instrum.* 3, S08002 (2008).
- [3] R. Santonico, *Nucl. Instrum. Meth. A* 661, S2 (2012).
- [4] D. Bošnjaković, Z. Lj. Petrović and S. Dujko, *J. Instrum.* 9, P09012 (2014).
- [5] A. Moshaii et al., *Nucl. Instrum. Meth. A* 661, S168 (2012).
- [6] L. Khosravi Khorashad et al., *EPL (Europhys. Lett.)* 96, 45002 (2011).
- [7] R. E. Robson, *Aust. J. Phys.* 44, 685 (1991).
- [8] K. Kumar, H. R. Skullerud and R. E. Robson, *Aust. J. Phys.* 33, 343 (1980).
- [9] A. J. Davies, C. J. Evans and F. L. Jones, *Proc. R. Soc. A Math. Phys. Eng. Sci.* 281, 164 (1964).
- [10] L. E. Kline, *J. Appl. Phys.* 45, 2046 (1974).
- [11] S. Ramo, *Proc. I.R.E.* 27, 584 (1939).
- [12] Z. M. Raspopović et al., *IEEE Trans. Plasma Sci.* 39, 2566 (2011).
- [13] O. Šašić et al. (2016), unpublished.
- [14] S. Biagi, *Nucl. Instrum. Meth. A* 421, 234 (1999).
- [15] H. Itoh et al., *J. Phys. D: Appl. Phys.* 26, 1975 (1993).

MEDIUM TO LOW ENERGY ANION BEAMS AND THEIR APPLICATION TO BIOMOLECULE FRAGMENTATION

L. Ellis-Gibblings¹, A. Traore¹, K. Krupa¹, J. C. Oller^{1,2}, F. Ferreira da Silva³, P. Limao-Vieira³ and G. Garcia¹

¹*Instituto de Física Fundamental, Consejo Superior de Investigaciones Científicas, Serrano 113-bis, 28006 Madrid, Spain*

²*Centro de Investigaciones Energéticas, Medioambientales y Tecnológicas, Avenida Complutense 22, 28040 Madrid, Spain*

³*Laboratório de Colisões Atômicas e Moleculares, CEFITEC, Departamento de Física, Faculdade de Ciências e Tecnologia, Universidade Nova de Lisboa, 2829-516, Caparica, Portugal*

Abstract. Appropriate radiative treatment for cancerous tumours demands a complete understanding and modelling of the physicochemical interactions that take place – this includes secondary species, such as negative ions and radicals formed by electron attachment and other processes. We describe an apparatus for electron transfer fragmentation studies from low energy anionic beams coincident with effusive molecular beams to provide data for these interactions.

1. INTRODUCTION

The mutagenic and genotoxic effects of low energy radiative interactions with biomolecules have been studied since Sanche and co-workers pioneered the field near the turn of the century [1,2]. It is now well established that low energy electron-molecular mechanisms are responsible for a portion of clinical radiotherapy's success, and the absolute description of these mechanisms is hoped to improve techniques in radiotherapy cancer treatment. The latest in this field are the clinical trials of nanoparticle [NP] enhanced radiotherapy using photons or ions underway in several research groups [3, 4]. This enhancement is in part due to the abundant secondary species produced by radiation of metal NPs in the cell medium [5], and increases the need to understand the subsequent interactions of these secondary species with vital cell constituents on the physicochemical level.

To elucidate the correlation between physicochemical damage via these interactions in small volumes with the eventual cell death or survival, event by event Monte Carlo simulation codes [6] and multiscale modelling procedures

have been developed [5]. Their appropriate implementation directly depends on the accuracy of the interaction data provided by experiment or theory. So far the interaction probabilities of ionic and neutral radicals, which are responsible for electron transfer [7], have not been well established. These are highly important species in radiation damage, and their effect is easily seen in experiments showing a decrease in cell death when the radical effect is quenched using a radical scavenger such as DMSO [4].

Here we describe an experimental technique developed to address this gap in knowledge, to cross low energy anions with an effusive biomolecular beam, whose subsequent fragmentation can be measured through time of flight mass spectrometry (TOF-MS).

2. EXPERIMENTAL DETAILS

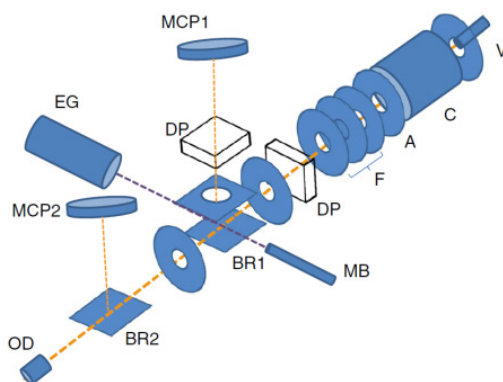


Figure 1. Schematics of the experimental setup. V, pulsed supersonic valve; C, hollow cathode discharge; A, anode; F, focusing lens; DP, deflecting plates; BR, beam reflector; MB, effusive molecular beam; MCP, multi-channel plate detector; EG, electron gun; OD, optical detector

The experimental setup has been developed at CSIC Madrid, consisting of differentially pumped interconnected high vacuum chambers. All square brackets correspond to labels in Figure 1. In the first chamber, a pulsed projectile precursor gas is admitted [V] into a hollow cathode apparatus [C, A], where it is formed into an anionic beam in the afterglow of the hollow cathode plasma via electron attachment. The discharge is formed by the voltage difference between the cathode and anode, and these are able to be varied concurrently with respect to ground, giving a final acceleration of the negative beam of 0-500eV. This beam is subsequently controlled and selected for mass via a three piece einzel lens [F] and a pair of deflecting plates and wein filter [DP]. The selected beam enters the second chamber through an aperture to ensure appropriate differential pumping, where it crosses with the effusive molecular beam [MB] in the extraction region [BR1] of a 1.12m time of flight mass spectrometer (TOF MS)

with microchannel plate [MCP1] detector. The interaction/extraction region is equipped with a small electron gun for neutral species analysis and electron impact ionization [EG]. Resistive heating of the target holding cell gives access to solid targets, as well as liquid and gas. The projectile beam composition and stability of the discharge are analysed by both a microchannel plate [MCP2] 5cm above the beam, 0.65m from the hollow cathode source, and an optical digital camera [OD] in the beam's forward direction. The hollow cathode is naturally pulsed by the Parker pulsed inlet valve, and the TOF extraction system is pulsed accordingly, so that information from each pulse is collected individually. TOF mass assignment is performed on the basis of the well-known anionic spectrum from neutral potassium-nitromethane collision experiments [8].

3. PRELIMINARY RESULTS

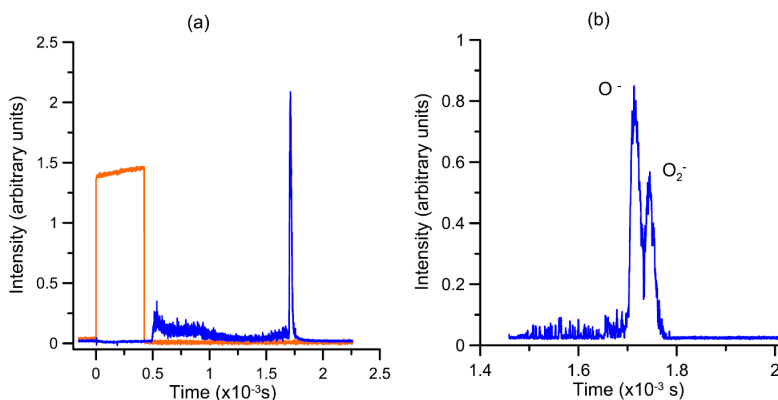


Figure 2. Time analysis of the negative ion beam. **A** Anion signal *dark* with respect to the valve control *light*. **b** Detail of the negative ion beam composition

Figure 2 shows the TOF mass spectra of the anions clearly formed in the hollow cathode discharge-induced plasma at -250 V, with O_2 as the feed gas. In Fig. 3a), at shorter flight times, the signal also contains contributions from electrons and discharge instability from the hollow cathode source, albeit not interfering with that from the anions. The figure also shows the pulse valve control signal to set the TOF scale. The anionic beam is comprised of O^- and O_2^- anions (see Fig. 3b), the latter yielding around 70 % of the former, and clearly visible from the weak background signal (~ 10 %). In the collision process from the anionic projectile to the neutral target beam, the potential role of the neutral atom as a stabilizing agent (third body) post-electron transfer from the incident anion is of particular interest.

4. CONCLUSION

A new apparatus for low energy anion/molecule collisions has been built at CSIC, Madrid, and is in the optimization stage. This experiment will be comparable to electron transfer experiments undertaken in other institutions and will provide data for Monte Carlo modelling of the impact of secondary species such as neutral and negative radicals in radiotherapy.

Acknowledgements

PLV acknowledges the Portuguese Foundation for Science and Technology (FCT-MEC) through SFRH/BSAB/105792/ 2014 during his sabbatical stay at CSIC, Madrid and the research grants PTDC/FIS-ATO/1832/2012 and UID/FIS/00068/ 2013. FFS acknowledges FCT-MEC through researcher grant IF-FCT IF/00380/2014. We also acknowledge the Spanish Ministerio de Economía y Competitividad (Project No. FIS 2012-31230). Some of this work forms part of the EU/ESF COST Actions CM1401 and CM1301, Our Astro-Chemical History and Chemistry for Electron-Induced Nanofabrication, respectively. LE-G and GG acknowledge the funding from the People Programme (Marie Curie Actions) of the European Union's Seventh Framework Programme FP7/2007- 2013/ under REA – Grant Agreement n°608163

REFERENCES

- [1] Boudaïffa, B. et al. Resonant formation of DNA strand breaks by low-energy (3 to 20 eV) electrons. *Science* (80-.). 287 , 1658–1660 (2000).
- [2] Sanche, L. Biological chemistry: Beyond radical thinking. *Nature* 461, 358–359 (2009).
- [3] Kim, J.-K. et al. Enhanced proton treatment in mouse tumors through proton irradiated nanoradiator effects on metallic nanoparticles. *Phys. Med. Biol.* 57, 8309–8323 (2012).
- [4] Porcel, E. et al. Gadolinium-based nanoparticles to improve the hadrontherapy performances. *Nanomedicine Nanotechnology, Biol. Med.* 10, 1601–1608 (2014).
- [5] Verkhovtsev, A. V., Korol, A. V. & Solov'yov, A. V. Revealing the Mechanism of the Low-Energy Electron Yield Enhancement from Sensitizing Nanoparticles. *Phys. Rev. Lett.* 114, 063401 (2015).
- [6] Blanco, F. et al. Modelling low energy electron and positron tracks in biologically relevant media. *Eur. Phys. J. D* 67, 199 (2013).
- [7] Almeida, D. et al. Mass spectrometry of anions and cations produced in 1-4 keV H -, O -, and OH - collisions with nitromethane, water, ethanol, and methanol. *Int. J. Mass Spectrom.* 311, 7–16 (2012).
- [8] Antunes, R. et al. Negative ion formation in potassium-nitromethane collisions. *Phys. Chem. Chem. Phys.* 12, 12513–9 (2010).

HIGH THROUGHPUT IMAGING FOR STUDYING THE SPATIAL EFFECT OF COLD ATMOSPHERIC PLASMA JETS ON CELL CULTURES

J. Kapaldo, X. Han and S. Ptasinska

*Department of Physics, Radiation Laboratory, University of Notre Dame,
Notre Dame IN, 46556, USA*

Abstract. We used high throughput fluorescence slide readers to acquire spatial dependent information about the interaction of cold atmospheric plasma jets with SCC25 cancer cells. Using image processing, artificial neural networks, and unsupervised learning techniques we classified over 2.5 million nuclei. This information will be used to study the spatial effect of plasma jets on biological samples.

1. INTRODUCTION

The use of cold atmospheric plasma jets (CAPJs) in biomedical applications with living cells and tissues has become more prevalent in recent years. CAPJs may contain many biologically relevant components including reactive oxygen and nitrogen species, free electrons, excited and charged molecules and atoms, photons, and large electric fields. The spatial distribution (concentration) of these components is not constant across the plasma jet and extend the visible plume. These regions with varying concentrations of the plasma's components can have different effects on biological samples; however, there is currently very little information about the spatial distribution of the plasma's effect since experimental techniques such as flow cytometry do not contain any spatial information.

We address this issue through the use of slide scanners with fluorescence microscopy capabilities. Slide scanners are automated microscopes that produce a single image of an entire slide. This allows us to retain the spatial information about the interaction between the biological samples and the CAPJ. However, these large scale images can suffer from several effects (non-uniform intensity, regions that are blurry ...) that must be taken into account before useful information can be obtained. Further, each image can have hundreds of thousands of cells, for example the images we worked with each had between 150,000 and 250,000 nuclei. Dealing with such large numbers requires image processing and feature extraction methods to segment each cell and then collect useful information about the cell, including size and shape, intensity, and texture and

pattern features. Based on these extracted features we can then use machine learning to classify the cells into several groups (cell cycle phase, damage level ...). These classification groups together with the cell's location on the slide allow to learn about the CAPJ's spatial effect on the cells.

In this paper, we will focus on the methods and techniques used for processing the images, extracting the data, and classifying the cells.

2. EXPERIMENT

In this work we expose SCC25 cancer cells to an AC CAPJ with Nitrogen feed gas [1,2]. After incubating the cells for some time after the exposure, the cells were fixed and stained with histone H2AX antibody with green fluorescence proteins (GFP) for labeling DNA double strand breaks, and with 4',6-diamidino-2-phenylindole (DAPI) for labeling nuclei. The slides (which the cells are mounted to) were then scanned using an Aperio Scanscope FL.

3. METHODS AND RESULTS

3.1 Slice images

Before starting analysis the original images are sliced into many smaller images. These small images are processed in parallel to significantly increase the speed of analysis. After image processing, the extracted nuclei positions can be stitched back together.

3.2 Intensity and optical distortion correction

Correcting the intensity and removing optical distortions across the image greatly enhances the distinguishability of G1/S/G2 phase cells. We found better results in this correction when we used the G1 intensity level across the image instead of using other background correction techniques. Obtaining the G1 intensity level is accomplished through filtering and fitting the nuclei position and DAPI intensity with a polynomial surface. The nuclei position and DAPI intensity were obtained using CellProfiler. The results of this correction on a histogram of the DAPI intensity may be seen in figure 1.

3.3 Feature extraction

The background corrected images of each channel were used in CellProfiler to extract several groups of features: area and shape, intensity, texture, granularity, radial intensity distribution, intensity correlation between channels, and features about foci (number of foci, average foci area, average foci intensity, and correlation between foci of each channel).

3.4 User classification and supervised learning

All of the features and nuclei locations were imported to Matlab for further processing. Software was developed for dynamic visualization of feature'

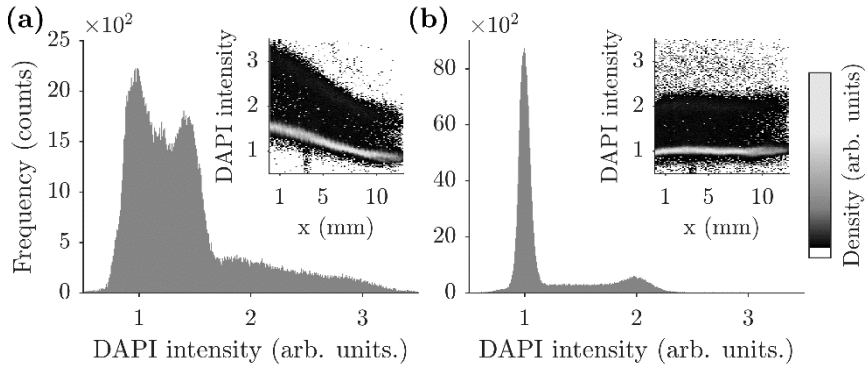


Figure 1. Histogram of DAPI intensity before (a) and after (b) background correction by the G1 cell cycle intensity. Inserts show a density plot of the DAPI intensity spatial distribution along the slow scan axis (x). The peak at DAPI = 1 corresponds to the G1 phase and the peak at 2 corresponds to the G2 phase.

data along with viewing the thumbnail images of the nuclei for which the data corresponds. This allows for efficient user classification of the nuclei.

Looking through the data it was found there were many segmentation errors (small portion of a nucleus classified as an entire nucleus, or multiple nuclei classified as a single nucleus) and that large sections of the images were too blurry to be used. The partial nuclei segmentations were corrected through a secondary image segmentation on all nuclei below a specific DAPI intensity. We then trained two artificial neural networks, one to detect blurry nuclei and the other to detect the multiple nuclei segmentation errors. In total we found that out of the 2.71 million nuclei in our dataset that $<1\%$ were partial segmentations, $\sim 6.5\%$ were blurry, and $\sim 3\%$ were multiple nuclei segmentations. (Figure 2 shows examples of nuclei in these three groups.)

With the data now cleaner, we classified ~ 2600 nuclei as being interphase, micronuclei, or in one of the sub-phases of mitosis: prometaphase, metaphase, anaphase, or telophase. (Prophase was not discernable from our nuclei images and was ignored.). This data was used to train an artificial neural network. The training data was randomly split into 0.6/0.2/0.2 ratio for training, cross-validation, and testing. The cross-validation set was chosen randomly from the 80% of data for training, and used to optimize the network size, network regularization, and a set of weighting coefficients on each class to deal with class imbalance. The measure used for determining network performance was the multiclass generalization of the Matthews correlation coefficient (MCC), which has been shown to be a good measure of network performance [3,4]. The trained network had an average MCC for the cross-validation set of 0.92 ± 0.01 , and an MCC for the test set of 0.89, both of which show good classification. Images of the different nuclei classes may be seen in figure 2. The total percentages of these classes (not including blurry or bad segmentations) were: prometaphase $\sim 0.03\%$, metaphase $\sim 0.38\%$, anaphase $\sim 0.12\%$, telophase $\sim 0.34\%$, interphase $\sim 98.35\%$, and micronuclei $\sim 0.44\%$ (total in mitosis ~ 0.87).

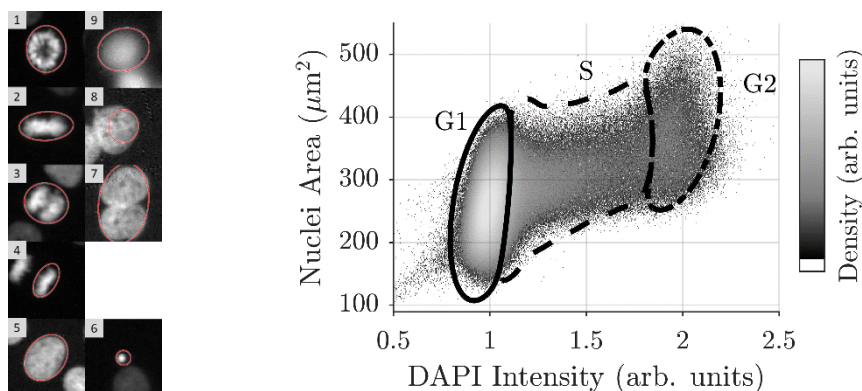


Figure 2. (Left) Representative images of the supervised classifications. 1: prometaphase, 2: metaphase, 3: anaphase, 4: telophase, 5: interphase, 6: micronuclei, 7: multiple nuclei, 8: partial nuclei, 9: blurry. (Right) Classification of sub-interphase using mixture of Gaussian model with uniform background.

3.5 Unsupervised learning of G1/S/G2

The different stages of interphase, G1/S/G2, were classified using a mixture of Gaussians model with uniform background. The features used for the fit were the DAPI intensity and the nuclei area. The results are shown in the right panel of figure 2. The population division of interphase nuclei was found to be 82.15% G1, 13.65% S, and 4.2% G2.

Acknowledgements

The authors would like to thank Sanford-Burnham Medical Research Institute for acquiring the fluorescence scanning images. This research was supported in part by the Notre Dame Center for Research Computing. This project has been performed in collaboration with Harper Cancer Research Institute at the University of Notre Dame. The research described herein was supported by the Division of Chemical Sciences, Geosciences and Biosciences, Basic Energy Sciences, Office of Science, United States Department of Energy through grant number DE-FC02-04ER15533.

REFERENCES

- [1] X. Han, Y. Liu, M. S. Stack, and S. Ptasinska, *J. Phys. Conf. Ser.* **565**, 012011 (2014).
- [2] X. Han, M. Klas, Y. Liu, M. Sharon Stack, and S. Ptasinska, *Appl. Phys. Lett.* **102**, (2013).
- [3] J. Gorodkin, *Comput. Biol. Chem.* **28**, 367 (2004).
- [4] G. Jurman, S. Riccadonna, and C. Furlanello, *PLoS One* **7**, 1 (2012).

LASER-INDUCED BREAKDOWN SPECTROSCOPY AT THE SOLID-AQUEOUS AEROSOL INTERFACE

Milica Matijević, Milovan Stoiljković, Miloš Momčilović, Jelena Savović,
Jovan Ciganović and Miroslav Kuzmanović*

*Physical Chemistry Department, VINČA Institute, P. O. Box 522, Belgrade,
University of Belgrade*

**Faculty of Physical Chemistry, University of Belgrade
Studentski trg 12-16, 11001 Belgrade, Serbia.*

Abstract. Laser-induced breakdown (LIB) atmospheric pressure plasma in interaction with aqueous aerosol was examined spectroscopically. The optical pulse of CO₂ laser operating at 10.6 μm was applied to create plasma at the solid interface. Resulting plasma interacts with the aqueous aerosol that streams alongside the interface. To estimate plasma atomization and ionization capacity, ionic-to-atomic line intensity ratio of Mg II 280.270 nm/Mg I 285.213 nm was measured. H-alpha line width was measured to estimate plasma electron number density. The results were compared with those measured in Direct Current (DC) arc plasma with continuous aerosol supply.

1. INTRODUCTION

Among the techniques for spectrochemical analysis, Laser-Induced Breakdown Spectroscopy (LIBS) have attracted great attention in the last dozen years [1]. This applies particularly to the technique for elemental analysis of solids which almost does not require sample preparing and consequently speeds up the analysis. For example, the existing LIBS platforms allow in-situ analysis of various types of solids (rock, organic and inorganic matter of different origin) [2]. The most commonly reported works of such kind describes application of nanosecond Q-switched solid-state Nd:YAG laser.

However, the analysis using LIBS have several disadvantages that the quantification makes unreliable. This primarily refers to strong matrix effect that affects ablation efficiency of the sample. Structural and chemical unevenness of the sample surface makes such troubles. Consequently, the lack of the sample-matching standards often makes the problem unsolvable.

In recent works LIB plasma was introduced in aqueous or dry aerosol in order to perform quantitative analysis [3, 4]. Although the dissolution of the solid sample could be time consuming, some of the above difficulties could be overcome in this way. Besides, the samples for analysis are mainly liquids.

A primary goal of this work is to gauge the feasibility of pulsed CO₂ laser to produce analytically useful plasma in aqueous aerosol at open atmosphere. In that sense, space resolved and time integrated ionic-to-atomic Mg line intensities were measured. Also, H-alpha line width was measured to estimate space distribution of electron number density. The results were compared to continuous atmospheric pressure DC arc plasma with aerosol supply.

2. EXPERIMENTAL AND OPERATION PROCEDURE

Transversally excited atmospheric pressure (TEA) CO₂ pulsed laser was used to create breakdown plasma at atmospheric pressure. Lasing wavelength of 10.6 μm with the net pulse duration of 2 μs (FWHM 0.1 μs) and pulse energy of about 150 mJ with repetition rate of 1 Hz was applied [2]. A plane grating monochromator focal length of 2 m coupled with the Apogee Alta F1007 CCD camera was used to record plasma spectra with resolution of 0.73 nm/mm.

Continuous stream of aqueous aerosol was produced by means of Meinhard type pneumatic nebulizer joined to the Scott-type cloud chamber and supported with argon gas (2 dm³/min). After the cloud chamber, an upward stream of aerosol 8 mm in diameter was established.

As an interface a tantalum sheet was set alongside the stream of the aerosol. A laser beam was fitted orthogonally onto the interface as well as on the optical axis of the monochromator. Plasma plume generated by the laser shot penetrate the aerosol and produce analyte atomization, excitation and ionization. The plume was projected in 1:1 ratio onto the entrance slit of monochromator. Starting from the interface as a reference, spatial scans of plasma emission was attained.

Atmospheric pressure DC arc argon plasma with continuous aerosol supply was scanned in the same manner starting from the plasma core as a reference.

3. RESULTS AND DISCUSSION

3.1 Ionic-to-atomic line intensity ratio

Plasma temperature and electron number density are related to the ionic-to-atomic line intensity ratio of the same element. This ratio is sensitive only to changes in plasma excitation conditions and is independent of the absolute amount of an analyte present in the plasma [5]. Commonly used emission-line pair of Mg II 280.270 nm and Mg I 285.213 nm were measured to indicate the robustness of LIB plasma generated in aqueous aerosol and argon atmosphere.

Assuming Local Thermodynamic Equilibrium (LTE), theoretical values of the Mg line ratios ranging of 9-10 corresponds to plasma temperature range of 7000-7500K [5]. In the case of LIB plasma such conditions were satisfied at distances close to the interface, as well as at greater distances through the aerosol, **Fig. 1**. Also, the intensity ratio distribution shows local maximum and minimum along the distance. That suggests spatial unevenness in the processes of

atomization, excitation and ionization. At least three zones within the plasma are obvious, **Fig. 1**.

In this respect, DC arc plasma is comparable to LIB plasma in the narrow current carrying core only. Thereafter, the ionization capacity monotonically decreases towards the plasma periphery, **Fig. 1**. If compared to LIB plasma ionic-to-atomic intensity ratios are ten times smaller at distances greater of 2 mm.

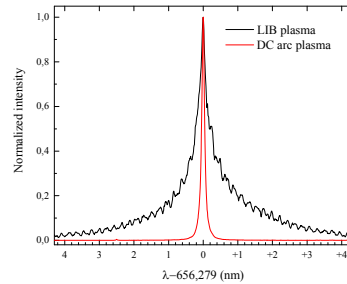
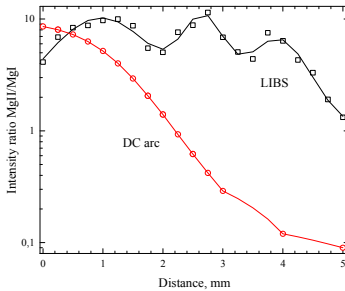


Figure 1. Spatial distribution of MgII/MgI line intensity ratio for LIB and DC arc plasma. The zeroth positions corresponds to tantalum bed interface and arc plasma axis, respectively

3.2 H-alpha line width

The presence of an electric field in the plasma induces the effect that causes spectral line broadening. In a strongly ionized source, species are surrounded by ions and electrons, which generate a local, strong electric field.

H-alpha line is measured to estimate electron number density in both types of plasmas. However, the purpose here has not to determine the exact line width but to indicate the differences. Comparative view of H-alpha line widths are shown in **Fig. 2**. Line shapes were fitted using pseudo-Voigt distribution which enables to derive Lorentz and Gauss components.

H-alpha line in LIB plasma was measurable along the distance of 7 mm, wherein the aerosol stream diameter is 8 mm. Up to the distance of 5.5 mm the Lorentz component of the line width ranges of 1.6-1.8 nm after which decreases rapidly. The Gauss component of the line width expresses maximum of 0.4 nm at distance of 4.5 mm. The results show that along distance of 6 mm the main contribution in the line width is the Stark effect.

In DC arc plasma H-alpha line was measurable up to distance of 2.5 mm. Both components of the line width decreases monotonically starting from the plasma core. The Lorentz component is dominant only in the current carrying core 2 mm in radius.

4. CONCLUSION

A set-up was designed to generate laser breakdown plasma at the interface solid-aqueous aerosol in argon atmosphere. Spatial distribution of ionic-to-atomic line intensity ratio of Mg was examined in context of analytical utility of plasma. H-alpha line width was measured to estimate spatial distribution of electron number density. It is apparent that in laser created breakdown plasma is possible to combine atomization of the aerosol and excitation and ionization of the atoms at distances away from strong background continuum emission.

On the other hand, DC arc plasma with aerosol supply is less effective in ionization, but supports excitation of the atoms. Ionic-to-atomic line intensity ratios are comparable only within narrow current carrying plasma core. Electron number density is much less in comparison to the laser created plasma.

Acknowledgements

This work is supported by Ministry of education, science and technological development under the grant NO 172019.

REFERENCES

- [1] A. De Giacomo, M. Dell'Aglio, O. De Pascale, R. Gaudiuso, V. Palleschi, C. Parigger, A. Woods, *Spectrochimica Acta Part B* 100, 180–188 (2014)
- [2] Jelena Savović, Milovan Stoiljković, Miroslav Kuzmanović, Miloš Momčilović, Jovan Ciganović, Dragan Ranković, Sanja Živković, Milan Trtica, *Spectrochim Acta B* 118, 127-136 (2016)
- [3] Michael E. Asgill, Sebastian Groh, Kay Niemax, David W. Hahn, *Spectrochimica Acta Part B* 109, 1–7 (2015)
- [4] Shi-Lei Zhong, Yuan Lu, Wei-Jin Kong, Kai Cheng, Ronger Zheng, *Front. Phys.* 11(4), 114202 (2016)
- [5] J. M. Mermet, *Analytica Chimica Acta*, 250, 85-94 (1991)

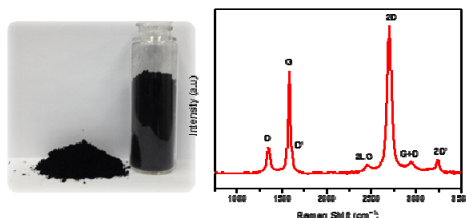
MICROWAVE PLASMAS APPLIED TO THE SYNTHESIS OF HIGH-QUALITY SUBSTRATE-FREE GRAPHENE

Cristóbal Melero¹, José Muñoz*¹ and María Dolores Calzada^{1,2}

¹Laboratory of Innovation in Plasmas (LIPs), University of Córdoba,
Edif. Einstein (C2) Campus de Rabanales, 14071 Córdoba, Spain

²Plasma Advances S.L., C/ Cecilia Payne, Edif. Aldebarán. Rabanales 21,
14014 Córdoba, Spain

Abstract. The synthesis of high-quality graphene on a large scale by using a plasma-based technique is presented. This technique allows us to obtain very thin graphene in powder and in only one step, without the use of neither metal catalysts, during the synthesis process, nor a substrate, for the graphene growing. Moreover, the cost for graphene production is significantly reduced because of the use of a wide variety of precursors. Thus, the plasma technology can be considered as a low cost, efficient, clean and environmentally friendly route for mass production of ultrathin graphene.



1. INTRODUCTION

Graphene is the basic building block (two-dimensional carbon material) from which can be formed all graphitic structures known to date. For instance, graphene can be stacked to form three-dimensional graphite, wrapped up to form fullerenes (zero-dimensional) or rolled to afford one-dimensional carbon nanotubes (CNTs). During the last years, the interest of the scientific community in such material has increased considerably due to its extraordinary properties, which make it suitable candidate for using in a wide range of applications such as electronic, catalysis, energy storage and composite materials.

Our research group has been focusing on the development of plasma technology, as a promising alternative to the conventional methods, for the production of nanostructured carbon material (graphene and nanotubes) [1]. In particular, plasmas generated at atmospheric pressure makes plasma technology an economic and attractive technique for the implementation of processes on an industrial scale. Plasma is defined as a partially ionized gas, mainly composed by electrons, ions, neutral atoms and photons. In non-equilibrium thermodynamic plasmas, electrons and heavy particles have the energy enough (7000 K and 1200 K respectively) for decomposing organic molecules (~ 500 K) into its atomic elements. This fact makes it extremely versatile because a wide variety of materials can be used as carbon source. Once those organic molecules are decomposed by the plasma species into their atomic elements, these atomic elements can recombine at the plasma exit to afford compounds of low-molecular weight. The use of plasmas at atmospheric pressure avoid the recombination of atomic species into large chain molecules at the plasma exit because the great number of electrons colliding with the plasma heavy particles which limits the size of by-products [2].

2. EXPERIMENTAL

In our research, microwave Ar plasma was created by using a TIAGO device developed in Moisan's group, and its detailed working theory and experiments were reported in bibliography [3]. We modified this device by adding a quartz reactor coaxially placed with the nozzle in which the plasma is created. This quartz reactor plays two significant roles: a) it reduces the contact of the plasma with the atmospheric air and b) it is used as chamber in which the graphene grows. The precursor is vaporized using a gas phase liquid delivery system and the precursor-argon mixture was passed through a steel tube heated at 110°C to maintain a temperature above the boiling point of ethanol to avoid its condensation. As precursors, the technique reported here in allow us to use a wide range of precursors of different nature such as alcohols, amines, hydrocarbons, aromatic compounds, nitriles etc.

3. RESULTS AND DICUSSION

The methodology developed by our research group combines the two main benefits of the most used techniques to date. On the one hand this technique allows us to obtain high-quality substrate-free graphene with similar quality than the graphene obtained by using CVD technique while on the other hand allow us to obtain similar quantities to the quantities provide by liquid exfoliation of graphite. In addition, this technique provides an unusual versatility which make possible the use of a wide range of precursors such as aliphatic alcohols, hydrocarbons, amines, nitriles, aromatic compounds etc. The graphene was fully characterized by Transmission Electron Microcopy (TEM), x-Ray photoelectric spectroscopy, Raman spectroscopy and thermogravimetric analysis.

Figure 1 shows the structure of the produced material as multi-layer graphene sheets (Figure 1).

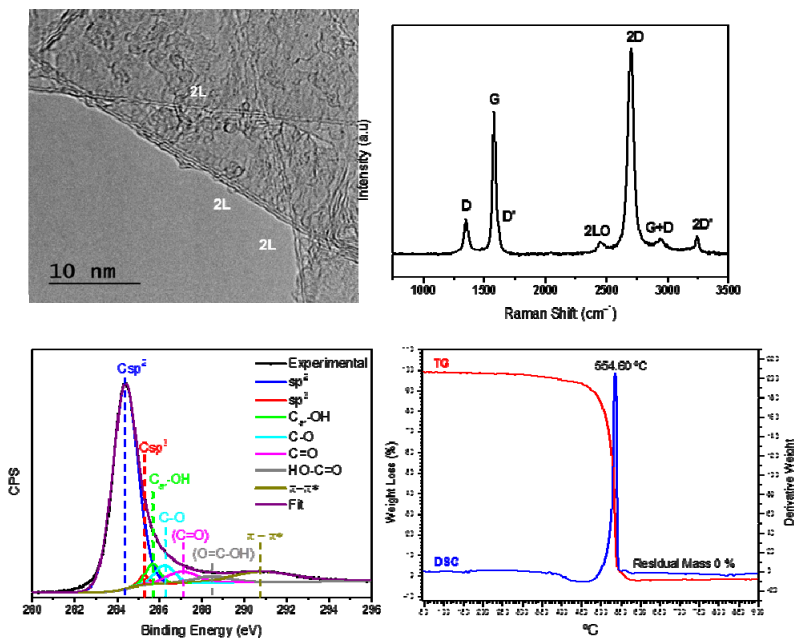


Figure 1. Graphene characterization.

4. CONCLUSIONS

We developed a fast, facile, and cost effective plasma technology to fabricate very thin and high-quality graphene. The technology solves one of the most important challenges facing the scientific community for graphene production, i.e., the synthesis of high-quality graphene on a large scale, catalyst-free and substrate-free. The quality of the as-synthesized graphene is comparable to the obtained one from the use of the traditional CVD technique.

Acknowledgements

This work was subsidized by the Andalusia Regional Council from Spain (Consejería de Economía e Innovación) under project no. P11-FQM-7489 (FEDER co-funded).

REFERENCES

- [1] Kabouzi, Y.; Moisan, M.; Rostaing, J. C.; Trassy, C.; Guérin, D.; Kéroack, D.; Zakrzewski, Z. *J. Appl. Phys.* 93, 9483–9496 (2003).
- [2] Rincón, R.; Melero, C.; Jiménez, M.; Calzada, M. D. *Plasma Sources Sci. Technol.* 24, 32005 (2015).
- [3] M. Moisan, Z. Zakrzewski and J. C. Rostaing, *Plasma Sources Sci. Technol.*, 10, 387 (2001).

INFLUENCE OF ELECTRON ENERGY DISTRIBUTION FUNCTION ON COMPOSITION OF ATMOSPHERIC PRESSURE He/O₂ PLASMAS

Ž. Mladenović^{1*}, S. Gocić¹, D. Marić² and Z. Lj. Petrović²

¹*Department of Physics, Faculty of Sciences and Mathematics, University of Niš, Višegradska 33, 18000 Niš, Serbia*

²*Institute of Physics, University of Belgrade, Pregrevica 118, 11080 Belgrade, Serbia*

Abstract. Atmospheric pressure non-equilibrium plasma represent efficient source of reactive species for different kind of applications. Nevertheless, for the purpose of modelling of this non-equilibrium system, Maxwell-Boltzmann distribution is commonly used for calculation of electron rate coefficients. In order to test sensitivity of plasma composition on assumed electron energy distribution function (EEDF), the zero-dimensional global model is applied for helium/oxygen mixture (0.5% of O₂) with humid air impurities. The initial calculation showed that inclusion of non-equilibrium EEDF mainly affects the processes with thresholds considerably higher than the mean electron energy while it does not change much for the processes with the threshold and peak in the region of the mean energy.

1. INTRODUCTION

Having in mind that chemical composition of complex plasmas is often inaccessible by measurements analysis based on numerical models has an important role. In that respect atmospheric pressure plasmas are particularly complex and difficult to describe by models. Results of a global model used for investigation of influence of humid air level on chemistry of reactive species in rf-driven atmospheric-pressure (AP) helium-oxygen mixture (0.5% of O₂) plasmas were presented in a recent paper [1,2]. Model comprises a reaction scheme with 1048 reactions for kinetics of nearly 60 species.

We have created a numerical code for solving the system of time-dependent rate equations with an idea to test sensitivity of plasma composition to selected EEDF. In doing so, we start from the chemical scheme in Appendix of Ref. [1]. Rate coefficients for electron molecule collisions are first calculated with a Maxwell-Boltzmann (MB) EEDF, and then with the non-equilibrium one, obtained by solving the Boltzmann equation BE.

2. MODEL

The time evolution of particle concentration in 0D global model is determined by rate equations, which include rates for processes of creation and destruction of each particle. Two-body rate coefficients for electron impact processes are calculated as [3]:

$$k_{i,exc} = \sqrt{2/m_e} \int_{\epsilon} Q(\epsilon) \sqrt{\epsilon} f(\epsilon) d\epsilon, \quad (1)$$

where m_e , ϵ , $Q(\epsilon)$ and $f(\epsilon)$ denote electron mass, energy, appropriate total cross section and EEDF, respectively. If MB distribution is assumed, the rate coefficients can be expressed in extended Arrhenius form [1,2]. In non-equilibrium case, rate coefficients for processes in Table 1 are obtained by solving the Boltzmann equation by BOLSIG+ solver [4,5]. MORGAN database [6] with cross sections data for He, O₂ and H₂O is used as input in BOLSIG+. Characteristic cross sections and MB and BE distributions for the same mean energy (electron temperature) are shown in Figure 1. Calculations are shown for the mixture of He 99.5%, O₂ 0.5% and H₂O 2.5ppm.

Table 1. List of selected electron-impact processes and rate coefficients [1,2] as a function of T_e [eV].

| <i>R.N.</i> | <i>reaction</i> | <i>rate coefficients</i> [cm ³ /s] | <i>Ref.</i> |
|-------------|---|--|-------------|
| 1. | He + e ⁻ → He* + e ⁻ | $4.2 \cdot 10^{-9} T_e^{0.31} \exp(-19.8/T_e)$ | [2] |
| 2. | He + e ⁻ → He ⁺ + 2e ⁻ | $1.5 \cdot 10^{-9} T_e^{0.68} \exp(-24.6/T_e)$ | [1] |
| 3. | O ₂ + e ⁻ → O ₂ ⁺ + 2e ⁻ | $9.0 \cdot 10^{-10} T_e^{2.0} \exp(-12.6/T_e)$ | [1] |
| 4. | O ₂ + e ⁻ → O ₂ (¹ Δ) + e ⁻ | $1.37 \cdot 10^{-9} \exp(-2.14/T_e)$ | [1] |
| 5. | O ₂ + e ⁻ → O ₂ (¹ Σ) + e ⁻ | $3.24 \cdot 10^{-10} \exp(-2.218/T_e)$ | [1] |

The system of rate-equations is solved by MATLAB ODE15s solver with relative and absolute tolerances equal to 10⁻¹² and 10⁻⁶, respectively. The pulse duration of 5 ms with time-step of 10 ns is chosen as is Ref. [1]. The T_e time dependence for rates calculation is obtained by fitting data from Fig. 2 in Ref. [1], within interval 1.8eV – 3.1eV. Electron concentration is fixed at the value of 10¹¹ cm⁻³. The initial plasma composition in global model is taken as He + 0.5% O₂ + 250ppm of humid air (78% N₂, 21% O₂, 10⁻²% CO₂, 10⁻³% N₂O, 10⁻⁵% NO₂, 10⁻⁶% NO), with 1% of relative humidity.

3. RESULTS AND DISCUSSION

As shown in Figure 1, BE distribution has a significantly lower high energy tail and minor overlapping with helium cross sections and in particular with ionization cross sections. As a consequence, the rate coefficients for He ionization and excitation are reduced by few orders of magnitude (Figure 2). In

energy region around 1 eV to 3 eV, BE has a similar shape and magnitude as MB distribution. Hence, rate coefficients for $O_2(^1\Delta)$ excitation have similar values (Figure 2). The processes such as ionization or excitation of metastables have rates for MB distribution that are many orders of magnitude larger than those for a non-equilibrium distribution. For the case of Ar plasmas, the influence of EEDF shape on rate coefficients is illustrated in paper [7].

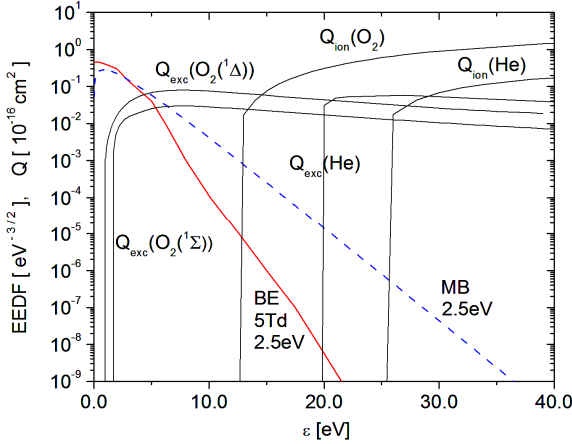


Figure 1. Cross sections for excitation and ionization of He and O_2 and EEDF: Maxwell-Boltzmann (MB) and Boltzmann equation (BE) (2.5eV mean energy).

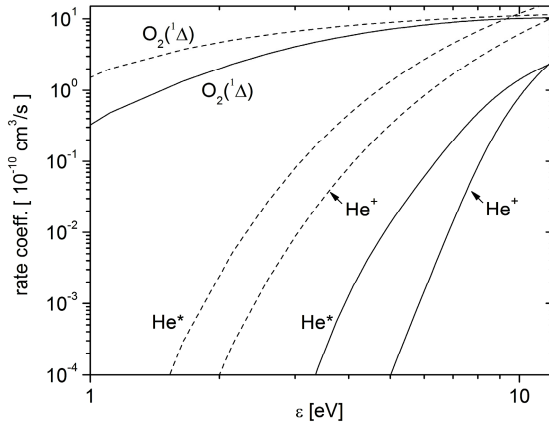


Figure 2. Rate coefficients for O_2 excitation and He excitation and ionization - based on MB (dashed line) and BE (solid line, Morgan set) EEDF.

The comparison of He/ O_2 plasma compositions based on the global model calculated with MB and BE distributions is shown in Figure 3. Significantly lower concentrations of He^+ , He^* , He_2^+ , O^+ , O_2^+ , O_4^+ species are obtained in case with BE rates. The level of He^+ ions is reduced by few orders of magnitude, as a direct consequence of a reduced ionization coefficient (Figure 2). Furthermore, concentrations of He_2^+ and O^+ ions are decreased since the

mean channels of their creations involve He^+ ions. Similarly, the reduction of He^* level caused by lower excitation coefficient is followed by O_2^+ decreasing, since Penning ionization of O_2 is an important channel for O_2^+ formation.

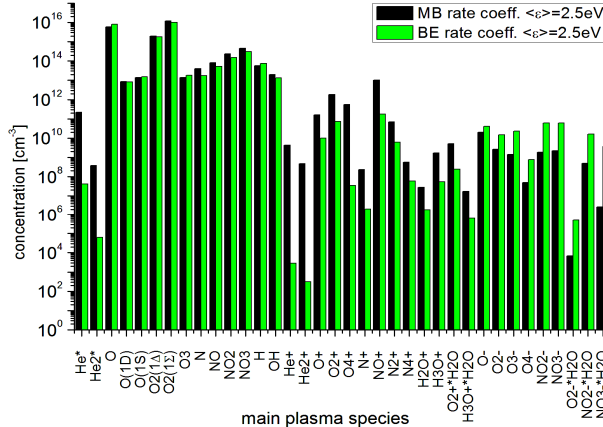


Figure 3. The comparison of plasma composition based on MB (black bars) and BE rate coefficients (green bars).

Concentrations of $\text{O}_2(^1\Delta)$ and $\text{O}_2(^1\Sigma)$ are slightly affected by BE distribution, in agreement with rate coefficient behavior in Figure 2. Similar low sensitivity to EEDF can be observed for other reactive species with low thresholds in their dominant channels. On the contrary, concentrations of negative ions are increased for BE rates. In general we may conclude that representation by MB distribution is rather robust if not entirely accurate for processes mainly induced directly by electrons if energy losses are of the same order as the mean energy. This representation fails seriously, as expected [7], for processes with much higher thresholds than the mean energy.

Acknowledgements

This work is supported by MES of Serbia, projects ON171037 and III41011.

REFERENCES

- [1] T. Murakami et al, *Plasma Sources Sci. Technol.* **22**, 015003 (2013).
- [2] T. Murakami et al, *Plasma Sources Sci. Technol.* **23**, 025005 (2014).
- [3] T. Makabe, Z. Petrović, *Plasma electronics: Applications in Microelectronic Device Fabrication*, p. 336, (Taylor&Francis Group, New York and London, 2006).
- [4] G. J. M. Hagelaar and L. C. Pitchford, *Plasma Sources Sci. Technol.* **14**, 722 (2005).
- [5] <http://www.lxcat.laplace.univ-tlse.fr>
- [6] Morgan database, www.lxcat.net, retrieved on February 11, 2014.
- [7] Z. Lj. Petrović et al, *Plasma Sources Sci. Technol.* **16**, S1 (2007).

ALUMINUM SURFACE CLEANING AND ACTIVATION BY AN ATMOSPHERIC PRESSURE Ar-N₂ MICROWAVE AFTERGLOW

J. Muñoz, J.A. Bravo, C. Melero and M.D. Calzada

Laboratorio de Innovación en Plasmas, Departamento de Física, Universidad de Córdoba, Campus de Rabanales - Edificio Einstein, 14071, Córdoba Spain

Abstract. The effects of exposing an aluminum surface to the afterglow of a microwave atmospheric pressure discharge have been studied, revealing a significant increase in the hydrophilic character of the surfaces due to surface cleaning and activation. These effects vanish with time when the samples are stored in air ambience. Analysis of the chemical environment of oxygen atoms in the surface by X-ray photon spectrometry reveals that OH radicals of the clean surface are replaced by fully oxidized oxygen atoms.

1. INTRODUCTION

Atmospheric-pressure microwave plasmas have been the subject of intensive research due to their flexibility and ease of use on several industry applications. Particularly, small scale microwave plasmas allow for local treatments of rough and structured materials. In this paper we present the effects of the exposure to an Ar-N₂ afterglow on the wettability of aluminum surfaces and analyze their ageing when stored in air ambience.

2. EXPERIMENT

The afterglow [1] of an atmospheric-pressure argon-nitrogen (up to 4% nitrogen) microwave (2.45 GHz) plasma sustained with 125 W using a surfatron [2], was used for treating the surface of aluminum samples. Samples were exposed at a distance of 3 cm measured from the end of the discharge. In order to discard the simple effects of temperature on the surface wettability, a comparison with samples heated (>150 °C) using a conventional hot plate was carried out.

Wettability of the samples was measured using the sessile drop technique during the 48 hours following the treatment. Small deionized water drops (<10 µl) were deposited on the surface of treated and control samples and photographs were taken using a digital camera. The images were analyzed using a spherical drop model [3] in order to determine the contact angle of the drop with the surface.

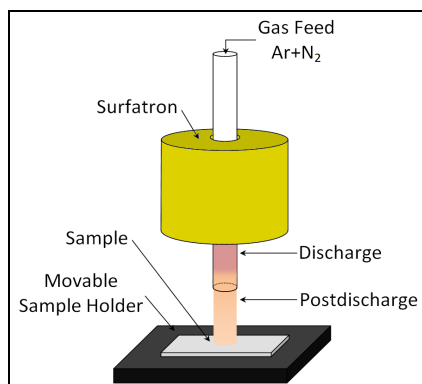


Figure 1. Experiment Setup.

3. RESULTS AND DISCUSSION

The contact angle of water drops with the aluminum surface significantly decreased after the treatment, reducing from 71° to 18° . No significant modification in the contact angle was detected in the case of the samples heated with the hot plate. The original properties of the plasma-treated samples partly recovered after the first 10 hours of treatment (Figure 2), with the contact angles increasing to 60° after this time lapse. After that, the contact angle slowly increased and recovered its original value after 48 hours.

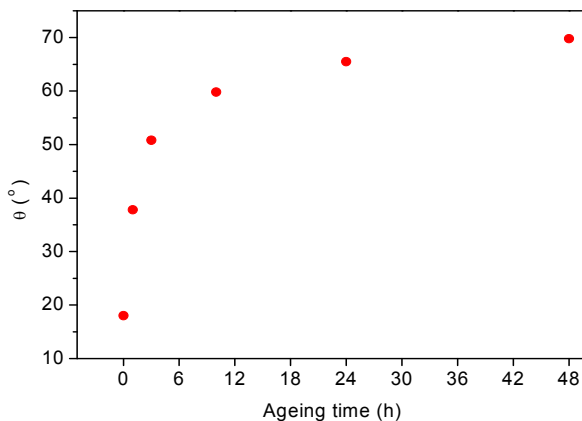


Figure 2. Variation of the contact angle after afterglow treatment.

X-ray photon spectrometry (XPS) was used in order to determine the variations in the chemical composition (Table 1) of the surface and identify the apparition of hydrophilic OH radicals (Figure 3) [4].

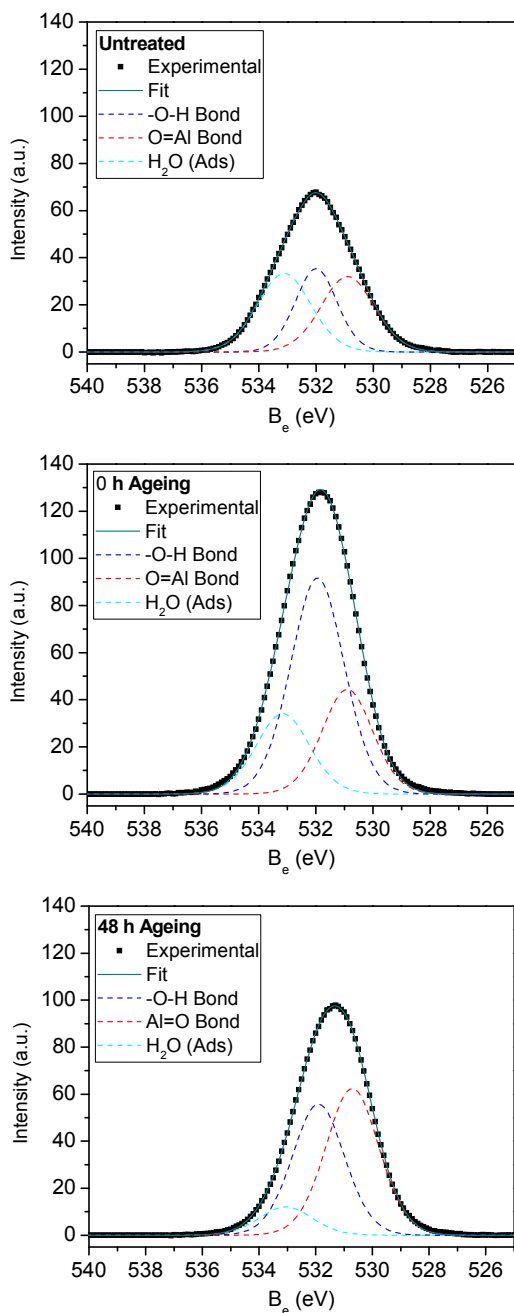


Figure 3. High resolution XPS spectra of the oxygen 1s line.

Table 1. Table caption 10 pt TimesRoman, Normal, Justified. After Table caption 6 pt.

| Sample | [C] (%) | [Al] (%) | [O] (%) | [F] (%) | [N] (%) |
|---------------------------------|---------|----------|---------|---------|---------|
| Untreated | 47 | 19 | 32 | < 2 | < 1 |
| Heated | 19 | 30 | 51 | < 2 | < 1 |
| Ar-N ₂ (0.5%) | 11 | 36 | 51 | < 2 | < 1 |
| Ar-N ₂ (0.5%) + 48 h | 16 | 32 | 50 | < 2 | < 1 |

The afterglow treatment induces a significant reduction in the carbon content due to hydrocarbon removal (surface cleaning). A similar effect can be detected in heated samples, with lower carbon removal effects. After the plasma treatment, there is no significant variation in the chemical composition of the surfaces according to Table 1.

However, analyzing the high resolution XPS spectra of oxygen 1s lines allows identifying modifications in the chemical environment of oxygen atoms belonging to the surface. From Figure 3, it can be seen how after the treatment, there is a significant reduction in water content of the surface, together with an increase in the relative content of OH radicals (surface activation). However, with ageing in air ambience, the amount of OH radical is reduced while the relative amount of fully oxidized oxygen radicals increases, thus leading to a less hydrophilic surface [4].

Acknowledgements

This work has been funded by the Andalusian Regional Council under project FQM-7489 and the FEDER Funds from the European Union.

REFERENCES

- [1] Bravo J.A., Muñoz J., Saez M. and Calzada M.D., IEEE Trans. Plasma Sci. 2011, 39, 2114.
- [2] Moisan M., Zakrzewski Z. And Pantel R., J. Phys. D. Appl. Phys., 1979, 12, 219.
- [3] Yuan Y., Surface Science Techniques SE - 1, vol. 51. Ed. G. Bracco and B. Holst. Berlin: Springer, 2013, 3.
- [4] Shin D.H., Bang C.U., Kim J.H., Hong Y.C., Uhm H.S., Park D.K. and Kim K.H., IEEE Trans. Plasma Sci. 2006, 34, 1241.

LOW TEMPERATURE PLASMA NEEDLE REDUCES THE SURVIVAL OF CANCER CELLS

Nenad Selaković¹, Nevena Puač¹, Nevenka Gligorijević², Milena Čavić²,
Gordana Malović¹, Radmila Janković², Siniša Radulović² and
Zoran Lj. Petrović^{1,3}

¹ *Institute of Physics, University of Belgrade, Pregrevica 118, 11080 Belgrade, Serbia*

² *Institute for Oncology and Radiology of Serbia, Pasterova 14, 11000 Belgrade, Serbia*

³ *Serbian Academy of Sciences, Knez Mihailova 35, 11000 Belgrade, Serbia*

Abstract. The aim of this study was to investigate whether plasma needle induces cancer cell death. This atmospheric pressure plasma source generates reactive oxygen species (ROS) and reactive nitrogen species (RNS) that are presumed to be major causes of cancer cell death. Here we report the influence of the power transmitted to the plasma and the exposure time on cell survival using two cancer cell lines, A549 and HeLa.

1. INTRODUCTION

The rapid development of plasma medicine, a new promising scientific field, occurred during the last decade. Using plasma physics in a wide range of sophisticated fundamental experiments involving the treatment of cells and tissues opened the door of *in vivo* therapeutic applications. Several atmospheric pressure plasma devices, such as plasma jet, plasma needle, dielectric barrier discharge (DBD) and plasma torch [1-4], have already been used for sterilization of wounds and medical equipment, treatment of dental caries and faster coagulation of blood.[5-7]

Our plasma needle is a more advanced version of the one that was originally presented by Stoffels [8] and we have used it in several applications like sterilization of planktonic bacteria, differentiation of human periodontal stem cells into an osteogenic line and for plant stem cells – calli.[9-11]

Lately, low-temperature plasmas are attracting great attention in the field of oncology [12]. In this study we used the plasma needle for the treatment of two cancer cell lines (HeLa and A549). The plasma needle discharge is a mixture consisting of reactive species and radicals that are formed in contact with the surrounding air and the treated sample. The change of power delivered to the plasma and the exposure time create different amounts of ROS and RNS that are

delivered to the treated cells, so we observed the effect on cell survival for the used set of parameters.

2. EXPERIMENT

The construction of the plasma needle was designed to be suitable for applications in direct contact with the sample. The body of the plasma needle is made of Teflon. Inside the body we put a Pyrex glass tube (o.d. 6 mm and i.d. 4 mm) through which we released 1 slm of helium as the feeding gas. A tungsten wire was used as the central electrode powered with 13.56 MHz sine wave and it was placed within a ceramic tube inside the glass tube. The role of the ceramic tube is to prevent discharge between the central electrode and the glass tube. The ceramic electrode is sticking 1 mm outside of the ceramic and glass tubes so the discharge occurs on its tip as a weak glow.

A549 (lung adenocarcinoma) and HeLa (cervical cancer) cell lines were used as representative cancer cell lines. The cells were maintained in RPMI-1640 medium (Sigma-Aldrich, Co, USA) with 10% heat inactivated newborn calf serum (Sigma-Aldrich, Co, USA) at 37°C in 5% CO₂.

The cells were seeded in 96-well cell culture plates, A549 (7000 cells/well), HeLa (4000 cells/well). We have varied two experimental parameters: exposure time (10 s, 30 s and 60 s) and power delivered to the plasma (1.3 W and 2.2 W). The distance between the plasma needle tip and the sample surface was 5 mm and we kept it constant during all experiments. The experiments were performed in triplicates, and untreated cells and medium-treated cells were used as controls.

After the treatment we have measured the cytotoxic activity of plasma needle on HeLa and A549 cell lines using an MTT assay according to the method of Mosmann (1983) and modified by Ohno and Abe (1991).

3. RESULTS AND DISCUSSION

Several different factors can affect the death of cancer cells such as the type of the cell and the type of the treatment (direct and indirect contact with the sample). Here we used the direct contact method of discharge on the sample which is more effective than the indirect contact (discharge in contact with the medium without cells).

In Fig.1 we show images of microtiter plate wells observed by optical microscopy. One can notice a reduction in the number of A549 cells between the control (untreated samples) and the treated samples for different powers of plasma (1.3 W and 2.2 W) and different exposure times (10 s, 30 s and 60 s).

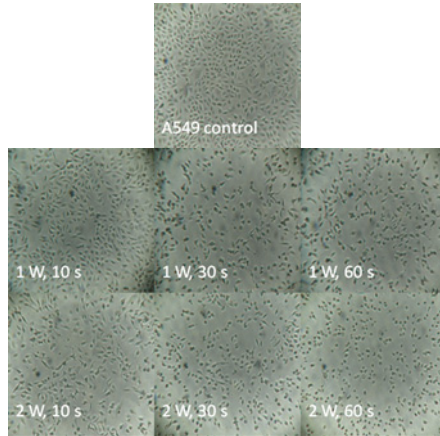


Figure 1. Images of microtiter plate wells obtained by optical microscopy for untreated A549 cells (control) and treated A549 cells for different powers of plasma and exposure times.

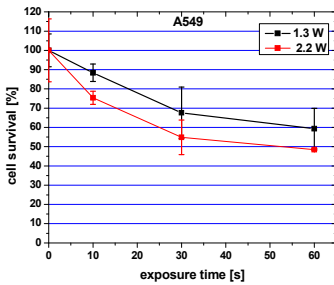


Figure 2. Cell survival comparison of A549 cells for two different applied powers and three different exposure times. The distance from plasma to sample was 5 mm.

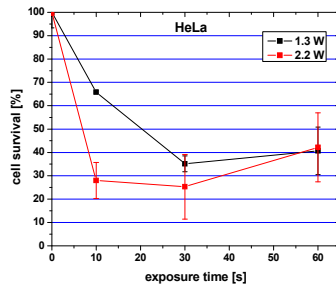


Figure 3. Cell survival comparison of HeLa cells for two different applied powers and three different exposure times. The distance from plasma to sample was 5 mm.

Fig. 2 represents a graphic view of the results of A549 cells already showed in Fig 1. and here one can notice an exponential drop caused by a longer exposure time for two different applied powers of discharge (1.3 W and 2.2 W). From the given chart it is obvious that higher power is more efficient in reducing cancer cell survival.

HeLa cells displayed greater vulnerability to the impact of plasma than A549 cells, especially for the higher power output (2.2 W) where a significant drop in cell survival (Fig. 3.) at the shortest exposure time (10 s) was observed. In both cases (1.3 W and 2.2 W), the effect of reducing cell survival was higher than 50%.

4. CONCLUSION

In this study we used our version of plasma needle for the treatment of two different carcinoma cell lines (HeLa and A549) in order to observe the effect on cell survival. Due to the different nature of the investigated cancer cell lines, which is reflected in a number of differences, among them and in the cells defense system (e.g the cell response to oxidative stress.) [13], these two lines showed different sensitivity to plasma treatment. The HeLa cells were more sensitive than A549 cells on the plasma treatment which was manifested in higher reduction of the cell survival determined by MTT assay.

Acknowledgements

This study was supported by Grant Nos. III41011, ON171037, III41026, and ON173024, MESTD, Republic of Serbia

REFERENCES

- [1] N. Puač, D. Maletić, S. Lazović, G. Malović, A. Đorđević, and Z. Lj. Petrović, *Appl Phys. Lett.*, 101, 24103, (2012).
- [2] E. Stoffels, I. E. Kieft, R. E. J. Sladek, E. P. Van Der Laan, and M. Steinbuch, *Plasma Sources Sci. Technol.* 15, 169, (2006).
- [3] I. A. Shkurenkov, Y. A. Mankelevich, and T. V Rakhimova, *Eur. Phys. J. D.* 62, 213, (2011).
- [4] S. Yonson, S. Coulombe, V. Léveillé, and R. L. Leask, *J. Phys. D: App. Phys.* 39, 3508, (2006).
- [5] M. Laroussi, *Plasma Processes Polym.* 2, 391, (2005).
- [6] E. Stoffels, A. J. Flikweert, W. W. Stoffels, and G. M. W. Kroesen, *Plasma Sources Sci. Technol.* 11, 383, (2002).
- [7] G. Fridman, G. Friedman, A. Gutsol, A. B. Shekhter, V. N. Vasilets, and A. Fridman, *Plasma Processes Polym.* 5, 503 (2008).
- [8] E. Stoffels, Y. A. Gonzalvo, T. D. Whitmore, D. L. Seymour, and J. A. Rees, *Plasma Sources Sci. Technol.* 15, 501, (2006).
- [9] S. Lazović, N. Puač, M. Miletić, D. Pavlica, M. Jovanović, D. Bugarski, S. Mojsilović, D. Maletić, G. Malović, P. Milenković, and Z. Petrović, *New J. Phys.* 12, 83037, (2010).
- [10] M. Miletić, S. Mojsilović, I. Okić Đorđević, D. Maletić, N. Puač, S. Lazović, G. Malović, P. Milenković, Z. Lj Petrović, and D. Bugarski, *J. Phys. D: Appl. Phys.* 46, 345401, (2013).
- [11] N. Puač, S. Živković, N. Selaković, M. Milutinović, J. Boljević, G. Malović, and Z. L. Petrović, *Appl. Phys. Lett.*, 104214106, (2014).
- [12] N. Kaushik, N. Uddin, G. B. Sim, Y. J.Hong, K. Y. Baik, C. H. Kim, E. H. Choi, *Sci. Rep.*, 5, 8587, (2015).
- [13] G. Speit and I. Bonzheim, *Mutagenesis*, 18(6), 545–548, (2003).

Section 4.

GENERAL PLASMAS

STATUS AND FUTURE PROSPECTS OF LASER FUSION RESEARCH AT ILE, OSAKA

Hiroshi Azechi

Institute of Laser Engineering, Osaka University, Osaka 565, Japan

X-RAY POLARIMETRY: A NEW WAY TO PROBE ASTROPHYSICAL PLASMA

René W. Goosmann, on behalf of the XIPE collaboration

*Observatoire astronomique de Strasbourg
11 rue de l'Université, F-67000 Strasbourg, France*

Strongly ionized and often also strongly magnetized plasma is ubiquitous in the sources observed in high energy astrophysics. On behalf of the consortium behind the X-ray Imaging Polarimetry Explorer (XIPE), I am going to lay out the future prospects of X-ray polarimetry in the 2-8 keV band. XIPE is under phase A study as a candidate for ESA's M4 mission to be launched in 2025. Two comparable X-ray polarimetry missions are being studied by NASA. These satellites would extract so far inaccessible information from the X-ray sky and thereby allow us to address many open questions concerning ionized plasma in the vicinity of compact objects, like neutron stars and black holes. I am going to show how polarimetry is going to complement established observational techniques and how it is actually going to make a number of unique contributions to astrophysics and also fundamental physics.

Acknowledgements: This work is partially supported by the French High Energy National Program (PNHE).

RELATIVISTIC PLASMAS IN AGN JETS: FROM SYNCHROTRON RADIATION TO γ -RAY EMISSION

G. La Mura^{*,1}, G. Busetto^{*,1}, S. Ciroi^{*,1}, P. Rafanelli^{*,1}, M. Berton¹, E. Congiu¹, V. Cracco¹, M. Frezzato¹

¹*Department of Physics and Astronomy - University of Padua, Vicolo dell'Osservatorio
3, 35122 - Padua, Italy*

**Member of the Fermi-LAT Collaboration*

It is now very well established that the nuclei of galaxies, including the Milky Way, host Super Massive Black Holes (SMBH), with masses in the range from a few $10^6 M_{\odot}$ up to nearly $10^{10} M_{\odot}$. Several lines of evidence suggest that the evolution of these objects is closely related to the history of their host galaxies. The strong gravitational field of SMBHs dominates the dynamical properties of the galaxy nuclei. If matter is captured and accreted onto SMBHs, a huge amount of gravitational binding energy is turned into radiation and an Active Galactic Nucleus (AGN) switches on. In spite of this fairly straightforward and common interpretation, AGNs are extremely complicated physical laboratories, where advanced concepts of Relativity, Quantum Mechanics and Magneto-hydrodynamics are required to fully explain their outstanding wealth of observational properties. The accretion of fuel onto SMBHs, indeed, occurs through the formation of highly magnetized relativistic plasma flows that, under specific circumstances, can lead to the acceleration of collimated jets, which may travel well outside the host galaxies.

Relativistic jets on the Megaparsec scale have long been known to be associated with giant radio galaxies and quasars and they are a key feature of blazars. Smaller scale jets, on the other hand, are starting to be more and more frequently identified in low luminosity objects. These jets are important in the establishment of specific features in the spectra of AGNs and they have a fundamental role in the accretion mechanism itself.

In this lecture, we focus on the Physics of relativistic AGN jet plasmas. After reviewing the fundamentals of radiation processes occurring when charged particles are accelerated by magnetic fields, we briefly consider the possible mechanisms of jet acceleration. We then discuss the observational properties of active galaxies that are relevant diagnostics of jet activity and we summarize the details of jet structure and their appearance in different radiation wavelengths. We finally review the most recent achievements of modern instruments, observing the sky at high energy γ -rays and we explain the importance of AGNs in the origin of extragalactic high energy radiation fields. We conclude this review with a discussion of the role of AGNs in the Cosmological framework and with an overview of how their properties evolve from the local to the remote Universe.

Acknowledgements: This work is partially supported by our Ministry under the grant NO 12345.

A HYBRID TRANSPORT-DIFFUSION SIMULATION IN LASER FUSION

Jinghong Li

*Institute of Applied Physics and Computational Mathematics,
Beijing 100094, China*

Radiation ablation and radiation transport are fundamental physical processes in laser inertial confinement fusion (ICF) [1], which is an approach to fusion that relies on the inertia of the fuel mass to provide confinement. Radiation modeling [2] is very important in the simulation of laser fusion. It is well known that a diffusion method is a good approximation for high Z and high density materials, while a transport method should be used for simulation of low Z and low density materials. Diffusion and transport methods are two common methods used in laser ICF simulation. Generally, transport modeling is better than diffusion modeling. However, transport modeling, such as S_N method of discrete ordinates, is much CPU time consumed than diffusion one.

In our Lagrangian radiation hydrodynamics simulation code, two-temperature flux-limited thermal conduction approximation is used for electron and ion where electrons and ions are in local thermodynamic equilibrium, and have their temperatures, respectively. The x-ray radiation field may not be Planckian distribution, and is described by multi-group method. Two methods are used for radiation modeling: multi-group flux-limited diffusion and multi-group transport (S_N). A hybrid transport-diffusion is a good choice, which can keep better modeling without much CPU time consumed.

Here, we present our hybrid transport-diffusion method and some simulation results by using multi-group diffusion, transport, and hybrid transport-diffusion radiation methods.

Acknowledgements: This work is supported National Natural Science Foundation of China under the Project No. 91130002.

REFERENCES

- [1] J. D. Lindl, Phys. Plasmas 2, 3933 (1995); J. D. Lindl, et al., Phys. Plasmas 11, 339 (2004).
- [2] J. I. Castor, Radiation Hydrodynamics, p. 69, (Cambridge University Press, New York, 2004).

INVESTIGATING THE REASONS OF VARIABILITY IN Si IV AND C IV BROAD ABSORPTION LINE TROUGHS

E. Lyratzi^{1,2}

¹*University of Athens, Faculty of Physics, Panepistimioupoli, Zographou 157 84,
Athens, Greece*

²*Eugenides Foundation, 387 Syngrou Av., 175 64, Athens, Greece*

Broad Absorption Lines (BALs) may originate from: (a) a smooth continuous flow [1] or (b) a flow of many individual clouds [2 and references therein]. The BALs complex profiles and the violent environment where they are created, along with latest observations [3] have strengthen the second point of view. According to that, BALs are composed of a series of absorption components, created in individual clouds. An indication of these clouds is the variation of some parts of BAL troughs [4]. Though most BAL variability studies focus on the variation of the whole absorption trough, it is very important to study the variation of each one of the components that create each BAL. Such a study is accomplished with the model proposed by Danezis et al. [5-6], which also ensures the uniqueness of the number of components and calculates the values of many physical parameters. In this study we apply this model to the C IV and Si IV resonance lines of three BAL Quasars. For each one we study two spectra taken on different epochs. We calculate the variations of the FWHM, optical depth, radial velocities and the equivalent width and we investigate the possibility of the variations of the BALs components indicating the existence of individual clouds.

Acknowledgements: This research project is progressing under the financial support of the Ted and Erica Spyropoulos Foundation and the Special Account for Research Grants of University of Athens, which we thank very much.

REFERENCES

- [1] N. Murray and J. Chiang, ApJ, 454, 105 (1995)
- [2] D. Stathopoulos, E. Danezis, E. Lyratzi, et al., JApA, 36, 495 (2015)
- [3] T. Misawa, N. Inada, M. Oguri et al., ApJ, 794, 20 (2014)
- [4] D. M. Capellupo, F. Hamann et al., MNRAS, 422, 3249 (2012)
- [5] E. Danezis, D. Nikolaidis, E. Lyratzi, et al., PASJ, 59, 827 (2007)
- [6] E. Danezis, E. Lyratzi, L. Č. Popović, et al., NewAR, 53, 214 (2009)

NUMERICAL SIMULATION OF LARGE SCALE LASER FILAMENTATION AND BEAM SMOOTHING FOR INERTIAL CONFINEMENT FUSION

Bin Li, Zhanjun Liu, Chunyang Zheng, Xiaoyan Hu, Liang Hao and Jiang Xiang

Institute of Applied Physics and Computational Mathematics, Beijing, China

Laser beam propagating in Hohlraum plasma is suffered to laser filamentation instability, which may enhance stimulated scattering instabilities and beam deflection[1]. In this invited progress report, we briefly introduce recent research progress on understanding physical mechanism of laser filamentation and controlling it for spatially and temporally smoothing laser beam, respectively, which is investigated by a three dimensional parallel laser plasma simulation code named LAP3D[2,3].

Continuous phase plate (CPP) smoothing beam is employed for investigation of spatially smoothing methods, in which the research includes as follows: 1) the threshold of filamentation for CPP beams; 2) influence of energy distribution of speckles to laser filamentation; 3) the features of filamentation while the beam propagating; 4) conditions for the onset of beam deflection for CPP beams.

Spectral dispersion smoothing beam (SSD) is employed for investigation of temporally smoothing laser beam, in which the research includes as follows: 1) the role of the modulated frequency of SSD on laser beam propagation; 2) the threshold of filamentation for SSD beams; 3) conditions for the onset of beam deflection for SSD beams.

Acknowledgements: This work is partially supported by the National Natural Science Foundation of China (Grant No.11175026, 11175027) and the Scientific Research Starting Foundation for the Returned Overseas Chinese Scholars, Ministry of Education of China (Grant No. [2012]1707).

REFERENCES

- [1] John Lindl, Phys Plasmas, 2, 11(1995).
- [2] Xiaoyan Hu, Liang Hao, Zhanjun Liu, Chunyang Zheng, Bin Li, Hong Guo, AIP ADVANCES, 5,8(2015).
- [3] Bin Li, Zhanjun Liu, Chunyang Zheng, Xiaoyan Hu, High Power Laser and Particle Beams,26,12(2014)

DIAGNOSING PLASMA IN THE SOLAR ATMOSPHERE USING SPECTROPOLARIMETRY

Ivan Milić^{1,2}

¹Max Planck Institute for Solar System research, Goettingen, Germany

²Astronomical Observatory, Belgrade, Serbia

State-of-the art spectropolarimetric observations of solar surface provide us with datasets of high angular, spectral and even temporal resolution with relatively high polarimetric sensitivity. Polarized profiles of spectral lines (i.e. spectral lines “seen” in all four Stokes parameters) are influenced by the thermodynamic and magnetic properties of solar atmosphere (photosphere and chromosphere). Interpretation of spectropolarimetric observations thus allows us to infer the physical properties of the plasma in these regions of solar atmosphere. In this talk we will focus both on microscopic and macroscopic processes influencing spectral line formation, namely: radiation transport, NLTE effects, scattering polarization, Zeeman and Hanle effect. We will then discuss the spectral lines response functions as the main theoretical tool for the inference and finally outline the main results provided by solar spectropolarimetry during last two decades.

DIAGNOSTICS OF PLASMA IN IONOSPHERIC D-REGION BY VLF RADIO WAVES

A. Nina¹, V. M. Čadež², L. Č. Popović² and V. A. Srećković¹

¹*Institute of Physics, University of Belgrade, Pregrevica 118,
11080 Belgrade, Serbia*

²*Astronomical Observatory, Volgina 7, 11060 Belgrade, Serbia*

We present our results of the ionospheric D-region investigations using databases for very low (VLF) and low (LF) frequency radio signals emitted by worldwide distributed transmitters and recorded by the receiver located in Belgrade.

This paper deals with the D-region plasma disturbances caused by different astrophysical phenomena such as the solar Ly α line, solar X-ray flares, solar terminator, and γ -ray bursts in particular.

We show our theoretical and numerical procedures for determination of the spatial and temporal electron density variations, calculations of different plasma parameters during relaxation periods after solar X-ray flare impacts and in quiet conditions, determinations of hydrodynamic waves, and detections of the short-term perturbations in the D-region.

More details of these analyses are given in [1-7].

Acknowledgements: This work is supported by the Ministry of Education, Science and Technological Development of the Republic of Serbia under the grants III 44002, 176001, 176002 and 176004.

REFERENCES

- [1] Nina, A., V. Čadež, V. A. Srećković and D. Šulić, *Balt. Astron.* 20, 609(2011).
- [2] Nina, A., V. Čadež, V. Srećković and D. Šulić, *Nucl. Instrum. Methods. B* 279, 110 (2012).
- [3] Nina, A., V. Čadež, D. Šulić, V. Srećković and V. Žigman, *Nucl. Instrum. Methods. B*, 279,106 (2012).
- [4] A. Nina and V. M. Čadež, *Geophys. Res. Lett.* 40 (18), 4803 (2013).
- [5] Nina, A. and Čadež, V. , *Adv.Space Res.* 54, 7, 1276(2014).
- [6] Nina, A., S. Simić, V. A. Srećković, and L. Č. Popović, *Geophys. Res. Lett.* 42, 8250 (2015).
- [7] A. Nina, *Diagnostic of plasma of ionospheric D region by electromagnetic VLF waves* (PhD Dissertation, 2014).

**LASER-MATTER INTERACTION AT THE
INTENSITY FRONTIER: ON THE PATH
TOWARDS LABORATORY ASTROPHYSICS**

Marija Vranić

*GoLP/Instituto de Plasmas e Fusão Nuclear,
Instituto Superior Técnico, Universidade de Lisboa,
1049-001 Lisbon, Portugal*

INFLUENCE OF RUNAWAY ELECTRONS ON DISCHARGE START-UP IN COMPASS

M. Vlaine^{1,2,3}, J. Mlynar², O. Ficker^{2,3}, J. Havlicek², V. Weinzettl², M. Imrisek^{2,4}, R. Panek², J.-M. Noterdaeme^{1,5} and the COMPASS Team

¹*Department of Applied Physics, Ghent University,
Sint-Pietersnieuwstraat 41, Technicum B4, Ghent B-9000, Belgium*
²*Institute of Plasma Physics of The CAS, Za Slovankou 3, CZ-18200
Prague 8, Czech Republic*

³*Faculty of Nuclear Sciences and Physical Engineering, Czech Technical
University in Prague, Brehova 8, CZ-11519 Prague 1, Czech Republic*

⁴*Faculty of Mathematics and Physics, Charles University, V
Holesovickach 2, CZ-18000 Prague 8, Czech Republic*

⁵*Max Planck Institute for Plasma Physics, Boltzmannstrae 2, D-85748
Garching, Germany*

Abstract. The contribution reports an observation of runaway electron influence on the initial phase of the plasma discharge in the COMPASS tokamak. This kind of phenomenon is of an importance for the runaway electron studies in smaller tokamaks. All relevant observations are presented and discussed.

1. INTRODUCTION

The electron is said to “run away” in velocity phase-space when the collisional drag force acting on it becomes smaller than the accelerating force coming from the electric field in plasma. A mechanism of runaway electron (RE) that creates the RE seed is called the Dreicer mechanism [1] (diffusion in the velocity phase-space). The RE seed can be afterwards multiplied by the avalanche mechanism in the exponential manner through the collisions of a thermal electron and the already existing RE that remains in the RE region. Due to the avalanche effect ITER could have a RE beam with tens of MeV and carrying current of 10 MA.

In fusion device, such as tokamak, electric field in toroidal direction E_{tor} is the main source of the electron acceleration. In small tokamaks the Dreicer mechanism prevails over avalanche mechanism. Furthermore, RE can be generated during the very beginning of the discharge, making RE

studies more difficult. Therefore, this paper will concentrate on the influence of the RE on the plasma parameters at the beginning of the COMPASS discharges, the so-called I_p ramp-up phase.

2. EXPERIMENTAL SETUP AND DIAGNOSTICS

The COMPASS tokamak [2] is a small-size experimental fusion device with major radius $R_0 = 0.56$ m, minor radius $a = 0.2$ m and ITER-like plasma shape. Toroidal magnetic field B_{tor} was 1.15 T for the analyses discharges and plasma current I_p during the flat-top was 130 kA. Electron densities were scanned down from 5×10^{19} to $1 \times 10^{19} \text{ m}^{-3}$. Plasma was limited on the inner limiter with circular shape, except during the I_p ramp-up phase when elliptical plasma is created due to better stability. The typical pulse length was around 0.30 – 0.35 s.

The loop voltage is measured in standard way by a flux loop, and the I_p is determined with a Rogowski coil. Actual amount of injected working gas (i.e. deuterium) puff will be used for quantification of particles inside the vacuum vessel instead of typically used the electron density n_e measurement, due to the relatively high fluctuations of the interferometer signal.

Main diagnostics used for the RE detection were NaI(Tl) scintillator for hard X-rays (HXR) and ZnS(Ag) neutron detector embedded in a plastic matrix and shielded with 10 cm of Pb. NaI(Tl) detector detects HXR with energy over 50 keV and it is located at approximate distance of 4 m from tokamak. Neutron detector is sensitive also to photons having energies over > 1 MeV and it is at about 4 m from tokamak with the same toroidal position as the NaI(Tl) detector. However, the neutron detector is also sensitive to the strong fluxes of HXR, therefore it will be referred to as the *Shielded HXR detector*.

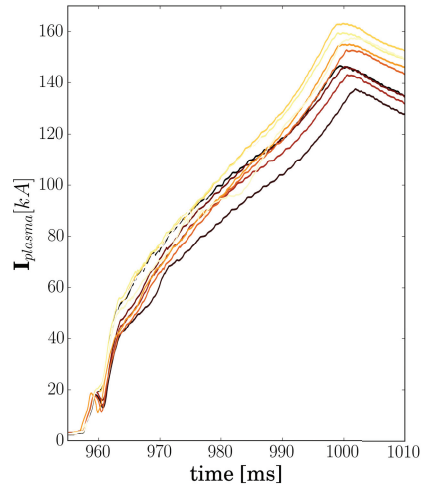


Figure 1. Plasma current during the first 55 ms of the discharge - the darker the line the higher n_e .

3. RESULTS AND DISCUSSION

Results from 10 discharges with a different densities are reported. The maximum value of n_e during I_p flat-top was approximately $5 \times 10^{19} \text{ m}^{-3}$, while minimum value reached was $1 \times 10^{19} \text{ m}^{-3}$. As the deuterium gas puff during the I_p ramp-up phase was lowered, one can see the rise of the I_p

at the end of the ramp-up phase I_p^{max} (see Fig. 1). Due to the fact that induced loop voltage V_{loop} was practically the same in the discharges and that the only significant difference in between the discharges was in the gas puff, i.e. plasma density, the REs are suspected to be the main cause of the difference in the I_p^{max} .

To confirm the above hypothesis, Shielded HXR and NaI(Tl) HXR measured data are plotted in Fig. 2 as a function of realized deuterium puff as well as the I_p^{max} . It is clear from Fig. 2a that lower gas puff corresponds to the more detected high energetic REs. Interestingly, the RE losses detected with NaI(Tl) HXR detector are almost the same until the end of ramp-up phase (Fig. 2b), while losses recorded during the rest of the discharge are larger when the gas puff is lower. Lower gas puff corresponds to lower n_e and lower content of neutrals in plasma. This is consistent with the RE theory having Dreicer electric field $E_D = \frac{n_e e^3 \ln \Lambda}{4\pi \epsilon_0^2 T_e} [\text{eV}]$ in its core. E_D corresponds to the strength of the electric field for which all electrons in plasma would become accelerated. Therefore, lower E_D means more generated REs. This corresponds to the plasma with lower n_e and larger electron temperatures T_e . Values of T_e were similar in all discharges, as measured by Thomson scattering. As mentioned in Sec. 1, E_{tor} is the most important parameter, but it was practically constant as indicated by the V_{loop} measurements.

On the other hand, during the I_p flat-top phase a drop of the V_{loop} is noticed. This comes from the fact that part of the measured I_p is carried by the REs. Therefore volt-second consumption from the tokamak central solenoid is reduced and the induced V_{loop} is lower. Finally, EFIT reconstruction (an iterative Grad-Shafranov solver [3]) estimates an artificial rise of the plasma pressure β for the RE dominated discharges as already reported and explained in Ref. [4].

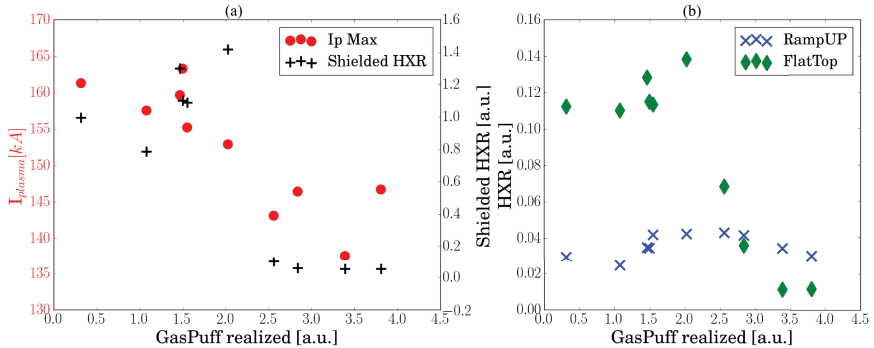


Figure 2. **Left:** Plasma current at the end of discharge ramp-up (red circles) and total Shielded HXR signal (black pluses) as function of deuterium gas puff. **Right:** NaI(Tl) HXR signal before the I_p reaches maximum (blue crosses) and during the rest of the discharge (green diamonds) as function of deuterium gas puff realized.

4. CONCLUSIONS AND OUTLOOK

Possible generation of REs during disruptions in ITER could present a serious threat to the in-vessel components. Therefore, RE studies are one of the main disruption-related topics in the physical fusion research. However, their studies in larger tokamaks could also invoke damage of the in-vessel components. While REs should not cause a serious harm in the smaller tokamaks their studies are more challenging, because RE origin is unclear due to their generation at the I_p ramp-up phase.

In this article, a clear influence of the RE on the initial I_p current is reported. Even though only n_e was a test parameter, I_p also changed significantly at the I_p^{max} (over 20%). V_{loop} and T_e were clearly similar for all the given discharges. Errors in EFIT calculation during RE dominated discharges were also observed, as expected.

The set of the analysed discharges is very convenient for the calculation and modelling purpose as majority of the main parameters are not changed and the main difference is in n_e that induces the difference in the RE population. Accordingly, an estimation of how much RE current is in the plasma for given discharges will be conducted. Two main approaches are foreseen: introducing an additional toroidal “wire” in EFIT and/or calculating full power balance equation.

Acknowledgements

The “Joint Doctoral Programme in Nuclear Fusion Science and Engineering” is acknowledged by the first author for supporting these studies. The next to thank is the MEYS project LM2015045, which supports the operation of COMPASS. The authors would also like to acknowledge the work of the WP14-MST2-9 research project team.

This work was carried out within the framework of the EUROfusion Consortium and received funding from Euratom research and training programme 20142018 under grant agreement 633053. The views and opinions expressed herein do not necessarily reflect those of the European Commission.

REFERENCES

- [1] H. Dreicer, Phys. Rev. 115, 238 (1959).
H. Dreicer, Phys. Rev. 117, 329 (1960).
- [2] R Panek *et al*, Plasma Phys. Control. Fusion 58, 014015 (2016).
- [3] V.D. Shafranov, Soviet At. Energ. 13 (6), 1149-1158 (1963).
- [4] M. Vlainic *et al.*, Nukleonika 60 (2), 249-255 (2015).

COMPETITION BETWEEN STIMULATED RAMAN SCATTERING AND TWO-PLASMON DECAY IN FUSION PLASMAS

C. Y. Zheng^{1,2,3}, C. Z. Xiao², Z. J. Liu^{1,2} and X. T. He^{1,2,3}

¹*Institute of Applied Physics and Computational Mathematics, Beijing 100094, China*

²*HEDPS, Center for Applied Physics and Technology, Peking University, Beijing 100871, China*

³*Collaborative Innovation Center of IFSA, Shanghai Jiao Tong University, Shanghai 200240, China*

In this presentation, we demonstrate competition between stimulated Raman scattering (SRS) and two-plasmon decay (TPD) in inhomogeneous plasma by using linear gain analysis and two dimensional particle-in-cell (PIC) simulations. Linear analysis shows that convective SRS prefers occurring in high laser intensity, large density scale length, and high temperatures situations, which may be common in large scale direct-drive scheme, shock ignition scheme, and hybrid-drive scheme. We can distinguish the occurrence region from absolute instabilities and convective instabilities and determine the threshold of convective SRS and TPD from the theory. The wider and lower density region of convective SRS and convective TPD makes it relevant to the hot electron generation. In our PIC simulations, several cases under the hybrid-drive scheme are presented. Great consistencies with linear analysis are shown in simulation results. A convective nature under the hybrid-drive scheme and saturation mechanism are identified due to LDI and strong pump depletion. Nonlinear evolution of the competition between SRS and TPD shows the importance of the convective SRS that it can reduce the hot-electron generation through suppressing the staged acceleration by TPD in the lower density region due to its high phase velocity. The competition between SRS and TPD is important, and it may be observed in the future experiments under the hybrid-drive scheme, shock ignition scheme, and large direct drive scheme as well.

SOLAR Ly α AND X-RAY INFLUENCE ON RADIO WAVE PROPAGATION IN IONOSPHERIC D-LAYER PLASMA

Jovan Bajčetić¹, Dušan Raičević¹ and Aleksandra Nina²

¹*University of Defence, Military Academy, Generala Pavla Jurišića Šturma 33,
11000 Belgrade*

²*Institute of Physics, University of Belgrade, Pregrevica 118,
11080 Belgrade, Serbia*

Abstract. In this paper we study how the ionospheric D-layer plasma affects the HF band communication signal propagation during quiet conditions and under influence of solar X-ray flares. It has been shown that the perturbed D-layer induces a significant refraction of the HF band radio waves which occurs after the onset of the detected X-radiation increase, and depends on altitude and signal frequency. We performed a simulation showing the signal propagation path between 70 km and 80 km where the solar Ly α line has dominant role in ionization and applied Wait's model of ionosphere can be used with a good approximation. Our modelling is based on calculation of the D-layer electron density using the VLF radio sounding, and measuring the ionizing X-band photon flux by the GOES-15 satellite during a solar X-ray flare. Here we consider period before and during solar X-ray flare occurred on May 5, 2010, and VLF radio signal emitted in Germany by DHO transmitter and received in Serbia for D-layer monitoring.

1. INTRODUCTION

As a part of atmosphere, the ionosphere is under permanent radiation coming from outer space. The most important role in plasma perturbation within this medium has the solar radiation. Specifically, between altitudes of 70 km and 80 km, the dominant sources of ionization are the solar Ly α line during quiet conditions and solar X-ray flares which are more intensive outer space non periodical perturbers. They have very important role in dynamics of the lowest ionospheric layer called D-layer, and consequently in processes occurred in this medium.

One of the processes that is present in the D-layer is the propagation of electromagnetic waves and the analysis of the sudden perturbation influence on the radio propagation is very important in telecommunications, primarily for radio communications.

In this paper we show differences in high frequency (HF) signal propagation paths within the middle part of D-layer in periods when Ly α and X radiations have a dominant role in ionization.

2. OBSERVATIONS AND MODELING

In our investigations we monitor the low ionosphere by VLF AWESOME receiver which is located in Institute of Physics and operates since 2008. The performed study utilizes signal emitted in Germany by DHO transmitter at 23.4 kHz.

From measured amplitude and phase changes we compute the electron plasma density $N_e(h; t)$ (in m^{-3}) at fixed altitude h (in km) applying Wait's model of ionosphere [1]:

$$N(h, t) = 1.43 \cdot 10^{13} e^{-\beta(t)H'(t)} e^{(\beta(t)-0.15)} \quad (1)$$

The signal reflection height H' (in km) and sharpness β (in km^{-1}) are independent parameters calculated by a numerical procedure based on comparison of the recorded amplitude and phase changes with corresponding values obtained by the LWPC numerical model for simulation of the VLF signal propagations [2].

To obtain the propagation path, we divided the D-layer on sub layers and calculated the deviation angle on the borders between neighbouring sub layers using the Snell's law where the refraction index n for frequency f in Hz is given by: $n(h, t) = \sqrt{1 - 81 \cdot N(h, t) / f^2}$ where N and f are given in m^{-3} and Hz, respectively.

3. RESULTS AND CONCLUSIONS

We apply modelling presented in Section 2 on solar X-ray flare occurred on May 5, 2010 and VLF radio signal emitted in Germany by DHO transmitter and received in Serbia. The detailed analyses of D-layer plasma properties in this period are given in [3, 4].

We show in Figs 1 and 2 the modelled propagation paths of HF signals at frequencies of 10 MHz and 15 MHz, which are emitted from the same position at the Earth surface and different angles with respect to vertical axes. We consider middle part of D-layer (between 70 km and 80 km) where the solar Ly α line has a dominant role in ionization and Wait's model of ionosphere can be applied with good approximation.

The influences of the solar Ly α line are shown in the upper panels of these figures, while changes in the propagation of HF waves affected by the plasma under increased X-ray radiation are presented in the bottom panels. As we see in both cases, the influence of solar X-ray flares can significantly change propagation path of HF signals. These changes are more visible for lower frequency and for larger emitted angle from the vertical axes. In considered

cases, both 10 MHz and 15 MHz signals do not reflect within 1000 km from the transmitter.

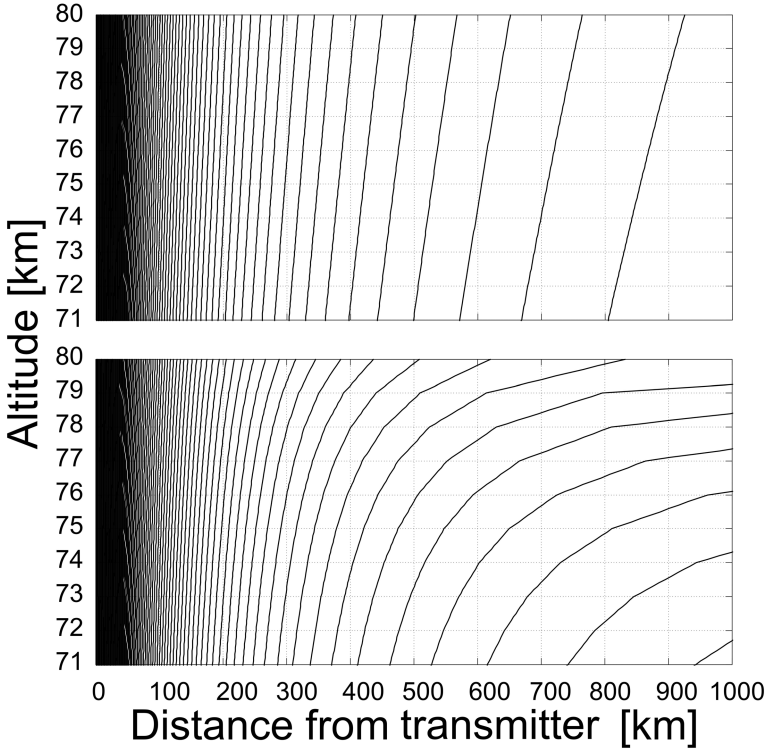


Figure 1. Propagation paths between 70 km and 80 km altitude of 10 MHz signals emitted from the same location in the Earth surface and with different angles. The upper panel show the paths in quiet D-layer when the electrons are primarily obtained from photoionization by solar Ly α line, while the bottom panel shows the paths in the moment of maximum plasma perturbation when the X radiation is dominant source of ionization. The paths going from left to right are related to the angles with respect to vertical axes from 0° to 89°.

From this analysis, we can conclude that the modelling of high frequency electromagnetic wave propagation in the middle part of the D-layer during a solar X-ray flare requires the plasma properties determination. The plasma influence on the HF radio propagation cannot be ignored within this region during this aperiodic perturbation, contrary to the conditions in quiet periods when solar Ly α line do not produce enough electrons to significantly affect HF signal propagation paths.

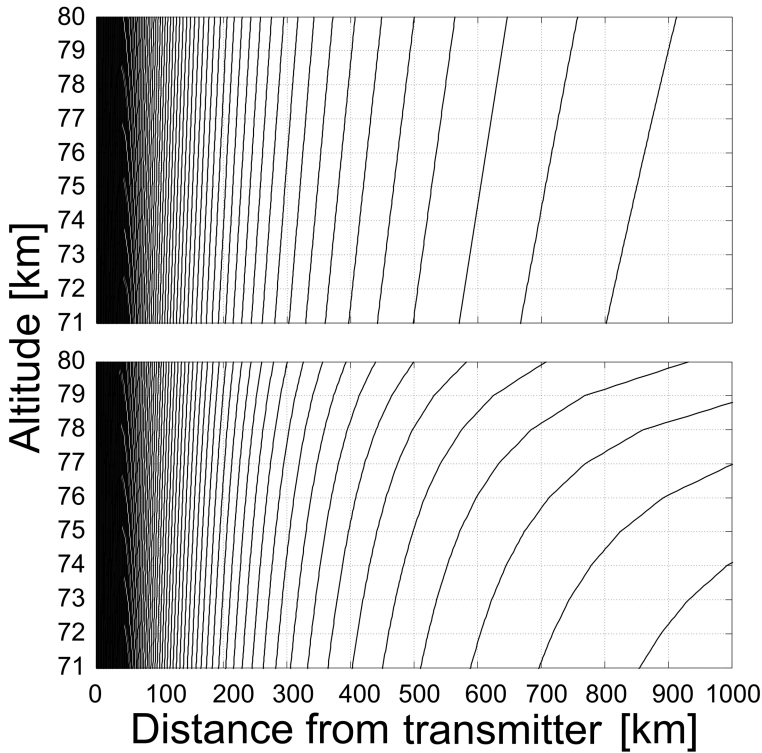


Figure 2. The same as in Fig. 1, but for signal frequency of 15 MHz.

Acknowledgements

This work is supported by the Ministry of Education, Science and Technological Development of the Republic of Serbia under the grants III 44002 and 176002.

REFERENCES

- [1] J. R. Wait and K. P. Spies, “Characteristics of the Earth-ionosphere waveguide for VLF radio waves”, NBS Technical Note 300, National Bureau of Standards, Boulder, CO.S (1964).
- [2] J. A. Ferguson, Computer Programs for Assessment of Long-Wavelength Radio Communications, Version 2.0, Space and Naval Warfare Systems Center, San Diego (1998).
- [3] A. Nina and V. M. Čadež, *Adv. Space Res.* 54, 7, 1276 (2014).
- [4] A. Nina, V.M. Čadež and J. Bajčetić, *Serb. Astron. J.*, 191, 51 (2015).

A SHORT OVERVIEW OF OUR CONTRIBUTION TO GREEN'S CATALOGUE OF GALACTIC SUPERNOVA REMNANTS

V. Borka Jovanović¹, P. Jovanović² and D. Borka¹

¹*Atomic Physics Laboratory (040), Vinča Institute of Nuclear Sciences,
University of Belgrade, P.O. Box 522, 11001 Belgrade, Serbia*

²*Astronomical Observatory, Volgina 7, P.O. Box 74, 11060 Belgrade,
Serbia*

Abstract. Aim of this work is to give a brief overview of a catalogue of known Galactic supernova remnants (SNRs), as well as to show our contribution to this listing. Also, we would like to point out that there are the notes on possible remnants not included, and also on questionable SNRs that are listed in this catalogue, so there is always a need for detailed studying of properties of such sources.

1. SUMMARY DATA FOR GALACTIC SNRS

SNRs are the structures resulting from the explosion of a star in a supernova. These non-thermal sources are spreading inside of the hot and low density bubbles, and they are extremely important for understanding our galaxy: they heat up the interstellar medium, distribute heavy elements throughout the galaxy, and accelerate cosmic rays.

A catalogue of Galactic SNRs, created in 1984 by D. A. Green (from Astrophysics Group of Cavendish Laboratory, Cambridge, United Kingdom), with some statistics of their parameters, is presented in [1], along with more detailed web-based version [2]. The current version of the catalogue contains 294 SNRs, and it is available as a summary listing of the parameters for each remnant, and as detailed listings (with over fifteen hundred references) for each object [3].

It is based on research in the published literature up to the end of 2013, and for each remnant in the catalogue the following parameters are given: *Galactic Coordinates* of the source centroid, *Other Names* that are commonly used for the remnant, *Right Ascension* and *Declination* of

the source centroid, *Angular Size* in arcminutes, *Flux Density* at 1 GHz in jansky, *Spectral Index* α (defined in the sense, $S_\nu \sim \nu^{-\alpha}$, where S_ν is the flux density at a frequency ν) and *Type* of the SNR (S - shell structure, F - filled-centre structure, C - composite).

Out of 294 known remnants in our Galaxy, only 20 have not been either detected in the radio band, or are poorly defined by current radio observations. In the current version of the catalogue, 79% of remnants are classified as shell (or possible shell), 12% are composite (or possible composite), and just 5% are filled-centre (or possible filled centre) remnants [1]. The morphology and brightness distribution in SNRs contain important information about the nature of the SNR and its possible hydrodynamical evolution.

2. OUR CONTRIBUTION TO SNR CATALOGUE

The vast majority of SNRs in our Galaxy were first recognized from radio observations. For our research, we used the radio continuum survey data, provided by Max Planck Institute for Radio Astronomy (MPIfR), Bon, Germany, available at the internet site: [4]. At that Survey Sampler, one can choose a coordinate system, projection type, and a survey (i.e. telescope) and then submit the request.

We calculated the brightness temperatures, surface brightnesses, and radio spectral indices for some of the SNRs which are already listed there. These are: Monoceros Nebula (G205.5+0.5), Cygnus Loop (G74.0-8.5), HB 21 (G89.0+4.7) and Lupus Loop (G330.0+15.0) (see Fig. 1).

For all of them, we confirmed the non-thermal nature of their radiation, and published results which are more recent and with higher statistics. Our new estimates, using the method we have previously developed, are published in the following papers: for Monoceros remnant in [5, 6], for Cygnus in papers [7, 8], for HB 21 in [9] and for Lupus in [10]. We developed the method for defining a loop border and for determining the values of brightness temperature and surface brightness, which is explained in details in [11] and references therein. This method of calculation we developed for main Galactic Loops I-IV [12], which is mentioned also in online version of the catalogue [4], and for which we showed that it could be applicable to all SNRs. Besides, this method is applicable to extragalactic radio sources as well [13, 14].

The 2014 May version of the catalogue, besides confirmed SNRs, contains also the notes on many possible or probable remnants. So, in the future work, one can study the properties of the possible remnants and find the reasons for, or against, being part of this catalogue.

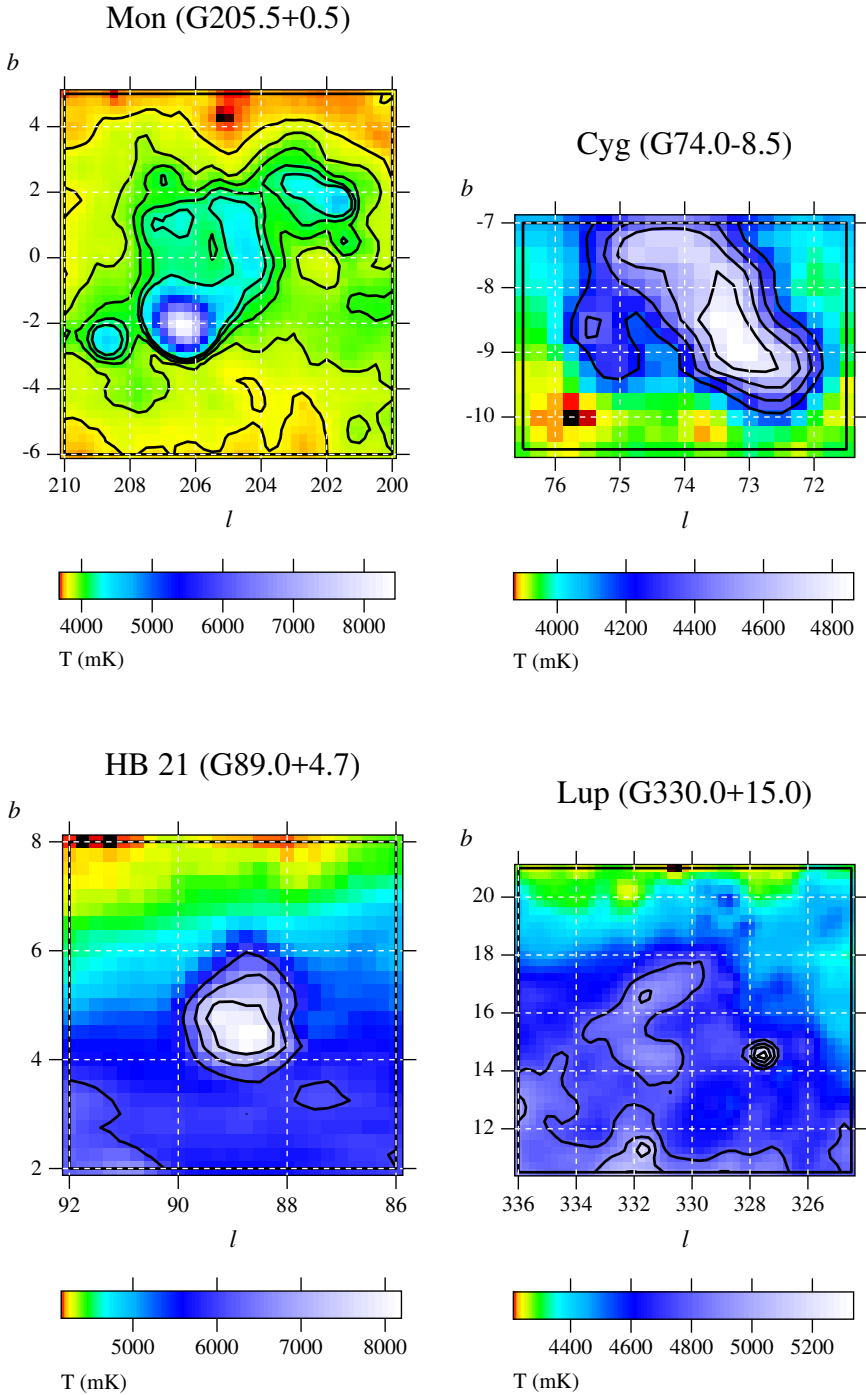


Figure 1. The 1420 MHz maps of SNRs, in new Galactic coordinates (l, b) , with brightness temperature contours. Below, the temperature scales are given (in mK). *Top left:* Monoceros, with five T_b contours from 3800 to 4200 mK; *top right:* Cygnus, 4200-4900 mK; *bottom left:* HB 21, 6000-9000 mK; *bottom right:* Lupus, 4780-5400 mK.

Acknowledgements

This work is supported by Ministry of Education, Science and Technological Development of the Republic of Serbia, through the project 176003 "Gravitation and the Large Scale Structure of the Universe".

REFERENCES

- [1] D. A. Green, *Bull. Astr. Soc. India* 42, 47 (2014).
- [2] D. A. Green, A Catalogue of Galactic Supernova Remnants (2014 May version), Astrophysics Group, Cavendish Laboratory, Cambridge, United Kingdom (2014). (available at <http://www.mrao.cam.ac.uk/surveys/snrs/>)
- [3] <http://www.mrao.cam.ac.uk/surveys/snrs/snrs.info.html>
- [4] <http://www3.mpifr-bonn.mpg.de/survey.html>
- [5] V. Borka Jovanović and D. Urošević, *Publ. Astron. Obs. Belgrade* 84, 459 (2008).
- [6] V. Borka Jovanović and D. Urošević, *Astron. Nachr.* 330, 741 (2009).
- [7] V. Borka Jovanović and D. Urošević, *Publ. Astron. Obs. Belgrade* 86, 101-106 (2009).
- [8] V. Borka Jovanović and D. Urošević, *Rev. Mex. AA* 47, 159 (2011).
- [9] D. Borka, V. Borka Jovanović and D. Urošević, *Rev. Mex. AA* 48, 53 (2012).
- [10] V. Borka Jovanović, D. Borka and P. Jovanović, *Publ. Astron. Obs. Belgrade*, in press (2016).
- [11] V. Borka Jovanović, *Publ. Astron. Obs. Belgrade* 91, 121 (2012).
- [12] V. Borka, *Mon. Not. R. Astron. Soc.* 376, 634 (2007).
- [13] V. Borka Jovanović, D. Borka, R. Skeoch, P. Jovanović, *Publ. Astron. Obs. Belgrade* 91, 255 (2012).
- [14] V. Borka Jovanović, P. Jovanović, D. Borka, *Zbornik radova XII Kongresa fizičara Srbije, Vrnjačka Banja, Srbija*, 28. april - 2. maj, 367 (2013).

FUNDAMENTAL PLANE OF ELLIPTICAL GALAXIES AND $f(R)$ GRAVITY

V. Borka Jovanović¹, P. Jovanović², D. Borka¹ and S. Capozziello^{3,4,5}

¹*Atomic Physics Laboratory (040), Vinča Institute of Nuclear Sciences, University of Belgrade, P.O. Box 522, 11001 Belgrade, Serbia*

²*Astronomical Observatory, Volgina 7, P.O. Box 74, 11060 Belgrade, Serbia*

³*Dipartimento di fisica, Università di Napoli "Federico II", Compl. Univ. di Monte S. Angelo, Edificio G, Via Cinthia, I-80126 Napoli, Italy*

⁴*Istituto Nazionale di Fisica Nucleare (INFN) Sez. di Napoli, Compl. Univ. di Monte S. Angelo, Edificio G, Via Cinthia, I-80126 Napoli, Italy*

⁵*Gran Sasso Science Institute (INFN), Viale F. Crispi 7, I-67100, L'Aquila, Italy*

Abstract. Aim of this work is to show the connection between the half-light radius, central velocity dispersion, and mean surface brightness of elliptical galaxies and the parameters of R^n gravity potential. We also want to show that R^n gravity fit the observations very well, without adding unknown forms of dark energy or dark matter.

1. FUNDAMENTAL PLANE OF ELLIPTICALS

It is well known that besides the spiral galaxies, elliptical galaxies could also have so called missing mass problem, where an extra mass is required to explain the observed differences between their dynamical masses and luminosities. The only two possibilities explaining this missing mass problem are dark matter (DM), or theories of modified gravity. In this work we adopt the second approach where we study whether the $f(R)$ gravity could solve the missing mass problem in elliptical galaxies without dark matter hypothesis. We adopt such an approach because in the galaxies we can deal with the extreme gravity regimes, and higher order curvature corrections in gravity action can emerge. That's why instead of general relativity we will use its simplest extension: $f(R)$ gravity model.

Many characteristics of normal elliptical galaxies are correlated, which has been empirically shown. For example, a galaxy with a higher luminosity has a larger effective radius. Also, more luminous elliptical galaxies

have larger central velocity dispersions. A set of correlations connecting the global properties of elliptical galaxies is called fundamental plane (FP), and it is an empirical relation [1]:

$$\log(r_e) = a \times \log(v) + b \times \log(I_e) + c, \tag{1}$$

with: r_e – effective or half-light radius (encloses half of the total luminosity emitted by a galaxy), v – central velocity dispersion, I_e – mean surface brightness within the effective radius. We illustrate this region of parameter space in Fig. 1.

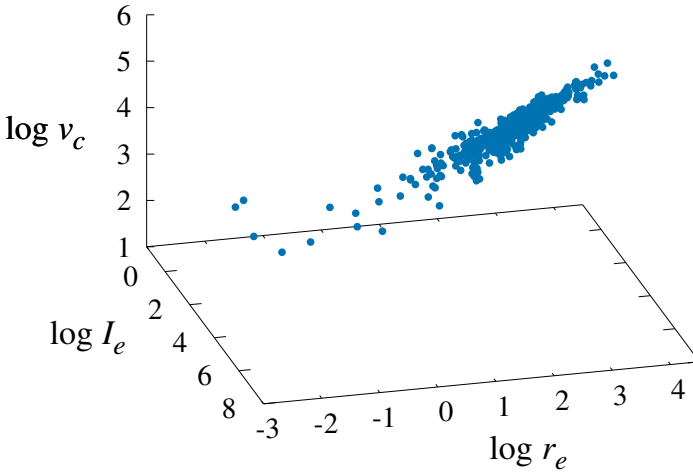


Figure 1. The three parameters of FP: surface brightness I_e , effective radius r_c and circular velocity v_c , for a sample of elliptical galaxies listed in Table 1 from [9].

2. $f(R)$ GRAVITY AND DYNAMICS OF STELLAR SYSTEMS

We adopt $f(R)$ gravity which is the straightforward generalization of Einstein’s General Relativity as soon as the function is $f(R) \neq R$, that is, it is not linear in the Ricci scalar R as in the Hilbert-Einstein action. R^n gravity is the power-law version of $f(R)$ modified gravity. In the weak field limit, its potential (generated by a pointlike mass m at the distance r) is [2]:

$$\Phi(r) = -\frac{Gm}{2r} \left[1 + \left(\frac{r}{r_c} \right)^\beta \right], \tag{2}$$

where r_c is scalelength depending on the gravitating system properties and β is universal constant which depends on power n :

$$\beta = \frac{12n^2 - 7n - 1 - \sqrt{36n^4 + 12n^3 - 83n^2 + 50n + 1}}{6n^2 - 4n + 2}. \quad (3)$$

About consideration of the power-law fourth-order theories of gravity, as well as about determining of the space parameters of $f(R)$ gravity see in [2, 3, 4, 5, 6, 7].

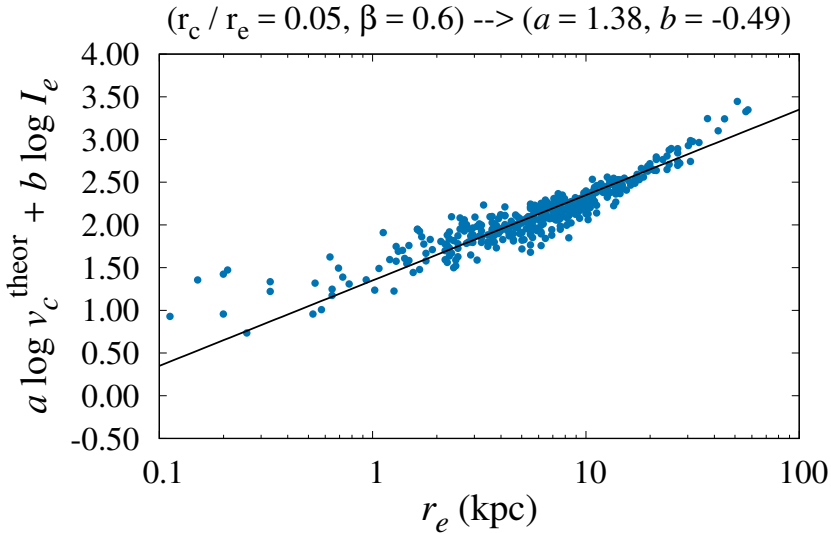


Figure 2. Fundamental plane of elliptical galaxies with calculated circular velocity v_c^{theor} and observed effective radius r_e and mean surface brightness within the effective radius I_e , for $r_c/r_e = 0.05$ and $\beta = 0.6$. Black solid line is result of 3D fit of FP (calculated FP coefficients are $a = 1.38$ and $b = -0.49$).

We want to connect fundamental plane of elliptical galaxies with R^n gravity potential, by showing the correlation between the corresponding parameters. In paper [8] the empirical result for coefficients a and b is: $a = 1.4$, $b = -0.85$. The test for our method is to recover these coefficients, starting from the gravitational potential derived from $f(R)$ gravity.

We use the data given in Table I of [9], which represents the result of the collected efforts of many astronomers over the years (available in ASCII format among the source files of its arxiv version). We fitted FP coefficients a, b, c to the observed values r_e, I_e and our calculated value v_c^{theor} , for different values of r_c/r_e and β , and one example we give in Fig. 2. The theoretical circular velocity we calculated for extended spherically symmetric systems, using Eq. (25) from [2], and taking into account the so called Hernquist profile for density distribution [10]. The coefficient a is exactly like in [8], while b has similar but not exactly the same value. However, we only calculated v_c^{theor} , while for I_e we considered observed values, but in any case

the agreement with data is very good. We obtained that the characteristic radius r_c of R^n gravity is proportional to the effective radius r_e (more precise, $r_c \approx 0.05 r_e$ gives the best fit with data). This fact points out that the gravitational corrections induced by R^n can lead photometry and dynamics of the system.

Acknowledgements

This work is supported by Ministry of Education, Science and Technological Development of the Republic of Serbia, through the project 176003 "Gravitation and the Large Scale Structure of the Universe", and by Istituto Nazionale di Fisica Nucleare, Sezione di Napoli, Italy, iniziative specifiche TEONGRAV and QGSKY. The authors also acknowledge the support by Bilateral cooperation between Serbia and Italy 451-03-01231/2015-09/1 "Testing Extended Theories of Gravity at different astrophysical scales".

REFERENCES

- [1] Busarello, M. Capaccioli, S. Capozziello, G. Longo and E. Puddu, *Astron. Astrophys.* 320, 415 (1997).
- [2] Capozziello, V. F. Cardone and A. Troisi, *Mon. Not. R. Astron. Soc.* 375, 1423 (2007).
- [3] D. Borka, P. Jovanović, V. Borka Jovanović and A. F. Zakharov, *Phys. Rev. D* 85, 124004 (2012).
- [4] D. Borka, P. Jovanović, V. Borka Jovanović and A. F. Zakharov, *Sveske fizičkih nauka (SFIN) year XXVI Series A: Conferences No. A1*, 61 (2013).
- [5] A. F. Zakharov, D. Borka, V. Borka Jovanović and P. Jovanović, *Adv. Space Res.* 54, 1108 (2014).
- [6] D. Borka, P. Jovanović, V. Borka Jovanović and A. F. Zakharov, Chapter 9 in "Advances in General Relativity Research", 343-362, Edited by Cameron Williams, ISBN: 978-1-63483-120-8, Nova Science Publishers (2015).
- [7] V. Borka Jovanović, S. Capozziello, P. Jovanović and D. Borka, submitted (2016).
- [8] R. Bender, D. Burstein and S. M. Faber, *Astrophys. J.* 399, 462 (1992).
- [9] Burstein, R. Bender, S. M. Faber and R. Nolthenius, *Astron. J.* 114, 1365 (1997).
- [10] L. Hernquist, *Astrophys. J.* 356, 359 (1990).

MOL-D: DATABASE FOR SPECIFIC COLLISIONAL PROCESSES AND WEB SERVICE WITHIN THE SERBIAN VIRTUAL OBSERVATORY AND THE VIRTUAL ATOMIC AND MOLECULAR DATA CENTER CONSORTIUM

D. Jevremović¹, V. Vujčić^{1,2}, A. A. Mihajlov³, V. A. Srećković³,
Lj. M. Ignjatović³, M. S. Dimitrijević^{1,4,5}, S. Erkapić¹ and N. Milovanović¹

¹*Astronomical Observatory, Volgina 7, 11160 Belgrade 74, Serbia*

²*Faculty of Organizational Sciences, University of Belgrade, Serbia*

³*University of Belgrade, Institute of Physics, P. O. Box 57, 11001, Serbia*

⁴*Observatoire de Paris, 92195 Meudon Cedex, France.*

⁵*IHIS Techno Experts, Batajnicki put 23, 11080 Zemun, Serbia.*

Abstract. We report the current stage of the MOL-D database and web service within the virtual atomic and molecular data center (VAMDC). MOL-D database is devoted to the modelling of stellar atmospheres, laboratory plasmas, technological plasmas and etc. The initial stage of development was done at the end of 2014, when we've built the service for all the existing photodissociation data for hydrogen H_2^+ and helium He_2^+ molecular ions. In the second stage of the development of MOL-D, we included new cross-section and rate coefficients for processes which involve species such as MgH^+ , HeH^+ , LiH^+ , NaH^+ , SiH^+ . In this paper, we present our ongoing work and plans for the future.

1. MOL-D

Belgrade MOL-D database is a collection of cross-sections and rate coefficients for specific collisional processes [1]. It can be accessed via website of Serbian Virtual Observatory (SerVO [2,3]) or as a web service which is part of the Virtual Atomic and Molecular Data Center (VAMDC [4,5]) network.

The database contains photodissociation cross-sections for the individual ro-vibrational states of the diatomic molecular ions and rate coefficients for the atom-Rydberg atom chemi-ionization and inverse electron-ion-atom chemi-recombination processes. The web interface offers access to data for photodissociation (bound-free) cross-sections of hydrogen H_2^+ and helium He_2^+ molecular ions as well as the corresponding averaged thermal photodissociation cross-sections (see for e.g. figure 1).

At this moment MOL-D is in the second stage of development. We are including new cross-section and rate coefficients data for processes which involve species such as MgH^+ , HeH^+ , LiH^+ , NaH^+ , SiH^+ which are important for the experimental plasma physics as well as for exploring of the interstellar medium, the early Universe chemistry and for the modeling of different stellar and solar atmospheres [1,4].

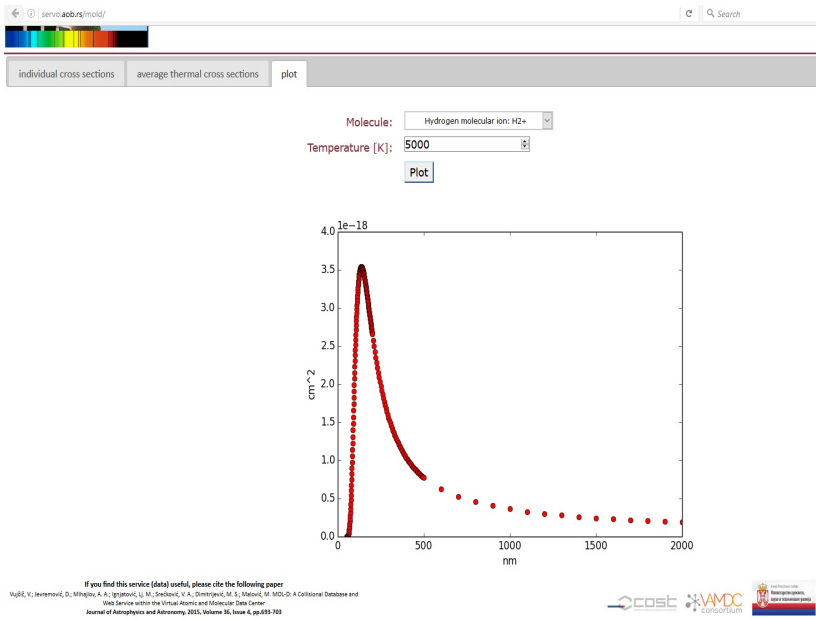


Figure 1. Screen shots of the MOL-D node at the Belgrade server station [3] showing average thermal photodissociation cross-section for H_2^+ molecular ion in the wide range of wavelengths and for the specified temperature.

We are planning incremental inclusion of data from our papers concerning atomic and molecular processes important for modeling different stellar atmospheres and laboratory plasmas as they become published. Along with database updates, we intend to develop new web utilities and interfaces for SerVO MOL-D website.

2. TECHNICAL DESCRIPTION

Data model of Belgrade MOL-D application with entities, attributes and relationships is shown in figure 2. The application is written in Django, a Python web framework and is extended and adapted on top of VAMDC NodeSoftware.

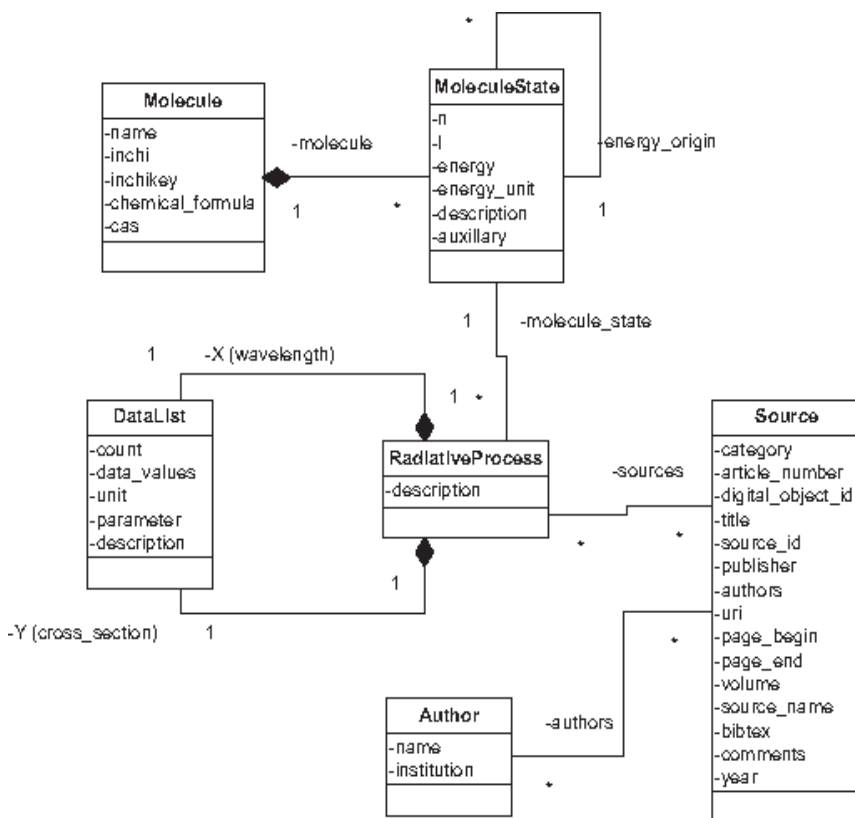


Figure 2. UML static diagram of MOL-D application.

Access to data is possible via VAMDC-compliant web service or via AJAX-enabled web interface (<http://servo.aob.rs/mold>). Both queries return data in XSAMS (XML Schema for Atoms, Molecules and Solids) format suited for interoperability of VAMDC nodes and applications. Additional on-site utilities include:

- making a selection based on molecule and QNJ/QNv numbers
- calculating average thermal cross section based on temperature for a specific molecule and wavelength

- making a plot of average thermal cross sections along all (discrete) wavelengths for a given temperature.

3. CONCLUSIONS AND PERSPECTIVES

Databases in atomic and molecular physics have become essential for the modeling and for the interpretation of data provided by observations and laboratory measurements of various plasmas [6]. Currently, very important resources of such data are dissipated, presented in different, non-standardized ways, available through a variety of highly specialized and often poorly documented interfaces. As a consequence the full exploitation of all data is limited. The free exchange of these data requires the definition of some standards and tools that help users and producers in this process. The continuation of such developments and services is crucial.

In the near future we intend to update current databases with new data as well as to include completely new database into Belgrade VAMDC node.

Acknowledgements

The authors are thankful to the Ministry of Education, Science and Technological Development of the Republic of Serbia for the support of this work within the projects 176002 and III44002. A part of this work has been supported by VAMDC. Support for VAMDC has been provided through the VAMDC and the SUP@VAMDC projects funded under the ‘Combination of Collaborative Projects and Coordination and Support Actions’ Funding Scheme of The Seventh Framework Program.

REFERENCES

- [1] V. Vujčić, D. Jevremović, A.A. Mihajlov, Lj.M. Ignjatović, V.A. Srećković, M.S. Dimitrijević, M. Malović, *Journal of Astrophysics and Astronomy*, Volume 36, Issue 4, pp. 693-703 (2015).
- [2] D. Jevremović, M.S. Dimitrijević, L.C. Popović et al., *New Astronomy Reviews* 53, 222 (2009).
- [3] <http://servo.aob.rs/mold/>
- [4] M.L. Dubernet, B.K. Antony, Y.A. Ba et al., *Journal of Physics B Atomic Molecular Physics*, 49, 074003, (2016).
- [5] <http://portal.vamdc.eu/>
- [6] B.P. Marinković, V. Vujčić, G. Sushko et al., *Nuclear Instruments and Methods in Physics Research B*, 354, 90 (2015).

THE NATURE OF GRAVITATIONAL AND GRAVITY WAVES

Gordana Jovanović

University of Montenegro, Džordža Vašingtona bb

Abstract. The terms gravity waves and gravitational waves are two commonly confused terms in physics. Gravity waves are generated in fluid mediums or on interfaces between two fluid mediums. On the other hand, gravitational waves are produced by cosmological phenomena in the universe. This is the main difference between gravity waves and gravitational waves. Gravity waves can be easily detected on the Earth whereas gravitational waves could not be detected until 14 September 2015. The concept of gravity waves isn't complex whereas the concept of gravitational waves is complex. The generation of gravity waves can be easily explained in fluid dynamics whereas the generation of gravitational waves isn't easy to understand. So, these two terms have totally different meanings. This article attempts to give a better understanding of those differences.

1. GRAVITATIONAL WAVES

Already in 1916., Albert Einstein predicted the existence of gravitational waves as a direct consequence of his theory of General Relativity but scientists were unable to detect these waves until 14 September 2015 [1]. Gravitational waves are faint deformations of the spacetime geometry, propagating at the speed of light and generated by catastrophic events in the Universe, in which strong gravitational fields and sudden acceleration (or deceleration) of asymmetric distribution of large masses are involved. In general terms, gravitational waves are radiated by objects whose motion involves acceleration, provided that the motion is not perfectly spherically symmetric (like an expanding or contracting sphere) or rotationally symmetric (like a spinning disk or sphere). Gravity is the weakest of the four fundamental forces. Therefore, gravitational waves are extremely small. For this reason, only extremely massive and compact objects having intense and asymmetric gravitation fields, like neutron stars and black hole binary systems, are expected to be able to generate detectable gravitational waves.

Gravitational waves are also produced by cosmological explosions such as supernova.

1.1 Gravitational Waves Detection

A few different experiments are currently searching for gravitational waves. LIGO (Laser Interferometer Gravitational-Wave Observatory) looks for gravitational waves by tracking how they affect spacetime: As a wave passes by, it stretches space in one direction and shrinks it in a perpendicular direction. LIGO aims to detect these changes using an interferometer. In fact, the project uses two detectors, one located in Washington State and the other in Louisiana, to sense the distortions in space that occur when a gravitational wave passes through Earth. Each detector is shaped like a giant L, with legs four kilometers long. To measure the relative lengths of the legs, a single laser beam is split at the intersection of the two legs. Half of the laser light is transmitted into one leg while the other half is reflected into the second leg. Mirrors are suspended as pendula at the end of each leg and near the beam splitter. Laser light bounces back and forth through the legs, reflecting off mirrors, and finally returns to the intersection, where it interferes with light from the other leg. Amazingly precise atomic clocks measure how long it takes to make the journey. Normally, the two legs are exactly the same length, and so the light takes exactly the same amount of time to traverse each. If a gravitational wave passes through, the detector and ground beneath it will expand and contract infinitesimally in one direction, and the two perpendicular legs will no longer be the same size. One of the lasers will arrive a fraction of a second later than the other, the two light beams would no longer completely subtract each other, yielding light patterns at the detector output. Encoded in these light patterns is the information about the relative length change between two legs, which in turn tells us about what produced the gravitational waves.

LIGO must be unbelievably sensitive to measure this change in the length of the legs, which is smaller than one ten-thousandth the diameter of a proton. To register such a tiny change, LIGO must filter out all other sources of noise, including earthquakes and nearby traffic. To help minimize local effects on the detector, LIGO has made many enhancements to the basic interferometer design (Advanced LIGO). There are two LIGO detectors located on the opposite sides of the USA separated nearly 2,000 miles. If a gravitational wave is real, its signature will be observed at both locations. If it is false positive (due to noise), only one station will detect it. According to the researchers at LIGO, the gravitational waves they have detected were generated when two black holes merged to create a single giant black hole. The theory of general relativity predicts that a system of two black holes that are orbiting around each other releases their energy as gravitational waves. So, the system loses its energy causing them to come closer [2]. This process takes billions of years and during the final fraction of a second, the

two black holes strike against each other and creates a single giant black hole. As a result of this tremendous cosmological strike, a portion of the mass of the system is converted into energy and propagates through space as gravitational waves. The amount of the mass that converted into energy is given by the famous Einstein's equation, $E = mc^2$.

The LIGO is not the only laser observatory for gravitational waves. There is European Space Agency's (ESA) Laser Interferometer Space Antenna, or LISA. LISA will act like a giant LIGO in space.

The lasers aren't the only way to detect changes in spacetime. The North American Nanohertz Observatory for Gravitational Waves (NANOGrav), looks for gravitational waves by looking at the burst of radio waves emitted by the neutron stars called pulsars. These radio wave pulses are normally strictly timed, so if they arrive early or late, it could be because a gravitational wave interfered with their journey to Earth.

Other experiments look for a specific type of gravitational waves created in the aftermath of the Big Bang. They do so by observing the radiation left over from the Big Bang. If the Big Bang made gravitational waves, scientists would expect to see swirls in this radiation's polarization. Programs like Background Imaging of Cosmic Extragalactic Polarization (BICEP), Harvard's series of experiments at the south pole, observe the leftover radiation in an attempt to find the polarization patterns.

1.2 The Importance of Gravitational Waves

Most of the astronomy done in the past has relied on different forms of electromagnetic radiation (visible light, radio waves, x-rays, etc.), but electromagnetic waves are easily reflected and absorbed by any matter that may be between their source and us. Even when light from the universe is obtained, it is often transformed during its journey through the universe.

Gravitational waves will change astronomy because the universe is nearly transparent to them: intervening matter and gravitational fields neither absorb nor reflect the gravitational waves to any significant degree. Humans will be able to observe astrophysical objects that would have otherwise been obscured, as well as the inner mechanisms of phenomena that do not produce light. The physics that went into the creation of a gravitational wave is encoded in the wave itself. If we could detect these waves, we could differentiate between gravitational wave signature and work out which phenomenon is generating them. For example, sudden pulse of gravitational waves may indicate they came from a supernova explosion, whereas a continuous oscillating signal may indicate two closely-orbiting black holes before merging. This is a beginning of the new era of gravitational astronomy.

2. GRAVITY WAVES

In a fluid dynamics, gravity waves are waves generated in a fluid medium or at the interface between two fluid media when the force of gravity (or buoyancy) tries to restore equilibrium. Namely, gravity waves result when a fluid particle or a cluster of particles moves on an interface of two fluids (between a body of water and air) or into a region of the fluid with a different density, the gravity tries to restore the lost equilibrium by replacing and repositioning some fluid particles at suitable places. This attempt of the gravity generates oscillations and oscillate about the equilibrium state, known as gravity waves or buoyancy waves. The gravity waves that are generated at interfaces between two different media are called surface gravity waves whereas the gravity waves that are generated within the fluid bodies (such between parts of different densities) are called internal gravity waves. To exist, the fluid must be stratified: the density must change with depth/height due to changes, for example, in temperature. Gravity waves need a medium for propagation as they are mechanical waves. Stratification of the medium imposes a cutoff frequency. For gravity waves it is Brunt-Vaisala frequency above which gravity waves cannot propagate [3]. Understanding how they behave is useful for explaining and predicting weather and climate phenomena. These waves, as a part of the gravito-acoustic waves spectra, are interesting because they are ubiquitous in the terrestrial and solar atmospheres, and certainly must exist in stellar atmosphere as well. Gravity waves transfer energy through matter and they can be attenuated significantly by physical barriers [4]. The gravity drives both gravitational waves and gravity waves, but they have different properties that shouldn't be confused.

Acknowledgements This work is done in the framework of the Montenegrin National Project "Physics of Ionized Gases and Ionized Radiation".

REFERENCES

- [1] B. P. Abbot et al, Phys. Rev. Lett. 116, 061102 (2016).
- [2] D. Kennefick, *Einstein, Gravitational Waves and the Theoretician's Regress*, p. 270, (Cambridge University Press, 2014).
- [3] G. Jovanović, AIP Conf. Proc. 1722, 190004 (2016).
- [4] G. Jovanović, Solar Physics 289, 11 (2014).

THE ROLE OF GRAVITY IN THE ACOUSTIC WAVES REFLECTION

Gordana Jovanović

University of Montenegro, Džordža Vašingtona bb

Abstract. Gravitational influence on reflection properties of acoustic waves at a plane boundary separating two isothermal regions of gravitationally stratified non-magnetized plasma is analyzed. The standard set of hydrodynamics equations has been used to derive dispersion equation of gravito-acoustic waves. Using boundary conditions at the discontinuity $z = 0$, general equation for reflection coefficient of gravito-acoustic waves has been derived. In approximation of the frequencies much higher than acoustic cut-off frequency, this equation becomes equal to reflection coefficient for the pure acoustic waves and gravitational influence is negligible. When gravitational effects are small but finite, the equation for reflection coefficient can be developed in order by a small terms. This is a first order correction of the pure acoustic case. The general equations derived in this paper are applied to the plane boundary between solar photosphere and chromosphere.

1. BASIC EQUATIONS

The standard set of HD equations describes the dynamics of adiabatic processes in a fully ionized hydrogen plasma in the presence of gravity with constant acceleration:

continuity equation

$$\frac{\partial \rho}{\partial t} + \nabla \cdot (\rho \vec{v}) = 0, \quad (1)$$

momentum equation

$$\rho \left(\frac{\partial \vec{v}}{\partial t} + \vec{v} \cdot \nabla \vec{v} \right) = -\nabla p + \rho \vec{g} \quad (2)$$

and an adiabatic law for a perfect gas

$$\frac{\partial p}{\partial t} + \vec{v} \cdot \nabla p = \frac{\gamma p}{\rho} \left(\frac{\partial \rho}{\partial t} + \vec{v} \cdot \nabla \rho \right). \quad (3)$$

1.1 The Basic State

We consider an unbounded isothermal plasma with a constant sound speed. The gravitational acceleration g is constant. The equilibrium quantities are assumed to depend only on the z coordinate. Thus, in Cartesian coordinates, we have:

$$\begin{aligned}\vec{g} &= -g\vec{e}_z, & g &= \text{const}, \\ \rho_0 &= \rho_0(z), & p_0 &= p_0(z).\end{aligned}$$

This basic state is assumed to satisfy the perfect-gas law:

$$p_0 = \rho_0 R_M T_0,$$

with $R_M = k/m$, where k is Boltzman constant and m is the mean mass of plasma particles. The unperturbed plasma is initially in hydrostatic equilibrium and assumed to be step-wise isothermal, $T_0 = \text{const}$. The basic state is described by equation:

$$\frac{d}{dz} \ln \rho_0(z) + \frac{1}{H} = 0, \quad (4)$$

with a density scale length

$$H = \frac{v_s^2}{\gamma g},$$

where $H = \frac{v_s^2}{\gamma g} = \text{const}$ is the isothermal density scale length in a nonmagnetized atmosphere and $\gamma = 5/3$ is the adiabatic constant.

The solution for the density profile that follows from Equation (4) is:

$$\rho_0(z) = \rho_0(0)e^{-z/H}. \quad (5)$$

1.2 Linearized HD Equations

Method of the small adiabatic harmonic perturbations, applied on the basic state quantities, gives the dispersion equation of gravito-acoustic waves:

$$k_p^2 = \frac{\omega^2(\omega^2 - \omega_{co}^2 - v_s^2 k_z^2)}{v_s^2(\omega^2 - \omega_{BV}^2)}, \quad (6)$$

where $k_p^2 = k_x^2 + k_y^2$ designates square of the horizontal wavenumber, $\omega_{co}^2 = \gamma^2 g^2 / 4v_s^2 = v_s^2 / 4H^2$ is the square of the acoustic wave cutoff frequency and $\omega_{BV}^2 = (\gamma - 1)g^2 / v_s^2 = (\gamma - 1)v_s^2 / \gamma^2 H^2$ is the square of the Brunt-Väisälä frequency. It's dimensionless form is:

$$K_z^2 = \Omega^2 - \Omega_{co}^2 - \frac{K_p^2(\Omega^2 - \Omega_{BV}^2)}{\Omega^2}, \quad (7)$$

where $K_p = k_p H$, $K_z = k_z H$ and $\Omega = \omega H / v_s$, i.e., K_p and K_z are dimensionless horizontal and vertical wavenumbers scaled to $1/H$ and Ω is dimensionless frequency scaled to v_s/H . The equation is fourth order in Ω and it presents gravito-acoustic wave equation [1].

2. REFLECTION COEFFICIENT

An incident gravito-acoustic wave with unit amplitude in region (1)-solar photosphere is partially reflected at the boundary $z = 0$ with amplitude A_r and partially transmitted into the region (2)-solar chromosphere with amplitude A_t . Applying equality of the unperturbed pressures at $z = 0$ and continuity of the vertical fluid displacement and pressure perturbation, the equations for complex amplitudes A_r and A_t can be obtained [2]. Reflection coefficient is defined as $R = |A_r|^2$ and it is presented in Figure 1. Parameter $s = T_1/T_2 = 0.6$ is constant because photosphere and chromosphere are assumed isothermal with temperatures $T_1 = 6 \times 10^3\text{K}$ and $T_2 = 10^4\text{K}$. Horizontal phase velocities are $V_h > 1.291$ for propagating waves. If $V_h = 1/\sqrt{s} = 1.291$, the reflection coefficient for these waves on the photosphere-chromosphere boundary is $R = 1$. Acoustic waves with $V_h < 1.291$ are evanescent. The frequency $\Omega_{co} = 1/2$ is the cutoff frequency below which modified acoustic waves can not propagate (evanescent waves). In the frequency range $0.5 < \Omega < 1.5$, when gravity mostly influences acoustic waves properties, reflection is higher than for the frequencies $\Omega \gg 1$, when the waves are almost pure acoustic in their nature. We can conclude that gravity increases the reflection coefficient of the acoustic waves. For the frequencies much higher than acoustic cut-off frequency, reflection coefficient of the acoustic waves modified by gravity and a pure acoustic waves are almost the same on the solar photosphere-chromosphere boundary. For the modified (by gravity) acoustic waves on the photosphere-chromosphere boundary the reflection coefficient is always greater than zero [3]. We found that gravito-acoustic waves propagate in the solar atmosphere. This is in agreement with a known scientific literature, [4].

3. FIGURES

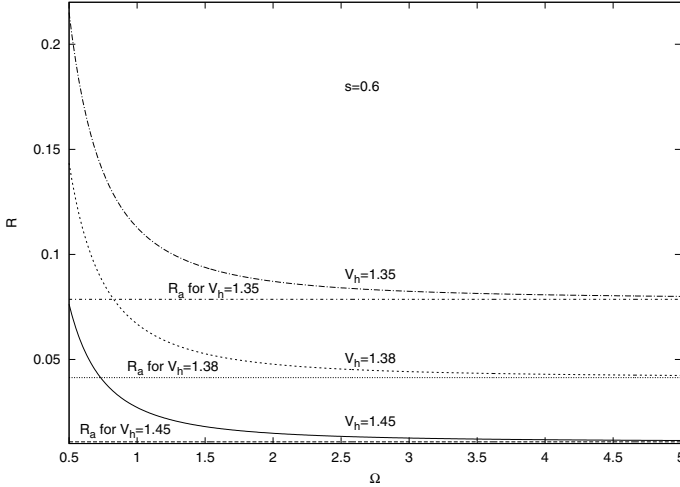


Figure 1. Reflection coefficient R for acoustic waves modified by gravity on the solar photosphere-chromosphere plane boundary (curves), when $s = 0.6$. Horizontal lines on this figure represent reflection coefficient of the pure acoustic waves that propagate from the solar photosphere to the solar chromosphere.

Acknowledgements This work is done in the framework of the Montenegrin National Project "Physics of Ionized Gases and Ionized Radiation".

REFERENCES

- [1] J. Christensen-Dalsgaard, *Lecture Notes on Stellar Oscillations*, p. 51, (Astronomisk Institut, Aarhus Universitet, 1989).
- [2] G. Jovanović, *Romanian Reports in Physics* 65, 4 (2013).
- [3] G. Jovanović, *Solar Physics* 289, 11 (2014).
- [4] C. S. Rosenthal, T. J. Bogdan, M. Carlsson, S. B. F. Dorch, V. Hansteen, S. W. McIntosh, A. McMurry, A. Nordlund and R. F. Stein, *Astrophys. J.* 564, 508 (2002).

STRATIFICATION IN THE BROAD LINE REGION OF ACTIVE GALACTIC NUCLEI: $H\beta$ VS. $H\gamma$ LINE SHAPES

Kovačević–Dojčinović Jelena and Popović Luka Č.

Astronomical Observatory, Volgina 7, 11060 Belgrade

Abstract. We analyze the shapes of the broad $H\beta$ and $H\gamma$ emission lines, in a sample of Active Galactic Nuclei (AGN) spectra. The aim is to investigate the kinematics and possible stratification of the emission regions where Balmer lines arise, using their profiles. We found that $H\gamma$ line profile is broader than $H\beta$, and has slightly larger blue asymmetry compared to $H\beta$. This can be caused by fitting procedure (underestimation of the Fe II lines which overlap with $H\gamma$, or the narrow component of the $H\beta$), or by physical processes, which lead to conclusion that $H\gamma$ is originating in the emission region closer to the black hole than $H\beta$.

1. INTRODUCTION

The Active Galactic Nucleus (AGN), which is present in the center of 5-10% of all galaxies, consists of a supermassive black hole surrounded by an accretion disk. The accretion disk is surrounded by gaseous regions, photoionized by a large amount of energy which is produced in process of accretion [1]. The photoionized gas closer to the accretion disk is called the Broad Line Region (BLR), because it produces the broad emission lines in spectra. The narrow emission lines are produced in the emission region further from the black hole, called the Narrow Line Region (NLR). It is assumed that the dominant mechanism of broadening of the emission lines in the AGN spectra is Doppler broadening, caused by turbulent, random or gravitational bounded motion of the emitting gas. Therefore, the widths of the lines reflect the kinematical properties of the emitting regions, and they are typically $\sim 4000 \text{ km s}^{-1}$ for the broad lines. For AGN type 1 (the AGNs with broad and narrow emission lines present in spectra), the most appropriate methods for black hole mass estimation are those which use the strong broad emission lines (see e.g. [2]). The basic assumption of these methods is that the BLR gas is virialized, i.e. that the main broadening

mechanism of the broad emission lines is the Keplerian motion of gas around the supermassive black hole. However, the complex shapes of broad emission lines, present in some cases, implies that the BLR is probably stratified, with complex kinematics [3]. Therefore, we need to investigate whether the virial assumption is correct for all broad emission lines in AGN spectra, and is it correct in general for all AGN population. The line which is the most frequently used as virial estimator is $H\beta$.

In this work, we compare the broad profiles of the $H\beta$ and $H\gamma$ emission lines, in a large sample of AGN spectra. The aim is to investigate the kinematics and possible stratification of the BLR, by analyzing the broad Balmer line profiles. In this way, we are trying to test the validity of using these lines as virial estimators for black hole mass estimation.

2. THE SAMPLE AND ANALYSIS

We analyze the 287 spectra of AGN type 1, chosen from Sloan Digital Sky Survey (SDSS), Data Release 7. This sample is initially used in [4], where the detailed search criteria are presented. For spectra decomposition and obtaining the broad profiles of $H\beta$ and $H\gamma$, we are using the multi-Gaussian model, where we suppose that each Gaussian represent the emission from a kinematically different emission region. The Balmer lines are fitted with two broad Gaussians [3,5], which represent the emission coming from the different parts of the BLR (Very Broad Line Region – VBLR, closer to the black hole and Intermediate Line Region – ILR, further from the black hole), and one narrow Gaussian, which represent the emission from the NLR. The numerous optical Fe II lines, as well as satellite narrow lines which overlap with the broad Balmer lines, are fitted and removed, in order to get the broad profiles of $H\beta$ and $H\gamma$. The optical Fe II lines are fitted with Fe II template [5,6]. The fitting decomposition is presented in [4] in details, and shown in Fig. 1.

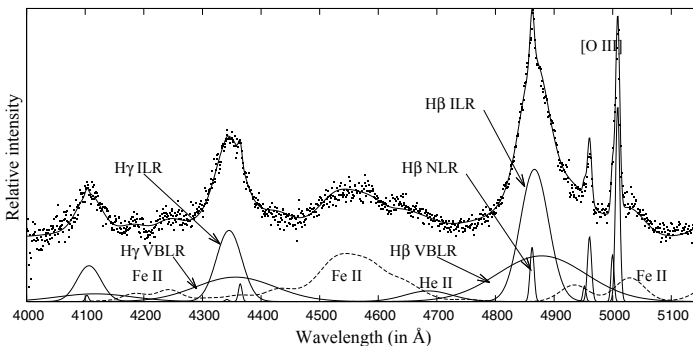


Figure 1. An example of the spectrum decomposition. The Fe II template is denoted with dashed line.

3. RESULTS AND CONCLUSIONS

We analyzed the properties of the broad $H\beta$ and $H\gamma$ lines (ILR + VBLR components) in the sample of 287 AGNs. We found that mean Full Width at Half Maximum (FWHM) and its standard deviation for the broad $H\beta$ is $4164 \pm 1370 \text{ km s}^{-1}$, while for the broad $H\gamma$ is larger: $5013 \pm 1351 \text{ km s}^{-1}$. The correlation between FWHM $H\beta$ and FWHM $H\gamma$ is $r=0.64$, $P=0$ (see Fig. 2), where r is the Spearman coefficient of correlation, and P is the probability that there is no correlation. We normalized the intensities

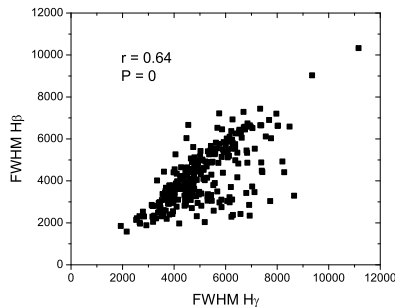


Figure 2. The correlation between the widths of the broad $H\beta$ and $H\gamma$ in AGN spectra.

of $H\beta$ and $H\gamma$ profiles to unity, and transform wavelength into velocity units. Then, we found their mean profiles for the whole sample, compared them (Fig. 3, left) and subtracted $H\beta$ from $H\gamma$ (Fig. 3, right). It is found that the flux of the difference obtained with subtraction of $H\beta$ from $H\gamma$ anticorrelates with the FWHM $H\beta$ ($r= - 0.62$, $P=0$, see Fig. 4, left), and correlates with the Equivalent Width (EW) of optical Fe II ($r=0.50$, $P=0$, see Fig. 4, right), but it there is no correlation with the FWHM of $H\gamma$ ($r=0.08$, $P=0.16$).

The results show that the $H\gamma$ broad profile is generally broader than $H\beta$ (see Fig. 3, left), and has slightly larger blue asymmetry compared to $H\beta$, which can be seen as higher blue peak in the mean difference (see Fig. 3, right). The correlation between the EW Fe II and the flux of the difference after subtraction of $H\beta$ from $H\gamma$ (Fig. 4, right) implies that the larger width of $H\gamma$ and presence of small blue asymmetry compared to $H\beta$ can be caused by the underestimation of Fe II lines which overlap with $H\gamma$ (the multiplets 27 and 28, near 4300 \AA) during the fitting procedure. Some other explanations are possible as well: an underestimation of the NLR component in the case of $H\beta$ decomposition, or influence of the physical processes which lead to the more efficient emission of the $H\gamma$ in the region closer to the black hole, where the line wings are produced (VBLR). This work is still in the progress, and the new results will be presented elsewhere.

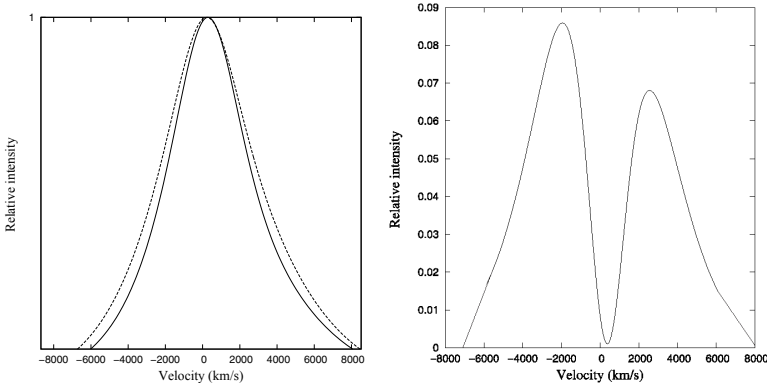


Figure 3. Left: the mean profile of $H\gamma$ (dashed line) and $H\beta$ (solid line). Right: the difference after subtraction of mean $H\beta$ from mean $H\gamma$ profile.

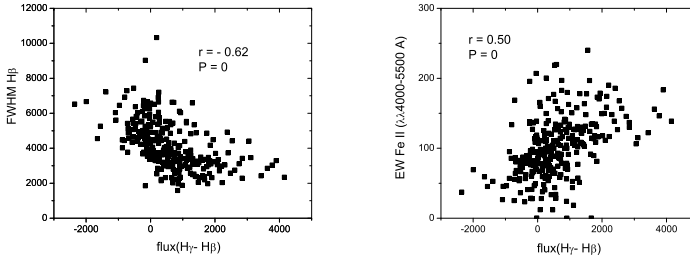


Figure 4. The correlation between the flux of the rest obtained with subtraction of $H\beta$ from $H\gamma$ and the width of $H\beta$ (left) and EW Fe II (right).

References

- [1] Peterson, B.M., *An Introduction to Active Galactic Nuclei*, (The University Press, Cambridge, 2003).
- [2] Peterson, B.M., Ferrarese, L., Gilbert, K.M., Kaspi, S., et al., *ApJ*, 613, 682 (2004).
- [3] Popović, L. Č., Mediavilla, E., Bon, E., Ilić, D., *A&A*, 423, 909 (2004)
- [4] Kovačević-Dojčinović, J., Popović L. Č., *ApJS*, 221, 35 (2015)
- [5] Kovačević J., Popović L. Č., Dimitrijević M. S., *ApJS*, 189, 15 (2010)
- [6] Shapovalova, A. I., Popović, L. Č., Burenkov, A. N., Chavushyan, V. H. et al., *ApJS*, 202, 10 (2012)

ATOM RYDBERG-ATOM PROCESSES IN THE STELLAR ATMOSPHERES

A. A. Mihajlov¹, V. A. Srećković¹, Lj. M. Ignjatović¹, Z. Simić² and M. S. Dimitrijević^{2,3}

¹*Institute of Physics Belgrade, BU, Pregrevica 118, Belgrade Serbia*

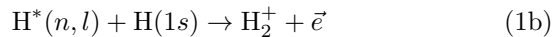
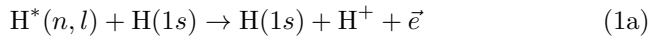
²*Astronomical Observatory, Volgina 7, 11160 Belgrade 74, Serbia*

³*IHIS-Technoexperts, Bežanijska 23, 11080 Zemun, Serbia*

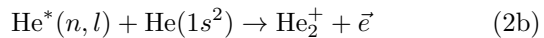
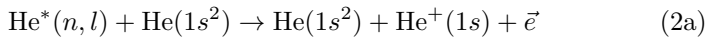
Abstract. The rate coefficients of the chemi-ionization processes taking into account the influence of the (n-n')-mixing processes, are determined. The calculations of the total chemi-ionization rate coefficients are carried out for the solar and DB white dwarf atmosphere models. It is demonstrated that the inclusion of (n-n') mixing processes influence on the values of chemi-ionization rate coefficients in all examined cases.

1. INTRODUCTION

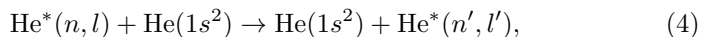
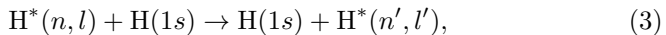
From our previous research it follows that the chemi-ionization processes in the atom Rydberg-atom collisions practically always run parallel with the corresponding (n-n')-mixing processes (see e.g. [1]). Here we will examine that consequence, which may influence on the enactment of chemi-ionization processes. Here we will treat chemi-ionization processes



in the hydrogen case, and in the helium case



where the principal quantum number $n \gg 1$. We will treat (n-n')-mixing processes in the hydrogen and in the helium case



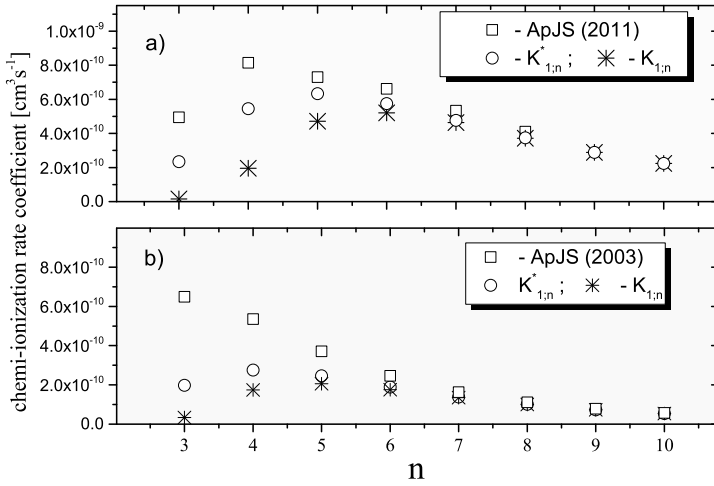


Figure 1. Comparison of the calculated values of rate coefficients of the chemi-ionization processes (1a,1b) and (2a,2b) with the data from [3,4].

where the final values of the quantum numbers n' , $l' \neq n, l$. The chemi-ionization processes (1a,1b) and (2a,2b) are investigated in the presence of open channels for the corresponding $(n-n')$ -mixing processes (3) and (4). The processes (1a,1b) and (2a,2b) are characterized by the partial rate coefficients which are function of quantum numbers n and l as well as function of temperature of the considered plasma T . As the final result we will present the rate coefficients which are obtained by the averaging of the partial rate coefficients with the given n over all l from 0 to $n-1$. These rate coefficients are calculated for $3 \leq n \leq 15$, for $4000 \text{ K} \leq T \leq 10000 \text{ K}$ in the hydrogen case, and for $7000 \text{ K} \leq T \leq 24000 \text{ K}$ in the helium case.

2. RESULTS AND DISCUSSION

The total average rate coefficients $K_{1,2}(n; T)$ of the processes (1a, 1b) together, and the processes (2a,2b) also together, are determined on the basis of expressions from [1]. All mentioned quantities are presented in Fig 1a for the hydrogen case for $T = 5000 \text{ K}$ and in Fig 1b for the helium case for $T = 10000 \text{ K}$. One can notice that there are visible differences between the values of the rate coefficients determined in [2,3] and the values obtained $K_{1,2}^*(n; T)$ with no simplifications in calculation and without mixing channel (circles in figures). The differences in relation to the rate coefficients $K_{1,2}(n; T)$ with mixing (star) and without mixing channel from [2,3] (squares) are very large for $n \leq 6$ and decrease quickly with the increase of n in the area $n > 6$. In order to show importance of processes (1)-(4) we

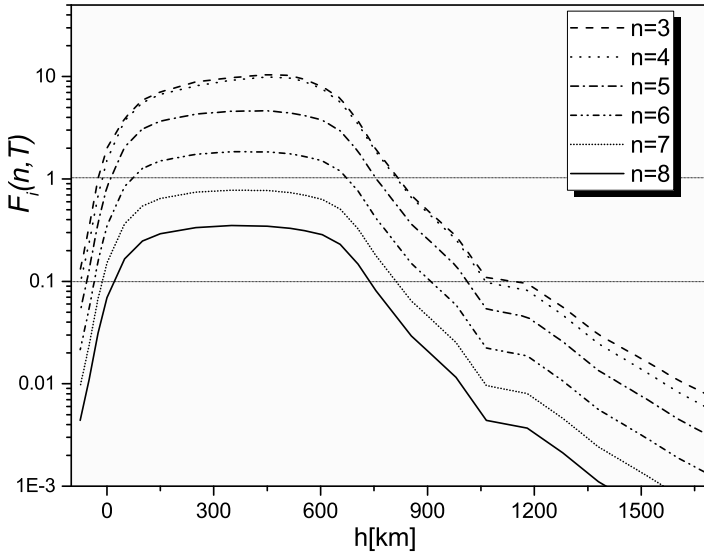
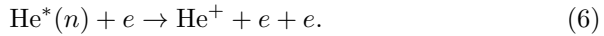


Figure 2. The parameter $F_i(n, T; H^*(n))$ as a function of the height h , for principal quantum numbers $n = 3 - 8$, for model of solar photosphere.

compared their efficiencies with the efficiencies of electron-Rydberg atom impact ionization in the hydrogen case and in the helium case



Fluxes generated in atom-Rydberg atom and electron-excited atom impact ionization are $I_{1,2}^{aa}(T; A^*)$ and $I_{1,2}^{ea}(T; A^*)$ and given by the expressions $I_{1,2}^{aa}(T; A^*) = K_{1,2}(n, T; A^*) \cdot N(A^*) \cdot N(A)$, $I_{1,2}^{ea}(T; A^*) = \alpha_{1,2}^{ea}(n, T; A^*) \cdot N(A^*) \cdot N(e)$, where $A^* = \text{H}^*(n)$ or $\text{He}^*(n)$, $K_{1,2}(n, T; A^*)$ the chemionization rate coefficient and $\alpha_{1,2}^{ea}(n, T; A^*)$ corresponding ionization rate coefficient for processes (5) and (6). The relative importance of the chemionization processes in comparison with electron-excited atom impact ionization is characterized by parameters $F_{1,2}(n, T) = I_{1,2}^{aa}(T; A^*)/I_{1,2}^{ea}(T; A^*)$. Calculations were carried out for photosphere of the Sun and some DB white dwarfs (see Fig's 2 and 3). These parameters are shown as functions of height h for the case of solar photosphere, and $\log(\tau)$ for DB white dwarfs, where τ is the Rosseland optical depth. The atmosphere data needed to determine $F_{1,2}(n, T; A^*(n))$ have been taken from DB white dwarf models (Koester 2015, private communication) and in the case of solar photosphere from [4]. Our results show that for the lower temperatures the chemionization processes are still dominant over electron-excited atom ionization processes, for $n = 3, 4$, and 6 almost in whole observed atmosphere which is

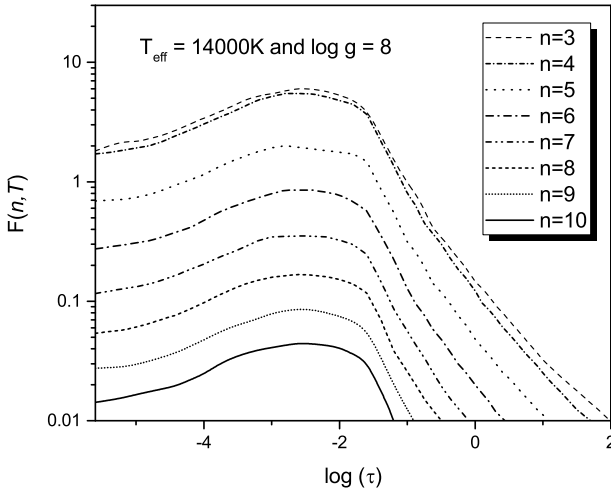


Figure 3. Same as in Fig. 2 but for the case of DB white dwarf atmosphere with $T_{eff} = 14000$ K and $\log g = 8$.

illustrated by Fig 2 and 3. For $n = 6, 7,$ and 8 chemi-ionization processes are comparable with electron-excited atom ionization processes. The obtained results show that the efficiency of the chemi-ionization processes in spite of the influence of $(n-n')$ -mixing in the most parts of the photosphere of the Sun and most parts of white dwarfs atmospheres remains dominant or at least comparable to the efficiency of the processes (5) and (6).

Acknowledgements

This work is supported by our Ministry under the grant 176002 and III4402.

REFERENCES

- [1] A. A. Mihajlov, V. A. Srećković, Lj. M. Ignjatović, A. N. Klyucharev, M. S. Dimitrijević and N. M.Sakan, 2015, JApA 36, 623 (2015)
- [2] A. A. Mihajlov, Lj. M. Ignjatović, M. S.Dimitrijević and Z. Djurić, ApJS 147, 369 (2003).
- [3] A. A. Mihajlov, L.j M.Ignjatović, V. A. Srećković and M. S. Dimitrijević, ApJS 193, 2 (2011).
- [4] J. E. Vernazza, E. H. Avrett and R. Loeser, ApJS 45, 635-725 (1981).

DETECTION OF PLASMA VARIATIONS IN PERIOD OF EARTHQUAKE OCCURRED NEAR KRALJEVO IN 2010 BY ELECTROMAGNETIC WAVES PROPAGATION

A. Nina¹, S. T. Mitrović², V. M. Čadež³, L. Č. Popović³, P. Kolarž¹,
A. Kolarski⁴ and J. Bajčetić²

¹*Institute of Physics, University of Belgrade, Pregrevica 118,
11080 Belgrade, Serbia*

²*University of Defence, Military Academy, Generala Pavla Jurišića Šturma 33,
11000 Belgrade*

³*Astronomical Observatory, Volgina 7, 11060 Belgrade, Serbia*

⁴*Institute for Geophysics, Batajnički drum 8, 11000 Belgrade, Serbia*

Abstract. In the recent time, the research of the lithospheric motions and atmospheric disturbances relations has been in focus of numerous geophysical studies. The obtained results indicate the changes in ionized gases near the Earth's surface and in the ionosphere, and point the technique for the low ionospheric monitoring by very low and low frequencies (VLF/LF) waves applicable for detection of plasma variation. Here, we present the amplitude of VLF signal emitted in Italy by ICV transmitter and received in Institute of Physics in Belgrade, Serbia during several days around November 3, 2010 when large earthquake occurred in Serbia near Kraljevo.

1. INTRODUCTION

VLF/LF electromagnetic waves propagate in the Earth-ionosphere waveguide bordered by two ionized layers: the low ionosphere at the top, and the Earth's surface and the gas near it at the bottom. The conductivities of these mediums (indicated in Figure 1, upper panel, as σ_i and σ_{es} respectively) are space and time dependent and their variations lead to changes in amplitude and phase of received waves. The sudden variations of these values can be consequence of numerous geophysical and astrophysical events.

As recent studies show, there are indications that one of these sources of perturbations can be earthquakes. One of the theoretical explanations is based on radon concentration increasing near the Earth's surface which induces intensive ionization, and consequently larger conductivity [1]. Namely, tectonic motion causes opening of new pathways for gas transportation from the deep layers of the earth crust to the atmosphere, resulting in rapid increase of radon exhalation.

Also, the hydrodynamic waves caused by lithospheric motions propagate from the lithosphere to the upper atmosphere and induce periodical changes in atmospheric constituents including electrons that have dominant role in medium influence on electromagnetic wave propagation [2].

In this paper we show the VLF signal variations during sunrise and sunset several days in vicinity of earthquake occurred on November 3, 2010 in Serbia, near Kraljevo.

2. EXPERIMENTAL SETUP AND OBSERVED DATA

In this study, we analysed 20.27 kHz VLF signal emitted by transmitter ICV in Isola di Tavolara, Italy and received by the receiver located in Institute of Physics in Belgrade, Serbia. As it can be seen in Figure 1, upper panel, the propagation path of this signal is relatively near to the epicenter of earthquake and ionospheric disturbances can be expected in that part of Balkan Peninsula.

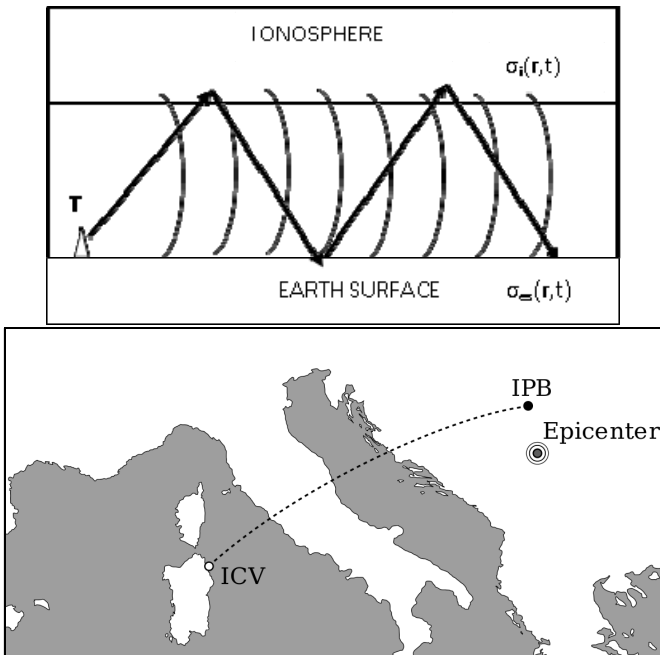


Figure 1. Upper panel: propagation of radio signals between two ionized layers in Earth-ionosphere waveguide. Bottom panel: map of VLF signal emitted in Italy by ICV transmitter and received in Institute of Physics in Belgrade, Serbia (IPB), and epicenter of earthquake occurred on November 3, 2010 near Kraljevo, Serbia.

3. RESULTS AND CONCLUSIONS

Here we consider the signal amplitude during the day of earthquake and the day before and after it. The detection of signal variations in the moment around 00:57 UT when earthquake occurred is analysed according comparison with relevant periods in other two days.

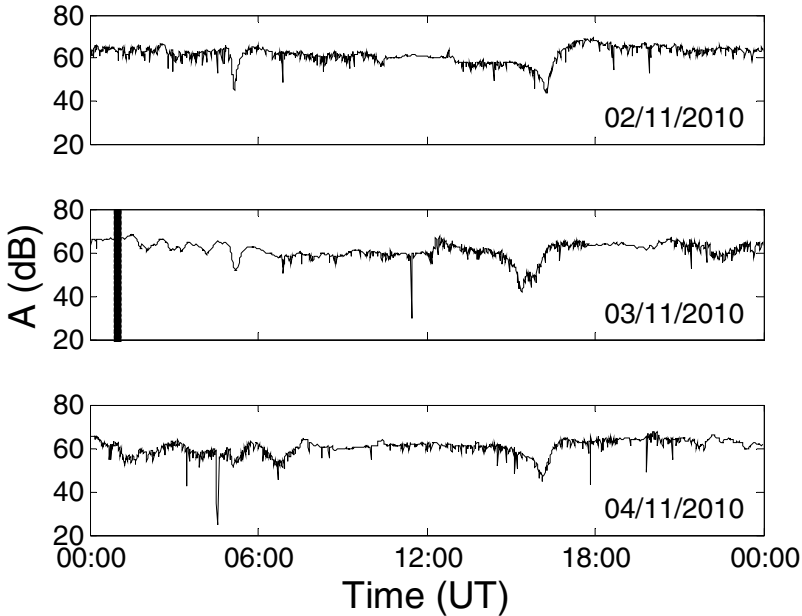


Figure 1. Amplitudes of VLF signal emitted in Italy by ICV transmitter and received in Institute of Physics in Belgrade, Serbia during the day before (upper panel), the day of earthquake (middle panel) and the next day (upper panel). The vertical line indicates time of earthquake at 00:57 UT.

As we can see in the middle panel of Figure 2, there are oscillations in the amplitude of the received VLF signal after earthquake noticed by vertical line. This shape is not recorded during two referent days which allows us to conclude that it is possible that considered signal was affected by processes in ionized boundary layers. The second difference is visible in period of sunrise. The inverse peak after 15 h UT in the day of earthquake begins earlier with respect to other two days. Also, two minimums are recorded although referent days indicate existing of just one. Correlation of the earthquake occurrence with such a signal perturbations is also analyzed in [3].

To conclude presented analysis, we can say that VLF signal emitted in Italy and received in Serbia has unexpected amplitude changes, which cause could be earthquake occurred near Kraljevo. Because of numerous other influences on medium within the signal propagate, these disturbances cannot be

certainly connected with the earthquake. The presented observations are appropriate for integration into statistics with similar events, which can significantly contribute in model development for detection of processes induced by earthquakes using radio signal for the low ionosphere monitoring.

Acknowledgements

This work is supported by the Ministry of Education, Science and Technological Development of the Republic of Serbia under the grants III 44002, 176001, 176002, 171020 and III 45003 and COST Action Time Dependent Seismology (TIDES) ES1401.

REFERENCES

- [1] Ghosh D, Deb A, Sengupta R Anomalous radon emission as precursor of earthquake. *J App Geophys* 69, 67 (2009).
- [2] Molchanov O. A., Hayakawa M., Miyaki K., *Adv. Polar Upper Atmos. Res.* 15, 146 (2001).
- [3] Molchanov, O., Hayakawa, M., Oudoh, T., Kawai, E., *Phys. Earth. Planet. In.*, 239 (1998).

SHORT-TERM DISTURBANCES OF THE LOW IONOSPHERE INDUCED BY γ -RAY BURSTS

A. Nina¹, S. Simić², V. A. Srećković¹, A. Djulaković³ and L. Č. Popović⁴

¹*Institute of Physics, University of Belgrade, Belgrade, Serbia*

²*Department of Physics, Faculty of Science,
University of Kragujevac, Kragujevac, Serbia*

³*Institute of Physics, University of Belgrade, Belgrade, Serbia*

⁴*Astronomical Observatory, Belgrade, Serbia*

Abstract. Although the γ radiation has enough energy for ionization of atmospheric particles, there are only several studies that show detection of changes in atmospheric plasma parameters induced by γ -ray bursts (GRBs). Here, we show results of our analysis related to the low ionospheric perturbations lasting less than 1 s close to the GRBs detection by the Swift satellite. We observed the low ionosphere by very low frequency (VLF) electromagnetic wave emitted in the USA by NAA transmitter and received in Institute of Physics in Belgrade, Serbia during 2 min before and 2 min after 54 GRB events detection. Our statistical study shows significantly increase of number of signal amplitude peaks 2, 3 and 4 times larger than the amplitude noise after the GRB detections and confirms the short-term ionospheric responses to this astrophysical phenomenon.

1. INTRODUCTION

The GRB events impact Earth's atmosphere about one time per day. The energy of these photons is large and they can ionize the atmospheric constituents. However the cross section for this process is very small. Because of that the detection of long-term ionospheric disturbances that can be connected with considered astrophysical phenomenon with certainty is very rare [1,2].

On the other side, atmosphere is under permanent influence of numerous different sources of perturbations and it is very hard to distinguish that one particular short-term ionospheric disturbance is consequence of some particular event, especially when its influence on plasma is lasting more than period of medium perturbation. Because of that it is necessary to do statistical study to examine short-term atmospheric plasma perturbation. The results given in [3] confirm detectability of these processes using analysis of amplitude peaks that are 2 and 3 times larger than amplitude noise for 6 signals which propagate during daytime and nighttime conditions as well as during periods when signal path was affected by solar terminator.

In this study we analyse influence of amplitude peaks that are 2, 3, 4 and 5 times larger than amplitude noise on detection of short-term reactions of the low ionosphere on GRB events.

2. OBSERVATIONS

Here, we analyse 24.0 kHz VLF signal emitted by transmitter NAA in Cutler, Maine, USA, and received by the AWESOME receiver located in Institute of Physics in Belgrade, Serbia. The sample of GRB events are formed for periods between 2009 and 2012 in the cases when signal is not strong perturbed by other perturbers during periods 2 min before and 2 min after considered detections by the Swift satellite.

We process signal amplitude described by set of data with time resolution of 0.02 s using procedure described in [3].

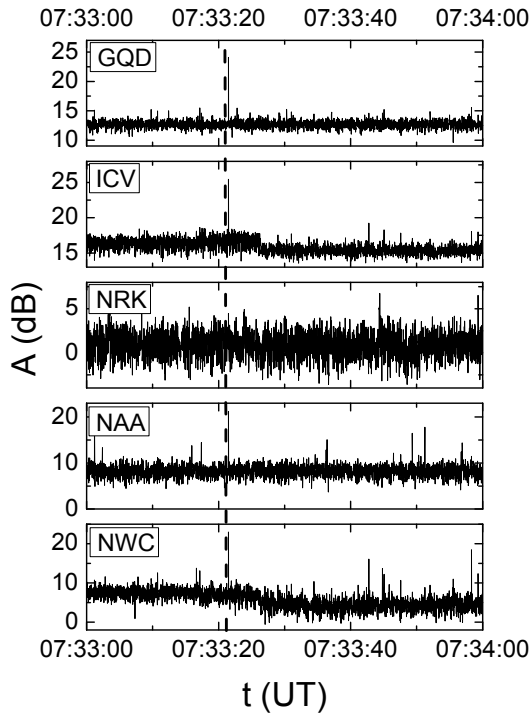


Figure 1. Short-time amplitude amplification in VLF/LF signals emitted from different locations, registered by the Belgrade VLF/LF receiver less than 1 sec after the GRB110412A event occurred on April 12, 2011.

3. RESULTS AND CONCLUSIONS

In Fig. 2 we show histograms of the number of recorded amplitude peaks N_A within the interval of 120 s before and after the GRB detections for binned time interval of 30 s. The panels from top to bottom related to the amplitude peaks which are $r = 5, 4, 3,$ and 2 times larger than the amplitude noise and their sum r_{sum} , respectively.

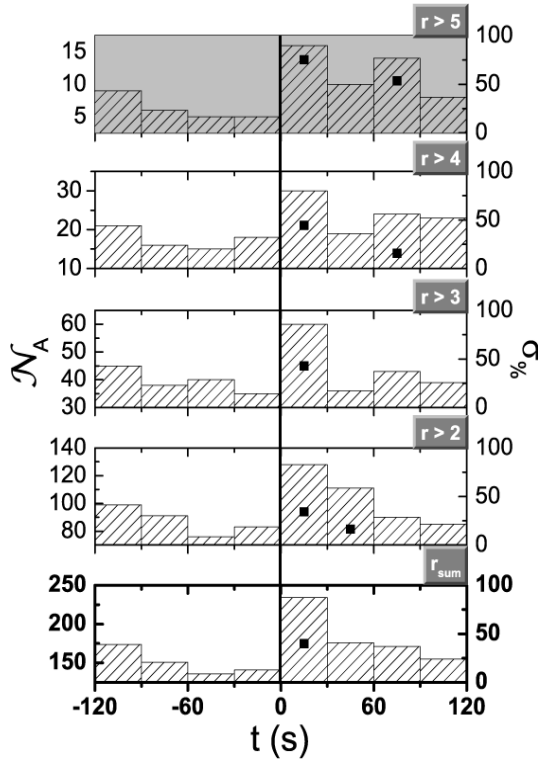


Figure 1. Histograms of number of peaks N_A for signals emitted by NAA transmitter accounted in time bins of 30 s for $r = 2, 3, 4,$ and 5 (upper 4 panels) and their sum (bottom panel). The vertical line denotes the time of the satellite recorded GRB and the black points indicate the statistically significant increase of peak numbers within the bins indicated by values of σ given by equation (2) (right axes).

As we can see the number of relevant peaks significantly increases (more than $\sigma = 30\%$ larger than the mean values in the particular histogram) after satellite detection of GRB events, noticed as vertical line at 0 s, for all criteria of amplitude intensity. Also significant increase is obtained in time periods 30 s – 60 s and 60 s – 90 s after the GRB event detection but only for $r = 2$ and $r = 4,$ respectively.

In addition we point out that the number N_A is too small for $r = 5$ and, consequently, we have no statistically reliable analysis.

To conclude the presented analysis, we can say that the statistical analysis of considered sample can be made for amplitude peaks 2, 3 and 4 times larger than the amplitude noise and that in all cases the increase in its number confirms the low ionospheric short-term response to the GRB events.

Acknowledgements

This work is partially supported by our Ministry under the grants III 44002, 176001 and 176002.

REFERENCES

- [1] Fishman G. J. and Inan U. S., *Nature*, 331, 418 (1988).
- [2] Inan, U. S., Lehtinen N. G., Moore R. C., Hurley K., Boggs S., Smith D. M. and Fishman G. J., *Geophys. Res. Lett.*, 34, L08103 (2007).
- [3] Nina, A., S. Simić, V. A. Srećković and L. Č. Popović, *Geophys. Res. Lett.* 42, 8250 (2015).

BOND - BOUND STATE TRANSITIONS IN THE FRAME OF COULOMB CUT-OFF MODEL POTENTIAL

N. M. Sakan¹, V. A. Srećković¹, Lj. M. Ignjatović¹ and A. A. Mihajlov¹

¹*Institute of Physics, University of Belgrade, Pregrevica 118, Zemun,
11000 Belgrade, Serbia*

Abstract. The cut-off Coulomb potential has proven itself as a model potential for the dense hydrogen plasma. It was tested and proven in calculation of the photo-ionization processes as well as inverse Bremsstrahlung processes of hydrogen atom in the photon wavelength region $300 \text{ nm} < \lambda < 1000 \text{ nm}$, with and without the influence of plasma. The further steps of improvement of the usage of model potential is carried out. Here are presented first test results of bond state transition modeling in the frame of cut-off Coulomb model potential. The presented results converge towards the theoretical values for plasma of small plasma coupling Γ , e.g. the plasma of small non-ideality. The investigated results are good indicator that the inclusion of the bond-bond radiation transitions could be well funded. It is expected that such approach would lead towards to the inclusion of bond state transition photo-absorption process within the frame of the presented Coulomb cut-off potential model.

1. INTRODUCTION

The cut-off Coulomb potential has been proven in modeling of continuous photo absorption of the dense plasma of moderate non-ideality, e.g. plasma coupling parameter Γ (see [1]), is comparable to or slightly greater than unity. Although the implementation of the cut-off Coulomb model potential is not entirely developed and performed, it's preliminary results were present in several papers [2, 3, 4, 5, 6, 7]. The usage of the mentioned model potential is in process of continuous development. As first step in extending of the model with additional processes is the bond state transition processes inclusion. The bond state transition processes is stated as most important goal in the development of the self containing model, capable of describing of optical as well as dynamical characteristics of dense hydrogen

plasma. The characteristics of the bond state transitions in plasma diagnostics is well known, almost mandatory method, [8]. The usage of the hydrogen lines as a probing method for the plasma characteristics are also well known and widely used in plasma of moderate and small non-ideality, [9].

As it was shown in [4], the extensive work was carried out in order to prove the model potential usage and to adopt the bond state level broadening models. Analysis of the results led to the conclusion to focus the research onto one of the potential models, e.g. the potential

$$U_0(r; r_{cut}) = \begin{cases} -\frac{e^2}{r} & 0 < r \leq r_{cut}, \\ 0 & r_{cut} < r, \end{cases} \quad (1)$$

Here r_{cut} is a model parameter, cut-off radius, determining the boundary between the zone where there is influence of individual ion-electron interaction, and the other zone where only collective phenomena of average plasma influence exists.

In accordance with the previously mentioned the continuation of research of the presented approach is the inclusion of the the bound-bound photo absorption process using the same model potential.

The investigated process, the bound-bound photo absorption, in accordance with previously used notation, is denoted as

$$\varepsilon_\lambda + H^*(n_i, l_i) \rightarrow H^*(n_f, l_f), \quad (2)$$

and was not considered within the frame of the used model potential. Here n and l are the principal and the orbital quantum number of hydrogen-atom excited states, hydrogen atom in it's initial state $|n_i, l_i\rangle$ is presented by $H^*(n_i, l_i)$, it's final state $|n_f, l_f\rangle$ by $H^*(n_f, l_f)$, and ε_λ presents absorbed photon energy.

The dipole transitions are favorable ones in radiative transition for the plasma in area where the usage of this model is preferred, e.g. where there is a single electron in average, in specific plasma sphere, r_{cut} . In accordance with that, the behavior of the dipole matrix element is investigated here. It is given by

$$\hat{D}(r; r_{cut}; n_i, l_i; n_f, l_f) = \langle n_f, l_f | \mathbf{r} | n_i, l_i \rangle, \quad (3)$$

where the wave functions $|n_i, l_i\rangle$ and $|n_f, l_f\rangle$ are initial and final hydrogen wave functions.

2.RESULTS AND DISCUSSION

The investigation of the bond transitions in the frame of cut-off Coulomb potential has shown good behavior. As it could be shown on figure 1a and 1b, the oscillator strength values converge towards the theoretical ones for the hydrogen without plasma influence.

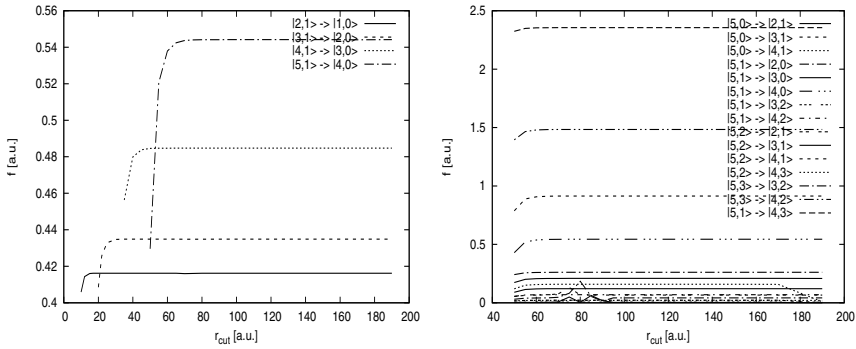


Figure 1. a) Convergence of the oscillator strength values.

b)

3.CONCLUSION

From the results of the investigation of the behavior of bond level transitions in the frame of cut-off Coulomb potential model it is obvious that it is possible to include the bond transition processes. There is a need to investigate further, more in depth, the shown behavior in order to prove that there is no numerical artifacts within the shown results. Also there is a need to include the broadening of the bond states, as first to reproduce the results with models already shown in [4], and after to further investigate various models for broadening mechanisms.

The preliminary results has shown that there is a possibility of inclusion of the bond transitions in the frame of cut-off Coulomb potential method for the describing of optical properties of the dense hydrogen plasma. There is a need for further development of the model and extending it's usage on more complex atoms also.

Acknowledgements

The authors are thankful to the Ministry of Education, Science and Technological Development of the Republic of Serbia for the support of this work within the projects 176002, 171014 and III44002.

REFERENCES

- [1] V. E. Fortov, I. T. Iakubov, Physics of Nonideal Plasma, Hemisphere, New York, 1989.
- [2] Yu. N. Gnedin, A. A. Mihajlov, Lj. M. Ignjatovi, N. M. Sakan, V. A. Srekovi, M. Yu. Zakharov, N. N. Bezuglov, A. N. Kly-

- charev, *New Astronomy Reviews* 53, 710, (2009), pp 259-265, DOI: 10.1016/j.newar.2009.07.003,
- [3] Ignjatović, L. M., Mihajlov, A. A., Sakan, N. M., Dimitrijević, M. S., Metropoulos, A., *MNRAS*, 396, (2009) pp2201-2210, DOI: 10.1111/j.1365-2966.2009.14870.x
- [4] Nenad M Sakan, The Calculation of the Photo Absorption Processes in Dense Hydrogen Plasma with the Help of Cut-Off Coulomb Potential Model, *J.Phys.: Conference Series* 257, 1, (2010),012036, DOI: 10.1088/1742-6596/257/1/012036
- [5] A A Mihajlovn N M Sakann V A Sreković, Y Vitel, *J.Phys.A* 44, 9, (2011), 095502, DOI: 10.1088/1751-8113/44/9/095502
- [6] Mihajlov, A. A., Srećković, V. A., Sakan, N. M., *J.Astrophys.Astr.* 36 (2015), pp 635–642, DOI: 10.1007/s12036-015-9350-0
- [7] Mihajlov, A. A., Srećković, V. A., Ignjatović, Lj. M., Klyucharev, A. N., Dimitrijević, M. S., Sakan, N. M., *J.Astrophys.Astr.* 36, 4, (2015) pp 623–634, DOI: 10.1007/s12036-015-9364-7
- [8] Hans R. Griem, *Principles of Plasma Spectroscopy*, Cambridge University Press, 1997, ISBN: 9780511524578, DOI: 10.1017/CBO9780511524578
- [9] N. Konjević, M. Ivković, N. Sakan, *Spectrochimica Acta Part B: Atomic Spectroscopy*, 76, (2012), pp 16-26, DOI: 10.1016/j.sab.2012.06.026
- [10] I. I. Sobel'man, *Atomic Spectra and Radiative Transitions*, Springer Verlag, Berlin, 1979.

MEASURING BLACK HOLE MASSES IN ACTIVE GALACTIC NUCLEI USING POLARIZATION IN BROAD LINE PROFILES

D. Savić¹, R. Goosmann², F. Marin², V. L. Afanasiev³, L. Č. Popović^{1,4},
D. Ilić⁴

¹*Astronomical Observatory Belgrade, Volgina 7, 11060 Belgrade, Serbia*

²*Observatoire Astronomique de Strasbourg, Université de Strasbourg,
CNRS, UMR 7550, 11 rue de l'Université, 67000 Strasbourg, France*

³*Astrophysical Observatory of the Russian Academy of Sciences, Nizhnij
Arkhyz, Karachaevo-Cherkesia 369167, Russia*

⁴*Department of Astronomy, Faculty of Mathematics, University of
Belgrade, Studentski Trg 16, 11000 Belgrade, Serbia*

Abstract. Spectropolarimetry of broad lines is a powerful tool to probe the structure of the Broad Line Region (BLR) located close to the supermassive black hole in Active Galactic Nuclei (AGN). It provides information on the gas kinematics which can be used to estimate the black hole mass. Here we present our recent investigation of the expected polarization of broad emission lines for different geometries of the BLR and scattering regions.

1. INTRODUCTION

Active galactic nuclei (AGNs) are known as one of the most luminous objects in the Universe, and its enormous emitted energy is thought to be powered by mass accretion onto a supermassive black hole (SMBH). The last few years have seen rapid advancement in our understanding of the role that supermassive black holes (SMBHs) play in the evolution of galaxies [1]. Part of this progress has come from increased confidence in the techniques for measuring SMBH masses, both directly and indirectly [2], and part has arisen from the discovery of new correlations between SMBH masses and the properties of the host galaxies [3, 4].

We investigate the possibilities and limits of the method to measure the black hole mass from the shape of the polarization angle (PA) across the broad line profiles in AGNs, as presented by Afanasiev et al. [5, 6]. Here

we present preliminary modeling results of the equatorial scattering model in the case of the Keplerian disc and compare them to observational data given in [5, 6].

2. METHOD

The broad lines are emitted from the broad line region (BLR) that is close to the SMBH, and therefore we can expect near Keplerian motion of the emitting gas in the BLR [7]. We assume that the light is being scattered in the inner part of the dusty torus (equatorial scattering, [8]), thus producing polarized light.

2.1 Model

We investigate the polarized broad line emission in (AGN) using the 3D Monte Carlo radiative transfer code STOKES [9, 10]. We consider a model where the central engine consists of a point-like continuum source. The BLR and the scattering region are modeled using a flared-disk geometry with Keplerian rotation (Figure 1). Inner and outer radius of the BLR and the scattering region are set to 0.0036 pc and 0.5 pc; and 0.5 pc and 3 pc, respectively. The total optical depth of the BLR and the scattering region are 0.02 and 3, respectively. The model setup is based on the systematic analysis conducted by Lira et al. (in preparation).

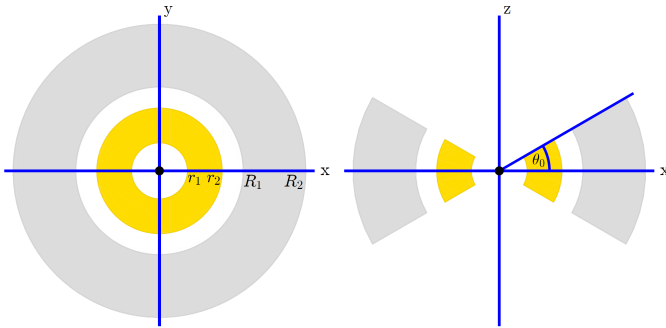


Figure 1. Cartoon showing the model geometry of the BLR (yellow) and the scattering disk (grey) in face-on (left) and edge-on (right) view.

3. PRELIMINARY RESULTS

We obtained similar degree of polarization in comparison with observations (Figure 2). The modeled unpolarized line width is much lower than the observed one due to the fact that we are observing from the near

face on direction. We produced similar profiles of the polarization angle (PA) as reported in [5, 6], and found that Keplerian motion can be traced across the PA profile (Figure 3, right panel). PA profile is flipped due to the opposite direction of rotation. The amplitude of the modeled PA is significantly lower in comparison with the observed one and thus our SMBH mass estimates are lower for an order of magnitude. This might be due to the fact that most of the scattering occurs mostly in the inner part of the scattering region, and this needs to be investigated further. This work is still in progress.

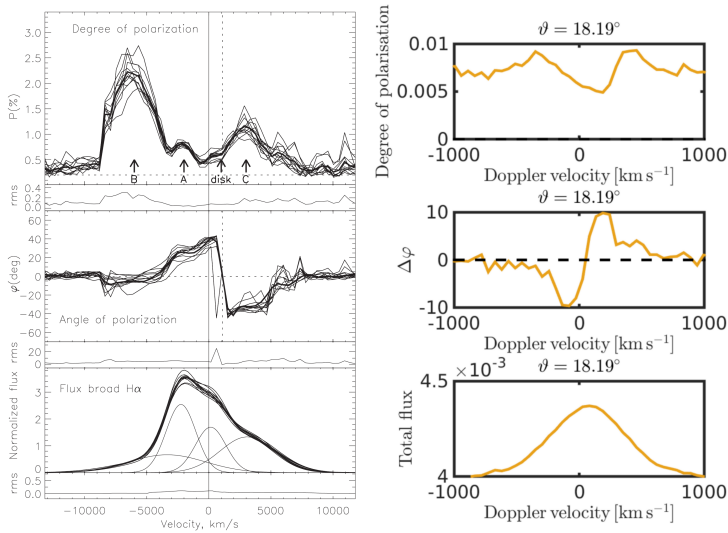


Figure 2. Observed (left panels) and modeled (right panels) polarization in the Ha line for Mrk 6. From top to bottom: the degree of polarization, the PA profile, and the broad Ha line profile. The last one in case of observed data is decomposed into four broad components (from [5, 6]).

4. ACKNOWLEDGEMENTS

This work was supported by the Ministry of Education and Science (Republic of Serbia) through the project Astrophysical Spectroscopy of Extragalactic Objects (176001), the French PNHE and the grant ANR-11-JS56-013-01 POLIOPTIX and the Russian Foundation for Basic Research (grant N12-02-00857). D. Savić thanks the French Government and the French Embassy in Serbia for supporting his research. Part of this work was supported by the COST Action MP1104 Polarization as a tool to study the Solar System and beyond.

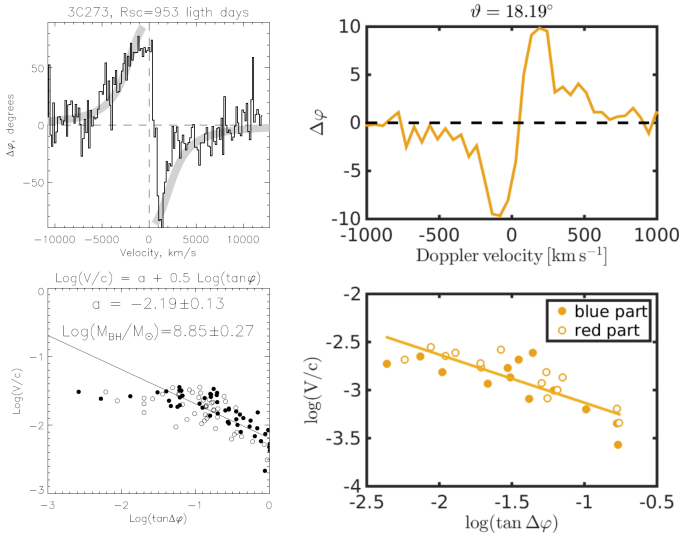


Figure 3. Left panels: the observed profile of PA (top) and velocities across the line profile vs. PA (bottom) for 3C273 (from [5, 6]). Right panels: the modeled profile of PA for a given inclination (top) and the fit of Keplerian rotation to the velocities across the line profile vs. PA (bottom), where full circles represent the blue part of the line, while open circles are for the red part.

REFERENCES

- [1] T. M. Heckman and P. N. Best, *ARA&A*, 52, 589 (2014).
- [2] B. M. Peterson, *SSRv*, 183, 253 (2014).
- [3] T. M. Heckman and G. Kauffmann, *Science*, 333, 182 (2011).
- [4] J. Kormendy and L. C. Ho, *ARA&A*, 51, 511 (2013)
- [5] V. L. Afanasiev, L. Č. Popović, A. I. Shapovalova, N. V. Borisov and D. Ilić, *MNRAS*, 440, 519 (2014).
- [6] V. L. Afanasiev and L. Č. Popović, *ApJL*, 800, L35 (2015).
- [7] C. M. Gaskell, *NewAR*, 53, 140 (2009).
- [8] J. E. Smith, A. Robinson, S. Young, D. J. Axon and E. A. Corbett, *MNRAS*, 359, 846 (2005).
- [9] F. Marin, R. W. Goosmann, C. M. Gaskell, D. Porquet and M. Dovčiak, *A&A*, 548, A121 (2012).
- [10] R. W. Goosmann, C. M. Gaskell and F. Marin, *AdSrP*, 54, 1341 (2014).

STARK BROADENING OF BISMUTH IV SPECTRAL LINES IN A TYPE STELLAR ATMOSPHERES

Zoran Simić¹, Milan S. Dimitrijević^{1,2} and Vladimir Srećković³

¹*Astronomical Observatory, Volgina 7, 11060 Belgrade, Serbia*

²*Observatoire de Paris, 92195 Meudon Cedex, France*

³*Institute of physics, University of Belgrade, P.O. Box 57, 11001, Belgrade, Serbia*

Abstract. Here we present Stark widths for four Bi IV spectral lines obtained by using modified semiempirical approach. Our results have been used for the consideration of the influence of the Stark broadening effect in A type stellar atmospheres.

1. INTRODUCTION

Spectral lines of ionized bismuth are interesting for astrophysics due to their presence in stellar atmospheres, so that data on their profiles are needed for example to determine bismuth abundance as well as for the diagnostics of stellar plasma and for analysis and synthesis of stellar spectra.

Strong absorption lines due to Bi II have been found in the HgMn star HR7775 in high-resolution spectra obtained with the IUE [1]. HR7775 was first recognized as a chemically peculiar (CP) star. The presence of Bi III spectral lines were reported in the ultraviolet spectrum of the χ Lupi [2]. Also, there are many examples with ionized bismuth spectral lines in spectra of CP stars.

Here, we investigated theoretically the influence of the Stark broadening effect on heavy metal spectral line profiles for Bi IV in spectra of A stars.

2. THE MODIFIED SEMIEMPIRICAL METHOD

According to the modified semiempirical (MSE) approach [3] the electron impact full width at half maximum (FWHM) of an isolated ion line is given by

$$\begin{aligned}
W = & N \frac{4\pi}{3c} \frac{\hbar^2}{m^2} \left(\frac{2m}{\pi kT}\right)^{1/2} \frac{\lambda^2}{\sqrt{3}} \cdot \left\{ \sum_{\ell_i \pm 1} \sum_{L_i, J_i} R_{\ell_i, \ell_i \pm 1}^2 \tilde{g}(x_{\ell_i, \ell_i \pm 1}) \right. \\
& + \sum_{\ell_f \pm 1} \sum_{L_f, J_f} R_{\ell_f, \ell_f \pm 1}^2 \tilde{g}(x_{\ell_f, \ell_f \pm 1}) + \left(\sum_{i'} R_{ii'}^2 \right)_{\Delta n \neq 0} g(x_{n_i, n_i+1}) \\
& \left. + \left(\sum_{f'} R_{ff'}^2 \right)_{\Delta n \neq 0} g(x_{n_f, n_f+1}) \right\}, \quad (1)
\end{aligned}$$

where n and ℓ are principal and angular momentum quantum numbers, and $R_{\ell_k, \ell_{k'}}$, $k = i, f$ is given by

$$\left(\sum_{k'} R_{kk'}^2 \right)_{\Delta n \neq 0} = \left(\frac{3n_k^*}{2Z} \right)^2 \frac{1}{9} (n_k^{*2} + 3\ell_k^2 + 3\ell_k + 11) \quad (2)$$

in the Coulomb approximation.

In Eq. (3)

$$x_{\ell_k, \ell_{k'}} = E / \Delta E_{\ell_k, \ell_{k'}}, \quad (3)$$

$k=i, f$ where $E = \frac{3}{2}kT$ is the electron kinetic energy and

$$\Delta E_{\ell_k, \ell_{k'}} = |E_{\ell_k} - E_{\ell_{k'}}| \quad (4)$$

is the energy difference between levels ℓ_k and $\ell_k \pm 1$ ($k = i, f$). Also

$$x_{n_k, n_{k+1}} \approx E / \Delta E_{n_k, n_{k+1}}, \quad (5)$$

where for $\Delta n \neq 0$ the energy difference between energy levels with n_k and n_k+1 , $\Delta E_{n_k, n_{k+1}}$, is estimated as

$$\Delta E_{n_k, n_{k+1}} \approx 2Z^2 E_H / n_k^{*3}. \quad (6)$$

In Eq. (4) the effective principal quantum number is defined by

$$n_k^* = [E_H Z^2 / (E_{ion} - E_k)]^{1/2}, \quad (7)$$

Z is the residual ionic charge i.e. the charge of the rest of atom as "seen" by optical electron (for example $Z=1$ for neutral atoms, 2 for singly charged ions etc), and E_{ion} is the appropriate spectral series limit.

In Eq. (3) T is the electron temperature, while $g(x)$ [4] and $\tilde{g}(x)$ [3] denote the corresponding effective Gaunt factors.

3. RESULTS

In order to see the influence of Stark broadening mechanism for Bi IV spectral line in stellar plasma conditions, we have calculated Stark widths for A type star ($T_{\text{eff}} = 10000$ K, $\log g = 4.5$) atmosphere model [5] and compared them with Doppler ones. Obtained results in function of the Rosseland optical depth are presented in Fig. 1. One can see, that exist photospheric layers where Doppler and Stark widths are comparable and even where the Stark width is dominant and must be taken into account.

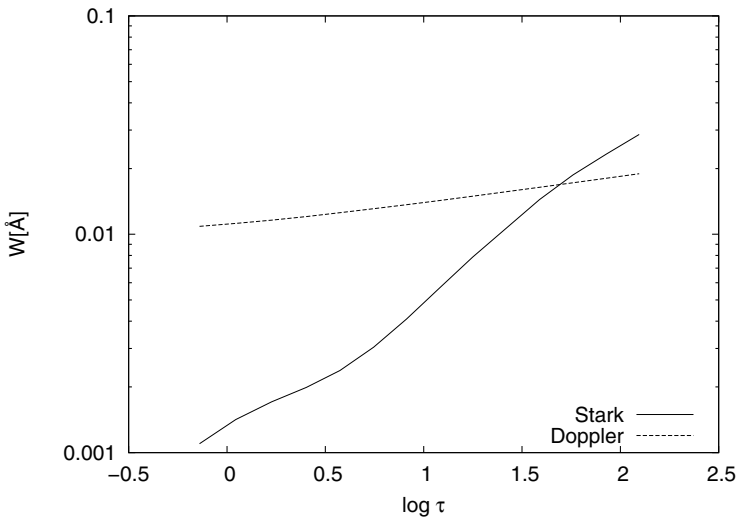


Figure 1. Thermal Doppler and Stark widths for Bi IV $7s\ ^1S - 7p\ ^1P^o$ 3296.8 Å line as functions of optical depth for an A type star ($T_{\text{eff}} = 10000$ K, $\log g = 4.5$).

Our results for Bi IV spectral lines are shown in Table 1.

Acknowledgements

This work is a part of the project 176002 "Influence of collisional processes on astrophysical plasma line shapes" supported by the Ministry of Education, Science and Technological Development of Serbia.

Table 1. Stark widths (FWHM) for Bi IV obtained by using modified semiempirical approach for perturber density of 10^{17}cm^{-3} and temperatures from 10000 up to 300000 K.

| Transition | T_e (K) | $W(\text{\AA})$ | Transition | T_e (K) | $W(\text{\AA})$ |
|--|-----------|-----------------|---|-----------|-----------------|
| $6s^2 \ ^1S - 6p \ ^1P^o$ 872.6(\AA) | 10000 | 0.289E-02 | $7s \ ^1S - 7p \ ^1P^o$ 3296.8(\AA) | 10000 | 0.184 |
| | 20000 | 0.204E-02 | | 20000 | 0.130 |
| | 50000 | 0.129E-02 | | 50000 | 0.823E-01 |
| | 100000 | 0.915E-03 | | 100000 | 0.627E-01 |
| | 200000 | 0.658E-03 | | 200000 | 0.538E-01 |
| | 300000 | 0.564E-03 | | 300000 | 0.533E-01 |
| $6s^2 \ ^1S - 7p \ ^1P^o$ 431.2(\AA) | 10000 | 0.198E-02 | $6p \ ^1P^o - 7s \ ^1S$ 1149.7(\AA) | 10000 | 0.132E-01 |
| | 20000 | 0.140E-02 | | 20000 | 0.939E-02 |
| | 50000 | 0.889E-03 | | 50000 | 0.593E-02 |
| | 100000 | 0.660E-03 | | 100000 | 0.452E-02 |
| | 200000 | 0.538E-03 | | 200000 | 0.380E-02 |
| | 300000 | 0.494E-03 | | 300000 | 0.352E-02 |

REFERENCES

- [1] J. M. Jacobs and M. M. Dworetsky, Nature, 299, 535 (1982).
- [2] D. S. Lecrone, C. R. Proffitt, G. M. Wahlgren, S. G. Johansson and T. Brage, AJ, 117, 1454 (1999)
- [3] M. S. Dimitrijević and N. Konjević, J. Quant. Spectrosc. Radiat. Transfer, 24, 451 (1980)
- [4] H. R. Griem, Phys. Rev., 165, 258 (1968)
- [5] R. L. Kurucz, Astrophys. J. Suppl. Series., 40, 1 (1979)

**The Workshop on X-ray
Interaction with Biomolecules in
Gas Phase (XiBiGP)**

STRUCTURE AND DYNAMICS OF GAS-PHASE BIOMOLECULES

Sadia Bari

DESY, Notkestraße 85, 22607 Hamburg, Germany

Little is known about biological radiation action on the molecular level. The response of biomolecules upon photons is of great interest i.e. for astrobiology and radiobiology. Key questions concern ion chemistry in the interstellar medium, possible transport of biomolecules from space to earth and molecular mechanisms underlying biological radiation damage. Electrospray ionization (ESI) is a gentle, state-of-the-art technique to introduce biomolecular ions from solution into the gas phase and into vacuum, providing a solvent- and substrate-free environment. This allows studying the molecule in a well-defined, isolated state, where only intramolecular interactions have to be considered. The combination of an ESI source with advanced light sources such as synchrotrons and free-electron lasers allows for a novel and unique way to investigate structure and dynamics of gas-phase biomolecules. In particular, synchrotron and free-electron laser sources have the great advantage of superior photon brilliance and a wide photon energy range. This enables systematic studies of energy dependent effects of ionization and dissociation processes [1,2]. Energy and photon intensity dependencies will be discussed for different peptides, proteins and oligonucleotides.

Acknowledgements: Parts of this research were carried out at the light sources FLASH and PETRA III at DESY, a member of the Helmholtz Association (HGF). We thank Helmholtz-Zentrum Berlin for the allocation of synchrotron radiation beamtime. The author thanks for funding from the Initiative and Networking Fund of the Helmholtz Association.

REFERENCES

- [1] S. Bari, O. Gonzalez-Magaña, G. Reitsma, J. Werner, S. Schippers, R. Hoekstra, and T. Schlathölter, *J. Chem. Phys.* 134, 024314 (2011).
- [2] O. González-Magaña, M. Tiemens, G. Reitsma, L. Boschman, M. Door, S. Bari, P.O. Lahaie, J.R. Wagner, M.A. Huels, R. Hoekstra, and T. Schlathölter, *Phys. Rev. A* 87, 032702 (2013).

XUV INDUCED ULTRAFAST DYNAMICS IN BIO-RELEVANT MOLECULES

M. C. Castrovilli¹, D. Ayuso², A. Trabattoni³, S. De Camillis⁴, A. Palacios², P. Declava⁵, J. Greenwood⁴, F. Martín², M. Nisoli^{1,3} and F. Calegari¹

¹ *IFN-CNR, Piazza Leonardo da Vinci 32, I-20133 Milano, Italy*

² *Departamento de Química, Módulo 13. Universidad Autónoma de Madrid, 28049 Madrid, Spain*

³ *Dipartimento di Fisica, Politecnico di Milano, Piazza Leonardo da Vinci 32, I-20133 Milano, Italy*

⁴ *Centre for Plasma Physics, School of Maths and Physics, Queen's University Belfast, BT7 1NN, UK*

⁵ *Dipartimento di Scienze Chimiche e Farmaceutiche, Università di Trieste, 34127, and CNR-IOM, Trieste (Italy)*

It has already been known that many biological processes and chemical reactions within a single molecule are initiated by ultrafast electron transfer. Theoretical studies have pointed out that very efficient charge dynamics can be driven by purely electronic effects, which can evolve on a temporal scale ranging from few femtoseconds down to tens of attoseconds.

Our study shows a clear experimental measurement of charge migration in aromatic amino acids, after attosecond excitation.

Our technique consists of a two-color, pump-probe set-up in which charge dynamics are initiated by isolated sub-300 as pulses (of energies between 17 eV and 35 eV) and probed by 4-fs, waveform-controlled near infrared (NIR) pulses, with central wavelength of 720 nm.

A clean plume of neutral amino acids (phenylalanine and tryptophan) was generated by evaporation from a thin metallic foil heated by a CW diode laser. The ions produced by the interaction of the molecules with pump and probe pulses were then collected by a linear time-of-flight device for mass analysis.

The evolution of the dication yield of phenylalanine ($m/z = 60$) as a function of the delay between pump and probe shows oscillations at a periodicity of 4.3 fs, while the same fragment in the case of tryptophan shows a periodicity of 3.9 fs.

Theoretical calculations support and better explain the complexity of the charge dynamics triggered by the attosecond pulse, identifying the beating between the amine and the carboxylic groups as the responsible of the observed oscillation frequencies in the case of phenylalanine. These fast oscillations can only be assigned to pure electron dynamics, since nuclear dynamics usually comes into play on a longer temporal scale and constitute the first experimental measurements of charge migration in biologically relevant molecules.

THE NQS STATION (NANO-SIZE QUANTUM SYSTEM), AS PART OF THE SQS INSTRUMENT (SMALL-QUANTUM-SYSTEM) AT THE SASE3 BRANCH OF THE EUROPEAN XFEL

A. De Fanis, T. Baumann, M. Ilchen, T. Mazza, M. Meyer, Y. Ovcharenko
and H. Zhang

European XFEL, Hamburg, Germany

The European X-Ray Free-Electron-Laser (XFEL) in Hamburg, Germany, is currently under commissioning and is due to operate from early 2017 [1]. The facility will provide a X-ray wavelengths from below the C K-edge to 25keV. Of the three simultaneously operational SASE branches, the so-called SASE3 will deliver focused intense short FEL beam ($\leq 1\mu\text{m}$, 10^{14}Wcm^{-2} , 2-100fs) to the SQS instrument in the soft X-ray region 260-3200eV [2]. The SQS instrument consists of 2 end-stations in series: AQS (Atomic Quantum System), for electron spectroscopy of atoms and molecules in the gas- or vapour- phase, and NQS (Nano-Quantum System), for electron- and ion- spectroscopy and coherent imaging of rare-gas-clusters, metal-clusters, or targets of biological importance (also in liquid-phase). In the NQS instrument we foresee a VMI [3] spectrometer with multihit capabilities for electrons or ions, a conventional ion-time-of-flight spectrometer, a B-mass ion spectrometer [4], and an X-ray detector in the forward direction for coherent imaging experiment [5]. An optical fs laser is also present for time-resolved experiments in the fs domain. The spectrometers, detectors, and laser, can operate simultaneously, compatible with the time-structure of XFEL (max $\leq 4.5\text{MHz}$ rate, average $\leq 27\text{kHz}$). This talk will present the current status of the NQS instrument in the framework of the AQS station at the European XFEL.

REFERENCES

- [1] M. Altarelli et al. *Technical Design Report: European X-Ray Free-Electron Laser* (European XFEL website, July 2007)
- [2] T. Mazza, H. Zhang, and M. Meyer, *Technical Design Report, Scientific Instrument SQS-WP85* at the European XFEL (European XFEL website, December 2012)
- [3] A.T.J.P. Eppink and D.H. Parker, *Rev. Sci. Instr.* **68**(1997) 3477
- [4] M. Lezius *et al.* *Phys. Rev. Lett.* **80**(1998) 261
- [5] J. Sztuk-Dambietz *et al.* *Proc. SPIE* **8778**(2015) 87780U

UNUSUAL FRAGMENTATION MECHANISMS IN IONIZED BIOMOLECULES IN THE GAS PHASE

Sergio Díaz-Tendero^{1,2}

¹*Departamento de Química, Módulo 13, Universidad Autónoma de Madrid, 28049 Madrid, Spain*

²*Condensed Matter Physics Center (IFIMAC), Universidad Autónoma de Madrid, 28049 Madrid, Spain*

Radiation damage of biological tissues starts at the femtosecond timescale, where ionization processes lead to the production of numerous secondary particles (electrons, ions, radicals). An important research activity focuses on the understanding of these processes at the molecular level [1]. In this context, ion-biomolecule collisions have become a fundamental technique to study radiation damage at the physical stage [2,3]. The dynamics of multiply charged (excited) molecular cations could be finely probe using physical techniques giving insight into ultrafast chemical processes at the fs timescale [4-6]. We have recently implemented a strategy based on the combination of experimental and theoretical studies to successfully disentangle the complicated fragmentation dynamics of complex molecular systems after ionization and excitation in collisions with energetic multiply charged ions [7,8]. We obtain the experimental data in the gas phase for neutral molecules in collisions with low-energy highly charged ions. State-of-the-art multicoincidence detection mass spectrometry techniques are used to determine the charge state of the molecule before fragmentation. The experimental data are analyzed by means of quantum chemistry calculations (density functional theory and *ab-initio* molecular dynamics). In this communication we present our recent results obtained by applying this methodological approach to study the fragmentation dynamics of excited doubly charged amino acids in the gas phase [7,8].

REFERENCES

- [1] P. Swiderek, *Angew. Chem. Int. Ed.* **45** 4056 (2006).
- [2] E. Pittenauer and G. Allmaier, *Comb. Chem. High T. Scr.* **12** 137 (2009).
- [3] M.A. Baldwin, *Biol. Mass Spectrom.* **402** 3 (2005).
- [4] Y.H. Jiang et al., *Phys. Rev. Lett.* **105** 263002 (2010).
- [5] M. Madjet et al., *Phys. Rev. Lett.* **107** 263002 (2011).
- [6] R. Itakura et al., *J. Chem. Phys.* **127** 104306 (2007).
- [7] S. Maclot et al., *J. Phys. Chem. Lett.* **4** 3903 (2013).
- [8] D.G. Piekarski et al., *PhysChemChemPhys* **17** 16767 (2015).

LARGE MOLECULES BREAK-DANCING IN THE SPOT LIGHT

Ronnie Hoekstra

Quantum Interactions and Structural Dynamics, Zernike Institute for Advanced Materials, University of Groningen, 9747AG, Groningen, the Netherlands

We use isolated gas-phase (bio-)molecules to investigate molecular properties and interaction dynamics without environmental effects. The main goal is to unravel how the initial ultrafast dynamics started by external triggers such as energetic photons subsequently leads to changes in the properties of the system. The interactions are studied by means of action spectroscopy in an apparatus in which electrospray ionization is combined with RF techniques to prepare targets of tailored molecular systems for investigation with energetic photons and ions, see figure 1.

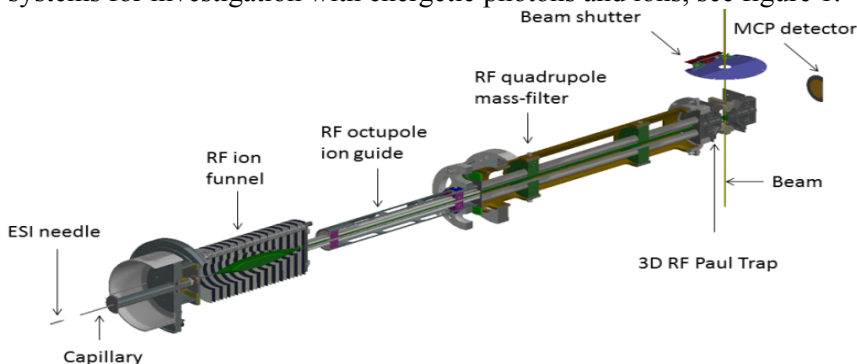


Figure 1. Schematics of the experimental apparatus.

On basis of a selection of experiments e.g. [1-4], in particular the following, closely linked topics will be addressed:

- i) fragmentation/ionization induced by soft-X-ray absorption,
- ii) the role of molecular mass/size and associated internal energies, and
- iii) simultaneous many-photon absorption processes in FEL pulses.

REFERENCES

- [1] O. Gonzalez Magaña et al., *J. Chem. Phys. A* 116, 053002 (2012)
- [2] O. Gonzalez Magaña et al., *Phys. Rev. A* 87, 032702 (2013)
- [3] G. Reitsma et al., *J. Chem. Phys.* 142, 024308 (2015)
- [4] T. Schlathölter et al., *Ang. Chem. Int. Ed.* in press (2016)

AUGER SPECTROSCOPY OF HNCO REVEALS DISSOCIATIVE PHOTOIONIZATION DYNAMICS IN THYMINE

F. Holzmeier^{1,2}, I. Fischer², S. Nandi¹, T. Wolf³ and M. Gühr^{3,4}

¹*Synchrotron SOLEIL, L'Orme des Merisiers Saint-Aubin, 91192 Gif-sur-Yvette, France*

²*University of Würzburg, Institute of Physical and Theoretical Chemistry, Am Hubland, 97074 Würzburg, Germany*

³*Stanford PULSE Institute, Menlo Park, California 94025, USA*

⁴*University of Potsdam, Institute of Physics and Astronomy, Campus Golm, 14476 Potsdam-Golm, Germany*

Markus Gühr and co-workers investigated the photoexcited dynamics of the DNA base thymine in a gas phase UV pump/soft X-ray probe experiment at the LCLS free electron laser [1]. When increasing the UV pump laser power, several new sharp lines were observed in the time resolved O 1s Auger spectrum setting in at a pump-probe delay of about 400 fs. This indicates a fragmentation of the DNA base to a smaller oxygen containing molecule with a low density of states by dissociative photoionization (DPI) when multiple UV photons are absorbed. Previous studies on the DPI of thymine [2,3] led to the assumption that isocyanic acid, HNCO, is formed. The steady-state Auger spectra at the oxygen, nitrogen, and carbon K-edge of isolated HNCO were therefore recorded for the first time at the PLEIADES soft X-ray beamline at Synchrotron SOLEIL. The highly-resolved spectra not only confirm the assumed dissociation process in thymine, but also help interpreting the observed dynamics in the LCLS experiment.

REFERENCES

- [1] B. K. McFarland *et al.*, Nat. Commun. 5, 4235 (2014).
- [2] H.-W. Jochims *et al.*, Chem. Phys. 314, 263-282 (2005).
- [3] R. Improta *et al.*, Int. J. Mass Spectrom. 201, 321-336 (2000).

SIZE SELECTIVE SPECTROSCOPY OF MOLECULAR CLUSTERS

Kuno Kooser^{1,2}, Dang Trinh Ha¹, Marta Tarkanovskaja^{1,2}, Eero Itälä¹,
Helena Levola¹ and Edwin Kukk¹

¹*Dept. of Physics and Astronomy, University of Turku, Turku, Finland*

²*Institute of Physics, University of Tartu, Tartu, Estonia*

Weak intermolecular interactions like $\text{CH}\cdots\text{X}$ ($\text{X}=\text{O}$, N , π) and peptide group $\text{O}=\text{C}-\text{N}-\text{H}$ are the most important binding motifs in biochemistry and have a vital stabilizing role in biological systems.

For example, pyrimidine (aromatic 6-membered heterocyclic with two N atoms in the ring), is a molecular skeletal building block of the nucleic acid bases cytosine, thymine and uracil. The other simple biomolecular building block acetamide ($\text{CH}_3-\text{CO}-\text{NH}_2$) is the only naturally occurring molecule (beside formamide) that contains a single peptide group ($\text{O}=\text{C}-\text{N}-\text{H}$) in its structure, which makes it one of the simplest molecular models for peptide bonds present as a repeat unit in proteins. Hence, acetamide is a useful model to study the hydrogen bonding (HB) between peptide groups, since it is capable of contributing to $\text{N}-\text{H}\cdots\text{O}=\text{C}$ and $\text{C}-\text{H}\cdots\text{O}=\text{C}$ types of intermolecular HB interactions.

Here we present the experimental results of partial ion yields of pyrimidine and acetamide clusters created by supersonic expansion source and studied by using vacuum ultraviolet radiation. The mechanism of formation of the protonated clusters and the photoinduced intermolecular dynamics (including the proton transfer processes) and the photofragmentation processes will be discussed. Geometry and the most stable arrangement of dimers will be analyzed.

More specifically, stacking and hydrogen-bonded interactions in pyrimidine dimers are investigated by using the second-order Møller-Plesset perturbational method (MP2) with the standard correlation consistent basis set aug-cc-pVDZ [1]. The calculations are performed by using the *ab initio* quantum chemistry code GAMESS [2].

Acknowledgements: The financial support by the Academy of Finland and Estonian Research Council (grants MJD428 and PUT735) is gratefully acknowledged.

REFERENCES

- [1] R. A. Kendall *et al* Chem. Phys. 96, 6796-6806 (1992).
- [2] M. W. Schmidt *et al*, J. Comput. Chem. 14, 1347 (1993).

ELECTRONIC STRUCTURE OF SMALL BIOLOGICALLY RELEVANT MOLECULES IN AQUEOUS SOLUTIONS STUDIED BY PHOTOELECTRON SPECTROSCOPY

Robert Seidel

*Helmholtz-Zentrum Berlin for Energy and Materials, Albert-Einstein-Strasse 15,
D-12489 Berlin, Germany*

Photoemission studies from liquid microjets were conducted to reveal the electronic structure of aqueous biologically relevant molecules. Valence photoelectron spectroscopy using soft X-rays is applied to determine the lowest ionization and electron detachment energies from several organic and inorganic molecules [1]. Two examples will be discussed in detail, the stabilization energy of phosphates of different charge states, and the lowest ionization energies of DNA [2], DNA bases, nucleosides and nucleotides [3]. All cases demonstrate the strong electronic-screening ability of liquid water which will be discussed. In addition to studying the ground-state electronic structure autoionization spectroscopies are applied to explore ultrafast charge and energy transfers in aqueous solutions. Relaxation processes involving simultaneous autoionization and proton transfer between adjacent molecules in aqueous systems, so-called proton transfer mediated charge separation (PTM-CS) process [4] will be reported. Within PTM-CS, molecular transients with a half-transferred proton are formed within a few femtoseconds after the core-level ionization event. Subsequent non-radiative decay of the highly non-equilibrium transients leads to a series of reactive species, and also providing routes for producing low-energy electrons. The non-local electronic decay processes are discussed for several small biologically relevant molecules which form hydrogen bonds with water: $\text{H}_2\text{O}(\text{aq})$, $\text{H}_2\text{O}_2(\text{aq})$, ammonia(aq), glycine (aq), and ammonium(aq).

Acknowledgements: This work is supported by the Deutsche Forschungsgemeinschaft (DFG), Research Unit FOR 1789.

REFERENCES

- [1] R. Seidel et al., *Annu. Rev. Phys. Chem.* 67, 13.1–13.23 (2016)
- [2] E. Pluharova et al., *J. Phys. Chem. Lett.* 4, 3766 (2013)
- [3] C. A. Schroeder et al., *J. Am. Chem. Soc.* 137, 201 (2015)
- [4] S. Thürmer et al., *Nat. Chem.* 5, 590 (2013)

FRAGMENTATION OF HALOTHANE MOLECULE BY SYNCHROTRON RADIATION

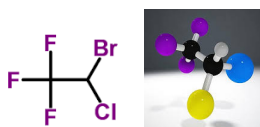
S. D. Tošić¹, P. Bolognesi², L. Avaldi², R. Richter³ and B. P. Marinković¹

¹ *Institute of Physics Belgrade, University of Belgrade, Pregrevica 118, 11080 Belgrade, Serbia*

² *CNR-Istituto di Struttura della Materia, Area della Ricerca di Roma1, Monterotondo Scalo, Italy*

³ *Elettra-Sincrotrone Trieste, Area Science Park, I-34012 Basovizza, Trieste, Italy*

Halothane (C₂HBrClF₃, 2-bromo-2-chloro-1,1,1-trifluoroethane) is one of the most extensively used halogenated anesthetics in medicine and the only one containing Br. It has a structure of a polyhalogenated organic molecule where the two carbon atoms experience very different chemical environments due to the bonding to different halogen atoms.



The fragmentation of C₂HBrClF₃ by high energy photons and electron beams has been studied by De Souza et al. [1], while recently, Ferreira da Silva et al. [2] investigated theoretically and experimentally the VUV photoabsorption spectrum. Maljković et al. [3] reported the differential cross sections for elastic electron scattering by halothane at 100 eV in a combined experimental and theoretical work. Here we present the results of the photofragmentation study of the halothane molecule obtained at Gas phase beamline of Elettra. NEXAFS as well as mass spectra were measured at different photon energies across C 1s, Cl 2p, Cl 2s, Br 3d, Br 3p, Br 3s and F 1s ionization edges.

Acknowledgements: This work is supported by Ministry of Education, Science and Technological Development of Republic of Serbia (Project No. OI 171020) and by the Serbia – Italy Joint Research Project “A nanoview of radiation-biomatter interaction”.

REFERENCES

- [1] G. G. B. de Souza et al. *Quim. Nova*, 24 (3), 311 (2001).
- [2] F. Ferreira da Silva et al. *J. Phys. Chem. A* 119, 8503 (2015).
- [3] J. Maljković et al. *Publ. Astron. Obs. Belgrade* No. 89, 33, (2010).

**The 4th International Workshop
on Non-Equilibrium Processes
(NonEqProc)**

Molecular excitations by electron-impact in non-equilibrium aerospace and fusion plasmas

Roberto Celiberto^{1,2} and Vincenzo Laporta²

¹*Dipartimento di Ingegneria Civile, Ambientale, Edile, del Territorio e di Chimica, Politecnico di Bari, Bari, Italy*

²*Istituto di Nanotecnologia - CNR, Bari, Italy*

A non-equilibrium plasma, in planetary explorations, can be generated by the interactions of the atmospheric gas with the protecting shield of space shuttles during their immersion in the atmosphere of a planet. The kinetic energy of the vehicles is then released by friction to the planet atmosphere so that excitation and ionization of molecular species take place. In this conditions, electron-impact processes, involving vibrationally excited molecules, play a role of great importance in redistributing the energy inside the plasma. Similar situation occur also in the peripheral regions of fusion devices (divertor and edge plasmas), where the relatively low temperatures allow for the formation of molecular species. The knowledge of electron-molecule collision cross sections, became then a basic information in the study of aerospace and fusion plasmas. A theoretical electron-molecule cross section database, for aerospace and fusion applications, will be presented at the Workshop. An example is shown in Fig. 1.

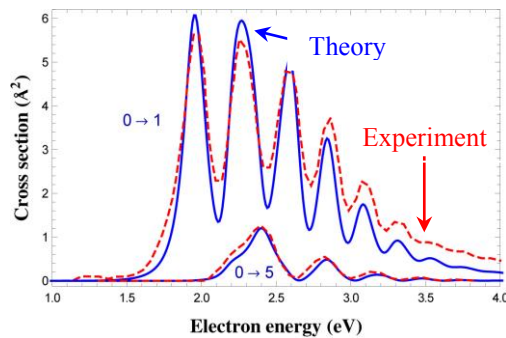


Figure 1. Comparison of theoretical and experimental electron-N₂ cross sections for 0→1 and 0→5 resonant vibrational excitation [1].

REFERENCES

- [1] R. Celiberto et al, Plasma Sources Sci. Technol. **25** (2016) 033004.

MODELLING LOW ENERGY PARTICLE TRACKS IN BIOLOGICALLY RELEVANT MEDIA

L. Ellis-Gibblings¹, K. Krupa¹, A. Traore¹, A Verkhovtsev^{1,2} and G. Garcia^{1,3}

¹*Instituto de Física Fundamental Consejo Superior de Investigaciones Científicas (IFF-CSIC), Madrid, Spain*

²*MBN Research Center, Altenhöferallee 3, 60438 Frankfurt am Main, Germany*

³*Centre for Medical Radiation Physics, University of Wollongong, NSW, Australia*

Photon and ion radiotherapy and positron emission tomography rely heavily on particle track simulation to ascertain the interaction/imaging region and the effects of treatment. Low energy species - secondary electrons, positrons, ions and radicals - are known to contribute much of the radiotherapy damage to cells, and the transport and annihilation dynamics of positrons impact sensitive tissue imaging [1]. Ongoing international collaborations contribute to accurate simulations of these particles in LEPTS - a monte carlo code simulating 10keV - 0eV electron and positron tracks from various sources [2]. Thus the locations of all energy depositions can be extracted, crucial at the radiation field edge, where there is a non-equilibrium of energy deposited within adjacent small volumes. We present an overview of the simulation, describe the techniques required and being developed to produce the input data, and update the community on advances in this model of low energy particle tracks aimed at clinical improvements.

Acknowledgements: Madrid: F. Blanco, A. Muñoz, M. Fuss; Lisbon (UNL): P. Limão-Vieira, F. Ferreira, D. Almeida; Flinders University (Adelaide): M. Brunger; ANU (Canberra): S. Buckman, J. Sullivan, R. McEachran; J. Cook University (Townsville): R. White; IOP (Belgrade): Z. Petrovic; Open University (UK): J. Gorfinkiel; Sherbrooke University: L. Sanche. The speaker is funded by the European Union's Seventh Framework Programme FP7/2007- 2013/ under REA – Grant Agreement n°608163”

REFERENCES

- [1] E. Alizadeh, T. Orlando, L. Sanche, *Ann. Rev. Phys. Chem.* **66**, 379-398 (2015)
- [2] M. Fuss *et al*, *J. App. Phys* 117, 21, (2015)

MODELLING HETEROGENEOUS REACTIONS OF OXYGEN-CONTAINING PLASMAS ON SILICA SURFACES

Vasco Guerra¹, Carlos Teixeira¹ and Daniil Marinov²

¹*Instituto de Plasmas e Fusão Nuclear, Instituto Superior Técnico,
Universidade de Lisboa, 1049-001 Lisboa, Portugal*

²*Laboratoire de Physique des Plasmas (CNRS, UPMC, UPSud)
Ecole Polytechnique, Route de Saclay 91128 Palaiseau, France*

This work presents and discusses models of surface recombination and molecule formation on silica surfaces, for oxygen-containing plasmas. The systems under study comprise O recombination forming O₂ and O₃, as well as NO₂ and CO₂ formation on the surface. A mesoscopic approach is adopted and two different approaches are explored: *i*) a deterministic description (DD), where the time-evolution of the adsorbed species and adsorption sites is ruled by a system of reaction-rate differential equations associated with the different elementary processes taken into account [1]; *ii*) a stochastic Monte Carlo approach, usually denoted by Dynamic or Kinetic Monte Carlo (KMC), where the time evolution of the system is made without dealing with the master equation directly, by following the evolution of one element of the statistical ensemble. The bases of KMC methods for surface kinetics have been recently reviewed in [2,3]. The KMC simulations are used to validate and examine the approximations made in the usual DD models, in particular in what concerns the treatment of diffusion of physisorbed atoms and Langmuir-Hinshelwood recombination.

Acknowledgements: This work was partially supported by the Portuguese FCT, under Projects UID/FIS/50010/2013, PTDC/FIS-PLA/1420/2014 and grant PD/BD/105884/2014 (PD-F APPLAuSE).

REFERENCES

- [1] V. Guerra, IEEE Trans. Plasma Sci. 35, 1397 (2007)
- [2] H. M. Cuppen, L. J. Karssemeijer and T. Lamberts, Chem. Rev. 113, 8840 (2013)
- [3] V. Guerra and D. Marinov, Plasma Sources Sci. Technol. 25, 045001 (2016)

TUNING THE AFTERGLOW PLASMA COMPOSITION IN AR/N₂/O₂ MIXTURES: CHARACTERISTICS AND APPLICATIONS OF A FLOWING SURFACE-WAVE MICROWAVE DISCHARGE SYSTEM

Kinga Kutasi¹, Cédric Noel², Thierry Belmonte² and Vasco Guerra³

¹*Wigner Research Centre for Physics of HAS, Budapest, Hungary*

²*Universite de Lorraine, Institut Jean Lamour, NANCY, France*

³*Instituto de Plasmas e Fusao Nuclear, IST, Universidade de Lisboa, Portugal*

In order to achieve efficient treatment of different surfaces two main requirements need to be satisfied: (i) the controlled production of active species and (ii) their transport to the surface to be treated. In a flowing afterglow system based on a low pressure surface-wave microwave discharge, there are several parameters that can influence the discharge conditions, and thus the production of the active species, namely: (i) the efficiency of the pumping system used and the capacitance of the afterglow system, (ii) the gas flow rate, (iii) the position of the microwave coupler (surfatron) along the discharge tube, (iv) the length of the discharge tube, and consequently, of the early-afterglow region, and (v) the gas mixture. Understanding the effect of these parameters and their proper setting, with the help of model calculations, give the possibility to produce the plasma composition required in the treatment reactor. In our presentation we are going to discuss the tuning possibilities of the afterglow plasma composition in binary and ternary mixtures by clarifying the characteristics of a flowing surface-wave microwave discharge system [1].

Acknowledgements: This work is supported by NKFIH – K – 104531.

REFERENCES

- [1] Kutasi K, Noel C, Belmonte T, Guerra V: Tuning the afterglow plasma composition in Ar/N₂/O₂ mixtures: characteristics of a flowing surface-wave microwave discharge system *Plasma Sources Sci. Technol.* 2016

NEW TRENDS IN LOW ENERGY ION IMPLANTATION

Svetlana Radovanov

*Applied Materials, TIG Group, Varian Semiconductor
35 Dory Road, Gloucester, Massachusetts, 02130, USA*

The main application for particle accelerators has been semiconductor ion implantation. Over the years ion implanters have become highly sophisticated tools incorporating the use of energy filters, collimators, quadrupoles, scanning systems and more recently molecular plasma sources, cryogenic and elevated implant temperature capabilities. One of the features that made these tools so successful in device fabrication is the high degree of control of the dopant depth profile. By selecting a unique ion mass, ion charge, ion energy and implant angle, a beam line tool offers highly automated control over the ion beam transport and implanted ion dose [1]. These beam lines operate with a large variety of species, four orders of magnitude energy range and five orders of magnitude of dose range. In recent years, some very high dose applications have been enabled by plasma doping systems [2]. For example, some dynamic random access memory applications require incredibly high doses $\sim 5 \times 10^{16}$ /cm² that can only be done by plasma doping. Unlike the other tools mentioned, ions are not mass analyzed, but instead the wafer is processed within the plasma chamber. The wafer is pulsed negatively by a bias supply with a square wave $T \sim 50 \mu\text{s}$ and $f \sim 5$ kHz. Implant energy is controlled by the bias voltage which can exceed 10 kV. The plasma is generated by an inductively coupled rf coil. When the bias voltage is on, a plasma sheath forms in front of the wafer surface, across which ions are accelerated and are implanted into the silicon.

In this paper we will discuss the beam line architecture and modeling associated with it. We also describe the fluid models that are used to model inductively coupled plasma source. The author acknowledges Dr Shahid Rauf for developing the fluid plasma - CRTRS code.

REFERENCES

- [1] A. Renau, Review Scientific Instruments, 81, 02B907 (2010)
- [2] J. England and W. Moller, Nucl. Inst. Methods, 365, 105 (2015)

HEAVY-PARTICLE PROCESSES IN LOW-PRESSURE WATER VAPOUR DISCHARGE

N. Škoro¹, D. Marić¹, V. Stojanović¹, J. Sivoš¹, G. Malović¹ and Z. Lj. Petrović^{1,2}

¹*Institute of Physics, University of Belgrade, Pregrevica 118, 11000 Belgrade, Serbia*

²*Serbian Academy of Sciences and Arts, Knez Mihailova 35, 11000 Belgrade, Serbia*

e-mail: nskoro@ipb.ac.rs

We present results of investigation of basic processes taking part in low-current water vapour discharges. Extensive experimental investigation of breakdown properties, spectrum and spatial emission profiles in low-pressure water vapour discharges yielded complete sets of data for different operating regimes [1,2]. Experimental data obtained for Townsend regime was used for comparison with the data obtained from our Monte Carlo simulation which includes both reactions with electrons and heavy particles [3]. Therefore, quantitative description of basic processes, particularly heavy-particle processes [4], governing water vapour discharges at low currents were attained. Moreover, the effective emission cross section from processes between heavy particles is acquired.

Acknowledgements: This work is supported by the Serbian Ministry of Education, Science and Technological Development under project numbers ON 171037 and III 41011.

REFERENCES

- [1] N. Škoro, D. Marić, G. Malović, W. G. Graham and Z. Lj. Petrović, *Phys.Rev. E*, 84, 055401 (R) (2011).
- [2] J. Sivoš, N. Škoro, D. Marić, G. Malović and Z. Lj. Petrović, *J. Phys. D: Appl. Phys.*, 48, 424011 (2015).
- [3] V. Stojanović, B. Jelenković and Z. Lj. Petrović, *J. Appl. Phys.*, 81, 1601-1603 (1997).
- [4] D. Marić, P. Hartmann, G. Malović, Z. Donko and Z. Lj. Petrović, *J. Phys. D: Appl. Phys.*, 36, 2639–2648 (2003).

DENPOH-NANBU THEORY IN MODELLING LOW PRESSURE DISCHARGES

Vladimir Stojanović

Institute of Physics Belgrade, University of Belgrade, 11001 Belgrade, Serbia

Analysis of transport of charged particles is an essential element in modelling collisional non-equilibrium plasmas. The transport data may be used directly in fluid and hybrid codes as well as in a process of normalization of cross sections. An important aspect of plasma models is that transport data are based on complete sets of cross sections. In principle, only complete cross section sets should be used for modelling since only they represent proper reference needed for comparison with others results. Modelling results are then always more realistic. The data for transport and cross sections of ions are needed since as electrons they may have a wide range of energies, thus affecting modeling of electric field profiles.

In this work we review cross section sets for ion scattering appropriate for modeling in low pressure discharges. Basic data for presented cross section sets are produced by Denpoh-Nanbu theory (DNT) [1] which is found appropriate for collision energies where interaction potential is close to induced dipole potential. DNT is developed to study various plasmas involving CF_4 and its mixtures. Basic outputs of DNT are momentum transfer elastic scattering cross section and range of reactive cross sections. They can be additionally modified according to available experimental and/or more precise theoretical data in normalization procedure where transport coefficients are calculated and in turn has to agree with experimental transport coefficients. In such a way cross section sets are validated by available experimental data for transport coefficients. Measurements such as for example spatially resolved emission in Townsend discharge are also found useful in spite of the fact that information hidden in excitation coefficients is partly obtained in non-equilibrium conditions. In this work we will present the cross section sets for ions in molecular gases possessing both negligible dipole moment (CF_4 , BF_3) and significant dipole moment such as for example water vapor.

Acknowledgements: This work is partly supported by Ministry of Education, Science and Technology of Republic Serbia projects ON171037 and III410011. Author acknowledge to Prof. Z. Lj. Petrović for valuable suggestions.

REFERENCES

- [1] K. Denpoh and K. Nanbu, J. Vac. Sci. Technol. A, 16 (1998) 1201.

A GENERALISED BOLTZMANN EQUATION FOR NON-EQUILIBRIUM CHARGED PARTICLE TRANSPORT VIA LOCALISED AND DELOCALISED STATES

Peter W. Stokes, Bronson Philippa, Daniel Cocks and Ronald D. White

*College of Science and Engineering, James Cook University, Townsville, QLD,
4811, Australia*

Non-equilibrium electron transport in certain liquids and dense gases can be influenced through electrons becoming trapped in (localised) bubble states, giving rise to dispersive electronic transport in liquid neon [1]. Similar trapping processes occur for positronium in bubbles [2] and positron annihilation on induced clusters [3]. We present a general phase-space kinetic model [4] for charged particle transport through combined localised and delocalised states, capable of describing scattering collisions, trapping, detrapping and losses. Generalisations of standard results for dilute gaseous systems are found, including the Wannier energy relation and the Einstein relations. Trapping and detrapping processes are shown to induce particle heating and cooling, as well negative differential conductivity. Fractional transport is observed for particle trapping time distributions with heavy tails, and fractional equivalents of the above relations have been found.

Acknowledgements: The authors gratefully acknowledge the useful discussions with Prof. Robert Robson, and the financial support of the Australian Research Council.

REFERENCES

- [1] Y. Sakai, W. F. Schmidt, and A. Khrapak, *Chemical Physics* 164, 139 (1992).
- [2] S. V. Stepanov, V. M. Byakov, D. S. Zvezhinskiy, G. Duplâtre, R. R. Nurmukhametov, and P. S. Stepanov, *Advances in Physical Chemistry* 2012, 1 (2012).
- [3] M. G. Colucci, D. P. van der Werf, and M. Charlton, *Journal of Physics B: Atomic, Molecular and Optical Physics* 44, 175204 (2011).
- [4] P. W. Stokes, B. Philippa, D. Cocks, and R. D. White, *Phys. Rev. E* 93, 032119 (2016).

A POSITRON REACTION MICROSCOPE

J. P. Sullivan

*Plasma Research Laboratories, Research School of Physics and Engineering,
Australian National University, Canberra, Australia*

Reaction microscope technology has made available a wealth of detailed and sensitive data for the testing of a fundamental understanding of collision processes, in particular ionisation through electron, photon or ion impact [1]. However, constraints in the availability and intensity of suitable sources mean that there have been no applications of this technique to positron scattering processes. Positrons are expected to display significantly different effects in low energy ionising collisions, in particular due to the presence of the positronium formation channel, an alternative ionisation pathway not found in electron scattering, for instance.

This talk will discuss work undertaken as a collaboration between the Australian National University, MPI Kernphysik and University of North Texas to develop a positron reaction microscope. The experiment is located at the ANU, as part of the atomic and molecular physics program at the Australian Positron Beamline Facility. The experimental parameters and operation will be described, along with preliminary results for positron ionisation of argon atoms. Future directions for this experimental program will also be outlined.

Acknowledgements: This work is supported by the Australian Research Council.

REFERENCES

[1] J. Ullrich, et al., *Rep. Prog. Phys.* **66**, 1463 (2003)

ATOMIC COLLISION PROCESSES IN HOT, DENSE PLASMAS

J. G. Wang¹, L. Liu¹, Y. Wu¹, S. B. Zhang² and R. K. Janev³

¹*Institute of Applied Physics and Computational Mathematics, P. O. Box 8009,
Beijing 100088, P. R. China*

²*School of Physics and Information Technology, Shanxi Normal University,
Xi'an 710062, P. R. China*

³*Macedonian Academy of Sciences and Arts, P. O. Box 428, 1000 Skopje,
Macedonia*

Hot, dense plasmas exhibit screened Coulomb interactions, resulting from the collective effects of correlated many-particle interactions. The screened interactions can alter the atomic structures and dynamics, and display some new physical phenomena. In this report, we review our recent works on the atomic collision processes in hot, dense plasma, including the photon excitation and ionization, electron impact excitation and ionization, and excitation, ionization and charge transfer of ion-atom scattering.

SINGLE-PARTICLE COUNTING: APPLICATIONS IN ATOMIC AND MOLECULAR PHYSICS

Achim Czasch

*Roentdek Handels GmbH, Im Vogelshaag 8,
D-65779 Kelkheim c/o IKF, University Frankfurt, Germany*

Position sensitive microchannel-plate (MCP) based particle/photon counting detectors are a pre-requisite for a number of applications in atomic/molecular physics and surface science fields. A private-public partnership between the University of Frankfurt and RoentDek GmbH collaborates already for 25 years on the development of such single-particle counting detectors and adequate read-out electronics for delay-line anode technique. Advances in digital electronics development and MCP manufacturing have eventually allowed for maturing of the same. Modular “Reaction microscopes” (COLTRIMS) are now readily available and can be tailored to complete electron/ion coincidence spectrometer setups for various applications. Ongoing detector developments shall increase the number of simultaneous detected particles and increase detection efficiency

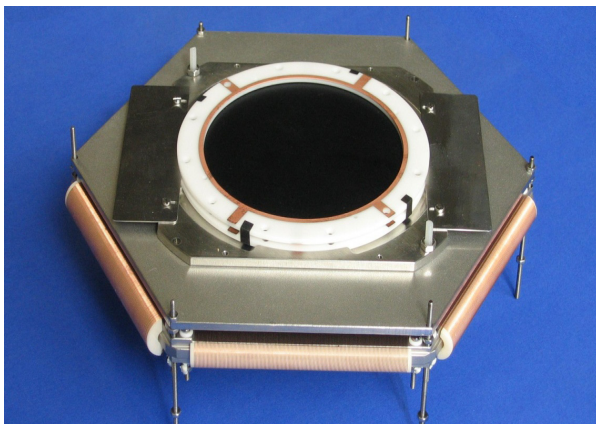


Figure 1. MCP delay-line for coincident space and time resolved detection of multiple particles per ionization event

REFERENCES

- [1] <http://Roentdek.com>

Author Index

AUTHOR INDEX

A

Abdurakhmanov I. B. 3
Adoui L. 7
Afanasiev V. L. 429
Akbari Kamran 186
Alizadeh Elahe 11
Alves Luís L. 100
Annaloro Julien 280
Aoneas M. M. 92, 96
Aparicio J. A. 224
Atmaca Umran 51
Avaldi L. 447
Avaldi Lorenzo 4
Ayadi Viktor 12
Ayuso D. 440
Azechi Hiroshi 371

B

Baiwen Li 136
Bajčetić J. 417
Bajčetić Jovan 385
Baksht E. Kh. 190
Bari Sadia 439
Baumann T. 441
Belmonte M. T. 224, 236, 264
Belmonte Thierry 454
Berger B. 216
Berndt Johannes 272
Berton M. 373
Bolognesi P. 447
Borka D. 150, 389, 393
Borka Jovanović V. 150, 389, 393
Bošnjaković D. 104, 108, 284, 336
Boubert Pascal 203
Božanić D. K. 166
Brablec A. 228
Brandenburg Ronny 209

Bravo J. A. 360
Bray A. W. 3
Bray I. 3
Bruggeman Peter J. 204
Bukvić S. 268
Bultel Arnaud 280, 308
Bunjac A. 16, 20
Burakov V. 178
Burgdörfer J. 139
Burger M. 268
Burger Miloš 141, 194
Busetto G. 373

C

Čadež V. M. 378, 417
Calegari F. 440
Calzada M. D. 360
Calzada María Dolores 352
Capes H. 208
Capozziello S. 393
Castrovilli M. C. 440
Čavić Milena 364
Čech J. 256
Cederquist H. 7
Celiberto R. 24
Celiberto Roberto 451
Céolin D. 6
Cheng Ning 136
Chunyang Zheng 136
Ciganović Jovan 348
Ciroi S. 373
Cocks Daniel 458
Congiu E. 373
Cracco V. 373
Cullen Patrick J. 260
Cvetanović N. 220, 228, 240
Czasch Achim 463

D

Daksha M. 216
Damany X. 219
De Camillis S. 440
De Fanis A. 441
de Oliveira N. 211
Decleva P. 440
Delaunay R. 7
Denifl Stephan 10
Derzsi A. 216
Despoja V. 154
Despoja Vito 137
Díaz-Tendero Sergio 442
Dimitrijević M. S. 397, 413
Dimitrijević Milan S. 433
Djeniže Stevan 194
Djordjević T. 154
Djulaković A. 421
Djurović S. 224, 232, 236, 252, 264
Djurovic Stevica 308
Dogan Mevlut 55
Dojčilović R. J. 162, 166, 174
Domaracka A. 7
Dombi Péter 12
Donko Z. 216
Dozias S. 219
DuBois R. D. 158
Dujko S. 104, 108, 120, 124, 284,
336
Dvořák P. 220

E

Ellis-Gibbins L. 340, 452
Erkapić S. 397
Erofeev M. V. 142, 190

F

Fabrikant I. I. 3
Fárník M. 144
Favia Pietro 205
Fedor J. 144
Ferreira da Silva F. 340
Ficker O. 380
Filipović Nikola 28

Fischer I. 444
Földi Péter 12
Frezcato M. 373
Fritzsche S. 32
Fursa D. V. 3

G

Gajo T. 232, 252
Gajo Teodora 217
Galmiz O. 228
Gans B. 211
Garcia G. 340, 452
Gatchell M. 7
Gavanski L. 224, 236, 252, 264
Gavanski Lazar 308
Gavrilović M. R. 218
Giglio E. 158
Gilić M. 112
Giuliani Alexandre 9
Gligorijević Nevenka 364
Gocić S. 356
Godbert-Mouret L. 208
Goosmann R. 429
Goosmann René W. 372
Gorjanc Marija 213
Greenwood J. 440
Grofulović Marija 100
Grygoryeva K. 144
Guaitella O. 222, 244
Guerra V. 215
Guerra Vasco 100, 453, 454
Gühr M. 444

H

Han X. 344
Han Xu 143
Hannachi I. 208
Hao Liang 376
Havlicek J. 380
He X. T. 384
Hickson K. 211
Himics László 148
Hoekstra Ronnie 443
Holzer Georg Alexander 10
Holzmeier F. 444

Hori Masaru 206
Hu Xiaoyan 376
Huber B. A. 7
Hussain Shahzad 272
Huth Michael 147

I

Ignjatović Lj. M. 397, 413, 425
Ilchen M. 441
Ilić D. 429
Imrisek M. 380
Iséni S. 219
Itälä Eero 445
Ito K. 211
Ivanović N. V. 288
Ivković M. 232, 276
Ivković S. S. 240

J

Jahnke Till 5
Jakimovski D. 67, 71
Janev R. K. 24, 59, 67, 71, 75, 87,
460
Janik Ireneusz 143
Janković Radmila 364
Jevremović D. 397
Josepson R. 220
Jovanović A. P. 292, 304, 320, 324
Jovanović Gordana 401, 405
Jovanović J. 128
Jovanović Jasmina 272
Jovanović P. 389, 393
Joyeux, D. 211

K

Kadyrov A. S. 3
Kapaldo J. 344
Kapaldo James 143
Karbunar L. 154
Kisić Danilo 145
Klas M. 296, 300
Klink Rouven 209
Kobilarov R. 252

Kočišek J. 144
Kolarski A. 417
Kolarž P. 417
Konjević N. 232, 276, 288
Koós Margit 148
Kooser Kuno 445
Kopyra Janina 39
Korolov I. 216
Koubiti M. 208
Kovačević Dojčinović Jelena 409
Kovačević Eva 272
Kovačević V. 219
Kovačević V. V. 244
Krstić I. 219
Krstić I. B. 244
Krupa K. 340, 452
Kucska N. P. 36
Kukk Edwin 445
Kuraica M. 219
Kuraica M. M. 240, 244
Kutasi Kinga 454
Kuzmanović Miroslav 348

L

La Mura G. 373
Laporta V. 24
Laporta Vincenzo 451
Lemell C. 139, 150
Lemell Christoph 138
Lengyel J. 144
Levola Helena 445
Li Bin 376
Li Jinghong 374
Lihua Cao 136
Limao-Vieira P. 340
Lin X. H. 87
Liu C. H. 75
Liu L. 75, 87, 460
Liu Z. J. 384
Liu Zhanjun 376
Logeais C. 208
Loison J. C. 211
Luque A. 284
Lyratzi E. 375

M

Macias-Montero M. 214
Maciejewska Paulina 39
Majkić M. D. 162, 166, 174
Majstorović G. Lj. 332
Maletić Dejan 248
Maljković Jelena 39
Malović G. 456
Malović Gordana 248, 316, 328,
364
Mančev Ivan 79, 83
Mar S. 224
Marandet Y. 208
Marić D. 128, 356, 456
Marić Dragana 312, 316, 328
Marin F. 429
Marinković B. P. 447
Marinov Daniil 453
Mariotti D. 214
Marković V. Lj. 292, 304, 320, 324
Martín F. 440
Matejčik Š. 296, 300
Matejčik Štefan 10
Matijević Milica 348
Mazza T. 441
Meichsner J. 207
Meireni M. 208
Melero C. 360
Melero Cristóbal 352
Meyer M. 441
Mihajlov A. A. 397, 413, 425
Mijatović Z. 232, 252
Mijatovic Zoran 308
Mika A. 7
Milić Ivan 377
Milojević Nenad 79, 83
Milosavljević Aleksandar R. 9
Milosavljević Vladimir 194
Milosavljević Vladimir M. 260
Milošević M. Z. 43, 47
Milovanović N. 397
Mirić J. 104, 108
Mirković M. A. 174
Mišković Z. L. 154
Mišković Zoran L. 137, 186
Mitrović S. T. 417

Mladenović Ž. 356
Mlynar J. 380
Momčilović Miloš 348
Morávek T. 256
Moravský L. 296, 300
Morel Vincent 308
Mukoyama T. 36
Muñoz J. 360
Muñoz José 352

N

Nagy G. U. L. 170
Nahon L. 211
Nandi S. 444
Navrátil Z. 220, 256
Nedeljković N. N. 162, 166, 174
Nedelko M. 178
Nemschokmichal S. 207
Nenadović Miloš 145
Nevar A. 178
Nguyen Y. N. 222
Nikitović Ž. 112, 116
Nikolić Zoran 194
Nina A. 378, 417, 421
Nina Aleksandra 385
Nisoli M. 440
Noel Cédric 454
Noterdaeme J.-M. 380
Nur Ozer Zehra 51, 55

O

Obradović B. 220
Obradović B. M. 240, 244
Obrusník A. 222
Oller J. C. 340
Ovcharenko Y. 441

P

Palacios A. 440
Panajotović Radmila 182
Panek R. 380
Pantić Dragan 194
Pattyn Cedric 272
Pavlović Sanja S. 260

Pavlović Vladan 28
Peláez R. J. 224
Peshkov A. A. 32
Petrović M. 112
Petrović Z. Lj. 104, 108, 120, 124,
128, 336, 356, 456
Petrović Zoran 328
Petrović Zoran Lj. 248, 312, 316,
364
Philippa Bronson 458
Pintassilgo C. D. 215
Poparić G. B. 63, 92, 96
Poparić Goran 194
Poparić Goran B. 260
Popović D. B. 16, 20
Popović L. Č. 378, 417, 421, 429
Popović Luka Č. 409
Popović M. P. 63
Pouvesle J.-M. 219
Ptasinska S. 344
Ptasinska Sylwia 11, 143
Puač Nevena 248, 364
Pysanenko A. 144

Q

Qi Y. Y. 59

R

Radjenović B. 296, 300
Radmilović-Radjenović M. 296,
300
Radovanov Svetlana 455
Radović I. 154
Radović Ivan 137
Radulović Siniša 364
Rafanelli P. 373
Ráhel' J. 256
Raičević Dušan 385
Rajta I. 170
Rakočević Zlatko 145
Ranković Miloš Lj. 9
Raspopović Z. 112, 116
Rawlins C. M. 3
Ribar Anita 10
Richter R. 447

Ripenko V. S. 142, 190
Ristić M. M. 63, 92, 96
Ristić Zoran 146
Robert E. 219
Roncin Philippe 135
Rosato J. 208, 221
Rousseau P. 7
Ryszka Michal 11

S

Sachser Roland 147
Sakan N. M. 425
Sarani Abdollah 209
Savage J. S. 3
Savić D. 429
Savić I. 232, 236, 252, 264
Savić Marija 312
Savović Jelena 348
Schiorlin Milko 209
Schulze J. 216
Seidel Robert 446
Seipt D. 32
Selaković Nenad 364
Shulepov M. A. 142, 190
Simić S. 421
Simić Z. 413
Simić Zoran 433
Simonović I. 104, 108, 120, 124
Simonović N. S. 16, 20, 43, 47
Šišović N. M. 288, 332
Sivoš J. 456
Sivoš Jelena 316, 328
Skočić M. 268
Škoro N. 456
Škoro Nikola 316, 328
Slikboer E. T. 222
Sobota A. 222, 244
Song Yuan-Hong 149
Spasojević Dj. 288
Srećković V. A. 378, 397, 413, 421,
425
Srećković Vladimir 433
Sretenović G. 219, 222
Sretenović G. B. 244
Sretenović Goran B. 223

Stamenković S. N. 292, 304, 320,
324
Stamm R. 208
Stankov B. 276
Stankov M. N. 292, 304, 320, 324
Stefanović Ilija 272
Stevanović Ljiljana 28
Stockett M. H. 7
Stoiljković Milovan 348
Stojanović V. 112, 116, 128, 456
Stojanović Vladimir 272, 328, 457
Stokes Peter W. 458
Štrbac Svetlana 145
Sullivan J. P. 8, 459
Surzhykov A. 32

T

Tarasenko N. 178
Tarasenko N. 178
Tarasenko V. F. 142, 190
Tarkanovskaja Marta 445
Teixeira Carlos 453
Tőkési K. 36, 150, 158, 170
Tőkési Károly 12, 139
Tošić S. D. 447
Tóth Sára 148
Trabattoni A. 440
Traore A. 340, 452
Trinh Ha Dang 445
Tschiersch R. 207

V

Vasiljević M. M. 332
Velusamy T. 214

Verkhovtsev A. 452
Vinic M. 276
Vlainic M. 380
Vojnović M. M. 63, 92, 96
Vranić Marija 379
Vujčić V. 397
Vujin Jasna 182

W

Wadehra J. M. 24
Wang J. G. 59, 75, 87, 460
Wang You-Nian 149
Wegner T. 207
Weinzettl V. 380
White R. D. 120, 124
White Ronald D. 458
Wolf T. 444
Wu Y. 87, 460

X

Xiang Jiang 376
Xiao C. Z. 384

Z

Zammit M. C. 3
Zettergren H. 7
Zhang H. 441
Zhang S. B. 460
Zhang Ying-Ying 149
Zheng C. Y. 384
Zheng Chunyang 376

CIP - Каталогизација у публикацији
Народна библиотека Србије, Београд

537.56(082)

539.186.2(082)

539.121.7(082)

533.9(082)

SUMMER School and International Symposium on the Physics of Ionized Gases
(28 ; 2016 ; Beograd)

Contributed Papers & Abstracts of Invited Lectures, Topical Invited Lectures, Progress Reports and Workshop Lectures / 28th Summer School and International Symposium on the Physics of Ionized Gases - SPIG 2016, [August 29 - September 2], 2016, Belgrade ; editors Dragana Marić ... [et al.]. - Belgrade : University of Belgrade, Faculty of Physics, 2016 (Beograd : Skripta Internacional). - 474 str. : ilustr. ; 24 cm

Tiraž 200. - Str. 5: Preface / editors Dragana Marić ... [et al.]. -
Napomene i bibliografske reference uz tekst. - Bibliografija uz svaki rad.
- Registar.

ISBN 978-86-84539-14-6

1. Marić, Dragana, 1973- [уредник] [аутор додатног текста]

а) Јонизовани гасови - Зборници б) Атоми - Интеракција - Зборници

с) Плазма - Зборници

COBISS.SR-ID 225356044

